



Universität Hamburg  
DER FORSCHUNG | DER LEHRE | DER BILDUNG

# Electron correlations and unconventional superconductivity in realistic solid-state materials and heterostructures

Dissertation  
zur Erlangung des Doktorgrades  
an der Fakultät für Mathematik, Informatik und Naturwissenschaften  
Fachbereich Physik  
der Universität Hamburg

vorgelegt von  
**Niklas Witt**

Hamburg  
2024

Copyright © 2024/2025 by Niklas Witt.

Typeset with  $\text{\LaTeX} 2_{\epsilon}$  in Palatino (Linotype) and Noto Sans.

An electronic version of this dissertation is available at

<https://ediss.sub.uni-hamburg.de/>

The use of color to emphasize hyperlinks has been omitted in the print version of this dissertation.

Original content of this thesis is released under a [Creative Commons](#) “[Attribution 4.0 International](#)” (CC BY 4.0) License. Third-party content is excluded and marked with its respective permissions.



Gutachter der Dissertation:

Prof. Dr. Tim O. Wehling  
Prof. Dr. Yusuke Nomura

Zusammensetzung der Prüfungskommission:

Prof. Dr. Alexander I. Lichtenstein  
Prof. Dr. Henning Moritz  
Prof. Dr. Yusuke Nomura  
Prof. Dr. Michael Potthoff  
Prof. Dr. Tim O. Wehling

Vorsitzender der Prüfungskommission:

Prof. Dr. Michael Potthoff

Datum der Disputation:

17.01.2025

Vorsitzender des Fach-Promotionsausschusses PHYSIK:

Prof. Dr. Markus Drescher

Dekan der Fakultät MIN:

Prof. Dr. Wolfgang J. Parak

Leiter des Fachbereichs PHYSIK:

Prof. Dr.-Ing. Norbert Ritter



# Abstract

The interplay of electron correlations and unconventional superconductivity is a pivotal area of condensed matter research, driven by the discovery of novel superconducting materials and the development of theoretical techniques. This thesis contributes to this expanding field by examining different aspects of superconductivity in strongly correlated electron systems. A core focus is the development and application of computational tools that enhance the efficiency and scope of material-realistic studies of superconductors, thereby enabling the investigation of previously inaccessible parameter regimes and properties of correlated superconducting matter. The findings of this thesis are contextualized within a broader overview of recent advancements in superconductivity research, along with a review of the theoretical methods and models employed.

For advancing the characterization of superconducting materials, we follow two complementary paths. One direction leverages low-rank representations of many-body correlation functions to address computational challenges posed by the intrinsic complexity of real materials and their low-temperature behavior. Specifically, we employ the intermediate representation basis for compact and efficient data handling to study spin-fluctuation-mediated superconductivity across a variety of multi-orbital materials. This includes a characterization of water-intercalated sodium cobalt oxides, where the numerical improvement enables the study of superconductivity and possible pairing symmetries at the experimentally relevant temperature scales on the order of a few Kelvin. For the recently discovered bilayer nickelate, we uncover the crucial role of inter-layer correlations in the formation of high-temperature superconductivity. Shifting focus to moiré materials as highly tunable quantum materials, we investigate possible superconductivity in twisted transition metal dichalcogenides. Our analysis reveals a strong charge carrier density dependence of the critical temperature for different pairing mechanisms, facilitating simple experimental scrutiny between them. In addition, we thoroughly evaluate the possibility of room-temperature superconductivity in copper-doped lead apatite, for which we do not find sustainable evidence. In this context, we discuss the general scientific challenges involved in achieving superconductivity at ambient conditions.

Furthermore, this thesis advances the microscopic understanding of superconductors by developing a Green's function-based method to access intrinsic superconducting length scales, which were previously inaccessible in strongly correlated materials. These length scales, namely the coherence length and magnetic penetration depth,

dictate many of the key properties of superconductors, including excitation energies, critical fields, and condensate stiffness. We validate our approach through application to alkali-doped fullerides. Here, our extended characterization reveals enhanced superconductivity with resilient phase coherence in the strong coupling regime of pairing interactions. The robust superconducting state is facilitated by multi-orbital physics. It stands in contrast to conventional limitations seen in single-band systems, where superconductivity is usually suppressed in the strong coupling regime due to the high effective masses of tightly-bound pairs. Our results pinpoint towards strategies for optimizing superconducting materials by surpassing traditional constraints with multi-orbital physics. The methodological advancements presented in this thesis broaden the scope of theoretically accessible parameters, enhancing the characterization of superconducting properties and laying a foundation for future innovations in superconductor design.

# Zusammenfassung

## German abstract

Die Erforschung des Zusammenspiels von Elektronenkorrelationen und unkonventioneller Supraleitung ist ein zentrales Gebiet der Festkörperforschung, welches durch die Entdeckung neuartiger supraleitender Materialien und die Entwicklung theoretischer Methoden stetig vorangetrieben wird. Die vorliegende Arbeit trägt zu diesem wachsenden Forschungsbereich bei, indem sie verschiedene Aspekte der Supraleitung in stark korrelierten Elektronensystemen untersucht. Ein zentraler Schwerpunkt liegt auf der Entwicklung und Anwendung von computergestützten Rechenmethoden, welche die Effizienz und den Umfang materialrealistischer Simulationen von Supraleitern verbessern. Dadurch wird die Untersuchung bisher unzugänglicher Parameterbereiche und Eigenschaften korrelierter supraleitender Materie ermöglicht. Die Ergebnisse dieser Arbeit sind in eine umfassende Übersicht der aktuellen Fortschritte in der Supraleitungsforschung eingebettet und werden durch eine Darstellung der verwendeten theoretischen Methoden und Modelle ergänzt.

Zur umfassenden Charakterisierung supraleitender Materialien werden zwei sich ergänzende Ansätze verfolgt. Eine Richtung fokussiert sich auf die Nutzung von Niedrigrang-Darstellungen für Vielteilchenkorrelationsfunktionen, um rechnerische Hürden zu bewältigen, die aus der Komplexität realer Materialstrukturen und der Herausforderung ihrer Beschreibung bei tiefen Temperaturen resultieren. Insbesondere wird die sogenannte „Intermediate Representation Basis“ verwendet, um eine kompakte und effiziente Datenverarbeitung während der numerischen Simulation zu ermöglichen. Als Anwendung dieser wird die durch Spinfluktationen vermittelte Supraleitung in ausgewählten Materialien mit multiorbitaler Elektronenstruktur untersucht. Hierzu zählt die Charakterisierung der Supraleitung und der möglichen Paarsymmetrien des supraleitenden Ordnungsparameters in wasserinterkaliertem Natrium-Kobaltoxid. Die Verbesserung der numerischen Effizienz ermöglicht Simulationen bei experimentell relevanten Temperaturen im Bereich von wenigen Kelvin. Ein weiteres untersuchtes Material ist die Bilagen-Nickeloxidstruktur, bei der kürzlich Hochtemperatursupraleitung entdeckt wurde. Unsere Berechnungen zeigen dabei die tragende Rolle von Interlagenkorrelationen bei der Ausbildung der Supraleitung auf. Zudem werden im Rahmen dieser Arbeit Moiré-Materialien untersucht, deren Eigenschaften experimentell vielseitig

einstellbar und präzise kontrollierbar sind. Im Speziellen untersuchen wir mögliche Supraleitung in verdrehten Übergangsmetallchalkogeniden. Dabei wird eine starke Ladungsträgerdichteabhängigkeit der kritischen Temperatur für verschiedene Paarungsmechanismen gefunden, was eine einfache experimentelle Differenzierung zwischen diesen Mechanismen ermöglicht. Darüber hinaus untersuchen und falsifizieren wir die Möglichkeit von Raumtemperatursupraleitung in kupferdotiertem Bleiapatit und diskutieren die allgemeinen Herausforderungen, die mit Supraleitung unter Umgebungsbedingungen verbunden sind.

Als zweites zentrales Ergebnis verbessert die vorliegende Arbeit das mikroskopische Verständnis von Supraleitern, indem eine modellunabhängige Methode basierend auf Greenschen Funktionen entwickelt wird, um intrinsische Längenskalen von Supraleitern zu berechnen. Diese Längenskalen, die durch die Kohärenzlänge und die magnetische Eindringtiefe gegeben sind, lassen sich insbesondere in stark korrelierten Materialien nur schwer bestimmen. Dennoch sind sie von hoher Relevanz für eine Vielzahl an Eigenschaften supraleitender Materialien, darunter Anregungsenergien, kritische Felder und die Kondensatsteifigkeit. Wir validieren unseren Ansatz durch Anwendung auf alkalidotierte Fulleride. Durch die erweiterte Charakterisierung des supraleitenden Phasendiagramms wird im Fall starker Paarwechselwirkung eine verbesserte Supraleitung mit stabiler Phasenkohärenz entdeckt. Dieser robuste supraleitende Zustand wird durch Multiorbitalwechselwirkungen ermöglicht und steht im Gegensatz zu den herkömmlichen Einschränkungen, die in Einbandssystemen auftreten. In diesen wird Supraleitung im Grenzfall starker Paarwechselwirkungen durch hohe effektive Massen stark gebundener Paare unterdrückt. Unsere Ergebnisse zeigen Strategien zur Optimierung supraleitender Materialien auf, die durch gezielte Nutzung von Multiorbitalphysik ermöglicht werden. Die methodischen Fortschritte erweitern zudem den numerisch zugänglichen Parameterraum, verbessern die Charakterisierung der supraleitenden Eigenschaften und legen den Grundstein für zukünftige Innovationen im Design von Supraleitern.



# Contents

<b>Abstract</b>	<b>v</b>
<b>Zusammenfassung</b> – German abstract	<b>vii</b>
<b>Preface</b>	<b>xi</b>
<b>List of publications</b>	<b>xv</b>
<b>List of abbreviations</b>	<b>xvii</b>
<b>1 Introduction</b>	<b>1</b>
1.1 Overview on superconducting materials . . . . .	2
1.2 Classification of superconductors . . . . .	9
1.3 Current challenges in superconductivity research . . . . .	10
<b>2 Many-body theory</b>	<b>15</b>
2.1 Effective low-energy models . . . . .	16
2.1.1 Downfolding from first principles . . . . .	18
2.1.2 Kanamori–Hubbard model . . . . .	20
2.2 Green’s function method . . . . .	23
2.2.1 Matsubara Green’s functions . . . . .	24
2.2.2 <i>S</i> -matrix expansion and self-energy . . . . .	26
2.2.3 Spectral representation and quasiparticles . . . . .	29
2.2.4 Luttinger–Ward functional . . . . .	33
2.3 Perturbative approaches . . . . .	35
2.3.1 Fluctuation exchange approximation . . . . .	36
2.4 Green’s function embedding methods . . . . .	39
2.4.1 Dynamical mean-field theory . . . . .	40
2.5 Low-rank representation of Green’s functions . . . . .	44
2.5.1 Intermediate representation basis . . . . .	46
Publication: <i>sparse-ir: Optimal compression and sparse sampling</i> of many-body propagators . . . . .	49
<b>3 Superconductivity</b>	<b>57</b>
3.1 Spontaneous symmetry breaking . . . . .	58
3.1.1 Ginzburg–Landau theory . . . . .	62
3.1.2 Anderson–Higgs mechanism and excitation modes . . . . .	74
3.1.3 Phase rigidity, supercurrent flow, and condensate stiffness . . . . .	76
3.1.4 Limits of GL theory — Ginzburg–Levanyuk criterion . . . . .	79
3.1.5 Berezinskii–Kosterlitz–Thouless phase transition . . . . .	80

3.1.6	Symmetry classification of the order parameter . . . . .	84
3.2	Bardeen–Cooper–Schrieffer theory . . . . .	89
3.2.1	Pair creation and Cooper pair instability . . . . .	89
3.2.2	BCS Hamiltonian and ground state . . . . .	93
3.2.3	Nambu–Gor’kov formalism . . . . .	97
3.2.4	Superconducting stiffness in BCS theory . . . . .	101
3.3	Migdal–Eliashberg theory . . . . .	103
3.4	Spin-fluctuation-mediated superconductivity . . . . .	105
3.4.1	Effective pairing interaction from fluctuation exchange . . . . .	106
<b>4</b>	<b>Superconducting pairing in layered materials</b>	<b>109</b>
4.1	Layered transition metal oxides . . . . .	110
4.1.1	Cobalt oxide hydrate – $\text{Na}_x\text{CoO}_2 \cdot y\text{H}_2\text{O}$ . . . . .	110
	Publication: <i>Efficient fluctuation-exchange approach to low-temperature spin fluctuations and superconductivity: From the Hubbard model to <math>\text{Na}_x\text{CoO}_2 \cdot y\text{H}_2\text{O}</math></i> . . . . .	114
4.2	Nickelate materials . . . . .	127
4.2.1	Bilayer nickelate – $\text{La}_3\text{Ni}_2\text{O}_7$ . . . . .	129
	Publication: <i>Quenched pair breaking by interlayer correlations as a key to superconductivity in <math>\text{La}_3\text{Ni}_2\text{O}_7</math></i> . . . . .	131
4.3	Moiré materials . . . . .	156
4.3.1	Twisted transition metal dichalcogenides . . . . .	158
	Publication: <i>Doping fingerprints of spin and lattice fluctuations in moiré superlattice systems</i> . . . . .	161
<b>5</b>	<b>Absence of room-temperature superconductivity</b>	<b>189</b>
5.1	Copper-doped lead apatite – $\text{Pb}_{10-x}\text{Cu}_x(\text{PO}_4)_6$ . . . . .	190
	Publication: <i>No superconductivity in <math>\text{Pb}_9\text{Cu}_1(\text{PO}_4)_6\text{O}</math> found in orbital and spin fluctuation exchange calculations</i> . . . . .	192
<b>6</b>	<b>Towards high-performance superconductivity</b>	<b>207</b>
6.1	Constraints on superconductivity . . . . .	208
6.1.1	Uemura relation . . . . .	210
6.1.2	The BCS–BEC crossover . . . . .	212
6.2	Resilient superconductivity from multi-orbital physics in $\text{A}_3\text{C}_{60}$ . . . . .	215
	Publication: <i>Bypassing the lattice BCS–BEC crossover in strongly correlated superconductors through multiorbital physics</i> . . . . .	216
<b>7</b>	<b>Concluding remarks</b>	<b>255</b>
	<b>Bibliography</b>	<b>259</b>
	<b>Acknowledgments</b>	<b>313</b>

# Preface

*An expert is a person who has found out by his own painful experience all the mistakes that one can make in a very narrow field.*

— Niels Bohr

I embarked on the journey of my doctorate with a deep fascination for how macroscopic properties of materials arise from the microscopic world, with new phases of matter being repeatedly discovered by studying the interplay of quantum mechanical particles on the atomic scale. The focus of this work is the phenomenon of superconductivity which, albeit having been researched for over a century, still poses many unresolved questions, with new and unique superconducting materials being continually reported. During the past decade, many novel platforms like hydrides, nickelates, or twisted moiré systems have emerged that challenge and enrich our understanding, truly making this a “golden age” of superconductivity research [1].

This thesis is a cumulative work composed of introductory notes as well as published and submitted original research on superconductivity in strongly correlated electron systems. This work is devoted to comprehensively explore fundamental aspects of superconducting materials and advance their theoretical understanding through the improvement and extension of computational tools. Specifically, this comprises compact data representation and compression techniques that enhance numerical efficiency, thereby enabling the description of previously unavailable parameter regimes, and the development of new methods to access a broader range of properties in correlated superconducting matter. As the general field of (strongly) correlated electron systems is broad and the number of superconducting materials is ever increasing, the presentation in this thesis is selective with a focus on models and methods applied in the publications and submitted preprints. Nonetheless, this thesis aims at being self-contained, pointing to relevant references for extended discussions.

The contributions of this thesis lie in both the theoretical advancements and the practical insights they provide. I hope that this work not only takes a step of many in advancing our understanding of superconductivity, but also inspires future studies to build upon these findings. Since the insights presented in this thesis surfaced from collaborative effort and for the sake of consistency, I will use the pronoun “we” throughout, except when highlighting my individual contributions.

## Outline

Each chapter of this cumulative thesis has been structured to guide the reader and systematically address the themes of the six publications making up this work. A full list of included publications (I–VI) can be found on page [xv](#) while a key point summary and the details of my personal contributions are given on the page prefacing the respective publication. Each work is embedded into individual chapters or sections, which provide the scientific context and advancements of the publication. This thesis consists of three introductory chapters, three chapters presenting the results, and a concluding chapter. They are organized as follows:

In the beginning, chapter 1 introduces the historical context, basic principles, and categorization of superconducting materials. Further, we provide an overview of current research developments and challenges in strongly correlated superconductors by highlighting a few of the many new material platforms that have emerged in recent years.

Chapter 2 presents a comprehensive introduction to many-body physics and the Green’s function method used to describe interacting systems and emergent phenomena such as superconductivity. Approaches to effective low-energy models and different approximations to the interacting problem are reviewed. An emphasis is put on the **fluctuation exchange (FLEX)** approach and **dynamical mean-field theory (DMFT)** to study the multi-orbital Kanamori–Hubbard model, which we employ in this thesis to investigate electron correlations and superconductivity. An integral part of the results shown in later chapters is based on low-rank representation of imaginary-time Green’s functions. This approach enables compact data compression and numerically efficient implementations, mitigating some of the limiting computational bottlenecks for material realistic calculations. We focus on the **intermediate representation (IR)** basis in combination with sparse sampling for which publication I provides an open-source code package.

To conclude the introductory part, chapter 3 gives an overview on the theory of superconductivity. We start from the central idea of **spontaneous symmetry breaking**, which allows for a qualitative understanding of superconducting properties like dissipationless charge currents and the Meissner–Ochsenfeld effect, as well as the emergence of the (competing) characteristic energy and length scales of superconductors. Following this, we address the microscopic origin for superconducting pairing as explained by the groundbreaking theory work of **Bardeen, Cooper, and Schrieffer (BCS)**. In this context, we review the Nambu–Gor’kov formalism to describe superconductivity in the framework of Green’s functions and we briefly describe **Migdal–Eliashberg theory** as an extension to BCS theory incorporating retarded interactions. Lastly, we review **spin fluctuations** as an electronic pairing mechanism pertinent to many unconventional superconductors. A focus of the

---

thesis is to explore the possibility of spin-fluctuation-mediated superconductivity in various multi-orbital materials. This is achieved by efficiently implementing the FLEX approximation within the IR basis, thereby enabling calculations at previously inaccessible temperatures down to the order of  $\sim O(1\text{ K})$ .

In chapter 4, we turn to the investigation of superconductivity in correlated heterostructured materials, which present versatile and tunable platforms with multiple degrees of freedom in the electronic system. We consider three different materials, each focused on varying aspects of correlated superconductivity. First, we discuss two distinct layered transition metal oxides. For the example of **water-intercalated sodium cobalt oxides** ( $\text{Na}_x\text{CoO}_2 \cdot y\text{H}_2\text{O}$ ), we showcase the numerical efficiency of the IR basis for multi-orbital systems in publication II. Our implementation enables us to address the possibility of spin-fluctuation-mediated superconductivity at the relevant temperature scale of the experimental critical temperature  $T_c \sim 4.5\text{ K}$ . At these temperatures, we can clearly discern dominance of  $f$ -wave symmetric pair fluctuations, but we do not observe the establishment of a superconducting transition from spin fluctuations. Additionally, as part of our code benchmark, we compare the superconducting phase diagram of the Hubbard model on a square lattice obtained from various many-body methods.

As the second example of layered transition metal oxides, we address the recently discovered superconductivity in **bilayer nickel oxides** ( $\text{La}_3\text{Ni}_2\text{O}_7$ ), which belong to the newer class of nickelate superconductors. The bilayer nickelate shows a much enhanced critical temperature  $T_c \sim 80\text{ K}$  compared to other nickelate materials which we attribute in publication III to the critical influence of inter-layer correlations.

Lastly, we turn to moiré superlattice systems, where twisting of individual material layers creates a new length scale through the long-range modulations of lattice stackings. These materials pose highly tunable quantum systems with rich phase diagrams of many correlated phases. In publication IV, we study the possibility of superconductivity in  **$\Gamma$ -valley twisted transition metal dichalcogenides** (TMDCs). We compare different pairing scenarios which show a unique dependence on the carrier density, enabling easy differentiation in experiment.

Chapter 5 deals with the potentials of room-temperature superconductivity and the strict scientific scrutiny that any likely candidate material is put under. Specifically, the case of **copper-substituted lead apatite** ( $\text{Pb}_{10-x}\text{Cu}_x(\text{PO}_4)_6\text{O}$ ), aka “LK-99”, is discussed which attracted a lot of attention due to its purported claims of being a superconductor under ambient conditions. Our contribution to the scientific scrutiny in publication V shows the absence of spin- and orbital-fluctuation-mediated superconductivity, for which we analyze the underlying reasons preventing it.

Transitioning to chapter 6, we present an analysis of known constraints on the critical temperature  $T_c$  of superconducting materials, providing insight into routes to further optimize  $T_c$ . In our analysis, we focus on limits originating from the

trade-off between pairing amplitude and macroscopic coherence as represented by the intrinsic energy scales of the superconducting gap and condensate stiffness. A physically insightful understanding of this paradigm is given by the **BCS–BEC crossover** phenomenology, showcasing how attractive interactions can increase pairing, but eventually lattice effects impair the kinetic energy of superconducting carriers, thereby reducing the condensate stiffness. We discuss the potentials of achieving high and robust stiffness in multi-orbital systems through mechanisms allowing for a substantial kinetic energy or via quantum geometric effects. In publication **VI**, we demonstrate how the competition of multi-orbital interactions can enable such enhanced superconductivity. Specifically, we show for a model of **alkali-doped fullerenes** ( $A_3C_{60}$ ) that increased inverted Hund’s coupling induces a localized superconducting state with enhanced critical temperatures and robustly high condensate stiffness. This analysis is enabled by the introduction of a novel theoretical framework to compute the fundamental length scales in presence of strong electron correlations.

In chapter **7**, we summarize the findings presented in this dissertation and we draw overarching conclusions that can be drawn from them. We discuss open questions and we give an outlook on potential future research directions.

# List of publications

This dissertation is based on the following journal articles, listed in order of appearance in the text. The individual contribution by the author of this thesis is detailed on the page prefacing the respective publication. This preface page is referenced together with the section that contains the publication below each list entry. Throughout the text, publications are referenced by the roman numerals listed here.<sup>1</sup>

- I** *sparse-ir: Optimal compression and sparse sampling of many-body propagators*  
Markus Wallerberger, Samuel Badr, Shintaro Hoshino, Sebastian Huber, Fumiya Kakizawa, Takashi Koretsune, Yuki Nagai, Kosuke Nogaki, Takuya Nomoto, Hitoshi Mori, Junya Otsuki, Soshun Ozaki, Thomas Plaikner, Rihito Sakurai, Constanze Vogel, **Niklas Witt**, Kazuyoshi Yoshimi, and Hiroshi Shinaoka  
Sec. 2.5.1, p. 49 et sqq. | [arXiv:2206.11762](https://arxiv.org/abs/2206.11762)      [SoftwareX 21](https://doi.org/10.1093/software/21/10/101266), 101266 (2023)
- II** *Efficient fluctuation-exchange approach to low-temperature spin fluctuations and superconductivity: From the Hubbard model to  $\text{Na}_x\text{CoO}_2 \cdot y\text{H}_2\text{O}$*   
**Niklas Witt**, Erik G. C. P. van Loon, Takuya Nomoto, Ryotaro Arita, and Tim O. Wehling  
Sec. 4.1.1, p. 114 et sqq. | [arXiv:2012.04562](https://arxiv.org/abs/2012.04562)      [Phys. Rev. B 103](https://doi.org/10.1103/PhysRevB.103.205148), 205148 (2021)
- III** *Quenched Pair Breaking by Interlayer Correlations as a Key to Superconductivity in  $\text{La}_3\text{Ni}_2\text{O}_7$*   
Siheon Ryee, **Niklas Witt**, and Tim O. Wehling  
Sec. 4.2.1, p. 131 et sqq. | [arXiv:2310.17465](https://arxiv.org/abs/2310.17465)      [Phys. Rev. Lett. 133](https://doi.org/10.1103/PhysRevLett.133.096002), 096002 (2024)
- IV** *Doping fingerprints of spin and lattice fluctuations in moiré superlattice systems*  
**Niklas Witt**, José M. Pizarro, Jan Berges, Takuya Nomoto, Ryotaro Arita, and Tim O. Wehling  
Sec. 4.3.1, p. 161 et sqq. | [arXiv:2108.01121](https://arxiv.org/abs/2108.01121)      [Phys. Rev. B 105](https://doi.org/10.1103/PhysRevB.105.L241109), L241109 (2022)
- V** *No superconductivity in  $\text{Pb}_9\text{Cu}_1(\text{PO}_4)_6\text{O}$  found in orbital and spin fluctuation exchange calculations*  
**Niklas Witt**, Liang Si, Jan M. Tomczak, Karsten Held, and Tim O. Wehling  
Sec. 5.1, p. 192 et sqq. | [arXiv:2308.07261](https://arxiv.org/abs/2308.07261)      [SciPost Phys. 115](https://doi.org/10.21468/SciPostPhys.115.1.197), 197 (2023)

---

<sup>1</sup>References to journal articles published during the examination process of this thesis have been updated in this list, on the respective preface, and in the bibliography as part of editorial adjustments.

**VI** *Bypassing the lattice BCS-BEC crossover in strongly correlated superconductors through multiorbital physics*

**Niklas Witt**, Yusuke Nomura, Sergey Brener, Ryotaro Arita, Alexander I. Lichtenstein, and Tim O. Wehling

Sec. 6.2, p. 216 et sqq. | [arXiv:2310.09063](https://arxiv.org/abs/2310.09063) [npj Quantum Mater.](https://doi.org/10.1038/s41535-024-00000-0) **9**, 100 (2024)

### **Works not included in this thesis**

- *Non-equilibrium carrier dynamics and band structure of graphene on 2D tin*  
Maria-Elisabeth Federl, **Niklas Witt**, Biao Yang, Niklas Hofmann, Johannes Gradl, Leonard Weigl, Neeraj Mishra, Camilla Coletti, Tim O. Wehling, and Isabella Gierz  
[arXiv:2405.01075](https://arxiv.org/abs/2405.01075) submitted to Phys. Rev. Lett.



# List of abbreviations

- $\mu$ SR** muon spin resonance
- ARPES** angular-resolved photoemission spectroscopy
- BCS** Bardeen–Cooper–Schrieffer (theory)
- BEC** Bose–Einstein condensation
- BKT** Berezinskii–Kosterlitz–Thouless (transition)
- BSE** Bethe–Salpeter equation
- BZ** Brillouin zone
- CDMFT** cellular dynamical mean-field theory
- cRPA** constrained random-phase approximation
- CT-QMC** continuous-time quantum Monte Carlo
- DTA** dynamical vertex approximation
- DCA** dynamical cluster approximation
- DFT** density functional theory
- DLR** discrete Lehmann representation
- DMFT** dynamical mean-field theory
- DMRG** density matrix renormalization group
- FFLO** Fulde–Ferrel–Larkin–Ovchinnikov (theory/pairing)
- FLEX** fluctuation exchange
- FMP** finite-momentum pairing
- GL** Ginzburg–Landau (theory/functional)
- HF** Hartree–Fock
- HTSC** high-temperature superconductor
- IPT** iterated perturbation theory
- IR** intermediate representation
- LTSC** low-temperature superconductor
- LW** Luttinger–Ward (functional)

- MATBG** magic-angle twisted bilayer graphene  
**MATTG** magic-angle twisted trilayer graphene  
**MBPT** many-body perturbation theory  
**NG** Nambu–Gor’kov (Green’s function)  
**NMR** nuclear magnetic response  
**NQR** nuclear quadrupole response  
**NRG** numerical renormalization group  
**ODLRO** off-diagonal long-range order  
**QMC** quantum Monte Carlo  
**QP** quasiparticle  
**RIXS** resonant inelastic X-ray scattering  
**RPA** random-phase approximation  
**SOC** spin-orbit coupling  
**SOPT** second-order perturbation theory  
**SQUID** superconducting quantum interference device  
**SSB** spontaneous symmetry breaking  
**STM** scanning tunneling microscopy  
**STS** scanning tunneling spectroscopy  
**TMDC** transition metal dichalcogenide  
**TPSC** two-particle self-consistency  
**vdW** van der Waals  
**WF** Wannier function

# CHAPTER Introduction

# 1

*This is why we're here: Unobtainium.<sup>1</sup> This little grey rock sells for 20 million a kilo.*

— Parker Selfridge

For more than a century, the study of superconductivity has been a cornerstone of scientific progress in condensed matter physics and beyond, constantly pushing the boundaries of our understanding of quantum mechanics and materials science [2]. A superconducting material is characterized by dissipationless charge transport (zero resistance) and perfect diamagnetism (Meissner–Ochsenfeld effect) below a critical transition temperature  $T_c$ , enabled by the persistent quantum coherence of electron pairs at the macroscopic scale. These properties have fueled significant technological advancements in various fields, including medical imaging, particle accelerators, and quantum computing hardware [3–5].

Superconductors belong to the recently established class of quantum materials [2, 3, 6, 7] which exhibit unique properties arising from quantum-mechanical effects, like electron correlations and topology. Advancements in the precise control of material parameters have propelled quantum materials design and discovery to the forefront of research efforts [8]. Examples of other emergent properties besides superconductivity include Mott insulators [9, 10], different flavors of the quantum Hall effect [11, 12], topological insulators [13, 14], spin liquids [15], altermagnetism [16, 17], charge density waves [18], multiferroics [19, 20], moiré systems [21–24], and light-induced states of matter [7, 25, 26]. In many cases, these quantum phenomena do not appear in isolation but intertwine in complex ways. Embedded within this paradigm is the interplay of electron correlations and superconductivity, which is the focus of investigation in this thesis.

Understanding this interplay is one of the leading challenges in condensed matter physics, as it lies at the heart of unraveling the microscopic mechanisms behind high-temperature superconductors (HTSCs). The discovery of high-temperature superconductivity in copper oxide layers (cuprates) [27, 28] has had arguably one of the most profound influences on shaping our current view on quantum matter [2], as it enticed the community to look more closely at the role of electron interactions. In

---

<sup>1</sup>Unobtainium is a fictional superconducting material at ambient conditions, which humankind relentlessly harvests for its valuable properties on the exoplanet Pandora in the movie series “Avatar”.

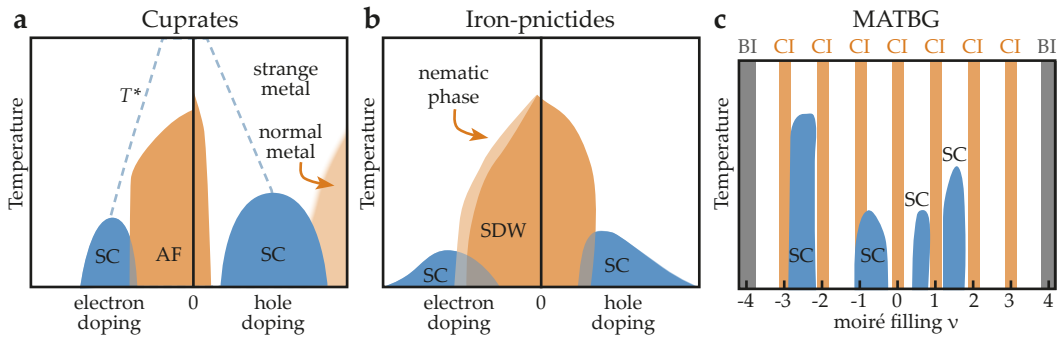


**Figure 1.1 – Schematic phase diagrams of unconventional superconductors.** (a) Phase diagram of cuprate materials with superconducting (SC), antiferromagnetic (AF), and pseudogap (appearance marked by  $T^*$ ) phases. Above the superconducting dome, cuprates are strange metals [36] and turn to a normal metallic (Fermi liquid) behavior in the large doping regime. (b) Phase diagram of iron-pnictides with a spin density wave (SDW) around half-filling in proximity to SC phases and nematic order on the electron-doped side. These phases coexist in some regions. (c) Phase diagram of magic-angle twisted bilayer graphene (MATBG) with correlated insulating (CI) phases at integer moiré filling  $\nu$  next to SC phases. At  $\nu = \pm 4$ , MATBG is a band insulator (BI). Adapted from Refs. [28, 35, 37, 38].

the past decades, numerous different correlated superconducting materials with rich phase diagrams have been reported [29, 30], as discussed below. Figure 1.1 illustrates three archetypal examples of such phase diagrams, belonging to cuprate materials, iron-pnictides, and magic-angle twisted bilayer graphene (MATBG), respectively. In each material, the superconducting phase emerges in proximity to correlated electronic phases (magnetic/insulating), indicating that strong electron interactions are crucial for the emergence of superconductivity [24, 29–35].

With the discovery of many different material platforms, research on correlated superconductors has branched out into various fronts, each with its own unique questions and challenges, while also sharing overarching questions across systems. In the following, we provide an overview of significant discoveries and recent developments in superconducting materials. We then introduce and clarify classification schemes of superconducting materials. Lastly, we discuss open questions in superconductivity research and describe the approach of this thesis to address some of these issues, particularly in the context of the specific materials studied.

## 1.1 Overview on superconducting materials

To gain an overview of the different superconducting material classes and to understand the current status of superconductivity research, we briefly review some of the important experimental discoveries and theoretical developments in the field. An intrinsic motivation of superconductivity research is to find superconductors operable under ambient conditions, with achieving room-temperature superconductivity being a significant milestone. Figure 1.2 presents the historical development of

critical temperatures in various superconducting materials. It shows the increasing trend in  $T_c$  over the decades, with notable jumps introduced by the discovery of new material classes like cuprates and hydrides. During the following discussion, Figure 1.2 acts as a reference point to visualize the context of major advancements in superconducting materials.

### The early years of superconductivity research

Superconductivity was first observed in mercury at a temperature of 4.15 K by Heike Kamerlingh Onnes in 1911, following his earlier success in liquefying helium [39, 40].<sup>2</sup> After the initial discovery, it took almost half a century before a full microscopic theory for superconductivity was developed by Bardeen, Cooper, and Schrieffer (BCS) in 1957 [41]. They showed that an effective electronic interaction mediated by phonons can be attractive, leading to the macroscopic condensation of electronic pairs. BCS theory provides the foundation of our microscopic understanding of the superconducting state, upon which more advanced theories are built. On the way to formulating BCS theory, several intermediate steps were taken, including measurements of the Meissner–Ochsenfeld effect, London’s local theory of electromagnetism, the observation of the isotope effect, and the formulation of phenomenological Ginzburg–Landau theory, see, e.g., chapter 1 in Ref. [42]. Following the introduction of BCS theory, a quantum field theoretical approach was developed with important contributions by Gor’kov, Nambu, and Eliashberg [43, 44].

Up to the 1980’s, superconductivity has been observed in many metals, alloys, and intermetallic compounds, with the search being guided by Matthias’ rules [30, 45].<sup>3</sup> In fact, more than half of the elemental metals with stable isotopes become superconducting (36 out of 58) at temperatures below 10 K, with some requiring additional pressure. This is illustrated in Figure 1.3. In addition, all stable semi-metals and a few non-metals become superconducting under pressure, while some of the long-lived radioactive elements, such as technetium (Tc), thorium (Th), and uranium (U), are superconductors at ambient pressure. Significant discoveries of that time period include the alloy NbTi and intermetallic compound Nb<sub>3</sub>Sn which are the commercially most widely used superconducting materials for high-field applications [4].<sup>4</sup>

---

<sup>2</sup>Unbeknownst to Onnes and his laboratory team, they had also observed the superfluid transition of liquid helium at around 2.2 K on the same day of measuring zero resistance in mercury [40], marking the discovery of two related quantum phenomena in the same experimental setup.

<sup>3</sup>A popularized version of Matthias’ rules states them as follows [46]: “One, a high symmetry is good; cubic symmetry is the best. Two, a high density of electronic states is good. Three, stay away from oxygen. Four, stay away from magnetism. Five, stay away from insulators. Six, stay away from theorists.”

<sup>4</sup>With critical magnetic fields up to 20 K, these two materials alone make up a billion-dollar industry producing superconducting wires [4, 30].



**Periodic table of superconductivity**

Periodic table of superconductivity																																															
H																	He																														
Li 4x10 <sup>-4</sup>	Be 0.026															B 11 250 GPa	C	N	O 0.6 120 GPa	F	Ne																										
Na	Mg															Al 1.19 film: 3.6	Si 8.5 250 GPa	P 6 7 GPa	S 17 160 GPa	Cl	Ar																										
K	Ca 15 150 GPa	Sc 0.3 21 GPa	Ti 0.4	V 5.3	Cr	Mn	Fe 2 21 GPa	Co	Ni	Cu	Zn 0.9	Ga 1.1 nano: 8.6 K	Ge 5.4 11.5 GPa	As 2.7 24 GPa	Se 7 13 GPa	Br 1.4 150 GPa	Kr																														
Rb	Sr 4 50 GPa	Y 2.8 15 GPa	Zr 0.6	Nb 9.2	Mo 0.92	Tc 7.8	Ru 0.5	Rh 3x10 <sup>-4</sup>	Pd	Ag	Cd 0.55	In 3.4 film: 4.2	Sn 3.7 film: 4.7	Sb 3.6 8.5 GPa	Te 7.4 35 GPa	I 1.2 25 GPa	Xe																														
Cs 1.5 5 GPa	Ba 5 15 GPa	(La)	Hf 0.13	Ta 4.4	W 0.01 film: 5.5	Re 1.7	Os 0.65	Ir 0.14	Pt	Au	Hg 4.15	Tl 2.39	Pb 7.2	Bi 5.3x10 <sup>-4</sup>	Po	At	Rn																														
Fr	Ra	(Ac)	Rf	Db	Sg	Bh	Hs	Mt	Ds	Rg	Ca	Nh	Fl	Mc	Lv	Ts	Og																														
.....																																															
<table border="1"> <tbody> <tr> <td>La 5.9</td> <td>Ce 1.7 5 GPa</td> <td>Pr</td> <td>Nd</td> <td>Pm</td> <td>Sm</td> <td>Eu 2.7 80 GPa</td> <td>Gd</td> <td>Tb</td> <td>Dy</td> <td>Ho</td> <td>Er</td> <td>Tm</td> <td>Yb 4.6 179 GPa</td> <td>Lu 0.1</td> </tr> <tr> <td>Ac</td> <td>Th 1.4</td> <td>Pa 1.4</td> <td>U 0.2</td> <td>Np 0.075</td> <td>Pu</td> <td>Am 0.8</td> <td>Cm</td> <td>Bk</td> <td>Cf</td> <td>Es</td> <td>Fm</td> <td>Md</td> <td>No</td> <td>Lr</td> </tr> </tbody> </table>																		La 5.9	Ce 1.7 5 GPa	Pr	Nd	Pm	Sm	Eu 2.7 80 GPa	Gd	Tb	Dy	Ho	Er	Tm	Yb 4.6 179 GPa	Lu 0.1	Ac	Th 1.4	Pa 1.4	U 0.2	Np 0.075	Pu	Am 0.8	Cm	Bk	Cf	Es	Fm	Md	No	Lr
La 5.9	Ce 1.7 5 GPa	Pr	Nd	Pm	Sm	Eu 2.7 80 GPa	Gd	Tb	Dy	Ho	Er	Tm	Yb 4.6 179 GPa	Lu 0.1																																	
Ac	Th 1.4	Pa 1.4	U 0.2	Np 0.075	Pu	Am 0.8	Cm	Bk	Cf	Es	Fm	Md	No	Lr																																	
.....																																															

■ Ambient Pressure  
■ High Pressure

**Figure 1.3 – Periodic table of superconductivity.** Materials that are superconducting as elemental compounds at ambient or higher pressure are marked. The number below the element denotes the transition temperature in Kelvin, whereas the necessary pressure for elements marked by orange color is indicated in a second row. Some compounds have higher temperatures when prepared as thin films. Data taken from Refs. [85–87].

### The rise of unconventional superconductors

In 1979, the first case of unconventional superconductivity was found in the heavy-fermion compound  $\text{CeCu}_2\text{Si}_2$  [88]. Many more heavy-fermion superconductors have been reported since then with one of the latest entries being  $\text{UTe}_2$  in 2019 [59, 89], which notably exhibits a re-entrant superconducting phase at high magnetic fields  $H > 30$  T. Heavy fermion materials have a low critical temperature below 10 K (with the exception of  $\text{PuCoGa}_5$ ) and several heavy fermion systems are believed to host unconventional superconductivity [58]. While no mutual agreement exists for the symmetry of the superconducting order parameter, some compounds are suggested to be triplet superconductors due to the presence of strong ferromagnetic fluctuations [58, 89, 90].

A paradigm shift was ignited by the discovery of cuprate superconductors by Bednorz and Müller in 1986 [27]. Subsequent to their report, a record hunt of unprecedentedly high critical temperatures was initiated, which led to a rapid increase of  $T_c$  values in a very short time frame. To date, the highest observed  $T_c$  value under ambient conditions was found in Hg-based copper oxides at 134 K [91] (under pressure up to 164 K [92]). Cuprate materials consist of layers of copper oxide which are hole- or electron-doped depending on the chemical composition. The superconducting state forms in the  $\text{CuO}_2$  planes with a characteristic dome dependence of  $T_c$  on the doping (cf. Figure 1.1a). The stoichiometric parent compound

is an antiferromagnetic Mott insulator, because of which superconductivity cannot be understood from BCS theory. Nowadays, the superconducting state is known to emerge from the presence of antiferromagnetic fluctuations. While there is a general consensus on the anisotropic  $d_{x^2-y^2}$ -wave pairing symmetry and importance of antiferromagnetic fluctuations for the formation of superconductivity [28, 31, 32, 34, 93, 94], no unifying theoretical framework exists that satisfyingly captures all aspects of the phase diagram [95].

With the advent of HTSCs and the simultaneous rise in computational power, numerous methods have been developed to address superconductivity in relation to the electronic interaction problem. These advancements have contributed to the current toolbox of microscopic theories and *ab initio* approaches to tackle material-realistic calculations [33, 34, 85, 93, 96–120] (see also chapters 2 and 3 for more details on some of these methods). On the experimental side, the discovery of novel superconducting platforms has accelerated with the increased control over quantum matter [3, 6, 7]. In particular, the past three decades showed a huge diversification in superconducting material families (cf. Figure 1.2). Given the scope of this thesis, it is not possible to cover all these developments. Therefore, we will focus on discussing three major advancements during this period: the families of other layered transition metal compounds, hydrides, and moiré materials.

This discussion will not cover other prominent superconducting materials such as organic superconductors [121, 122], magnesium diboride ( $\text{MgB}_2$ ) [123], or the recently discovered family of Kagome materials  $\text{AV}_3\text{Sb}_5$  ( $A=\text{K, Rb, Cs}$ ) [62–65]. Notably,  $\text{MgB}_2$  stands out among conventional superconductors with the highest critical temperature of 39 K at ambient pressure.<sup>5</sup> While we do not go into detail here, we will address superconductivity in alkali-doped fullerenes ( $\text{A}_3\text{C}_{60}$ ,  $A=\text{K, Rb, Cs}$ ) [126–129] later in chapter 6 and publication VI.

### Layered transition metal superconductors

One of the major developments in the past decades has been the discovery of new families of unconventional superconductors among layered transition-metal-based compounds, expanding beyond cuprates. The first notable discovery was in the layered transition metal oxide perovskite  $\text{Sr}_2\text{RuO}_4$  in 1994 [130], whose pairing mechanism poses one of the most puzzling problems in superconductivity research [131]. The exploration of unconventional superconductivity in 3d transition metal compounds as potential cuprate analogues gained momentum in 2003 with the report of superconductivity in water-intercalated sodium cobalt oxide ( $\text{Na}_x\text{CoO}_2 \cdot y\text{H}_2\text{O}$ , cobaltate), featuring a relatively low  $T_c$  of 4.5 K [132–134]. Notably, the cobaltate is the only transition metal oxide superconductor with a

---

<sup>5</sup>Initially, it was hoped that  $\text{MgB}_2$  would replace NbTi and  $\text{Nb}_3\text{Sn}$  in superconducting applications [4], but it could not meet the expectations due to its poor mechanical properties [124, 125].



triangular lattice structure.<sup>6</sup> A comprehensive overview on cobaltates will be given in section 4.1.1 and publication II.

Shortly after the discovery of the cobaltate, superconductivity was identified in iron-based materials [35, 135, 136]. The initial finding came in 2006 with LaOFeP ( $T_c = 5$  K) [137], followed by a breakthrough in 2008 when superconductivity was reported in LaFeAsO<sub>1-x</sub>F<sub>x</sub> with a much higher  $T_c$  of 26 K [138]. The prompt verification by numerous laboratories led to a rapid increase in the observed critical temperatures of iron-based superconductors [136], similar to the rise seen with cuprates. These materials consist of conducting layers of iron and pnictides (typically arsen (As) and phosphorus (P)) or chalcogenides (mostly selenium (Se) and tellurium (Te)), with the highest observed critical temperature exceeding 100 K in thin FeSe films on a SrTiO<sub>3</sub> substrate [139]. Iron-based superconductors are multi-orbital systems with many pockets on the Fermi surface, leading to discussions of inter-band  $s_{\pm}$ - or  $d$ -wave pairing symmetries in these materials [35, 135]. The electronic structure has influenced investigations into many multi-orbital specific correlation phenomena such as Hund's metals [140] or orbital-selective Mott states [141–143].

The HTSC discoveries in cuprates and iron-based materials are often described as marking the onset of the “Copper Age” and “Iron Age” of superconductivity research, respectively, due to their high influence on the overall research landscape. The most recent breakthrough of this kind occurred in 2019 with the observation of superconductivity in layered nickel oxide materials (nickelates) [49], which initiated the “Nickel Age” of superconductivity research [144–146]. One of the newest additions to this material family is the bilayer nickelate (La<sub>3</sub>Ni<sub>2</sub>O<sub>7</sub>) with the high critical temperature of around 80 K under pressure [56], yielding again a sizable jump within just a few years. We will discuss nickelates in more detail in section 4.2 and superconductivity in the bilayer nickelate specifically in publication III.

### Hydrides under pressure

Another significant advancement in the last decade was the discovery of high-temperature superconductivity in pressurized hydrides [85, 98, 147]. Relatively early after the introduction of BCS theory, Ashcroft proposed that metallic hydrogen would exhibit superconductivity at very high temperatures due to the light weight of hydrogen atoms [148]. He later extended this argument to hydrogen-containing alloys, suggesting that chemical pre-compression in these materials could reduce the enormous pressure required to metallize hydrogen [149]. This line of thought led to the computational prediction for pressurized H<sub>2</sub>S to be a HTSC [150, 151], which was experimentally verified just a year later with the observation of super-

---

<sup>6</sup>Recently, superconductivity was reported in experiments on a structurally similar layered triangular lattice cobalt oxychalcogenide (Na<sub>2</sub>CoSe<sub>2</sub>O) [84]. Interestingly, the first-principles electronic structure shows predominantly oxygen and selenium weight at the Fermi level.

conductivity in  $\text{H}_3\text{S}$  (formed from  $\text{H}_2\text{S}$  under pressure) with a  $T_c$  of about 203 K at 155 GPa [152]. Another seminal achievement was the discovery of clathrate  $\text{LaH}_{10}$ , which demonstrated near-room-temperature superconductivity around 250 K ( $-23^\circ\text{C}$ ) at 170 GPa [153, 154], setting the current record for the highest  $T_c$  of all known superconductors. The case of hydride materials is unique among superconductors, because its discovery was guided by theoretical predictions before experimental verification [147]. This serves as a striking example of the predictive power enabled by *ab initio* materials design for conventional superconductors [85, 96, 105], a capability that can be further enhanced by machine-learning approaches [155, 156].

### Two-dimensional materials and moiré systems

The last family of superconductors which we want to discuss comprises two-dimensional (2D) materials. Since the successful exfoliation of graphene in 2004 [157], the field of (quasi) 2D materials is thriving [158–160]. These materials characterize by their unique properties arising from quantum confinement and their high tunability via mechanisms such as environmental dielectric screening, electrostatic doping, heterostructuring capabilities, or external field tuning [8, 22, 158, 160–162]. A notable subclass of 2D materials are van der Waals (vdW) materials, where the bulk structure is composed of individual layers held together by weak vdW forces, such as graphene (graphite) or transition metal dichalcogenides (TMDCs). While some bulk compounds, like 2H-NbSe [66], were known to be superconducting before the advent of 2D materials, many mono- or few-layer vdW materials have since been shown to exhibit superconductivity as well [69–71, 73–76].

In 2018, the field of 2D materials expanded significantly with the discovery of moiré systems and their prospects of tuning quantum matter [21–24, 162]. This breakthrough came with the successful fabrication of magic-angle twisted bilayer graphene (MATBG) [77, 163], which exhibits a variety of correlated, topological, and superconducting phases (cf. Figures 1.1c and 4.4b). Moiré materials are characterized by a long-wavelength modulation of the lattice, which emerges from twisting layers relative to each other or from introducing a lattice mismatch between different material layers. Initially, superconductivity was only observed in twisted bilayer and twisted trilayer graphene [38, 77, 78, 163, 164]. However, recently two independent groups have reported (unconventional) superconductivity in twisted  $\text{WSe}_2$  (t- $\text{WSe}_2$ ) [79, 80], following an initial work in 2020 that only observed a zero-resistance state [165]. We further discuss the class of moiré materials in section 4.3, where we study superconductivity in  $\Gamma$ -valley twisted homobilayer TMDCs in publication IV.

## 1.2 Classification of superconductors

Given the vast number of superconducting materials, different terminological classifications have been introduced, some of which have already been used in the previous discussion. We aim to clarify their meanings here. We note that the boundaries within some categories are not always clear-cut and may depend on individual interpretations.

- **Conventional vs. Unconventional:** The notion of “conventionality” is commonly assigned to superconductors that can be explained by the (adiabatic, harmonic) phonon-mediated mechanisms of BCS and Migdal–Eliashberg theory [166]. In contrast, unconventional superconductors often involve more complex pairing mechanisms, mediated by magnetic fluctuations or other non-phononic interactions. Another frequently used criterion is the symmetry of the superconducting order parameter; superconductors with symmetries deviating from isotropic  $s$ -wave pairing are considered unconventional [167]. While examples like hydrides and alkali-doped fullerides do not fit neatly into this classification<sup>7</sup>, these criteria nonetheless provide a useful framework for understanding the complexity and the challenges involved in studying different types of superconductors.
- **Low-temperature (LTSC) vs. high-temperature superconductor (HTSC):** Historically, the discovery of cuprates marked a significant leap in achievable critical temperatures, surpassing the previous record of  $T_c = 23.3$  K in  $\text{Nb}_3\text{Ge}$  films [168]. At the time, it was widely believed that  $T_c$  values could not exceed 30 K (known as the Cohen–Anderson limit) [28, 169], leading to the designation of cuprates as HTSCs and distinguishing them from conventional superconductors. Consequently,  $T_c$  values above 30 K are often classified as “high temperature” [30], which coincides with the  $T_c$  of  $\text{La}_{0.185}\text{Ba}_{0.15}\text{CuO}_4$  from Bednorz and Müller’s pioneering work [27]. Outside the cuprate family, the term HTSC is commonly used for iron-based superconductors, hydrides, and recently nickelates. Since numerous other materials with  $T_c$  values exceeding 30 K have been discovered, including conventional superconductors like  $\text{MgB}_2$ , an alternative and perhaps more practical distinction for “high” and “low” temperature superconductors could be the boiling point of liquid nitrogen at  $T_{\text{N}_2} = 77$  K.
- **Weak vs. strong coupling:** In the context of superconductivity, coupling strength refers to the electronic pairing interaction. In BCS and Migdal–Eliashberg theory, the dimensionless electron-phonon coupling constant  $\lambda = N(0)U_{\text{eff}}$ , determined by the density of states at the Fermi level  $N(0)$  and an effective (static) interaction

<sup>7</sup>Hydrides are typically considered to be conventional, but with anti-adiabatic and anharmonic phonons playing an important role [85, 96, 166]. Fullerides, on the other hand, exhibit isotropic  $s$ -wave superconductivity, but strong electron correlations also have a significant impact on the formation of electron pairs, rendering the pairing mechanism rather unconventional [119, 128].

$U_{\text{eff}}$ , is used to gauge this strength (see, e.g., chapter 3 in Ref. [42]). Typically,  $\lambda \geq 1$  is considered the regime of strong coupling. In the context of a general attractive interaction, independent of the pairing mechanism, the coupling strength is indirectly used to characterize the spatial extent of electron pairs. This concept is employed in the BCS–BEC crossover phenomenology, see section 6.1.2, which describes the transition from a BCS regime of extended, largely overlapping electron pairs to a Bose–Einstein condensation (BEC) regime of strongly localized pairs by tuning the pairing strength or pair density.

- **Weakly correlated vs. strongly correlated:** The strength of electron correlations describes the influence of electron-electron interactions. A commonly used qualitative measure is the ratio of electronic interaction strength, such as the local Hubbard interaction  $U$ , to the kinetic energy, characterized by the bandwidth  $W$  in periodic systems. Typically, a system is considered strongly correlated for  $U/W > 1$ . Similar to coupling strength, correlation strength is also associated with a degree of electron localization. While weakly-correlated systems are well-described by the Bloch band picture, strongly-correlated systems are better characterized by the atomic limit. Many correlated superconductors lie in an intermediate regime where neither picture is fully applicable.

### 1.3 Current challenges in superconductivity research

The preceding discussion showed that research on superconductivity is vast and has grown immensely in the past decades. Here, we compile a brief, non-exhaustive list of overarching problems that connect different superconducting materials. This list is selective and subjective to the author’s view, reflecting both the current state of the field and the specific scope of this dissertation. Following this, we summarize which points we aim to address in this thesis.

#### 1. Is there a unified theory of unconventional superconductivity?

Cuprates are the cornerstone of research into unconventional superconductivity. While many aspects of their phase diagram can be qualitatively and sometimes quantitatively explained by different theories, a unified approach covering all experimental observations is still lacking. This gap is well summarized in the review by Singh [95]. Moreover, several parts of the phase diagram remain not fully understood. Many of these unresolved issues are not only pertinent to cuprates but also appear in other correlated superconducting materials (iron-based, nickelates, moiré graphene systems, ...) [7, 28]. Overarching open questions include the nature of the ground state as temperature approaches zero in the absence of superconductivity (elucidating the nature of the pseudogap) [170–173], the microscopic character of the strange metal

phase [36] at  $T > T_c$  from which superconductivity emerges, and the role of quantum critical points [174, 175].

#### 2. What are the mechanisms of light-enhanced superconductivity?

Light-enhancement of superconductivity [25] refers to the phenomenon where excitation of a superconducting material with ultrashort laser pulses can induce a transient state exhibiting superconducting properties at a significantly higher critical temperature. This type of transient superconductivity has been observed in various materials such as cuprates [176–179], organic salts [180, 181], and  $A_3C_{60}$  [182–188]. Most experimental evidence for these transient states is based on the observation that the material exhibits optical conductivity characteristic of a superconductor. More recent and rigorous experimental studies have provided additional compelling evidence. Notably, the latest measurements demonstrate light-induced field expulsion in YBCO [179], resembling a photo-induced Meissner–Ochsenfeld effect. Despite these experimental advances, a microscopic understanding of the mechanisms underlying light-enhanced superconductivity remains elusive, as discussed in various studies including Ref. [189] and references therein.

#### 3. Can we find topological superconductors?

A longstanding goal in superconductivity research is to obtain rigorous experimental evidence for topological superconductivity [190, 191], which is, e.g., relevant for the development of robust quantum computers [192]. Potential candidates for topological superconductors can be roughly categorized in intrinsic and artificial materials [190]. Among these, triplet superconductors are particularly promising, although experimental confirmation of such materials remains challenging. A notable example is  $Sr_2RuO_4$ , which was considered to be a  $p$ -wave triplet superconductor for over 20 years. However, recent experimental results have essentially discredited this scenario [131], prompting a renewed investigation into its pairing symmetry, see, e.g., Refs. [193–195].

#### 4. How to characterize the superconducting state and distinguish underlying pairing mechanisms?

In unconventional superconductors, the symmetry of the electron pairing wave function and the associated superconducting gap can be more complex than the isotropic  $s$ -wave pairing described by BCS theory. The gap symmetry is intrinsically linked to the microscopic pairing mechanism, making it a critical factor in scrutinizing different theoretical scenarios. Commonly, a coherent understanding of the pairing mechanism is achieved by comparison of experimental results and theoretical predictions. This is typically done by examining critical temperatures, gap symmetries, and their responses to various environmental changes such as strain/pressure, temperature, carrier

density, or external electromagnetic fields. However, in experimental settings, the properties of the gap symmetry can often only be inferred indirectly (see section 3.1.6), leaving room for interpretation. This challenge is exemplified by the case of  $\text{Sr}_2\text{RuO}_4$  [131] (see point 3). Therefore, incorporating more rigorous and diverse comparative dimensions would be desirable to reduce ambiguity and enhance our understanding of the superconducting state.

### 5. How to address bottlenecks in material-realistic calculations?

The complexity of real materials frequently limits the accessible phase space of computational methods. In particular, computational bottlenecks arise when attempting to study the low-temperature regime pertinent to the experimentally relevant scale set by  $T_c$ , which for many materials is only on the order of a few to tens of Kelvin. Overcoming these challenges necessitates the development of advanced theoretical and numerical approaches to make material-realistic studies of low-temperature superconductors feasible.

### 6. What limits superconductivity and how to achieve superconductivity at ambient conditions?

This question is the elephant in the room. Answering it is intimately linked to solving the aforementioned problems, as our understanding of the constraints on critical temperatures and the ability to predict candidate materials are fundamentally limited by our current knowledge. Early heuristic approaches, like Matthias' rules and the Cohen–Anderson limit, were useful to an extent, but ultimately proved inadequate for predicting HTSCs, such as cuprates. Given these limitations, it is essential to re-evaluate and expand our current understanding, establish theoretical or empirical bounds on  $T_c$  [196–203], and seek ways to surpass these bounds [VI, 204].

Given the size of the field, addressing these questions in detail would be beyond the scope of a single thesis. Therefore, we will focus on a subset of these broad questions as they relate directly to the specifics of this dissertation:

To expand the theoretical characterization of the superconducting state (**point 4**), we introduce a novel method in publication VI to calculate the intrinsic length scales of a superconductor – the coherence length and penetration depth – in the presence of (strong) electron correlations. These length scales determine critical magnetic fields and currents as well as the characteristic energy scales of superconductors, as detailed in chapter 3. Our method can be implemented in *ab initio* approaches and microscopic theories, thereby enabling a more rigorous comparison between theory and experiment and allowing for more precise scrutiny of different pairing mechanisms. On another note, we illustrate that the doping degree of freedom in (twisted) 2D materials can serve as a useful comparison axis. Specifically, we show

that for twisted  $\Gamma$ -valley homobilayer TMDCs, different pairing mechanisms result in distinct doping dependencies of the critical temperature. This is easily verifiable in experiment due to the possibility of in-situ changes in carrier density via electrostatic doping, in contrast to chemical doping required in most other materials.<sup>8</sup>

To overcome some of the computational bottlenecks (**point 5**), we utilize new compact representations of many-body propagators to enable efficient numerical implementations. In publication **I**, we present a code package for the intermediate representation (IR) basis and sparse modeling approach, which is subsequently utilized in publications **II** to **V** to study unconventional superconductivity in various multi-orbital materials. By leveraging these computational improvements, we make significant contributions to understanding the superconducting properties of individual materials.

Lastly, to address the constraints on possible room-temperature superconductivity (**point 6**), we undertake two approaches. First, in chapter **5** and publication **V**, we investigate an alleged room-temperature superconductor and discuss the factors that hinder the emergence of spin-fluctuation-mediated superconductivity in this specific case. Second, in chapter **6**, we examine general limitations of superconductivity by analyzing the competition between superconducting energy scales of pairing amplitude and condensate stiffness. In publication **VI**, we demonstrate for a model of  $A_3C_{60}$  that these constraints can be circumvented and increased superconducting temperatures can be achieved by tuning the pairing interaction without impairing the condensate stiffness in multi-orbital systems. Our results reveal promising pathways for pushing the boundaries of current  $T_c$  limits and achieving higher  $T_c$ 's.

---

<sup>8</sup>To stress this point, we note that the phase diagrams of cuprates and iron-pnictides shown in Figure 1.1, panels a and b, are obtained from many different samples, while the phase diagram of MATBG in panel c was measured from a single sample.





# CHAPTER 2

## Many-body theory

子曰：「溫故而知新，可以為師矣。」<sup>1</sup>  
— 孔子 (Confucius)

Understanding the interactions among many quantum particles is a key focus in condensed matter physics. Our macroscopic world, composed of a vast number of electrons and nuclei, fundamentally operates under the quantum mechanical many-body Schrödinger equation  $H|\psi\rangle = E|\psi\rangle$ . Describing the Hamiltonian  $H$  of a solid, including terms for kinetic energy and particle interactions, is straightforward. However, solving this equation for real-world systems is impractical due to the enormous number of particles  $\sim 10^{23}$  involved—noted as early as 1929 by Dirac [205].

Even if one could theoretically solve the many-body Schrödinger equation exactly, predicting the emergence of collective phenomena like magnetism and superconductivity is inherently challenging [2, 206–208]. These phenomena are hallmarks of interacting many-body systems, yet understanding their nature and interplay remains a difficult task. To address the interacting problem, theories for solid-state systems have adopted numerous methods and approximations [209–212].

A central tool to describe interacting systems of many particles is given by Green's functions. They probe the correlations of particles, whereby they directly relate to observable quantities in experiments (cf. Figure 2.3 in section 2.2). In this chapter, we review the theoretical framework of Green's functions, establishing the foundation for investigating superconductivity in the presence of strong electron correlations in subsequent chapters. We begin with a brief review of effective low-energy models (section 2.1), which are crucial for simplifying the many-body problem by focusing on relevant energy scales and degrees of freedom. In particular, we focus on the approximation of a local Coulomb interaction which is captured in the Hubbard model and its multi-orbital extension by Kanamori [140]. To describe interacting models in thermal equilibrium, we introduce the formalism of Matsubara Green's functions in section 2.2 and we discuss important concepts like their spectral representation, the quasiparticle picture, and the Luttinger–Ward functional for constructing approximations to the interacting many-body problem.

<sup>1</sup>*Zi yue*: “*Wēn gù'ér zhī xīn, kěyǐ wéi shī yǐ.*” — The Master said, “If a man keeps cherishing his old knowledge, so as continually to be acquiring new, he may be a teacher of others.” (from 論語 – 為政第二 (*Lúnyǔ – Wéi zhèng dì èr*), Confucian Analects – book II: Wei Chang).

In this context, we discuss two complementary approaches given by perturbative methods (section 2.3) and embedding schemes (section 2.4). Specifically, we describe the fluctuation exchange (FLEX) approximation and dynamical mean-field theory (DMFT), which are employed in the publications contained in this thesis. In section 2.5, we address the computational challenges inherent in dealing with realistic material systems. We propose low-rank representations of Green's functions as a viable tool to overcome computational bottlenecks, focusing on the example of the intermediate representation (IR) basis.

## 2.1 Effective low-energy models

Generally, two philosophies are followed to tackle the interacting many-body problem: applying approximate methods to solve the full problem, or formulating simplified models with reduced degrees of freedom that can be addressed using more exact methods. Here, we focus on the latter approach by deriving and studying material-realistic models for the electronic interaction problem. In this section, we discuss strategies to obtain such effective models.

In a solid, electrons move through a lattice of positively charged ions. By employing the Born–Oppenheimer approximation, electronic and ionic dynamics are adiabatically decoupled, owing to their different masses and associated timescales. As a result, electrons move in a potential of fixed atomic positions, while ionic dynamics can be effectively described through harmonic oscillations, resulting in phonons [44]. The remaining, purely electronic Hamiltonian with only electron-electron interactions can be written in second quantization<sup>2</sup> as

$$H = \underbrace{\sum_{\alpha\beta} h_{\alpha\beta} c_{\alpha}^{\dagger} c_{\beta}}_{H_{\text{kin}} \equiv H_0} + \frac{1}{2} \underbrace{\sum_{\alpha\beta\gamma\delta} U_{\alpha\delta,\gamma\beta} c_{\alpha}^{\dagger} c_{\beta}^{\dagger} c_{\gamma} c_{\delta}}_{H_{\text{int}} \equiv H_1}, \quad (2.1)$$

consisting of single and two-body terms which describe the kinetic and interaction part, respectively. The corresponding matrix elements  $h_{\alpha\beta}$  and  $U_{\alpha\delta,\gamma\beta}$  (cf. Eq. (2.7)) are determined by the chosen basis of single-particle states labeled by the combined quantum numbers  $\alpha$ . For instance, one can use real space basis with atomic (or Wannier) orbitals  $\{\phi_{\alpha}(\mathbf{R})\}$  where then  $\alpha = (\mathbf{R}_i, l, \sigma)$  specifies an electron at lattice site  $\mathbf{R}_i$  in the (Wannier) orbital  $l$  with spin  $\sigma$ .

Even though we simplified the solid state Hamiltonian, dealing with the electronic problem remains challenging. This difficulty arises from the fact that the kinetic energy and Coulomb interaction cannot be easily diagonalized simultaneously within the framework of single-particle states. Hence, we rely on further approximations.

---

<sup>2</sup>For an introduction to the notation of second quantization, we refer to Refs. [44, 213–215].

The arguably most successful and matured approach is given by density functional theory (DFT) [216–218], as its precision to describe ground state properties of (weakly-correlated) materials is on par with experimental accuracy [210]. DFT is the typical starting point for deriving material-realistic model Hamiltonians, so that we briefly want to summarize the idea of DFT. General introductions can be found in Refs. [219–221].

In DFT, the electron density  $n(\mathbf{r})$  replaces the many-body wave function as the central quantity to solve for, thereby reducing the degrees of freedom from  $3N$  for  $N$  particles to simply 3. The foundations of DFT were given by Hohenberg and Kohn [216], who had shown that the ground state energy  $E_0$  is an exact functional of  $n(\mathbf{r})$ , i.e., the variational principle

$$E_0 = E[n_0(\mathbf{r})] \leq E[n(\mathbf{r})] \quad (2.2)$$

for the ground state density  $n_0(\mathbf{r})$  holds.<sup>3</sup> The problem of DFT is to find a suitable representation of the functional  $E[n(\mathbf{r})]$ . In practice, the Kohn–Sham ansatz [217] is employed, where the electron density is represented by a set  $\{\psi_\alpha\}$  of non-interacting single-particle wave-functions. Then, the kinetic energy and Hartree-term of the electron interaction can be easily specified, while all remaining parts of  $E[n(\mathbf{r})]$  are lumped into the generally unknown exchange-correlation functional  $E_{xc}[n(\mathbf{r})]$ . Over time, a plethora of approximations with different levels of sophistication and accuracy have been developed for  $E_{xc}$  [224, 225].

The success of DFT derives from its accuracy [210] and it being a first-principles or *ab initio* approach which does not rely on any free adjustable parameters. That is, ground state properties of a material can be computed by only specifying the lattice of the system and atoms occupying it. While DFT performs well in describing most weakly-correlated materials (in particular  $s, p$ -electron metals)<sup>4</sup>, it fails for systems with strong electron correlations like many  $d$ -shell and  $f$ -shell compounds [218]. For instance, DFT is generally unable to describe the properties of Mott- or charge-transfer insulating states which are induced by strong on-site Coulomb interactions [9, 10]. In these cases, one needs to go beyond DFT, where the electronic structure obtained from DFT is a good starting point. In the following, we will describe this process and show how to derive the Kanamori–Hubbard model Hamiltonian via the approximation of a local Coulomb interaction (section 2.1.2).

<sup>3</sup>Later, Levy [222] and Lieb [223] generalized the Hohenberg–Kohn theorem to a constrained-search formulation.

<sup>4</sup>An exception is the infamous “band gap problem” of DFT, see, e.g., Refs. [219, 220, 226]

### 2.1.1 Downfolding from first principles

The full Hilbert space spanned by the electronic Hamiltonian Eq. (2.1) is exponentially large and unsolvable in practice. It is, however, often possible to separate a correlated subspace with reduced complexity and less degrees of freedom. The process of constructing an effective model of the correlated subspace from a larger Hilbert space is referred to as downfolding [227]. Even though the physical idea of downfolding is clear-cut, the question of how to apply it in practice can be ambiguous [84, 228, 229].

Many different downfolding schemes have been developed [84, 227], like constrained theories [230–232] or DFT-based embedding schemes (“DFT++”) [114, 115, 233, 234]. Here, we only want to briefly outline the commonly employed procedure of downfolding and we do not discuss the concomitant uncertainties like double-counting corrections. Instead, we refer the reader to Refs. [106, 107, 114, 115, 227, 235] and references therein for in-depth discussions.

The first step involves finding a suitable subspace which contains most electron correlations. For thermally activated phenomena like superconductivity (cf. Figure 2.11 in section 2.5), this typically involves bands in a low-energy window around the Fermi energy. In addition, one needs to decide how many degrees of freedom (bands/orbitals, spins, ...) need to be included in an effective model description to faithfully capture the physics of the correlated subspace. For this, an analysis of the band character or orbital weight composition of a material’s electronic structure is crucial.<sup>5</sup>

Given that a subspace has been found, the corresponding effective Hamiltonian needs to be constructed, i.e., the coefficients  $h_{\alpha\beta}$  and  $U_{\alpha\delta,\gamma\beta}$  in Eq. (2.1) need to be computed in a suitable basis of the reduced electronic Hilbert space. In this work, we employ the approximation of a localized Coulomb interaction, which is reasonable in systems with highly localized electronic wave functions, such as those found in (open)  $d$ -shells or  $f$ -shells of transition metals, lanthanides, or actinides. Hence, it is desirable to construct a tight-binding Hamiltonian of localized orbitals for which, e.g., Wannier functions (WFs) are used [106, 115, 236].

The eigenstates of (non-interacting) periodic quantum systems [106, 215] are given by Bloch functions

$$\psi_{nk}(\mathbf{r}) = e^{i\mathbf{k}\mathbf{r}} u_{nk}(\mathbf{r}) \quad (2.3)$$

with a lattice-periodic function  $u_{nk}(\mathbf{r}) = u_{nk}(\mathbf{r} + \mathbf{R})$  labeled by wave vector  $\mathbf{k}$  and band  $n$ .

---

<sup>5</sup> For instance, we consider in publication II the three-orbital  $t_{2g}$  ( $d_{xy}, d_{xz}, d_{yz}$ ) manifold of the Co atoms in the cobalt-oxide layers of  $\text{Na}_x\text{CoO}_2 \cdot y\text{H}_2\text{O}$ , or in publication IV, we study the inter-layer correlations between the two-orbital  $e_g$  ( $d_{x^2-y^2}, d_{z^2}$ ) manifolds of the Ni atoms in each layer of the bilayer nickelate  $\text{La}_3\text{Ni}_2\text{O}_7$ .

WFs are the Fourier transform of Bloch functions<sup>6</sup>

$$w_{n\mathbf{R}}(\mathbf{r}) = \frac{1}{N_k} \sum_{\mathbf{k}} e^{-i\mathbf{k}\mathbf{R}} \psi_{n\mathbf{k}}(\mathbf{r}) \quad (2.4)$$

that consequently get labeled by the Bravais lattice vector  $\mathbf{R} = \sum_i m_i \mathbf{a}_i$  with  $m_i \in \mathbb{Z}$  and primitive lattice vectors  $\mathbf{a}_i$ . WFs form a complete orthogonal basis, but they are not eigenstates of the periodic system's Hamiltonian since localization in energy is traded for localization in space [106]. Both the Bloch functions  $\psi_{n\mathbf{k}}$  and hence WFs  $w_{n\mathbf{R}}$  are not unique. An equivalent set of Bloch functions can be generated by applying a unitary transformation  $U_{nn'}^k$ , that mixes the bands at a particular wave vector  $\mathbf{k}$  as

$$\psi_{n\mathbf{k}} = \sum_{n'} U_{nn'}^k \psi_{n'\mathbf{k}} \quad (2.5)$$

which corresponds to a phase shift  $e^{i\varphi_n(\mathbf{k})}$  for an isolated band. This gauge freedom of the Bloch function transfers to the choice of WFs, allowing for the construction of “maximally localized Wannier functions” put forward by Marzari and Vanderbilt [237]. The general idea is to choose a gauge  $U_{nn'}^k$ , that minimizes the quadratic spread of WFs

$$\Omega = \sum_n [\langle n\mathbf{0} | r^2 | n\mathbf{0} \rangle - \langle n\mathbf{0} | r | n\mathbf{0} \rangle^2] = \sum_n [\langle r^2 \rangle_n - \langle r \rangle_n^2] \quad (2.6)$$

written in ket notation  $|n\mathbf{R}\rangle$  of the WF  $w_{n\mathbf{R}}(\mathbf{r}) = \langle \mathbf{r} | n\mathbf{R} \rangle$ . The resulting orbital basis can consist of atomic-like orbitals or more complex density distributions depending on the mixing of different band characters. Since the construction of the full orbital basis can almost be regarded as a science in its own right, we refer the reader to the review by Marzari et al. [106] for further details.

We can specify the matrix elements of the electronic Hamiltonian (2.1) of our correlated subspace using the WF basis. Let us establish a short-hand notation  $1 = (\mathbf{R}_1, n_1, \sigma_1)$  for the WF basis. Then, the matrix elements are given by

$$h_{12} = \int d^3r w_1^*(\mathbf{r}) \left[ -\frac{\hbar^2}{2m} \nabla + V(\mathbf{r}) \right] w_2(\mathbf{r}) \equiv -t_{12} \quad (2.7a)$$

$$U_{14,32} = \iint d^3r d^3r' w_1^*(\mathbf{r}) w_2^*(\mathbf{r}') \frac{e^2}{|\mathbf{r} - \mathbf{r}'|} w_3(\mathbf{r}') w_4(\mathbf{r}) \quad (2.7b)$$

We have introduced the common notation of  $t_{12}$  (with a minus sign) for the “hopping” matrix elements of the single-body term which are determined by the overlap (transfer) integrals of WFs at lattice sites  $\mathbf{R}_1$  and  $\mathbf{R}_2$ . Because WFs are (by construction)

<sup>6</sup>Note that the sum over crystal momenta  $\mathbf{k}$  is restricted to the first Brillouin zone. We keep this convention except when noted otherwise.

localized around lattice sites, the hopping elements  $t_{12}$  decay quickly with distance  $|\mathbf{R}_1 - \mathbf{R}_2|$ . Often, it is sufficient to limit the description to hopping processes between a few nearest-neighbor sites.

The kinetic Hamiltonian is often referred to as Wannier (projected) or lattice Hamiltonian. We can fully specify it in Wannier basis as

$$H_{\text{kin}} = - \sum_{il,jm,\sigma} t_{il,jm} c_{il\sigma}^\dagger c_{jm\sigma} = \sum_{n,k,\sigma} \varepsilon_{nk} c_{nk\sigma}^\dagger c_{nk\sigma} \quad (2.8)$$

with quantum labels of lattice site index  $i \hat{=} \mathbf{R}_i$ , orbital  $l$ , and spin  $\sigma$ . In the second step, we diagonalized the Hamiltonian with dispersion  $\varepsilon_{nk}$ <sup>7</sup> depending on band index  $n$  and (crystal) momentum  $k$  by Fourier transforming the fermionic operators

$$c_j^\dagger = \frac{1}{N_k} \sum_k e^{-ik\mathbf{R}_j} c_k^\dagger, \quad c_j = \frac{1}{N_k} \sum_k e^{ik\mathbf{R}_j} c_k \quad (2.9)$$

and inserting a unitary transformation  $U_{ln}$  to switch between (Wannier) orbital and (Bloch) band basis.

Both  $t_{12}$  and  $U_{14,32}$  can be directly evaluated using computed WFs [238]. However, important renormalization effects might be missing due to the projection onto the correlated subspace. While these effects are often not substantial for the hopping parameters  $t_{12}$  [106], they notably lead to an overestimation of the Coulomb matrix elements  $U_{14,32}$  when calculating Eq. (2.7b). This overestimation occurs because the screening from the remaining bands outside the projected correlated subspace is neglected. A widely used approach to derive effective Coulomb matrix elements [239–243] is given by the constrained random-phase approximation (cRPA) [227, 231, 244]. Interactions from cRPA are frequency-dependent [231], which is not treatable within most applied quantum field theoretical methods. A common approximation is to take the static limit  $U_{\text{eff}} = U_{\text{cRPA}}(\omega = 0)$  which might underestimate the true interaction value. Developing unambiguous methods to determine the interaction value for a downfolded model is ongoing research [212, 245, 246].

### 2.1.2 Kanamori–Hubbard model

The complexity of the full, long-ranged interaction matrix in Eq. (2.7b) is too difficult to treat within most methods. We can severely simplify the interaction Hamiltonian by making a few assumptions:

---

<sup>7</sup>Note that we implicitly assume that the chemical potential  $\mu$  has been absorbed into  $\varepsilon_{nk}$ .

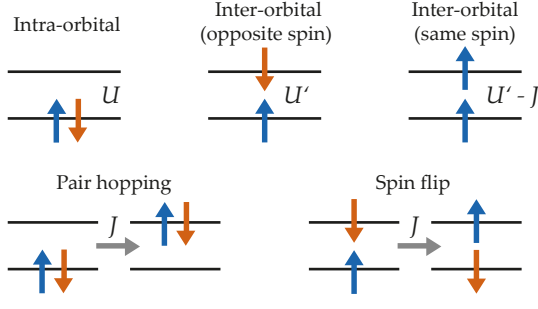


**Figure 2.1 – Multi-orbital interactions.** Schematic picture of different (instantaneous) intra-site interactions. They include interactions between electrons with opposite spins in the same orbital ( $U$ ), opposite spins in different orbitals ( $U'$ ), parallel spins in different orbitals ( $U' - J$ ), and processes involving pair hopping and spin flips ( $J$ ).

First, we assume the on-site interaction  $U_{ii,ii}$  of electrons at the same lattice site  $i$  to be the dominant contribution, i.e.,  $U_{ii,ii} \gg U_{ii,jj}, U_{ij,ij}$ , etc.<sup>8</sup> This is justified if the WFs are well localized around their respective lattice site. Second, we want to preserve SU(2) spin symmetry, which is satisfied in a paramagnetic state without spin-orbit coupling (SOC). Last, we assume that our correlated subspace consists of a (degenerate) orbital manifold for which the SO(3) orbital symmetry is sustained, such as the triplet  $t_{2g}$  and doublet  $e_g$  splittings of the  $d$ -shell in an octahedral environment (cf. footnote 5 on page 18).

Under these assumptions, only four local Coulomb integrals exist [140, 249] (site index  $i$  is suppressed)

$$U = U_{ll,ll} = \iint d^3r d^3r' |w_l(\mathbf{r})|^2 U_c(\mathbf{r} - \mathbf{r}') |w_l(\mathbf{r}')|^2, \quad (2.10a)$$

$$U' = U_{ll,mm} = \iint d^3r d^3r' |w_l(\mathbf{r})|^2 U_c(\mathbf{r} - \mathbf{r}') |w_m(\mathbf{r}')|^2, \quad (2.10b)$$

$$J = U_{lm,lm} = \iint d^3r d^3r' w_l^*(\mathbf{r}) w_m^*(\mathbf{r}') U_c(\mathbf{r} - \mathbf{r}') w_l(\mathbf{r}') w_m(\mathbf{r}), \quad (2.10c)$$

$$J' = U_{lm,ml} = \iint d^3r d^3r' w_l^*(\mathbf{r}) w_l^*(\mathbf{r}') U_c(\mathbf{r} - \mathbf{r}') w_m(\mathbf{r}') w_m(\mathbf{r}), \quad (2.10d)$$

while all other terms, e.g.,  $U_{ml,ll}$  have to vanish by symmetry. Note that  $U_c(\mathbf{r} - \mathbf{r}')$  denotes an effective screened interaction, e.g., from cRPA [227, 231, 241]. The interaction terms describe intra-orbital (Hubbard) interaction  $U$ , inter-orbital interaction  $U'$ , Hund's exchange  $J$ , and correlated pair hopping  $J'$ . By choosing real-valued (Wannier) functions  $w$ , we can identify  $J = J'$ . Due to the (orbital) rotation symmetry, the relation  $U' = U - 2J$  holds and only two independent parameters exist.<sup>9</sup> In most cases, the strength of interactions follows the scheme  $U > U' > J$  [250].

<sup>8</sup>The effect of non-local interactions can approximately be taken into account by an effective screening of the on-site interaction  $U$  as  $U^* = U - \bar{V}$  where  $\bar{V}$  is a weighted average of non-local interactions [247, 248].

<sup>9</sup>The rotation symmetry is only approximate for screened interactions but the assumption works reasonably well in many cases.

The corresponding Hamiltonian is called Kanamori–Hubbard Hamiltonian [249, 251, 252] which takes the form<sup>10</sup> (local index  $i$  suppressed)

$$\begin{aligned}
 H_{\text{int}} = & U \sum_m \hat{n}_{m\uparrow} \hat{n}_{m\downarrow} + \sum_{m < l, \sigma\sigma'} (U' - J\delta_{\sigma\sigma'}) \hat{n}_{m\sigma} \hat{n}_{l\sigma'} \\
 & - J \sum_{m \neq l} c_{m\uparrow}^\dagger c_{m\downarrow} c_{l\downarrow}^\dagger c_{l\uparrow} + J \sum_{m \neq l} c_{m\uparrow}^\dagger c_{m\downarrow}^\dagger c_{l\downarrow} c_{l\uparrow}
 \end{aligned} \quad (2.11)$$

with occupancy operator  $\hat{n}_\alpha = c_\alpha^\dagger c_\alpha$ . The first two terms account for density-density interactions among electrons in the same ( $U$ ) and different ( $U' - J\delta_{\sigma\sigma'}$ ) orbitals, while the last two terms involve correlated pair hopping and spin-flip processes. These interactions are schematically depicted in Figure 2.1. By introducing total charge, spin, and orbital isospin operators

$$\hat{N} = \sum_{m\sigma} \hat{n}_{m\sigma}, \quad \hat{S} = \frac{1}{2} \sum_{m, \sigma\sigma'} c_{m\sigma}^\dagger \boldsymbol{\tau}_{\sigma\sigma'} c_{m\sigma'}, \quad \hat{L}_n = i \sum_{lm, \sigma} \epsilon_{lmn} c_{l\sigma}^\dagger c_{m\sigma} \quad (2.12)$$

with Pauli-matrix vector  $\boldsymbol{\tau} = (\tau_x, \tau_y, \tau_z)$  and Levi–Civita symbol  $\epsilon_{lmn}$ , we can compactly write the Kanamori–Hubbard Hamiltonian as [140]

$$H_{\text{int}} = (U - 3J) \frac{\hat{N}(\hat{N} - 1)}{2} - 2J\hat{S}^2 - \frac{1}{2}J\hat{L}^2 + \frac{5}{2}J\hat{N}. \quad (2.13)$$

This formulation of the interaction illustrates Hund’s rules which dictate the ground-state configuration of atomic shells: The total spin  $S$  is maximized first, followed by the maximization of the orbital angular momentum  $L$ . We study the Kanamori–Hubbard Hamiltonian for different materials in publications II to VI.

### Hubbard Hamiltonian

Taking the single-orbital limit of the Kanamori–Hubbard model retrieves the Hubbard model with only the local Hubbard interaction  $U$ :

$$H_U = - \sum_{ij, \sigma} t_{ij} c_{i\sigma}^\dagger c_{j\sigma} + U \sum_i \hat{n}_{i\uparrow} \hat{n}_{i\downarrow}. \quad (2.14)$$

The Hubbard model is the simplest description of interacting particles on a lattice. A schematic illustration of the involved processes is drawn in Figure 2.2a. Despite its simplicity, the Hubbard model is only exactly solvable in one dimension [254, 255] and in the infinite dimensional limit [256]. Over the past decades, the Hubbard model has been immensely studied [171, 257] due to its paradigmatic relevance for HTSCs [34, 93, 110, 118, 173, 258–260] and the surge of cold-atom quantum

<sup>10</sup>Note that the Kanamori–Hubbard Hamiltonian is not valid for an entire  $d$ -shell, where the full (local) interaction matrix  $U_{14,32}$  needs to be computed [140, 253].



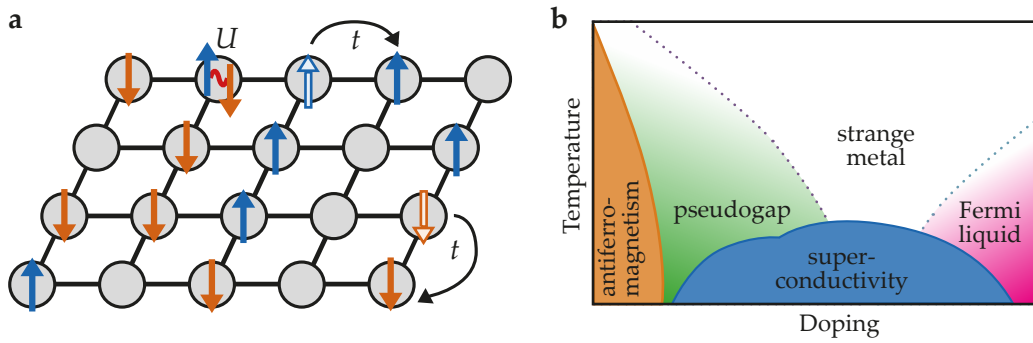


**Figure 2.2 – Schematic of the Hubbard model on a square lattice.** (a) Depiction of the Hubbard model with (nearest-neighbor) hopping processes  $t$  and on-site Coulomb repulsion  $U$ . (b) Proposed phase diagrams of the Hubbard model with antiferromagnetic, superconducting, pseudogap, strange metal, and Fermi liquid phases [171].

simulators [261–266]. Simultaneously, it serves as a significant benchmarking hub for the development and comparison of numerical methods [II, 209, 211]. Recent algorithmic advances and increased computing power have led to consistent results and growing consensus on the Hubbard model's properties. A schematic temperature and doping dependent phase diagrams of the Hubbard model on a square lattice is shown in Figure 2.2b, which is qualitatively similar to that of cuprates, cf. Figure 1.1a.

## 2.2 Green's function method

Green's functions are the backbone of quantum field theoretical methods to investigate systems of interacting particles. They encode spatio-temporal correlations of many-body systems and their response to external perturbations, like electromagnetic fields or variations in temperature. With this, Green's functions not only provide a practical framework, but they also link to experimental observables [44, 267, 268], as is summarized in Figure 2.3. Most notably, single-particle Green's functions connect to spectral functions, which can be measured using spectroscopy experiments like angular-resolved photoemission spectroscopy (ARPES). Higher-order Green's functions, involving two or more particles, are associated with linear and nonlinear response functions. In this section, we will introduce the notation and summarize the framework of fermionic Green's functions. For detailed derivations and a discussion of bosonic Green's functions, we refer to textbooks on many-body methods and quantum field theories (for condensed matter systems), such as Refs. [43, 44, 213, 214, 269]. Throughout this chapter, we set  $\hbar \equiv 1$ .

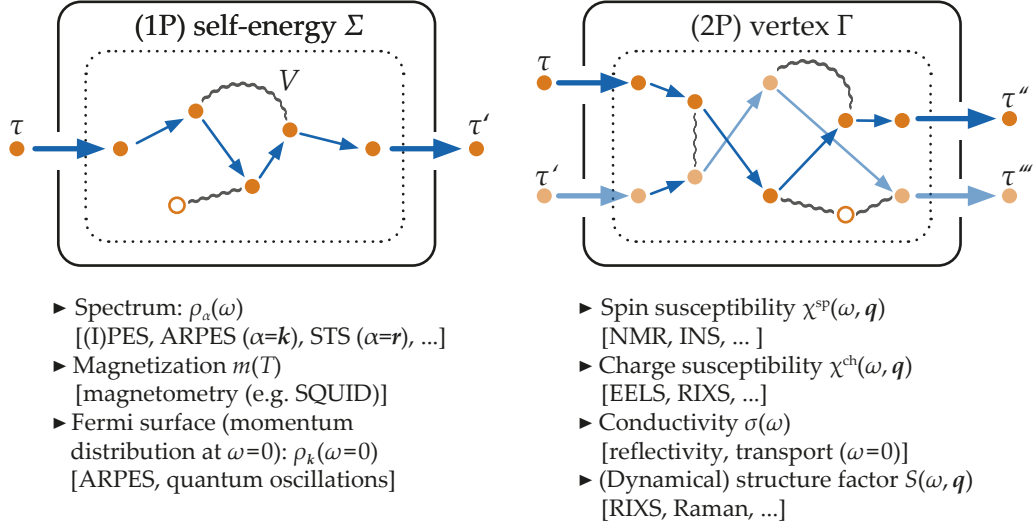


**Figure 2.3 – Schematic picture of Green’s functions and their relation to experimental observables.** Green’s functions measure the probability amplitude of particle trajectories between different times  $\tau, \tau'$  in an interacting many-body environment, schematically drawn for single-particle (1P) and two-particle (2P) correlation functions. The quantities that encode the interaction  $U$  between particles are the self-energy  $\Sigma$  and vertex  $\Gamma$ , respectively. Below each picture, we indicate physical observables, the respective correlation function and experimental techniques to measure them [44, 267, 268]. Abbreviations: (inverse) photoemission spectroscopy ((I)PES), angular-resolved photoemission spectroscopy (ARPES), scanning tunneling spectroscopy (STS), superconducting quantum interference device (SQUID), nuclear magnetic resonance (NMR), inelastic neutron scattering (INS), electron energy loss spectroscopy (EELS), resonant inelastic X-ray scattering (RIXS).

### 2.2.1 Matsubara Green’s functions

In this thesis, we deal with systems at finite temperature and in thermal equilibrium where the Matsubara formalism is most practical. In this framework, we work with imaginary time instead of real time, which can be obtained from Wick rotation  $it \mapsto \tau$ . The motivation for the imaginary-time formulation stems from the similarity between the time translation operator  $e^{-iHt} \mapsto e^{-\tau H}$  and statistical weight  $e^{-\beta H}$  with inverse temperature  $\beta^{-1} = k_B T$ , which then can be regarded as time propagation in imaginary time up to times  $\tau = \beta$ . Hence, certain information<sup>11</sup> about the dynamics of a system can be extracted from its thermodynamic observables. The single-particle Matsubara Green’s function is defined by

$$G_{\alpha_1 \alpha_2}(\tau_1, \tau_2) = -\langle \mathcal{T}_\tau c_{\alpha_1}(\tau_1) c_{\alpha_2}^\dagger(\tau_2) \rangle \quad (2.15)$$

Here,  $c_\alpha^\dagger$  ( $c_\alpha$ ) are fermionic creation (annihilation) operators of quantum states  $\alpha$  in the Heisenberg time-evolution picture  $\hat{A}(\tau) = e^{\tau H} \hat{A} e^{-\tau H}$ . Further,  $\langle \cdot \rangle = \text{Tr}\{\hat{\rho} \cdot\}$

<sup>11</sup>In fact, it turns out that going to the imaginary-time formalism works as a very efficient filter that suppresses high-energy (short-time) information. We can use this fact to compactly compress the weakly filtered low-energy information; see section 2.5.1.

denotes the thermal expectation value with statistical operator  $\hat{\rho} = e^{-\beta H}/Z$ , where  $Z$  is the partition function and  $H$  the system's Hamiltonian.<sup>12</sup> Lastly,  $\mathcal{T}_\tau$  is the time-ordering operator

$$\mathcal{T}_\tau c_1(\tau_1)c_2^\dagger(\tau_2) = c_1(\tau_1)c_2^\dagger(\tau_2)\Theta(\tau_1 - \tau_2) - c_2^\dagger(\tau_2)c_1(\tau_1)\Theta(\tau_2 - \tau_1), \quad (2.16)$$

where  $\Theta$  is the Heaviside step function. The single-particle Green's function probes for the internal correlations by measuring the probability amplitude of a particle (or hole) propagating through the system between times  $\tau_1$  and  $\tau_2$  and changing the state from  $\alpha_1$  to  $\alpha_2$ . Hence, they are often also referred to as propagators. Green's functions constitute practical tools because they filter out much of the (redundant) information contained in the statistical operator  $\hat{\rho}$  regarding the full interacting system. We want to note that the Green's function (2.15) represents a specific example of a correlation function. For instance, we can also define higher-order Green's functions like the two-particle correlation function

$$G_{\alpha_1\alpha_2,\alpha_3\alpha_4}^{(2)}(\tau_1, \tau_2, \tau_3, \tau_4) = \langle \mathcal{T}_\tau c_{\alpha_1}(\tau_1)c_{\alpha_2}^\dagger(\tau_2)c_{\alpha_3}(\tau_3)c_{\alpha_4}^\dagger(\tau_4) \rangle, \quad (2.17)$$

which contains four fermionic operators.

Since we are working in thermal equilibrium, the Green's function only depends on time differences  $\tau_1 - \tau_2$  such that we can effectively work with a single time  $\tau = \tau_1 - \tau_2$  (shifting  $\tau_2 = 0$ ). Fermionic imaginary-time Green's functions have the property to be antiperiodic in time with periodicity  $\beta$ . For times  $-\beta < \tau < 0$ , it follows from the cyclic properties of the trace that

$$G_{\alpha\gamma}(\tau) = -G_{\alpha\gamma}(\tau + \beta). \quad (2.18)$$

That means we can restrict the description to an interval  $0 < \tau < \beta$ . A finite time interval results in discrete frequencies when Fourier expanding the Green's function. These discrete frequencies are called Matsubara frequencies given by  $\omega_n = (2n + 1)/\beta$  with an integer  $n$ .<sup>13</sup> The corresponding back and forth Fourier expansion (transformation) is given by

$$G(i\omega_n) = \int_0^\beta d\tau G(\tau)e^{i\omega_n\tau} \quad \text{and} \quad G(\tau) = \frac{1}{\beta} \sum_n G(i\omega_n)e^{-i\omega_n\tau}. \quad (2.19)$$

<sup>12</sup>The chemical potential  $\mu$  has been absorbed into the Hamiltonian, since we work in the grand canonical ensemble to treat the Fock space of many particles.

<sup>13</sup>Note that bosonic Matsubara Green's functions are periodic on the interval  $[0, \beta]$  and the corresponding frequencies are given by  $\nu_n = 2\pi n/\beta$  with  $n \in \mathbb{Z}$ .

Although the Matsubara frequencies are purely imaginary, we can analytically continue the Green's function to real frequencies  $\omega$  and corresponding observables like the excitation spectrum. We discuss this relation further in section 2.2.3.

Let us briefly address the spatial dependence of the Green's function. Since we are working in periodic lattice systems,  $G$  only depends on distances  $\mathbf{R}_1 - \mathbf{R}_2$  and we can easily Fourier transform between real-space and wave vector/(crystal) momentum representation as

$$G(\mathbf{k}) = \sum_j G(\mathbf{R}_j) e^{i\mathbf{k}\mathbf{R}_j} \quad \text{and} \quad G(\mathbf{r}) = \frac{1}{N_k} \sum_{\mathbf{k}} G(\mathbf{k}) e^{-i\mathbf{k}\mathbf{r}}, \quad (2.20)$$

where we have promoted the spatial dependence from an index to an argument. Let us introduce some shorthand notation for the following discussion: We can consider the Green's function as a matrix in the remaining spin-orbital degrees of freedom  $\alpha = (l, \sigma)$  which we denote by underlining  $G_{\alpha\gamma} \equiv [\underline{G}]_{\alpha\gamma}$ . In addition, we will use the four-vector notation  $k = (i\omega_n, \mathbf{k})$  and  $r = (\tau, \mathbf{r})$  combining the frequency-momentum and time-space dependence, respectively.

### 2.2.2 S-matrix expansion and self-energy

Evaluating the Green's function (2.15) for the interacting (downfolded) lattice Hamiltonian (2.1) is difficult as the computational cost scales with the exponentially increasing size of the Fock space. Different approaches exist to introduce controlled approximations to the computation of Green's functions. For instance, the equation of motion for the single-particle Green's function generates an infinite hierarchy of coupled differential equations between different orders of  $n$ -particle Green's functions, which can be systematically truncated at specific orders [213]. Another typical approach is a perturbative expansion around a known reference frame. Here, we want to briefly sketch the idea of many-body perturbation theory (MBPT) for an expansion around the non-interacting limit  $U = 0$ , where the remaining (kinetic) part of the Hamiltonian  $H_0$  in (2.8) is diagonal in  $\mathbf{k}$  space and spin  $\sigma$ . The starting point is the non-interacting or bare (paramagnetic) Green's function. In (non-diagonal) orbital basis, it is given by

$$\underline{G}_0(i\omega_n, \mathbf{k}) = [i\omega_n \mathbb{1} - \underline{h}(\mathbf{k})]^{-1} \equiv \frac{\mathbb{1}}{i\omega_n \mathbb{1} - \underline{h}(\mathbf{k})}, \quad (2.21)$$

where  $\mathbb{1}$  denotes the unity matrix in orbital space and  $[\underline{h}]_{lm}(\mathbf{k}) = -\sum_j t_{jl,0m} e^{i\mathbf{k}\mathbf{R}_j}$  is the Fourier transform of the hopping matrix in Eq. (2.7a). We have introduced the notation that a fraction denotes the inversion of the orbital matrix in the denominator.

In diagonal band basis, the bare Green's function simplifies to

$$G_{0,m}(i\omega_n, \mathbf{k}) = \frac{1}{i\omega_n - \varepsilon_{m\mathbf{k}}} . \quad (2.22)$$

We see from these expressions that the poles of the Green's functions encode the excitation energies  $\omega = \varepsilon_{m\mathbf{k}}$  of the system.

In order to incorporate interactions, we switch to the interaction picture where the time dependence of an operator is expressed with respect to the non-interacting Hamiltonian  $H_0$ , i.e.,  $\hat{A}_I(\tau) = e^{\tau H_0} \hat{A} e^{-\tau H_0}$ . We then can introduce the time-evolution operator in the interaction picture, also known as the  $S$ -matrix operator

$$\begin{aligned} S(\tau, \tau') &= e^{\tau H_0} e^{-(\tau-\tau')H} e^{-\tau' H_0} \\ &= \mathcal{T}_\tau \exp\left(-\int_{\tau'}^{\tau} d\tau'' H_{1,I}(\tau'')\right) \\ &= \sum_{n=0}^{\infty} \frac{(-1)^n}{n!} \int_{\tau'}^{\tau} d\tau_1 \dots d\tau_n \mathcal{T}_\tau [H_{1,I}(\tau_1) \dots H_{1,I}(\tau_n)] \end{aligned} \quad (2.23)$$

with the interacting Hamiltonian  $H_{1,I}$  in the interaction picture. The formal expression by a time-ordered exponential in the second line can be derived from a Trotter decomposition of the time interval  $[\tau', \tau]$  [44], which is a short-hand notation for the series expansion in the last line.

We can express the interacting Green's function (2.15) by the  $S$ -matrix operator as

$$G_{12}(\tau) = -\frac{\text{Tr} [e^{-\beta H_0} \mathcal{T}_\tau c_1(\tau) c_2^\dagger(0) S(\beta, 0)]}{\text{Tr} [e^{-\beta H_0} S(\beta, 0)]} = -\frac{\langle \mathcal{T}_\tau c_1(\tau) c_2^\dagger(0) S(\beta, 0) \rangle_0}{\langle S(\beta, 0) \rangle_0} , \quad (2.24)$$

where  $\langle \cdot \rangle_0$  denotes the thermal expectation value with respect to  $H_0$ . For brevity, we dropped the index "I" with all time-dependent operators henceforth being in the interaction picture. Inserting Eq. (2.23) allows us to expand the Green's functions in terms of the interacting Hamiltonian  $H_1$ :

$$G_{12}(\tau) = -\frac{1}{\langle S(\beta, 0) \rangle_0} \sum_{n=0}^{\infty} \frac{(-1)^n}{n!} \int_0^\beta d\tau_1 \dots d\tau_n \langle \mathcal{T}_\tau c_1(\tau) c_2^\dagger(0) H_1(\tau_1) \dots H_1(\tau_n) \rangle_0 . \quad (2.25)$$

This expression can be simplified because the expectation value of  $4n + 2$  fermionic operators at order  $n$ , corresponding to a (non-interacting)  $2n + 1$ -particles Green's function, is taken with respect to the non-interacting Hamiltonian. In this case, *Wick's theorem* [43, 44] applies and we can rewrite the expectation value as the (permutation) product of  $2n + 1$  non-interacting single-particle Green's functions. One can introduce Feynman diagrams as a handy tool to pictorially express and bookmark the Wick-factorized terms that occur in the expansion (2.25) [44, 213, 270].

**Figure 2.4 – Components of Feynman diagrams.** Diagrammatic depiction of bare ( $G_0$ ) and dressed ( $G$ ) propagator, interaction vertex ( $U$ ) and self-energy ( $\Sigma$ ) in frequency-momentum space  $k = (i\omega_n, \mathbf{k})$ .

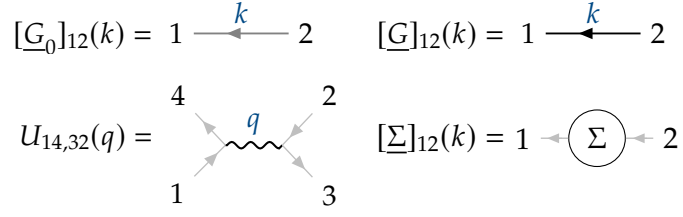


Figure 2.4 shows diagrammatic depictions of the basic components that make up Feynman diagrams (see, e.g., Figure 2.5 for example diagrams).

We can differentiate between two types of diagrams occurring in the expansion (2.25): connected and factorizable disconnected diagrams. Analyzing the prefactor  $\langle S(\beta, 0) \rangle_0$  shows that it cancels exactly with all disconnected diagrams, which is known as the *linked cluster theorem* [44]. Hence, one only needs to consider all connected diagrams. This task quickly becomes unfeasible for high orders  $n$  because  $(2n + 1)!$  terms need to be considered. Nonetheless, the perturbative expansion (2.25) enables physically motivated approximations by selecting certain classes of diagrams. We discuss examples in section 2.3.

### The self-energy

An important object that encodes the feedback of the interacting environment on the propagation of a particle is the self-energy  $\Sigma$ . Within the diagrammatic formulation, it consists of all connected (irreducible) diagrams which cannot be separated by cutting a single-particle propagator line. Figure 2.5 shows a few of the low-order diagrams that contribute to  $\Sigma$ . Using the self-energy, we can rewrite the expansion of the interacting Green's function (2.25) in frequency (and momentum) space as

$$\underline{G}(k) = \underline{G}_0(k) + \underline{G}_0(k)\underline{\Sigma}(k)\underline{G}(k), \quad (2.26)$$

which is known as the Dyson equation. It is a self-consistent equation for the interacting Green's function<sup>14</sup> which is obtained from “dressing” the non-interacting Green's function with interaction feedback of the system contained in  $\Sigma$ . The self-energy can be regarded as a complex-valued, frequency-dependent and non-local single-particle potential, which becomes apparent from the solution of the Dyson equation:

$$\underline{G}^{-1}(i\omega_n, \mathbf{k}) = \frac{\mathbb{1}}{[\underline{G}_0(i\omega_n, \mathbf{k})]^{-1} - \underline{\Sigma}(i\omega_n, \mathbf{k})} \stackrel{\text{Eq. (2.21)}}{=} \frac{\mathbb{1}}{i\omega_n \mathbb{1} - \underline{h}(\mathbf{k}) - \underline{\Sigma}(i\omega_n, \mathbf{k})}. \quad (2.27)$$

<sup>14</sup>See the discussion of the Luttinger–Ward functional in section 2.2.4 and also appendix G of Ref. [269] for notes on the convergence of this series expansion. A similar procedure as described here can be performed for the two-particle Green's function (2.17). The corresponding results for the Dyson equation and self-energy are the Bethe–Salpeter equation (BSE) and the vertex  $\Gamma$  (often also denoted  $F$ ), which can be further classified by the Parquet decomposition [271, 272].

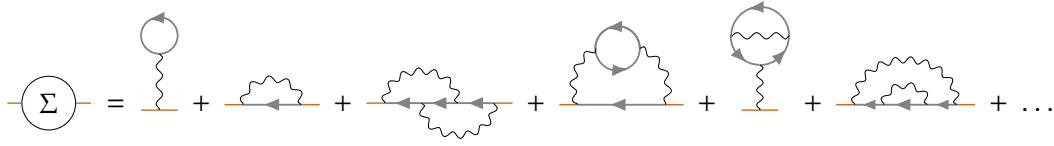


**Figure 2.5 – Low-order diagrams of the self-energy.** Feynman diagrams of the (irreducible) self-energy in first and second order of the interaction. Note that not all second-order diagrams are shown.

A qualitative interpretation of  $\Sigma$  is given by the spectral function which we discuss in the next section. The self-energy acts as the general turning knob for approximations, where the task of computing  $G$  is effectively shifted to determining  $\Sigma$ . In section 2.2.4, we will introduce the Luttinger–Ward functional as a powerful tool to generate approximations for  $\Sigma$ . We note that the self-energy is an auxiliary quantity, as it depends on the choice of the reference Green's function  $G_0$  used in the Dyson equation (2.26). Hence, the interacting Green's function can also be expressed by other quantities. For example, Ref. [273] introduces a time-dependent exchange-correlation potential instead of the self-energy.

### 2.2.3 Spectral representation and quasiparticles

Before turning to approximation schemes for the self-energy, we want to summarize a few important properties of Green's functions. To this end, we want to link the Green's function to experimental observables (cf. Figure 2.3) for which we need to extend the description to real frequencies  $\omega$ . This can be achieved by an analytic continuation of the Matsubara Green's function  $G(i\omega_n)$  to the retarded Green's function  $G^R(\omega + i0^+)$  evaluated slightly above the real axis ( $0^+$  is an infinitesimal part). This connection can be proven via the Lehmann representation [213].

If an analytic expression exists, one obtains the corresponding correlation function on real-frequencies by replacing  $i\omega_n \mapsto \omega + i0^+$ . For example, the interacting Green's function (2.27) becomes

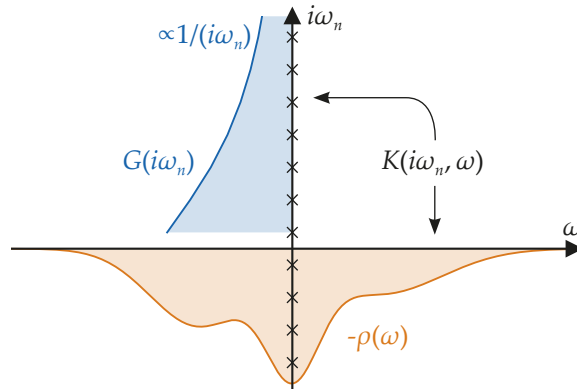
$$\underline{G}^R(\omega, \mathbf{k}) = \frac{\mathbb{1}}{(\omega + i0^+)\mathbb{1} - \underline{h}(\mathbf{k}) - \underline{\Sigma}(\omega, \mathbf{k})}. \quad (2.28)$$

On the other hand, one can write down the spectral representation of the imaginary-time Green's function [47] (indices of the Green's function suppressed)

$$G(\tau) = - \int_{-\infty}^{\infty} d\omega \underbrace{\frac{e^{-\omega\tau}}{1 + e^{-\beta\omega}} \rho(\omega)}_{K(\tau, \omega)}. \quad (2.29)$$

The kernel function  $K(\tau, \omega)$  connects  $G(\tau)$  to the spectral function  $\rho(\omega)$  describing the excitation spectrum of a system that is measured, e.g., in ARPES [44]. An

**Figure 2.6 – Lehmann representation.** Schematic representation of the Lehmann representation’s kernel  $K(i\omega_n, \omega)$  mapping the spectral function  $\rho(\omega)$  to the Matsubara Green’s function  $G(i\omega_n)$  on discrete frequencies  $\omega_n$  marked by crosses on the imaginary axis. The Matsubara Green’s function is smooth and decays with a characteristic  $1/(i\omega_n)$  tail at large frequencies. Note that the spectral function is plotted with a minus sign for illustrative purposes.



analogous expression can be obtained in Matsubara frequency space as

$$G(i\omega_n) = \int_{-\infty}^{\infty} d\omega K(i\omega_n, \omega)\rho(\omega) = \int_{-\infty}^{\infty} d\omega \frac{\rho(\omega)}{i\omega_n - \omega} \quad (2.30)$$

with the Fourier transformed kernel  $K(i\omega_n, \omega) = 1/(i\omega_n - \omega)$ .

In principle, one might try to obtain the spectral function by inverting the integral equation, either in  $\tau$  or  $i\omega_n$  formulation. It turns out, however, that the kernel is ill-conditioned and the inversion is an ill-posed problem [274]. These circumstances can be partially understood by noticing that the kernel is a very good filtering function, schematically drawn in Figure 2.6: The spectral function can generally have many (sharp) features, while the Matsubara Green’s function is smooth. This smoothness makes the imaginary-time formalism so convenient for computational methods because no sharp features need to be resolved.<sup>15</sup> This “filtering” property of the kernel arises from an exponential decay of singular values [I, 275], which shows us that the Matsubara Green’s function carries less information than its real-frequency counterpart. In section 2.5.1, we will discuss how this property can be used to generate a compact basis representation for imaginary-time Green’s functions.

Still, obtaining real-frequency information is of importance for comparison to experiments. Many different approaches exist and are continuously being developed, with numerous numerical libraries emerging. Commonly applied methods the Padé approximation [276–278], the maximum entropy method [278–283], stochastic approaches [284, 285], also combined with sparse modeling [286–288], neural networks [289], or Nevanlinna analytic continuation [290–292].

From the spectral representation of the imaginary-time Green’s function, it is possible to derive an approximate expression for the spectral weight at the Fermi

<sup>15</sup>There can, of course, arise numerical problems with the slow convergence of the Green’s function at high frequencies due to the  $1/(i\omega_n)$  decay. Typically, this can be mitigated by fitting of the moments of the high-frequency decay.



level ( $\omega = 0$ ) [268, 293]

$$-\frac{\beta}{\pi} G\left(\tau = \frac{\beta}{2}\right) \approx \rho(\omega = 0). \quad (2.31)$$

For low temperatures ( $\beta \rightarrow \infty$ ), this relation becomes exact. Thus,  $G(\tau = \beta/2)$  can be used as a qualitative indication for metallic or insulating behavior. Another signal is the low-frequency behavior of the imaginary part of the self-energy. To illustrate this connection, let us analyze the impact of the self-energy on the excitation spectrum. The spectral function can be obtained from the imaginary part of the retarded Green's function<sup>16</sup>

$$\rho_k(\omega) = -\frac{1}{\pi} \text{Im} G^{\text{R}}(\omega, \mathbf{k}) \stackrel{\text{Eq. (2.28)}}{=} \frac{1}{\pi} \frac{-\text{Im} \Sigma(\omega, \mathbf{k})}{[\omega - \varepsilon_k - \text{Re} \Sigma(\omega, \mathbf{k})]^2 + [\text{Im} \Sigma(\omega, \mathbf{k})]^2}. \quad (2.32)$$

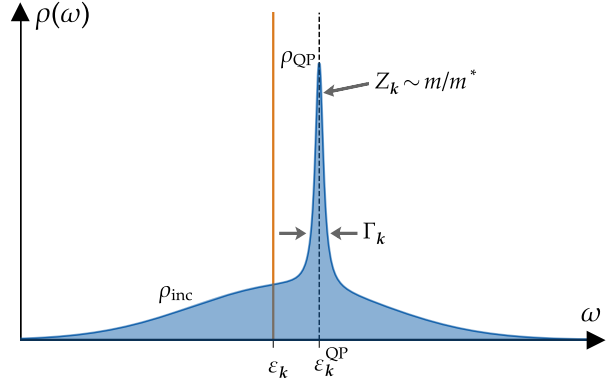
In the non-interacting case ( $\Sigma = 0$ ), this expression reduces to a  $\delta$ -peak picking out the energy  $\varepsilon_k$ . When interactions are introduced, two significant effects occur: The peak's position shifts due to the real part of the self-energy ( $\text{Re} \Sigma$ ), and its width increases because of the imaginary part of the self-energy ( $\text{Im} \Sigma$ ), resulting in a finite lifetime  $\tau \sim (\text{Im} \Sigma)^{-1}$  (cf. Figure 2.7).

If the imaginary part of the self-energy is small, the (shifted) excitation peak remains sharp describing long-lived particles. These are called quasiparticles (QPs) which can be regarded as non-interacting electrons with renormalized properties. The QP picture describes a Fermi liquid [44] that relies on the adiabatic connection between the ground states of interacting and non-interacting systems. Consequently, its validity is assured only when no gapped states arise during the transition from the non-interacting to the interacting system, as stated in the *Gell-Mann and Low theorem* [44]. Evaluating the imaginary part of the self-energy at the Fermi level ( $\omega = 0$ ) is crucial for distinguishing between the existence of finite-lived, low-energy single-particle excitations, characteristic of metallic states<sup>17</sup>, and the presence of a gap in the spectrum, typical of insulating states. Specifically, a divergence in  $|\text{Im} \Sigma(\omega \rightarrow 0)| \rightarrow \infty$  indicates that the lifetime  $\tau = 0$ , signifying an insulating state. This is to be differentiated from band insulators which can arise from the non-interacting single-particle picture alone or through a mean-field treatment of interaction effects [294].

<sup>16</sup>Some authors use a slightly different definition  $A(\omega) = -2 \text{Im} G^{\text{R}}(\omega)$  [213] for the spectral function, changing equations by a factor of  $2\pi$  since  $A(\omega) = 2\pi\rho(\omega)$ . Often, the notation of  $A$  and  $\rho$  is interchangeably used without differentiating the definitions.

<sup>17</sup>The scattering rate in a Fermi liquid scales as  $\tau_k^{-1} \propto \varepsilon_k^2 + \pi^2(k_{\text{B}}T)^2$  [44] with quadratic dependence on energy and temperature. As a consequence, the resistivity shares the same quadratic dependence  $\rho(T) = \rho_0 + AT^2$  as that of a metal. Hence, Fermi liquids can be regarded as metals with charge carriers similar to the underlying electrons but with renormalized properties. This is in contrast to many unconventional superconductors which have a so-called strange metal phase above the superconducting dome (cf. Figure 1.1a) with linear-in- $T$  scaling of the resistivity [36].

**Figure 2.7 – Quasiparticle spectral function.** The spectral function  $\rho(\omega)$  of a non-interacting system is a sharp delta peak (orange line) at the excitation energy  $\varepsilon_k$ . In the interacting case (blue), the corresponding QP peak  $\rho_{\text{QP}}$  is shifted to  $\varepsilon_k^{\text{QP}}$  while being broadened to a width of  $\Gamma_k$  and reduced weight  $Z_k \sim m/m^* < 1$ , where  $m^*$  is the effective mass. The QP peak is on top of an incoherent background  $\rho_{\text{inc}}$  due to interactions.



Interaction processes occur mostly at low-energies in an energy window of several  $k_B T$  around the Fermi level. Close to the Fermi level, the self-energy can be linearized

$$\Sigma(\omega, \mathbf{k}) \approx \text{Re} \Sigma(0, \mathbf{k}) + (1 - Z_k^{-1})\omega - i\Gamma_{0,k}, \quad (2.33)$$

where we introduced  $\Gamma_{0,k} = -\text{Im} \Sigma(0, \mathbf{k})$  and the QP weight or renormalization factor

$$Z_k = \frac{1}{1 - \left. \frac{\partial \text{Re} \Sigma(\omega)}{\partial \omega} \right|_{\omega=0}}. \quad (2.34)$$

Inserting the linearized self-energy in Eq. (2.32) yields

$$\rho_k(\omega) \approx \underbrace{\frac{Z_k}{\pi} \frac{\Gamma_k}{(\omega - \varepsilon_k^{\text{QP}})^2 + \Gamma_k^2}}_{\rho_{\text{QP}}} + \rho_{\text{inc}}(\omega) \quad (2.35)$$

with the QP scattering rate  $\Gamma_k = Z_k \Gamma_{0,k} = 1/(2\tau_k)$  connected to the QP lifetime  $\tau_k$  and the effective QP dispersion

$$\varepsilon_k^{\text{QP}} = Z_k[\varepsilon_k + \text{Re} \Sigma(0, \mathbf{k})]. \quad (2.36)$$

The spectral function of QP excitations (2.35) consists of the coherent part  $\rho_{\text{QP}}$  of the renormalized QPs, described by a Lorentzian shape, on top of an incoherent background  $\rho_{\text{inc}}$ . This is drawn in Figure 2.7. From the QP dispersion (2.36), it can be seen that the QP weight  $Z_k = m/m^* < 1$  describes an effective mass renormalization  $m^*$  due to interaction effects. In addition,  $Z$  represents the magnitude of the discontinuity in the occupation number at the Fermi surface, which for  $T = 0$  and  $\Gamma_k \rightarrow 0$  can be expressed as  $n_k = Z_k \Theta(-\varepsilon_k^{\text{QP}}) + \text{smooth background}$  [44].

The information of low-energy QPs is also encoded in the Matsubara Green's function and self-energy. A similarly performed linearization of the self-energy

yields the following relations

$$\Sigma(i\omega_n, \mathbf{k}) \approx \text{Re} \Sigma(i\omega_n \rightarrow 0, \mathbf{k}) + (1 - Z_k^{-1})i\omega_n - i\Gamma_{0,k}, \quad (2.37a)$$

$$\Gamma_k = Z_k \Gamma_{0,k} = -Z_k \text{Im} \Sigma(i\omega_n \rightarrow 0, \mathbf{k}) = \frac{1}{2\tau_k}, \quad (2.37b)$$

$$\varepsilon_k^{\text{QP}} = Z_k [\varepsilon_k + \text{Re} \Sigma(i\omega_n \rightarrow 0, \mathbf{k})], \quad (2.37c)$$

$$Z_k = \left[ 1 - \frac{\partial \text{Im} \Sigma(i\omega_n, \mathbf{k})}{\partial \omega_n} \Big|_{i\omega_n \rightarrow 0} \right]^{-1}. \quad (2.37d)$$

Most low-energy information is contained in the lowest Matsubara frequency [295], because of which the limit  $i\omega_n \rightarrow 0$  is often replaced by an evaluation at  $i\omega_0$ . Otherwise, the low-frequency behavior can be extracted by performing a polynomial fit to the first few Matsubara frequencies.

To end this section, we want to highlight that the Green's function encodes the relation between excitation and equilibrium properties. An illustrative example is the occupation  $n_{k\alpha}$  of an energy state  $\varepsilon_{k\alpha}$ . It is obtained from

$$n_{k\alpha} = \langle c_{k\alpha}^\dagger c_{k\alpha} \rangle = G_{\alpha\alpha}(\tau = 0^-, \mathbf{k}) = \int_{-\infty}^{\infty} d\omega f(\omega) \rho_\alpha(\omega) \quad (2.38)$$

with the Fermi function  $f(\omega) = 1/(e^{\beta\omega} + 1)$ . The connection to the spectral function  $\rho_\alpha$  is established by the Green's function, as the last equality can be derived from contour integration.

### 2.2.4 Luttinger–Ward functional

The Luttinger–Ward (LW) functional [296], denoted by  $\Phi[G]$ , is a central object in quantum field theoretical treatments of fermionic systems [269, 297]. It relates static quantities given by the grand-canonical potential  $\Omega = -\beta^{-1} \ln Z$  and dynamical quantities given by the single-particle Green's function  $G$  and self-energy  $\Sigma$  in the following way [269] (indices suppressed)<sup>18</sup>

$$\Omega[G] = \Omega_0 + \Phi[G] - \text{Tr}[\Sigma G] - \text{Tr}[\ln(1 - G_0 \Sigma)]. \quad (2.39)$$

Here,  $\Omega_0 = -\beta^{-1} \sum_k \ln(1 + e^{-\beta\varepsilon_k})$  is the non-interacting grand potential, and  $\text{Tr}[A] = 1/(\beta N_k) \sum_k \text{Tr} \underline{A}(k)$  denotes a trace over the spin-orbital matrix in combination with a summation over Matsubara frequencies and momentum. The LW functional  $\Phi[G]$  thereby connects the thermodynamic potentials of the interacting and non-interacting system.

<sup>18</sup>We here do not write the additional dependence of the  $\Omega$  and  $\Phi$  functionals on the specific model interaction  $U$ , which is implicitly assumed.

$$\Phi[G] = \text{Diagram 1} + \text{Diagram 2} + \text{Diagram 3} + \text{Diagram 4} + \text{Diagram 5} + \text{Diagram 6} + \dots$$

**Figure 2.8 – Skeleton diagram expansion of Luttinger–Ward functional.** Low-order expansion of the LW functional in terms of skeleton diagrams where solid lines denote dressed propagators. It includes first-order (Hartree–Fock (HF)), second-order, and a few third-order diagrams.

Formally,  $\Phi[G]$  can be derived from the Legendre transform of the free energy with respect to the bare propagator  $G_0$  [298] and it is possible to express it by an infinite series of closed skeleton diagrams [297, 299]:

$$\Phi[G] = \sum_n \frac{1}{2n} \Phi^n[G] = \sum_n \frac{1}{2n} \text{Tr}(G \Sigma^{S,n}[G]). \quad (2.40)$$

$\Sigma^{S,n}$  denotes the  $n$ -th order skeleton diagram self-energy contribution. In a skeleton diagram, bare propagator lines are replaced by dressed Green’s functions which include possible insertions of lower-order self-energy diagrams. For instance, the last two diagrams in Figure 2.5 include insertions of the second (Fock) diagram, which can be captured by rewriting the first two diagrams with a dressed propagator line. Figure 2.8 shows a few low-order diagrams contained in  $\Phi[G]$ . Importantly, the full self-energy can be derived from the LW functional by taking the functional derivative

$$\Sigma_{12}(k) = \frac{\delta \Phi[G]}{\delta G_{21}(k)}. \quad (2.41)$$

This relation is obtained from the condition of  $\Omega[G]$  being stationary for the exact Green’s function  $G$ , i.e.,  $\delta \Omega / \delta G = 0$ , which also reproduces the Dyson equation (2.26). Since the LW functional is a generating functional of the self-energy, it allows for a systematic construction of approximate self-energies, e.g., by only keeping certain classes of diagrams in  $\Phi[G]$  (see section 2.3). Any such “ $\Phi$ -derivable” self-energy and hence Green’s function is guaranteed to obey conservation laws [300, 301], because of which they are also called conserving approximation.

In addition to the perturbative expansion of the LW functional given in Eq. (2.40), it is possible to derive  $\Phi[G]$  in a non-perturbative way [302]. This is important because the LW functional and derived methods can encounter significant convergence problems, leading to unphysical solutions. A first indication for this is that the self-energy is a functional of the dressed Green’s function  $\Sigma[G]$ , rendering the Dyson equation,  $G = G_0 + G_0 \Sigma[G] G$ , a non-linear equation which is not guaranteed to converge [269]. Recently, it was more rigorously shown that these convergence issues stem from a multivalued nature of the LW functional [303–310], which is linked

to vertex divergences [113, 307, 311–315]. To mitigate these problems, applying appropriate constraints to the approximation methods is essential [302, 309, 316–319]. This consideration is crucial for the accurate identification and interpretation of phase transitions [320–322].<sup>19</sup> For example, in the case of the FLEX approximation, convergence to unphysical solutions is likely when the spin or charge susceptibility [Eqs. (2.47)] diverge, because of which it is necessary to constrain calculations to the paramagnetic case.

As a concluding thought, we want to mention that  $\Phi$ -derivable approximations fulfill conservation laws and the associated sum rules only on the one-particle level. They violate rigorous relations on the two-particle level like crossing symmetries. It is generally impossible to construct an approximation that is consistent on the single- and two-particle level, which is only possible for the exact solution. An in-depth discussion of this issue can be found in Ref. [324]. One can try to construct conserving approximations that at least fulfill some of the two-particle sum rules. This is baked into the two-particle self-consistency (TPSC) method [325–327], which enforces the Pauli principle to hold, as encoded in local sum rules of the spin and charge susceptibilities. This is achieved by adjusting effective spin and charge vertices while neglecting (self-consistent) renormalization for the single-particle Green's function. Recently, self-consistent renormalization feedback from the self-energy was included in variations of TPSC, which yields better agreement with diagrammatic Monte Carlo (DiagMC) for the expense of some of the rigor in fulfilling sum rules [328].

## 2.3 Perturbative approaches

In the previous sections, we have introduced many-body perturbation theory (MBPT) in the context of the LW functional to construct approximations to the full interacting many-body theory. In practice, one resorts to taking a particular class of diagrams since it is impossible to sum all diagrams.<sup>20</sup> Generally, two philosophies for constructing perturbative approaches can be followed.

The first method involves performing a truncated low-order expansion. For example, the first-order expansion corresponds to the Hartree–Fock (HF) approximation, which is represented by the first two diagrams of the LW functional in Figure 2.8. The second-order expansion, depicted by the third and fourth diagram in the same figure, is commonly known as second-order perturbation theory (SOPT), the  $GF^2$  method, or iterated perturbation theory (IPT) [330–332].

<sup>19</sup>Understanding the nature of the vertex divergencies and classifying convergence brackets of the LW functional and derived methods is a very active area of current research, see, e.g., Refs. [309, 310, 323] and references therein.

<sup>20</sup>DiagMC [329] tries to approximate this task through importance sampling within the configuration space of Feynman diagrams, systematically including contributions from both low- and high-order diagrams.

Alternatively, one can utilize partial resummation techniques which involve summing an infinite series of certain classes of (repeating) diagrams. The selection of diagrams is guided by their representation of specific physical processes that are expected to be dominating. An important example is the GW approach [227, 269, 333], which sums up an infinite series of bubble diagrams, like the third and sixth term depicted in Figure 2.8. The infinite series can be reformulated in terms of an effective interaction  $W$  that is screened by electronic interactions. The GW method can be performed with different degrees of self-consistency applied to the propagator  $G_{(0)}$ , the interaction  $W_{(0)}$ , or both, which all come with advantages and disadvantages [269, 334]. In this thesis, we apply the fluctuation exchange (FLEX) approximation [271, 335–337], which sums up an infinite series of ladder diagrams ( $T$ -matrix approach), like the fifth term in Figure 2.8, in addition to the bubble diagrams also contained in GW. It is discussed further below.

We note that perturbative approaches are limited by the interaction strength up to which either the truncation of the expansion becomes invalid or the partial summation of a class of diagrams runs outside its radius of convergence [305, 321]. In addition, they are not able to capture strong-coupling physics and phenomena like the interaction-induced Mott transition [9].

### 2.3.1 Fluctuation exchange approximation

The FLEX approximation [33, 271, 335–337] self-consistently incorporates the exchange of spin and charge fluctuations represented by an infinite series of bubble and ladder diagrams (cf. Figure 2.9). This makes FLEX suitable for studying systems with strong spin or charge fluctuations, e.g., close to magnetic phase transitions and quantum critical points [33]. Therefore, FLEX is often applied to study spin- and orbital-fluctuation-mediated superconductivity [33, 338–342], e.g., in cuprates [335, 343–346], organic superconductors [347–349], cobaltates [II, 350–352], iron-based superconductors [108, 353], or nickelates [109, 354].

Initially, FLEX had been formulated for normal-state calculations of the single-orbital Hubbard model on the square lattice to describe  $d$ -wave superconductivity in cuprates [335–337], effectively providing a microscopic foundation for phenomenological spin fluctuation theory [33]. Later, FLEX was extended to general lattice Hamiltonians [355] and multi-orbital systems [234, 356–358].<sup>21</sup> Due to the form of diagrams, FLEX can be regarded as a self-consistent generalization of the random-phase approximation (RPA), where the bare propagator is replaced by the dressed one [33].

---

<sup>21</sup>Often, only Ref. [357] is cited as it was the first work to include the FLEX equations for a local multi-orbital interaction of the Kanamori form (2.11). Note, however, that the equations in [357] contain a wrong second-order correction term, which incorrectly mixes spin and charge channel vertices. The correct equations only appear later [358], leading to some erroneous implementations as discussed in publication II.

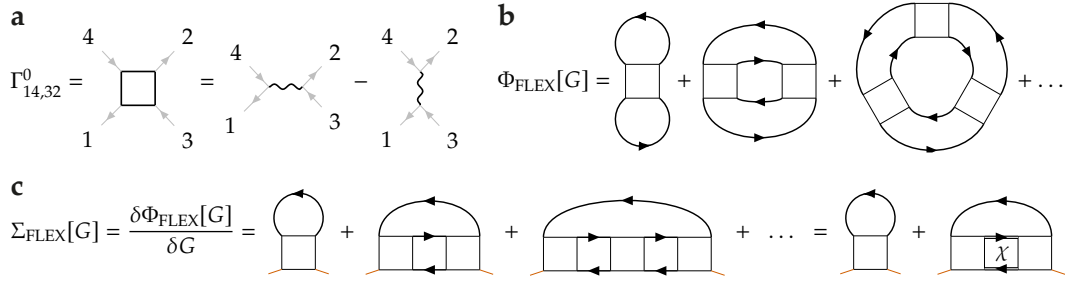


**Figure 2.9 – Diagrammatic representation of the FLEX approximation.** (a) Diagrammatic representation of the (bare) anti-symmetrized vertex  $\Gamma^0$  in Eqs. (2.43–2.44). (b) FLEX approximation of the LW functional  $\Phi$  consisting of closed loop diagrams with  $\Gamma^0$ . (c) Self-energy of the FLEX approximation obtained from taking the functional derivative  $\Sigma_{\text{FLEX}} = \delta\Phi_{\text{FLEX}}/\delta G$ . The resulting infinite series of bubble and ladder diagrams can be summed up to yield the susceptibility  $\chi$ .

The FLEX approximation can be regarded as a zeroth-order to the parquet approach, where the irreducible vertex is replaced by the bare one and no coupling between different channels exists [271]. A common approximation comprises neglecting contributions of the particle-particle ladder diagrams to the normal-state self-energy, which often goes unmentioned in the literature [321].<sup>22</sup> We adopt this approximation here and we summarize the FLEX formalism for local multi-orbital interaction of the Kanamori form (2.11) in the following. A derivation can be found in Ref. [47]. In section 3.4.1, we discuss spin-fluctuation-mediated superconductivity as described by FLEX-like diagrams contributing to the particle-particle channel.

To treat multi-orbital interactions, it is convenient to introduce the anti-symmetrized (particle-hole) vertex  $\Gamma$  [43]

$$H_{\text{int}} = \frac{1}{4} \sum_{1234} \Gamma_{14,32} c_1^\dagger c_2^\dagger c_3 c_4, \quad (2.42)$$

which connects to the general interaction  $U_{14,32}$  matrix elements in Eq. (2.1) as

$$\Gamma_{14,32} = U_{14,32} - U_{13,42}. \quad (2.43)$$

By assuming the Kanamori-Hubbard interaction for  $U_{14,32}$ , the vertex reduces to  $\Gamma_{14,32} \equiv \delta_{i_1 i_2} \delta_{i_1 i_3} \delta_{i_1 i_4} \Gamma_{14,32}^0$  with the local and bare (unrenormalized) antisymmetrized vertex  $\Gamma_{14,32}^0$ . The bare antisymmetrized vertex is given by

$$\begin{aligned} \Gamma_{14,32}^0 &= -\frac{1}{2} U_{l_1 l_4, l_3 l_2}^s \tau_{\sigma_1 \sigma_4} \cdot \tau_{\sigma_2 \sigma_3} + \frac{1}{2} U_{l_1 l_4, l_3 l_2}^c \delta_{\sigma_1 \sigma_4} \delta_{\sigma_2 \sigma_3} \\ &= \frac{1}{2} [U^s + U^c]_{l_1 l_4, l_3 l_2} \delta_{\sigma_1 \sigma_4} \delta_{\sigma_2 \sigma_3} - U_{l_1 l_4, l_3 l_2}^s \delta_{\sigma_1 \sigma_3} \delta_{\sigma_2 \sigma_4} \end{aligned} \quad (2.44)$$

<sup>22</sup>In the original work by Bickers et al. [335], the contribution of both particle-hole (ph) and particle-particle (pp) ladder diagram series were considered. Numerous later works disregard the latter and the name ‘‘FLEX’’ is ambiguously used to refer to both approaches, with and without pp ladder.

with the (bare) spin and charge vertex  $U^s$  and  $U^c$ , respectively. In the second line, we have used the Pauli matrix identity  $\tau_{14} \cdot \tau_{23} = 2\delta_{13}\delta_{24} - \delta_{14}\delta_{23}$ . The bare interaction vertices are specified as

$$U_{14,32}^s = \begin{cases} U \\ U' \\ J \\ J \end{cases}, \quad U_{14,32}^c = \begin{cases} U & \text{if } 1 = 2 = 3 = 4 \\ -U' + 2J & \text{if } 1 = 3 \neq 2 = 4 \\ 2U' - J & \text{if } 1 = 4 \neq 2 = 3 \\ J & \text{if } 1 = 2 \neq 3 = 4 \end{cases}. \quad (2.45)$$

Since FLEX works with the bare vertex and neglects any corrections, the interaction parameters  $U, U', J$  should be regarded as effectively screened quantities [33]. This makes the direct comparison to other methods using the same interaction parameters not straightforward.

The diagrammatic representation of the antisymmetrized vertex is a four-legged box (Figure 2.9a) and diagrams generated with it are referred to as Hugenholtz diagrams. The Hugenholtz diagrams of the bubble and ph-ladder series for the LW functional and corresponding self-energy are drawn in Figure 2.9, panels b and c. Starting from the second-order diagram, the irreducible (particle-hole) susceptibility defined by

$$\chi_{ll',mm'}^0(q) = -\frac{1}{\beta N_k} \sum_k G_{lm}(k+q) G_{m'l'}(k) \quad (2.46)$$

is inserted between bare vertices  $\Gamma^0$ , which is infinitely repeated. Hence, the diagrams can be resummed in terms of a geometric series, leading to the BSE of the susceptibility  $\tilde{\chi}$ . In case of SU(2) symmetry, the BSE can be solved for spin and charge channel separately, leading to RPA-like expressions

$$\underline{\chi}^s(q) = \underline{\chi}^0(q) \sum_n \left[ \underline{U}^s \underline{\chi}^0(q) \right]^n = \underline{\chi}^0(q) [\mathbb{1} - \underline{U}^s \underline{\chi}^0(q)]^{-1} \quad (2.47a)$$

$$\underline{\chi}^c(q) = \underline{\chi}^0(q) \sum_n \left[ -\underline{U}^c \underline{\chi}^0(q) \right]^n = \underline{\chi}^0(q) [\mathbb{1} + \underline{U}^c \underline{\chi}^0(q)]^{-1} \quad (2.47b)$$

of the spin and charge susceptibility, respectively. We have written the susceptibilities and bare interaction vertices as matrices in orbital space, since the 4-tensor indices can be grouped as  $14, 32 \equiv a, b$ , rendering expressions like  $\underline{U}^s \underline{\chi}^0(q)$  a simple product of matrices with size  $N_\alpha^2 \times N_\alpha^2$ , where  $N_\alpha$  is the number of (Wannier) orbitals. The effective interaction that is obtained after resummation is given by

$$\underline{\mathcal{V}}(q) = \frac{3}{2} \underline{U}^s \left[ \underline{\chi}^s(q) - \frac{1}{2} \underline{\chi}^0(q) \right] \underline{U}^s + \frac{1}{2} \underline{U}^c \left[ \underline{\chi}^c(q) - \frac{1}{2} \underline{\chi}^0(q) \right] \underline{U}^c + \frac{3}{2} \underline{U}^s - \frac{1}{2} \underline{U}^c. \quad (2.48)$$



Note that the subtracting terms  $\sim \chi^0/2$  occur in order to not double count the second order contributions. With this interaction, the FLEX self-energy can be calculated as

$$\Sigma_{lm}(k) = \frac{1}{\beta N_k} \sum_q \sum_{l'm'} \mathcal{V}_{l'l',mm'}(q) G_{l'm'}(k-q). \quad (2.49)$$

In practical calculations, Eqs. (2.46) to (2.49) are solved self-consistently. The typical starting point is the non-interacting Green's function  $G_0$  (2.21) and mixing is applied when calculating the full Green's function from the Dyson equation (2.27), i.e.,  $G^n = \kappa G^n + (1 - \kappa)G^{n-1}$  for iteration step  $n$  with  $\kappa \leq 0.5$ . In each iteration, the chemical potential  $\mu$  is adjusted by solving Eq. (2.38) for a set filling  $n = \sum_{k\alpha} n_{k\alpha}$ . Note that in order to assure convergence to a physical solution, it is important to constrain the calculations to the paramagnetic case by preventing the spin and charge susceptibility from diverging.<sup>23</sup> The largest eigenvalues of the respective BSE kernels  $\alpha_{s,c} = \max_q [\pm \underline{U}^{s,c} \underline{\chi}^0(q)]$ , called Stoner enhancement factors, can be used as a proxy for the strength of spin and charge fluctuations and the system's tendency towards phase instabilities.

## 2.4 Green's function embedding methods

A hallmark of strongly correlated systems is the interaction-driven metal-to-insulator (Mott) transition [9, 10], which emerges as the interaction strength becomes comparable to the kinetic energy of electrons. In the process, the system begins to behave more like an atomic system and bandstructure theory becomes invalid. In the evolution between non-interacting limit and atomic limit, a gap opens and the Gell-Mann and Low theorem is inapplicable. Hence, the perturbative treatment of interaction effects becomes insufficient in case of strong correlations.

A different approach needs to be taken where quantum embedding methods [114, 269, 361, 362] are promising. The general idea is to treat correlations only in a subsystem by self-consistently mapping the full system to an auxiliary system describing the subsystem. An important example in this context is spatial embedding, where an impurity (cluster) is locally embedded in a non-interacting background of particles. This is the idea of dynamical mean-field theory (DMFT) [111, 363], which we will review in the following. As DMFT has become a widely used approximation, we refer to (pedagogical) reviews and books such as Refs. [111, 114, 115, 227, 269, 364, 365] for more details.

<sup>23</sup>FLEX obeys the Mermin-Wagner theorem [359] preventing antiferromagnetic long-range order to occur in two dimensions [360], since the self-energy damping effect of the self-consistent feedback from fluctuation exchange effectively keeps the susceptibility from diverging. In numerical calculations however, this can only be assured by implementing constraints.

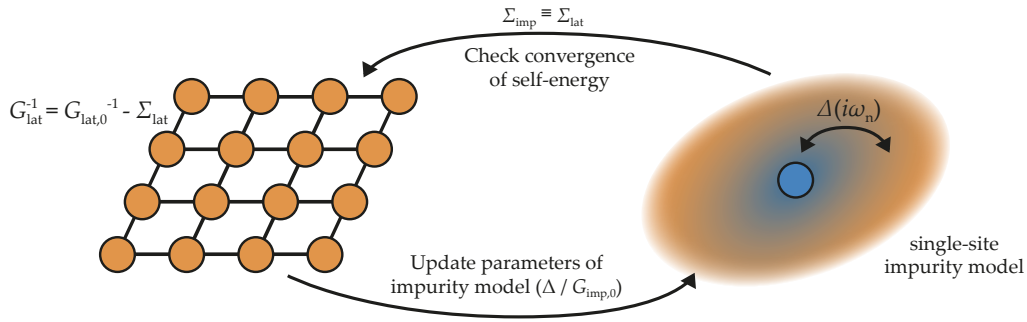


**Figure 2.10 – Schematic visualization of spatial embedding in DMFT.** The lattice model, described by the (momentum-dependent) lattice Green’s function  $G_{\text{lat}}$ , is mapped onto an auxiliary system represented by the single-site impurity model embedded into a bath (visualized as a homogeneous background). The coupling to the bath is described by the hybridization function  $\Delta(i\omega_n)$  which encodes the information of the original lattice model. Solving the impurity model yields a self-energy that is self-consistently fed back into the lattice model.

### 2.4.1 Dynamical mean-field theory

DMFT is designed to describe correlated electron systems with strong local interactions. It has become one of the most widely applied methods for studying strong correlation effects in material calculations [114, 115]. The general approximation of DMFT is to freeze out non-local fluctuations (in a spatial mean-field) and to treat all local correlation effects, which allows to capture Mott physics [9, 111].

Historically, DMFT was developed by investigating the limit of infinite dimensions  $d$ , or equivalently, infinite coordination  $z$  of a lattice, where  $z$  is the number of nearest-neighbor sites. A scaling argument by Metzner and Vollhardt [256], which was generalized by Müller-Hartmann [366], showed that a normalization of the kinetic hopping  $t = t^*/\sqrt{z}$  is necessary to have a non-trivial, finite contribution of the kinetic energy in the limit  $z \rightarrow \infty$ . As a consequence, only local skeleton diagrams contribute to the self-energy, i.e., it simplifies to  $\Sigma_{ij}(i\omega_n) = \delta_{ij}\Sigma(i\omega_n)$ . Building on these results, Georges and Kotliar [363] recognized that in infinite dimensions, a many-body lattice model like the Hubbard model can be mapped onto an Anderson impurity model subject to a self-consistent bath.<sup>24</sup> This is the core idea of DMFT: Local correlations in an interacting lattice model can be described by mapping it to a self-consistently embedded, auxiliary quantum-impurity model (Figure 2.10). The mapping becomes exact in the limit of infinite coordination, e.g., for the Bethe lattice, but remains a good approximation for (realistic) three-dimensional lattices and serves as a reasonable starting point for two-dimensional systems.

<sup>24</sup>See also related works by Jarrel [367] and Ohkawa [368]. We note that making the connection to impurity models accelerated the study of strongly correlated lattice systems as impurity models have been well-studied at that time [369] with a variety of efficient numerical techniques such as quantum Monte Carlo (QMC) methods to solve them.

Many different techniques exist to derive the equations of DMFT [111, 115, 269], such as the cavity construction within a path-integral formalism [44, 214], from the lowest-order approximation of the dual fermion approach [370, 371], or via the LW functional [114, 302], rendering DMFT a non-perturbative conserving approximation. We do not show the full derivation here but summarize and motivate the results.

### Mapping to a self-consistent impurity problem

The central idea of DMFT is the self-consistent mapping of the lattice Hamiltonian [Eq. (2.1)] with local interactions [Eq. (2.11)] on an effective Anderson impurity model:

$$H_{\text{AIM}} = H_{\text{imp}} + H_{\text{bath}} + H_{\text{hyb}} . \quad (2.50)$$

The model consists of impurity and bath electrons, which are coupled by a hybridization term. The parts are specified for a multi-orbital model by

$$H_{\text{imp}} = \sum_{\alpha\sigma} \varepsilon_{d,\alpha} d_{\alpha\sigma}^\dagger d_{\alpha\sigma} + \frac{1}{2} \sum_{\alpha\beta\gamma\delta,\sigma\sigma'} U_{\alpha\delta,\gamma\beta} d_{\alpha\sigma}^\dagger d_{\beta\sigma'}^\dagger d_{\gamma\sigma'} d_{\delta\sigma} \quad (2.51a)$$

$$H_{\text{bath}} = \sum_{k,n\sigma} \varepsilon_{k,n} c_{kn\sigma}^\dagger c_{kn\sigma} \quad (2.51b)$$

$$H_{\text{hyb}} = \sum_{k,\alpha n\sigma} V_{k,\alpha n} d_{\alpha\sigma}^\dagger c_{kn\sigma} + V_{k,n\alpha}^* c_{kn\sigma}^\dagger d_{\alpha\sigma} \quad (2.51c)$$

with electrons on the impurity being described by  $d^{(\dagger)}$  operators for the impurity levels  $\varepsilon_{d,\alpha}$  labeled by  $\alpha$ , bath electrons denoted by  $c^{(\dagger)}$  operators for (dispersing) bath energies  $\varepsilon_{kn}$ , and hybridization (“hopping”)  $V_{k,\alpha n}$  between impurity and bath. The bath can be integrated out in a path-integral formalism<sup>25</sup> [111], yielding the effective action

$$\begin{aligned} S_{\text{imp}}[d^*, d] = & - \int_0^\beta d\tau d\tau' \sum_{\alpha\beta,\sigma} d_{\alpha\sigma}^*(\tau) [\underline{G}_{\text{imp},0}^{-1}]_{\alpha\beta}(\tau - \tau') d_{\beta\sigma}(\tau') \\ & + \frac{1}{2} \int_0^\beta d\tau \sum_{\alpha\beta\gamma\delta,\sigma\sigma'} U_{\alpha\delta,\gamma\beta} d_{\alpha\sigma}^*(\tau) d_{\beta\sigma'}^*(\tau) d_{\gamma\sigma'}(\tau) d_{\delta\sigma}(\tau) \end{aligned} \quad (2.52)$$

with Grassman variables  $d$  and  $d^*$  [44] and the non-interacting impurity Green's function  $G_{\text{imp},0}$ . On Matsubara frequencies, it is given by

$$\underline{G}_{\text{imp},0} = [i\omega_n \mathbb{1} - \underline{\varepsilon}_d - \underline{\Delta}(i\omega_n)]^{-1} , \quad (2.53)$$

<sup>25</sup>Equivalently, one can employ the equation-of-motion technique for the impurity Green's function to decouple bath degrees of freedom.

which includes the frequency-dependent hybridization function

$$\Delta_{\alpha\beta}(i\omega_n) = \sum_{kn} \frac{V_{k,\alpha n}^* V_{k,n\beta}}{i\omega_n - \varepsilon_{kn}} \quad (2.54)$$

obtained from integrating out the bath degrees of freedom. In the expression for  $G_{\text{imp},0}$ , the hybridization function takes on the role of a self-energy as an effective potential that encodes the information about the bath by weighting the bath energy poles with  $V_{k,\alpha n}$ . We note that  $G_{\text{imp},0}$  is often referred to as *dynamical* Weiss field in analogy to static mean-field theory.

The numerically demanding part of DMFT consists of solving the impurity problem defined by the action in Eq. (2.52). For this purpose, many different numerical solvers have been developed [269], like the IPT [111, 363], exact diagonalization (ED) [372, 373], numerical renormalization group (NRG) [374], density matrix renormalization group (DMRG) [375, 376], or continuous-time quantum Monte Carlo (CT-QMC)-based methods [377]. In publications III and VI, we employ CT-QMC within the hybridization expansion (CT-HYB) variant [378–382], which utilizes a strong-coupling expansion. It has the advantage over weak-coupling expansion methods like CT-INT [383] or CT-AUX [384] that the computational cost decreases with correlation strength and it is easier to treat non-density-density interactions like the Hund’s coupling [377, 385]. A pedagogical introduction to CT-QMC solvers can be found in chapter 5 of Ref. [365].

The mapping of the full lattice model is effectively performed by demanding that the local Green’s function  $G_{\text{loc}}$ , obtained from summing over the momentum dependence of the lattice Green’s function  $G_{\text{lat}}$  [Eq. (2.27)], is equal to the impurity Green’s function  $G_{\text{imp}}$ , i.e.,

$$\underline{G}_{\text{loc}}(i\omega_n) = \frac{1}{N_k} \sum_{\mathbf{k}} \underbrace{[i\omega_n \mathbb{1} - \underline{h}(\mathbf{k}) - \underline{\Sigma}(i\omega_n)]^{-1}}_{\underline{G}_{\text{lat}}(i\omega_n, \mathbf{k})} \stackrel{!}{=} \underline{G}_{\text{imp}}(i\omega_n) \quad (2.55)$$

with the non-interacting lattice Hamiltonian  $h(\mathbf{k})$  (2.7a). Here, we have already inserted the local approximation of the self-energy, leading to the association  $\underline{\Sigma}_{\text{lat}}(i\omega_n, \mathbf{k}) \approx \underline{\Sigma}_{\text{imp}}(i\omega_n) \equiv \underline{\Sigma}(i\omega_n)$ . Since we have the identity between local and impurity Green’s function, the lattice and impurity problems are connected by the impurity model’s Dyson equation. Calculating  $G_{\text{loc}}$  allows for determining the Weiss function (frequency dependence suppressed)

$$\underline{G}_{\text{imp},0} = [\underline{G}_{\text{loc}}^{-1} + \underline{\Sigma}]^{-1} \quad (2.56)$$

or equivalently hybridization function  $\Delta(i\omega_n)$ . On the other hand, we can obtain the self-energy given that the impurity problem (2.52) with  $G_{\text{imp},0}$  as an input has been solved, i.e., an interacting Green's function  $G_{\text{imp}}(i\omega_n)$  has been computed:

$$\underline{\Sigma} = \underline{G}_{\text{imp},0}^{-1} - \underline{G}_{\text{imp}}^{-1}. \quad (2.57)$$

To conclude, we summarize the DMFT self-consistency loop, as schematically shown in Figure 2.10:

1. Start with an initial self-energy  $\Sigma$  (e.g., non-interacting  $\Sigma = 0$  or previous solution).
2. Calculate the local (on-site) Green's function  $G_{\text{loc}}(i\omega_n)$  from Eq. (2.55).
3. Calculate the non-interacting impurity Green's function  $G_{\text{imp},0}(i\omega_n)$  from Eq. (2.56).
4. Solve the interacting impurity model defined by the effective action in Eq. (2.52) to obtain  $G_{\text{imp}}(i\omega_n)$ .
5. Calculate new self-energy  $\Sigma(i\omega_n)$  from Eq. (2.57).
6. Go back to step 2 until convergence of the self-energy. Additionally, the equality  $G_{\text{loc}}(i\omega_n) = G_{\text{imp}}(i\omega_n)$  can be used to check convergence.

### Beyond the local limit of dynamical mean-field theory

A limiting factor of DMFT is that it only addresses local fluctuations, which is not sufficient for many materials and phenomena like unconventional superconductivity, where non-local fluctuations play a critical role [34, 117]. Over the past decades, the toolbox of DMFT-based approaches has been greatly extended to also take into account non-local fluctuations. These developments can be categorized into two distinct routes of improving DMFT:

The first approach is given by cluster extensions of DMFT [112]. The idea is to increase the size of the embedded impurity model by considering interacting cluster of size  $N_c$  in a non-interacting, self-consistent bath. Then, spatial correlations are treated exactly up to length-scales of the cluster size, such that  $N_c$  acts as a control parameter and the solution becomes identical to the lattice model for  $N_c \rightarrow \infty$ . The enlarged cluster can either be constructed via patching in momentum space within the dynamical cluster approximation (DCA) [93, 94, 118, 386] or by larger real-space clusters within cellular DMFT (CDMFT) [387–390].

The second approach comprises diagrammatic extensions [113] that incorporate non-local corrections to the self-energy. These methods adopt various strategies, including the assumption of locality in higher-order particle vertices, as utilized in the

triply irreducible local expansion (TRILEX) [391, 392], the quadruply irreducible local expansion (QUADRILEX) [393], and the dynamical vertex approximation (DΓA) [394–396]. Other strategies involve combining DMFT with functional renormalization group methods [397]; performing (diagrammatic) perturbation theory for a reference system (dual space) with the local solution by DMFT as the starting point, as implemented in dual fermion (DF) [370, 371], dual boson (DB) [398], or dual TRILEX (D-TRILEX) [399–401]; and integrating DMFT with MBPT approaches [305] such as DMFT+GW [402, 403], DMFT+FLEX [404, 405], or DMFT+TPSC [406–409].

## 2.5 Low-rank representation of Green’s functions

The Green’s function method, as previously introduced, is a powerful tool for investigating correlated materials and emerging phases therein. Significant advancements in recent decades have been primarily fueled by improvements in computing power, which have made it possible to employ more sophisticated techniques, such as extensions of DMFT, across broader parameter ranges and with enhanced accuracy [211]. However, the application to realistic systems still poses considerable computational challenges due to the intrinsic complexity of real materials. This complexity stems from the interplay of many degrees of freedom and energy scales of different (competing) phenomena in condensed matter physics, spanning multiple orders of magnitude. An overview of characteristic energy scales in condensed matter systems is provided in Figure 2.11. For instance, low-temperature phenomena such as superconductivity occur at much smaller thermal energies (0.1–10 meV) than electronic band excitation and electronic screening (0.1–10 eV), encompassing up to four orders of magnitude.

In imaginary-time Green’s function-based methods, the relevant energy scales are set by the system’s Hamiltonian (overall energy range / ultraviolet (UV) scale limit, e.g., bandwidth  $W$ ), the characteristic energy of the investigated many-body phenomenon (desired accuracy / infrared (IR) scale limit), and the temperature (energy resolution  $\Delta\omega_n \sim \beta^{-1}$ ). The most common approach to numerically represent Matsubara Green’s functions is by sampling frequency points on a uniform grid. For this naive sampling, the required number of frequencies  $N_{\omega_n}$  for a numerical accuracy  $\epsilon$  scales as  $N_{\omega_n} \sim \mathcal{O}(\Lambda\epsilon^{-p})$ , with  $p \geq 1$  and  $\Lambda = \beta\omega_{\max}$  being a dimensionless cutoff that depends on inverse temperature  $\beta$  and frequency cutoff  $\omega_{\max}$  (UV limit). The linear scaling of sampling points with respect to  $\beta$  makes calculations at low-temperatures prohibitively expensive. In combination with the many degrees of freedom, which necessitate the employment of multi-orbital models, the accessible parameter space and range of applicable methods for material-realistic calculations is limited. These issues are amplified in the case of two-particle or

## 2.5 Low-rank representation of Green's functions

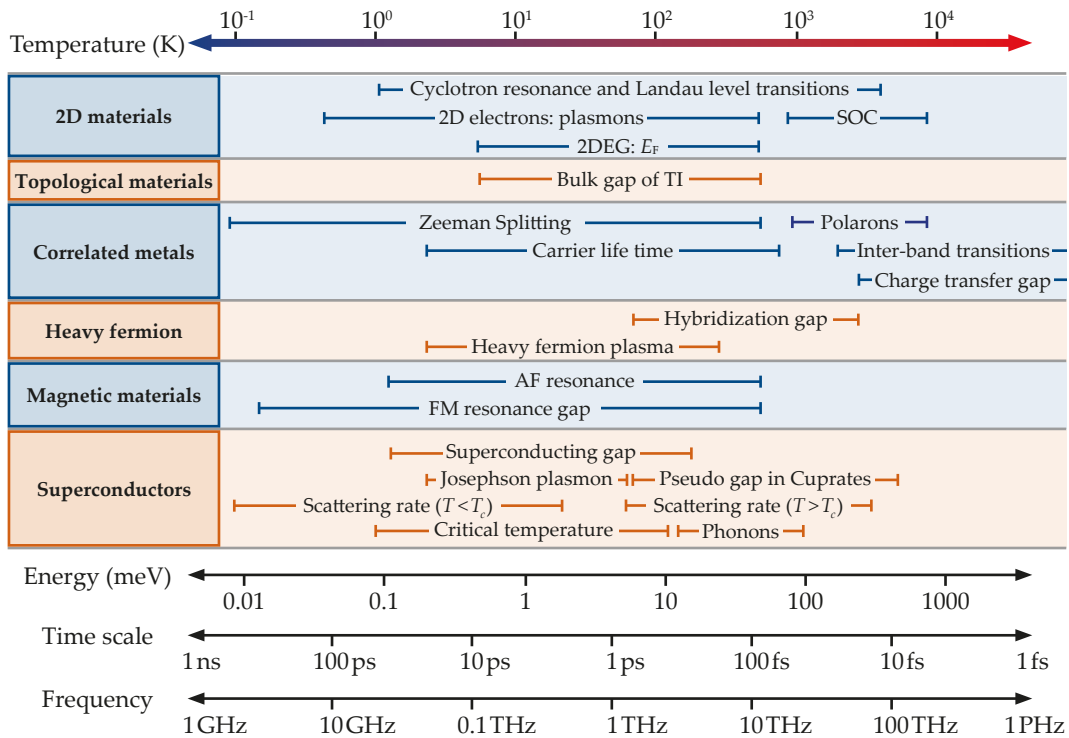


**Figure 2.11 – Energy scales of elementary excitations and collective modes in quantum materials.** Schematic representation of typical energy scales for different phenomena found in condensed matter systems. This figure is adapted from Ref. [410].

higher-order response functions [411], as they depend on multiple time, space, and orbital indices.

Recently, theoretical progress has been made to address these computational bottlenecks by constructing compact and compressed representations for the single-particle Matsubara Green's function. These include the expansion in orthogonal polynomials, like the Legendre [412, 413] or Chebyshev [414] bases, power-mesh representations [415, 416], construction of optimal quadrature rules for Matsubara summation [417], or wavelet representations [418]. For instance, the orthogonal polynomial expansion improves the frequency scaling<sup>26</sup> to  $\mathcal{O}(\sqrt{\Lambda} \log \epsilon^{-1})$ , because of which it has become a standard implementation in QMC-based impurity solvers [380, 381, 419, 420].

An optimal basis representation for single-particle Green's functions is given by the intermediate representation (IR) basis [I, 274, 275, 421] in combination with sparse sampling [330, 422], and the closely related discrete Lehmann representation (DLR) [423, 424]. These approaches start from the a priori knowledge of the ill-conditioning of the spectral representation kernel  $K(\tau, \omega)$  that connects Matsubara Green's function and spectral function in Eq. (2.29), which is reflected in an exponen-

<sup>26</sup>A comparison of scaling behavior for different methods can be found in Ref. [413].

tially fast decaying singular values [275]. This enables a low-rank decomposition of the kernel, yielding very compact sets of basis functions whose size scales only with  $O(\log \Lambda \log \epsilon^{-1})$ . In addition, the method of sparse sampling allows for the construction of compact grids in imaginary time and Matsubara frequency, from which the IR coefficients can be derived. We developed the code library `sparse-ir` [I], which provides routines to compute the IR basis and associated grids. This is discussed in detail in the embedded publication I below.

A complimentary approach to the low-rank decomposition of many-body propagators is given by quantum tensor train (QTT) representation [425–427], which is more commonly known in the condensed matter community as matrix product states used, e.g., in DMRG [375]. The low-rank tensor representation enables, in principle, not only a compression of imaginary time or frequency information but of the whole tensor structure of many-body correlation functions. The application of this approach to practical many-body calculations remains to be shown, but the prospects from proof-of-principle compression of typical many-body objects [425] appear promising. One point where it could contribute to more efficient implementations is the representation of lattice degrees of freedom. The momentum-grid construction and corresponding resolution of lattice quantities like Green’s functions is a remaining bottleneck at low temperatures, affecting the accuracy of momentum derivatives or Brillouin zone integration pertinent to all condensed matter calculations. Approaches to mitigate these problems have been developed, e.g., adaptive  $k$ -space sampling methods [428–431], but they are typically model or problem specific approaches.

### 2.5.1 Intermediate representation basis

The IR basis in combination with sparse sampling provides a simple framework for efficient implementations of quantum field theoretical methods. It has been applied in many different contexts, such as phonon-mediated superconductivity [432–435] (available in the Migdal–Eliashberg solver of the EPW code [436–438]), unconventional superconductivity [III] within the FLEX approximation [II, IV, V, 439], estimation of magnetic interactions [440–442], analytic continuation [286, 287, 290, 291], or TPSC calculations [328, 406, 409]. In addition, extensions to two-particle propagators with the overcomplete IR approach [443–446] have been developed.

We briefly want to summarize the general idea of the IR basis and sparse sampling to compare it to the closely related DLR. More details can be found in the original works [275, 330, 421], the pedagogical reviews in Refs. [274, 422], and publication I describing the implementation within the `sparse-ir` code library. Explanations and guides of how to use the IR basis in practical many-body calculations are provided by the extensive tutorials of the code package [I].



The IR basis is derived from the singular value expansion of the spectral kernel

$$K(\tau, \omega) = \frac{e^{-\tau\omega}}{1 + e^{-\beta\omega}} = \sum_{l=0}^{\infty} U_l(\tau) S_l V_l(\omega) \quad (2.58)$$

with singular values  $S_l$ , and the IR basis functions  $\{U_l(\tau)\}_l$  and  $\{V_l(\omega)\}_l$ . The expansion (2.58) is unique for a given dimensionless parameter  $\Lambda = \beta\omega_{\max}$ , where the frequency cutoff  $\omega_{\max}$  is chosen such that the spectrum  $\rho(\omega)$  is bounded in the interval  $[-\omega_{\max}, \omega_{\max}]$ . The sets of functions  $\{U_l(\tau)\}_l$  and  $\{V_l(\omega)\}_l$  constitute complete orthogonal polynomial bases for which currently no analytic expression exists. Their properties have been studied numerically [447], which showed that Legendre polynomials are recovered from the IR basis functions in the limit  $\Lambda \rightarrow \infty$ .

The singular values  $S_l$  decay exponentially fast (cf. Figure 1 in publication I), giving rise to the ill-conditioning of analytic continuation; see the discussion in section 2.2.3. The exponential decay reflects that  $K(\tau, \omega)$  can be represented to high accuracy by a low-rank decomposition, i.e., only relying on a few basis functions. In fact, the truncation error for truncating at order  $L$  scales as  $\epsilon_L \sim S_L/S_0 \sim e^{-aL}$ .

We can utilize the low-rank structure and expand the imaginary-time Green's function in the  $U_l(\tau)$  basis, or the corresponding Fourier transformed expression, as

$$G(\tau) = \sum_{l=0}^{L-1} G_l U_l(\tau) + \epsilon_L, \quad (2.59a)$$

$$G(i\omega_n) = \sum_{l=0}^{L-1} G_l U_l(i\omega_n) + \epsilon_L. \quad (2.59b)$$

These series expansions are well controlled by a given  $\Lambda$  and desired accuracy  $\epsilon_L$ . In order to accurately perform calculations on Matsubara frequencies (e.g. solving the Dyson equation) or the imaginary time domain (e.g. evaluating self-energy diagrams) it is sufficient to use a non-linear, sparsely sampled grid  $\{\bar{\omega}_n\}/\{\bar{\tau}_k\}$  that can be generated from the extrema of the IR basis functions. The resulting  $\tau$  mesh is more densely sampled close to the interval edges of 0 and  $\beta$ , while the  $\omega_n$  grid is dense at small frequencies and almost logarithmically spaced at high frequencies, see Figure 2 in Ref. [330]. To give a feeling for the reduction in size, we note that for an IR parameter  $\Lambda = 10^4 - 10^5$ , the basis size and number of necessary grid points are on the order of 100 or fewer, cf. Fig. 1 in publication II. These values for  $\Lambda$  correspond to  $\beta$  values between  $10^3$  to  $10^4$  for  $\omega_{\max} = 10$ . In comparison, achieving the same level of accuracy with a uniform grid typically demands a few thousands to tens of thousands Matsubara frequencies.

The construction of the IR basis and associated sparse grids is to be differentiated from the DLR [423, 424]. The DLR is obtained from an interpolative decomposition

of the kernel  $K(\tau, \omega)$ , which yields basis functions  $K(\tau, \omega_l) \sim e^{-\tau\omega_l}$ . This has the advantage of an analytic expression for the basis functions (exponentials), at the expense of them forming a non-orthogonal basis. The sparse sampling grid of the IR basis is substituted by the interpolation grid used to compute the DLR basis functions via the pivoted QR method. These differences do not show up in practice for the user of these frameworks. Whether to choose the IR or DLR basis depends on the particular type of application and given code environment.<sup>27</sup>

### **sparseIR code utility**

We summarize the utilities of the code library `sparse-ir` with python, julia, and fortran programming language support. The main features include:

- On-the-fly construction of basis functions  $\{U_l(\tau)\}$ ,  $\{U_l(i\omega_n)\}$ , and  $\{V_l(\omega)\}$  as well as sparse sampling grids  $\{\bar{\tau}_k\}$ ,  $\{i\bar{\omega}_n\}$  for a given input  $\Lambda$  and  $\epsilon$ .
- Fitting routines to recover IR coefficients from arbitrary imaginary-time or Matsubara frequency grids.
- Evaluation of IR coefficients on arbitrary imaginary-time or Matsubara frequency grids.
- Extensive tutorials showcasing the utility for a variety of many-body calculations.

This code library is a newly developed, enhanced version of the earlier python package `irbasis` [447] which only provided pre-computed basis functions for fixed values of  $\Lambda$ . The following publication provides more details on the usage and implementation.

---

<sup>27</sup>For example, the DLR basis has been applied to DMFT calculations for implementing the Dyson equation part [448].

## **sparse-ir: Optimal compression and sparse sampling of many-body propagators**

Markus Wallerberger, Samuel Badr, Shintaro Hoshino, Sebastian Huber, Fumiya Kakizawa, Takashi Koretsune, Yuki Nagai, Kosuke Nogaki, Takuya Nomoto, Hitoshi Mori, Junya Otsuki, Soshun Ozaki, Thomas Plaikner, Rihito Sakurai, Constanze Vogel, Niklas Witt, Kazuyoshi Yoshimi, Hiroshi Shinaoka

### Key points summary

- Development of stand-alone code library collection `sparse-ir` for python and julia with Fortran support to enable optimal compression and sparse modeling of imaginary-time and Matsubara frequency propagators based on the intermediate representation (IR) basis.
- Overview on theoretical background and code architecture as well as examples illustrating the API for simple applications.
- Extensive tutorials showcasing the usage of the `sparse-ir` package for many different many-body techniques available at:  
<https://spm-lab.github.io/sparse-ir-tutorial/>.

### Author Contributions

I tested the python code library of `sparse-ir` and provided general feedback together with small code contributions to the main developers M. Wallerberger and H. Shinaoka. I gave comments on the manuscript and referee report. For the extensive tutorials shipping with `sparse-ir`, I wrote the jupyter notebooks for the python-based examples of “DMFT with IPT solver”, “FLEX approximation”, and “TPSC approximation”.

### Copyright Notice

This work is licensed under the Creative Commons Attribution 4.0 International License (CC-BY), which permits unrestricted use, distribution, and reproduction in any medium, provided the original work is properly cited:

M. Wallerberger et al., *SoftwareX* **21**, 101266 (2023).

Copyright © 2022 The Authors. This is an accepted version of the article published by Elsevier B.V at doi: [10.1016/j.softx.2022.101266](https://doi.org/10.1016/j.softx.2022.101266).



Original software publication

## sparse-ir: Optimal compression and sparse sampling of many-body propagators



Markus Wallerberger<sup>a,\*</sup>, Samuel Badr<sup>a</sup>, Shintaro Hoshino<sup>b</sup>, Sebastian Huber<sup>a</sup>, Fumiya Kakizawa<sup>b</sup>, Takashi Koretsune<sup>c</sup>, Yuki Nagai<sup>k,l</sup>, Kosuke Nogaki<sup>d</sup>, Takuya Nomoto<sup>g</sup>, Hitoshi Mori<sup>h</sup>, Junya Otsuki<sup>e</sup>, Soshun Ozaki<sup>f</sup>, Thomas Plaikner<sup>a</sup>, Rihito Sakurai<sup>b</sup>, Constanze Vogel<sup>a</sup>, Niklas Witt<sup>i</sup>, Kazuyoshi Yoshimi<sup>j</sup>, Hiroshi Shinaoka<sup>b,m</sup>

<sup>a</sup> Department of Solid State Physics, TU Wien, 1040 Vienna, Austria

<sup>b</sup> Department of Physics, Saitama University, Saitama 338-8570, Japan

<sup>c</sup> Department of Physics, Tohoku University, Miyagi 980-8577, Japan

<sup>d</sup> Department of Physics, Kyoto University, Kyoto 606-8502, Japan

<sup>e</sup> Institute for Interdisciplinary Science, Okayama University, Okayama 700-8530, Japan

<sup>f</sup> Department of Physics, University of Tokyo, Bunkyo, Tokyo 113-0033, Japan

<sup>g</sup> Research Center for Advanced Science and Technology, University of Tokyo, 4-6-1 Meguro-ku, Tokyo, 153-8904, Japan

<sup>h</sup> RIKEN Center for Emergent Matter Science (RIKEN CEMS), 2-1 Hirosawa, Wako, Saitama 351-0198, Japan

<sup>i</sup> I. Institute of Theoretical Physics, University of Hamburg, 22607 Hamburg, Germany

<sup>j</sup> Institute for Solid State Physics, University of Tokyo, Tokyo 113-8654, Japan

<sup>k</sup> CCSE, Japan Atomic Energy Agency, Kashiwa, Chiba 277-0871, Japan

<sup>l</sup> Mathematical Science Team, RIKEN Center for Advanced Intelligence Project (AIP), Tokyo 103-0027, Japan

<sup>m</sup> JST, PRESTO, 4-1-8 Honcho, Kawaguchi, Saitama 332-0012, Japan

### ARTICLE INFO

#### Article history:

Received 28 June 2022

Received in revised form 21 October 2022

Accepted 14 November 2022

#### Keywords:

Intermediate representation

Sparse sampling

Python

Julia

Fortran

### ABSTRACT

We introduce sparse-ir, a collection of libraries to efficiently handle imaginary-time propagators, a central object in finite-temperature quantum many-body calculations. We leverage two concepts: firstly, the intermediate representation (IR), an optimal compression of the propagator with robust *a priori* error estimates, and secondly, sparse sampling, near-optimal grids in imaginary time and imaginary frequency from which the propagator can be reconstructed and on which diagrammatic equations can be solved. IR and sparse sampling are packaged into stand-alone, easy-to-use Python, Julia and Fortran libraries, which can readily be included into existing software. We also include an extensive set of sample codes showcasing the library for typical many-body and *ab initio* methods.

© 2022 The Author(s). Published by Elsevier B.V. This is an open access article under the CC BY license (<http://creativecommons.org/licenses/by/4.0/>).

### Code metadata

Current code version	1.0
Permanent link to code/repository used for this code version	<a href="https://github.com/ElsevierSoftwareX/SOFTX-D-22-00160">https://github.com/ElsevierSoftwareX/SOFTX-D-22-00160</a>
Code Ocean compute capsule	
Legal Code License	MIT
Code versioning system used	git
Software code languages, tools, and services used	Python or Julia or Fortran
Dependencies	scipy (optional: xprec)
Link to developer documentation/manual	<a href="https://sparse-ir.readthedocs.io">sparse-ir.readthedocs.io</a> ; <a href="https://spm-lab.github.io/sparse-ir-tutorial">spm-lab.github.io/sparse-ir-tutorial</a>
Support email for questions	<a href="https://github.com/SpM-lab/sparse-ir/issues">github.com/SpM-lab/sparse-ir/issues</a>

\* Corresponding author.

## 1. Motivation and significance

Computational quantum many-body physics is a major driver of advances in materials science, quantum computing, and high-energy physics. Yet, in pushing these fields forward, we face a three-pronged challenge: firstly, the requirement to model more complicated systems in an effort to understand advanced many-body effects, secondly, speeding up the calculations to allow large-scale automatized system discovery, and thirdly, the need for reliable error control to fortify predictive power of the results.

For diagrammatic methods working in imaginary (Euclidean) time—widely used to solve quantum many-body systems—these three prongs translate to the need to compactly store, quickly manipulate, and reliably control the error, respectively, of many-body propagators and the diagrammatic equations in which they appear. Previous efforts either focused on optimizing imaginary time grids [1,2] or modeling generic smooth functions [3,4].

The intermediate representation (IR) [5,6] instead leverages the analytical structure of imaginary-time propagators to construct a maximally compact, orthonormal basis: the number of basis functions needed to represent a propagator scales logarithmically with the desired accuracy and logarithmically with  $\Lambda$ , the ultraviolet cutoff in units of temperature. (Related approaches either optimize for a different norm [7] or trade some compactness for simpler algorithms [8,9].) Sparse sampling [10] is a complementary concept which connects the IR to sparse time and frequency grids, which allows us to efficiently move between representations and restrict the solution of diagrammatic equations to those grids. Uniquely, error control is baked into the IR: each basis function comes with an *a priori* error level, which also means changing accuracy is simply a matter of changing the number of nonzero basis coefficients. The IR for the one-particle basis also serves as a building block for compressing arbitrary  $n$ -point propagators [11,12] and fast solutions to the corresponding diagrammatic equations [13].

Precomputed IRs for different cutoffs  $\Lambda$  have been released previously as the *irbasis* library [14]. Using this library, IR and sparse sampling has been successfully employed in numerous physics and chemistry applications [15–28].

In this paper, we introduce *sparse-ir*, a major step forward from the previous library: it computes the basis on the fly, usually within seconds. This not only removes the need for precomputing and shipping databases, it also allows tailoring the cutoff  $\Lambda$  and even the type of kernel to the specific application. We also simplify the use of sparse sampling, which previously had to be implemented on top of *irbasis* by the user. Finally, we improve the infrastructure for two-particle calculations by adding the possibility of augmented and vertex bases [11,13]. We also provide a set of small, self-contained Jupyter notebooks showcasing the use of IR and sparse sampling for selected physics and quantum chemistry applications, lowering the barrier of entry for new users. The library is available as three standalone Python, Julia and Fortran ports, each with minimal dependencies.

The remainder of this paper is organized as follows: after an overview over IR and sparse sampling in Section 2, we showcase the use of *sparse-ir* in a simple Feynman diagrammatic method in Section 3. In Section 4, we then give an overview of the anatomy and function of the package. We state our final assessments in Section 5.

## 2. Software description

We are concerned with (retarded) many-body propagators and related functions in equilibrium:

$$G^R(\omega) = -i \int_{t'}^{\infty} dt e^{i\omega t} \langle A(t)B(t') \mp B(t')A(t) \rangle, \quad (1)$$

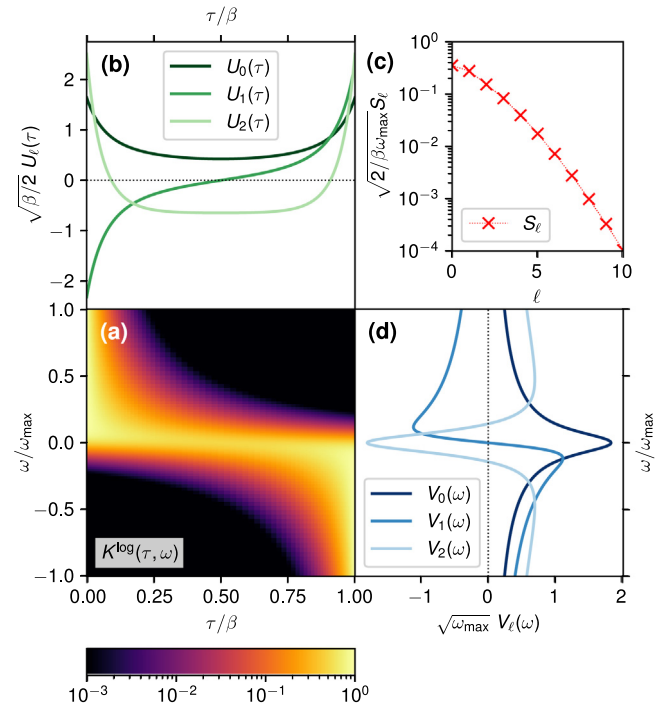


**Fig. 1.** Singular value expansion (4) of the (a) analytic continuation kernel  $K(\tau, \omega)$  (3) for  $\beta\omega_{\max} = 30$  into (b) left-singular functions  $U_l$ , which share the kernel’s imaginary-time axis  $\tau$ , (c) singular values  $S_l$ , and (d) right-singular functions  $V_l$ , which share the kernel’s real-frequency axis  $\omega$ .

where both  $A, B$  are bosonic (–) or fermionic (+) operators,  $\langle \cdot \rangle = \text{Tr}(e^{-\beta H} \cdot) / \text{Tr}(e^{-\beta H})$  is the expectation value,  $1/\beta$  is temperature and  $H$  is the Hamiltonian. At its core, *sparse-ir* seeks to (i) maximally compress the information contained in these propagators and (ii) reliably reconstruct this compressed form from sparse time and frequency grids to allow its use in diagrammatic calculations.

To achieve (i) compression, *sparse-ir* relies on the fact that information is lost in transitioning from the (observable) spectral function  $\rho(\omega) = -\frac{1}{\pi} \Im G^R(\omega)$  on the real-frequency axis to the propagator  $G(\tau)$  on the imaginary-time axis:

$$G(\tau) := -\langle T_{\tau} A(\tau) B(0) \rangle = - \int d\omega K(\tau, \omega) \rho(\omega), \quad (2)$$

where  $K$  is an integral kernel mediating the transition (cf. Section 4):

$$K(\tau, \omega) = \frac{\exp(-\tau\omega)}{\exp(-\beta\omega) \pm 1} \Theta(\omega_{\max} - |\omega|), \quad (3)$$

$T_{\tau}$  is the time-ordering operator,  $\omega_{\max}$  is a UV cutoff (upper bound to the bandwidth), and  $0 < \tau < \beta$  is imaginary time. This information loss is epitomized by the singular value expansion (SVE) [29] of the kernel  $K$  [5,30]:

$$K(\tau, \omega) = \sum_{l=0}^{\infty} U_l(\tau) S_l V_l(\omega), \quad (4)$$

where  $\{U_l\}$  are the left-singular functions, an orthonormal system on the imaginary-time axis, and  $\{V_l\}$  are the right-singular functions, an orthonormal system on the real-frequency axis. The amount of information retained in the transformation from  $V_l$  to  $U_l$  is encoded in the associated (scaled) singular value  $S_l/S_0$ . The decomposition (4) is illustrated in Fig. 1: the kernel (3) in panel (a) is decomposed into “direct products” of left-singular functions (b) and right-singular functions (d), scaled by singular values (c).

(For example, the lowest-order approximation to  $K(\tau, \omega)$  would be  $U_0(\tau)V_0(\omega)S_0$ .)

Crucially, the singular values  $S_l$  decay at least exponentially quickly,  $\log(S_l) = \mathcal{O}(-l/\log(\beta\omega_{\max}))$ . This information loss on the other hand allows the imaginary-time propagator to be compressed by storing the expansion coefficients of the left-singular functions (“IR basis functions”)  $U_l$  [6]:

$$G(\tau) = \sum_{l=0}^{L-1} U_l(\tau) G_l + \epsilon_L(\tau), \quad (5a)$$

where  $G_l = -S_l \int d\omega V_l(\omega)\rho(\omega)$  are the expansion coefficients and  $\epsilon_L$  is an error term which vanishes exponentially quickly,  $\epsilon_L \sim S_L/S_0$ . Its Fourier transform is given by

$$\hat{G}(i\omega) = \int_0^\beta d\tau e^{i\omega\tau} G(\tau) = \sum_{l=0}^{L-1} \hat{U}_l(i\omega) G_l + \hat{\epsilon}_L(i\omega), \quad (5b)$$

where  $i\omega = \frac{i\tau}{\beta}(2n + \zeta)$  is a Matsubara frequency,  $\zeta = 0/1$  for bosons/fermions, and  $\hat{\cdot}$  denotes the Fourier transform. The singular value construction means that the IR basis is (a) *optimal* in terms of compactness:<sup>1</sup> for, e.g.,  $\beta\omega_{\max} < 10^8$ , no more than 200 coefficients must be stored to obtain full double precision accuracy; (b) orthonormal; and (c) unique, thereby providing a robust and compact storage format.

To achieve (ii) reconstruction, we note that the “polynomial-like” properties of  $U_l$  [13,31] guarantee that there exists [32,33] a sparse set of  $\mathcal{O}(L)$  times  $\mathcal{T} = \{\tau_i\}$  and frequencies  $\mathcal{W} = \{i\omega_n\}$  from which we can robustly infer the coefficients [10]. *sparse-ir* solves the following ordinary least-squares problems:

$$G_l = \arg \min_{\{G_l\}} \sum_{\tau \in \mathcal{T}} \left| G(\tau) - \sum_{l=0}^{L-1} U_l(\tau) G_l \right|^2, \quad (6a)$$

$$G_l = \arg \min_{\{G_l\}} \sum_{i\omega \in \mathcal{W}} \left| \hat{G}(i\omega) - \sum_{l=0}^{L-1} \hat{U}_l(i\omega) G_l \right|^2. \quad (6b)$$

Given a sensible choice for the sampling points, Eqs. (5) and (6) now allow us to move between sparse imaginary-time and frequency grids and compressed representations without any significant loss of precision [10].

### 3. Example usage

As a simple example, let us perform self-consistent second-order perturbation theory for the single impurity Anderson model at finite temperature. Its Hamiltonian is given by

$$H = -\mu(c_\uparrow^\dagger c_\uparrow + c_\downarrow^\dagger c_\downarrow) + U c_\uparrow^\dagger c_\downarrow^\dagger c_\downarrow c_\uparrow + \sum_{p\sigma} (V_{p\sigma} f_{p\sigma}^\dagger c_\sigma + V_{p\sigma}^* c_\sigma^\dagger f_{p\sigma}) + \sum_{p\sigma} \epsilon_p f_{p\sigma}^\dagger f_{p\sigma}, \quad (7)$$

where  $U$  is the electron interaction strength,  $\mu$  is the chemical potential,  $c_\sigma$  annihilates an electron on the impurity,  $f_{p\sigma}$  annihilates an electron in the bath,  $\dagger$  denotes the Hermitian conjugate,  $p \in \mathbb{R}$  is bath momentum, and  $\sigma \in \{\uparrow, \downarrow\}$  is spin. The hybridization strength  $V_{p\sigma}$  and bath energies  $\epsilon_p$  are chosen such that the non-interacting density of states is semi-elliptic with a half-bandwidth of one,  $\rho_0(\omega) = \frac{2}{\pi} \sqrt{1 - \omega^2}$ ,  $U = 1.2$ ,  $\beta = 10$ , and the system is half-filled,  $\mu = U/2$ .

We present the associated algorithm in Fig. 2. First, we construct the IR basis for fermions and  $\beta = 10$ , intuit that  $\omega_{\max} = 8$  is larger than the interacting bandwidth and content ourselves

```

1 import sparse_ir as ir, numpy as np
2 basis = ir.FiniteTempBasis('F', 10, 8, 1e-6)
3 U = 1.2
4 def rho0w(w):
5     return np.sqrt(1-w.clip(-1,1)**2) * 2/np.pi
6 rho0l = basis.v.overlap(rho0w)
7 G0l = -basis.s * rho0l
8 Gl_prev = 0
9 Gl = G0l
10 stau = ir.TauSampling(basis)
11 siw = ir.MatsubaraSampling(basis)
12 while np.linalg.norm(Gl - Gl_prev) > 1e-6:
13     Gl_prev = Gl
14     Gtau = stau.evaluate(Gl)
15     Sigmatau = U**2 * Gtau**3
16     Signal = stau.fit(Sigmatau)
17     Sigmaiw = siw.evaluate(Signal)
18     G0iw = siw.evaluate(G0l)
19     Giw = 1/(1/G0iw - Sigmaiw)
20     Gl = siw.fit(Giw)

```

Fig. 2. Self-consistent second-order perturbation theory for a single-impurity Anderson model (7) with a semi-elliptic density of states and  $U = 1/2$  at half filling and  $\beta = 10$  using *sparse-ir*.

with an accuracy of  $\epsilon = 10^{-6}$  (line 2). We then compute the basis coefficients as  $\rho_{0,l} = \int d\omega V_l(\omega)\rho_0(\omega)$  (line 6). The non-interacting propagator  $G_{0,l} = -S_l\rho_{0,l}$  (line 7) serves as initial guess for  $G_l$  (line 9). We then construct the grids and matrices for sparse sampling (lines 10, 11), after which we enter the self-consistency loop (line 12): At half filling, the second-order self-energy is simply

$$\Sigma(\tau) = U^2 G^3(\tau) \quad (8)$$

(line 15). We construct this object at the sampling points  $\{\tau_i\}$  by first expanding  $G_l$  (line 14). The dynamical part of the self-energy is propagator-like [34], so it can be modeled by the IR basis (the Hartree and Fock term, if present, needs to be handled separately). The Dyson equation

$$\hat{G}^{-1}(i\omega) = \hat{G}_0^{-1}(i\omega) - \hat{\Sigma}(i\omega) \quad (9)$$

(line 19) is then solved by expanding both  $G_0$  and  $\Sigma$  on the sparse set of frequencies (lines 17, 18). To complete the loop, the IR coefficients for  $G$  are then updated (line 20). We converge if the deviation between subsequent iterations (line 13) is consistent with the basis accuracy (line 12).

The resulting self-energy  $\hat{\Sigma}(i\omega)$  on the Matsubara axis is presented in Fig. 3 (only the imaginary part is plotted, since the real part is merely a constant  $U/2$  at half filling). Instead of a dense mesh (plusses), the Dyson equation has to be solved only on the sampling points (crosses). Since the IR coefficients for both the Green’s function and the self-energy are guaranteed to decay quickly (see inset), this is enough to reconstruct the functions everywhere with the given accuracy bound of  $\epsilon = 10^{-6}$ . We note that this bound and the UV cutoff  $\omega_{\max}$  are the only discretization parameters we need to supply.

The code in Fig. 2 is short, simple—no explicit Fourier transforms or models are required—yet guarantees the given accuracy goal. Extending the approximation to  $\Sigma = GW$  would require only the addition of a bosonic basis, the construction of the RPA diagram,  $\Pi(\tau) = G^2(\tau)$ , and solving the Bethe–Salpeter equation,  $\hat{W}(i\omega) = U + U\hat{\Pi}(i\omega)\hat{W}(i\omega)$ , where again sparse grids and transformations can be used.

In addition to this example, *sparse-ir* ships a set of tutorials [35], demonstrating the use of the Python, Julia, and Fortran libraries in typical many-body calculations. Each tutorial contains a short description of the underlying many-body theory as

<sup>1</sup> The truncated IR expansion minimizes  $\|\epsilon_L\|$  in the  $L_2$ -norm sense if no additional information, i.e., a flat prior, for  $\rho(\omega)$  is used.

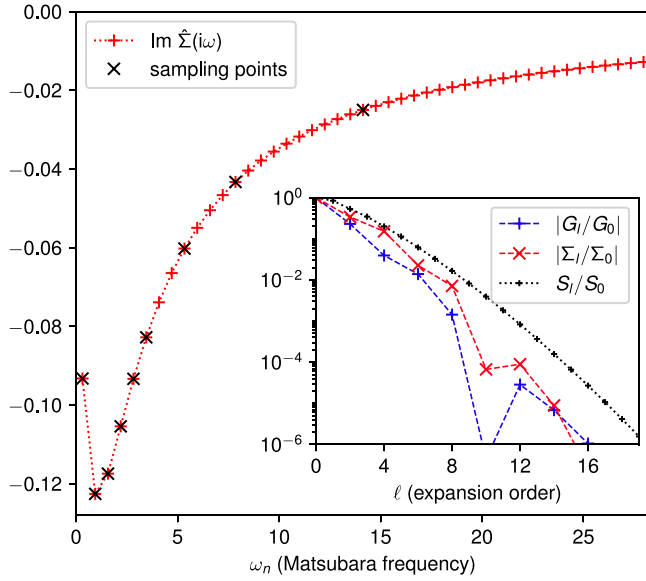


**Fig. 3.** Imaginary part of the Matsubara self-energy  $\hat{\Sigma}(i\omega)$  for the GF(2) calculation in Fig. 2. Black crosses mark the location of sampling points  $\mathcal{W}$  on which the Dyson equation (9) is solved and from which the full signal is reconstructed. Inset: normalized IR expansion coefficients of  $G$  (pluses) and  $\Sigma - \Sigma_{\text{HF}}$  (crosses) and singular values (dots) for comparison. Lines are guides for the eye.

well as sample code utilizing *sparse-ir* and its expected output. Currently, we include tutorials on: (a) the GF(2) and GW approximation [36,37], (b) fluctuation exchange (FLEX) [19,23,38], (c) the two-particle self-consistent (TPSC) approximation [39,40], (d) Eliashberg theory for the Holstein–Hubbard model [41–44], (e) the Lichtenstein formula [45], (f) calculation of the orbital magnetic susceptibility [46–53], and (g) numerical analytic continuation based on the SpM method [5].

#### 4. Architecture and features

The main functions of the library are (a) construction and handling of the kernel (3), (b) performing the singular value expansion (4), (c) storage and evaluation of the IR basis functions (5), and (d) construction of the sampling points and solution of the fitting problem (6). The *sparse-ir* package was split along these lines into modules, see Fig. 4, which we will briefly describe in the following.

**Kernel.** Two kernels are packaged with *sparse-ir*:

$$K_A^{\text{log}}(x, y) = \frac{\exp(-\frac{\Lambda}{2}(x+1)y)}{1 + \exp(-\Lambda y)} \Theta(1 - |y|), \quad (10a)$$

$$K_A^{\text{RB}}(x, y) = \frac{y \exp(-\frac{\Lambda}{2}(x+1)y)}{1 - \exp(-\Lambda y)} \Theta(1 - |y|). \quad (10b)$$

Kernels are expressed in terms of dimensionless variables  $x$  and  $y$  in the interval  $[-1, 1]$ , where  $\tau = \frac{\beta}{2}(x+1)$  and  $\omega = \omega_{\text{max}}y$ . Instead of parametrization by both inverse temperature  $\beta$  and UV cutoff frequency  $\omega_{\text{max}}$ , this allows one to consider only a single scale parameter  $\Lambda = \beta\omega_{\text{max}}$ .

The logistic kernel (10a) is the default kernel used for both fermionic and bosonic propagators for simplicity: even though it is the analytic continuation kernel for fermions, it can also be used to compactly model bosonic propagators [8,26,54]. The regularized bosonic kernel (10b) is common in numerical analytic continuation of bosonic functions [55,56] and is used by the *irbasis* library for bosonic propagators. Thermal contributions to

the susceptibility,  $\chi(\omega = 0)$ , can be modeled by augmenting the basis [13]. User-defined kernels may be added.

Each kernel  $K$  can be evaluated by supplying  $x, y$ , however care must be taken not to lose precision around  $x = \pm 1$ : in addition to  $x$  we use  $x_{\pm} := 1 \pm x$  to full precision to avoid cancellation in the enumerators of Eqs. (10).

**Piecewise polynomials.** To represent the IR basis functions (4), we employ piecewise Legendre polynomials:

$$P_{nq}(x; \{x_m\}) := \sqrt{\frac{1}{\Delta x_n}} P_q\left(\frac{x - \bar{x}_n}{\Delta x_n}\right) \Theta(\Delta x_n - |x - \bar{x}_n|), \quad (11)$$

where  $x_0 < x_1 < \dots < x_N$  are the segment edges,  $\Delta x_n := \frac{1}{2}(x_n - x_{n-1})$ ,  $\bar{x}_n := \frac{1}{2}(x_n + x_{n-1})$ , and  $P_q$  denotes the  $q$ th Legendre polynomial.

Given suitable discretizations of the axes,  $\{x_n\}$  and  $\{y_n\}$ , as well as a Legendre order  $Q$ , the left and right IR basis functions can then be expanded as follows:

$$u_l(x) \approx \sum_{n=1}^N \sum_{q=0}^Q u_{lnq} P_{nq}(x; \{x_0, \dots, x_N\}), \quad (12a)$$

$$v_l(y) \approx \sum_{n'=1}^{N'} \sum_{q'=0}^Q v_{ln'q'} P_{n'q'}(y; \{y_0, \dots, y_{N'}\}), \quad (12b)$$

where  $u_{lnq}$  and  $v_{ln'q'}$  are expansion coefficients.

Legendre polynomials have the advantage that their Fourier transform is given analytically [3]:

$$\begin{aligned} \hat{P}_{nq}(\pm\omega; \{x_m\}) &:= \int_{x_0}^{x_N} dx e^{\pm i\omega x} P_{nq}(x; \{x_m\}) \\ &= 2\sqrt{\Delta x_n} e^{\pm i\omega \bar{x}_n} (\pm 1)^q j_q(\omega \Delta x_n), \end{aligned} \quad (13)$$

where  $\omega \geq 0$  is a frequency and  $j_q(x)$  is the  $q$ th spherical Bessel function. Thus, no numerical integration is necessary, though  $\exp(i\omega x)$  must be analytically mapped back to small  $i\omega x$  to avoid cancellation.

**Singular value expansion (SVE).** Given the discretization outlined above, we can relate the SVE (4) needed for constructing the IR basis to the singular value decomposition (SVD) of the following  $(NQ) \times (N'Q)$  matrix [6,29]:

$$\begin{aligned} A_{nq, n'q'} &= \sqrt{(q + \frac{1}{2})(q' + \frac{1}{2})} \\ &\times \iint dx dy P_{nq}(x, \{x_m\}) P_{n'q'}(y, \{y_m\}) K(x, y), \end{aligned} \quad (14)$$

where the singular values of  $A$  are equal to the singular values  $s_l$  of the kernel, and the left and right singular vectors are the (scaled) expansion coefficients of  $u_l(x)$  and  $v_l(y)$ , respectively (12).  $L$  is chosen such that  $s_L < \epsilon s_0$ , where  $\epsilon$  is the desired accuracy of the basis. In practice, we approximate the integral (14) by the associated Gauss–Legendre rule and rewrite the problem as equation for the Gauss nodes [8,29,32]. As the kernels (10) are all centrosymmetric,  $K(x, y) = K(-x, -y)$ , the SVE problem is block-diagonalized for a four-fold speedup [57].

We empirically find that choosing  $\{x_m\}$  and  $\{y_m\}$  close to the extrema of the highest-order basis functions,  $u_{L-1}(x)$  and  $v_{L-1}(y)$ , respectively, to provide an excellent discretization, only necessitating  $Q = 16$  for  $\epsilon = 10^{-16}$ . Since computing the basis functions requires solving the SVE, each kernel maintains approximations to  $\{x_m\}$  and  $\{y_m\}$  as hints. As only a fraction  $1/Q$  of the singular values of Eq. (14) are needed, we use a truncated SVD algorithm (rank-revealing QR decomposition followed by two-sided Jacobi rotations [58]) at the cost of  $\mathcal{O}(N^2NQ^3)$ .

In order to guarantee an accuracy of  $\epsilon$  for both singular values and basis functions, one has to compute the SVE with a machine

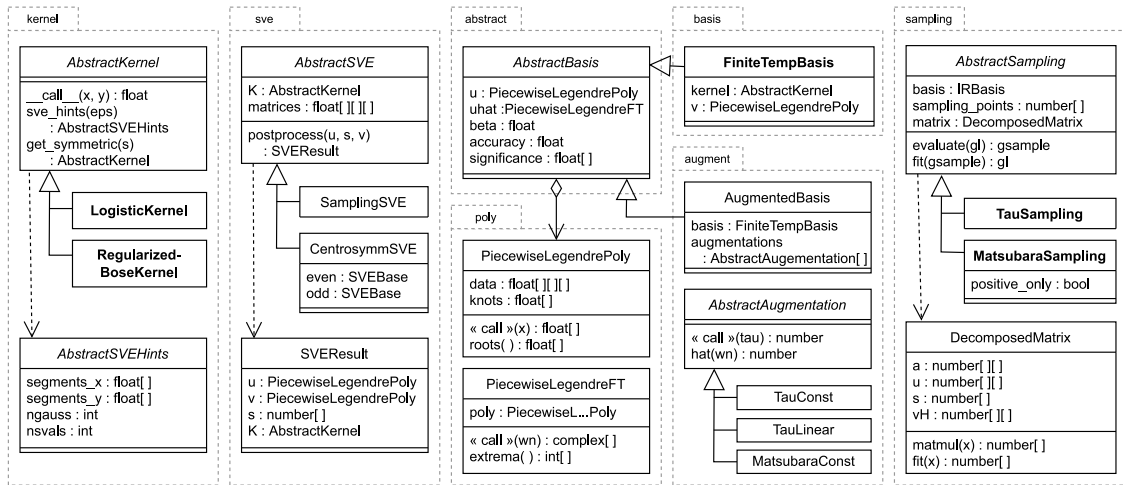


Fig. 4. Simplified UML class diagram of the core of *sparse-ir*. Classes with names in boldface are available from the top namespace.

precision of  $\epsilon^2$  [58]. Thus we compute the SVD in standard double precision for  $\epsilon \geq 10^{-8}$  and quadruple precision otherwise. For the latter we have developed the *xprec* extension to numpy. Note that quadruple precision is only needed in the SVE – the basis functions are stored and evaluated in double precision.

**Sampling.** The sampling times  $\{\tau_i\}$  and frequencies  $\{\omega_n\}$  are chosen such that the highest-order basis functions,  $U_{L-1}(\tau_i)$  and  $\hat{U}_{L-1}(\omega_n)$ , respectively, are locally extremal. To optimize conditioning,  $\tau_1$  and  $\tau_L$  are moved from  $\pm 1$  to the midpoint of between the  $\pm 1$  and the closest root of  $U_{L-1}$ . Sampling in frequency is conditioned somewhat worse due to the discrete nature of the frequency axis, which is why  $\{\omega_n\}$  are augmented by four additional frequencies.

With the sampling points chosen, sparse sampling now involves transitioning between IR basis coefficients and the value at the sampling points. For evaluation (5) at the sampling points we multiply with precomputed matrices,  $F_{ij} := U_j(\tau_i)$  and  $\hat{F}_{ij} := \hat{U}_j(\omega_n)$ , respectively, at a cost of  $\mathcal{O}(L^2)$ . For fitting the IR coefficients, we need to solve the least-squares problems (6). However, multiplying with a precomputed pseudoinverse can lead to loss of backward stability [59], and we observe this in the case of basis augmentation. Instead, we precompute and store the SVD of  $F$  and  $\hat{F}$  and construct the pseudoinverse on the fly, again at a cost of  $\mathcal{O}(L^2)$ .

For propagators  $G(\tau)$  which are real-valued in imaginary time, Matsubara sampling can be directed to infer negative frequencies from the symmetry relation  $\hat{G}(i\omega) = \hat{G}^*(-i\omega)$  by setting the positive-only flag. This cuts the number of sampling frequencies in half and yields a four-fold speedup at no loss of accuracy.

**Julia and fortran libraries.** This software package includes Julia [60] and Fortran [61] libraries. The Julia library implements the full set of functionalities of the Python library with a similar interface. The Fortran library implements only their subset required for its use in *ab initio* programs: The Fortran library uses the tabulated values of the IR basis functions computed by the Python library. The Fortran interface is fully compatible with the Fortran95 standard and has no additional external dependencies. More detailed descriptions can be found in readme files of the repositories and the tutorials described below.

## 5. Impact and outlook

We expect that *sparse-ir* will be widely used in many-body and *ab initio* calculations based on diagrammatic theories such

as GW and quantum embedding theories such as the dynamical mean-field theory and its extensions. The computational complexity of diagrammatic calculations based on these technologies grows slower than any power law with respect to the inverse temperature. This makes these technologies particularly efficient and useful in studying systems with a large bandwidth at low temperatures. The library will make new studies for understanding the low-temperature properties of solids and molecules feasible.

To facilitate its application to various fields, the library supports languages popular in many different areas (Python and Julia for prototyping, Fortran, C, and C++ for existing *ab initio* codes.) The library is shipped with many self-contained tutorials on specific topics in different fields of physics.

## 6. Conclusions

We present intermediate representation (IR) and sparse sampling for efficient many-body and *ab initio* calculations based on imaginary-time propagators. These methods are implemented in Python/Julia/Fortran libraries to allow researchers in a large community of many-body physics and *ab initio* calculations to use them.

## Declaration of competing interest

The authors declare that they have no known competing financial interests or personal relationships that could have appeared to influence the work reported in this paper.

## Data availability

No data was used for the research described in the article.

## Acknowledgments

MW was supported by the FWF, Austria through project P30997. NW acknowledges funding by the Cluster of Excellence EXC 2056 of the DFG, Germany – project ID 390715994, and support by the DFG research unit QUAST FOR5249, Germany (project DFG WE 5342/8-1). RS, FK and HS were supported by JST, PRESTO, Japan Grant No. JPMJPR2012. HS was supported by JSPS, Japan KAKENHI Grants No. 21H01041 and No. 21H01003. SH was supported by No. JP21K03459. TK was supported by JSPS, Japan KAKENHI Grants No. 21H01003, 21H04437, and 22K03447. SO was supported by JSPS, Japan KAKENHI Grants No. 18H01162 and JSPS through the Program for Leading Graduate Schools (MERIT), Japan. KN was supported by JSPS, Japan Grants No. JP21J23007.



## References

- [1] Ku W, Eguluz AG. Band-gap problem in semiconductors revisited: Effects of core states and many-body self-consistency. *Phys Rev Lett* 2002;89:126401. <http://dx.doi.org/10.1103/PhysRevLett.89.126401>.
- [2] Kananenka AA, Phillips JJ, Zgid D. Efficient temperature-dependent Green's functions methods for realistic systems: Compact grids for orthogonal polynomial transforms. *J Chem Theory Comput* 2016;12(2):564–71. <http://dx.doi.org/10.1021/acs.jctc.5b00884>.
- [3] Boehnke L, Hafermann H, Ferrero M, Lechermann F, Parcollet O. Orthogonal polynomial representation of imaginary-time Green's functions. *Phys Rev B* 2011;84:075145. <http://dx.doi.org/10.1103/PhysRevB.84.075145>.
- [4] Dong X, Zgid D, Gull E, Strand HUR. Legendre-spectral Dyson equation solver with super-exponential convergence. *J Chem Phys* 2020;152(13):134107. <http://dx.doi.org/10.1063/5.0003145>.
- [5] Otsuki J, Ohzeki M, Shinaoka H, Yoshimi K. Sparse modeling approach to analytical continuation of imaginary-time quantum Monte Carlo data. *Phys Rev E* 2017;95:061302. <http://dx.doi.org/10.1103/PhysRevE.95.061302>.
- [6] Shinaoka H, Otsuki J, Ohzeki M, Yoshimi K. Compressing Green's function using intermediate representation between imaginary-time and real-frequency domains. *Phys Rev B* 2017;96(3):35147. <http://dx.doi.org/10.1103/PhysRevB.96.035147>.
- [7] Kaltak M, Kresse G. Minimum isometry method: A compressive sensing approach for Matsubara summation in many-body perturbation theory. *Phys Rev B* 2020;101:205145. <http://dx.doi.org/10.1103/PhysRevB.101.205145>.
- [8] Kaye J, Chen K, Parcollet O. Discrete Lehmann representation of imaginary time Green's functions. 2021, arXiv [arXiv:2107.13094](https://arxiv.org/abs/2107.13094).
- [9] Kaye J, Chen K, Strand HUR. libdfr: Efficient imaginary time calculations using the discrete Lehmann representation. 2021, arXiv [arXiv:2110.06765](https://arxiv.org/abs/2110.06765).
- [10] Li J, Wallerberger M, Chikano N, Yeh C-N, Gull E, Shinaoka H. Sparse sampling approach to efficient ab initio calculations at finite temperature. *Phys Rev B* 2020;101(3):035144. <http://dx.doi.org/10.1103/physrevb.101.035144>.
- [11] Shinaoka H, Otsuki J, Haule K, Wallerberger M, Gull E, Yoshimi K, et al. Overcomplete compact representation of two-particle Green's functions. *Phys Rev B* 2018;97:205111. <http://dx.doi.org/10.1103/PhysRevB.97.205111>.
- [12] Shinaoka H, Geffroy D, Wallerberger M, Otsuki J, Yoshimi K, Gull E, et al. Sparse sampling and tensor network representation of two-particle Green's functions. *SciPost Phys* 2020;8:12. <http://dx.doi.org/10.21468/SciPostPhys.8.1.012>.
- [13] Wallerberger M, Shinaoka H, Kauch A. Solving the Bethe–Salpeter equation with exponential convergence. *Phys Rev Res* 2021;3:033168. <http://dx.doi.org/10.1103/PhysRevResearch.3.033168>.
- [14] Chikano N, Yoshimi K, Otsuki J, Shinaoka H. irbasis: Open-source database and software for intermediate-representation basis functions of imaginary-time Green's function. *Comput Phys Comm* 2019;240:181–8. <http://dx.doi.org/10.1016/j.cpc.2019.02.006>.
- [15] Nomoto T, Koretsune T, Arita R. Local force method for the ab initio tight-binding model: Effect of spin-dependent hopping on exchange interactions. *Phys Rev B* 2020;102(1):014444. <http://dx.doi.org/10.1103/physrevb.102.014444>.
- [16] Nomoto T, Koretsune T, Arita R. Formation mechanism of the helical Q structure in Gd-based skyrmion materials. *Phys Rev Lett* 2020;125(11):117204. <http://dx.doi.org/10.1103/physrevlett.125.117204>.
- [17] Nomura Y, Nomoto T, Hirayama M, Arita R. Magnetic exchange coupling in cuprate-analog d9 nickelates. *Phys Rev Res* 2020;2(4):043144. <http://dx.doi.org/10.1103/physrevresearch.2.043144>.
- [18] Isakov S, Yeh C-N, Gull E, Zgid D. Ab initio self-energy embedding for the photoemission spectra of NiO and MnO. *Phys Rev B* 2020;102(8):085105. <http://dx.doi.org/10.1103/physrevb.102.085105>.
- [19] Witt N, van Loon EGCP, Nomoto T, Arita R, Wehling TO. Efficient fluctuation-exchange approach to low-temperature spin fluctuations and superconductivity: From the Hubbard model to Na<sub>x</sub>CoO<sub>2</sub> · yH<sub>2</sub>O. *Phys Rev B* 2021;103:205148. <http://dx.doi.org/10.1103/PhysRevB.103.205148>.
- [20] Pokhilko P, Isakov S, Yeh C-N, Zgid D. Evaluation of two-particle properties within finite-temperature self-consistent one-particle green's function methods: Theory and application to GW and GF<sub>2</sub>. *J Chem Phys* 2021;155(2):024119. <http://dx.doi.org/10.1063/5.0054661>.
- [21] Yeh C-N, Isakov S, Zgid D, Gull E. Electron correlations in the cubic paramagnetic perovskite Sr(V, Mn)O<sub>3</sub>: Results from fully self-consistent self-energy embedding calculations. *Phys Rev B* 2021;103(19). <http://dx.doi.org/10.1103/PhysRevB.103.195149>.
- [22] Yeh C-N, Shee A, Sun Q, Gull E, Zgid D. Relativistic self-consistent GW: Exact two-component formalism with one-electron approximation for solids. 2022, arXiv [arXiv:2202.02252](https://arxiv.org/abs/2202.02252).
- [23] Witt N, Pizarro JM, Berges J, Nomoto T, Arita R, Wehling TO. Doping fingerprints of spin and lattice fluctuations in moiré superlattice systems. *Phys Rev B* 2022;105:L241109. <http://dx.doi.org/10.1103/PhysRevB.105.L241109>.
- [24] Nagai Y, Shinaoka H. Smooth self-energy in the exact-diagonalization-based dynamical mean-field theory: Intermediate-representation filtering approach. *J Phys Soc Japan* 2019;88(6):064004. <http://dx.doi.org/10.7566/jpsj.88.064004>.
- [25] Nagai Y. Intrinsic vortex pinning in superconducting quasicrystals. 2021, arXiv [arXiv:2111.13288](https://arxiv.org/abs/2111.13288).
- [26] Etsuko Itou YN. QCD viscosity by combining the gradient flow and sparse modeling methods. 2021, arXiv [arXiv:2110.13417](https://arxiv.org/abs/2110.13417).
- [27] Sakurai R, Mizukami W, Shinaoka H. Hybrid quantum-classical algorithm for computing imaginary-time correlation functions. 2021, arXiv [arXiv:2112.02764](https://arxiv.org/abs/2112.02764).
- [28] Nagai Y, Shinaoka H. Sparse modeling approach for quasiclassical theory of superconductivity. 2022, arXiv [arXiv:2205.14800](https://arxiv.org/abs/2205.14800).
- [29] Hansen PC. Discrete inverse problems: insights and algorithms. SIAM; 2010. <http://dx.doi.org/10.1137/1.9780898718836>.
- [30] Bryan RK. Maximum entropy analysis of oversampled data problems. *Eur Biophys J* 1990;18:165–74. <http://dx.doi.org/10.1007/BF02427376>.
- [31] Karlin S. *Total positivity*. Stanford University Press; 1968.
- [32] Rokhlin V, Yarvin N. Generalized Gaussian quadratures and singular value decompositions of integral operators. *SIAM J Sci Comput* 1996;20:44. <http://dx.doi.org/10.1137/S1064827596310779>.
- [33] Shinaoka H, Chikano N, Gull E, Li J, Nomoto T, Otsuki J, et al. Efficient ab initio many-body calculations based on sparse modeling of Matsubara Green's function. 2021, arXiv [arXiv:2106.12685](https://arxiv.org/abs/2106.12685).
- [34] Luttinger JM. Analytic properties of single-particle propagators for many-fermion systems. *Phys Rev* 1961;121:942–9. <http://dx.doi.org/10.1103/PhysRev.121.942>.
- [35] 2022, <https://spm-lab.github.io/sparse-ir-tutorial>.
- [36] Hedin L. New method for calculating the one-particle Green's function with application to the electron-gas problem. *Phys Rev* 1965;139:A796–823. <http://dx.doi.org/10.1103/PhysRev.139.A796>.
- [37] Aryasetiawan F, Gunnarsson O. The GW method. *Rep Prog Phys* 1998;61(3):237–312. <http://dx.doi.org/10.1088/0034-4885/61/3/002>.
- [38] Bickers NE, Scalapino DJ, White SR. Conserving approximations for strongly correlated electron systems: Bethe–Salpeter equation and dynamics for the two-dimensional Hubbard model. *Phys Rev Lett* 1989;62:961–4. <http://dx.doi.org/10.1103/PhysRevLett.62.961>.
- [39] Vilks YM, Tremblay A-MS. Non-perturbative many-body approach to the Hubbard model and single-particle pseudogap. *J Physique I* 1997;7(11):1309–68. <http://dx.doi.org/10.1051/jp1:1997135>.
- [40] Tremblay A-MS. Two-particle-self-consistent approach for the Hubbard model. In: Avella A, Mancini F, editors. *Strongly correlated systems: theoretical methods*. Berlin, Heidelberg: Springer Berlin Heidelberg; 2012, p. 409–53. [http://dx.doi.org/10.1007/978-3-642-21831-6\\_13](http://dx.doi.org/10.1007/978-3-642-21831-6_13).
- [41] Eliashberg GM. Interactions between electrons and lattice vibrations in a superconductor. *Soviet Phys JETP* 1960;11:696.
- [42] Scalapino DJ. The electron-phonon interaction and strong-coupling superconductors. In: Parks RD, editor. *Superconductivity*. 1st ed. Boca Raton, FL: CRC Press; 1969, p. 112. <http://dx.doi.org/10.1201/9780203737965>.
- [43] Zhong J, Schüttler H-B. Polaronic anharmonicity in the Holstein–Hubbard model. *Phys Rev Lett* 1992;69:1600–3. <http://dx.doi.org/10.1103/PhysRevLett.69.1600>.
- [44] Kaga Y, Werner P, Hoshino S. Eliashberg theory of the Jahn–Teller–Hubbard model. *Phys Rev B* 2022;105:214516. <http://dx.doi.org/10.1103/PhysRevB.105.214516>, URL <https://link.aps.org/doi/10.1103/PhysRevB.105.214516>.
- [45] Lichtenstein AI, Katsnelson MI, Gubanov VA. Exchange interactions and spin-wave stiffness in ferromagnetic metals. *J Phys F: Met Phys* 1984;14(7):L125–8. <http://dx.doi.org/10.1088/0305-4608/14/7/007>.
- [46] Fukuyama H. Theory of orbital magnetism of Bloch electrons: Coulomb interactions. *Progr Theoret Phys* 1971;45(3):704–29. <http://dx.doi.org/10.1143/PTP.45.704>.
- [47] Gómez-Santos G, Stauber T. Measurable lattice effects on the charge and magnetic response in graphene. *Phys Rev Lett* 2011;106:045504. <http://dx.doi.org/10.1103/PhysRevLett.106.045504>.
- [48] Raoux A, Piéchon F, Fuchs J-N, Montambaux G. Orbital magnetism in coupled-bands models. *Phys Rev B* 2015;91:085120. <http://dx.doi.org/10.1103/PhysRevB.91.085120>.
- [49] Piéchon F, Raoux A, Fuchs J-N, Montambaux G. Geometric orbital susceptibility: Quantum metric without Berry curvature. *Phys Rev B* 2016;94:134423. <http://dx.doi.org/10.1103/PhysRevB.94.134423>.
- [50] Ogata M, Fukuyama H. Orbital magnetism of Bloch electrons: I. General formula. *J Phys Soc Japan* 2015;84(12):124708. <http://dx.doi.org/10.7566/JPSJ.84.124708>.

- [51] Matsuura H, Ogata M. Theory of orbital susceptibility in the tight-binding model: Corrections to the Peierls phase. *J Phys Soc Japan* 2016;85(7):074709. <http://dx.doi.org/10.7566/JPSJ.85.074709>.
- [52] Ogata M. Orbital magnetism of Bloch electrons: II. Application to single-band models and corrections to Landau–Peierls susceptibility. *J Phys Soc Japan* 2016;85(6):064709. <http://dx.doi.org/10.7566/JPSJ.85.064709>.
- [53] Ogata M. Orbital magnetism of Bloch electrons: III. Application to graphene. *J Phys Soc Japan* 2016;85(10):104708. <http://dx.doi.org/10.7566/JPSJ.85.104708>.
- [54] Meyer HB. Calculation of the shear viscosity in SU(3) gluodynamics. *Phys Rev D* 2007;76:101701. <http://dx.doi.org/10.1103/PhysRevD.76.101701>.
- [55] Jarrell M, Gubernatis J. Bayesian inference and the analytic continuation of imaginary-time quantum Monte Carlo data. *Phys Rep* 1996;269(3):133–95. [http://dx.doi.org/10.1016/0370-1573\(95\)00074-7](http://dx.doi.org/10.1016/0370-1573(95)00074-7).
- [56] Motoyama Y, Yoshimi K, Otsuki J. Robust analytic continuation combining the advantages of the sparse modeling approach and the Padé approximation. *Phys Rev B* 2022;105:035139. <http://dx.doi.org/10.1103/PhysRevB.105.035139>.
- [57] Chikano N, Otsuki J, Shinaoka H. Performance analysis of a physically constructed orthogonal representation of imaginary-time Green's function. *Phys Rev B* 2018;98(3):035104. <http://dx.doi.org/10.1103/PhysRevB.98.035104>.
- [58] Golub GH, van Loan CF. *Matrix computations*. 3rd ed. Johns Hopkins University Press; 1996.
- [59] Wilkinson JH. *Rounding errors in algebraic processes*. Prentice–Hall; 1963.
- [60] 2022, <https://github.com/SpM-lab/SparseIR.jl>.
- [61] 2022, <https://github.com/SpM-lab/sparse-ir-fortran>.

# CHAPTER Superconductivity

# 3

*This is a piece of pure physics haiku.*<sup>1</sup>

— Piers Coleman

Superconductivity is a prototypical example of emergent phenomena where the collective pair condensation of electrons cannot be anticipated from the Schrödinger equation of individual particles. The formation of the superconducting state necessitates two distinct quantum phenomena: particle pairing and macroscopic phase coherence. Their interplay creates a many-body state with broken global phase symmetry manifesting in unique properties such as the Meissner effect with perfect diamagnetism, dissipationless supercurrent flow, or the Josephson effect.

Electron pairing requires an attractive interaction allowing the electrons to avoid repulsive Coulomb forces in time (retarded interaction), space (anisotropic interaction), or orbital degrees of freedom (exchange interaction). The onset of macroscopic coherence, on the other hand, warrants long-range order enabled by the (phase) stiffness or rigidity of the superconducting condensate. The condensate stiffness is closely linked to the pair density and electronic structure properties, like its associated quantum geometry and effective masses [449–452]. Both requirements for superconductivity introduce two distinct and often competing energy scales [453–456], the pairing amplitude or energy gap  $\Delta$  and the condensate stiffness  $D_s$ . An equivalent characterization is given by amplitude and phase mode energies or intrinsic length scales of a superconductor, the correlation length  $\xi$  and magnetic penetration depth  $\lambda_L$ .

In this chapter, we review the theoretical concepts necessary to understand the preceding premise and we introduce the methodological tools to study superconducting materials as applied in later chapters. There are many excellent textbooks on the subject of superconductivity which may be consulted for a more detailed treatment of some of the topics discussed here, such as Refs. [30, 42, 457–462].

A central classification of superconductivity is given by the notion of spontaneous symmetry breaking which we discuss first in section 3.1. We introduce the superconducting order parameter associated with broken U(1) phase rotation symmetry,

---

<sup>1</sup>To not only humble the topic but fit the lyrical motif, the chapter's title could aptly be named:

*Theory at glance – Superconductivity – Comprehensively*

which allows for a qualitative understanding of many properties of superconducting matter. The description within Ginzburg–Landau theory shows how the aforementioned intrinsic lengths or, equivalently, energy scales emerge and connect to experimental observables like critical fields and currents. We briefly address the Berezinskii–Kosterlitz–Thouless (BKT) transition pertinent to two-dimensional systems and we summarize the classification of the order parameter by spin-orbit and point group symmetries which can be broken in unconventional superconductors on top of a broken  $U(1)$  symmetry.

Building on the phenomenological motivation, we turn to a microscopic understanding of superconductivity. Its foundations are given by Bardeen–Cooper–Schrieffer (BCS) theory which introduced the general idea of electrons forming Cooper pairs through the presence of an effective attractive interaction. In section 3.2, we summarize BCS theory and introduce the Nambu–Gor’kov formalism which extends the framework of Green’s functions to describe superconductivity. This approach allows us to address more generalized pairing interactions beyond the local static approximation of BCS theory. An extension to retarded interactions originating from electron-phonon coupling is given by Miglda–Eliashberg theory (section 3.3).

A key focus of this thesis is the investigation of spin-fluctuation-mediated superconductivity [32–34, 117] in various materials [II, III, IV, V]. The central premise is that electron scattering off magnetic fluctuations (paramagnons) induces an anisotropic pairing potential, possibly facilitating more complex pairing symmetries compared to those found in conventional, phonon-mediated superconductors. In section 3.4, we provide an overview on the framework of spin-fluctuation-mediated superconductivity with an effective interaction kernel derived from microscopic spin fluctuation exchange (FLEX-type diagrams).

## 3.1 Spontaneous symmetry breaking

The notion of ‘symmetry’ is a powerful concept universally present throughout physics. The presence of symmetries in a system implies that associated conservation laws hold as captured in Noether’s theorem. Yet, the *spontaneous* breakdown of symmetries has an equally profound consequence due to its connection to phase transitions and the emergence of collective ordering. For instance, the crystallization of solids breaks  $O(3)$  rotation and reflection symmetry as well as  $\mathbb{R}^d$  translation symmetry in  $d$  dimensions, magnetic systems reduce  $SU(2)$  spin rotation symmetry, and superfluidity or superconductivity is associated with breaking of  $U(1)$  phase-rotation symmetry. Here, we will use the phenomenology of spontaneous symmetry breaking (SSB) to identify and characterize fundamental properties of

the superconducting condensate without the need to consider any details on the microscopic origin. For this overview, we partially follow Refs. [44, 463].

SSB occurs when a stable state  $|\psi\rangle$  has reduced symmetry compared to the Hamiltonian  $H$  associated with the system.<sup>2</sup> This means that the unitary transformation  $\hat{U} = e^{i\alpha\hat{Q}}$  of a symmetry generator  $\hat{Q}$  applied to  $|\psi\rangle$  gives rise to an inequivalent state while the energy of the two states  $|\psi\rangle$  and  $\hat{U}|\psi\rangle$  is the same. In fact, a whole set of such symmetry-broken states can be generated by performing all symmetry transformations  $\hat{U}$  starting from some initial symmetry-broken state  $|\psi\rangle$ . The central quantity to characterize those states and distinguish between symmetric and symmetry-broken phase is the *order parameter* which was originally introduced by Landau in his general theory for second-order phase transitions [464].

The order parameter is zero in the disordered (symmetric) phase and becomes finite in the ordered (symmetry-broken) phase, where it quantifies the “degree of order” [464]. Microscopically, the order parameter describes the development of long-range order due to SSB but its choice is not necessarily unique. Often, the characterizing observable is motivated from the SSB itself. For instance, one chooses the magnetization along the  $z$ -direction,  $m_z = \langle \hat{S}_z \rangle$ , for an Ising-type ferromagnet or the Fourier-transformed density,  $\rho_G = \sum_k \langle c_k^\dagger c_{k+G} \rangle$ , for discrete lattices. Nevertheless, it is possible to give a recipe for determining proper order parameter. Following Beekman et al. [463], the (local) order parameter  $\Psi(\mathbf{r})$  can be found from the existence of an interpolating field  $\hat{\Phi}(\mathbf{r})$  acting locally in space via

$$\Psi(\mathbf{r}) = \langle \psi | [\hat{Q}, \hat{\Phi}(\mathbf{r})] | \psi \rangle \begin{cases} \neq 0 & T < T_c \\ = 0 & T \geq T_c \end{cases}. \quad (3.1)$$

Here, the commutator  $[\hat{Q}, \hat{\Phi}(\mathbf{r})]$  can be regarded as an operator  $\hat{\Psi}(\mathbf{r})$  pertinent to the broken symmetry  $\hat{Q}$ . The freedom in choosing  $\hat{\Phi}$  allows for defining  $\hat{\Psi}$  to be distinct for different classes of nonequivalent ordered states. This is useful if more than one symmetry is broken, as is particularly the case for most unconventional superconductors (see section 3.1.6).

To illustrate the definition (3.1), we want to discuss two examples. First, we consider a ferromagnetic system where the principle axis of spin-alignment is chosen to be along the  $z$ -direction. In this case, the  $SU(2)$  rotation symmetry of spin space is reduced to just  $U(1)$  rotations about the  $z$ -axis, i.e., the symmetry of  $\hat{S}_x$  and  $\hat{S}_y$  is spontaneously broken. We can obtain the order parameter (the magnetization) by choosing  $\hat{Q} = \hat{S}_x$  and  $\hat{\Phi} = \hat{S}_y$  such that  $[\hat{S}_x, \hat{S}_y] = i\hat{S}_z$  and  $\Psi \sim \langle \hat{S}_z \rangle \equiv m_z$ .

The second example concerns the order parameter for a superfluid (or superconductor). This ordered phase emerges from the coherent condensation of particles

<sup>2</sup>We will only consider the thermodynamic limit here. For an in-depth discussion of the impact on finite-sized systems, we refer to the lecture notes by Beekman et al. [463].

(bosons or fermionic pairs) which breaks global U(1) phase-rotation invariance. This is reflected in the symmetry-breaking macroscopic condensate developing a particular phase  $\varphi$ . An equivalent statement is that the particle number is not conserved in the condensate. This relation might not be straightforward to see a priori but it becomes clear by determining the order parameter. For simplicity, we discuss a bosonic system in the following.<sup>3</sup> The (broken) symmetry of the (indefinite) total particle number is described by  $\hat{Q} \equiv \hat{N} = \int d^d r \hat{\rho}(\mathbf{r}) = \int d^d r \hat{\psi}^\dagger(\mathbf{r})\hat{\psi}(\mathbf{r})$  [463] with bosonic field operators  $\hat{\psi}^{(\dagger)}$ . As the interpolating field we choose the field operator  $\hat{\psi}$  itself. It follows from Eq. (3.1) that

$$[\hat{Q}, \hat{\psi}(\mathbf{r})] = \int d^d r' [\hat{\psi}^\dagger(\mathbf{r}')\hat{\psi}(\mathbf{r}'), \hat{\psi}(\mathbf{r})] = -\hat{\psi}(\mathbf{r}) \quad (3.2)$$

using  $[\hat{\psi}^\dagger(\mathbf{r}), \hat{\psi}(\mathbf{r}')] = -\delta(\mathbf{r} - \mathbf{r}')$ . Hence, the order parameter is the expectation value of a field operator,  $\Psi = \langle \hat{\psi} \rangle$ , which can only be finite in case of a varying particle number since  $\hat{\psi}$  links states  $|N\rangle$  and  $|N + 1\rangle$  (or  $|N + 2\rangle$  for superconductors). Such quantum states of indefinite particle numbers are described by *coherent states* [44, 459, 463] (cf. the BCS ground state in Eq. (3.98)) which can be thought of as the many-body generalization of wave packets. They are the eigenstates of the field operator given by

$$|\psi\rangle = \mathcal{N} \exp\left(\int d^d r g(\mathbf{r})\hat{\psi}^\dagger(\mathbf{r})\right) |0\rangle \sim \sum_n (\hat{\psi}^\dagger)^n |0\rangle \quad (3.3)$$

with normalization constant  $\mathcal{N}$ . The presence of field operators with varying powers  $n$  reveals the quantum nature of coherent states, which manifests as a coherent superposition of infinitely many states with different particle numbers. The complex function  $g(\mathbf{r}) = |g(\mathbf{r})|e^{i\varphi(\mathbf{r})}$  is the eigenvalue of  $\hat{\psi}(\mathbf{r})$  and can be identified as the macroscopic wave function of the condensate [459] (see Eq. (3.5) below) with average particle number  $N_s = \int d^d r |g(\mathbf{r})|^2$ . Acting with the symmetry transformation  $e^{i\alpha\hat{N}}$  on a coherent state translates the phase of the wave function as  $g(\mathbf{r})e^{i\alpha}$  which can be used to show that  $\hat{N}$  and  $\hat{\varphi}$  form a pair of conjugate variables, i.e., that they obey a commutation relation  $[\hat{N}, \hat{\varphi}] = i$  and uncertainty principle  $\Delta N \Delta \varphi \geq 1/2$ . [44]. This demonstrates our initial assertion that the particle condensate has a precise phase at

---

<sup>3</sup>Some subtleties exist between superfluidity from Bose–Einstein condensation and Cooper pairing in superconductors: First, composite fermionic pairs making up the superconducting condensate are not necessarily proper bosons (see section 3.2.1 and the book by Leggett [460] for an in-depth discussion). Second, superconductors are charged superfluids where the order parameter couples locally to the electromagnetic gauge field. This manifests in gapping out the Nambu–Goldstone mode in the Anderson–Higgs mechanism (section 3.1.2). This non-gauge invariant nature of the order parameter is sometimes equivocally referred to as spontaneous breaking of *local* U(1) gauge symmetry/redundancy [214], which is actually not possible due to Elitzur’s theorem [465]; see ch. 7.2 of the review by Beekman et al. [463] for a discussion of the local order parameter’s gauge-invariance. Note, however, that these nuances are not important for most practical applications.

the expense of an indeterminate particle number.<sup>4</sup> It is not a bad description in a macroscopic system with  $N \sim 10^{23}$ : Writing the uncertainty principle of phase and particle number  $\Delta\varphi\Delta N/N \gtrsim 1/N$  in terms of particle number fluctuations  $\Delta N/N$  shows that the phase and particle density can be simultaneously measured with high accuracy since, particle fluctuations and phase variations are small on the order of  $N^{-\frac{1}{2}} \sim 10^{-11}$ .

We want to conclude the discussion on the superfluid/superconducting order parameter by making a connection to the classification in terms of off-diagonal long-range order (ODLRO) [459, 460, 467] initially introduced by Onsager and Penrose for the description of superfluidity in helium [468, 469]. The idea of ODLRO is that long-range correlation between particles exists. This can be quantified by the single-particle density matrix  $\rho(\mathbf{r}, \mathbf{r}')$  being factorizable on long-distances [467]

$$\rho(\mathbf{r}, \mathbf{r}') = \langle \hat{\psi}^\dagger(\mathbf{r})\hat{\psi}(\mathbf{r}') \rangle \xrightarrow{|\mathbf{r}-\mathbf{r}'| \rightarrow \infty} \langle \hat{\psi}^\dagger(\mathbf{r}) \rangle \langle \hat{\psi}(\mathbf{r}') \rangle + \text{small terms} , \quad (3.4)$$

indicating that there is a macroscopic coherence between points  $\mathbf{r}, \mathbf{r}'$ . Such macroscopic phase coherence ensures that all condensed particles behave in unison, effectively rendering the entire system a single, coherent quantum entity. A key distinction from the previous description is that ODLRO employs states of fixed particle number by utilizing correlation functions such as  $\rho(\mathbf{r}, \mathbf{r}')$  [460]. Yet, Eq. (3.4) is written in a way that connects to our previously found order parameter  $\langle \hat{\psi}(\mathbf{r}) \rangle = g(\mathbf{r})$  and coherent states with macroscopic wave function  $g(\mathbf{r})$ . To make this concrete, we consider a homogeneous condensate of superfluid density  $n_s$ , where then  $\rho(\mathbf{r}, \mathbf{r}') = n_s$  for  $|\mathbf{r} - \mathbf{r}'| \rightarrow \infty$ . Identifying this with  $\langle \hat{\psi}^\dagger(\mathbf{r}) \rangle \langle \hat{\psi}(\mathbf{r}') \rangle = |g|^2$  from ODLRO in Eq. (3.4), we can write the macroscopic wave function as

$$g = \sqrt{n_s}e^{i\varphi} \equiv \Psi \quad (3.5)$$

with fixed phase  $\varphi$ . An extended discussion of this relationship can be found in chapter 5 of Annett's book [459]. Thus, we can associate the superfluid order parameter with the superfluid density  $|\Psi|^2 = n_s$ . For superconductors, where the condensate is made up by electron (Cooper) pairs, the order parameter describes the pair density. However, it is more common to denote the "superconducting density"  $n_s$  as the density of (single) electrons that form the Cooper pairs in the superconducting condensate, such that  $n_n = n - n_s$  represents the density of unpaired electrons. We maintain this convention here and denote the (Cooper) pair density by  $n_p$ , which leads to the superconducting order parameter relationship  $|\Psi|^2 = n_p = n_s/2$ .

<sup>4</sup>This point of view was not easily accepted after the introduction of BCS theory for superconducting pairing and its practicality can be criticized, see ch. 2.2 in the book by Leggett [460]. Physical implications of a quantum state with definite phase are discussed, e.g., by Leggett and Sols [466].

### 3.1.1 Ginzburg–Landau theory

We are interested in the properties of the superconducting condensate that emerge upon entering the symmetry-broken phase. Landau’s theory for phase transitions provides a phenomenological, yet insightful description to characterize changes in thermodynamic properties. Central to this idea is the parameterization of the partition function,  $Z = \text{Tr} e^{-\beta H}$ , and appropriate thermodynamic potentials in terms of the order parameter  $\Psi$ . Formally, this is achieved by integrating out the microscopic degrees of freedom in  $Z$  [214, 463] to obtain an effective path-integral

$$Z = \int \mathcal{D}^2[\Psi] e^{-\beta \mathcal{F}_L[\Psi]} \quad (3.6)$$

with the Landau free energy  $\mathcal{F}_L$  being a functional of the complex order parameter. In this sense, the order parameter can be seen as a coarse-grained representation of the microscopic details. Landau’s theory is a mean-field theory where the functional integral is simplified by a saddle-point integration, but Eq. (3.6) represents a good starting point to systematically include fluctuations around the mean-field value of the order parameter [459, 462].

The ground state and its properties are found from minimizing  $\mathcal{F}_L$ . Close to the phase transition ( $T \approx T_c$ ),  $\Psi$  is small and it was Landau’s astute proposal [464] to expand  $\mathcal{F}_L$  in powers of  $\Psi$ :<sup>5</sup>

$$\mathcal{F}_L[\Psi]/V = f_L[\Psi] = f_n + a\Psi^*\Psi + \frac{b}{2}(\Psi^*\Psi)^2 = f_n + a|\Psi|^2 + \frac{b}{2}|\Psi|^4. \quad (3.7)$$

The term  $f_n$  is the free energy density of the disordered (“normal”) phase and coefficients  $a$ ,  $b$  are material dependent parameters obtained from evaluating Eq. (3.6) for a given microscopic model; see ch. 5.7 in the book by Leggett [460] for expressions obtained from BCS theory as initially derived by Gor’kov [470]. We constrain the description here to second-order phase transitions where terms up to quartic order are sufficient and we set  $f_n$  to zero.

The stationary point of  $f_L$  is found from the condition

$$\frac{\delta f_L}{\delta \Psi^*} = 2\Psi(a + b|\Psi|^2) \stackrel{!}{=} 0 \quad \Rightarrow \quad |\Psi_0| = \pm \sqrt{-\frac{a}{b}} \vee \Psi_0 = 0. \quad (3.8)$$

In order to have a finite solution below the critical temperature  $T_c$ , the sign of  $a$  needs to change as  $b > 0$  is required for a stable system. We achieve this by  $a(T) = \alpha(T - T_c) = -\alpha T_c(1 - t)$  with reduced temperature  $t = T/T_c$ .

---

<sup>5</sup>Proper Taylor expansion around  $\Psi = 0$  would yield different numerical prefactors but we follow a common convention [44] to drop a factor of  $\frac{1}{2}$  when dealing with complex order parameters.



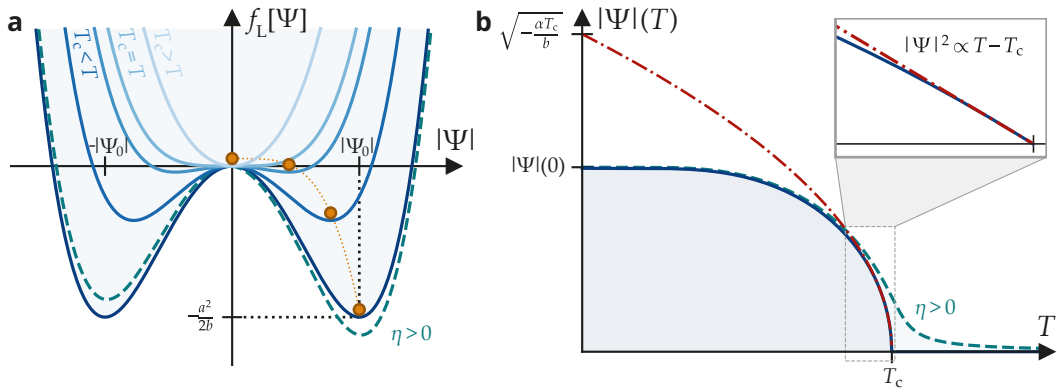


**Figure 3.1 – Landau free energy and order parameter** (a) Landau free energy  $f_L$  for a BCS superconducting order parameter  $\Psi$  at different temperatures  $T$ . The evolution of the minimum with  $T$  being reduced below the transition temperature  $T_c$  is indicated by orange dots. (b) Temperature-dependent order parameter  $\Psi(T)$ . The solid blue line describes the BCS order parameter, whereas the red dash-dotted line is the Landau order parameter. The linear-in-temperature behavior of the squared order parameter at temperatures close to  $T_c$  is shown in the inset. Its extrapolation to  $\sqrt{-\alpha T_c/b}$  at zero temperature overestimates the real value  $\Psi(0)$ . In both panels, the effect of a pairing potential  $\eta$  [471] is drawn with a teal dashed line.

Thus, the finite order parameter takes the form

$$|\Psi(T)| = \sqrt{-\frac{\alpha}{b}(T - T_c)} = |\Psi(0)|\sqrt{1 - t} \quad (3.9)$$

with  $|\Psi(0)|^2 = -\alpha T_c/b$  for  $T < T_c$  and the Landau free energy density becomes  $f_L = -a^2/(2b)$ . In Figure 3.1, we show the shape of  $f_L$  and the order parameter as a function of temperature  $T$  for the example of a BCS superconducting system. As  $T$  crosses  $T_c$ , minima at  $\pm|\Psi_0|$  arise that grow with decreasing  $T$  – the renowned double-well potential is formed.

Close to the phase transition, a superconducting system shows an infinitely strong response to external applied fields. We can see this by adding a source term  $\sim -\eta\Psi$  to  $f_L$ , where the external pairing potential  $\eta$  is coupled in via the proximity effect. This results in a tilt of the potential energy landscape and it smears out the order parameter at  $T_c$  (see Figure 3.1). The response of the system is encoded in the (zero-field) susceptibility<sup>6</sup>

$$\chi_0(T) = \left. \frac{\partial \Psi}{\partial \eta} \right|_{\eta=0} = \begin{cases} -\frac{1}{4a} & T < T_c \\ \frac{1}{2a} & T \geq T_c \end{cases}, \quad (3.10)$$

which solely derives from the second order term  $a$ . Since  $a \rightarrow 0$  for  $T \rightarrow T_c$ ,  $\chi_0$  diverges at the critical point  $T_c$  which shows that any small stray fields  $\eta$  can push

<sup>6</sup>The result is obtained from minimizing Eq. (3.7) with respect to  $\eta$  after adding the source term.

the system into the symmetry-broken phase.<sup>7</sup> Analyzing the divergence behavior of susceptibilities is a common method to identify phase transition lines in microscopic methods (sometimes referred to as Thouless criterion [472]). Equivalently, one can investigate the eigenvalues of the corresponding Bethe–Salpeter equation kernel, i.e., a vertex and (irreducible) bubble term. For the superconducting pairing instability, this is embodied by the linearized gap equation (see Eqs. (3.128) and (3.131)) which we use to determine  $T_c$  in publications II, III, IV, V. We note that care must be taken in interpreting diverging susceptibilities (or vertices) within approximate many-body techniques as signs of a phase transition [117, 321, 322], see also the discussion in section 2.2.4.

#### Spatial fluctuations of the order parameter

So far we ignored the fact that the order parameter is a complex-valued function  $\Psi = |\Psi|e^{i\varphi}$  which is possible because Eq. (3.7) is  $U(1)$  symmetric. The double-well potential (Figure 3.1a) has, in fact, rotational symmetry in the complex plane that is broken by the order parameter taking a finite value with a particular phase (cf. Figure 3.4a in section 3.1.2). To account for variations in the amplitude or twists of the phase, we need to add a gradient term to  $\mathcal{F}_L$ . The free energy then becomes (neglecting the normal phase contribution  $f_n$  and pairing field  $\eta(\mathbf{r})$ )

$$\begin{aligned}\mathcal{F}_{\text{GL}}[\Psi] &= \int d^d r f_{\text{GL}}[\Psi(\mathbf{r}), \nabla\Psi(\mathbf{r})] \\ &= \int d^d r \left( a|\Psi(\mathbf{r})|^2 + \frac{b}{2}|\Psi(\mathbf{r})|^4 + \frac{\hbar^2}{2m_{\text{p}}^*}|\nabla\Psi(\mathbf{r})|^2 \right),\end{aligned}\quad (3.11)$$

which is known as Ginzburg–Landau (GL) free energy [473]. The gradient term is written to resemble a kinetic energy, i.e., the coefficient  $m_{\text{p}}^*$  is the effective mass of the condensing particles. In superconductors, these particles are Cooper pairs, for which we associate  $m_{\text{p}}^* = 2m^*$ , where  $m^*$  is the effective (or renormalized) electron mass.<sup>8</sup> By inserting  $\Psi(\mathbf{r}) = |\Psi(\mathbf{r})|e^{i\varphi(\mathbf{r})}$  and using the chain rule  $\nabla\Psi = \nabla(|\Psi|e^{i\varphi}) = e^{i\varphi}(\nabla|\Psi| + i|\Psi|\nabla\varphi)$ , we can separate terms relating to amplitude and phase as

$$f_{\text{GL}} = \underbrace{a|\Psi(\mathbf{r})|^2 + \frac{b}{2}|\Psi(\mathbf{r})|^4}_{\text{amplitude fluctuations}} + \underbrace{\frac{\hbar^2}{2m_{\text{p}}^*}\nabla|\Psi(\mathbf{r})|^2 + \frac{\hbar^2|\Psi(\mathbf{r})|^2}{2m_{\text{p}}^*}|\nabla\varphi(\mathbf{r})|^2}_{\text{phase fluctuations}}. \quad (3.12)$$

---

<sup>7</sup>This is because the transition to a superconductor is of second order. First-order transitions are not necessarily accompanied by a diverging susceptibility

<sup>8</sup>Our notation slightly differs from that found in most other discussions of GL theory, where  $m^*$  is used to denote the (effective) pair mass instead of the single electron’s mass [V, 44, 458, 462]. The distinction using  $m_{\text{p}}^*$  allows us to explicitly represent electron correlations contributing to an effective mass  $m^*$ , while avoiding a factor of 2 discrepancy in subsequent equations.

The dominating fluctuations are determined by the characteristic length scale established through the gradient term – the *correlation length*  $\xi$ . It is defined as

$$\xi(T) = \sqrt{\frac{\hbar^2}{2m_p^*|a(T)|}} = \xi_0|1-t|^{-\frac{1}{2}} \quad (3.13)$$

with the coherence length  $\xi(T=0) = \xi_0 = (2m_p^*\alpha T_c)^{-1/2}$  [44]. The correlation length sets the scale for macroscopic coherence, i.e., the coarse-grained resolution obtained from integrating out microscopic degrees of freedom in Eq. (3.6). For lengths below  $\xi$ , amplitude fluctuations of the order parameter dominate while on distances above  $\xi$  only phase fluctuations remain (see the discussion of phase rigidity in section 3.1.3). The divergence of  $\xi$  at  $T_c$  indicates that microscopic details are not important close to the phase transition whereas fluctuation effects have significant influence and the mean-field treatment of GL theory loses validity as discussed in section 3.1.4. In BCS theory, it turns out that the coherence length describes the distance between paired electrons, i.e., the size of Cooper pairs, and is given by [459, 460]

$$\xi_0 = \frac{\hbar v_F}{\pi \Delta_0} = 0.18 \frac{\hbar v_F}{k_B T_c} \quad (3.14)$$

with the zero-temperature superconducting gap  $\Delta_0$  (3.95) and Fermi velocity  $v_F$ .

### The correlation length

To illustrate the nature of  $\xi$ , we briefly discuss three examples of nonuniform solutions  $\Psi(\mathbf{r})$  for Eq. (3.12). First, we consider the case of constant phase where we can choose  $|\Psi| \equiv \Psi$  to be real-valued. The stationary point condition  $\delta\mathcal{F}_{GL}/\delta\Psi = 0$  yields a differential equation for  $\Psi$ . For convenience, we consider a one-dimensional problem and introduce the normalized function  $g = \Psi/\Psi_0$  with  $\Psi_0^2 = -a/b$  such that the differential equation becomes [458]

$$\xi^2 \frac{d^2 g}{dx^2} + g - g^3 = 0. \quad (3.15)$$

To study how the order parameter changes towards the edge of a superconductor, we set the boundary conditions  $g(x_0) = 0$  and  $g(x \rightarrow \infty) = 1$ , i.e., the homogeneous value  $\Psi_0$  should be taken far inside the superconductor, away from the edge at  $x_0$ . The solution is given by

$$g(x) = \tanh\left(\frac{x - x_0}{\sqrt{2}\xi}\right) \quad \text{for } x \geq x_0. \quad (3.16)$$

It shows that  $\xi$  is indeed the characteristic length scale on which the order parameter and hence condensate density  $n_s = 2|\Psi|^2$  varies. Considering small variations

from the homogeneous value  $g(x) = 1 + \delta g(x)$  yields  $\delta g(x) \sim -e^{-\sqrt{2}(x-x_0)/\xi}$ . That is, disturbances to  $\Psi_0$  decay over distances  $\xi$ , because of which the correlation length is sometimes called “healing length”.

In contrast, we can consider the case where direct amplitude fluctuations are frozen out (i.e.,  $\nabla|\Psi(\mathbf{r})| = 0$ ) and only the phase varies. The corresponding stationary point condition is similar to Eq. (3.8) with the additional term  $\sim \xi^2|\nabla\varphi|^2$ . The order parameter solution is

$$|\Psi| = |\Psi_0| \sqrt{1 - \xi^2|\nabla\varphi(\mathbf{r})|^2}. \quad (3.17)$$

Thus, short-ranged phase fluctuations on distances below  $\xi$  reduce the amplitude since phase and amplitude modes are coupled in the free energy (see section 3.1.2). Large enough fluctuations destroy the macroscopic coherence and lead to a collapse of the pairing condensate. By choosing the particular form of phase fluctuations  $\varphi(\mathbf{r}) = \mathbf{q} \cdot \mathbf{r}$  describing Cooper pairs with finite center-of-mass momentum  $\mathbf{q}$  (cf. Eq. (3.73)), it is possible to probe this spatially induced breakdown of superconductivity as utilized in publication VI to calculate  $\xi$  from microscopic models.

Lastly, we assess the linear response to a varying pairing field  $\eta(\mathbf{r})$  compared to the homogeneous case in Eq. (3.10). The result of a bit of algebra is (cf. p. 368 in Ref. [44])

$$\chi(\mathbf{q}) = \frac{\chi_0 \xi^{-2}}{q^2 + \xi^{-2}} \quad (3.18)$$

in reciprocal space with  $\chi_0$  from Eq. (3.10). The Fourier-transform in three dimensions yields a Yukawa-like function in position space

$$\chi(\mathbf{r}) = \frac{\chi_0}{4\pi\xi^2} \frac{e^{-|\mathbf{r}|/\xi}}{|\mathbf{r}|}. \quad (3.19)$$

Both expressions show that the response is short-ranged on the scale of  $\xi$ . The susceptibility provides an alternative definition for the correlation length via [474]

$$\xi^{-1} = - \lim_{r \rightarrow \infty} \frac{\chi(r)}{r}. \quad (3.20)$$

#### Coupling to electromagnetic fields

Superconductors are charged superfluids which couple to electromagnetic fields. To take this into account in GL theory, we introduce the vector potential  $\mathbf{A}$  via minimal-coupling, i.e., we replace  $\nabla \mapsto \nabla + i\frac{q}{\hbar}\mathbf{A}$  with  $q = -2e$  for Cooper pairs of

electrons.<sup>9</sup> The free energy reads

$$\mathcal{F}_{\text{GL}}[\Psi, \mathbf{A}] = \int d^d r \left[ a |\Psi(\mathbf{r})|^2 + \frac{b}{2} |\Psi(\mathbf{r})|^4 + \frac{\hbar^2}{2m_{\text{p}}^*} \left| \left( \nabla - i \frac{2e}{\hbar} \mathbf{A} \right) \Psi(\mathbf{r}) \right|^2 + \underbrace{\frac{B^2}{2\mu_0}}_{f_{\text{EM}}} \right], \quad (3.21)$$

where the electromagnetic energy  $f_{\text{EM}}$  of the magnetic field  $\mathbf{B} = \nabla \times \mathbf{A}$  was added. Since the vector potential appears in the gradient term, it establishes a second characteristic length scale – the London penetration depth  $\lambda_{\text{L}}$ . We can identify it more easily by focusing on the vector potential degree of freedom: Let us consider a homogeneous condensate  $\Psi = \sqrt{n_{\text{s}}}/2$ , such that the free energy density depends only on the vector potential as

$$f_{\text{GL}}[\mathbf{A}] \sim \frac{e^2 n_{\text{s}}}{2m^*} A^2 + \frac{(\nabla \times \mathbf{A})^2}{2\mu_0} = \frac{1}{2\mu_0} \left( \frac{1}{\lambda_{\text{L}}^2} A^2 + (\nabla \times \mathbf{A})^2 \right) \quad (3.22)$$

inserting  $m_{\text{p}}^* = 2m^*$ . In the second step, we inserted the London penetration depth<sup>10</sup>

$$\lambda_{\text{L}} = \sqrt{\frac{m^*}{e^2 n_{\text{s}} \mu_0}} \stackrel{\text{Eq. (3.8)}}{=} \sqrt{\frac{a m_{\text{p}}^*}{4e^2 \mu_0 b}} \quad (3.23)$$

appearing as the prefactor of  $A^2$ , i.e., it is associated with the variations of  $\mathbf{A}$ . Magnetic fields can only penetrate superconducting matter on distances up to  $\lambda_{\text{L}}$  such that they are expelled from the inside of a superconductor.  $1/\lambda_{\text{L}}$  encodes the coupling strength of the superconducting condensate to electromagnetic fields which is (symbolically) captured by the inverse proportionality of  $\lambda_{\text{L}}$  to  $e$ : A large penetration depth describes a weak coupling where the field can penetrate without much screening over a greater distance while short  $\lambda_{\text{L}}$  describe the opposite situation with a strong coupling to the vector potential. The system parameter determining the coupling strength is given by the ratio  $n_{\text{s}}/m^*$  of superconducting carrier density and effective mass, which represents the condensate stiffness  $D_{\text{s}}$  (cf. Eq. (3.44)) further discussed in section 3.1.3.

<sup>9</sup>It is an interesting anecdote that in their original work Ginzburg and Landau, as they did not yet know about electron pairs, made the choice of  $q = -e$  “which there is no reason to consider as different from the electronic charge” [473]. Yet, Ginzburg and Landau had different opinions on the matter where Ginzburg believed in some effective charge. He deduced its value to be  $e_{\text{eff}} = 2-3e$  from comparison with experiments [475].

<sup>10</sup>We note that within GL theory, the temperature dependence of  $\lambda_{\text{L}}$  is proportional to  $n_{\text{s}}^{-1/2} \sim |\Psi| \propto |1-t|^{-1/2}$  just as the coherence length in Eq. (3.13). However, an empirically better description of experimental data is given by the dependence  $\lambda_{\text{L}}(T) = \lambda_{\text{L}}(0)|1-t^4|^{-1/2}$  originating from the Gorter–Casimir two-fluid model [41, 458].

That the superconducting phase contains no magnetic field lines is the well-known Meissner–Ochsenfeld effect which we can derive from the stationary point condition of the free energy for  $A$ . Taking the functional derivative yields [44]

$$\frac{\delta \mathcal{F}_{\text{GL}}}{\delta A} = 0 = -j + \frac{1}{\mu_0} \nabla \times \mathbf{B}, \quad (3.24)$$

where we introduce the supercurrent density (cf. section 3.1.3)

$$\mathbf{j} = -i \frac{e\hbar}{m^*} (\Psi^* \nabla \Psi - \Psi \nabla \Psi^*) - \frac{4e^2}{m^*} |\Psi|^2 \mathbf{A}. \quad (3.25)$$

Eq. (3.24) states Ampère’s law, underlining that  $\Psi$  describes a macroscopic quantity, the wavefunction of the condensate, as established before solely from the consequence of broken phase rotation symmetry. Taking the curl of Ampère’s law yields a differential equation for the magnetic field

$$\left( \nabla^2 - \frac{1}{\lambda_L} \right) \mathbf{B} = 0, \quad (3.26)$$

to which the solution is an exponentially decaying function  $B(\mathbf{r}) \sim e^{-|\mathbf{r}|/\lambda_L}$  over the characteristic length  $\lambda_L$ . The expulsion of magnetic fields from the inside of a superconductor (“Meissner phase”) is an immediate consequence and magnetic field lines only penetrate the surface region up to  $\lambda_L$ . It is the result of perfect diamagnetic response of the charged condensate where loop supercurrents generate a compensating opposing field (cf. Eq. (3.24)).

As the current  $\mathbf{j}$  is proportional to the vector potential  $\mathbf{A}$ <sup>11</sup> (cf. Eq. (3.25)), a similar expression of exponential decay holds for the current. It signifies that stationary currents only exist in regions where the magnetic field can penetrate, i.e., surface shells of thickness  $\sim \lambda_L$ . We stress that it does not mean the absence of a persistent supercurrent flow whose existence is, in fact, a direct consequence of macroscopic coherence embodied by the order parameter  $\Psi$  [463]. This so-called rigidity of the superconducting condensate is further discussed in section 3.1.3.

We remark that the preceding discussion adopts the simplified perspective of local electrodynamics as initially discussed by the London brothers [476]. Pippard [477] later expanded the theory to a non-local description which is in better agreement with experimental observations and accommodates disorder and impurity effects. Notably, Pippard introduced a length scale  $\xi_P$ , known as the Pippard coherence

---

<sup>11</sup>The *local* relation  $\mathbf{j} = -A/(\mu_0 \lambda_L^2) \propto \mathbf{A}$  is known as London equation which captures the diamagnetic nature of current response and, effectively, the dissipationless nature of the supercurrent, cf. section 18.5 in Ref. [213]. It implies  $\partial_t \mathbf{j} = E/(\mu_0 \lambda_L^2)$  which is in contrast to Ohm’s law  $\mathbf{j} \propto \mathbf{E}$  describing the typical dissipating currents in a material. Note that the London equation formally requires one to work in the London gauge  $\nabla \cdot \mathbf{A} = 0$  or an equivalent constraint for a gauge field  $\mathbf{A}' = \mathbf{A} + \nabla \chi$  [461].

length, which characterizes the area over which  $j$  and  $A$  are non-locally correlated. In case of small  $\xi_P$ , the local limit of the London equation is recovered [461]. Note that  $\xi_P$  is closely related to  $\xi_0$  [Eq. (3.14)] [458].

### Critical surface of a superconductor

A superconductor screens magnetic fields away such that field intensity decays on distances  $\lambda_L$ . However, a superconductor cannot withstand arbitrarily high magnetic fields. The limiting magnetic field strength is determined by the energetics of the superconducting condensate and magnetic field. For this characterization, it is more convenient to work with the Gibbs free energy  $G(\mathbf{H}) = F(\mathbf{H}) - \mathbf{H} \cdot \mathbf{B}$  which is a function of the external magnetizing field  $\mathbf{H} = \mathbf{B}/\mu_0$ . In the discussion of Figure 3.1, we have seen that the energy density of the superconducting condensate without a magnetic field is given by  $f_s = g_s = -a^2/(2b)$ . On the other hand, if we are in the normal state outside the superconductor, e.g., a metal, the free energy density of the magnetic field is given by  $g_n = f_n - HB = -H^2/(2\mu_0)$ . The superconducting phase breaks down when  $g_n \leq g_s$  where the equality condition defines the thermodynamic critical field

$$H_{c,\text{th}} = \sqrt{\frac{a^2}{\mu_0 b}}. \quad (3.27)$$

A domain wall separates the normal and superconducting state when  $H = H_{c,\text{th}}$ . Its surface tension  $\sigma_{\text{sn}} = \Delta G/A$  (Gibbs free energy per area  $A$  of the interface) can be written as [44, 458]

$$\sigma_{\text{sn}} = \frac{\mu_0 H_c^2}{2} \int_{-\infty}^{\infty} dx \left[ \left( \frac{H(x)}{H_{c,\text{th}}} - 1 \right)^2 - \left( \frac{\Psi(x)}{\Psi_0} \right)^4 \right], \quad (3.28)$$

which describes the difference of magnetic field energy and condensation energy at the interface. Depending on the spatial dependence of the magnetizing field  $H(x)$  and order parameter  $\Psi(x)$ ,  $\sigma_{\text{sn}}$  can be either positive or negative. These cases give rise to the classification of type I ( $\sigma_{\text{sn}} > 0$ ) and type II ( $\sigma_{\text{sn}} < 0$ ) superconductors.<sup>12</sup> The spatial dependence is controlled by  $\lambda_L$  and  $\xi$  such that their ratio

$$\kappa = \frac{\lambda_L}{\xi}, \quad (3.29)$$

called the Ginzburg–Landau parameter, effectively determines the type of superconductor. The critical value can be found from the condition  $\sigma_{\text{sn}} = 0$  yielding  $\kappa = 1/\sqrt{2}$  (cf. p. 392 in Ref. [44]).

<sup>12</sup>Sometimes the declaration of Pippard superconductors (type I) and London superconductors (type II) is used when the predominant character of electrodynamics is emphasized.

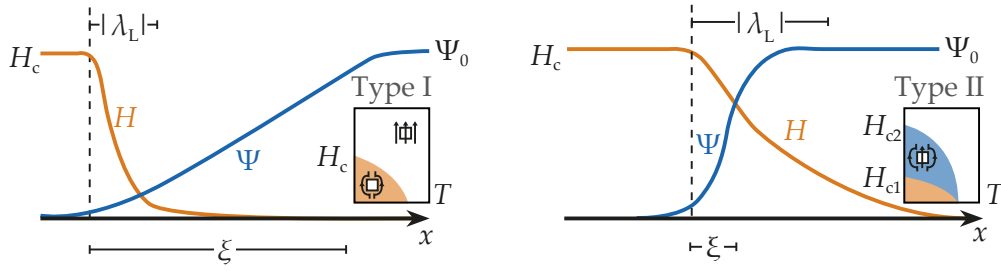


**Figure 3.2 – Classification types of superconductors.** Schematic behavior of the order parameter  $\Psi$  and magnetic field  $H$  at the domain wall of type I (left) and type II (right) superconductors. The insets show the typical  $H$ - $T$  phase diagrams, where type I superconductors only have a Meissner phase (orange) with no penetrating field lines and type II superconductors can host an additional vortex lattice phase (blue) with partially penetrating magnetic flux lines.

The schematic behavior of magnetic field and order parameter (condensate density) for type I and II superconductors is drawn in Figure 3.2. In type I superconductors ( $\kappa < 1/\sqrt{2}$ , i.e.,  $\xi > \sqrt{2}\lambda_L$ ), the coherence length is large and the condensate can smoothly adapt to quickly decaying magnetic fields. Most pure elemental superconductors (cf. Figure 1.3) are classified as type I, with the exceptions of niobium (Nb) and vanadium (V) [30]. In contrast, type II superconductors ( $\kappa > 1/\sqrt{2}$ ) have large penetration depths such that areas exist where the condensate order parameter is recovered while magnetic field lines remain. For intermediate magnetic field strength, it is then energetically more favorable to create a mixed phase of coexisting superconducting and normal domains such that two critical magnetic fields  $H_{c1} < H_{c2}$  exist. This mixed phase is realized for  $H_{c1} < H < H_{c2}$ , where an Abrikosov lattice [270] of superconducting vortices emerges in which the magnetic flux is contained. The magnitude of the flux  $\Phi$  is quantized due to the fixed phase of the condensate in units of the flux quantum  $\Phi_0 = h/(2e) = \pi\hbar/e$  [44, 458]. Most unconventional superconductors as well as conventional alloy and compound superconductors are of type II, including the technologically relevant compounds NbTi and Nb<sub>3</sub>Sn [4, 30].

The critical magnetic fields are related to each other and can be expressed by the two characteristic length scales  $\xi$  and  $\lambda_L$ . The thermodynamic critical field (3.27) is given by [458]

$$\mu_0 H_{c,\text{th}} = \frac{\Phi_0}{2\sqrt{2}\pi\lambda_L\xi}. \quad (3.30)$$

It determines the first and second critical field of type II superconductors via

$$\mu_0 H_{c1} = \mu_0 H_{c,\text{th}} \frac{\ln \kappa}{\sqrt{2}\kappa} = \frac{\Phi_0}{4\pi\lambda_L^2} \ln \frac{\lambda_L}{\xi}, \quad (3.31a)$$

$$\mu_0 H_{c2} = \sqrt{2}\kappa\mu_0 H_{c,\text{th}} = \frac{\Phi_0}{2\pi\xi^2}. \quad (3.31b)$$



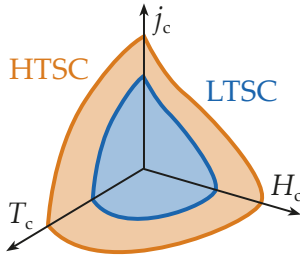


**Figure 3.3 – Critical surface of a superconductor.** Superconducting performance is limited by the critical temperature  $T_c$ , critical magnetic field  $H_c$ , and critical current density  $j_c$ . The volume encompassed by the critical surface is typically much larger in a high-temperature superconductor (HTSC) compared to a low-temperature superconductor (LTSC).

As magnetic fields and currents are linked by Ampère’s law (3.24), a critical supercurrent density  $j_c$  has to exist. Upholding a stationary current implies charge flow, i.e., Cooper pairs have to move through the material with finite center-of-mass momentum  $q$ . The associated kinetic energy  $\hbar^2 q^2 / 2m^*$  at some point exceeds the pairing energy of the condensate, leading to a breakup of Cooper pairs (cf. also Eq. (3.80)). In GL theory, this limit is reached at the depairing current [458]

$$j_{\text{dp}} = \frac{2\sqrt{2}H_{c,\text{th}}}{3\sqrt{3}\lambda_L} = \frac{\Phi_0}{3\sqrt{3}\mu_0\xi\lambda_L^2}. \quad (3.32)$$

We use this relation in publication VI to obtain the penetration depth by calculating supercurrents in the framework of microscopic theories. The depairing current constitutes the theoretical upper maximum to achievable critical currents  $j_c$  as they crucially depend on sample geometry and defect densities through effects like vortex pinning [458, 478]. In fact, elaborate experimental setups are necessary for  $j_c$  reaching  $j_{\text{dp}}$  [479].

The limiting values  $T_c$ ,  $H_c$ , and  $j_c$  define the critical surface of a superconductor drawn in Figure 3.3. An ideal superconducting material has a large volume encompassed by the critical surface where typically low-temperature superconductors (of type I) have a smaller volume than high-temperature superconductors. For engineering of superconducting materials, e.g., to optimize the critical surface, the knowledge of the length scales  $\lambda_L$  and  $\xi$  is pivotal as Eqs. (3.30–3.32) and the preceding discussion showed.

We note in passing that  $H_{c(2)}$  is not the only limiting magnetic field. In addition, the Clogston–Chandrasekhar limit [480, 481], also called the Pauli paramagnetic limiting field, exists for singlet-paired superconductors. It arises from the competition of the superconducting gap  $\Delta$  and Zeeman splitting energy determining the critical value [481]

$$H_p = \frac{\Delta}{2\mu_B} \stackrel{\text{BCS}}{=} \frac{1.76T_c}{2\mu_B} \approx 2.6 T_c \frac{\text{T}}{\text{K}} \quad (3.33)$$

in BCS theory.<sup>13</sup> Here,  $\mu_B$  is the Bohr magneton. Early on, it was realized that  $H_p$  can be surpassed in systems with SOC [30] where, for instance, in recent years Ising-type superconductivity was discovered in several transition metal dichalcogenides (TMDCs) [73, 482–485]. On the other hand, the observation of critical magnetic fields exceeding the Pauli paramagnetic limit is often interpreted as an indication for triplet superconductivity where the parallel-aligned Cooper pair spins stay unaffected by the Zeeman splitting. Recently, this has been discussed in magic-angle twisted trilayer graphene (MATTG) [78, 486] and in uranium-based ferromagnetic heavy Fermion compounds [90] with the notable mention of UTe<sub>2</sub> [59, 89], where the re-entrant superconducting phase at high magnetic fields  $H > 30$  T is surpassing the paramagnetic limit by far.

#### Order parameter with finite momentum

Although magnetism and superconductivity are competing, the possibility of their coexistence has been independently conjectured by Fulde and Ferrel (FF) [487] and Larkin and Ovchinnikov (LO) [488] for superconductors where Cooper pairs have finite center-of-mass momenta. This is known as FFLO theory [489, 490] where the generalized FFLO order parameter takes the form

$$\Psi_{\text{FFLO}}(\mathbf{r}) = \sum_{\mathbf{q}} |\Psi_{\mathbf{q}}| e^{i\mathbf{q}\mathbf{r}} \quad (3.34)$$

with a linear combination of different momenta  $\mathbf{q}$ . Such an order parameter breaks time-reversal symmetry as the  $\mathbf{q}$ -dependent phase corresponds to a magnetic field because of the coupling between phase gradient and vector potential. The initial proposals by FF and LO are specific cases of the order parameter (3.34). FF-type pairing assumes that a single momentum  $\mathbf{q}$  is taken, such that the order parameter has a helical phase

$$\Psi_{\text{FF}}(\mathbf{r}) = |\Psi| e^{i\mathbf{q}\mathbf{r}} , \quad (3.35)$$

corresponding to a homogeneous phase twist along the direction of  $\mathbf{q}$ . This order parameter describes Cooper pairs with finite center-of-mass momentum  $\mathbf{q}$  (cf. Eq. (3.73)). The initial LO-type pairing, on the other hand, considers opposite momenta  $\pm\mathbf{q}$  such that the order parameter becomes

$$\Psi_{\text{LO}}(\mathbf{r}) = |\Psi|(e^{i\mathbf{q}\mathbf{r}} + e^{-i\mathbf{q}\mathbf{r}}) = 2|\Psi| \cos(\mathbf{q}\mathbf{r}) . \quad (3.36)$$

---

<sup>13</sup>If one instead compares the pair condensation energy  $N(0)\Delta^2/2$  (cf. Eq. (3.99)) and paramagnetic magnetization energy  $\chi H^2/2 = N(0)\mu_B^2 H^2$ , the resulting limiting field strength is  $H_p = \Delta/(\sqrt{2}\mu_B) \approx 1.86 T_c$  T/K [480].

It describes a periodic amplitude modulation with wave vector  $\mathbf{q}$ , which is commonly also referred to as a pair density wave (PDW) [491]. Different to FF pairing with constant amplitude, the LO and generalized FFLO states necessarily break the point group symmetry of the lattice.<sup>14</sup> Many systems with FFLO pairing have been theoretically suggested [489, 490, 492–501] and also experimentally verified in layered organic superconductors [502–505], heavy-fermion compounds [506–510], iron-based superconductors [510–512], proximitized topological insulators [513, 514], TMDCs [515–518], or possibly cuprates [519].

The theoretical framework of Cooper pairs with finite momentum is a convenient tool. For instance, it is used to describe an anisotropic supercurrent flow relevant for the recently discovered superconducting diode effect [520–522], or to probe the condensate response to small phase perturbations pertinent to the superconducting stiffness [499, 523] discussed in section 3.1.3. Based on the finite-momentum pairing formalism, we developed a microscopic approach to the intrinsic length scales ( $\xi$  and  $\lambda_L$ ) in publication VI where we also further discuss the Ginzburg–Landau phenomenology pertinent to an order parameter of FF-type (3.35).

### Dimensionless GL equations

To conclude, we emphasize that the GL free-energy for superconductors (3.21) contains two coupled components: the order parameter  $\Psi$  and vector potential  $\mathbf{A}$ . Each of them introduces an intrinsic length scale given by the correlation length  $\xi$  and the London penetration depth  $\lambda_L$ , respectively. These characteristic scales,  $\xi$  and  $\lambda_L$ , cast the stationary point conditions determined by  $\delta\mathcal{F}_{\text{GL}}/\delta\Psi^* = 0$  and  $\delta\mathcal{F}_{\text{GL}}/\delta\mathbf{A} = 0$ , known as the Ginzburg–Landau equations, into a dimensionless form [461]. By introducing  $g = \Psi/\Psi_0$ ,  $\mathbf{a} = (\Phi_0/2\pi\xi)\mathbf{A}$  and  $\kappa = \lambda_L/\xi$ , the GL equations can be written as follows:

$$(-i\nabla - \mathbf{a})^2 g + g - g^3 = 0, \quad (3.37a)$$

$$\underbrace{\kappa^2 \nabla \times (\nabla \times \mathbf{a})}_{=j} + \frac{i}{2}(g^* \nabla g - g \nabla g^*) + g^2 \mathbf{a} = 0. \quad (3.37b)$$

Here,  $j$  is the dimensionless supercurrent. In analogy to atomic physics,  $\lambda_L$  and  $\xi$  hold a similar significance to the Bohr radius  $a_0$  in relation to atomic binding energies. For the discussion of various boundary conditions and solutions to the GL equations, we refer to the books by Tinkham [458].

<sup>14</sup>The literature on FFLO-type pairing is not very strict in differentiating these two cases. Mostly, LO pairing or PDW are discussed while FF superconductivity appears more rarely [490].

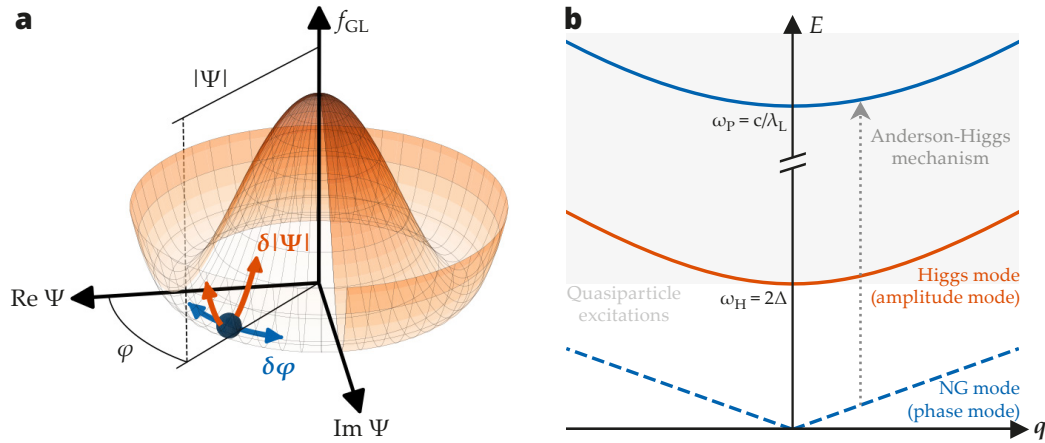


**Figure 3.4 – Mexican hat potential and excitation modes of a complex order parameter.** (a) The “Mexican hat”-shaped GL free-energy potential of the complex order parameter  $\Psi = |\Psi|e^{i\varphi}$ . The Higgs (orange) and Nambu–Goldstone (NG; blue) mode excitations associated with amplitude  $\delta|\Psi|$  and phase  $\delta\varphi$  variations, respectively, are schematically drawn. (b) Schematic excitation spectrum of a superconductor in GL theory. The Anderson–Higgs mechanism gaps out the Nambu–Goldstone mode with an energy on the order of the plasma frequency  $\omega_p$ . As a consequence, the Higgs mode becomes the low-energy excitation with gap  $2\Delta$ , overlapping with the quasiparticle continuum.

### 3.1.2 Anderson–Higgs mechanism and excitation modes

The complex order parameter of a superconductor has two degrees of freedom, the amplitude  $|\Psi|$  and phase  $\varphi$  [524, 525]. They can fluctuate in the free energy potential landscape (Eq. (3.12)) as drawn in Figure 3.4a, which is commonly referred to as “Mexican hat” potential due to its geometric shape. Each of the possible fluctuations,  $\delta|\Psi|$  and  $\delta\varphi$ , give rise to a collective excitation mode.

The amplitude mode is called Higgs mode in analogy to the Higgs particle in the standard model of particle physics<sup>15</sup>. Recently, the Higgs-mode spectroscopy in superconductors has become experimentally feasible through the developments of terahertz spectroscopy [410, 528, 529], which constitutes a further classification tool of the superconducting state in and out of equilibrium and its interplay with other collective modes [184, 524, 525, 530–532]. The Higgs mode has a mass due to the radial curvature of the free energy which corresponds to an excitation gap of energy  $\omega_H$  at zero momentum. In BCS theory, this excitation energy is identical to the superconducting gap  $\hbar\omega_H = 2\Delta$  leading into the quasiparticle continuum [525]. Using Eq. (3.14), we can associate this energy to the correlation length  $\omega_H \sim \xi^{-1}$ .

The phase mode, on the other hand, is called the Nambu–Goldstone mode. Its appearance and the number of Nambu–Goldstone modes is corollary to SSB of a continuous symmetry as captured in Goldstone’s theorem [463, 533, 534]. The

<sup>15</sup>In fact, Higgs first proposed the mechanism for the appearance of the particle now bearing his name within a generic model of broken U(1) symmetry [526], drawing conceptual inspiration from the phenomenon of superconductivity due to Anderson [527].

Nambu–Goldstone mode is typically a massless mode, i.e., gapless and vanishing for zero momentum. The best known example in condensed matter physics are acoustic phonons ( $\omega_q = v_s|q|$ ) that emerge from breaking of continuous translation symmetry. In the case of broken U(1) symmetry, the Nambu–Goldstone mode corresponds to phase translation of the order parameter, i.e., moving in azimuthal direction within the brim of the Mexican hat potential.

In superconductors, the Nambu–Goldstone mode is gapped out due to the coupling of the order parameter’s phase to the gauge field  $A$ . This phenomenon is known as the Anderson–Higgs mechanism [526, 527] where the gauge field acquires mass, giving rise to a plasmon mode of excitation energy  $\omega_p$  (see Eq. (3.40) below). Consequently, the Higgs mode becomes the lowest excitation as sketched in Figure 3.4b. We can see this by considering fluctuations in the free energy given in Eq. (3.21). By inserting  $\Psi(\mathbf{r}) = (|\Psi_0| + \delta|\Psi(\mathbf{r})|)e^{i\varphi(\mathbf{r})}$  and only keeping terms up to second order in fluctuations, we obtain [525, 535]

$$f_{\text{GL}} = \underbrace{-2a}_{>0} \delta|\Psi|^2 + \frac{\hbar^2}{2m_{\text{P}}^*} (\nabla\delta|\Psi|)^2 + \frac{2e^2|\Psi|^2}{m_{\text{P}}^*} \left( A - \frac{\Phi_0}{2\pi} \nabla\varphi \right)^2 + \frac{1}{2\mu_0} (\nabla \times A)^2. \quad (3.38)$$

The first two terms describe the gapped amplitude mode of excitation energy  $-2a \sim 2\Delta$  and the last two terms belong to the phase mode. As the free energy must be gauge invariant, only the combination  $A - \frac{\Phi_0}{2\pi} \nabla\varphi$  of vector potential  $A$  and phase  $\varphi$  is gauge independent. Hence, the gauge transformation  $A \mapsto A + \frac{\Phi_0}{2\pi} \nabla\varphi$  allows to eliminate the phase from the free energy by generating a bare quadratic term of the vector potential. To see its nature, we Fourier transforming the free energy (3.38) yielding [535]

$$f_{\text{GL}} = \sum_q \left( -2a + \frac{\hbar^2}{2m_{\text{P}}^*} q^2 \right) \delta|\Psi_q| \delta|\Psi_{-q}| + \frac{1}{2\mu_0} \left( \frac{1}{\lambda_{\text{L}}^2} A_q^{\parallel} A_{-q}^{\parallel} + \left[ \frac{1}{\lambda_{\text{L}}^2} + q^2 \right] A_q^{\perp} A_{-q}^{\perp} \right), \quad (3.39)$$

where  $A_q = A_q^{\parallel} + A_q^{\perp}$  is split into longitudinal and transversal components with respect to the direction of  $q$ . The vector potential term  $\propto q^2$  is the usual magnetic energy corresponding to photons with energy  $\hbar\omega_q = qc$ . The absorption of the phase gradient introduced the constant terms proportional to  $\lambda_{\text{L}}^{-2}$ , such that notably all components of the vector potential appear in Eq. (3.39). By including time dependent variations in the free energy, one finds that this corresponds to a mass-carrying photon dispersion  $\hbar^2\omega_q^2 = m_{\text{A}}^2 c^4 + q^2 c^2$  [44, 535] with  $m_{\text{A}} = \hbar/(c\lambda_{\text{L}})$  inside the superconductor. This equates to an excitation gap

$$\omega_{q=0} = \frac{m_{\text{A}} c^2}{\hbar} = \frac{c}{\lambda_{\text{L}}} \stackrel{\text{Eq. (3.23)}}{=} \sqrt{\frac{m^*}{e^2 n_{\text{s}} \epsilon_0}} = \omega_{\text{p}}, \quad (3.40)$$

corresponding to the plasmon energy for charged particles of density  $n_s$ . Thus, the Goldstone mode has become a “massive plasmon excitation” [527] by absorbing the vector potential, associating it with the length scale  $\lambda_L$ . The Meissner–Ochsenfeld effect illustrated in section 3.1.1 is a direct consequence of this, cf. Eq. (3.22) with the constant  $A^2/\lambda_L^2$  term.

We note that the first term of Eq. (3.39) implies the dispersion

$$\hbar\omega_q = 2|a|(1 + \xi^2 q^2) \quad (3.41)$$

for the amplitude mode. It shows that the cost of finite-momentum amplitude excitations is dictated by the correlation length  $\xi$ , similar to the suppression of the order parameter in Eq. (3.17).

#### 3.1.3 Phase rigidity, supercurrent flow, and condensate stiffness

The existence of a dissipationless supercurrent is an essential property of a superconducting system. We introduced the current density in Eq. (3.25) but it is insightful to insert the order parameter  $\Psi = |\Psi|e^{i\varphi}$  yielding

$$\mathbf{j} = 2e|\Psi|^2 \underbrace{\frac{\hbar}{m_P^*} \left( \nabla\varphi - \frac{2\pi}{\Phi_0} \mathbf{A} \right)}_{v_s} = 2en_P \mathbf{v}_s = en_s \mathbf{v}_s. \quad (3.42)$$

Here, we have inserted the superfluid velocity  $v_s$  and replaced  $|\Psi|^2 = n_P = n_s/2$ . We see that not only an external vector potential but importantly also a twist of the phase  $\nabla\varphi$  can induce a supercurrent flow. Hence, macroscopically coherent pair movement is driven by the deformation of the ground-state phase, rather than by excitations above the ground state which are responsible for conventional currents.

Bending or twisting the phase is associated with an energy cost due to the well-defined phase of the order parameter. This resilience of the superconducting condensate to phase changes is referred to as *phase rigidity*, which ultimately enables persistent supercurrents. From a microscopic perspective, the phase rigidity can be viewed as the kinetic energy of Cooper pairs in the condensate. The associated (kinetic) phase-bending energy is given by

$$E_{\text{phase}} = \frac{m_P^* n_P}{2} \int d^d r v_s^2(\mathbf{r}) = \frac{\hbar^2 n_s}{8m^*} \int d^d r (\nabla\varphi(\mathbf{r}))^2 = \frac{D_s}{2} \int d^d r (\nabla\varphi(\mathbf{r}))^2, \quad (3.43)$$

where we set  $\mathbf{A} = 0$  in  $v_s$  and we introduced the phase or condensate *stiffness*  $D_s$ , see Eq. (3.44) below.<sup>16</sup> The stiffness measures the energy cost associated with phase gradients or, framed differently, the condensate’s resilience to phase twists. It

<sup>16</sup>Different naming conventions and nomenclature exist for the phase stiffness throughout the literature. For instance, it is also called (phase) rigidity modulus or helicity modulus, and other

is analogous to how mass measures the inertia of particles, opposing changes in their velocity. A large value of  $D_s$  indicates that the superconductor has a strong resistance to phase fluctuations, thereby maintaining its phase rigidity. In GL theory, we find  $D_s \propto n_s/m^*$  depending on the effective mass of charge carriers. This is intuitive, as lighter particles can carry a stronger supercurrent. Recently, it has been shown that additional geometric contributions to the stiffness exist in multi-band systems [450–452, 536].

The stiffness  $D_s$  can be expressed by the measurable London penetration depth (3.23). However, by our definition in Eq. (3.43), the units of the stiffness depend on the dimensionality of the system.<sup>17</sup> Notably,  $D_s$  has the unit of energy in  $d = 2$ , whereas it needs for  $d = 3$  an additional length scale  $L$  to produce the correct units. The definition of a suitable length  $L$  can be tricky and depends on the geometry of the system at hand [537]. In the following, we focus on the discussion of the two-dimensional stiffness given by

$$D_s = \frac{\hbar^2 n_s}{4m^*} = \frac{\hbar^2 n_P}{m_P^*} = \frac{\hbar^2}{4e^2 \mu_0 \lambda_L^2} \stackrel{\text{CGS}}{=} \frac{\hbar^2 c^2}{16\pi e^2 \lambda_L^2}. \quad (3.44)$$

We also state the stiffness in CGS units for comparison to the commonly found expression in theoretical literature, e.g., Ref. [389]. The two-dimensional stiffness (3.44) is also important for some three-dimensional systems, where it is possible to determine a suitable length  $L$  and reduce  $D_s^{3D} = D_s^{2D}/L$ . The simplest case is given for thin films with thickness  $w$  smaller than the correlation length  $\xi$ . As phase fluctuations are confined in-plane, the perpendicular direction can be integrated out yielding  $L = w$ . The corresponding areal density  $n_s^{3D} w \equiv n_s^{2D}$  is often used as an effective two-dimensional superconducting density entering Eq. (3.44) instead of discussing  $D_s^{3D} = D_s^{2D}/w$ . A similar argument applies for quasi-two-dimensional layered systems, where superconductivity is confined to weakly coupled planes, as found in cuprates or nickelates. The relevant length is the average interplane distance  $z$  which needs to be larger than the out-of-plane coherence length  $\xi^\perp$ . The corresponding penetration depth  $\lambda_L^\perp$  sets  $D_s$ . Other cases of three-dimensional superconductors are more complicated where  $L$  should be considered as a spatial cutoff for the integral. A good estimate is to choose the cut off on the order of the correlation length  $L \sim \xi$  [537].

The stiffness encodes the linear response of a system to small applied vector potentials  $A$  as can be seen by gauge transforming Eq. (3.47) to  $j = -\tilde{D}_s A$ . The prefactor to the vector potential is called the superfluid weight, which is a different

---

symbols  $\rho_{(s)}$ ,  $J_{(s)}$ ,  $I_{(s)}$ ,  $\Upsilon_{(s)}$ , or  $Q_{(s)}$  are commonly used. We discuss an equivalent definition called superfluid weight  $\tilde{D}_s$  in Eq. (3.45).

<sup>17</sup>The general units are  $[\mathcal{E}L^{2-d}]$  with energy  $\mathcal{E}$  and length  $L$  for given dimension  $d$ .

convention of defining the superfluid stiffness:

$$\tilde{D}_s = \frac{(2e)^2}{\hbar^2} D_s = \frac{e^2 n_s}{m^*} = \frac{1}{\mu_0 \lambda_L^2}. \quad (3.45)$$

Its naming derives from the relation to the static ( $\omega = 0$ ), long-wavelength limit ( $q \rightarrow 0$ ) of the electromagnetic response function (see Eq. (3.49) below), giving rise to the Meissner effect and its conceptual similarity to the Drude weight  $D$  in normal conductors [449, 538]. To evaluate the linear response and calculate  $D_s$ , different but equivalent viewpoints are employed.

On the one hand, the stiffness is obtained from the second derivative of thermodynamic potentials [44, 389, 450, 451, 457, 523, 539–542]. Since phase gradient and vector potential are gauge equivalent, the derivative can be taken with respect to either of them which changes whether one probes for the definition of the stiffness  $D_s$  or weight  $\tilde{D}_s$ . This can be seen from the phase fluctuation free energy by changing

$$\mathcal{F}_{\text{phase}} = \frac{D_s}{2} \int d^2r \left( \nabla\varphi - \frac{2e}{\hbar} \mathbf{A} \right)^2 \stackrel{\text{Eq. (3.45)}}{=} \frac{\tilde{D}_s}{2} \int d^2r \left( \mathbf{A} - \frac{\hbar}{2e} \nabla\varphi \right)^2. \quad (3.46)$$

For the current density, we need to take the first derivative of the free energy

$$\mathbf{j} = -\frac{\delta \mathcal{F}_{\text{phase}}}{\delta \mathbf{A}} = -\tilde{D}_s \left( \mathbf{A} - \frac{\hbar}{2e} \nabla\varphi \right) = \frac{2e}{\hbar} D_s \left( \nabla\varphi - \frac{2e}{\hbar} \mathbf{A} \right) = \frac{2e}{\hbar} \frac{\delta \mathcal{F}_{\text{phase}}}{\delta (\nabla\varphi)}, \quad (3.47)$$

where then the second derivative yields the stiffness (or superfluid weight)

$$D_s = \frac{\delta^2 \mathcal{F}_{\text{phase}}}{\delta (\nabla\varphi)^2} \Big|_{\nabla\varphi \rightarrow 0} = -\frac{\hbar^2}{4e^2} \frac{\delta^2 \mathcal{F}_{\text{phase}}}{\delta \mathbf{A}^2} \Big|_{\mathbf{A} \rightarrow 0} = \frac{\hbar^2}{4e^2} \tilde{D}_s. \quad (3.48)$$

These relations can be directly evaluated in mean-field theory [44, 450, 451, 523, 539, 543, 544] or expressed by Green's functions to calculate the stiffness from microscopic models, where typically further approximations apply [389, 451, 540–542]. We will derive and discuss the corresponding BCS expression in section 3.2.4.

Another approach to  $D_s$  evaluates the relevant linear response correlation functions, which in case of an applied static vector potential is the current-current correlation function. Here, the superfluid stiffness is obtained via<sup>18</sup> [449, 455, 538]

$$D_s = D_{\text{dia}} + D_{\text{para}} = -\langle E_{\text{kin}} \rangle - \lim_{q \rightarrow 0} \chi_{jj}(\mathbf{q}, \omega = 0) \quad (3.49)$$

---

<sup>18</sup>Note that the short-wavelength limit  $q \rightarrow 0$  is applied after taking the static limit  $\omega = 0$ . Changing the order of limits yields the Drude weight  $D$  encoding the normal current response where  $D$  and  $D_s$  can be used to differentiate between different types of conductive behavior [449, 538].



with the kinetic energy  $\langle -E_{\text{kin}} \rangle$  (diamagnetic term) and the paramagnetic current-current response function

$$\chi_{jj}(\mathbf{r}, \tau) = \langle \mathcal{T}_\tau \hat{j}_x(\mathbf{r}, \tau), \hat{j}_x(0, 0) \rangle \quad (3.50)$$

for the example of an applied current (operator)  $\hat{j}$  in  $x$  direction. This approach has been often applied in the context of DMFT studies by neglecting vertex corrections [455, 545].

Both approaches become equivalent in the limit of small  $q$  [451]. In practice, this can be used to directly calculate  $D_s$  from inducing a (small) current response instead of evaluating the response function. It is achieved by imposing a constraint on the order parameter with small coupled  $A$ , or equivalently, a small homogeneous phase twist which generates a finite supercurrent flow in the system. Either the current response or change in free energy due to additional kinetic energy of the Cooper pair flow allows for computing the stiffness then [451, 523, 540, 542]. We follow this idea and extend it in publication VI by calculating the supercurrent for arbitrary  $q$ . We achieve this by imposing a finite-momentum order parameter  $\Psi_q = |\Psi|e^{iqr}$  constraint, where the phase gradient  $\nabla\varphi = \nabla(qr) = q$  is characterized by momentum  $q$ . We introduced this type of order parameter in the context of FFLO theory in section 3.1.1. We recover the linear-response-based approaches described here in the  $q \rightarrow 0$  limit.

### 3.1.4 Limits of GL theory — Ginzburg–Levanyuk criterion

In our preceding discussions, we assumed small fluctuations of the order parameter allowing for a low-order Taylor expansion of the GL free energy. Large fluctuations, however, can result in a significant deviation from the mean-field description [462]. Levanyuk [546] and Ginzburg [547] independently proposed criteria that effectively set limits to the applicability of such a mean-field treatment and hence GL theory. The essential observation is that fluctuations affect the mean-field order parameter only on length scales  $x \gg \xi$ , since the correlation length  $\xi$  is the coarse graining scale for the order parameter in the path integral (3.6). Conversely, the strength of fluctuations on shorter length scales should be small for a valid description which can be quantified via [44, 463]

$$\frac{1}{\xi^d} \int_0^\xi d^d r \langle \psi(\mathbf{r}) \hat{\psi}(0) \rangle - \langle \psi(\mathbf{r}) \rangle \langle \hat{\psi}(0) \rangle \ll \frac{1}{\xi^d} \int_0^\xi d^d r \langle \hat{\psi}(\mathbf{r}) \rangle^2. \quad (3.51)$$

The variance of the order parameter should be smaller than its average ( $\delta\Psi^2 \gg \Psi^2$ ) in a correlation volume  $\xi^d$ , effectively measuring when local fluctuations become able to destroy local order. Evaluating this inequality gives a qualitative criterion for the applicability of a mean-field description [44, 462, 463]. A way to formulate

this is given by

$$\frac{\Delta T}{T_c} \gg \left( \frac{k_B}{\xi_0^d \Delta C_V} \right)^{\frac{2}{4-d}} \simeq Gi_d, \quad (3.52)$$

where we introduced the Ginzburg–Levanyuk number  $Gi_d$ . This inequality quantifies the temperature region  $\Delta T$  around  $T_c$  below which fluctuation effects become too strong and mean-field theory becomes invalid.  $\Delta C_V$  is the specific heat jump at the phase transition and  $\xi_0^d \Delta C_V = S_G$  can be interpreted as the entropy in the coherence volume  $\xi_0^d$  associated with the emergence of order [44]. Note that  $Gi_d$  does not define a strict boundary but rather provides an estimate for the relevant order of magnitude for  $\Delta T$ .

We can make two important observations here: First, the coherence length  $\xi_0$  is crucial in setting the temperature region  $\Delta T$ . For superconductors with large  $\xi_0$ , deviations from mean-field theory are expected only very close to  $T_c$ . Typical values for  $Gi_d$  are given by  $10^{-16}$  for strongly type I superconductors to  $10^{-4}$  for strongly type II superconductor [463]. This is one reason why BCS theory is able to describe conventional superconductors so well – corrections stemming from fluctuation effects are relevant only on a tiny interval  $\Delta T \lesssim 10^{-12} T_c$  [462] many orders of magnitude smaller than that accessible in experiment.

Second,  $Gi_d$  shows a dependence on the (spatial) dimension  $d$ . The case  $d = 4$  is called the upper critical dimension above which mean-field theory becomes exact up to  $T_c$ , whereas for lower dimensions  $d < 4$  thermal fluctuations qualitatively impact the phase transition and render a mean-field description invalid. The Ginzburg–Levanyuk number hints at fluctuation effects becoming stronger, the lower the dimension is. In fact, also a lower critical dimension exists at or below which fluctuations are so intense that they prevent long-range order entirely. For superconductors, this lower dimension is  $d = 2$  because of which a different approach to phase transitions needs to be taken as described in the next section.

#### 3.1.5 Berezinskii–Kosterlitz–Thouless phase transition

Two-dimensional systems are special because the Hohenberg–Mermin–Wagner theorem [359, 548] forbids SSB at finite temperature as formation of long-range order is destroyed by thermal fluctuations.<sup>19,20</sup> Despite this limitation, two-dimensional

---

<sup>19</sup>Often, this theorem is only named after Mermin–Wagner as their paper was published first. However, their work was, in fact, inspired by Hohenberg’s work as stated by Mermin and Wagner [359]. The main difference is that Hohenberg discussed the case of superconductivity and superfluidity while Mermin and Wagner showed the absence of magnetism in one and two dimensions.

<sup>20</sup>We note that the Hohenberg–Mermin–Wagner theorem is of importance for strict two-dimensional systems and theoretical descriptions thereof, but its applicability to real materials is strongly limited [549].

systems can still host a different kind of phase transition or ordering that is qualitatively similar to true long-range order. This alternative ordering was independently proposed by Berezinskii [550] and by Kosterlitz and Thouless [551, 552].

The Berezinskii–Kosterlitz–Thouless (BKT) transition [463, 537, 553] is distinct from conventional phase transitions because the decay of the correlation function (single-particle density matrix) follows a power law

$$\langle \hat{\psi}^\dagger(\mathbf{r})\hat{\psi}(\mathbf{r}') \rangle \propto |\mathbf{r} - \mathbf{r}'|^{\eta(T)} \quad \text{for } |\mathbf{r} - \mathbf{r}'| \rightarrow \infty \quad (3.53)$$

with some system and temperature dependent exponent  $\eta(T)$  rather than being constant over long distances (cf. Eq. (3.4)) in the low-temperature phase. Such systems are said to have algebraic long-range order or to be quasi-long-range ordered. The emergence of this order constitutes a phase transition because the power law behavior of the correlation function cannot be analytically connected to the exponential decay seen in the disordered phase at higher temperatures. Yet, the free energy remains continuous at the transition point because of which it is classified as an “infinite-order” phase transition [463].

The mechanism driving the phase transition is the unbinding of vortex-antivortex pairs (Figure 3.5a) or pairs of higher order topological defects that can form at finite temperatures on the background of the SSB superconducting state at zero temperature. To understand this premise, we turn to the two-dimensional XY model for which the BKT transition was originally formulated in the context of (classical) magnetic systems with spin  $S = 1$ . For superconducting systems, the discrete XY model describes an array of superconducting islands with locally fluctuating phases connected by Josephson junctions, sometimes referred to as the Josephson lattice model [214, 389]. The corresponding Hamiltonian is given by

$$H_{XY} = -D_s \sum_{ij} \cos(\varphi_i - \varphi_j) \quad (3.54)$$

with the superconducting phase  $\varphi_i$  on site  $i$  and the stiffness  $D_s$  playing the role of the coupling constant between sites. At low temperatures, we can expand  $\cos(\varphi_i - \varphi_j) \approx 1 - \frac{1}{2}(\varphi_i - \varphi_j)^2$  and take the continuum limit of this model, replacing  $\varphi_i - \varphi_j \rightarrow \nabla\varphi(\mathbf{r})$  in the process, to obtain

$$H_{XY} = E_0 + \frac{D_s}{2} \int d^2r (\nabla\varphi(\mathbf{r}))^2 \quad (3.55)$$

with ground state energy  $E_0 = 2D_s N$  for a homogeneous (SSB) phase on all  $N$  lattice sites. The continuum model corresponds to the phase bending energy in Eq. (3.43) from which we introduced the stiffness  $D_s$ .

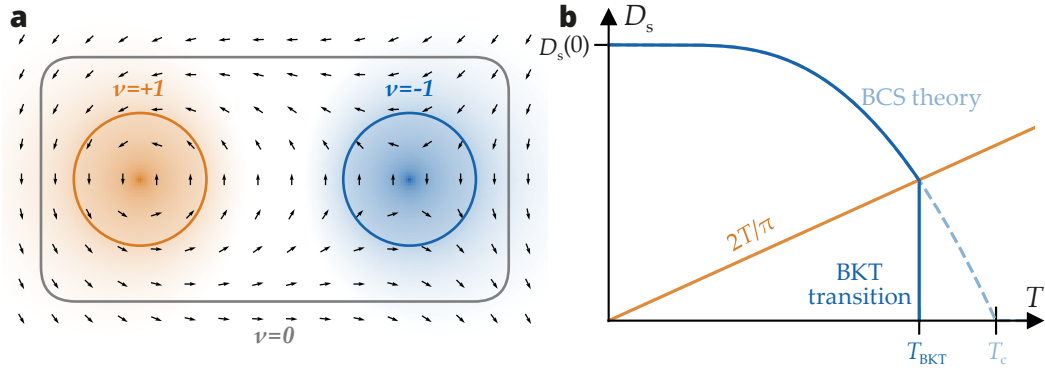


**Figure 3.5 – Vortex-antivortex pair and schematic BKT transition.** (a) Pair of vortex ( $\nu = +1$ ) and antivortex ( $\nu = -1$ ) as topological defects that can appear in the XY model. On larger distances than their separation, the vortex pair appears topologically neutral ( $\nu = 0$ ). (b) Illustration of the BKT transition determined from the temperature  $T$  dependence of the superconducting stiffness  $D_s$ . The transition occurs when the universal BKT line (solid orange) intersects with  $D_s$ , leading to a jump at  $T_{\text{BKT}}$ . The lighter blue dashed line is the mean-field BCS value of  $D_s$ , which has a higher  $T_c$  than  $T_{\text{BKT}}$ .

Local minima of the Hamiltonian exist for continuous fields  $\varphi(\mathbf{r})$  satisfying

$$\frac{\delta H_{XY}}{\delta \varphi(\mathbf{r})} = 0 \quad \Leftrightarrow \quad \nabla^2 \varphi(\mathbf{r}) = 0. \quad (3.56)$$

While the homogeneous field  $\varphi(\mathbf{r}) = \text{const.}$  is a trivial solution describing the ground state, a second class of solutions is given by vortices. A vortex is a topological excitation characterized by the phase winding around a singular point. It has a topological charge  $\nu$  corresponding to the winding number

$$\nu = \frac{1}{2\pi} \oint_C \nabla \varphi \cdot d\mathbf{l} \quad (3.57)$$

obtained by integrating over a closed contour  $C$  around the vortex core. Neutral bound pairs of topological defects with opposite charges, e.g., a vortex-antivortex pair with  $\nu = \pm 1$  (Figure 3.5a), can form as finite-energy excitations from the ordered (homogeneous) ground state. This induces a local disturbance of the superfluid's phase but it does not destroy global coherence for sufficiently strongly bound pairs. Separating defect pairs and creating singular vortices costs significant energy<sup>21</sup>, such that the thermally populated defects stay bound, yielding the algebraic long-range order (3.53).

As the temperature increases, vortex-antivortex pairs become more widely separated, with the distance between them growing as large as the separation between different pairs. Hence, pairs unbind and single defect excitations exist in the system, compromising the condensate's coherence until even quasi-long-range order is lost.

<sup>21</sup>With their topological charge  $\nu$ , vortices are analogous to normal Coulomb charges, allowing for a description of vortex fluctuations by a Coulomb gas model [553].

An insightful heuristic argument by Kosterlitz and Thouless [552] illustrates this idea: Let us consider the excitation of a singular vortex fulfilling  $\nabla\varphi(\mathbf{r}) = v/r$  with  $v = 1$ . Inserting this in Eq. (3.55) yields an energy  $E - E_0 = \pi D_s \ln(L/a)$  for a system of size  $L^2$  and lattice spacing  $a$ . The associated entropy is given by the number of possible places to insert the vortex, i.e.,  $S = k_B \ln(L^2/a^2) = 2k_B \ln(L/a)$ . Taken together, the free energy of creating a single vortex is given by

$$F = E - TS = E_0 + (\pi D_s - 2k_B T) \ln(L/a) . \quad (3.58)$$

At low temperature, the energy cost for creating the vortex is higher than the entropy gain due to the logarithmic scaling with the system size. For high enough temperatures, however, the entropy of creating a vortex dominates and any order will be destroyed. This changes the sign of the free energy which diverges in the thermodynamic limit  $L \rightarrow \infty$ , hinting at a phase transition around the sign-changing point  $\pi D_s = 2k_B T$ .

This argument is simplified, of course, as not a single vortex is created. Instead, multiple defect pairs unbind, as discussed above, which interact and induce screening. These effects were properly accounted for in a renormalization group (RG) treatment where the stiffness  $D_s$  gets renormalized in the process [553–555]. The fix point of the RG flow yields a transition at the *universal* condition of

$$D_s(T_{\text{BKT}}^-) = \frac{2}{\pi} k_B T_{\text{BKT}}^- . \quad (3.59)$$

This relation is shown in Figure 3.5b in comparison to the mean-field expectation from BCS theory. Coming from low temperatures, the superconducting stiffness jumps discontinuously from  $D_s(T_{\text{BKT}}^-)$  to  $D(T_{\text{BKT}}^+) = 0$  at the transition temperature  $T_{\text{BKT}}$  which is distinct to the continuous vanishing of mean-field theory. Consequently,  $T_{\text{BKT}}$  is lower than the mean-field value  $T_c$ , stemming from the enhanced influence of thermal fluctuations and topological defects.

Nowadays, the BKT transition has been measured in many different systems like thin  $^4\text{He}$  films, ultracold atomic gases, or superconducting films, verifying the universal jump in the superfluid stiffness [553]. For the discussion of superconducting materials, the BKT transition is important as many (unconventional) high-temperature superconductors, like cuprates or FeSe thin films, are quasi-two-dimensional materials. Here, the universal criterion (3.59) puts a strong constraint on the possibility of superconductivity [198] as it implies (cf. Figure 3.5b)

$$k_B T_{\text{BKT}} \leq \frac{\pi}{2} D_s , \quad (3.60)$$

which is sometimes referred to as Nelson–Kosterlitz criterion [555]. That is, for the (BKT) transition to occur, there must be a sufficient stiffness to support the bound

vortex-antivortex pairs at lower temperatures. As the stiffness is linked to the kinetic energy of electrons,  $D_s$  can be effectively quenched by strong correlation effects, which can lead to a suppression of  $T_c$ . We discuss the consequences and limitations for superconductivity further in chapter 6.

#### 3.1.6 Symmetry classification of the order parameter

In the phenomenological characterization of the superconducting state, we have concentrated on properties that arise from breaking of the U(1) phase-rotation symmetry. While it is the defining broken symmetry for a superconductor, in principle more symmetries of the underlying Hamiltonian can be broken. The occurrence of such additional symmetry breaking is the hallmark of unconventional superconductors, manifesting, for instance, as broken rotation symmetry due to anisotropic pairing. In unconventional superconductors, the superconducting gap can exhibit nodes in momentum space or possess more complex spin-orbital structures [II, III, IV, V, 108, 193–195, 346, 389, 556–559], leading to qualitatively different properties compared to conventional superconductors. The analogy to anisotropic pairing in superfluidity in  $^3\text{He}$  [560, 561] along with the discovery of heavy fermion and cuprate superconductors has prompted more detailed symmetry characterization of the superconducting state [167, 562]. Determining the pairing symmetry is a crucial tool for understanding the underlying microscopic mechanisms driving superconductivity in different material systems [478]. Pedagogical introductions can be found in Refs. [167, 562–565].

Central to describing the symmetries of the superconducting state are the internal degrees of freedom of the order parameter. For paired electrons in equilibrium and translational invariant systems, the relevant correlation function takes the form<sup>22</sup>

$$\Psi_{m\sigma, m'\sigma'}(\tau - \tau', \mathbf{r} - \mathbf{r}') = \langle \mathcal{T}_\tau c_{m\sigma\mathbf{r}}(\tau) c_{m'\sigma'\mathbf{r}'}(\tau') \rangle \quad (3.61)$$

with time-ordering operator  $\mathcal{T}_\tau$  and the fermionic annihilation operators carrying (Wannier) orbital or (Bloch) band  $m$ , spin  $\sigma$ , position  $\mathbf{r}$ , and time  $\tau$  dependencies. The exchange of any of these indices must obey the Pauli principle encoded by the anticommutation of the fermionic operators, i.e., the symmetry constraint

$$\Psi_{m\sigma, m'\sigma'}(\tau - \tau', \mathbf{r} - \mathbf{r}') = -\Psi_{m'\sigma', m\sigma}(\tau' - \tau, \mathbf{r}' - \mathbf{r}) \quad (3.62)$$

---

<sup>22</sup>Often, the energy gap  $\Delta$  is equivalently used for symmetry classifications. In most cases, this does not need to be differentiated from the pair wave function  $g \sim \langle cc \rangle \equiv \Psi$  discussed here, as they can be linked by  $\Delta = \mathcal{U} \langle cc \rangle$  for an effective attractive interaction  $\mathcal{U}$  (cf. BCS expression (3.87)). Care must be taken, however, in case of non-diagonal  $\mathcal{U}$  and when changing between orbital and band representation.

must be fulfilled. Fourier transforming yields the equivalent antisymmetric condition

$$\Psi_{m\sigma, m'\sigma'}(i\omega_n, \mathbf{k}) = -\Psi_{m'\sigma', m\sigma}(-i\omega_n, -\mathbf{k}) . \quad (3.63)$$

In matrix and four-vector notation  $k = (i\omega_n, \mathbf{k})$ , it can be compactly written as  $\underline{\Psi}(k) = -\underline{\Psi}^T(-k)$ . We can classify the order parameter symmetry by analyzing the behavior of a symmetry operation acting on any of its degrees of freedom. This entails the permutation of spins  $\hat{S}$ , relative coordinates (parity)  $\hat{P}$ , orbital indices  $\hat{O}$ , and relative time  $\hat{T}$ <sup>23</sup> according to:

$$\hat{S} \Psi_{m\sigma, m'\sigma'} = \pm \Psi_{m\sigma, m'\sigma'} , \quad (3.64a)$$

$$\hat{P} \Psi(\mathbf{r} - \mathbf{r}') = \pm \Psi(\mathbf{r}' - \mathbf{r}) \quad \text{or} \quad \hat{P} \Psi(\mathbf{k}) = \pm \Psi(-\mathbf{k}) , \quad (3.64b)$$

$$\hat{O} \Psi_{m\sigma, m'\sigma'} = \pm \Psi_{m'\sigma, m\sigma'} , \quad (3.64c)$$

$$\hat{T} \Psi(\tau - \tau') = \pm \Psi(\tau' - \tau) \quad \text{or} \quad \hat{T} \Psi(i\omega_n) = \pm \Psi(-i\omega_n) . \quad (3.64d)$$

By Fourier transforming, space and time permutation correspond to simple inversion of momentum  $\mathbf{k}$  and frequency  $i\omega_n$ , because of which we focus on this notation in the following. Each symmetry operator can be either symmetric (+) or antisymmetric (-), but taken together have to fulfill the antisymmetry (3.63) of the order parameter. That is, the relation  $\hat{S}\hat{P}\hat{O}\hat{T} \underline{\Psi}(k) = -\underline{\Psi}^T(-k)$  holds. This so-called *SPOT* criterion [193, 194, 564] or Berezinskii classification scheme [560] can be symbolically written as

$$\hat{S}\hat{P}\hat{O}\hat{T} = -1 . \quad (3.65)$$

Altogether, this results in  $2^3 = 8$  distinct pairing classifications, as outlined in Table 3.1. Consequently, we distinguish between spin triplet states (with even spin,  $\langle |\hat{S}| \rangle = 1$ ) and singlet states (with odd spin,  $\langle |\hat{S}| \rangle = 0$ ) states, as well as between even parity (e.g. *s*, *d*, *g*-wave) and odd parity (e.g. *p*, *f*-wave) symmetries, inter-orbital and intra-orbital pairings, and even and odd frequency superconductors. Our focus here lies on even frequency superconductors with odd-frequency pairings being more exotic [564, 566, 567]. Moving forward, we will therefore omit the frequency dependence.

### Representation theory for the order parameter

The specific symmetry behavior of the order parameter depends on the symmetry group  $\mathcal{G}$  of the underlying Hamiltonian. For condensed matter systems, this is typically given by  $\mathcal{G} = \mathcal{G}_c \otimes \text{SU}(2)_S \otimes \text{SO}(3)_O \otimes \Theta$  with the crystal space group  $\mathcal{G}_c$

<sup>23</sup>Note that  $\hat{T}$  is different to time reversal and sometimes referred to as braiding operator [564]. While for equilibrium systems the permutation  $\tau \rightarrow -\tau$  looks like time inversion, true time-reversal  $\hat{\Theta} = i\sigma_y \hat{K}$  would also entail a complex conjugation  $\hat{\Theta}\Psi(\tau) = \pm \Psi^*(-\tau)$ . By the same reasoning,  $\hat{P}$  is a permutation of (relative) positions, often identical to space inversion.

**Table 3.1 – Possible symmetry combinations according to the SPOT classification.** The overall sign of applying spin  $\hat{S}$ , (spatial) parity  $\hat{P}$ , orbital  $\hat{O}$ , and frequency  $\hat{T}$  commutation must be odd (–). The top four rows describe even frequency pairing, while the bottom four rows belong to more exotic odd-frequency pairing [560, 564, 566, 567].

Spin	Parity	Orbital	Frequency
–	+	+	+
+	–	+	+
+	+	–	+
–	–	–	+
+	+	+	–
–	–	+	–
–	+	–	–
+	–	–	–

containing translational and point group symmetry of the Bravais lattice,  $SU(2)$  spin symmetry,  $SO(3)$  orbital symmetry, and time-reversal symmetry  $\Theta$ . A symmetry operator  $\hat{g} \in \mathcal{G}$  acts on the order parameter according to

$$\hat{g}\underline{\Psi}(\mathbf{k}) = \underline{U}^T(g)\underline{\Psi}(R^{-1}(g)\mathbf{k})\underline{U}(g), \quad (3.66)$$

where  $R^{-1}(g) \in O(3)$  is a rotation matrix and  $\underline{U}(g)$  denotes the direct product of two operators acting on spin-orbital space. In the following, we assume the absence of SOC such that we can separate the contributions of  $\underline{U}(g)$  and spin is independent of momentum.

The order parameter symmetry can be classified by the corresponding irreducible representations (irreps)  $\Gamma^p$  of the group  $\mathcal{G}$ .<sup>24</sup> The orthogonality of irreps enables the construction of the character projection operator  $\hat{\mathcal{P}}^p$  specific to a given irrep  $p$ . The order parameter transforming in accordance to the irrep  $p$  can then be derived using the projection operator:

$$\hat{\mathcal{P}}^p \Psi = \sum_{\hat{g} \in \mathcal{G}} [\chi^p(g)]^* \hat{g} \Psi = \delta^{pq} \Psi, \quad (3.67)$$

which is orthogonal to other irreps  $q$ . Here,  $\chi^p(g)$  is the character (i.e., the trace of the representation matrix of  $\Gamma^p$ ) of the symmetry transformation  $g$  associated with the irrep  $p$ . We can generally write the order parameter as a linear combination of basis functions  $\psi^p$  obtainable from applying  $\hat{\mathcal{P}}^p$ . It takes the form

$$\Psi_{m\sigma, m'\sigma'}(k) = \sum_p \sum_{r=1}^{N_p} \eta_r^{(p)} \psi_{m\sigma, m'\sigma'}^{(p,r)}(k), \quad (3.68)$$

where the summations go over irreps  $p$  of dimensionality  $N_p$ . The expansion coefficients  $\eta_r^{(p)}$  effectively take over the role as an order parameter in the GL free energy (density).

<sup>24</sup>We do not discuss the mathematical foundations of representation theory of groups here, but we refer the interested reader to books and pedagogical notes such as Refs. [565, 568, 569].



The corresponding expansion is given by

$$f_{\text{GL}} = f_n + \sum_p \left[ a^p(T) \sum_{r=1}^{N_p} |\eta_r^p|^2 + f^p(\eta^4) \right]. \quad (3.69)$$

The quadratic term keeps a simple, isotropic form whereas  $f^p(\eta^4)$  contains all fourth-order terms which overall must be positive definite to ensure the stability of the free energy; see Refs. [167, 562] for examples of various point groups. Each irrep has a distinct critical temperature  $T_c^p$  with the irrep state possessing the highest  $T_c$  being the one realized. Additional phase transitions between irreps at lower temperatures can also occur if multiple competing minima are present. In cases involving higher dimensional irreps ( $N_p > 1$ ) with the multidimensional order parameter presented as a multicomponent vector  $\boldsymbol{\eta}^p \in \mathbb{C}^{N_p}$ , a specific linear combination of components  $\eta_r^p$  emerges based on material-specific coefficients influencing the free energy. For instance, let us consider the  $D_6$  point group of a triangular lattice. The two-dimensional  $E_2$  irrep contains the basis functions with  $\eta_1 = d_{x^2-y^2}, \eta_2 = d_{xy}$  form factor symmetries. An ordered state can be established by either one of the two components,  $d_{x^2-y^2}$  or  $d_{xy}$ , or by a linear combination that is either real ( $d \pm d$ ) or complex ( $d \pm id$ ) which correspond to nematic (rotational symmetry-breaking) or chiral (time-reversal symmetry-breaking) states.

We now turn to specifying the basis functions. The individual degrees of freedom can be separated as follows

$$\psi_{m\sigma, m'\sigma'}^{(p,r)}(\mathbf{k}) = \sum_{\kappa\nu\rho} d_{\kappa\nu\mu}^{(p,r)} g^\kappa(\mathbf{k}) O_{mm'}^\nu S_{\sigma\sigma'}^\mu \quad (3.70)$$

with amplitude  $d_{\kappa\nu\mu}^{(p,r)}$ . Each factor –  $g(\mathbf{k})$  for spatial dependence,  $O_{mm'}$  for orbital structure, and  $S_{\sigma\sigma'}$  for spin – can be analyzed separately and then linked using a tensor product.

The conventional way of writing the spin part is given by

$$S_{\sigma\sigma'} = [i(d_0\tau_0 + \mathbf{d} \cdot \boldsymbol{\tau})\tau_y]_{\sigma\sigma'} \quad (3.71)$$

with the  $2 \times 2$  identity matrix  $\tau_0$  and Pauli matrix vector  $\boldsymbol{\tau} = (\tau_x, \tau_y, \tau_z)$ . The first scalar term describes the singlet component and the vector  $\mathbf{d} = (d_x, d_y, d_z)$  constitutes the triplet component. Without SOC, we can directly diagonalize the spin sector and the pairing state (3.70) is either characterized by fixed scalar  $d_0$  (spin pairing) or vector  $\mathbf{d}$  (triplet pairing). Then, only the combined spatial and orbital part need to be classified in accordance to the irreps of the lattice's point group symmetry.

The spatial part  $g(\mathbf{k})$  is commonly referred to as the form factor. For a single-band system or (degenerate) intra-orbital pairing ( $O_{mm'} = \delta_{mm'}$ ), the parity of the spatial part is determined by the spin state. The Pauli principle enforces singlet superconductors to have even parity  $g(\mathbf{k}) = g(-\mathbf{k})$ , whereas triplet states have odd parity  $g(\mathbf{k}) = -g(-\mathbf{k})$ . The form factor transforms according to the basis functions of the respective point group symmetry's irrep, which is often labeled in terms of angular momentum such as  $l = s, p, d$ , and  $f$ . Pairing symmetries of higher angular momentum have symmetry-dictated nodes where the order parameter and hence superconducting gap vanishes, i.e., finite spectral weight remains at the Fermi energy. An example is the  $d$ -wave pairing pertinent to cuprate materials [28, 478]. Here, the spatial form factor is given by  $g_{d_{x^2-y^2}}(\mathbf{k}) \propto \cos(k_x) - \cos(k_y)$ , which belongs to the  $B_1$  irrep of the  $C_{4v}$  point group symmetry of the square lattice.

Multi-orbital or multi-band systems are generally more complicated by allowing for more pairing possibilities. Order parameter with off-diagonal orbital components describe electrons from different orbitals participating in pairing. The group theoretical classification of such pairing is more conveniently carried out in orbital space because the band-basis functions carry an additional momentum dependence from the unitary transformation to Bloch space. In band basis, the expansion (3.70) becomes

$$f_{m\sigma, m'\sigma'}^{(p,r)}(\mathbf{k}) = \sum_{\kappa\nu\rho} d_{\kappa\nu\rho}^{(p,r)} g^\kappa(\mathbf{k}) B_{aa'}^\nu(\mathbf{k}) S_{\sigma\sigma'}^\rho. \quad (3.72)$$

The group theoretical classification of superconducting pairing states is a powerful tool; however, it cannot make dynamical predictions on the dominant pairing for a given model. Such predictions require a more detailed analysis of a given pairing interaction and microscopic calculations (cf. publications II to V).

#### Experimental probes of pairing symmetries

Determining the superconducting pairing symmetries in materials is crucial to understanding the underlying mechanisms driving superconductivity. We aim here to briefly outline common experimental methods [267] to identify these pairing symmetries. Given the vast array of sophisticated experimental techniques, we give only a rough overview. Broadly, experimental approaches can be categorized by the targeted observable or specific symmetry probe:

- Measuring the single-particle excitation spectrum and gap structure:  
*ARPES, scanning tunneling microscopy/spectroscopy (STM/STS), specific heat measurements, low-temperature London penetration depth measurements*

- Analyzing the spin structure of Cooper pairs:  
*Nuclear magnetic response (NMR), nuclear quadrupole response (NQR), Knight shift measurements*
- Investigating time-reversal symmetry breaking:  
*Muon spin resonance ( $\mu$ SR), polar Kerr effect measurements*
- Resolving phase difference in the order parameter at different  $k$  points:  
*Superconducting quantum interference device (SQUID) measurements, quasiparticle interference, neutron scattering*
- Probing of collective modes:  
*Raman spectroscopy, Higgs spectroscopy*

Most of these techniques can either directly measure the presence or absence of a specific symmetry or exhibit signatures that can be correlated with particular pairing symmetries. For example, superconductors with nodal gaps typically exhibit a “V”-shaped spectrum in their density of states and display power-law behavior in the temperature dependence of specific heat. In contrast, fully gapped states show a corresponding gapped spectral function and an exponential temperature decay in the specific heat.

### 3.2 Bardeen–Cooper–Schrieffer theory

The original paper by Bardeen, Cooper, and Schrieffer [41] introduced a comprehensive theory of superconductivity, which is able to describe properties of conventional superconductors quantitatively well. It introduced the concept of Cooper pairs that form due to an attractive interaction. These pairs can coherently condense by opening an energy gap  $\Delta$  in the single-particle spectrum. In BCS theory, the attraction is mediated by phonons with the approximation of being local and constant in an energy window on the order of the Debye frequency  $\omega_D$ .

As an important part of contemporary physics, the description is standard in every book on solid state physics and interacting many-body systems in the condensed matter context. Here, we only aim at giving a brief introduction which provides the foundations for advanced theories applied to tackle more complex systems and materials. This is particularly relevant for strongly correlated superconductors where conventional BCS theory fails. In-depth discussions on BCS theory can be found, for instance, in the classic text books by Schrieffer [457] or Tinkham [458].

#### 3.2.1 Pair creation and Cooper pair instability

Our microscopic view on superconductivity is shaped by the picture of electrons condensing into Cooper pairs. In these pairs, electrons behave as composite particles

which mostly act as bosonic particles but still obey the Pauli principle. It was Cooper's ingenious idea [570] that led to this microscopic picture as he showed that the Fermi sea  $|\text{FS}\rangle = \prod_{|k| \leq k_F, \sigma} c_{k\sigma}^\dagger |0\rangle$ , i.e., the non-interacting ground state of electrons, is unstable in the presence of an arbitrarily small attraction between the electrons.

Central to this idea is the Cooper pair creation operator

$$\Upsilon_q^\dagger = \iint d^d r d^d r' g(\mathbf{r} - \mathbf{r}') \psi_\uparrow^\dagger(\mathbf{r}) e^{iq(\mathbf{r}+\mathbf{r}')/2} \psi_\downarrow^\dagger(\mathbf{r}') \quad (3.73a)$$

$$= \iint d^d R d^d x g(\mathbf{x}) e^{iq\mathbf{R}} \psi_\uparrow^\dagger(\mathbf{R} + \mathbf{x}/2) \psi_\downarrow^\dagger(\mathbf{R} - \mathbf{x}/2), \quad (3.73b)$$

which creates a fermionic singlet pair<sup>25</sup> of center-of-mass momentum  $\mathbf{q}$ . The internal wave function  $g(\mathbf{r} - \mathbf{r}')$  describes the spatial distribution of the Cooper pair depending on the electron's individual positions  $\mathbf{r}, \mathbf{r}'$ . In the second line, we transformed the arguments of the fermionic field operators  $\psi^\dagger$  to the center-of-mass position  $\mathbf{R} = (\mathbf{r} + \mathbf{r}')/2$  and relative position  $\mathbf{x} = \mathbf{r} - \mathbf{r}'$ . Fourier transforming this expression with  $\psi_\sigma^\dagger(\mathbf{r}) = \frac{1}{N_k} \sum_{\mathbf{k}} c_{k\sigma}^\dagger e^{-i\mathbf{k}\mathbf{r}}$  yields

$$\Upsilon_q^\dagger = \sum_{\mathbf{k}} g_{\mathbf{k}} c_{\mathbf{k}+\frac{\mathbf{q}}{2}\uparrow}^\dagger c_{-\mathbf{k}+\frac{\mathbf{q}}{2}\downarrow}^\dagger \quad (3.74)$$

with  $g_{\mathbf{k}} = \int d^d x g(\mathbf{x}) e^{i\mathbf{k}\mathbf{x}}$ . The Cooper pair wave function, as we will see, serves as the superconducting order parameter. In the following, we show the instability of the Fermi sea against pair addition.

We consider the Hamiltonian

$$H = \sum_{\mathbf{k}, \sigma} \varepsilon_{\mathbf{k}} c_{k\sigma}^\dagger c_{k\sigma} + \hat{V} \quad (3.75)$$

with single-particle dispersion  $\varepsilon_{\mathbf{k}}$  (Fermi energy  $E_F = 0$ ) and electron-electron interaction term  $\hat{V}$ . An electron pair can only be added above the filled Fermi sea as  $|\Psi(\mathbf{q})\rangle = \Upsilon_q^\dagger |\text{FS}\rangle$ . Applying  $H$  on this pair state  $H|\Psi(\mathbf{q})\rangle = E(\mathbf{q})|\Psi(\mathbf{q})\rangle$  yields

$$E(\mathbf{q})|\Psi(\mathbf{q})\rangle = \sum_{|\mathbf{k} \pm \frac{\mathbf{q}}{2}| > k_F} (\varepsilon_{\mathbf{k}+\frac{\mathbf{q}}{2}} + \varepsilon_{-\mathbf{k}+\frac{\mathbf{q}}{2}}) g_{\mathbf{k}} |\mathbf{k}, \mathbf{q}\rangle + \sum_{|\mathbf{k}|, |\mathbf{k}'| > k_F} \langle \mathbf{k}, \mathbf{q} | \hat{V} | \mathbf{k}', \mathbf{q} \rangle g_{\mathbf{k}'} |\mathbf{k}, \mathbf{q}\rangle, \quad (3.76)$$

where we introduced  $|\mathbf{k}, \mathbf{q}\rangle = c_{\mathbf{k}+\frac{\mathbf{q}}{2}\uparrow}^\dagger c_{-\mathbf{k}+\frac{\mathbf{q}}{2}\downarrow}^\dagger |\text{FS}\rangle$ .

---

<sup>25</sup>We focus on the case of single-orbital, isotropic singlet pairing as in the original work by BCS [41].

The drastic but physically well-motivated approximation by BCS [41] is to set<sup>26</sup>

$$\langle \mathbf{k}, \mathbf{q} | \hat{V} | \mathbf{k}', \mathbf{q} \rangle \equiv V_{\mathbf{k}, \mathbf{k}'} = \begin{cases} -U/N_k, & |\varepsilon_{\mathbf{k}}|, |\varepsilon_{\mathbf{k}'}| < \hbar\omega_D \\ 0, & \text{else} \end{cases} \quad (3.77)$$

with  $U > 0$ , i.e., to adopt an attractive local interaction in an energy window of the Debye frequency  $\omega_D$ . This effective interaction derives from electron-phonon scattering which is attractive for energies smaller than the typical phononic energy scale as characterized by  $\omega_D$ . We additionally assume that it is independent of the center-of-mass momentum  $\mathbf{q}$ . By comparing coefficients and removing the pair function  $g_{\mathbf{k}}$ , we obtain the condition

$$1 = \frac{U}{N_k} \sum_{0 < \varepsilon_{\pm \mathbf{k} + \frac{\mathbf{q}}{2}} < \hbar\omega_D} \frac{1}{\varepsilon_{\mathbf{k} + \frac{\mathbf{q}}{2}} + \varepsilon_{\mathbf{k} - \frac{\mathbf{q}}{2}} - E(\mathbf{q})}. \quad (3.78)$$

To find a solution to this condition, we take the continuum limit and linearize the dispersion for small  $\mathbf{q}$  by dropping  $\mathcal{O}(q^2)$ , which effectively shifts the zero from the Fermi energy by  $v_F q/2$ . Thus, Eq. (3.78) becomes

$$1 = U \int_{\frac{v_F q}{2}}^{\frac{v_F q}{2} + \hbar\omega_D} d\varepsilon \frac{N(\varepsilon)}{2\varepsilon - E(\mathbf{q})}. \quad (3.79)$$

Assuming the density of states to be constant within the integration window,  $N(\varepsilon) \approx N(0)$ , we can solve for the binding energy  $E(\mathbf{q})$  given by

$$E(\mathbf{q}) = -\frac{2\hbar\omega_D}{e^{\frac{2}{UN(0)}} - 1} + v_F q. \quad (3.80)$$

This result shows the possibility of having a bound electron pair, necessitating only the existence of an attractive interaction (3.77). The first term describes the energy gain of adding an electron pair to the Fermi sea and the second indicates that the center-of-mass movement of Cooper pairs compromises this binding energy, eventually breaking up the pair [44, 457, 571]. Interestingly, the dispersion is linear in  $q$ . In the limit  $2 \gg UN(0)$ , we can simplify the binding energy to yield

$$E(q = 0) = -2\hbar\omega_D e^{-\frac{2}{UN(0)}} \simeq \Delta_0. \quad (3.81)$$

This result is very similar to the outcome of BCS theory with the zero-temperature gap  $\Delta_0$  in Eq. (3.95), but here an additional factor of 2 appears in the exponential. The reason is that following Cooper's argument, we only considered a single pair added above the Fermi energy. BCS theory, on the other hand, takes into account

<sup>26</sup>The normalizing factor  $1/N_k \simeq 1/V$  of the volume  $V$  is necessary to make the interaction term extensive [44].

pairing between all electrons. It is possible to generalize the argument presented here to also include the removal of electron pairs below the Fermi energy which recovers the BCS result, cf. chapter 12 in Ref. [571].

Based on the equation (3.80), we can determine the momentum  $Q$  at which the binding energy of the Cooper pair is significantly reduced. Replacing the binding energy with  $\Delta_0$ , we find  $E(Q) = 0$  for

$$\frac{Q}{\hbar} = \frac{\Delta_0}{\hbar v_F} \sim \xi_0^{-1}, \quad (3.82)$$

which is the reciprocal Cooper pair size  $\xi_0$  in Eq. (3.14) up to some numerical factor. Typical values are on the order of  $\xi_0 \sim 0.1\text{--}1\ \mu\text{m}$ , i.e., Cooper pairs are weakly-bound and largely overlapping due to their big pair size spanning hundreds of lattice constants.

#### Nature of composite pairs

We briefly want to discuss the physical nature of the pair operator (3.74), where we keep  $q = 0$  for simplicity. Let us define the operators

$$b_k^\dagger = c_{k\uparrow}^\dagger c_{-k\downarrow}^\dagger, \quad b_k = c_{-k\downarrow} c_{k\uparrow}, \quad (3.83)$$

which fulfill the following commutation relations

$$[b_k^\dagger, b_{k'}^\dagger] = [b_k, b_{k'}] = 0, \quad (3.84a)$$

$$[b_k, b_{k'}^\dagger] = \delta_{kk'}(1 - \hat{n}_{k\uparrow} - \hat{n}_{-k\downarrow}). \quad (3.84b)$$

Hence, the operators  $b_k^{(\dagger)}$  obey bosonic commutation relations as long as  $k \neq k'$ . For equal momenta, they still have to obey the Pauli principle which enforces that only one fermionic pair can exist for a given momentum. To reflect this, Eq. (3.84b) can be expressed as an anticommutator  $\{b_k, b_{k'}^\dagger\} = \delta_{kk'}$  [572]. Thus, Cooper pairs are *not* proper bosons undergoing Bose–Einstein condensation (BEC), but they still condense into a macroscopic coherent state (cf. Eq. (3.98)), albeit as weakly-bound pairs. The reason lies in the number of particles  $N$  being so large that particle number fluctuations become negligibly small.

Nevertheless, a deep connection exists to the purely bosonic picture of a BEC, because the wavefunction of the BCS and BEC states continuously connect.<sup>27</sup> This is known as the BCS–BEC crossover which is further discussed in section 6.1.2 and publication VI. Already from Eq. (3.84b), we can see that, in the dilute and localized case with  $n_{k\sigma} \ll 1$ , we obtain a bosonic relation  $[b_k, b_{k'}^\dagger] \approx \delta_{kk'}$ , enabling the

---

<sup>27</sup>Before Cooper’s proposal, it was suggested by Schafroth, Blatt, and Butler [573] that superconductivity can be described by a BEC of electron pairs in localized bound states. In the original BCS paper [41], it is stressed that their pairing picture is different to a BEC.

description by a BEC. Since the electron density is small, fermions can easily ignore the Pauli exclusion as exchange interactions are negligible [574, 575]. Hence, Cooper pairs lose their internal fermionic degrees of freedom and behave as strongly coupled bosons.

### 3.2.2 BCS Hamiltonian and ground state

In the following, we discuss the BCS model Hamiltonian for singlet pairing in a single-band system:

$$H_{\text{BCS}} = \sum_{k\sigma} \varepsilon_k c_{k\sigma}^\dagger c_{k\sigma} + \sum_{k,k'} V_{k,k'} \underbrace{c_{k\uparrow}^\dagger c_{-k\downarrow}^\dagger}_{b_k^\dagger} \underbrace{c_{-k'\downarrow} c_{k'\uparrow}}_{b_{k'}}. \quad (3.85)$$

Here, we focus on the isotropic interaction  $V_{k,k'} = -U$  of Eq. (3.77).<sup>28</sup> For a discussion of anisotropic pairing in general and the illustrative example of  $d$ -wave pairing on a square lattice, we refer to chapter 15 of Coleman’s book [44]. For our discussion, we follow the presentation in Ref. [44]. To solve the Hamiltonian, we adopt a mean-field approach by performing the standard decoupling<sup>29</sup>

$$b_k^\dagger b_k = b_k^\dagger \langle b_k \rangle + \langle b_k^\dagger \rangle b_k - \langle b_k^\dagger \rangle \langle b_k \rangle + \cancel{(b_k^\dagger - \langle b_k^\dagger \rangle)(b_k - \langle b_k \rangle)}, \quad (3.86)$$

where fluctuations  $\delta b = b - \langle b \rangle$  are neglected. For a BCS superconductor, this is well justified as the Cooper pairs have significant overlap due to their large size  $\xi_0$ ; see also the discussion in section 3.1.4. From this decoupling, we can introduce the (mean-field) pairing potential

$$\Delta = -\frac{U}{N_k} \sum_k \langle c_{-k\downarrow} c_{k\uparrow} \rangle = -U \langle c_{r=0\downarrow} c_{r=0\uparrow} \rangle \simeq U\Psi, \quad (3.87)$$

which will turn out as the superconducting gap (Eq. (3.91)). It connects to the local pairing amplitude, which corresponds to the order parameter  $\Psi$  analyzed in section 3.1. The resulting BCS mean-field Hamiltonian takes the form

$$H_{\text{BCS}} = \sum_{k\sigma} \varepsilon_k c_{k\sigma}^\dagger c_{k\sigma} + \sum_k \left[ \Delta c_{k\uparrow}^\dagger c_{-k\downarrow}^\dagger + \Delta^* c_{-k\downarrow} c_{k\uparrow} \right] + \frac{|\Delta|^2}{U}. \quad (3.88)$$

### Gapped quasiparticle spectrum

The pairing term  $\Delta c_{k\uparrow}^\dagger c_{-k\downarrow}^\dagger$  can be interpreted in two different ways: Either as two electrons combining to form a Cooper pair ( $e^- + e^- \rightleftharpoons \text{pair}^{2-}$ ) or, alternatively, an electron scattering into a pair and hole ( $e^- \rightleftharpoons \text{pair}^{2-} + h^+$ ) which is known as

<sup>28</sup>In the following, we drop the constraint of  $|\varepsilon_k| < \hbar\omega_D$  on the  $k$ -sums for brevity.

<sup>29</sup>Alternatively, one can perform a Hubbard–Stratonovich transformation with saddle-point approximation of the corresponding path integral [44, 214].

Andreev reflection [44]. The latter perspective allows for an insightful analogy between superconductivity and magnetism, where superconducting pairs are characterized by an isospin in charge space analogous to the magnetic spin. This picture originated from Anderson [576] and Nambu [577]. To elucidate this analogy, we introduce the Nambu spinor

$$\psi_{\mathbf{k}} = \begin{pmatrix} c_{\mathbf{k}\uparrow} \\ c_{-\mathbf{k}\downarrow}^\dagger \end{pmatrix}, \quad \psi_{\mathbf{k}}^\dagger = \begin{pmatrix} c_{\mathbf{k}\uparrow}^\dagger & c_{-\mathbf{k}\downarrow} \end{pmatrix} \quad (3.89)$$

fulfilling the anticommutation  $\{\psi_{\mathbf{k}}, \psi_{\mathbf{k}'}\} = \delta_{\mathbf{k}\mathbf{k}'}$ . Instead of up and down electrons, the Nambu spinor encompasses electrons and holes. The spinor notation enables a more compact representation of the Hamiltonian (3.88) in terms of a single vector field [44]

$$H_{\text{BCS}} = \sum_{\mathbf{k}} \psi_{\mathbf{k}}^\dagger [\mathbf{h}_{\mathbf{k}} \cdot \boldsymbol{\tau}] \psi_{\mathbf{k}} + \text{const.} \quad (3.90)$$

Here,  $\boldsymbol{\tau} = (\tau_x, \tau_y, \tau_z)$  is the Pauli matrix vector and the vector field  $\mathbf{h}_{\mathbf{k}} = (\Delta_1, \Delta_2, \varepsilon_{\mathbf{k}})$  acts as a Zeeman field in isospin space. Its in-plane components are given by  $\Delta_1 = \text{Re } \Delta = (\Delta^* + \Delta)/2$  and  $\Delta_2 = \text{Im } \Delta = (\Delta^* - \Delta)/(2i)$ .

Drawing the analogy to an antiferromagnet, we can identify the vector  $\mathbf{B}_{\mathbf{k}} = -\mathbf{h}_{\mathbf{k}}$  as a momentum-dependent Weiss field<sup>30</sup> to which the isospin  $\boldsymbol{\tau}_{\mathbf{k}} = \psi_{\mathbf{k}}^\dagger \boldsymbol{\tau} \psi_{\mathbf{k}}$  couples. The direction of  $\mathbf{B}_{\mathbf{k}}$  sets the quantization axis in isospin space at a given momentum  $\mathbf{k}$ , thereby determining the quasiparticle charge. In a metallic state ( $\Delta = 0$ ),  $\mathbf{B}_{\mathbf{k}}$  points up below the Fermi surface (occupied, electronic states) and down above (unoccupied, hole-like states). In a superconductor, however, the direction of  $\mathbf{B}_{\mathbf{k}}$  rotates and mixes electron and hole states close to the Fermi energy (inset of Figure 3.6). Completely turning the Weiss field around, corresponding to the creation of a quasiparticle pair, costs the energy  $2|\mathbf{B}_{\mathbf{k}}|$ . Hence, a single quasiparticle excitation is described by

$$E_{\mathbf{k}} = |\mathbf{B}_{\mathbf{k}}| = \sqrt{\varepsilon_{\mathbf{k}} + |\Delta|^2}. \quad (3.91)$$

As a result, the excitation spectrum is gapped by  $|\Delta|$  as illustrated in Figure 3.6. In the ground state, each isospin aligns with the Weiss field  $\mathbf{B}_{\mathbf{k}} = -E_{\mathbf{k}} \hat{\mathbf{n}}_{\mathbf{k}}$ . The unit vector  $\hat{\mathbf{n}}_{\mathbf{k}}$  stands at an angle  $\theta_{\mathbf{k}}$  to the electron charge axis (“z-axis”). We can specify the components of the isospin  $\boldsymbol{\tau}_{\mathbf{k}}$  by the angle  $\theta_{\mathbf{k}}$ . We use the gauge freedom and choose the gap to be real valued, i.e.,  $\Delta \equiv \Delta_1$  and  $\Delta_2 = 0$ . Then, the z-component and transverse component are given by

---

<sup>30</sup>Weiss fields are effective fields in mean-field theory that approximate the collective influence of all interactions within a system by averaging them into a single representative field.



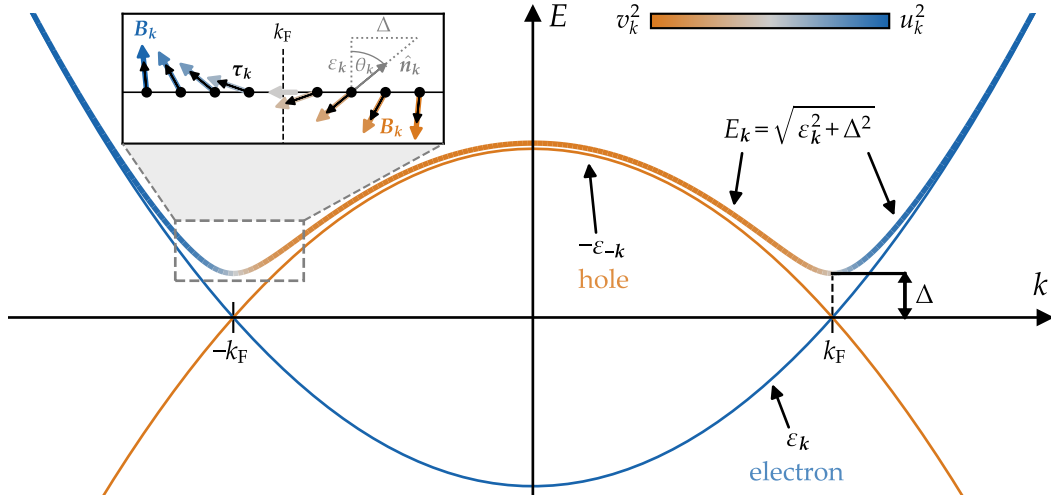


**Figure 3.6 – Quasiparticle excitation spectrum of a superconductor.** Electron (blue) and hole (orange) excitation spectra are mixed in a superconductor by Andreev scattering. This is characterized by the rotation of the isospin Weiss field  $\mathbf{B}_k$  about an angle  $\theta_k$  as the momentum passes through the Fermi surface (inset). As a result, the quasiparticle spectrum  $E_k$  shows a gap  $\Delta$  at the Fermi wavevector  $k_F$ . Electrons and holes participate equally at this point, yielding an indefinite charge state of the quasiparticle. The quasiparticle factors  $u_k$  and  $v_k$  characterize the hole-like or electron-like character of the quasiparticle, respectively.

$$\langle \tau_{k,z} \rangle = \langle n_{k\uparrow} + n_{k\downarrow} - 1 \rangle = -\cos \theta_k = -\frac{\varepsilon_k}{E_k} = -\frac{\varepsilon_k}{\sqrt{\varepsilon_k^2 + \Delta^2}}, \quad (3.92a)$$

$$\langle \tau_{k,x} \rangle = \langle c_{k\uparrow}^\dagger c_{-k\downarrow}^\dagger + c_{-k\downarrow} c_{k\uparrow} \rangle = -\sin \theta_k = -\frac{\Delta}{E_k} = -\frac{\Delta}{\sqrt{\varepsilon_k^2 + \Delta^2}}. \quad (3.92b)$$

The  $z$ -component indicates the number of pairs, as the up ( $\tau_{k,z} = 1$ ) and down ( $\tau_{k,z} = -1$ ) states describe doubly occupied ( $n_{k\uparrow} = n_{k\downarrow} = 1$ ) and empty pair states ( $n_{k\uparrow} = n_{k\downarrow} = 0$ ), respectively. The transverse component describes pair creation and annihilation from which we find the pairing amplitude  $\langle c_{-k\downarrow} c_{k\uparrow} \rangle = -\frac{1}{2} \sin \theta_k$  since  $\Delta_2 = 0$ . We can insert this into Eq. (3.87) to obtain the BCS gap equation at  $T = 0$ :

$$\Delta = \frac{U}{N_k} \sum_k \frac{\Delta}{2\sqrt{\varepsilon_k^2 + \Delta^2}}. \quad (3.93)$$

We solve the gap equation by replacing the restricted  $\mathbf{k}$  summation with an energy integral over the interval  $|\varepsilon_k| < \hbar\omega_D$ :

$$1 = \frac{UN(0)}{2} \int_{-\hbar\omega_D}^{\hbar\omega_D} d\varepsilon \frac{1}{\sqrt{\varepsilon^2 + \Delta^2}} = UN(0) \sinh^{-1} \left( \frac{\hbar\omega_D}{\Delta} \right). \quad (3.94)$$

For the weak-coupling condition  $UN(0) \ll 1$ , we find the ground state gap as

$$\Delta_0 = \Delta(T = 0) = \frac{\hbar\omega_D}{\sinh\left(\frac{1}{UN(0)}\right)} \approx 2\hbar\omega_D e^{-\frac{1}{UN(0)}}. \quad (3.95)$$

### BCS wave function

We utilize the isospin representation to construct the ground state wave function: Each isospin is rotated by  $\theta_k$  relative to the vacuum  $|0\rangle$ , representing zero excited pairs. Consequently, the corresponding wave function is obtained by applying a spin rotation about the  $y$ -axis at each momentum:

$$|\Psi_{\text{BCS}}\rangle = \prod_k e^{i\frac{\theta_k}{2}\tau_{k,y}} |0\rangle = \prod_k \left( \cos \frac{\theta_k}{2} + \sin \frac{\theta_k}{2} c_{k\uparrow}^\dagger c_{-k\downarrow}^\dagger \right) |0\rangle. \quad (3.96)$$

The BCS wave function thereby incorporates a superposition of states with different particle numbers  $N$  and  $N + 2$ . Let us introduce abbreviations for the coefficients [41]

$$u_k = \cos \frac{\theta_k}{2} = \sqrt{\frac{1}{2}(1 + \cos \theta_k)} = \sqrt{\frac{1}{2} \left( 1 + \frac{\varepsilon_k}{E_k} \right)}, \quad (3.97a)$$

$$v_k = \sin \frac{\theta_k}{2} = \sqrt{\frac{1}{2}(1 - \cos \theta_k)} = \sqrt{\frac{1}{2} \left( 1 - \frac{\varepsilon_k}{E_k} \right)}. \quad (3.97b)$$

called the coherence factors satisfying the normalization  $|u_k|^2 + |v_k|^2 = 1$ .  $u_k$  and  $v_k$  describe the vacancy and occupation of a pair state at momentum  $k$  or, equivalently, the electron-like and hole-like character of the excited quasiparticle (cf. Figure 3.6), respectively. It turns out that the coherence factors  $(v_k, u_k)$  and their complex conjugates  $(-v_k^*, u_k^*)$  represent the eigenvectors of the Nambu matrix  $\mathbf{h}_k \cdot \boldsymbol{\tau}$ , i.e., they diagonalize  $H_{\text{BCS}}$  in Eq. (3.88). This is known as the Bogoliubov transformation further discussed in, e.g., Refs. [44, 215, 457, 458].

Using the coherence factors, we can rewrite the ground state as a coherent state

$$\begin{aligned} |\Psi_{\text{BCS}}\rangle &= \prod_k (u_k + v_k c_{k\uparrow}^\dagger c_{-k\downarrow}^\dagger) |0\rangle = \prod_k u_k \underbrace{\left( 1 + \frac{v_k}{u_k} c_{k\uparrow}^\dagger c_{-k\downarrow}^\dagger \right)}_{=g_k} |0\rangle \\ &= \underbrace{\prod_k u_k}_{\equiv \mathcal{N}} \prod_k e^{g_k c_{k\uparrow}^\dagger c_{-k\downarrow}^\dagger} |0\rangle = \mathcal{N} e^{\sum_k g_k b_k^\dagger} |0\rangle = \mathcal{N} e^{\Upsilon_{q=0}^\dagger} |0\rangle \end{aligned} \quad (3.98)$$

of the Cooper pair creation operator  $\Upsilon^\dagger$  (3.74). In the process, we identified the Cooper pair wave function as  $g_k = v_k/u_k$  and introduced the normalization  $\mathcal{N}$ . The coherent state representation is enabled by the Pauli principle yielding  $(c_{k\uparrow}^\dagger c_{-k\downarrow}^\dagger)^n = 0$  for  $n \geq 2$  in the expansion of the exponential, thus connecting to the phenomenological discussion of section 3.1.

Knowing the ground state wave function, we can calculate the energy that is gained from pair condensation. It is given by

$$E_{\text{cond}} = \langle \Psi_{\text{BCS}} | H_{\text{BCS}} | \Psi_{\text{BCS}} \rangle - \langle \text{FS} | H_{\text{BCS}} | \text{FS} \rangle = -\frac{1}{2} N(0) \Delta . \quad (3.99)$$

A similar result holds for anisotropic gap functions [167], which shows that many nodes at the Fermi level ( $E_F = 0$ ) are energetically unfavorable for condensation. Moreover, we can determine the occupation number

$$n_{k\sigma} = \langle \Psi_{\text{BCS}} | \hat{n}_{k\sigma} | \Psi_{\text{BCS}} \rangle = \langle 0 | (u_k^* + v_k^* c_{-k\downarrow} c_{k\uparrow}) c_{k\sigma}^\dagger c_{k\sigma} (u_k + v_k c_{k\uparrow}^\dagger c_{-k\downarrow}^\dagger) | 0 \rangle = |v_k|^2 . \quad (3.100)$$

Thus, the average number of condensed electrons is  $n_k = \langle \hat{n}_{k\uparrow} \rangle + \langle \hat{n}_{k\downarrow} \rangle = 2|v_k|^2$ , which is consistent with the fact that there is a probability of  $|v_k|^2$  to find a pair of electrons at momentum  $k$ . The total particle number follows as

$$N_s = \langle \hat{N} \rangle = \sum_{k\sigma} \langle \hat{n}_{k\sigma} \rangle = 2 \sum_k |v_k|^2 . \quad (3.101)$$

Analogously, one can show that the fluctuation of particle number is given by

$$\delta N^2 = \langle (\hat{N} - \langle \hat{N} \rangle)^2 \rangle = \langle \hat{N}^2 \rangle - \langle \hat{N} \rangle^2 = 4 \sum_k |u_k|^2 |v_k|^2 . \quad (3.102)$$

It is easy to show that  $\delta N^2$  is maximal for  $|v_k|^2 = 1/2 = |u_k|^2$ , i.e., for particles from the non-interacting Fermi surface ( $\varepsilon_k = 0$ ).

### 3.2.3 Nambu–Gor’kov formalism

To solve the BCS Hamiltonian at finite-energy, we introduce the Nambu–Gor’kov (NG) Green’s function formalism in the following, which allows to describe superconducting systems in the framework of Green’s functions. While BCS theory can be solved without the usage of Green’s functions, doing so provides a good example for the formalism, which can be transferred to more general Hamiltonians than the BCS Hamiltonian in Eq. (3.88).

The Green’s function formalism was introduced in section 2.2, but it does not work right-away for symmetry-broken phases like superconductivity. The problem can be understood from the perturbative expansion of the interacting electron propagator [Eq. (2.25)], which does not converge for the naive insertion of the BCS interaction [578]. This is captured in the Cooper pair binding energy in Eq. (3.95), which is non-perturbative in the instantaneous BCS interaction  $U$ .

In order to describe the emergence of symmetry-broken phases like superconductivity, one needs to include the correlation functions, which describe long-range

order pertinent to the SSB [578]. To describe superconductivity, we thus have to introduce correlation functions that describe scattering of electron pairs or equivalently Andreev scattering of electrons and holes (cf. Eqs. (3.4) and (3.87)). These are given by

$$F_{\alpha\beta}(\tau, \mathbf{k}) = -\langle \mathcal{T}_\tau c_{k\alpha\uparrow}(\tau) c_{-k\beta\downarrow}(0) \rangle, \quad F_{\alpha\beta}^*(\tau, \mathbf{k}) = -\langle \mathcal{T}_\tau c_{-k\alpha\downarrow}^\dagger(\tau) c_{k\alpha\uparrow}^\dagger(0) \rangle \quad (3.103)$$

and they are called anomalous or Gor'kov Green's functions. Both the propagation of electrons and holes as well as Andreev scattering terms of electrons and holes can be represented collectively in a matrix propagator in isospin space. This is the NG Green's function which is defined as the correlation function of Nambu spinors (3.89), forming the  $(2 \times 2)$  matrix<sup>31</sup>

$$\begin{aligned} \mathcal{G}_{\alpha\beta}(\tau, \mathbf{k}) &= -\langle \mathcal{T}_\tau \psi_{k\alpha}(\tau) \otimes \psi_{k\beta}^\dagger(0) \rangle \\ &= \begin{pmatrix} -\langle \mathcal{T}_\tau c_{k\alpha\uparrow}(\tau) c_{k\beta\uparrow}^\dagger(0) \rangle & -\langle \mathcal{T}_\tau c_{k\alpha\uparrow}(\tau) c_{-k\beta\downarrow}(0) \rangle \\ -\langle \mathcal{T}_\tau c_{-k\alpha\downarrow}^\dagger(\tau) c_{k\beta\uparrow}^\dagger(0) \rangle & -\langle \mathcal{T}_\tau c_{-k\alpha\downarrow}^\dagger(\tau) c_{-k\beta\downarrow}(0) \rangle \end{pmatrix} \\ &= \begin{pmatrix} G_{\alpha\beta}(\tau, \mathbf{k}) & F_{\alpha\beta}(\tau, \mathbf{k}) \\ F_{\alpha\beta}^*(\tau, \mathbf{k}) & \bar{G}_{\alpha\beta}(\tau, \mathbf{k}) \end{pmatrix}. \end{aligned} \quad (3.104)$$

Here,  $\bar{G}_{\alpha\beta}(\tau, \mathbf{k}) = -\langle \mathcal{T}_\tau c_{-k\alpha\downarrow}^\dagger(\tau) c_{-k\beta\downarrow}(0) \rangle$  is the propagator of a hole, which connects to the electron's Green's function via  $\bar{G}(\tau, \mathbf{k}) = -G^T(-\tau, \mathbf{k})$ . The benefit of the NG Green's function formalism is that the usual framework of many-body approximations discussed in chapter 2 can be transferred to the matrix Green's function. For instance, we can write the Dyson equation (2.26) as

$$\underline{\mathcal{G}}^{-1}(k) = \underline{\mathcal{G}}_0^{-1}(k) - \underline{\mathcal{S}}(k) \quad (3.105)$$

with the non-interacting Green's function

$$\underline{\mathcal{G}}_0(k) = \begin{pmatrix} i\omega_n \mathbb{1} - \underline{h}_0(\mathbf{k}) & 0 \\ 0 & i\omega_n \mathbb{1} + \underline{h}_0(-\mathbf{k}) \end{pmatrix} \quad (3.106)$$

containing only diagonal entries with particle and hole propagation. We denote the one-body Hamiltonian as  $\underline{h}_0(\mathbf{k})$  with an index 0, which differs from the notation in chapter 2. This is to emphasize that it comprises only the electronic (or hole) component without any mean-field superconducting pairing, i.e., that it is not to be confused with the BCS Weiss-field  $h_k$  contribution, see Eq. (3.112) below.

<sup>31</sup>For spin triplet pairing, the NG Green's function becomes a  $4 \times 4$  matrix, see, e.g., section 15.5 in Ref. [44] on spin triplet superfluidity in <sup>3</sup>He.

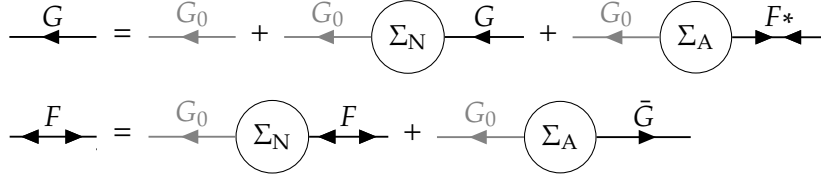


**Figure 3.7 – Nambu–Gor'kov Dyson equation.** Diagrammatic representation of Eq. (3.109). The anomalous propagator  $F$  (and self-energy  $\Sigma_{A(N)}$ ) have two outgoing lines, while their complex conjugate has two inward-directed lines. The hole propagator  $\bar{G}$  goes into the other direction of the electron propagator  $G$ .

In addition, the self-energy matrix

$$\underline{\mathcal{S}}(k) = \begin{pmatrix} \underline{\Sigma}_N(k) & \underline{\Sigma}_{AN}(k) \\ \underline{\Sigma}_{AN}^*(k) & -\underline{\Sigma}_N^*(-k) \end{pmatrix} \quad (3.107)$$

with normal and anomalous (off-diagonal) components enters the Dyson equation. The anomalous self-energy describes the effective pairing potential of Cooper pairs and it is closely related to the superconducting gap. In case of inversion symmetric systems, this relation can be expressed via [579]<sup>32</sup>

$$\underline{\Delta}(i\omega_n, \mathbf{k}) = \frac{\text{Re } \underline{\Sigma}_{AN}(i\omega_n, \mathbf{k})}{\mathbb{1} - \frac{\text{Im } \underline{\Sigma}_N(i\omega_n, \mathbf{k})}{\omega_n}} \simeq Z \underline{\Sigma}_{AN} \quad (3.108)$$

with quasiparticle weight  $Z$ .<sup>33</sup> If  $Z = 1$ , we can directly associate  $\underline{\Sigma}_{AN} \equiv \underline{\Delta}$ . The matrix formulation of the Dyson equation (3.105) corresponds to two coupled equations of the normal and anomalous Green's function

$$\underline{G}(k) = \underline{G}_0(k) + \underline{G}_0(k) \underline{\Sigma}_N(k) \underline{G}(k) + \underline{G}_0(k) \underline{\Sigma}_{AN}(k) \underline{F}^*(k), \quad (3.109a)$$

$$\underline{F}(k) = \underline{G}_0(k) \underline{\Sigma}_N(k) \underline{F}(k) + \underline{G}_0(k) \underline{\Sigma}_{AN}(k) \underline{\bar{G}}(k). \quad (3.109b)$$

The equations for  $\bar{G}$  and  $F^*$  are connected to  $G$  and  $F$  by symmetry. In Figure 3.7, we show the diagrammatic representation of these equations. For small anomalous self-energy  $\underline{\Sigma}_{AN}$ , we can linearize this set of equations to recover the Dyson equation. This is easily done by rewriting Eq. (3.109a) to obtain

$$\underline{G}(k) = [\underline{G}_0^{-1}(k) - \underline{\Sigma}_N(k)]^{-1} (\mathbb{1} + \underline{\Sigma}_{AN}(k) \underline{F}^*(k)) \approx [\underline{G}_0^{-1}(k) - \underline{\Sigma}_N(k)]^{-1}. \quad (3.110)$$

<sup>32</sup>Inversion symmetry  $\underline{\Sigma}(k) = \underline{\Sigma}(-k)$  implies that the spin-orbital matrix is symmetric, i.e.,  $\underline{\Sigma} = \underline{\Sigma}^T$ . Only then, we can write the expression as stated here. For the general expression, see Refs. [579, 580].

<sup>33</sup>We note that the relation  $\underline{\Delta} \simeq Z \underline{\Sigma}_{AN}$  is typically used for correlated superconductors with electronic pairing interaction. It follows from applying the linearization of the self-energy (2.37a) to  $\mathcal{S} \sim (1 - Z^{-1})i\omega_n \tau_0$ . In Migdal–Eliashberg theory with phononic pairing interaction, it is more common to expand  $\mathcal{S} \sim (1 - \bar{Z})i\omega_n \tau_0$ , which results in the relation of  $\underline{\Delta} \simeq \underline{\Sigma}_{AN}/\bar{Z}$  [581].

Rearranging Eq. (3.109b) then yields for the linearized anomalous Green's function

$$\underline{F}(k) = \underbrace{[\underline{G}_0^{-1}(k) - \underline{\Sigma}_N(k)]^{-1}}_{\underline{G}(k)} \underline{\Sigma}_{AN}(k) \underline{\bar{G}}(k) = -\underline{G}(k) \underline{\Sigma}_{AN}(k) \underline{G}^\dagger(-k) \quad (3.111)$$

with  $\underline{\bar{G}}(i\omega_n, \mathbf{k}) = -\underline{G}^\dagger(-i\omega_n, -\mathbf{k})$ .

### BCS theory in Nambu-Gor'kov formalism

To illustrate the NG framework, we apply it to the single-band BCS Hamiltonian (3.88). The one-body Hamiltonian entering the NG Green's function is given by (cf. Eq. (3.90))

$$h_{\mathbf{k}} = \mathbf{h}_{\mathbf{k}} \cdot \boldsymbol{\tau} = \varepsilon_{\mathbf{k}} \tau_z + \Delta_1 \tau_x + \Delta_2 \tau_y, \quad (3.112)$$

where we can associate  $h_0(\mathbf{k}) \equiv \varepsilon_{\mathbf{k}}$  and  $\Sigma_{AN} \equiv \Delta$ . Since this Hamiltonian only contains Pauli matrices  $\tau_i$ , its square can be easily calculated as  $h_{\mathbf{k}}^2 = \varepsilon_{\mathbf{k}}^2 + \Delta_1^2 + \Delta_2^2 = E_{\mathbf{k}}^2$ . This is useful when evaluating the NG Green's function, which yields

$$\mathcal{G}(k) = [i\omega_n \tau_0 - h_{\mathbf{k}}]^{-1} = \frac{1}{(i\omega_n)^2 - E_{\mathbf{k}}^2} \begin{pmatrix} i\omega_n + \varepsilon_{\mathbf{k}} & \Delta \\ \Delta^* & i\omega_n - \varepsilon_{\mathbf{k}} \end{pmatrix} \quad (3.113)$$

where we explicitly used  $\mathbb{1} = \tau_0$  to denote the unity matrix. We can directly read off normal and anomalous Green's function this way

$$G(k) = -\frac{i\omega_n + \varepsilon_{\mathbf{k}}}{\omega_n^2 + E_{\mathbf{k}}^2}, \quad (3.114a)$$

$$F(k) = -\frac{\Delta}{\omega_n^2 + E_{\mathbf{k}}^2}. \quad (3.114b)$$

Using Eq. (3.87), we obtain a self-consistent equation for the superconducting gap

$$\Delta = -\frac{U}{N_{\mathbf{k}}} \sum_{\mathbf{k}} \underbrace{\langle c_{\downarrow \mathbf{k}} c_{\uparrow \mathbf{k}} \rangle}_{F(\tau=0^+, \mathbf{k})} = -\frac{U}{\beta N_{\mathbf{k}}} \sum_{\mathbf{k}, n} F(i\omega_n, \mathbf{k}) \stackrel{\text{Eq. (3.114b)}}{=} \frac{U}{\beta N_{\mathbf{k}}} \sum_{\mathbf{k}, n} \frac{\Delta}{\omega_n^2 + E_{\mathbf{k}}^2}. \quad (3.115)$$

This is the well-known BCS gap equation. We can perform the Matsubara summation via contour integration [44, 213]

$$\frac{1}{\beta} \sum_n \frac{1}{\omega_n^2 + E_{\mathbf{k}}^2} = -\frac{1}{2\pi i \beta} \oint dz \frac{f(z)}{(z - E_{\mathbf{k}})(z + E_{\mathbf{k}})} = -\frac{f(E_{\mathbf{k}}) - f(-E_{\mathbf{k}})}{2E_{\mathbf{k}}} \quad (3.116)$$

with Fermi function  $f(E) = 1/(e^{\beta E} + 1)$ .

By using  $f(E) - f(-E) = -\tanh(\beta E/2)$ , we obtain the more common expression of the gap equation

$$\Delta = \frac{U}{N_k} \sum_k \frac{\Delta}{2E_k} \tanh\left(\frac{\beta E_k}{2}\right). \quad (3.117)$$

Generally, one has to solve this self-consistent equation numerically, see Figure 3.1b. However, we can also find analytical expressions in two limiting cases. In the limit of  $T \rightarrow 0$ , we recover Eq. (3.93) from which we were able to determine the zero-temperature gap  $\Delta_0$  in Eq. (3.95). On the other hand, we can calculate the critical temperature  $T_c$  where  $\Delta(T = T_c) = 0$ . The Matsubara summation in Eq. (3.115) yields (see p. 518 in Ref. [44])

$$k_B T_c = \underbrace{\frac{e^{-\gamma}}{2\pi}}_{\approx 1.13} \hbar \omega_D e^{-\frac{1}{UN(0)}} \quad (3.118)$$

with Euler constant  $\gamma = 0.577$ .  $T_c$  has the same exponential dependence on coupling strength  $\lambda = UN(0)$  and the proportionality to  $\omega_D$  as the zero-temperature gap. The ratio of  $\Delta_0$  and  $T_c$  is universal in BCS theory:

$$\frac{\Delta_0}{k_B T_c} = \pi e^{-\gamma} \approx 1.76. \quad (3.119)$$

With the expression for the superconducting Green's function, one can easily derive further experimental quantities like the spectral function (cf. Figure 2.3). We refer to Ref. [44] showing some of these calculations.

### 3.2.4 Superconducting stiffness in BCS theory

In the previous section, we have introduced the BCS gap equation (3.117) to determine the pairing amplitude or superconducting gap  $\Delta$ . As discussed in section 3.1.3, the superconducting condensate has the stiffness  $D_s$  as a second fundamental energy scale. Here, we want to derive the BCS expression from Eq. (3.48) for which we utilize the Green's function formalism.

To this end, we put the constraint of a small phase twist  $\nabla\phi(\mathbf{r}) = \nabla(\mathbf{q} \cdot \mathbf{r}) = \mathbf{q}$  on the system (see section 3.1.3 and also publication VI), which is analogous to a vector potential  $\mathbf{A} = -\Phi_0 \mathbf{q}$ . This effectively shifts the dispersion  $\varepsilon_k \mapsto \varepsilon_{k-\frac{q}{2}}$  (cf. section 3.2.1), such that the diagonal elements of  $h_k$  (3.112) change according to

$$\begin{pmatrix} \varepsilon_k & \\ & \varepsilon_{-k} \end{pmatrix} \mapsto \begin{pmatrix} \varepsilon_{k-\frac{q}{2}} & \\ & \varepsilon_{-k-\frac{q}{2}} \end{pmatrix} = \begin{pmatrix} \varepsilon_{k-\frac{q}{2}} & \\ & \varepsilon_{k+\frac{q}{2}} \end{pmatrix} \equiv \varepsilon_{k-\frac{q}{2}} \tau_z \quad (3.120)$$

using inversion symmetry  $\varepsilon_{\mathbf{k}} = \varepsilon_{-\mathbf{k}}$ . We note that writing  $\tau_z$  in the index of the dispersion is only a symbolic abbreviation for compact writing. The introduction of a finite  $\mathbf{q}$  (i.e., vector potential) breaks time-reversal symmetry due to which the diagonal is strictly not proportional to  $\tau_z$  anymore and also some contributions proportional to  $\tau_0$  mix in (see Supplementary Note 4 in publication VI). For the initial steps of calculating the stiffness, we summarize the steps detailed on p. 535ff in Ref. [44]. We start from the free energy density, which is given by [44]

$$f = -\frac{1}{\beta N_{\mathbf{k}}} \sum_{\mathbf{k},n} \underbrace{\text{Tr} \ln [\varepsilon_{\mathbf{k}-\frac{\mathbf{q}}{2}\tau_z} \tau_z + \Delta \tau_x - i\omega_n \tau_0]}_{-\mathcal{G}^{-1}} + \frac{\Delta^2}{U}. \quad (3.121)$$

For simplicity, we chose the gap to be real-valued ( $\Delta \equiv \Delta_1$ ,  $\Delta_2 = 0$ ). The stiffness is given by the second derivative (cf. Eq. (3.48)), which evaluates to

$$D_{s,ij} = \left. \frac{\partial^2 f}{\partial q_i \partial q_j} \right|_{\mathbf{q}=0} = \frac{1}{4\beta N_{\mathbf{k}}} \sum_{\mathbf{k},n} \left( \underbrace{\frac{\partial^2 \varepsilon_{\mathbf{k}}}{\partial k_i \partial k_j} \text{Tr}[\tau_z \mathcal{G}(k)]}_{\text{diamagnetic part}} + \underbrace{\frac{\partial \varepsilon_{\mathbf{k}}}{\partial k_i} \frac{\partial \varepsilon_{\mathbf{k}}}{\partial k_j} \text{Tr}[\mathcal{G}(k) \mathcal{G}(k)]}_{\text{paramagnetic part}} \right). \quad (3.122)$$

This expression can be more compactly rewritten by integrating the diamagnetic term by parts as [44]

$$D_{s,ij} = -\frac{1}{8\beta N_{\mathbf{k}}} \sum_{\mathbf{k},n} \frac{\partial \varepsilon_{\mathbf{k}}}{\partial k_i} \frac{\partial \varepsilon_{\mathbf{k}}}{\partial k_j} \text{Tr} [[\tau_z, \mathcal{G}(k)]^2] = \frac{1}{\beta N_{\mathbf{k}}} \sum_{\mathbf{k},n} \frac{\partial \varepsilon_{\mathbf{k}}}{\partial k_i} \frac{\partial \varepsilon_{\mathbf{k}}}{\partial k_j} \frac{\Delta^2}{[\omega_n^2 + E_{\mathbf{k}^2}]^2}. \quad (3.123)$$

Ref. [44] continues from here to determine the  $T = 0$  value of the stiffness. Here, we want to find an expression for arbitrary temperatures. For this, we evaluate the Matsubara summation as

$$\frac{1}{\beta} \sum_n \frac{1}{(i\omega_n - E_{\mathbf{k}})^2 (i\omega_n + E_{\mathbf{k}})^2} = \frac{-1}{4E_{\mathbf{k}}^2} \left[ \frac{f(E_{\mathbf{k}}) - f(-E_{\mathbf{k}})}{E_{\mathbf{k}}} - f'(E_{\mathbf{k}}) - f'(-E_{\mathbf{k}}) \right]. \quad (3.124)$$

Using the identity  $f'(E) + f'(-E) = 2f'(E) = -\beta/[2 \cosh^2(\beta E/2)]$ , we arrive at

$$D_{s,ij}(T) = \frac{1}{4N_{\mathbf{k}}} \sum_{\mathbf{k}} \frac{\partial \varepsilon_{\mathbf{k}}}{\partial k_i} \frac{\partial \varepsilon_{\mathbf{k}}}{\partial k_j} \left[ \frac{\tanh\left(\frac{\beta E_{\mathbf{k}}}{2}\right)}{E_{\mathbf{k}}} - \frac{\beta}{2 \cosh^2\left(\frac{\beta E_{\mathbf{k}}}{2}\right)} \right] \frac{\Delta^2}{E_{\mathbf{k}}^2}. \quad (3.125)$$

This expression extends to multi-band systems, which necessitate an additional summation over bands  $n$ . Moreover, inter-band processes can significantly con-



tribute through the quantum geometric tensor of the Bloch bands, giving rise to a quantum geometric term  $D_{s,\text{geom}}$  [451]. This contribution enables robust superconductivity in (twisted) flat band systems such as magic-angle twisted bilayer graphene (MATBG) [450, 536, 543, 544, 582], see also section 4.3. The underlying reason is that the conventional stiffness contribution, as derived here, depends on the effective mass of electrons  $D_s \sim n_s/m^*$  (cf. Eq. (3.44)). Hence,  $D_s$  vanishes in the limit of flat bands ( $m^* \rightarrow \infty$ ), which strongly limits superconductivity without other contributions (cf. Eq. (3.59)).

To see the dependence on effective mass, i.e., the relevance of kinetic energy, we consider the zero-temperature limit. In this case,  $\beta/\cosh^2(\beta E_k/2) \rightarrow 0$  and  $\tanh(\beta E_k/2) \rightarrow 1$ , such that

$$D_{s,ij}(T=0) = \frac{1}{4N_k} \sum_k \frac{\partial \varepsilon_k}{\partial k_i} \frac{\partial \varepsilon_k}{\partial k_j} \underbrace{\frac{\Delta^2}{E_k^3}}_{=-2\partial_{\varepsilon_k} v_k^2} = \frac{1}{2N_k} \sum_k v_k^2 \frac{\partial^2 \varepsilon_k}{\partial k_i \partial k_j}, \quad (3.126)$$

where we inserted the derivative of the coherence factor  $v_k^2$  [Eq. (3.97b)] with respect to the dispersion  $\varepsilon_k$  and integrated by parts. The second derivative of the dispersion is connected to the effective mass of the carriers. For a parabolic dispersion  $\varepsilon_k = \hbar^2 k^2/(2m^*)$ , we obtain the simple result  $D_s(0) = \hbar^2 n_s/(4m^*)$  known from Eq. (3.44) with  $n_s/2 = N/(2V) = \sum_k v_k^2/N_k$  from Eq. (3.101).

### 3.3 Migdal–Eliashberg theory

BCS theory offers a solid framework for understanding superconductivity in many conventional superconductors with weak coupling strength  $\lambda = UN(0)$ . However, the approximation of an instantaneous interaction limits its quantitative accuracy for many materials with stronger coupling or higher critical temperatures. To overcome these limitations, the Migdal–Eliashberg theory extends BCS theory by incorporating the full dynamical nature of electron-phonon interactions. This approach accounts for the frequency-dependence of interactions in a  $GW_0$ -like approximation in the NG framework, where the screened interaction  $W_0$  considers both electron-phonon and Coulomb interactions [85]. Since this thesis does not primarily focus on phonon-mediated superconductivity, we will only briefly review the Migdal–Eliashberg theory to show how its framework is similarly applied to spin-fluctuation-mediated superconductivity by replacing the interaction kernel in the gap equation. For in-depth discussions of the Migdal–Eliashberg theory, particularly in the context of nonempirical approaches of superconducting DFT (SCDFT) and *ab initio* embedding, we refer to Refs. [85, 96, 97, 438, 581].

The starting point of the (conventional) Migdal–Eliashberg theory is the application of diagrammatic perturbation theory (cf. section 2.3) to the Hamiltonian of electrons and phonons, where the (harmonic) electron-phonon interaction is considered as the perturbation. Compared to the purely electronic interaction problem, the electron-phonon coupled system is significantly simplified by Migdal’s theorem [583]. It states that vertex corrections can be neglected due to the much smaller energy scale of phonons compared to electrons. By dressing Green’s functions and interaction lines in a fashion similar to the *GW* method, one arrives at the expression for the anomalous self-energy in Migdal–Eliashberg theory [583, 584].<sup>34</sup>

$$\Sigma_{\text{AN},m}(k) = \frac{1}{\beta N_{\mathbf{k}}} \sum_{k',m'} \mathcal{K}_{mm'}(k-k') F_{m'}(k'). \quad (3.127)$$

Here,  $F$  is the anomalous Green’s function and the interaction kernel  $\mathcal{K} = \mathcal{V}_{\text{e-ph}} + \mathcal{V}_{\text{C}}$  consists of the screened, effective electron-electron interaction  $\mathcal{V}_{\text{e-ph}}$  mediated by phonons and the screened Coulomb interaction  $\mathcal{V}_{\text{C}}$ . By including  $\mathcal{V}_{\text{C}}$  in the interaction kernel, the negative effect of electron repulsion on pairing is captured.<sup>35</sup> The indices refer to the band basis and band off-diagonal terms are neglected, as commonly done when studying electron-phonon superconductivity [96, 97]. Eq. (3.127) is commonly referred to as the Eliashberg equation [584] or gap equation due to the close relation between  $\Sigma_{\text{AN}}$  and the gap  $\Delta$ . We can obtain the BCS gap equation (3.115) with  $\Delta \equiv \Sigma_{\text{AN}}$  by neglecting  $\mathcal{V}_{\text{C}}$  and inserting the static approximation  $\mathcal{V}_{\text{e-ph}} = U$  in an energy window  $|\varepsilon_k| < \hbar\omega_{\text{D}}$ .

When calculating the transition temperature  $T_{\text{c}}$  of a material, it is sufficient to work with the linearized anomalous Green’s function  $F \simeq G \Sigma_{\text{AN}} \bar{G}$  [Eq. (3.111)], i.e., dropping higher-order terms of the anomalous self-energy. The corresponding linearized gap equation reads

$$\Sigma_{\text{AN},m}(k) \approx -\frac{1}{\beta N_{\mathbf{k}}} \sum_{k',m'} \mathcal{K}_{mm'}(k-k') G_{m'}(k') G_{m'}^*(-k') \Sigma_{\text{AN},m'}(k'). \quad (3.128)$$

This equation represents an eigenvalue problem  $\lambda_{\text{SC}} \Sigma_{\text{AN}} \simeq \mathcal{B} \Sigma_{\text{AN}}$ , where the superconducting transition is found for the temperature at which the eigenvalue  $\lambda_{\text{SC}}$  reaches unity. The diagrammatic representation of the full and linearized gap equation is drawn in Figure 3.8.

For many materials, solving the Eliashberg equation is demanding due to the high number of Matsubara frequencies necessary at low temperature. The introduction

---

<sup>34</sup>We do not state the equation for the normal self-energy here. For that, we refer to Refs. [339, 438, 581]

<sup>35</sup>Due to the comparably fast nature of Coulomb forces, often a static approximation is used [85]. However, some materials can exhibit strong plasmonic excitations and explicitly treating these dynamic effects enhances critical temperatures [96, 101, 585], while the inclusion of spin fluctuations decreases  $T_{\text{c}}$  [102, 103, 438].

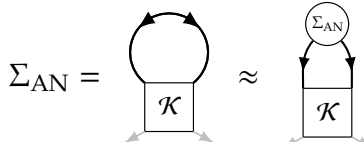


**Figure 3.8 – Eliashberg equation.** Diagrammatic representation of the Eliashberg equation (3.127). The second diagram represents the linearized version (3.128) with  $F \simeq G\Sigma_{\text{AN}}G$  inserted. The interaction kernel  $\mathcal{K}$  depends on the pairing mechanism.

of the IR basis [I] mitigates these problems [432, 433, 435, 438]. A common approximation to simplify calculations of  $T_c$  in Migdal–Eliashberg theory is to replace the Coulomb interaction  $\mathcal{V}_C$  by an effective pseudo-potential  $\mu^*$  [586, 587], trying to capture retardation effects. Often,  $\mu^*$  is not calculated but treated as an effective parameter. In addition, instead of solving the Eliashberg equation exactly (for  $\mu^*$ ), the semi-empirical McMillan–Allen–Dynes equation [588, 589] is used to calculate the critical temperature [96, 97]

$$k_B T_c = \frac{\hbar \langle \omega \rangle}{1.2} \exp \left( -\frac{1.04(1 + \lambda)}{\lambda - \mu^*(1 + 0.62\lambda)} \right), \quad (3.129)$$

where  $\langle \omega \rangle$  denotes a logarithmic average of phonon frequencies (“typical phonon energy”) and  $\lambda$  is the electron-phonon coupling strength. This expression resembles the BCS expression in Eq. (3.118), but it includes the Coulomb pseudo-potential  $\mu^*$  which can significantly suppress achievable critical temperatures. We use the McMillan–Allen–Dynes formula in publication IV to investigate (conventional) phonon-mediated-superconductivity induced by moiré phonons in twisted transition metal dichalcogenides.

### 3.4 Spin-fluctuation-mediated superconductivity

Theories of phonon-mediated pairing fall short in explaining experimental observations in most unconventional and strongly correlated superconductors, such as non-uniform superconducting gaps like nodal singlet  $d$ -wave in cuprates or  $s_{\pm}$ -wave in iron-pnictides. Instead, other pairing scenarios pertinent to purely electronic interaction effects have been suggested. Among these, spin-fluctuation-mediated superconductivity is believed to capture many aspects across different unconventional superconductors, owing in part to the proximity of the superconducting phase to magnetic order [33, 34, 117]. In this scenario, the attractive interaction is induced by electrons scattering off of magnetic fluctuations instead of phonons.<sup>36</sup> In contrast to phonon-mediated superconductivity, the pairing interaction induced by spin fluctuations involves the polarization of the electronic medium itself rather than the ionic lattice. The resulting pairing potential is anisotropic in space and captures exchange interaction effects in multi-orbital systems.

<sup>36</sup>These spin fluctuations are not necessarily proper bosons with a sharp dispersion relation  $\omega(\mathbf{q})$  but rather have spectral weight spread out in momentum and frequency. Critical temperatures of different superconductors were shown to scale with the spread of  $\omega_{\text{SF}}$  of spin fluctuations [32, 34].

Historically, the idea of electron pairing arising from purely repulsive interactions was first noted by Kohn and Luttinger [217]. They discussed how Friedel oscillations of the electron density (as a higher order interaction process from screening) can create spatial regions which are attractive to electrons and thus facilitate pairing. To utilize the spatial structure for pairing, the pair wave function has to carry a non-zero angular momentum. Shortly after, Berk and Schrieffer [590] laid the groundwork for spin-fluctuation-mediated superconductivity by introducing an effective interaction based on the RPA susceptibility, primarily framing it as a mechanism where ferromagnetic fluctuations inhibit spin singlet pairing. These observations were later identified to be the key to the triplet superfluidity seen in  $^3\text{He}$  [561]. The discovery of unconventional superconductivity in heavy fermion compounds, Bechgaard salts, and notably high-temperature cuprates catalyzed significant progress in developing superconducting pairing mechanisms deriving from spin fluctuations. We refer to Refs. [32–34, 95, 117] for a broader overview and in-depth discussions. In the following, we summarize the details of the pairing interaction induced by spin fluctuations.

#### 3.4.1 Effective pairing interaction from fluctuation exchange

The pairing interaction from spin fluctuations is represented by the irreducible vertex  $\Gamma_{pp}$  in the particle-particle (pairon/cooperon) channel. The conventional approach involves only accounting for particle-hole exchange contributions to  $\Gamma_{pp}$ , while neglecting computationally more expensive feedback from particle-particle fluctuations [33, 34, 117].

In the publications included in this thesis [II, III, IV, V], we employ the FLEX (RPA-like) approximation, where we use the bare local vertex  $\Gamma^0$  (2.44) as the building block of the particle-hole ladder making up  $\Gamma_{pp}$ . The interaction kernel  $\mathcal{K} \equiv \Gamma_{pp}$  of the Eliashberg equation (Figure 3.8) is thus analogously constructed to the interaction entering the FLEX self-energy in section 2.3.1 (cf. Figure 2.9c). For preserved SU(2) symmetry, we can decompose the interaction into singlet (S) and triplet (T) pairing channels, for which the respective expressions are given by [47]

$$\underline{\mathcal{V}}^S(q) = \frac{3}{2}\underline{U}^s \underline{\chi}^s(q) \underline{U}^s - \frac{1}{2}\underline{U}^c \underline{\chi}^c(q) \underline{U}^c + \frac{3}{4}\underline{U}^s + \frac{1}{4}\underline{U}^c, \quad (3.130a)$$

$$\underline{\mathcal{V}}^T(q) = -\frac{1}{2}\underline{U}^s \underline{\chi}^s(q) \underline{U}^s - \frac{1}{2}\underline{U}^c \underline{\chi}^c(q) \underline{U}^c - \frac{1}{4}\underline{U}^s + \frac{1}{4}\underline{U}^c \quad (3.130b)$$

with the spin and charge bare vertices in Eq. (2.45) and susceptibilities  $\chi^{s/c}$  in Eq. (2.47).

The corresponding linearized gap equation for multi-orbital systems reads ( $\eta = S, T$ )

$$\lambda_{\text{SC}}^{(\eta)\Sigma_{\text{AN},lm}}(k) = -\frac{1}{\beta N_k} \sum_{k',l',m',jj'} \mathcal{V}_{ll',m'm}^{(\eta)}(k-k') G_{lj}(k') G_{m'j'}^*(-k) \Sigma_{\text{AN},jj'}^{(\eta)}(k'). \quad (3.131)$$

Our implementation of the gap equation in the IR basis (see section 2.5.1 and publication I) enables the efficient evaluation of the gap equations for various different pairing symmetries following the *SPOT* principle, as discussed in section 3.1.6. By analyzing the corresponding eigenvalues  $\lambda_{\text{SC}}^\mu$  of a given symmetry  $\mu$  (including spin pairing channel  $\eta$ ), we can identify the dominant instability as the one for which  $\lambda_{\text{SC}}$  reaches unity first.



# Superconducting pairing in layered materials

# 4

Ἀγεωμέτρητος μηδεὶς εἰσὶτω.<sup>1</sup>

— Motto on the entrance of Plato's academy

Layered materials have taken an important role in condensed matter research due to the unique electronic properties that stem from their structural anisotropy. These materials often feature strong intra-layer bonding and moderate to weak inter-layer coupling, which can be attributed to, e.g., weak wave-function overlap due to large inter-layer distances or weak bonding electronic interactions such as vdW forces. This results in a quasi-two-dimensional electronic structure, where the reduced, effective dimensionality within the layers can amplify electron correlations and fluctuation effects, making layered materials a prime platform for various quantum phenomena [6, 97]. For instance, spin-fluctuation-mediated superconductivity tends to be stronger in (quasi-)two-dimensional materials compared to fully three-dimensional systems, because the fractional phase volume for spin-fluctuation scattering is larger [339].

Indeed, many unconventional and, in particular, high-temperature superconductors are layered materials with varying degree of coupling strength in the direction perpendicular to the layers. The most prominent examples are cuprates, which share a common structure consisting of copper oxide layers (with one or more Cu-O planes) stacked between block layers. The composition of these block layers then determines the doping of the copper oxide layers [28]. In contrast to such intrinsically layered materials, the class of vdW materials offer a much higher degree of control over material properties, allowing for the design of quantum matter on demand through methods such as heterostructuring and twisting to form moiré structures [22, 24, 158]

In this chapter, we examine superconductivity in both intrinsic and artificially engineered layered materials. Specifically, we consider spin-fluctuation-driven superconductivity in layered transition metal oxides in section 4.1, with a focus on hydrated sodium cobalt oxide ( $\text{Na}_x\text{CoO}_2 \cdot y\text{H}_2\text{O}$ ) and the recently discovered

---

<sup>1</sup>*Ageōmétrētos mēdeis eisitō.* — Let no one untrained in geometry enter.

bilayer nickelate ( $\text{La}_3\text{Ni}_2\text{O}_7$ , cf. section 4.2.1). Additionally, we study different superconducting pairing mechanisms in twisted TMDC homobilayers in section 4.3.

### 4.1 Layered transition metal oxides

The orbital character of valence electrons forming covalent bonds in a solid significantly influences the material's properties. In band theory, this is reflected by the bandwidth that develops from the overlap of orbital wave functions. Outer  $s$  and  $p$  electrons are itinerant because of their strong wave function overlap with neighboring atoms, whereas  $f$  electrons are highly localized and screened by core electrons. In contrast, valence  $d$ -shell electrons possess an intermediate character, placing transition metal elements with open  $d$ -shells in a unique position for properties emerging from chemical bonding. The bandwidth in transition metal compounds is often determined by indirect charge transfer between  $d$  orbitals via ligand  $p$  orbitals, which further narrows the  $d$  bandwidth and enhances interaction effects and electron correlations. As a result, even simple monoxides such as NiO or CuO are incorrectly classified as metals in band theory due to partially filled bands. Instead, they are magnetic charge transfer insulators induced by sizable interactions in the narrow  $d$ -bands [10].

Due to their mixed-valence and coordination possibilities, transition metals can form a variety of compositions. Among these, transition metal oxides have been intensively studied as they can host different correlated phases [591, 592]. Several families of (unconventional, high-temperature) superconducting transition metal oxides have been reported, with most prominent examples containing copper (cuprates) [28], ruthenium ( $\text{Sr}_2\text{RuO}_4$ ) [131], cobalt (hydrated  $\text{Na}_x\text{CoO}_2$ ), and nickel (nickelates); we also refer to the overview in chapter 1 and Figure 1.2. In these materials, the superconducting pairing primarily resides in individual transition metal oxide layers. Often, superconductivity emerges in proximity to magnetic phases (cf. Figure 1.1a for cuprates), which led to proposals of purely electronic pairing mechanisms, e.g., based on spin fluctuations. Here, we will discuss superconductivity in layered cobalt oxides. The family of nickelate materials, especially the bilayer nickelate  $\text{La}_3\text{Ni}_2\text{O}_7$ , will be addressed separately in section 4.2.

#### 4.1.1 Cobalt oxide hydrate – $\text{Na}_x\text{CoO}_2 \cdot y\text{H}_2\text{O}$

In order to understand unconventional superconductivity found in cuprates, researchers were on the search of superconductivity in oxides of related  $3d$  transition metals. In 2003, Takada et al. [132] discovered superconductivity in water-intercalated sodium cobalt oxide ( $\text{Na}_x\text{CoO}_2 \cdot y\text{H}_2\text{O}$ ) with a critical temperature of up to 4.7 K. This material is synthesized through the hydration of the layered sodium cobalt oxide  $\text{Na}_x\text{CoO}_2$ , a compound previously studied for its high thermoelectric



power [591]. Despite extensive research on  $\text{Na}_x\text{CoO}_2 \cdot y\text{H}_2\text{O}$ , the nature of its superconducting state remains controversial due to conflicting experimental and theoretical findings of its Fermi surface topology and superconducting pairing symmetry. In the following, we briefly summarize the structural and electronic properties of  $\text{Na}_x\text{CoO}_2 \cdot y\text{H}_2\text{O}$  (the crystal and band structure are depicted in Fig. 4 of publication II embedded below). Afterwards we give an overview on the unresolved issues contributing to the ongoing controversy. An in-depth discussion can be found in the reviews in Refs. [133, 134].

The properties of  $\text{Na}_x\text{CoO}_2 \cdot y\text{H}_2\text{O}$  mostly derive from its parent compound  $\text{Na}_x\text{CoO}_2$ . Its structure consists of cobalt oxide layers formed by edge-shared  $\text{CoO}_6$  octahedra, which are separated by sodium ions. In the  $\text{CoO}_2$  planes, positioning Co ions on a perfect triangular lattice. This triangular lattice geometry is unique among layered transition metal oxide superconductors and introduces lattice frustration effects. However, superconductivity only emerges upon hydration, which introduces water molecules between the oxide layers while Na ions are extracted. The intercalated water block layers push the cobalt oxide layers further apart and reduce their height, thereby enhancing the two-dimensional character of the system.

The low-energy electronic structure of  $\text{Na}_x\text{CoO}_2 \cdot y\text{H}_2\text{O}$  is formed by the  $t_{2g}$  orbitals of the Co atoms which are hole-doped by the Na ions. The reduced layer height induces a trigonal distortion in the oxygen octahedra, leading to crystal field splitting  $\Delta_{\text{CF}}$  which partially lifts the Co  $t_{2g}$  degeneracy into  $a_{1g}$  and  $e'_g$ . The LDA Fermi surface of  $\text{Na}_x\text{CoO}_2$  [593], that is studied in effective multi-orbital models of  $\text{Na}_x\text{CoO}_2 \cdot y\text{H}_2\text{O}$  [133, 134], shows a  $\Gamma$ -concentric  $a_{1g}$  hole pocket and small oval  $e'_g$  hole pockets along the  $\Gamma$ -K direction. The  $e'_g$  pockets allow for nearly perfect nesting conditions, which is crucial for enabling spin-fluctuation-driven superconductivity as investigated in publication II. However, the Fermi surface topology remains a controversial issue as will be discussed below.

### Open questions and challenges

The origin and nature of the superconducting state in  $\text{Na}_x\text{CoO}_2 \cdot y\text{H}_2\text{O}$  remains elusive. Here, we summarize key issues contributing to this controversy (see also the review by Sakurai et al. [134]):

- **Structural instability:** The  $\text{Na}_x\text{CoO}_2 \cdot y\text{H}_2\text{O}$  compound generally suffers from instability due to water evaporation which significantly impacts sample conditions and reproducibility. The water concentration is crucial for the emergence of superconductivity as it influences the Na concentration  $x$  and induces compression of the  $\text{CoO}_6$  layers, affecting the crystal field splitting. Both factors play a critical role in determining the Fermi surface topology.

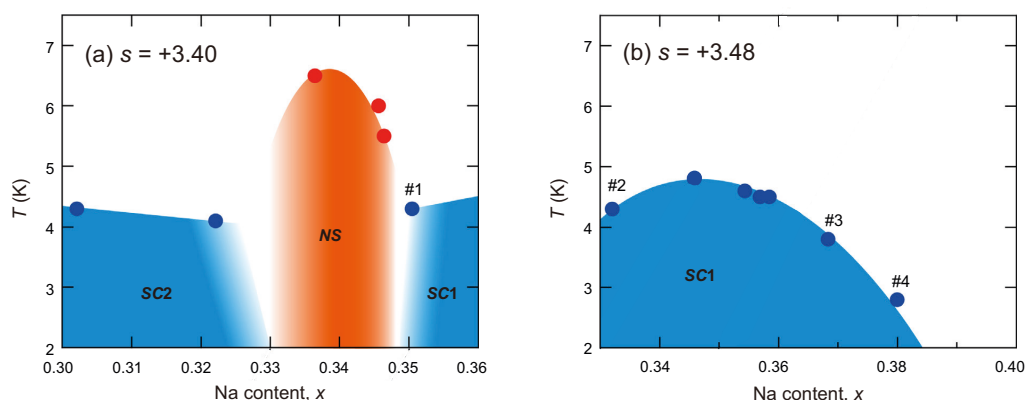


**Figure 4.1 – Experimental phase diagram of  $\text{Na}_x(\text{H}_3\text{O})_z\text{CoO}_2 \cdot y\text{H}_2\text{O}$ .** Superconducting phase diagram as a function of Na concentration for different valences of (a)  $s = 3.40$  and (b)  $s = 3.48$ . The superconducting phases are termed SC1 and SC2, while NS is a non-superconducting phase, whose nature is not clearly determined (presumably magnetic ordering [596]). Reproduced from [134] with permission from © 2015 Elsevier. Not covered by the CC BY 4.0 license.

- Unclear Co valence:** The hole doping from Na leads to a Co atom valence of  $s = 4 - x$  (electron filling  $n = 9 - s = 5 + x$ ). However, later studies identified the presence and importance of  $\text{H}_3\text{O}^+$  ions (with concentration  $z$ ) in the water block layers, refining the chemical composition to  $\text{Na}_x(\text{H}_3\text{O})_z\text{CoO}_2 \cdot y\text{H}_2\text{O}$  [134, 594]. Consequently, the valence is adjusted to  $s = 4 - x - z$  and the presence of  $\text{H}_3\text{O}^+$  modifies the possible doping-dependent diagrams, as shown in Figure 4.1. The additional doping with  $\text{H}_3\text{O}^+$  introduces uncertainty about the precise location of the superconducting phase within the Na concentration  $x$ -dependent phase diagram of the parent compound  $\text{Na}_x\text{CoO}_2$ . Without accounting for  $\text{H}_3\text{O}^+$ , the superconducting phase was originally placed at low doping, where the normal state is characterized as a Pauli paramagnetic metal [595]. However, the additional  $\text{H}_3\text{O}^+$  doping could potentially shift the superconducting phase into a Curie-Weiss magnetic regime at higher doping [596].
- Fermi surface topology:** Experimental and theoretical studies have not provided clear evidence for the existence of  $e'_g$  hole pockets on the Fermi surface. Theoretical modeling indicates that the presence of  $e'_g$  pockets is highly sensitive to the surrounding conditions (doping, crystal field splitting strength from layer squeezing, correlation effects). Experimental evidence is also inconclusive. While several ARPES measurements of  $\text{Na}_x\text{CoO}_2$  do not detect  $e'_g$  pockets at the Fermi level, Shubnikov-de-Haas data, photo-emission spectroscopy, and X-ray Compton scattering measurements support their presence.
- Pairing symmetry:** Various theoretical models proposed different pairing mechanisms and symmetries [133, 597], each with both supporting and contradictory

experimental results [134]. One highly contested pairing scenario is spin-triplet  $p$ - or  $f$ -wave pairing driven by the presence of ferromagnetic fluctuations originating from the  $e'_g$  pockets. However, most theoretical studies have been unable to investigate this scenario at the experimentally relevant temperature scale of  $T_c \sim 5$  K, leaving the dominance of  $p$ -wave or  $f$ -wave symmetry undetermined.

Our embedded publication II addresses the question of spin-fluctuation-driven superconductivity at experimentally relevant temperatures around  $T_c$  and their dependence on Fermi surface topology. To facilitate this study, we utilize the enhanced efficiency of the FLEX approximation implemented in the IR basis, which allows us to perform calculations at 2 K using a maximum of 62 Matsubara frequencies. We benchmark our method using a previously established Wannier construction of the  $t_{2g}$  bands, incorporating  $e'_g$  pockets on the Fermi surface [350].<sup>2</sup>

Our investigation reveals a dominance of  $f_{y(x^2-3y^2)}$ -wave symmetry fluctuations at low temperatures, although we do not observe a superconducting phase transition within the studied temperature range. An additional study of the Fermi surface topology shows the largest superconducting eigenvalue on the order of 0.7 at the lowest calculation temperature of 2 K.

Before performing the multi-orbital model study of  $\text{Na}_x\text{CoO}_2 \cdot y\text{H}_2\text{O}$ , we also benchmark our code implementation against the single-band Hubbard model on a square lattice. In this context, we draw a comprehensive superconducting phase diagram comparing different many-body methods, specifically for the particle-hole symmetric lattice model with only nearest-neighbor hopping  $t$  and intermediate interaction  $U/t = 4$ .

---

<sup>2</sup>We note that the studied model [350] does not consider the influence of  $\text{H}_3\text{O}^+$  ions, as their presence was not yet known at the time the Wannier construction was proposed.

Niklas Witt, Erik G. C. P. van Loon, Takuya Nomoto, Ryotaro Arita, Tim O. Wehling

### Key points summary

- Implementation of multi-orbital FLEX approximation within the IR basis (“FLEX+IR”), demonstrating numerical efficiency by reaching temperatures on the order of  $10^{-4}$  in units of the bandwidth.
- Benchmark of single-orbital Hubbard model and phase diagram comparison of FLEX and other many-body methods (DMFT+FLEX, TPSC, DCA).
- Study of  $\text{Na}_x\text{CoO}_2 \cdot y\text{H}_2\text{O}$  ( $T_c^{\text{exp}} = 4.5\text{ K}$ ) for possibility of spin-fluctuation-mediated superconductivity. Finding of dominant  $f_{y(x^2-3y^2)}$ -wave pairing eigenvalues at low temperatures down to  $\sim O(1\text{ K})$ , but without transition to the superconducting phase.






### Author Contributions

I wrote the FLEX+IR code under supervision of T. Nomoto, R. Arita, and T. Wehling and I performed all calculations shown in the publication. I prepared all the figures and wrote the initial draft. All authors discussed the results and gave comments on the text. I was responsible for handling the paper submission and correspondence with the editor and referees. Most of the code writing and parts of the results in this paper have been obtained as part of my master thesis [47].

### Copyright Notice

Reprinted with permission from N. Witt et al., Physical Review B **103**, 205148 (2021). Copyright © 2021 by the American Physical Society. This is the accepted and published version of the article available at doi: [10.1103/PhysRevB.103.205148](https://doi.org/10.1103/PhysRevB.103.205148).

## Efficient fluctuation-exchange approach to low-temperature spin fluctuations and superconductivity: From the Hubbard model to $\text{Na}_x\text{CoO}_2 \cdot y\text{H}_2\text{O}$

Niklas Witt <sup>1,2,\*</sup>, Erik G. C. P. van Loon <sup>1,2</sup>, Takuya Nomoto <sup>3</sup>, Ryotaro Arita <sup>3,4</sup> and Tim O. Wehling <sup>1,2</sup>

<sup>1</sup>*Institut für Theoretische Physik, Universität Bremen, Otto-Hahn-Allee 1, 28359 Bremen, Germany*

<sup>2</sup>*Bremen Center for Computational Materials Science, Universität Bremen, Am Fallturm 1a, 28359 Bremen, Germany*

<sup>3</sup>*Department of Applied Physics, The University of Tokyo, 7-3-1 Hongo, Bunkyo-ku, Tokyo 113-8656, Japan*

<sup>4</sup>*RIKEN Center for Emergent Matter Science, 2-1 Hirosawa, Wako, Saitama 351-0198, Japan*



(Received 9 December 2020; revised 23 March 2021; accepted 30 April 2021; published 26 May 2021)

Superconductivity arises mostly at energy and temperature scales that are much smaller than the typical bare electronic energies. Since the computational effort of diagrammatic many-body techniques increases with the number of required Matsubara frequencies and thus with the inverse temperature, phase transitions that occur at low temperatures are typically hard to address numerically. In this work, we implement a fluctuation exchange (FLEX) approach to spin fluctuations and superconductivity using the “intermediate representation basis” (IR) [Shinaoka *et al.*, *Phys. Rev. B* **96**, 035147 (2017)] for Matsubara Green functions. This FLEX + IR approach is numerically very efficient and enables us to reach temperatures on the order of  $10^{-4}$  in units of the electronic bandwidth in multiorbital systems. After benchmarking the method in the doped repulsive Hubbard model on the square lattice, we study the possibility of spin-fluctuation-mediated superconductivity in the hydrated sodium cobalt material  $\text{Na}_x\text{CoO}_2 \cdot y\text{H}_2\text{O}$  reaching the scale of the experimental transition temperature  $T_c = 4.5$  K and below.

DOI: [10.1103/PhysRevB.103.205148](https://doi.org/10.1103/PhysRevB.103.205148)

### I. INTRODUCTION

The physics of unconventional superconductivity has been a longstanding problem in condensed-matter physics. Over the course of decades, many different systems have been discovered, such as heavy-fermion compounds [1,2], cuprates [3,4], iron-based superconductors [5,6], twisted two-dimensional (2D) materials [7,8], and infinite-layer nickelate [9].

Finding a microscopic description for these materials is a difficult task since correlations as well as complexity need to be accounted for appropriately. The inherent complexity of real materials arises from the interplay of many internal degrees of freedom and typically covering multiple energy scales. For instance, screening of the Coulomb interaction often involves electronic bands reaching up to 100 eV in energy. On the other side, superconductivity emerges when thermal energies are on a scale of 10 meV for  $T_c$  cuprate systems down to a few 10  $\mu\text{eV}$  in several heavy-fermion systems. Hence, four or even more orders of magnitude of electronic energies are typically involved in the electronic structure of superconducting materials. For the theoretical modeling, this has practical consequences. Distinct energy scales require large but accurate frequency grid sampling and processing. This frequently limits the phase space that can be studied by diagrammatic many-body methods.

One particular material example for this complex interplay of different degrees of freedom and energy scales is given by

the water intercalated sodium cobalt oxide,  $\text{Na}_x\text{CoO}_2 \cdot y\text{H}_2\text{O}$ , which features superconductivity with transition temperatures reaching  $T_c = 4.5$  K [10]. This material consists of layered cobalt oxide planes being separated by sodium ions and water molecules. The Co atoms are arranged on a triangular lattice and hole-doped, rendering it a possible realization of a resonating-valence-bond state, related to high-temperature superconductivity [11,12]. However, until now neither an experimental nor a theoretical consensus has been reached on the origin of the superconducting pairing.

Theoretically proposed pairing types include a spin triplet  $p$ - or  $f$ -wave driven by ferromagnetic fluctuations [13–16], a spin singlet extended  $s$ -wave [17,18], a chiral ( $d + id$ )-wave [19,20], an odd frequency gap [15,21], or conventional phonon-assisted  $s$ -wave pairing [22,23]. For each of them, experimental results can be found that support or deny their realization [24], making the analysis quite delicate. This controversy about the pairing type originates from several problems. They include a general instability of the  $\text{Na}_x\text{CoO}_2 \cdot y\text{H}_2\text{O}$  compound due to water evaporation with an accompanying large dependence on sample conditions [24]. On the theoretical side, a multiorbital model is necessary to accurately describe the electronic structure [25], which makes computational studies very challenging. It might be one of the reasons why no microscopic studies of the superconducting instability have been reported on the temperature scale of  $T_c \sim 5$  K.

In this work, we implement a fluctuation exchange (FLEX) approach [14,26–32] using the intermediate representation (IR) basis [33–36] and study the possibility of spin-fluctuation-mediated superconductivity in

\*niwitt@uni-bremen.de

$\text{Na}_x\text{CoO}_2 \cdot y\text{H}_2\text{O}$ . The IR basis provides a compact representation of imaginary-time quantities that additionally enables the usage of sparsely sampled data grids [37]. As a result, the numerical cost of calculations can be considerably reduced permitting, e.g., new *ab initio* approaches [38]. Here, we use this combined FLEX + IR approach to perform calculations at very low temperatures. We study the magnetic properties of  $\text{Na}_x\text{CoO}_2 \cdot y\text{H}_2\text{O}$  and investigate the possibility of triplet superconductivity occurring on the scale of the experimental  $T_c$ .

The remainder of this work is structured as follows: In Sec. II we will briefly review the FLEX approximation and explain the application of the IR basis. To illustrate the accuracy and efficiency of our approach, we first show benchmark studies on the single-orbital Hubbard model in Sec. III. Subsequently, we use our method to research the possibility of spin-fluctuation-driven superconductivity in the  $\text{Na}_x\text{CoO}_2 \cdot y\text{H}_2\text{O}$  system at very low temperatures. For this, we study the Fermi surface, filling, and interaction dependence of the spin susceptibility and superconducting instability in Sec. IV.

## II. METHODS

### A. Fluctuation exchange approximation

The FLEX approximation introduced by Bickers *et al.* [26,27] is a perturbative diagrammatic approach that treats spin and charge fluctuations self-consistently. It can be derived from a Luttinger-Ward functional [39] containing an infinite series of closed bubble and ladder diagrams. As such, it is a conserving approximation [40,41]. Due to its perturbative nature, FLEX cannot sufficiently capture strong-coupling physics, but it performs well in the weak-coupling regime. It is suitable for studying systems with strong spin fluctuations in Fermi liquids and near quantum critical points.

In this paper, we employ the multiorbital extension of FLEX [29,42] for which we consider the (antisymmetrized) local interaction Hamiltonian

$$H_{\text{int}} = \frac{1}{4} \sum_i \sum_{\xi_1 \xi_2 \xi_3 \xi_4} \Gamma^0_{\xi_1 \xi_4, \xi_3 \xi_2} c_{i\xi_1}^\dagger c_{i\xi_2}^\dagger c_{i\xi_3} c_{i\xi_4}, \quad (1)$$

where the operators  $c_{i\xi}^\dagger$  ( $c_{i\xi}$ ) create (destroy) an electron at site  $i$  in a state  $\xi = (l, \sigma)$ , which is a combined orbital and spin index. The bare vertex  $\Gamma^0$  is expressed as

$$\Gamma^0_{\xi_1 \xi_4, \xi_3 \xi_2} = -\frac{1}{2} U_{l_1 l_4, l_3 l_2}^S \boldsymbol{\sigma}_{\sigma_1 \sigma_4} \cdot \boldsymbol{\sigma}_{\sigma_2 \sigma_3} + \frac{1}{2} U_{l_1 l_4, l_3 l_2}^C \delta_{\sigma_1 \sigma_4} \delta_{\sigma_2 \sigma_3} \quad (2)$$

with the interaction matrices

$$U_{ij,kl}^S = \begin{cases} U & \text{if } i = j = k = l, \\ U' & \text{if } i = k \neq l = j, \\ J & \text{if } i = j \neq l = k, \\ J' & \text{if } i = l \neq k = j, \end{cases} \quad U_{ij,kl}^C = \begin{cases} U & \text{if } i = j = k = l, \\ -U' + 2J & \text{if } i = k \neq l = j, \\ 2U' - J & \text{if } i = j \neq l = k, \\ J' & \text{if } i = l \neq k = j, \end{cases}$$

where  $U$  and  $U'$  are the local intra- and interorbital interactions,  $J$  is the interorbital exchange interaction or Hund's coupling, and  $J'$  is the pair-hopping between two orbitals. Due to symmetry, they are related by  $U = U' + J + J'$  and  $J = J'$ .

In FLEX, the self-energy can be calculated from

$$\Sigma_{lm}(k) = \frac{T}{N} \sum_q \sum_{l',m'} V_{ll',mm'}(q) G_{l'm'}(k-q), \quad (3)$$

where  $k = (i\omega_n, \mathbf{k})$  and  $q = (iv_m, \mathbf{q})$  denote crystal momentum and Matsubara frequencies  $\omega_n = (2n+1)\pi T$  ( $\nu_m = 2m\pi T$ ) for fermions (bosons),  $T$  is the temperature, and  $N$  is the number of sites. The interaction consists of contributions from the spin and charge channel as

$$V(q) = \frac{3}{2} U^S [\chi^S(q) - \frac{1}{2} \chi^0(q)] U^S + \frac{3}{2} U^S + \frac{1}{2} U^C [\chi^C(q) - \frac{1}{2} \chi^0(q)] U^C - \frac{1}{2} U^C. \quad (4)$$

The charge and spin susceptibility entering Eq. (4) are defined by

$$\chi^C(q) = \frac{\chi^0(q)}{\mathbb{1} + \chi^0(q) U^C}, \quad \chi^S(q) = \frac{\chi^0(q)}{\mathbb{1} - \chi^0(q) U^S}, \quad (5)$$

with the unity operator  $\mathbb{1}$  and the irreducible susceptibility

$$\chi_{ll',mm'}^0(q) = -\frac{T}{N} \sum_k G_{lm}(k+q) G_{m'l'}(k). \quad (6)$$

We use Eqs. (3)–(6) to self-consistently solve the Dyson equation

$$G(k)^{-1} = G^0(k)^{-1} - \Sigma(k) \quad (7)$$

with the bare Green function given by

$$G^0(i\omega_n, \mathbf{k}) = \frac{\mathbb{1}}{i\omega_n \mathbb{1} - [H^0(\mathbf{k}) - \mu \mathbb{1}]}. \quad (8)$$

$H^0(\mathbf{k})$  is the noninteracting Hamiltonian, and  $\mu$  denotes the chemical potential, which needs to be adjusted in every iteration to keep the electron density  $n$  fixed. The fractions in Eqs. (5) and (8) are to be understood as inversions.

In the presence of strong magnetic fluctuations, it is possible to study the superconducting phase transition within FLEX. For this purpose, we consider the linearized Eliashberg theory with the gap equation reading

$$\lambda \Delta_{lm}^\eta(k) = \frac{T}{N} \sum_q \sum_{l',m'} V_{ll',m'm}^\eta(q) F_{l'm'}^\eta(k-q). \quad (9)$$

It is diagonal in the spin singlet- and triplet-pairing channel ( $\eta = s, t$ ) with the anomalous Green function  $F^\eta(k) = -G(k) \Delta^\eta(k) G^T(-k)$  and respective interactions

$$V^s(q) = \frac{3}{2} U^S \chi^S(q) U^S - \frac{1}{2} U^C \chi^C(q) U^C + \frac{1}{4} (3U^S + U^C), \\ V^t(q) = -\frac{1}{2} U^S \chi^S(q) U^S - \frac{1}{2} U^C \chi^C(q) U^C - \frac{1}{4} (U^S - U^C). \quad (10)$$

$\lambda$  and  $\Delta$  in the linearized gap equation (9) represent an eigenvalue and eigenvector of the Bethe-Salpeter equation, respectively [26,43]. We solve this eigenvalue problem by using the power iteration method. The superconducting transition temperature is found if the eigenvalue  $\lambda$  reaches unity.

### B. Intermediate representation basis

The basic objects of diagrammatic many-body methods like FLEX are Green functions and derived quantities that

are computed numerically on finite imaginary-time and Matsubara frequency grids. Using conventional uniform grids to represent Green functions, calculations require grid sizes that increase linearly with inverse temperature upon cooling the system. In practice, this prohibits calculations at low temperatures, as the required amount of data becomes too large to be stored or processed. One of several approaches [44–46] to tackle these problems is to use a compact representation of Green functions as given by (orthogonal) continuous basis functions, like Legendre polynomials [47,48], Chebyshev polynomials [49], or numerical basis functions [50].

The IR basis [33–36] is such an orthogonal numerical basis in which Green functions can be efficiently and compactly represented. The basis functions are defined by the singular value expansion of the kernel that connects Green function and spectral function [51]:

$$K^\alpha(\tau, \omega) = \omega^{\delta_{\alpha,B}} \frac{e^{-\omega\tau}}{1 \pm e^{-\beta\tau}} = \sum_{l=0}^{\infty} S_l^\alpha U_l^\alpha(\tau) V_l^\alpha(\omega). \quad (11)$$

Here,  $\{U_l^\alpha(\tau)\}$ ,  $\{V_l^\alpha(\omega)\}$  denote the IR basis functions, and  $S_l^\alpha$  are the exponentially decaying singular values. The expansion is uniquely defined by fermionic or bosonic statistics  $\alpha \in \{F, B\}$  and a dimensionless parameter  $\Lambda = \beta\omega_{\max}$ , where  $\beta$  is the inverse temperature, and  $\omega_{\max}$  is a cutoff frequency that captures the spectral width of the system.

The representation within the IR basis provides a controlled way to store Green functions. This means that the truncation error  $\delta$  of the expansion

$$G^\alpha(x) = \sum_{l=0}^{l_{\max}} G_l^\alpha U_l^\alpha(x) \quad [x = \tau, i\omega_n] \quad (12)$$

with  $N_{\text{IR}}^\alpha = l_{\max} + 1$  basis functions is controllable. It is determined from the singular values by  $\delta \leq S_{l_{\max}}/S_0$ . Due to their exponential decay, only a small number  $N_{\text{IR}}^\alpha$  is necessary to compactly represent Green function data with high accuracy, as is shown in Fig. 1. Compared to other basis sets like Legendre or Chebyshev polynomials, the IR basis holds a superior compactness, especially at low temperatures.

Another advantage of the IR basis is the possibility to generate sparse imaginary-time and frequency grids with a size equal to the number of basis functions [37]. This scheme ideally requires an even (odd) number for fermionic (bosonic) quantities because of which the lines in Fig. 1 are step functions. The sparse grids offer the benefit of decreased data storage while performing intermediate steps of solving diagrammatic calculations efficiently, like computing Fourier transformation by simple matrix multiplications [52].

In practical calculations, a desired accuracy  $\delta$  is chosen, and  $\Lambda$  is set such that  $\Lambda \geq \beta\omega_{\max}$  holds for a fixed  $\omega_{\max}$ . Then, the  $\{U_l^\alpha\}$  functions are precomputed on imaginary-time and Matsubara frequency grids. The evaluation of Eq. (11) is numerically expensive. However, the open-source IRBASIS software package [35] provides numerical basis functions as solutions to Eq. (11) that can be quickly accessed and implemented easily. Throughout this paper, we employed  $\Lambda = 10^4$  and  $\delta = 10^{-8}$ , which corresponds to small basis and grid sizes of  $N_{\text{IR}}^F = 62$  and  $N_{\text{IR}}^B = 57$ .

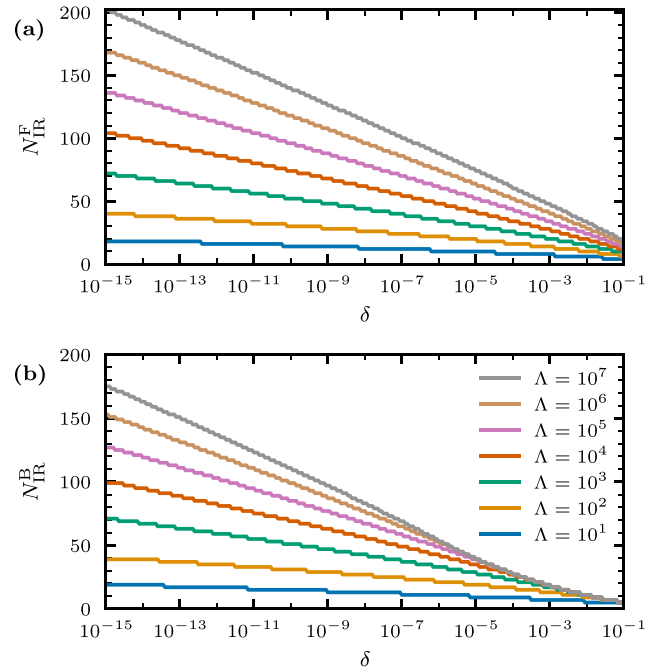


FIG. 1. Number of IR basis functions  $N_{\text{IR}}^\alpha$  needed to sufficiently expand (a) fermionic or (b) bosonic Green functions within an error bound  $\delta$ . The imaginary-time and Matsubara frequency grid sizes can be chosen equally large.

### III. BENCHMARK: SINGLE-ORBITAL SQUARE LATTICE HUBBARD MODEL

The Hubbard model is a fundamental model used to study correlated electron physics, particularly the interplay of magnetism and unconventional superconductivity. Despite its simplicity, it captures many essential physics important to interacting quantum systems. Thus, a multitude of many-body approaches has been developed to simulate the properties of the Hubbard model [53,54]. Therefore, it constitutes an excellent system to benchmark our FLEX + IR approach to former FLEX and further studies of magnetism and superconductivity.

In this regard, we consider the repulsive single-orbital Hubbard model on a square lattice, which also serves as a relevant study case for cuprates [4]. Taking into account nearest- and next-nearest-neighbor hoppings  $t$  and  $t'$ , the single-particle dispersion is given by

$$\varepsilon_{\mathbf{k}} = 2t[\cos(k_x) + \cos(k_y)] + 4t' \cos(k_x) \cos(k_y). \quad (13)$$

In the following,  $t$  is the unit of energy. We set the local interaction to an intermediate value of  $U/t = 4$ . For an assessment of the performance of the FLEX + IR method introduced, here we first compare to an earlier FLEX work of one of the current authors [28]. To this end, we adapted the  $N = 64^2$  lattice sites in our calculations and replaced the uniform 2048 Matsubara frequency grid of Ref. [28] with the IR basis sampling.

The Hubbard model contains different magnetic fluctuations whose relative strength can be controlled by the Fermi surface shape, i.e., by changing  $t'$  and the electron filling  $n$ . To contemplate different physical situations, we inspect the

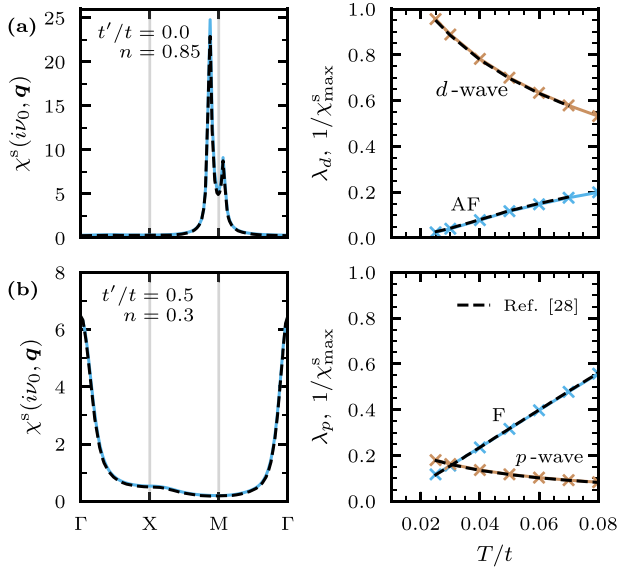


FIG. 2. Comparison of static spin susceptibility (left column) at  $T/t = 0.03$  and eigenvalue of the Eliashberg equation as well as inverse magnetic susceptibility at the leading instability (right column) as calculated with our FLEX + IR implementation with results from Ref. [28] (dashed lines). The rows show two different situations with dominant (a) antiferromagnetism (AF:  $t'/t = 0$ ,  $n = 0.85$ ) and (b) ferromagnetism (F:  $t'/t = 0.5$ ,  $n = 0.3$ ) for  $U/t = 4$ .

possibility of both dominant antiferromagnetism (AF) and ferromagnetism (F) by using the parameters  $t'/t = 0$ ,  $n = 0.85$  and  $t'/t = 0.5$ ,  $n = 0.3$ , respectively.

First we examined the spin susceptibility  $\chi^s$ . The results for the static spin susceptibility  $\chi^s(iv_0 = 0, \mathbf{q})$  are shown along high-symmetry paths in the Brillouin zone in the left column of Fig. 2. For a direct comparison, we also included the results of Ref. [28]. Clearly, the agreement between both data sets is excellent. The dominant structures and magnitude of the incommensurate antiferromagnetic and the weaker ferromagnetic fluctuations are reproduced exactly.

The presence of strong magnetic fluctuations can drive unconventional superconductivity. To study its appearance, we calculated the superconducting eigenvalue  $\lambda$ . In the case of dominant AF fluctuations, we consider a singlet-pairing gap with  $d_{x^2-y^2} \equiv d$ -symmetry while we choose the degenerate triplet  $p$ -wave state for dominant F fluctuations. Their respective eigenvalues are shown in the right column of Fig. 2 together with the inverse of  $\chi^s(0, \mathbf{Q})$  at the wave vector  $\mathbf{Q}$  of the leading instability, which signifies magnetic ordering. As can be seen, the AF fluctuations are strong enough to enable  $d$ -wave superconductivity with a  $T_c \approx 0.02t$ , whereas the  $p$ -wave solution is not realized. This is mainly due to stronger self-energy renormalization for  $t' > 0$  and a smaller prefactor in the triplet-pairing potential  $V^1(\mathbf{q})$  in Eq. (10). Once again, we included data from Ref. [28], which agree very well. This demonstrates that by employing the IR basis we can reduce the necessary frequency points by a factor of  $\sim 33$  while achieving the same results under persistent accuracy.

In a second step, we use our FLEX + IR approach to study the superconducting and magnetic phase diagram of the square lattice Hubbard model with  $t'/t = 0$ . An addi-

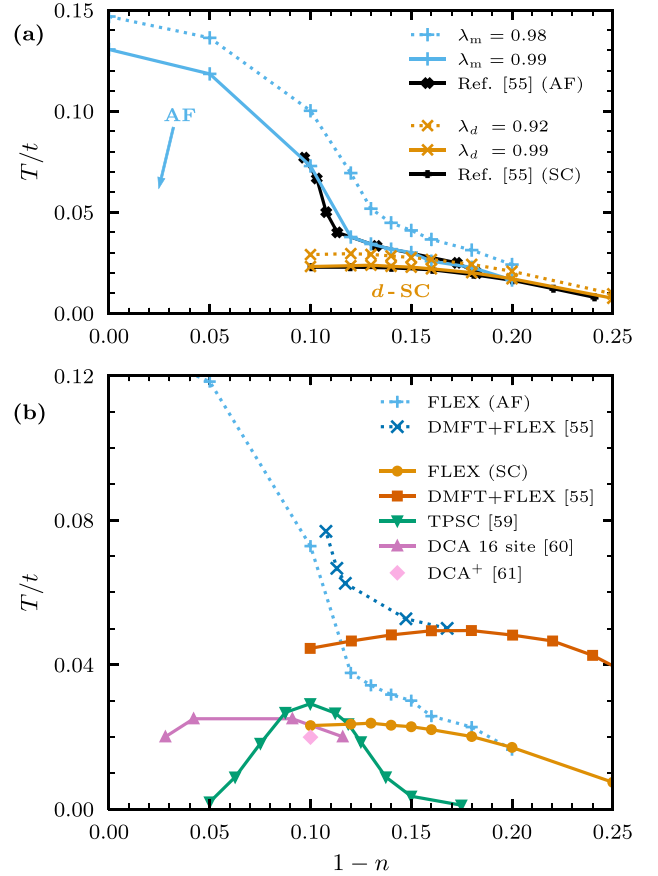


FIG. 3. Phase diagram of the Hubbard model with  $t'/t = 0$  and  $U/t = 4$ . (a) Comparison of different magnetic (AF) and superconducting (SC) eigenvalues calculated by the FLEX + IR approach with results from Ref. [55]. (b) Comparison of calculated phase boundaries from FLEX + IR to a variety of methods including DMFT + FLEX [55], TPSC [59], DCA on a 16-site cluster [60], and DCA+ [61].

tional comparison to numerical methods beyond FLEX will be made.

To map out the phase diagram, we performed calculations for different fillings and temperatures. Regions of strong magnetic and superconducting fluctuations can be identified by analyzing and extrapolating the corresponding magnetic ( $\lambda_m = U\chi_{\max}^0$ ) and superconducting ( $\lambda_d$ ) eigenvalues. In Fig. 3(a) we show the  $n - T$  diagram for two extracted values of  $\lambda_m$  and  $\lambda_d$  to indicate the evolution of the phase boundaries for  $\lambda \rightarrow 1$ . Additionally, we included independent FLEX results by Kitatani *et al.* [55] ( $\lambda_{m,d} = 0.99$ ) to verify our accuracy. This latter comparison yields excellent agreement.

The results show that  $T_c$  grows monotonically with the electron filling with some flattening of the curve around a hole doping of 0.15, as has been reported previously [56]. We cannot, however, make a statement about the underdoped region near half-filling due to strong AF fluctuations preventing the FLEX cycle from converging. This can be seen from  $\lambda_m \rightarrow 1$ , which masks the superconducting domain below 0.1 hole-doping. This issue is inherently a part of the theory due to the diverging denominator of the spin susceptibility. Here,



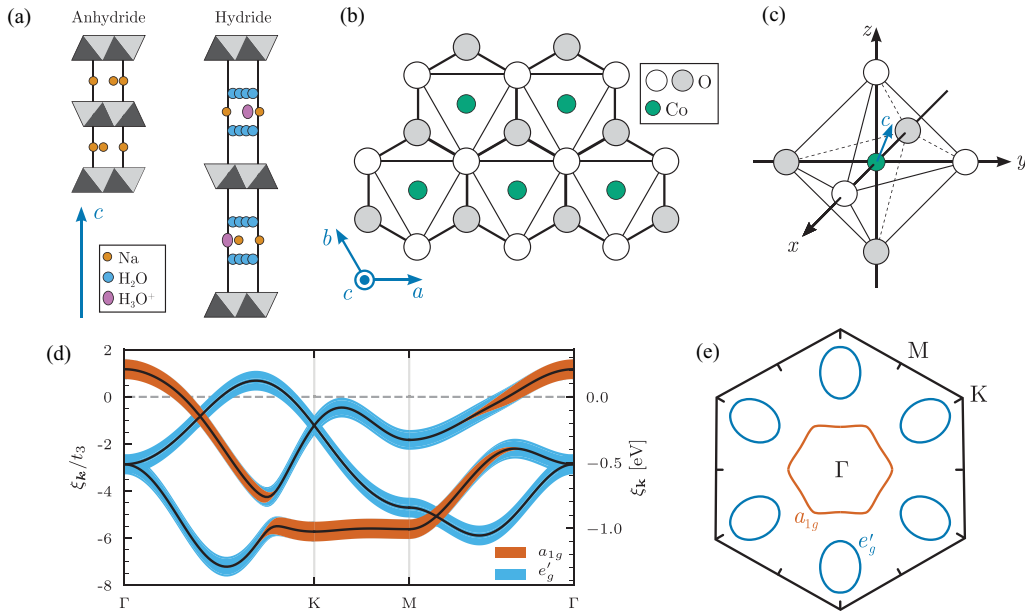


FIG. 4. Crystal and electronic structure of the  $\text{Na}_x\text{CoO}_2 \cdot y\text{H}_2\text{O}$  compound. (a) Vertical layered structure of  $\text{CoO}_2$  planes (light and dark gray) with intercalated  $\text{Na}^+$ ,  $\text{H}_2\text{O}$ , and  $\text{H}_3\text{O}^+$ . (b) Top view on  $\text{CoO}_2$  planes showing a triangular sublattice of Co ions with surrounding O ions. (c)  $\text{CoO}_6$  octahedron, which is trigonally deformed by the layered structure. (d) Electronic band structure with orbital character projections indicated by surrounding color patches. Model details are given in the Appendix. Energies are measured with respect to the chemical potential  $\xi_k = \varepsilon_k - \mu$ . (e) Fermi surface corresponding to the band structure of panel (d).

the strong fluctuations result from better nesting conditions on the Fermi surface with less doping, which becomes even more profound for larger  $U$ .

At this point, we should comment on the designation of phase boundaries at finite temperatures, since the Mermin-Wagner theorem [57,58] actually prohibits the formation of (perfect) long-range-ordered phases associated with spontaneous breaking of continuous symmetries at finite temperatures in two dimensions. The results shown here are best understood in the context of quasi-two-dimensional systems: It has been shown that purely two-dimensional systems show very similar results to quasi-two-dimensional systems with a weak but finite three-dimensional character as long as the out-of-plane coherence length is large [28].

In Fig. 3(b) we compare our phase diagram obtained from FLEX for  $\lambda_{m,d} = 0.99$  with phase diagrams reported in the literature which have been calculated using DMFT + FLEX (dynamical mean-field) [55], two-particle self-consistency (TPSC) [59], the diagrammatic cluster approximation (DCA) on a 16-site cluster [60], and DCA<sup>+</sup> [61]. On a qualitative level, all approaches under consideration yield maximally achievable superconducting critical temperatures on the same order of magnitude. Also the shape of the phase boundary of the AF region agrees between FLEX and FLEX + DMFT.

On a close, more quantitative level, however, there are profound differences between the phase diagrams revealed by the different methods: The most prevalent difference between all methods lies in the structures of the superconducting dome in the phase diagram. The filling dependence of this dome shape varies significantly. Due to the reasons of the previous

discussion, FLEX does not establish this dome structure. It can be retrieved by incorporating strong correlation effects as contained in DMFT, DCA, and also in TPSC. The level at which correlations are incorporated, however, strongly influences the exact doping dependence.

#### IV. SODIUM COBALT OXIDE

The pairing type of superconductivity and its interplay with magnetism in  $\text{Na}_x\text{CoO}_2 \cdot y\text{H}_2\text{O}$  is a very controversial issue as we have elucidated in the Introduction. In the following, we apply the FLEX + IR approach to study this problem.

##### A. Crystal and electronic structure

$\text{Na}_x\text{CoO}_2 \cdot y\text{H}_2\text{O}$  is commonly synthesized by soft-chemical methods from the parent compound  $\text{Na}_{0.7}\text{CoO}_2$ . The latter is a layered material consisting of cobalt oxide planes that are separated by sodium ions; cf. Fig. 4(a). The  $\text{CoO}_2$  planes are composed of edge-shared  $\text{CoO}_6$  octahedra that place the Co ions on a perfect triangular lattice as depicted in Figs. 4(b) and 4(c). During hydration, water molecules and hydronium ions are intercalated between the  $\text{CoO}_2$  planes. As a consequence, the separation between the  $\text{CoO}_2$  planes in the  $c$ -direction increases while the  $\text{CoO}_6$  octahedra contract in that direction. The material becomes thus more anisotropic, i.e.,  $\text{H}_2\text{O}$  intercalation enhances two-dimensionality in the  $\text{CoO}_2$  planes.

The Co atoms have partially filled  $t_{2g}$  bands that are electron-doped by the Na ions. In the simplest approximation, their filling is  $n = 5 + x$ , where  $x$  is the Na content. Upon Na

doping, a rich phase diagram [24,62] with weak correlations for low dopings ( $x \sim 0.3$ ) and strong correlations for high dopings ( $x \sim 0.7$ ) emerges. In this phase characterization, the superconducting region is placed around  $x \approx 0.3$ . However, this classification had been made without consideration of possible additional doping from the  $\text{H}_3\text{O}^+$  ions because their presence was only discovered at a later time [24]. Due to this, the filling of the  $t_{2g}$ -bands might be larger in the superconducting phase, locating it in the strongly correlated region [16,63].

To model the electronic structure, we use a three-band tight-binding model for the  $t_{2g}$  bands as formulated by Mochizuki *et al.* [14], which describes the low-energy characteristics of LDA band-structure calculations [64] quite well. This model includes a crystal field term accounting for the trigonal deformation of the  $\text{CoO}_6$  octahedra because of the plane height reduction. It leads to a splitting of the  $t_{2g}$  orbitals into a higher  $a_{1g}$  and lower twofold  $e'_g$  levels. The exact details on this model are presented in the Appendix. The corresponding band structure is shown orbitally resolved for a Co valence of  $s = 3.645$  or respective electron filling of  $n = 5.355$  in Fig. 4(d). Panel (e) contains the associated Fermi surface. It consists of one large  $a_{1g}$  hole pocket around the Brillouin zone center and six elliptically shaped  $e'_g$  hole pockets near the K points. The latter play an important role in creating strong ferromagnetic fluctuations since they have a large density of states and offer good nesting conditions for  $\mathbf{Q} \approx (0, 0)$  [14,21,25].

There has been much discussion on the actual existence of the  $e'_g$  pockets on the Fermi surface in the literature. It stems from the fact that ARPES measurements [65–69] locate them below the Fermi level. However, these results might be due to surface effects [70] since PES [71] and Shubnikov–de Haas measurements [72] seem to support their existence. Theoretical studies showed that the  $e'_g$  pockets are suppressed in charge self-consistent LDA + DMFT calculations [73], while LDA + DFMT performed with a realistic Hund’s coupling  $J$  can stabilize them [74]. The problem of locating the  $e'_g$  pockets in energy is very delicate since variations in the crystal field splitting (layer height), electron filling, and bandwidth renormalization influence the fermiology of  $\text{Na}_x\text{CoO}_2 \cdot y\text{H}_2\text{O}$ . In this work, we study the interplay of spin fluctuations and superconductivity for different models of the Fermi surface. We start with the type of Fermi surface considered also in Ref. [14] and vary the Fermi surface shape and topology afterward.

To this end, we first reproduce the results given in Ref. [14] within FLEX + IR and then extend the calculations to lower temperatures. We adapted the interaction strength of  $U = 6$  in units of the hopping  $t_3$  ( $U \sim 1.1$  eV; see the Appendix) and we vary the Hund’s coupling  $J$  as a ratio of  $U$ . For the initial comparison, we use a  $\mathbf{k}$ -mesh of  $32 \times 32$  as in Ref. [14], but the low-temperature calculations demand a denser grid sampling for which we found  $N_k = 210^2$  lattice sites to be converged.

### B. Spin susceptibilities

To check the accuracy of our implementation, we calculated the static spin susceptibility and compare our results to Ref. [14], where calculations were carried out for a temperature of  $T/t_3 = 0.02$  and different  $J/U$  values. It should be

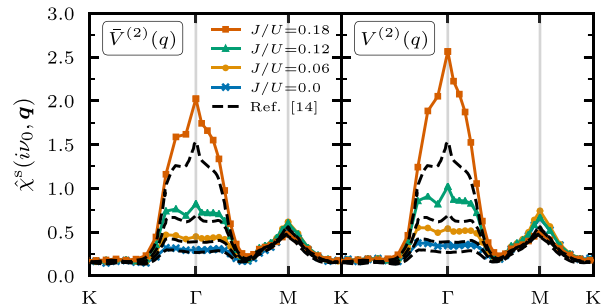


FIG. 5. Comparison of the largest eigenvalue of the static spin susceptibility to results from Ref. [14] at  $T/t_3 = 0.02$  using a  $32 \times 32$   $\mathbf{k}$ -mesh. The second-order correction used in the calculations is different between both panels [see the text and Eqs. (14) and (15)].

noted that a different second-order correction  $\bar{V}^{(2)}(q)$  to the FLEX interaction has been employed in Ref. [14], which is given by

$$\bar{V}^{(2)}(q) = -\frac{1}{4}(U^S + U^C)\chi^0(q)(U^S + U^C). \quad (14)$$

Comparing it to the second-order contribution from Refs. [42,75–78] as implemented in our code

$$V^{(2)}(q) = -\frac{3}{4}U^S\chi^0(q)U^S - \frac{1}{4}U^C\chi^0(q)U^C \quad (15)$$

it becomes evident that  $\bar{V}^{(2)}(q)$  incorrectly includes mixing between spin and charge channel contributions. In Fig. 5 we show the largest eigenvalue of the static spin susceptibility  $\hat{\chi}^s$  for both interactions together with data by Mochizuki *et al.* from Ref. [14]. It can be seen that the results are very well reproduced if  $\bar{V}^{(2)}(q)$  is implemented (left panel). Comparing it to the implementation of  $V^{(2)}$  (right panel) shows that the incorrect mixing of fluctuation channels leads to a reduction of fluctuation strength.

Generally, the system contains F as well as AF fluctuations. By increasing  $J$ , ferromagnetism is strongly enhanced while the AF fluctuations are slightly decreased. The latter are generated by scattering on the  $a_{1g}$  surface as well as between different  $e'_g$  pockets, whereas the F fluctuations emerge mostly from intrapocket scattering in the  $e'_g$  sheets. The charge fluctuations are negligibly small and not shown here.

The previously discussed results were at a relatively high temperature of  $T/t_3 = 0.02$ , which corresponds to  $\sim 50$  K. To properly understand the superconducting transition, a lower temperature range on the order of the experimental critical temperatures needs to be investigated. In Fig. 6 we show the temperature evolution of the largest eigenvalues of static irreducible susceptibility  $\hat{\chi}^0$  and spin susceptibility  $\hat{\chi}^s$  for two exchange interaction ratios  $J/U$ .  $\hat{\chi}^0$  does not show a strong dependence on  $T$ . The peak at the M point becomes slightly enhanced while the structure around the  $\Gamma$  point changes a bit.

Contrary to this,  $\hat{\chi}^s$  shows a strong  $T$  dependence. By cooling the system, the ferromagnetic fluctuation strength exhibits a nonmonotonous behavior with a strong enhancement of the peak at  $\mathbf{Q} = (0, 0)$  for  $T/t_3 \approx 0.02$ . This nonmonotonous evolution traces back to an almost divergent  $\hat{\chi}^s$  stemming from the denominator in Eq. (5) approaching zero. In other words,

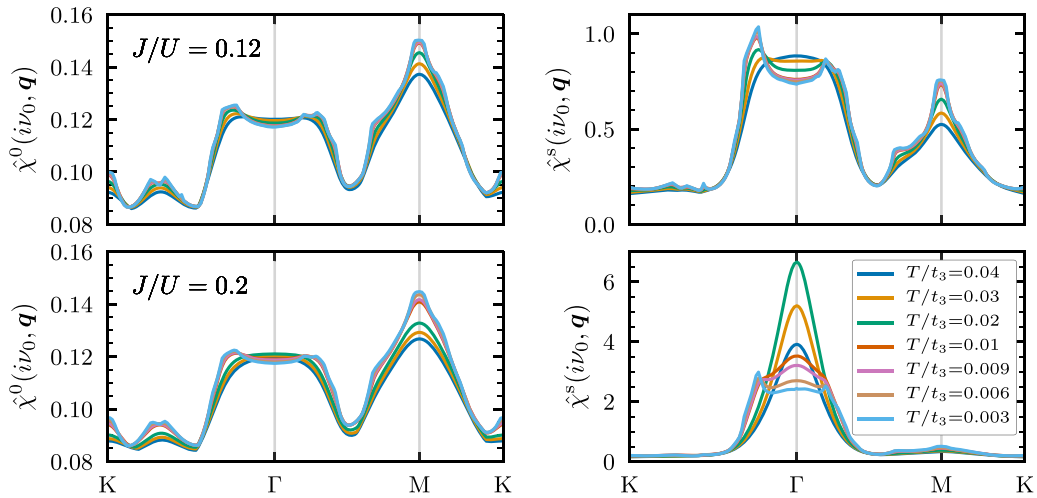


FIG. 6. Evolution of the largest eigenvalues of static ( $i\nu_0 = 0$ ) irreducible susceptibility  $\hat{\chi}^0$  and spin susceptibility  $\hat{\chi}^s$  for two exchange interactions  $J/U$ .

the simulated case is close of a ferromagnetic instability. Indeed, we could not converge calculations for larger Hund's couplings  $J/U \geq 0.22$  since  $J$  favors the formation of ferromagnetic order. For  $J/U = 0.2$  we find that the maximum in  $\hat{\chi}^s$  jumps at some intermediate temperature  $T \sim 0.01$  from having an absolute maximum at  $\mathbf{Q} = (0, 0)$  to an absolute maximum at finite  $\mathbf{q}$ -vectors. Hence, some long-wavelength spin waves are the favored type of fluctuation in this regime. The  $\mathbf{q}$ -vectors associated with these spin waves match well to the minor and major axes of the  $e'_g$  pockets. Since the Fermi surface becomes less thermally smeared out, the scattering between opposite edges is favored.

### C. Triplet superconductivity possible?

The ferromagnetic fluctuations investigated in the previous section seem promising to mediate triplet superconductivity in  $\text{Na}_x\text{CoO}_2 \cdot y\text{H}_2\text{O}$ . To address this question, we solve the Eliashberg equation for different pairing symmetries. Possible triplet pairings compatible with the point group of the triangular lattice are  $f_1 \equiv f_{y(x^2-3y^2)}$ ,  $f_2 \equiv f_{x(3x^2-y^2)}$ , and  $p$ -wave, for which  $p_x$  and  $p_y$  are degenerate. The  $\mathbf{k}$ -dependence of the respective order parameter is depicted in Fig. 7(a).

The temperature dependence of the corresponding superconducting eigenvalues is shown in Fig. 7(b) for three different Hund's couplings. At high temperatures, the  $p$ - and  $f_1$ -wave solutions coexist with a near degeneracy that is lifted for low  $T$ . There, the  $f_1$ -gap clearly shows up as the dominant pairing symmetry. Since it has line nodes between the  $\Gamma$  and  $M$  points, the  $f_1$ -gap fits well to the  $e'_g$  pockets of the Fermi surface in the sense that the nodes do not intersect them. Contrarily, the  $f_2$ -gap has line nodes that intersect also the  $e'_g$  pockets, which explains why the  $f_2$ -symmetric gap appears unfavorable in our calculations.

While we do find an enhancement in the  $f_1$ - (dominant) and  $p$ -wave (subdominant) superconducting eigenvalues of the linearized Eliashberg equation upon lowering the temperature, we do not find triplet superconductivity to be realized on the order of experimental  $T_c$ . The eigenvalue of the leading  $f_1$ -

symmetric gap stays below 0.6 at  $T/t_3 = 10^{-3}$  corresponding to approximately 2 K. Comparing  $\lambda_{f_1}$  for different  $J/U$  indicates an increase of superconducting pairing strength since the F fluctuations are enhanced. Therefore, it might be possible that the  $f_1$ -pairing is realized for larger  $J/U$ , but we cannot access this regime since it is masked in our FLEX calculations by the magnetic instability.

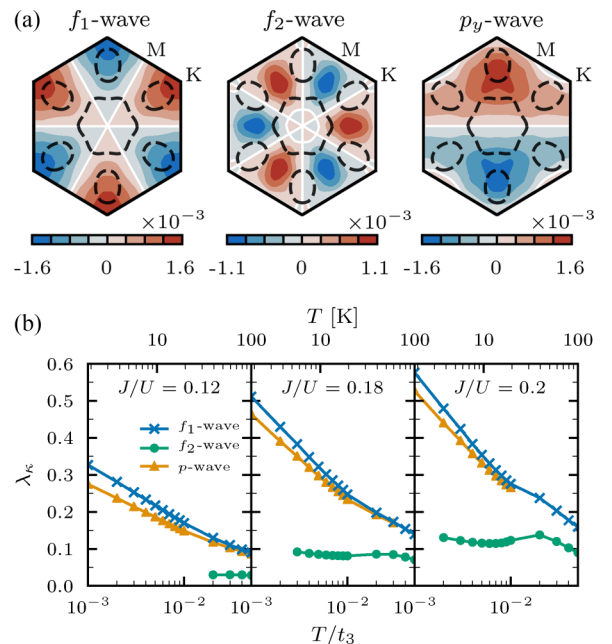


FIG. 7. (a) Possible triplet-pairing symmetries of the superconducting gap. Shown is the orbital trace of the converged order parameter  $\Delta(i\omega_1, \mathbf{k})$  for  $T/t_3 = 0.003$  and  $J/U = 0.2$ . The line nodes (solid white) intersect differently with the Fermi surface (dashed black) depending on the gap symmetry. (b) Temperature dependence of the superconducting eigenvalue  $\lambda_\kappa$  for different gap symmetries  $\kappa = f_1, f_2, p$ . The panels show different exchange interactions  $J/U$ . Note that the  $T$ -axis is logarithmic.

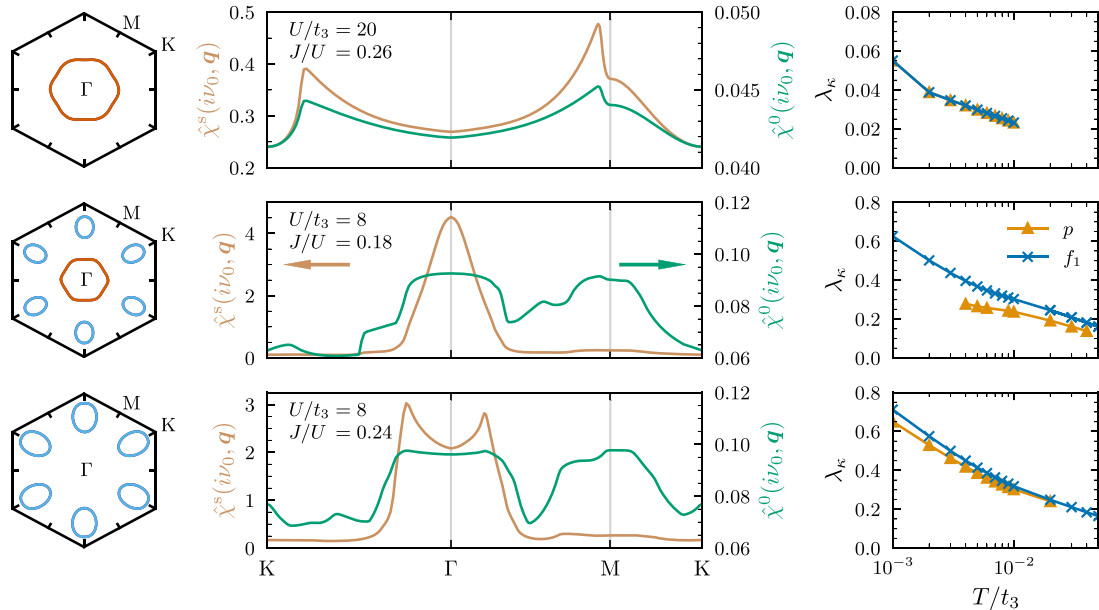


FIG. 8. Dependence of magnetic fluctuations and eigenvalues of the superconducting Eliashberg equation on Fermi surface topology. Each row shows the noninteracting Fermi surface, maximal eigenvalue of irreducible and spin susceptibility, and superconducting eigenvalue at  $T/t_3 = 0.003$  for the maximally convergible interaction parameters. The top row corresponds to a Fermi surface composed of the  $a_{1g}$  pocket only ( $\Delta_{CF} = -1.2$ ), the middle row to both pocket types being present ( $\Delta_{CF} = 0.4$ ), and the bottom row to only the  $e'_g$  pockets existing ( $\Delta_{CF} = 9.0$ ).

#### D. Influence of the Fermi surface

The Fermi surface topology naturally affects the magnetic and superconducting fluctuations, whereas the exact shape of the Fermi surface for  $\text{Na}_x\text{CoO}_2 \cdot y\text{H}_2\text{O}$  is an open question, as explained in Sec. IV A. Therefore, it is insightful to investigate how the magnetism and superconductivity depend on Fermi surface topology. We compare the situation with  $a_{1g}$  and  $e'_g$  pockets present [Fig. 4(e)] considered so far to the cases in which either the  $a_{1g}$  or  $e'_g$  pockets are absent (Fig. 8). The Fermi surface with suppressed  $e'_g$  pockets corresponds to the results observed in ARPES measurements [65–69]. The latter case, on the other hand, avoids any nodes of the  $f_1$ -symmetric gap on the Fermi surface, which leads to the realization of  $f$ -wave superconductivity in the single-band case [13].

We control the Fermi surface shape in our model via the filling  $n$  and crystal field splitting  $\Delta_{CF}$ . In the following calculations, we set the filling to  $n = 5.6$ . If we consider the Fermi surface with only the  $e'_g$  pockets being present, then their effective hole doping of 0.4 is equal to the hole doping of the  $e'_g$  pockets in our previous calculation for  $n = 5.355$  and  $\Delta_{CF} = 0.4$ . By this, we can directly estimate the influence of neglecting the  $a_{1g}$  pocket. Furthermore,  $n = 5.6$  corresponds to the  $t_{2g}$  filling reported for measurements of superconductivity when considering the additional  $\text{H}_3\text{O}^+$  doping [24]. We choose the crystal field splitting as  $\Delta_{CF} = -1.2, 0.4, 9.0$  to create the three different Fermi surface topologies as shown in the left column of Fig. 8. For each, we performed calculations with different interaction parameters  $U$  and  $J$ .

In the remaining panels of Fig. 8, we present  $\hat{\chi}^0$  and  $\hat{\chi}^s$  at  $T/t_3 = 0.003$  and the superconducting eigenvalue  $\lambda_{\kappa}$  for the maximal values of  $U$  and  $J$  for which we were able to con-

verge the FLEX loop. In the case of a single  $a_{1g}$  Fermi sheet, strong magnetic fluctuations do not emerge. If  $e'_g$  pockets exist, intrapocket scattering strongly enhances F fluctuations. This can be seen both in the case with  $a_{1g}$  and  $e'_g$  pockets being present and in the case of only  $e'_g$  pockets existing, as we can stabilize FLEX solutions with sizable F or more generally long-wavelength spin fluctuations.

Evaluating the eigenvalues of the linearized Eliashberg equation shows that any spin-fluctuation-induced superconducting pairing is strongly suppressed in the absence of the  $e'_g$  pockets. Since the AF fluctuations are dominant in this scenario, we also tried to solve the Eliashberg equation for  $d$ -wave symmetry. However, we could not find a converged solution. If the material actually exhibits an  $a_{1g}$  Fermi surface only, a different mechanism has to be considered to explain the superconductivity. In the cases with the  $e'_g$  pockets present and correspondingly stronger F fluctuations, we again find the dominant  $f_1$ -wave together with subdominant  $p$ -wave symmetric solutions of the linearized Eliashberg equation. By excluding the  $a_{1g}$  pocket from the Fermi surface, the superconducting pairing strength in the aforementioned  $f_1$ - and  $p$ -wave channels is increased, likely due to the absence of gap nodes intersecting with the Fermi surface in this case. Nonetheless, even in the absence of the  $a_{1g}$  Fermi pockets, we do not find the superconducting transition on the order of experimental  $T_c$ . As previously discussed, the transition might occur for larger values of  $U$  or  $J$ , which are, however, outside the region where we could stabilize the FLEX self-consistency loop.

#### V. CONCLUSION

We implemented the FLEX approximation using the IR basis to study magnetism and superconductivity in the Hubbard

model and  $\text{Na}_x\text{CoO}_2 \cdot y\text{H}_2\text{O}$ . Benchmark calculations on the Hubbard model showed an excellent agreement with previous FLEX calculations but at a much lower numerical cost.

This gain in numerical efficiency allowed us to turn to more realistic multiband systems and to approach so far unexplored low-temperature regimes. We studied the dependence of magnetic and superconducting fluctuations on temperature, Fermi surface topology, and interaction strength in  $\text{Na}_x\text{CoO}_2 \cdot y\text{H}_2\text{O}$ . We found the existence of  $e'_g$  pockets on the Fermi surface to be crucial in order to generate strong ferromagnetic fluctuations. Concerning superconducting pairing, we find the  $f_{y(x^2-3y^2)}$ -wave symmetry to be dominant over other triplet-pairing symmetries at low temperatures. We do not, however, find the superconducting transition on the order of the experimental  $T_c$ , but our calculations indicate that the spin-fluctuation-driven transition takes place at significantly lower temperatures. This situation might still change for larger interactions, which are, however, inaccessible within FLEX because of too strong magnetic fluctuations. Studies employing other methods could give more insight on this question. If the  $e'_g$  Fermi pockets are absent, we only find weak magnetic fluctuations, which cannot establish superconductivity. In this case, the pairing mechanism has to be of a different origin.

In summary, we have shown that the FLEX + IR approach enables the study of complex multiorbital systems at low-temperature scales not accessible with conventional Matsubara frequency grid sampling. This should bring further systems featuring possibly an interplay of spin fluctuations and superconductivity into the reach of FLEX calculations at experimentally relevant temperature scales. Since another limiting factor of Green function methods is the momentum integration in the Brillouin-zone, a combination with, e.g., adaptive  $k$ -space sampling methods [79–81] could further extend the range of possible systems. Interesting grounds to be explored range from moiré superlattice systems to realistic multiband models of infinite-layer nickelate compounds.

#### ACKNOWLEDGMENTS

N.W. thanks the University of Tokyo for hospitality during his research stay, where ideas presented in this work were conceived. N.W. and T.W. acknowledge support by the Deutsche Forschungsgemeinschaft (DFG) via RTG 2247

(QM3) (Project No. 286518848) and European Commission via the Graphene Flagship Core Project 3 (Grant Agreement ID: 881603) is supported by the Central Research Development Fund of the University of Bremen. The authors acknowledge the North-German Supercomputing Alliance (HLRN) for providing computing resources that have contributed to the research results reported in this paper.

#### APPENDIX: TIGHT-BINDING MODEL FOR $\text{Na}_x\text{CoO}_2 \cdot y\text{H}_2\text{O}$

The tight-binding model to describe the electronic structure of  $\text{Na}_x\text{CoO}_2 \cdot y\text{H}_2\text{O}$  is constructed following Ref. [14] and reads

$$H_{\text{TB}} = \sum_{\gamma, \gamma', \sigma} \left( \varepsilon_k^{\gamma\gamma'} + \frac{\Delta_{\text{CF}}}{3} (1 - \delta_{\gamma\gamma'}) \right) c_{k\gamma\sigma}^\dagger c_{k\gamma'\sigma}. \quad (\text{A1})$$

Here, the summation goes over spin  $\sigma$  and the  $d$ -orbitals  $\gamma$  of the  $t_{2g}$  manifold. The first term describes the kinetic energy, and the second term includes the crystal electric field  $\Delta_{\text{CF}}$  due to the trigonal distortion of the  $\text{CoO}_6$  octahedra [cf. Fig. 4(c)]. The band dispersion is given by

$$\begin{aligned} \varepsilon_k^{\gamma\gamma} &= 2t_1 \cos k_\alpha^{\gamma\gamma} + 2t_2 [\cos k_\beta^{\gamma\gamma} + \cos (k_\alpha^{\gamma\gamma} + k_\beta^{\gamma\gamma})] \\ &\quad + 2t_4 [\cos (2k_\alpha^{\gamma\gamma} + k_\beta^{\gamma\gamma}) + \cos (k_\alpha^{\gamma\gamma} - k_\beta^{\gamma\gamma})] \\ &\quad + 2t_5 \cos (2k_\alpha^{\gamma\gamma}), \\ \varepsilon_k^{\gamma\gamma'} &= 2t_3 \cos k_\beta^{\gamma\gamma'} + 2t_6 \cos k_\beta^{\gamma\gamma'} + 2t_7 \cos (k_\alpha^{\gamma\gamma'} + 2k_\beta^{\gamma\gamma'}) \\ &\quad + 2t_8 \cos (k_\alpha^{\gamma\gamma'} - k_\beta^{\gamma\gamma'}) + 2t_9 \cos (2k_\alpha^{\gamma\gamma'} + k_\beta^{\gamma\gamma'}), \end{aligned}$$

where  $k_\alpha^{xy,xy} = k_\alpha^{xy,zx} = \mathbf{k}_1$ ,  $k_\beta^{xy,xy} = k_\beta^{xy,zx} = \mathbf{k}_2$ ,  $k_\alpha^{yz,yz} = k_\alpha^{yz,yz} = \mathbf{k}_2$ ,  $k_\beta^{yz,yz} = k_\beta^{xy,yz} = -(\mathbf{k}_1 + \mathbf{k}_2)$ ,  $k_\alpha^{zx,zx} = k_\alpha^{yz,zx} = -(\mathbf{k}_1 + \mathbf{k}_2)$ , and  $k_\beta^{zx,zx} = k_\beta^{yz,zx} = \mathbf{k}_1$ , with  $\mathbf{k}_1$  and  $\mathbf{k}_2$  being the reciprocal-lattice vectors defined by the triangular lattice in Fig. 4(a).

We employ the hopping parameters  $t_1 = 0.45$ ,  $t_2 = 0.05$ ,  $t_3 = 1$ ,  $t_4 = 0.2$ ,  $t_5 = -0.15$ ,  $t_6 = -0.05$ ,  $t_7 = 0.12$ ,  $t_8 = 0.12$ , and  $t_9 = -0.45$ , where  $t_3$  is the unit of energy. Setting  $\Delta_{\text{CF}} = 0.4$  and  $t_3 \equiv 0.18$  eV reproduces LDA band-structure calculations [64] well, particularly around the Fermi level. The value of  $\Delta_{\text{CF}}$  significantly influences the Fermi surface topology.

- 
- [1] F. Steglich, J. Aarts, C. D. Bredl, W. Lieke, D. Meschede, W. Franz, and H. Schäfer, Superconductivity in the Presence of Strong Pauli Paramagnetism:  $\text{CeCu}_2\text{Si}_2$ , *Phys. Rev. Lett.* **43**, 1892 (1979).
- [2] B. D. White, J. D. Thompson, and M. B. Maple, Unconventional superconductivity in heavy-fermion compounds, *Physica C* **514**, 246 (2015).
- [3] J. G. Bednorz and K. A. Müller, Possible high  $T_c$  superconductivity in the Ba-La-Cu-O system, *Z. Phys. B* **64**, 189 (1986).
- [4] B. Keimer, S. A. Kivelson, M. R. Norman, S. Uchida, and J. Zaanen, From quantum matter to high-temperature superconductivity in copper oxides, *Nature (London)* **518**, 179 (2015).
- [5] Y. Kamihara, H. Hiramatsu, M. Hirano, R. Kawamura, H. Yanagi, T. Kamiya, and H. Hosono, Iron-based layered superconductor:  $\text{LaOFeP}$ , *J. Am. Chem. Soc.* **128**, 10012 (2006).
- [6] G. R. Stewart, Superconductivity in iron compounds, *Rev. Mod. Phys.* **83**, 1589 (2011).
- [7] Y. Cao, V. Fatemi, S. Fang, K. Watanabe, T. Taniguchi, E. Kaxiras, and P. Jarillo-Herrero, Unconventional superconductivity in magic-angle graphene superlattices, *Nature (London)* **556**, 43 (2018).
- [8] L. Balents, C. R. Dean, D. K. Efetov, and A. F. Young, Superconductivity and strong correlations in moiré flat bands, *Nat. Phys.* **16**, 725 (2020).

- [9] D. Li, K. Lee, B. Y. Wang, M. Osada, S. Crossley, H. R. Lee, Y. Cui, Y. Hikita, and H. Y. Hwang, Superconductivity in an infinite-layer nickelate, *Nature (London)* **572**, 624 (2019).
- [10] K. Takada, H. Sakurai, E. Takayama-Muromachi, F. Izumi, R. A. Dilanian, and T. Sasaki, Superconductivity in two-dimensional  $\text{CoO}_2$  layers, *Nature (London)* **422**, 53 (2003).
- [11] P. W. Anderson, Resonating valence bonds: A new kind of insulator?, *Mater. Res. Bull.* **8**, 153 (1973).
- [12] P. W. Anderson, The resonating valence bond state in  $\text{La}_2\text{CuO}_4$  and superconductivity, *Science* **235**, 1196 (1987).
- [13] K. Kuroki, Y. Tanaka, and R. Arita, Possible spin-triplet  $f$ -wave pairing due to disconnected Fermi surfaces in  $\text{Na}_x\text{CoO}_2 \cdot y\text{H}_2\text{O}$ , *Phys. Rev. Lett.* **93**, 077001 (2004).
- [14] M. Mochizuki, Y. Yanase, and M. Ogata, Ferromagnetic Fluctuation and Possible Triplet Superconductivity in  $\text{Na}_x\text{CoO}_2 \cdot y\text{H}_2\text{O}$ : Fluctuation-Exchange Study of the Multiorbital Hubbard Model, *Phys. Rev. Lett.* **94**, 147005 (2005).
- [15] I. I. Mazin and M. D. Johannes, A critical assessment of the superconducting pairing symmetry in  $\text{Na}_x\text{CoO}_2 \cdot y\text{H}_2\text{O}$ , *Nat. Phys.* **1**, 91 (2005).
- [16] M. Ogata, A new triangular system:  $\text{Na}_x\text{CoO}_2$ , *J. Phys.: Condens. Matter* **19**, 145282 (2007).
- [17] M. Mochizuki and M. Ogata, Deformation of electronic structures due to  $\text{CoO}_6$  distortion and phase diagrams of  $\text{Na}_x\text{CoO}_2 \cdot y\text{H}_2\text{O}$ , *J. Phys. Soc. Jpn.* **75**, 113703 (2006).
- [18] K. Kuroki, S. Onari, Y. Tanaka, R. Arita, and T. Nojima, Extended  $s$ -wave pairing originating from the  $a_{1g}$  band in  $\text{Na}_x\text{CoO}_2 \cdot y\text{H}_2\text{O}$ : Single-band U-V model with fluctuation exchange method, *Phys. Rev. B* **73**, 184503 (2006).
- [19] G. Baskaran, Electronic Model for  $\text{CoO}_2$  Layer Based Systems: Chiral Resonating Valence Bond Metal and Superconductivity, *Phys. Rev. Lett.* **91**, 097003 (2003).
- [20] M. L. Kiesel, C. Platt, W. Hanke, and R. Thomale, Model Evidence of an Anisotropic Chiral  $d + id$ -wave Pairing State for the Water-Intercalated  $\text{Na}_x\text{CoO}_2 \cdot py\text{H}_2\text{O}$  Superconductor, *Phys. Rev. Lett.* **111**, 097001 (2013).
- [21] M. D. Johannes, I. I. Mazin, D. J. Singh, and D. A. Papaconstantopoulos, Nesting, Spin Fluctuations, and Odd-Gap Superconductivity in  $\text{Na}_x\text{CoO}_2 \cdot y\text{H}_2\text{O}$ , *Phys. Rev. Lett.* **93**, 097005 (2004).
- [22] K. Yada and H. Kontani, Electron-phonon mechanism for superconductivity in  $\text{Na}_{0.35}\text{CoO}_2$ : Valence-band Suhl-Kondo effect driven by shear phonons, *J. Phys. Soc. Jpn.* **75**, 033705 (2006).
- [23] K. Yada and H. Kontani,  $s$ -wave superconductivity due to Suhl-Kondo mechanism in  $\text{Na}_x\text{CoO}_2 \cdot y\text{H}_2\text{O}$ : Effect of Coulomb interaction and trigonal distortion, *Phys. Rev. B* **77**, 184521 (2008).
- [24] H. Sakurai, Y. Ihara, and K. Takada, Superconductivity of cobalt oxide hydrate,  $\text{Na}_x(\text{H}_3\text{O})_z\text{CoO}_2 \cdot y\text{H}_2\text{O}$ , *Physica C* **514**, 378 (2015).
- [25] Y. Yanase, M. Mochizuki, and M. Ogata, Multi-orbital analysis on the superconductivity in  $\text{Na}_x\text{CoO}_2 \cdot y\text{H}_2\text{O}$ , *J. Phys. Soc. Jpn.* **74**, 430 (2005).
- [26] N. E. Bickers, D. J. Scalapino, and S. R. White, Conserving Approximations for Strongly Correlated Electron Systems: Bethe-Salpeter Equation and Dynamics for the Two-Dimensional Hubbard Model, *Phys. Rev. Lett.* **62**, 961 (1989).
- [27] N. E. Bickers and D. J. Scalapino, Conserving approximations for strongly fluctuating electron systems. I. Formalism and calculational approach, *Ann. Phys.* **193**, 206 (1989).
- [28] R. Arita, K. Kuroki, and H. Aoki,  $d$ - and  $p$ -wave superconductivity mediated by spin fluctuations in two- and three-dimensional single-band repulsive Hubbard model, *J. Phys. Soc. Jpn.* **69**, 1181 (2000).
- [29] T. Takimoto, T. Hotta, and K. Ueda, Strong-coupling theory of superconductivity in a degenerate Hubbard model, *Phys. Rev. B* **69**, 104504 (2004).
- [30] K. Yamazaki, M. Ochi, D. Ogura, K. Kuroki, H. Eisaki, S. Uchida, and H. Aoki, Superconducting mechanism for the cuprate  $\text{Ba}_2\text{CuO}_{3+\delta}$  based on a multiorbital Lieb lattice model, *Phys. Rev. Research* **2**, 033356 (2020).
- [31] H. Sakakibara, H. Usui, K. Suzuki, T. Kotani, H. Aoki, and K. Kuroki, Model Construction and a Possibility of Cupratelike Pairing in a New  $d_g$  Nickelate Superconductor ( $\text{Nd,SrNiO}_2$ ), *Phys. Rev. Lett.* **125**, 077003 (2020).
- [32] K. Björnson, A. Kreisel, A. T. Rømer, and B. M. Andersen, Orbital-dependent self-energy effects and consequences for the superconducting gap structure in multiorbital correlated electron systems, *Phys. Rev. B* **103**, 024508 (2021).
- [33] H. Shinaoka, J. Otsuki, M. Ohzeki, and K. Yoshimi, Compressing Green's function using intermediate representation between imaginary-time and real-frequency domains, *Phys. Rev. B* **96**, 035147 (2017).
- [34] N. Chikano, J. Otsuki, and H. Shinaoka, Performance analysis of a physically constructed orthogonal representation of imaginary-time Green's function, *Phys. Rev. B* **98**, 035104 (2018).
- [35] N. Chikano, K. Yoshimi, J. Otsuki, and H. Shinaoka, ir-basis: Open-source database and software for intermediate-representation basis functions of imaginary-time Green's function, *Comput. Phys. Commun.* **240**, 181 (2019).
- [36] J. Otsuki, M. Ohzeki, H. Shinaoka, and K. Yoshimi, Sparse modeling in quantum many-body problems, *J. Phys. Soc. Jpn.* **89**, 012001 (2020).
- [37] J. Li, M. Wallerberger, N. Chikano, C.-N. Yeh, E. Gull, and H. Shinaoka, Sparse sampling approach to efficient ab initio calculations at finite temperature, *Phys. Rev. B* **101**, 035144 (2020).
- [38] T. Wang, T. Nomoto, Y. Nomura, H. Shinaoka, J. Otsuki, T. Koretsune, and R. Arita, Efficient ab initio Migdal-Eliashberg calculation considering the retardation effect in phonon-mediated superconductors, *Phys. Rev. B* **102**, 134503 (2020).
- [39] J. M. Luttinger and J. C. Ward, Ground-state energy of a many-fermion system. II, *Phys. Rev.* **118**, 1417 (1960).
- [40] G. Baym and L. P. Kadanoff, Conservation laws and correlation functions, *Phys. Rev.* **124**, 287 (1961).
- [41] G. Baym, Self-consistent approximations in many-body systems, *Phys. Rev.* **127**, 1391 (1962).
- [42] K. Kubo, Pairing symmetry in a two-orbital Hubbard model on a square lattice, *Phys. Rev. B* **75**, 224509 (2007).
- [43] N. Bulut, D. J. Scalapino, and R. T. Scalettar, Nodeless  $d$ -wave pairing in a two-layer Hubbard model, *Phys. Rev. B* **45**, 5577 (1992).
- [44] C.-H. Pao and N. E. Bickers, Renormalization-group acceleration of self-consistent field solutions: Two-dimensional Hubbard model, *Phys. Rev. B* **49**, 1586 (1994).

- [45] L. Takeuchi, Y. Yamakawa, and H. Kontani, Self-energy driven resonancelike inelastic neutron spectrum in the  $s + +-$  wave state in Fe-based superconductors, *Phys. Rev. B* **98**, 165143 (2018).
- [46] F. Schrodli, A. Aperis, and P. M. Oppeneer, Increased performance of Matsubara space calculations: A case study within Eliashberg theory, *Phys. Rev. B* **99**, 184508 (2019).
- [47] L. Boehnke, H. Hafermann, M. Ferrero, F. Lechermann, and O. Parcollet, Orthogonal polynomial representation of imaginary-time Green's functions, *Phys. Rev. B* **84**, 075145 (2011).
- [48] X. Dong, D. Zgid, E. Gull, and H. U. R. Strand, Legendre-spectral Dyson equation solver with super-exponential convergence, *J. Chem. Phys.* **152**, 134107 (2020).
- [49] E. Gull, S. Isakov, I. Krivenko, A. A. Rusakov, and D. Zgid, Chebyshev polynomial representation of imaginary-time response functions, *Phys. Rev. B* **98**, 075127 (2018).
- [50] M. Kaltak and G. Kresse, Minimax isometry method: A compressive sensing approach for Matsubara summation in many-body perturbation theory, *Phys. Rev. B* **101**, 205145 (2020).
- [51] The additional factor  $\omega$  in the bosonic case prevents divergence for  $\omega \rightarrow 0$ . The spectral function needs to be redefined as well; see Ref. [33].
- [52] For a technical comparison of the IR basis based sparse sampling approach and other methods, see Table I of Ref. [48].
- [53] J. LeBlanc, A. E. Antipov, F. Becca, I. W. Bulik, G. K.-L. Chan, C.-M. Chung, Y. Deng, M. Ferrero, T. M. Henderson, C. A. Jiménez-Hoyos, E. Kozik, X.-W. Liu, A. J. Millis, N. Prokof'ev, M. Qin, G. E. Scuseria, H. Shi, B. Svistunov, L. F. Tocchio, I. Tupitsyn *et al.*, Solutions of the Two-Dimensional Hubbard Model: Benchmarks and Results from a Wide Range of Numerical Algorithms, *Phys. Rev. X* **5**, 041041 (2015).
- [54] T. Schäfer, N. Wentzell, F. imkovic, Y.-Y. He, C. Hille, M. Klett, C. J. Eckhardt, B. Arzhang, V. Harkov, F.-M. L. Régent, A. Kirsch, Y. Wang, A. J. Kim, E. Kozik, E. A. Stepanov, A. Kauch, S. Andergassen, P. Hansmann, D. Rohe, Y. M. Vil'k, J. P. LeBlanc, S. Zhang, A.-M. Tremblay, M. Ferrero, O. Parcollet, and A. Georges, Tracking the Footprints of Spin Fluctuations: A MultiMethod, MultiMessenger Study of the Two-Dimensional Hubbard Model, *Phys. Rev. X* **11**, 011058 (2021).
- [55] M. Kitatani, N. Tsuji, and H. Aoki, FLEX+DMFT approach to the  $d$ -wave superconducting phase diagram of the two-dimensional Hubbard model, *Phys. Rev. B* **92**, 085104 (2015).
- [56] Y. Yanase, T. Jujo, T. Nomura, H. Ikeda, T. Hotta, and K. Yamada, Theory of superconductivity in strongly correlated electron systems, *Phys. Rep.* **387**, 1 (2003).
- [57] N. D. Mermin and H. Wagner, Absence of Ferromagnetism or Antiferromagnetism in One- or Two-Dimensional Isotropic Heisenberg Models, *Phys. Rev. Lett.* **17**, 1307 (1966).
- [58] P. C. Hohenberg, Existence of long-range order in one and two dimensions, *Phys. Rev.* **158**, 383 (1967).
- [59] B. Kyung, J.-S. Landry, and A.-M. S. Tremblay, Antiferromagnetic fluctuations and  $d$ -wave superconductivity in electron-doped high-temperature superconductors, *Phys. Rev. B* **68**, 174502 (2003).
- [60] E. Gull, O. Parcollet, and A. J. Millis, Superconductivity and the Pseudogap in the Two-Dimensional Hubbard Model, *Phys. Rev. Lett.* **110**, 216405 (2013).
- [61] P. Staar, T. Maier, and T. C. Schulthess, Two-particle correlations in a dynamic cluster approximation with continuous momentum dependence: Superconductivity in the two-dimensional Hubbard model, *Phys. Rev. B* **89**, 195133 (2014).
- [62] M. L. Foo, Y. Wang, S. Watauchi, H. W. Zandbergen, T. He, R. J. Cava, and N. P. Ong, Charge Ordering, Commensurability, and Metallicity in the Phase Diagram of the Layered  $\text{Na}_x\text{CoO}_2$ , *Phys. Rev. Lett.* **92**, 247001 (2004).
- [63] A. Wilhelm, F. Lechermann, H. Hafermann, M. I. Katsnelson, and A. I. Lichtenstein, From Hubbard bands to spin-polaron excitations in the doped Mott material  $\text{Na}_x\text{CoO}_2$ , *Phys. Rev. B* **91**, 155114 (2015).
- [64] D. J. Singh, Electronic structure of  $\text{NaCo}_2\text{O}_4$ , *Phys. Rev. B* **61**, 13397 (2000).
- [65] M. Z. Hasan, Y.-D. Chuang, D. Qian, Y. W. Li, Y. Kong, A. P. Kuprin, A. V. Fedorov, R. Kimmerling, E. Rotenberg, K. Rossnagel, Z. Hussain, H. Koh, N. S. Rogado, M. L. Foo, and R. J. Cava, Fermi Surface and Quasiparticle Dynamics of  $\text{Na}_{0.7}\text{CoO}_2$  Investigated by Angle-Resolved Photoemission Spectroscopy, *Phys. Rev. Lett.* **92**, 246402 (2004).
- [66] H.-B. Yang, S.-C. Wang, A. K. P. Sekharan, H. Matsui, S. Souma, T. Sato, T. Takahashi, T. Takeuchi, J. C. Campuzano, R. Jin, B. C. Sales, D. Mandrus, Z. Wang, and H. Ding, ARPES on  $\text{Na}_{0.6}\text{CoO}_2$ : Fermi Surface and Unusual Band Dispersion, *Phys. Rev. Lett.* **92**, 246403 (2004).
- [67] H.-B. Yang, Z.-H. Pan, A. K. P. Sekharan, T. Sato, S. Souma, T. Takahashi, R. Jin, B. C. Sales, D. Mandrus, A. V. Fedorov, Z. Wang, and H. Ding, Fermi Surface Evolution and Luttinger Theorem in  $\text{Na}_x\text{CoO}_2$ : A Systematic Photoemission Study, *Phys. Rev. Lett.* **95**, 146401 (2005).
- [68] T. Shimojima, K. Ishizaka, S. Tsuda, T. Kiss, T. Yokoya, A. Chainani, S. Shin, P. Badica, K. Yamada, and K. Togano, Angle-Resolved Photoemission Study of the Cobalt Oxide Superconductor  $\text{Na}_x\text{CoO}_2$ : Observation of the Fermi Surface, *Phys. Rev. Lett.* **97**, 267003 (2006).
- [69] J. Geck, S. V. Borisenko, H. Berger, H. Eschrig, J. Fink, M. Knupfer, K. Koepernik, A. Koitzsch, A. A. Kordyuk, V. B. Zabolotnyy, and B. Büchner, Anomalous Quasiparticle Renormalization in  $\text{Na}_{0.73}\text{CoO}_2$ : Role of Interorbital Interactions and Magnetic Correlations, *Phys. Rev. Lett.* **99**, 046403 (2007).
- [70] D. Pillay, M. Johannes, and I. Mazin, Electronic Structure of the  $\text{Na}_x\text{CoO}_2$  Surface, *Phys. Rev. Lett.* **101**, 246808 (2008).
- [71] M. Kubota, K. Takada, T. Sasaki, H. Kumigashira, J. Okabayashi, M. Oshima, M. Suzuki, N. Kawamura, M. Takagaki, K. Fukuda, and K. Ono, Photoemission and x-ray absorption study of the two-dimensional triangular lattice superconductor  $\text{Na}_{0.35}\text{CoO}_2 \cdot 1.3\text{H}_2\text{O}$ , *Phys. Rev. B* **70**, 012508 (2004).
- [72] N. Oeschler, R. A. Fisher, N. E. Phillips, J. E. Gordon, M.-L. Foo, and R. J. Cava, Specific heat of  $\text{Na}_{0.3}\text{CoO}_2 \cdot 1.3\text{H}_2\text{O}$ : Two energy gaps, nonmagnetic pair breaking, strong fluctuations in the superconducting state, and effects of sample age, *Phys. Rev. B* **78**, 054528 (2008).
- [73] L. Boehnke and F. Lechermann, Getting back to  $\text{Na}_x\text{CoO}_2$ : Spectral and thermoelectric properties, *Phys. Status Solidi A* **211**, 1267 (2014).
- [74] H. Ishida, M. D. Johannes, and A. Liebsch, Effect of Dynamical Coulomb Correlations on the Fermi Surface of  $\text{Na}_{0.3}\text{CoO}_2$ , *Phys. Rev. Lett.* **94**, 196401 (2005).

- [75] K. Yada and H. Kontani, Origin of weak pseudogap behaviors in  $\text{Na}_{0.35}\text{CoO}_2$ : Absence of small hole pockets, *J. Phys. Soc. Jpn.* **74**, 2161 (2005).
- [76] R. Sknepnek, G. Samolyuk, Y. bin Lee, and J. Schmalian, Anisotropy of the pairing gap of FeAs-based superconductors induced by spin fluctuations, *Phys. Rev. B* **79**, 054511 (2009).
- [77] Y. Yanagi and O. Ōno, Effects of ferromagnetic fluctuations on the electric and thermal transport properties in  $\text{Na}_x\text{CoO}_2$ , *J. Phys.: Conf. Ser.* **200**, 012235 (2010).
- [78] B. Horváth, B. Lazarovits, and G. Zaránd, Fluctuation-exchange approximation theory of the nonequilibrium singlet-triplet transition, *Phys. Rev. B* **84**, 205117 (2011).
- [79] A. Eiguren and I. G. Gurtubay, Helmholtz Fermi surface harmonics: An efficient approach for treating anisotropic problems involving Fermi surface integrals, *New J. Phys.* **16**, 063014 (2014).
- [80] J. Lafuente-Bartolome, I. G. Gurtubay, and A. Eiguren, Symmetric Helmholtz Fermi-surface harmonics for an optimal representation of anisotropic quantities on the Fermi surface: Application to the electron-phonon problem, *Phys. Rev. B* **102**, 165113 (2020).
- [81] K. Zantout, S. Backes, and R. Valentí, Effect of Nonlocal Correlations on the Electronic Structure of LiFeAs, *Phys. Rev. Lett.* **123**, 256401 (2019).



## 4.2 Nickelate materials

Layered nickel oxides have long been considered potential analogues to cuprates, given the proximity of nickel and copper in the periodic table [598–600]. For instance, infinite-layer compounds  $\text{CaCuO}_2$  and  $\text{NdNiO}_2$  are isostructural and isoelectronic, inviting a comparison of their similarities and differences [144, 601, 602]. In 2019, Li et al. [49] successfully synthesized superconducting thin films of hole-doped infinite-layer nickelates  $\text{Nd}_{0.8}\text{Sr}_{0.2}\text{NiO}_2$ , achieving a critical temperature of 9–15 K. Subsequent defect-free samples showed that  $T_c$  can be enhanced up to 20 K [55] (cf. Figure 4.2). Since then, the family of infinite-layer nickelates, denoted as  $R\text{NiO}_2$  ( $R$  = trivalent rare-earth element), has expanded to include La- and Pr-based variants hole-doped with Sr or Ca [50–52, 54].

Recent efforts have identified two promising strategies to enhance superconductivity in nickelates. One approach involves utilizing pressure as an additional tuning parameter alongside doping. Experimental work demonstrated an increase of  $T_c$  to 31 K at 12 GPa in Pr-based nickelates [54]. Building on these results, DFT calculations suggest that high-temperature superconductivity might be achievable in  $\text{PrNiO}_2$  without doping at even higher pressures [603]. In addition, research efforts are focused on finding other nickel oxide multilayer structures. Recently, superconductivity has been observed in Ruddlesden-Popper phase nickelates  $R_{n+1}\text{Ni}_n\text{O}_{3n+1}$  for  $n = 2, 3, 5$  [53, 56, 57].<sup>3</sup> While the pentalayer compound  $\text{Nd}_6\text{Ni}_5\text{O}_{12}$  becomes superconducting at ambient pressure, the bilayer  $\text{La}_3\text{Ni}_2\text{O}_7$  and trilayer  $\text{La}_4\text{Ni}_3\text{O}_9$  require finite pressure.

In the following, we briefly review the electronic structure and emergence of superconductivity in infinite-layer nickelates, contrasting these with the bilayer case discussed in section 4.2.1 and publication III. We do not address the normal/non-superconducting phases of infinite-layer nickelates here, which feature elements such as strange metal behavior and charge ordering. These phases, like the superconducting phase, are still subjects of active experimental investigation [146]. This overview is based on the reviews in Refs. [144, 146] in which further details and references can be found.

Infinite-layer cuprates and nickelates share similarities in their crystal and electronic structure, yet also decisive differences exist. Most importantly, the band structure of nickelates features not only a cuprate-like Ni  $3d_{x^2-y^2}$  band at the Fermi level, but also additional electron pockets appear at the  $\Gamma$  and A points. These pockets arise from the rare-earth  $5d_{z^2}$  orbital (which hybridizes with Ni  $3d_{z^2}$ ) and  $5d_{xy}$  (or alternatively an interstitial  $s$  orbital [604]). These pockets cause a self-doping effect on the Ni  $d_{x^2-y^2}$  band by approximately 10%. Moreover, the charge-transfer energy  $\Delta_{dp}$  is larger in infinite-layer nickelates than in cuprates, and the oxygen

<sup>3</sup>The structure of Ruddlesden-Poppers nickelates  $R_{n+1}\text{Ni}_n\text{O}_{3n+1}$  consists of a repeated sequence of  $n$  layers of  $\text{LaNiO}_3$  followed by a  $\text{LaO}$  layer, stacked along the  $c$ -axis.

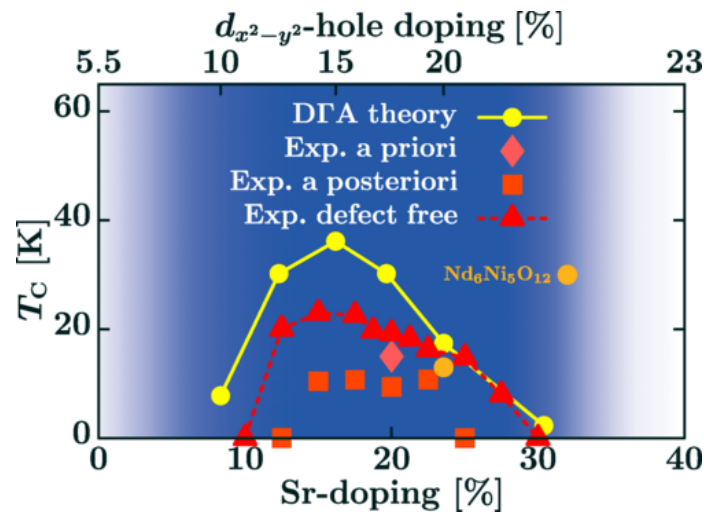


**Figure 4.2 – Superconducting phase diagram of  $\text{Sr}_x\text{Nd}_{1-x}\text{NiO}_2$ .** Critical temperature  $T_c$  vs. Sr-doping  $x$  and effective doping of the single-orbital  $d_{x^2-y^2}$  model. The  $d$ -wave phase diagram from DΓA calculations [260] is compared to experimental data collected at different time points relative to the calculations [49, 55, 605] (see Ref. [606]). The pentalayer  $\text{Nd}_6\text{Ni}_5\text{O}_{12}$  [53] with 20% doping of the  $d_{x^2-y^2}$  orbital also fits into this description. The blue background indicates the doping area for which the single-band description is assumed to be valid. Reprinted with permission from [606]. Copyright © 2024 the American Physical Society. Not covered by the CC BY 4.0 license.

$p$ -orbitals are situated considerably lower in energy concomitant to a weaker Ni-O hybridization than the respective Cu-O.

Theoretical studies have largely discounted conventional phonon-mediated mechanisms for nickelate superconductivity [604, 607, 608]. Instead, infinite-layer superconductors are considered unconventional superconductors, calling for alternative pairing mechanisms. It is an ongoing debate whether superconductivity in infinite-layer nickelates can be described by a single-orbital [260, 602, 606] or multi-orbital [109, 609–612] picture. For a more detailed discussion of various multi-orbital scenarios, we refer the reader to Ref. [144]. Here, we want to briefly summarize the single-band approach suggested in Ref. [260] (see also Refs. [602, 606]) due to its success in describing the experimental phase diagram. This approach adopts the standpoint that correlations in the Ni  $d_{x^2-y^2}$  band are most important, while the  $\Gamma$  and A pockets on the Fermi surface only act as effective charge reservoirs. Figure 4.2 shows the superconducting phase diagram of  $d$ -wave pairing obtained from a spin-fluctuation mechanism calculated using DΓA.<sup>4</sup> The results closely match the experimentally measured superconducting dome [49, 55, 605].

<sup>4</sup>Optimizing this single-band model points to palladium-based compounds as promising candidates for enhanced superconducting properties [613].

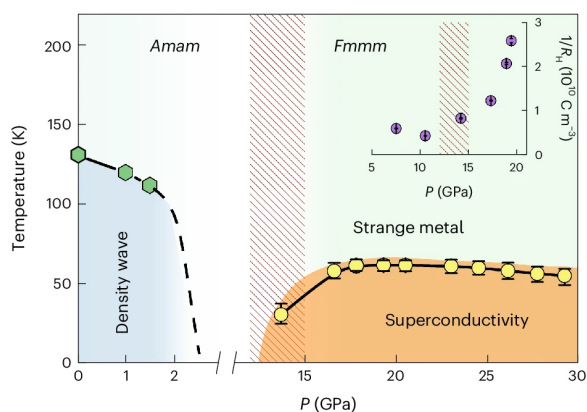


**Figure 4.3 – Phase diagram of bilayer nickelate.** Temperature-pressure phase diagram of  $\text{La}_3\text{Ni}_2\text{O}_{7-\delta}$ . At low pressure, a density wave emerges, which is suppressed as pressure increases. A structural phase transition occurs around 10 GPa, leading to the onset of the superconducting state. The inset displays the inverse Hall coefficient at 80 K. Reprinted from [614] with permission from © 2024 Springer Nature. Not covered by the CC BY 4.0 license.

### 4.2.1 Bilayer nickelate – $\text{La}_3\text{Ni}_2\text{O}_7$

Recently, high-temperature superconductivity was discovered in the Ruddlesden-Poppers perovskite bilayer  $\text{La}_3\text{Ni}_2\text{O}_7$  under high pressure, achieving a  $T_c$  around 80 K [56] above 14 GPa. The current view of the phase diagram is drawn in Figure 4.3 [146, 614]. By applying pressure, the system undergoes a phase transition from a *Amam* to a more symmetric *Fmmm* phase, which involves the reorientation of apical oxygen octahedra from a tilted arrangement to a rectified, linear alignment with  $180^\circ$  angles between them. Other experimental studies report that, instead of the *Fmmm* structure, an even higher *I4/mmmm* symmetry is adopted in the superconducting phase at low temperatures [615, 616]. Superconductivity emerges alongside the structural phase transition and exhibits a weak decreasing trend in  $T_c$  as pressure is further increased. The structural transition is accompanied by a rapid change in the Hall carrier coefficient [617], possibly indicating a reconstruction of the low-energy electronic structure and Fermi surface.

At ambient pressure, a density-wave-like phase emerges, the nature of which is poorly understood. There are speculations about whether it constitutes a spin or charge density wave, or perhaps a coexistence of both [618, 619]. A spin density wave has been detected around 150 K using  $\mu\text{SR}$  [619, 620], NMR [621], and resonant inelastic X-ray scattering (RIXS) [622]. However, its connection to the density wave state is still unclear. This represents just one of many questions in the early-stage research on bilayer nickelates. Other unresolved issues include the aforementioned nature of the low-temperature and high-pressure structure (*Fmmm* vs. *I4/mmmm*) [615, 616], the origin of the strange metal phase [617] observed at temperatures above the superconducting phase (similar to many other correlated superconductors [36]), and the filamentary nature of superconductivity [56, 616, 623]. Furthermore, the precise structural composition remains unclear, with superconductivity being found in two polymorphs of repeating two-layer nickel oxides (“2222”) [56, 624–626] and alternating monolayer-trilayer (“1313”) stackings [624, 625, 627, 628]. In particular, a

recent study was able to stabilize the 2222 structure by substitution of La with Pr in  $\text{La}_2\text{PrNi}_2\text{O}_7$  [626]. For a timely review on bilayer nickelates, see Ref. [629].

We here concentrate on the electronic structure and superconductivity in bilayer nickelates of the 2222 structure. As further detailed in publication III, the low-energy electronic structure consists of strongly hybridizing Ni  $d_{z^2}$  and  $d_{x^2-y^2}$  orbitals from both layers. Currently, it is unclear whether superconductivity is dominantly driven by the  $d_{z^2}$  (weak-coupling picture) or  $d_{x^2-z^2}$  (strong coupling picture) orbitals. In the embedded publication, we demonstrate that strong inter-layer correlations induce a Lifshitz transition in the pressurized phase, thereby suppressing ferromagnetic fluctuations originating from the  $d_{z^2}$  bonding orbital and enhancing  $s_{\pm}$ -wave superconductivity driven by antiferromagnetic fluctuations. These results derive from a comparison between cellular dynamical mean-field theory (CDMFT) and DMFT calculations, with the former allowing for a direct treatment of inter-layer correlations. We use the IR basis for solving the linearized Eliashberg equation, which enables us to explore a large range of (effective) interaction parameters and pairing symmetries within a spin-fluctuation-driven pairing mechanism. This approach facilitates the construction of comprehensive superconducting phase diagrams for both DMFT and CDMFT solutions. Furthermore, we assess the influence of pressure by scaling the out-of-plane hopping, revealing that the effect of inter-layer correlations diminishes significantly at lower pressures.

### Key points summary

- Study of inter-layer correlations in the novel bilayer nickelate material  $\text{La}_3\text{Ni}_2\text{O}_7$  under pressure and its influence on superconductivity within cluster dynamical mean-field theory (CDMFT) based on a wannierized *ab initio* model.
- Comparison of *ab initio*, DMFT and CDMFT Fermi surfaces, spectral functions and self-energies shows suppression of hole-like  $\gamma$ -pockets around the  $(\pi, \pi)$ -point with inter-layer correlations increasing the effective Ni  $d_{z^2}$  bonding-antibonding splitting between layers.
- Observation of enhanced singlet  $s_{\pm}$ -wave superconductivity through inter-layer correlations as pair-breaking ferromagnetic fluctuations are quenched, which originate from the  $\gamma$ -pockets.
- Qualitative assessment of pressure by scaling of out-of-plane hopping shows strong influence on the strength of inter-layer correlations.

### Author Contributions

The DMFT and CDMFT calculations were done by S. Ryee, which I transformed to the IR basis to solve the linearized gap equation basis for determining dominant eigenvalues  $\lambda$  and symmetries of the superconducting gap  $\Delta$ . I provided the data for  $\Delta$  and  $\lambda$  in Fig. 3(a,c), which was assembled by S. Ryee. I contributed the discussion of susceptibilities, pairing interaction, and superconducting gap to the manuscript, and I gave comments on the complete text. For the supplemental material, I wrote sections SM10.C, SM11, and SM13, created Figs. S10, S11, and S14, and I provided data for Figs. S15 and S16. All authors discussed the results and interpretation. The project was conceived by S. Ryee with my input on superconductivity.

### Copyright Notice

This manuscript has been published as S. Ryee et al., *Phys. Rev. Lett.* **133**, 096002 (2024). In the following, the last submitted and accepted author version is embedded, which was uploaded as a preprint to the arXiv servers at doi:10.48550/arXiv.2310.17465.

# Quenched pair breaking by interlayer correlations as a key to superconductivity in $\text{La}_3\text{Ni}_2\text{O}_7$

Siheon Ryee,<sup>1,\*</sup> Niklas Witt,<sup>1,2</sup> and Tim O. Wehling<sup>1,2</sup>

<sup>1</sup>*Institute of Theoretical Physics, University of Hamburg, Notkestrasse 9, 22607 Hamburg, Germany*

<sup>2</sup>*The Hamburg Centre for Ultrafast Imaging, Luruper Chaussee 149, 22761 Hamburg, Germany*

(Dated: August 11, 2024)

The recent discovery of superconductivity in  $\text{La}_3\text{Ni}_2\text{O}_7$  with  $T_c \simeq 80$  K under high pressure opens up a new route to high- $T_c$  superconductivity. This material realizes a bilayer square lattice model featuring a strong interlayer hybridization unlike many unconventional superconductors. A key question in this regard concerns how electronic correlations driven by the interlayer hybridization affect the low-energy electronic structure and the concomitant superconductivity. Here, we demonstrate using a cluster dynamical mean-field theory that the interlayer electronic correlations (IECs) induce a Lifshitz transition resulting in a change of Fermi surface topology. By solving an appropriate gap equation, we further show that the leading pairing instability,  $s\pm$ -wave, is enhanced by the IECs. The underlying mechanism is the quenching of a strong ferromagnetic channel, resulting from the Lifshitz transition driven by the IECs. Based on this picture, we provide a possible reason of why superconductivity emerges only under high pressure.

The recent discovery of superconductivity in bilayer nickelate  $\text{La}_3\text{Ni}_2\text{O}_7$  under high pressure [Fig. 1(a)] heralds a new class of high- $T_c$  superconductors [1]. Without doping, this material exhibits superconductivity under pressure exceeding 14 GPa with maximal critical temperature of  $T_c \simeq 80$  K [1–5]. Notable feature in  $\text{La}_3\text{Ni}_2\text{O}_7$  is a multiorbital nature of low-lying states already at the level of density functional theory (DFT) [1, 6–20] [Fig. 1(b)]. Namely, three electrons per unit cell are distributed over Ni- $e_g$  orbitals in the top and bottom square-planar lattices, whereas Ni- $t_{2g}$  orbitals are fully occupied, thereby inactive for the low-energy physics. The two layers are coupled dominantly via interlayer nearest-neighbor hopping (or hybridization) between Ni- $d_{z^2}$  orbitals ( $t_{\perp}^z \simeq -0.63$  eV) [6, 8, 13]. The hopping between Ni- $d_{x^2-y^2}$  is much smaller ( $|t_{\perp}^x| < 0.05$  eV) [6, 8]. Most importantly,  $t_{\perp}^z$  is deemed to be crucial for the noninteracting Fermi surface (FS) topology and theories of superconductivity in  $\text{La}_3\text{Ni}_2\text{O}_7$  [12, 13, 16, 18, 19, 21–29].

In this respect, an important open question concerns how interlayer electronic correlations (IECs) driven by  $t_{\perp}^{x/z}$  modify the low-energy electronic structure and how they affect superconductivity. Since  $t_{\perp}^z$  is the largest among all the hopping amplitudes [6, 8], one can identify the interlayer nearest-neighbor electronic correlations in the Ni- $d_{z^2}$  states as the leading “nonlocal” correlations.

In this paper, we employ a cluster (cellular) dynamical mean-field theory (CDMFT) [30–32] to address nonperturbatively the nonlocal as well as the local electronic correlations within the two-site clusters (dimers) of the bilayer square lattice model for  $\text{La}_3\text{Ni}_2\text{O}_7$  [Fig. 1(a)]. One of the key findings of our study is a Lifshitz transition resulting in a change of the FS topology which does not occur when only local correlations are taken into account. By solving an appropriate gap equation, we show that the IECs promote  $s\pm$ -wave pairing. The underlying mechanism is the quenching of ferromagnetic (FM) fluctuations resulting from the Lifshitz transition due to IECs. Based on this picture, we provide a possible reason of why superconductivity emerges only under high pressure.

We consider a Hamiltonian on the bilayer square lattice:

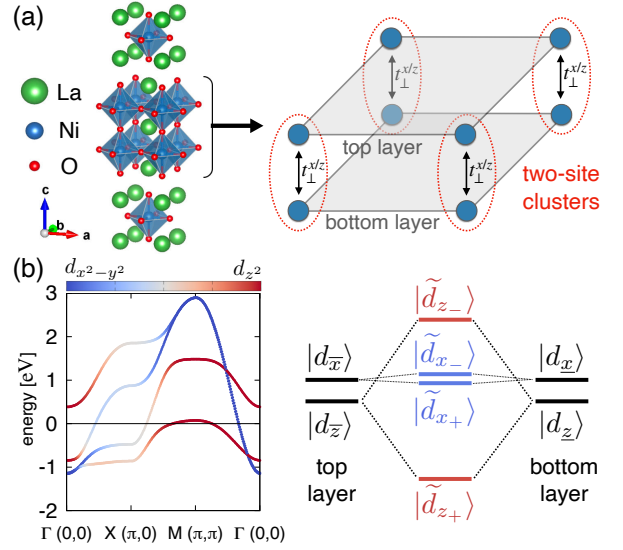


FIG. 1. (a) Left: Crystal structure of  $\text{La}_3\text{Ni}_2\text{O}_7$  under high pressure drawn using VESTA [33]. Right: The bilayer square lattice model for  $\text{La}_3\text{Ni}_2\text{O}_7$ . Dimers consisting of top and bottom layer Ni sites (blue circles) coupled via  $t_{\perp}^{x/z}$  are highlighted with red-dotted ovals. (b) Left: MLWF bands of the DFT electronic structure. The colorbar indicates the orbital character. Right: Sketch of the formation of four BA orbitals within the dimer consisting of the Ni- $e_g$  orbitals in the top and bottom layers.

$\mathcal{H} = H_0 + H_{\text{int}}$ . Here,  $H_0$  is a tight-binding term for the Ni- $e_g$  subspace describing the band structure for which we use the maximally localized Wannier function (MLWF) description for the DFT result of  $\text{La}_3\text{Ni}_2\text{O}_7$  under high pressure (29.5 GPa) [8] [Fig. 1(b)].  $H_{\text{int}}$  is the local interaction term between Ni- $e_g$  orbital electrons on the same Ni site, and is given by the standard Kanamori form consisting of  $U$  (intraorbital Coulomb interaction),  $J$  (Hund’s coupling), and  $U'$  (interorbital Coulomb interaction;  $U' = U - 2J$ ). We use  $U = 3.7$  eV,  $J = 0.6$  eV, and  $U' = 2.5$  eV by taking *ab initio* estimates for the  $e_g$  MLWF model [34]. See Supplemental Material (SM) for more information [35].

The impurity problem is solved using the hybridization-expansion continuous-time quantum Monte Carlo method [36, 37]. We investigate the system at a temperature of  $T = 1/145$  eV  $\simeq 80$  K corresponding to the maximum experimental  $T_c$  [1]. To mitigate the Monte Carlo sign problem resulting from the large interlayer hybridization in CDMFT, we solve the model in a bonding-antibonding (BA) basis defined as the + or - combinations of the top and bottom layer  $e_g$  orbitals:

$$|\tilde{d}_{i\eta\pm\sigma}\rangle = (|d_{i\bar{\eta}\sigma}\rangle \pm |d_{i\eta\sigma}\rangle)/\sqrt{2}. \quad (1)$$

Here, ket symbols indicate the corresponding Wannier states with site index  $i$  for the bilayer square lattice and spin  $\sigma \in \{\uparrow, \downarrow\}$ .  $\bar{\eta}$  and  $\eta$  represent Ni- $e_g$  orbitals ( $\eta \in \{x^2 - y^2, z^2\}$ ) in the top and bottom layers, respectively. Hereafter  $x^2 - y^2$  is denoted by  $x$  and  $z^2$  by  $z$ . Site and spin indices are omitted unless needed. In this BA basis the CDMFT self-energy becomes orbital-diagonal and momentum-independent, so our CDMFT is equivalent to “four-orbital single-site DMFT”. The interlayer hopping  $t_{\perp}^{\eta}$  between  $e_g$  orbitals  $|d_{\bar{\eta}}\rangle$  and  $|d_{\eta}\rangle$  turns into a hybridization gap of  $2|t_{\perp}^{\eta}|$  between BA orbitals  $|\tilde{d}_{\eta+}\rangle$  and  $|\tilde{d}_{\eta-}\rangle$ . Thus a small (large) splitting is realized for  $\eta = x$  ( $\eta = z$ ) [schematically shown in the right panel of Fig. 1(b)].

We first investigate how interlayer correlations affect the low-energy electronic structure by contrasting DMFT (in which all the interlayer correlations are neglected [38]) and CDMFT results for the same model. Note that, in a reasonable range around the *ab initio* interaction parameters, neither a Mott transition nor a bad metal behavior emerges within our calculations [35], which is in line with experiments [1–4].

Figure 2 presents the FSs obtained within DMFT and CDMFT. We find from DMFT that the local correlations alone do not affect the FS topology [Fig. 2(a)]. The size and the shape of three FS pockets obtained from DFT, namely  $\alpha$ ,  $\beta$ , and  $\gamma$  pockets, remain intact. This result is consistent with previous DFT+DMFT studies [7, 9, 24].

The IECs, however, significantly modify this picture [Fig. 2(b)]. While the  $\alpha$  pocket remains nearly unchanged, the  $\beta$  and the  $\gamma$  pockets are largely affected by IECs. The  $\beta$  pocket becomes more diamond-shaped with spectral weight at the first Brillouin zone (FBZ) boundary being shifted toward the  $X$  point. We also find redistribution of electron occupations in favor of half-filled  $\bar{z}$  and  $\underline{z}$  orbitals with  $\langle n_{\bar{z}} \rangle = \langle n_{\underline{z}} \rangle \simeq 0.93$  compared to the DMFT value of 0.85. Most interestingly, the  $\gamma$  pocket disappears which results in a Lifshitz transition of the FS. Looking at the orbital character of the FS [Fig. 2(c)] reveals that  $x_-$  and  $z_-$  (for the  $\beta$  pocket around  $X$  point) and  $z_+$  (for the  $\gamma$  pocket around the  $M$  point) BA orbitals underlie the FS modification.

More information can be obtained from the momentum-dependent CDMFT spectral function [Fig. 2(d)]. Near the  $X$  point, the second lowest band moves upward such that  $x_-$  and  $z_-$  states get closer to the Fermi level. The flat  $z_+$  character at the  $M$  point, on the other hand, sinks below the Fermi level,

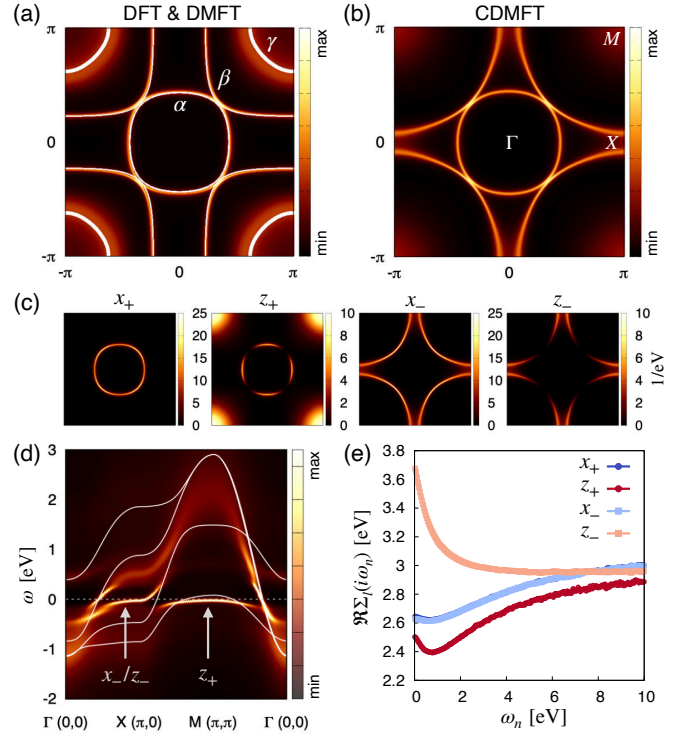


FIG. 2. (a) FSs obtained from the MLWF model of the DFT band structure (white lines) and DMFT (color map). (b) FS from CDMFT. The FSs of DMFT and CDMFT in (a) and (b) are approximated via  $-\sum_{lm} \delta_{lm} \Im G_{lm}(\mathbf{k}, i\omega_0)$  where  $l, m \in \{x_+, z_+, x_-, z_-\}$ . (c) The orbital character of the CDMFT FS. (d) The momentum-dependent spectral function obtained from CDMFT using the maximum entropy method [39, 40] (color map). The white solid lines indicate the DFT bands. The Fermi level is at  $\omega = 0$ . (e) The real part of the CDMFT self-energy on the Matsubara frequency axis.

leading to the disappearance of the  $\gamma$  pocket.

To further pinpoint the microscopic role of IECs, we investigate the CDMFT self-energy  $\Sigma_l(i\omega_n)$  where  $\omega_n = (2n + 1)\pi/T$  is the fermionic Matsubara frequency with  $n$  being integer and  $l \in \{x_+, z_+, x_-, z_-\}$ . Without IECs,  $\Sigma_{x_+/z_+}(i\omega_n) = \Sigma_{x_-/z_-}(i\omega_n)$ , so IECs are manifested by a difference of the self-energies between the BA orbitals. We first find that  $\Sigma_{x_+}(i\omega_n) \simeq \Sigma_{x_-}(i\omega_n)$  over the entire frequency range due to small  $t_{\perp}^x$  resulting in negligible IECs.

In contrast to the  $x_{\pm}$  components, large  $t_{\perp}^z$  gives rise to strong IECs in the  $z_{\pm}$  components. We investigate the real part  $\Re \Sigma_l(i\omega_n)$  which modifies the on-site energy level of the orbital  $l$ ; see Fig. 2(e). See SM for the imaginary part [35]. We note first that the Hartree-Fock self-energy,  $\Re \Sigma_l(i\omega_{\infty})$ , does not modify the FS topology because  $\Re \Sigma_{x_{\pm}}(i\omega_{\infty}) - \Re \Sigma_{z_{\pm}}(i\omega_{\infty})$  is only about 0.1 eV and  $\Re \Sigma_{x_+/z_+}(i\omega_{\infty}) = \Re \Sigma_{x_-/z_-}(i\omega_{\infty})$ .

In a low-frequency regime ( $\omega_n \ll 10$  eV), however,  $\Re \Sigma_{z_+}(i\omega_n)$  is smaller and  $\Re \Sigma_{z_-}(i\omega_n)$  is larger than the value at infinite frequency. This, in turn, shifts effectively the on-site energy levels of  $z_{\pm}$  upward ( $z_-$ ) and downward ( $z_+$ ) with respect to their DFT counterparts, thereby enhancing the hy-

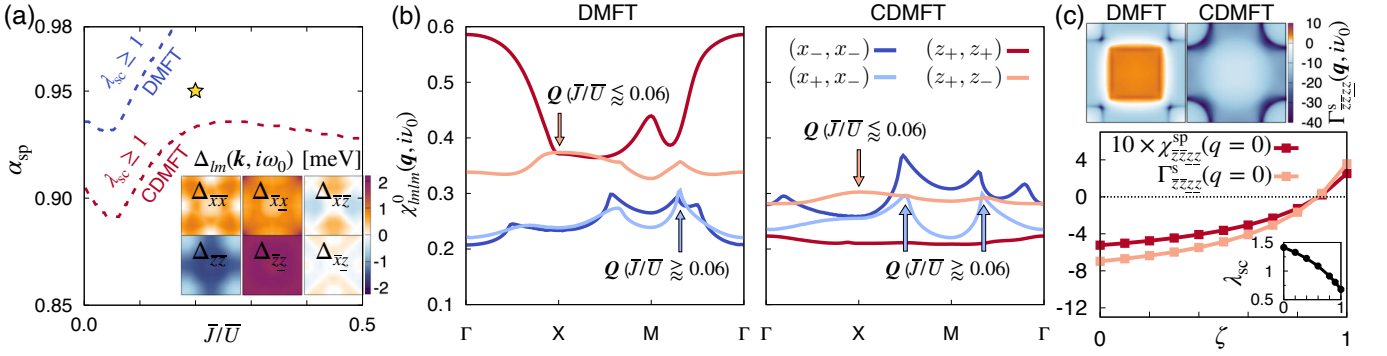


FIG. 3. (a) Superconducting phase diagram in the  $\alpha_{\text{sp}} - \bar{J}/\bar{U}$  space at  $T = 1/145$  eV  $\simeq 80$  K. The superconductivity sets in (i.e.,  $\lambda_{\text{sc}} \geq 1$ ) in the regions above the dashed lines; blue for the DMFT and red for the CDMFT. Inset: the CDMFT gap functions in the FBZ for the parameter set marked by the yellow star which corresponds to  $\alpha_{\text{sp}} = 0.95$  and  $\bar{J}/\bar{U} = 0.2$ . (b) The irreducible susceptibilities at the lowest bosonic frequency  $\chi_{lm}^0(\mathbf{q}, i\nu_0)$  calculated using DMFT (left) and CDMFT (right) Green's functions.  $\mathbf{Q}$  and the associated  $\chi^0(\mathbf{q}, i\nu_0)$  components are highlighted with colored arrows. (c) Upper panel: the spin-singlet pairing interaction  $\Gamma_{zzzz}^{\text{ss}}(\mathbf{q}, i\nu_0)$  between top and bottom layer  $z$  orbitals in the FBZ. Lower panel:  $\chi_{zzzz}^{\text{sp}}(q=0)$ ,  $\Gamma_{zzzz}^{\text{ss}}(q=0)$ , and  $\lambda_{\text{sc}}$  (inset) as a function of scaling factor  $\zeta$  for DMFT  $\chi_{z_+z_+z_+z_+}^0(q)$ .  $\alpha_{\text{sp}} = 0.95$  and  $\bar{J}/\bar{U} = 0.2$  for both panels.

bridization gap. In fact, this low-energy behavior is the origin of the shifts of spectral weight and concomitant FS change seen in Fig. 2(b). Near the  $X$  point  $z_-$  has substantial weight in the  $\beta$  pocket of the noninteracting FS. Thus the large upturn of  $\Re\Sigma_{z_-}(i\omega_n)$  as  $\omega_n \rightarrow 0$  makes an upward shift in energy near the  $X$  point, leading to the change of the  $\beta$  pocket in CDMFT; see also SM [35]. The physics here bears a close resemblance to that of  $\text{VO}_2$  in which intersite correlations within dimers promote intradimer singlets with an enhanced hybridization gap [41–43].

Having analyzed the effects of IECs on the electronic structure, we below investigate how they affect superconductivity. In light of the reported signatures of a spin density wave (SDW) in  $\text{La}_3\text{Ni}_2\text{O}_7$  at ambient pressure [44–51], it may be natural to consider spin-fluctuation-mediated pairing.

A phase transition to the superconducting state occurs when the corresponding pairing susceptibility diverges, which requires numerical evaluation of the pairing vertex  $\Gamma^{\text{s/t}}$  for singlet (s) or triplet (t) Cooper pairs [52, 53] (bold symbols will be used to denote vectors and matrices). The spin and charge susceptibilities ( $\chi^{\text{sp/ch}}$ ) and the related irreducible vertices ( $\Gamma^{\text{sp/ch}}$ ) contribute to  $\Gamma^{\text{s/t}}$ . Calculating frequency- and momentum-dependent  $\Gamma^{\text{sp/ch}}$  and  $\chi^{\text{sp/ch}}$ , however, is highly nontrivial for multiorbital systems. We thus follow an idea previously employed to study cuprates, ruthenates, and iron-based superconductors [54–57]. Namely,  $\Gamma^{\text{sp/ch}}$  are parametrized by effective intraorbital Coulomb interaction  $\bar{U}$  and Hund's coupling  $\bar{J}$ , i.e.,  $\Gamma^{\text{sp/ch}} \rightarrow \bar{\Gamma}^{\text{sp/ch}}(\bar{U}, \bar{J})$  (we assume the interorbital value  $\bar{U}' = \bar{U} - 2\bar{J}$ ). The effective vertices  $\bar{\Gamma}^{\text{sp/ch}}(\bar{U}, \bar{J})$  are independent of frequency and momentum, see SM [35]. This leads to the gap equation

$$\lambda_{\text{sc}} \Delta_{lm}(k) = -\frac{T}{2N} \sum_{q, l_1 l_2 m_1 m_2} \Gamma_{l_1 m_1 m_2}^{\text{s/t}}(q) \times G_{l_1 l_2}(k-q) G_{m_1 m_2}(q-k) \Delta_{l_2 m_2}(k-q), \quad (2)$$

where  $\lambda_{\text{sc}}$  is the eigenvalue,  $G(k)$  the (C)DMFT Green's function, and  $\Delta(k)$  the gap function.  $k \equiv (\mathbf{k}, i\omega_n)$  and  $q \equiv (\mathbf{q}, i\nu_n)$  with  $\mathbf{k}$  and  $\mathbf{q}$  being the crystal momentum and  $\nu_n = 2n\pi/T$  the bosonic Matsubara frequency.  $N$  indicates the number of  $k$ -points in the FBZ.  $\Gamma_{l_1 m_1 l_2 m_2}^{\text{s/t}}(q = k - k')$  describe the particle-particle scattering of electrons in orbitals  $(l, m)$  with four-momenta  $(k, -k)$  to  $(l_1, m_1)$  with  $(k', -k')$ . The transition to the superconducting state is indicated by the maximum eigenvalue  $\lambda_{\text{sc}}$  reaching unity. Since  $\bar{\Gamma}^{\text{sp/ch}}(\bar{U}, \bar{J})$  are more sparse in the original  $e_g$  basis than the BA basis, so are the resulting  $\chi^{\text{sp/ch}}$  and  $\Gamma^{\text{s/t}}$ . We therefore discuss  $\chi^{\text{sp/ch}}$  and  $\Gamma^{\text{s/t}}$  in the  $e_g$  picture.

We find the predominance of singlet over triplet pairings arising from antiferromagnetic (AFM) fluctuations. Figure 3(a) presents the resulting superconducting phase diagram for the leading singlet channel. Since we cannot pinpoint the precise magnitude of  $\bar{U}$  and  $\bar{J}$ , we scan a range of values. The vertical axis is given by the Stoner enhancement factor  $\alpha_{\text{sp}}$  which indicates the maximum eigenvalue of  $\bar{\Gamma}^{\text{sp}}(\bar{U}, \bar{J})\chi^0(\mathbf{q}, i\nu_0)$  and gauges the proximity to a magnetic instability. Here,  $\chi^0$  is the irreducible susceptibility,  $\chi_{lm'l'm'}^0(q) = -\frac{T}{N} \sum_k G_{l'l'}(k+q) G_{m'm}(k)$ , which is the lowest-order term of the spin susceptibility,  $\chi^{\text{sp}} = \chi^0[\mathbf{1} - \bar{\Gamma}^{\text{sp}}(\bar{U}, \bar{J})\chi^0]^{-1}$ . Thus,  $\alpha_{\text{sp}}$  is determined entirely from  $\bar{U}$  and  $\bar{J}$ , provided  $\chi^0(\mathbf{q}, i\nu_0)$  is given [35]. For both DMFT and CDMFT cases, the leading pairing symmetry in the  $e_g$ -orbital basis is always the intraorbital  $s$ -wave/interorbital  $d_{x^2-y^2}$ -wave pairing; see the inset of Fig. 3(a). Projecting to the noninteracting FS, this pairing corresponds to the  $s\pm$ -wave where the gap changes sign between the neighboring FS pockets [35]. This leading pairing symmetry is in line with many previous studies [8, 12, 13, 18, 21–23, 25]. The qualitative features of the gap functions remain unchanged over the entire parameter range while  $\mathbf{Q}$  (the crystal momentum at which the maximum eigenvalue of  $\bar{\Gamma}^{\text{sp}}(\bar{U}, \bar{J})\chi^0(\mathbf{q}, i\nu_0)$  emerges)



changes from  $\mathbf{Q} = (\pi, 0)$  for  $\bar{J}/\bar{U} \lesssim 0.06$  to an incommensurate wave vector around the  $M$  point for  $\bar{J}/\bar{U} \gtrsim 0.06$  for both DMFT and CDMFT as highlighted in Fig. 3(b); see SM for the details [35].

The most notable feature of the phase diagram presented in Fig. 3(a) is the enhanced superconducting instabilities in CDMFT compared to DMFT. This result is quite surprising because the  $\gamma$  pocket which disappears by IECs within our CDMFT calculation has been argued to drive the spin-fluctuation-mediated superconductivity throughout the literature [9, 13, 16, 18, 21]. It thus raises the question: What is the role of the  $\gamma$  pocket in the pairing?

We first find that the  $\gamma$  pocket has a ‘‘Janus-faced’’ role: It hosts both obstructive and supportive magnetic fluctuations for the singlet pairing. This can be, in fact, traced back to the behavior of  $\chi_{lm}^0(\mathbf{q}, i\nu_0)$  by investigating the  $(l, m) = (z_+, z_+)$  and  $(z_+, z_-)$  components of the DMFT calculation in Fig. 3(b). While the  $\gamma$  pocket allows for small- $\mathbf{q}$  particle-hole excitations resulting in the  $\mathbf{q} = (0, 0)$  interlayer FM  $\chi_{z_+z_+z_+z_+}^0(\mathbf{q}, i\nu_0)$ , the  $\mathbf{q} = (\pi, 0)$  nesting between the  $\gamma$  and  $\beta$  pocket gives rise to AFM  $\chi_{z_+z_-z_+z_-}^0(\mathbf{q}, i\nu_0)$ . Thus, the  $\gamma$  pocket promotes two different competing (i.e., FM vs. AFM) magnetic channels. Importantly, however, the FM  $\chi_{z_+z_+z_+z_+}^0(\mathbf{q}, i\nu_0)$  predominates in DMFT as clearly shown in the left panel of Fig. 3(b).

The disappearance of the  $\gamma$  pocket from the FS due to IECs within CDMFT results in the suppression of both channels, especially the  $\chi_{z_+z_+z_+z_+}^0$  component involving solely the  $\gamma$  pocket [Fig. 3(b)]. This change is more apparent from the sign of the pairing interaction. In the singlet channel, the FM fluctuation is directly manifested by a repulsive (rather than attractive) interaction  $\Gamma_{\bar{z}\bar{z}z z}^s(q=0)$  [upper panel of Fig. 3(c)], which hinders the singlet Cooper pairing between  $\bar{z}$  and  $z$  orbitals. Quenching of the FM  $\chi_{z_+z_+z_+z_+}^0$  as in CDMFT yields the attractive pairing interaction  $\Gamma_{\bar{z}\bar{z}z z}^s$  over the entire FBZ; see Fig. 3(c). Hence, the enhanced pairing tendency in CDMFT is mainly attributed to the suppression of this FM channel upon undergoing the Lifshitz transition.

To further corroborate this argument, we analyze how the DMFT superconducting instabilities are affected by the FM fluctuation by introducing a scaling factor  $\zeta$  for  $\chi_{z_+z_+z_+z_+}^0(q)$ . Namely,  $\chi_{z_+z_+z_+z_+}^0(q)$  is rescaled to  $\zeta\chi_{z_+z_+z_+z_+}^0(q)$  before constructing  $\chi^{\text{sp/ch}}$  and  $\Gamma^s$ . Indeed, as shown in the lower panel of Fig. 3(c), the interlayer FM spin susceptibility  $\chi_{\bar{z}\bar{z}z z}^{\text{sp}}(q=0)$  turns AFM with decreasing  $\zeta$  followed by an attractive pairing interaction  $\Gamma_{\bar{z}\bar{z}z z}^s(q=0)$  and an increase of  $\lambda_{\text{sc}}$ . See SM for additional data [35]. Note also that since the  $\gamma$  pocket is the only FS pocket dispersive along the  $k_z$  direction [19], the disappearance of the  $\gamma$  pocket by IECs makes  $\text{La}_3\text{Ni}_2\text{O}_7$  effectively two-dimensional.

We now turn to the question of ‘‘Why does superconductivity emerge only in the high-pressure phase?’’. A useful insight is obtained from a recent experiment which reports that pressure mainly shrinks the out-of-plane Ni-O bond length while the in-plane one is weakly affected [58]. Thus, the

main effect of pressure can be addressed with the change of  $t_{\perp}^z$  which is sensitive to the out-of-plane Ni-O bond length. Since  $t_{\perp}^z \simeq -0.63$  eV at 29.5 GPa under which superconductivity emerges [6, 8, 13], a smaller magnitude of  $t_{\perp}^z$  should correspond to the lower pressure case. In light of this observation, we investigate two ‘‘low pressure’’ cases, namely  $t_{\perp}^z = -0.45$  eV and  $t_{\perp}^z = -0.55$  eV, using CDMFT.

In Fig. 4(a), we find that large  $\chi_{z_+z_+z_+z_+}^0(\mathbf{q}, i\nu_0)$  emerges for the two low-pressure cases, in sharp contrast to the high-pressure result ( $t_{\perp}^z \simeq -0.63$  eV) which we have already noticed in Fig. 3. Interestingly, this result provides a plausible scenario of why  $\text{La}_3\text{Ni}_2\text{O}_7$  is not superconducting in the low-pressure phase because FM  $\chi_{z_+z_+z_+z_+}^0(\mathbf{q}, i\nu_0)$  obstructs the singlet pairing as detailed above. While the  $\gamma$  pocket gives rise to strong FM fluctuations, the actual magnetic transition occurs at a finite  $\mathbf{q}$  as shown in Fig. 4(b) which presents the maximum eigenvalue of the spin susceptibility at each  $\mathbf{q}$ ,  $\chi_{\text{max}}^{\text{sp}}(\mathbf{q}, i\nu_0)$ , for  $t_{\perp}^z = -0.45$  eV.  $\chi_{\text{max}}^{\text{sp}}(\mathbf{q}, i\nu_0)$  shows a peak at  $\mathbf{q} = \mathbf{Q}_{\text{SDW}}$  which is different from but close to the SDW wave vector  $\mathbf{Q}_{\text{SDW}}^{\text{exp}} = (0.5, 0.5)\pi$  reported by experiments [50, 51]. See SM for further discussion [35].

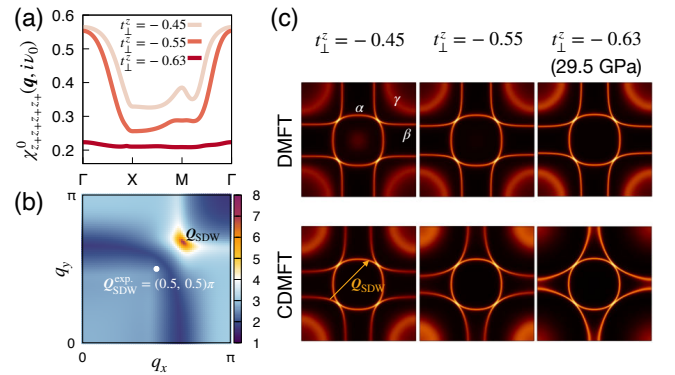


FIG. 4. (a)  $\chi_{z_+z_+z_+z_+}^0(\mathbf{q}, i\nu_0)$  calculated using CDMFT Green’s functions for three different values of  $t_{\perp}^z$  (in units of eV). (b)  $\chi_{\text{max}}^{\text{sp}}(\mathbf{q}, i\nu_0)$  at  $\alpha_{\text{sp}} = 0.95$  and  $\bar{J}/\bar{U} = 0.2$  for  $t_{\perp}^z = -0.45$  eV. (c) FSs obtained from DMFT and CDMFT for the same values of  $t_{\perp}^z$ . We used  $U = 3.7$  eV,  $J = 0.6$  eV, and  $U' = U - 2J$  for all the cases.  $\mathbf{Q}_{\text{SDW}}$  in (b) is highlighted with the orange arrow.

To trace the origin of the difference between the two low-pressure cases and the high-pressure ( $t_{\perp}^z \simeq -0.63$  eV) case, we investigate the CDMFT FSs [lower panels in Fig. 4(c)]. The strength of IECs is controlled by  $|t_{\perp}^z|$ , so the shape of the  $\beta$  and the  $\gamma$  pockets in CDMFT FS is basically the same as the DMFT FS for the smallest  $|t_{\perp}^z|$  ( $t_{\perp}^z = -0.45$  eV). As  $|t_{\perp}^z|$  increases, however, the  $\gamma$  pocket gets suppressed in CDMFT which is consistent with the evolution of  $\chi_{z_+z_+z_+z_+}^0(\mathbf{q}, i\nu_0)$  presented in Fig. 4(a); see SM for further discussion on the microscopic origin, especially on the change of the  $\beta$  pocket [35]. At  $t_{\perp}^z \simeq -0.63$  eV, the FS which we have already seen in Fig. 2(b) is realized. In contrast, the FS is almost unaffected by  $t_{\perp}^z$  in DMFT. Hence, it can be seen that the concerted effect of pressure (as modelled via  $t_{\perp}^z$ ) and IECs induces the Lifshitz transition. This transition quenches the FM channel resulting

in an enhancement of the singlet pairing mediated by AFM fluctuations.

We finally discuss implications of the above pressure-induced FS change for the available experimental data. Since the SDW is known to emerge in the ambient-pressure phase [44–51], direct comparison of our FS for small  $|t_{\perp}^z|$  with experimental FS obtained from angle-resolved photoemission spectroscopy under ambient pressure [59] may be misleading. Also, considering that there is a discrepancy as to whether or not the  $\gamma$  pocket crosses the Fermi level in  $\text{La}_4\text{Ni}_3\text{O}_{10}$  even between experiments [60, 61], the same issue may also pertain to  $\text{La}_3\text{Ni}_2\text{O}_7$ . Further study is required. Rather, a tantalizing signature of the Lifshitz transition of FS is seen in the pressure dependence of Hall coefficient ( $R_{\text{H}}$ ) [62]. While the sign of  $R_{\text{H}}$  is positive for the entire pressure range, a sudden drop of  $R_{\text{H}}$  occurs near  $\sim 10$  GPa followed by the emergence of superconductivity [62]. Since the  $\gamma$  pocket is a hole-like FS [Fig. 2(d)] and is destructive for pairing, the drop of  $R_{\text{H}}$  and the emergence of superconductivity is quite naturally explained from our Lifshitz transition scenario.

To conclude, we have demonstrated that IECs play a critical role in  $\text{La}_3\text{Ni}_2\text{O}_7$  by inducing a Lifshitz transition. The superconducting instability is found to be enhanced by this transition due to the quenching of the FM fluctuation, which may also explain why superconductivity emerges only under high pressure.

*Acknowledgments.* We are grateful to F. Lechermann and I. Eremin for useful discussion. S. R. thanks Se Young Park for helpful comment on the charge self-consistency. This work is supported by the Cluster of Excellence ‘CUI: Advanced Imaging of Matter’ of the Deutsche Forschungsgemeinschaft (DFG) - EXC 2056 - project ID 390715994, by DFG priority program SPP 2244 (WE 5342/5-1 project No. 422707584) and the DFG research unit FOR 5242 (WE 5342/7-1, project No. 449119662). Calculations were done on the supercomputer Lise at NHR@ZIB as part of the NHR infrastructure under the project hhp00056.

---

\* sryee@physnet.uni-hamburg.de

- [1] H. Sun, M. Huo, X. Hu, J. Li, Z. Liu, Y. Han, L. Tang, Z. Mao, P. Yang, B. Wang, J. Cheng, D.-X. Yao, G.-M. Zhang, and M. Wang, *Nature* **621**, 493 (2023), number: 7979 Publisher: Nature Publishing Group.
- [2] J. Hou, P.-T. Yang, Z.-Y. Liu, J.-Y. Li, P.-F. Shan, L. Ma, G. Wang, N.-N. Wang, H.-Z. Guo, J.-P. Sun, Y. Uwatoko, M. Wang, G.-M. Zhang, B.-S. Wang, and J.-G. Cheng, *Chinese Physics Letters* **40**, 117302 (2023).
- [3] Y. Zhang, D. Su, Y. Huang, H. Sun, M. Huo, Z. Shan, K. Ye, Z. Yang, R. Li, M. Smidman, M. Wang, L. Jiao, and H. Yuan, *High-temperature superconductivity with zero-resistance and strange metal behavior in  $\text{La}_3\text{Ni}_2\text{O}_7$*  (2023), arXiv:2307.14819 [cond-mat].
- [4] G. Wang, N. N. Wang, X. L. Shen, J. Hou, L. Ma, L. F. Shi, Z. A. Ren, Y. D. Gu, H. M. Ma, P. T. Yang, Z. Y. Liu, H. Z. Guo, J. P. Sun, G. M. Zhang, S. Calder, J.-Q. Yan, B. S. Wang, Y. Uwatoko, and J.-G. Cheng, *Phys. Rev. X* **14**, 011040 (2024).
- [5] M. Zhang, C. Pei, Q. Wang, Y. Zhao, C. Li, W. Cao, S. Zhu, J. Wu, and Y. Qi, *Journal of Materials Science & Technology* **185**, 147 (2024).
- [6] Z. Luo, X. Hu, M. Wang, W. Wú, and D.-X. Yao, *Physical Review Letters* **131**, 126001 (2023), publisher: American Physical Society.
- [7] D. A. Shilenko and I. V. Leonov, *Physical Review B* **108**, 125105 (2023), publisher: American Physical Society.
- [8] Y. Gu, C. Le, Z. Yang, X. Wu, and J. Hu, *Effective model and pairing tendency in bilayer Ni-based superconductor  $\text{La}_3\text{Ni}_2\text{O}_7$*  (2023), arXiv:2306.07275 [cond-mat].
- [9] F. Lechermann, J. Gondolf, S. Bötzel, and I. M. Eremin, *Phys. Rev. B* **108**, L201121 (2023).
- [10] Y. Zhang, L.-F. Lin, A. Moreo, and E. Dagotto, *Phys. Rev. B* **108**, L180510 (2023).
- [11] Y. Cao and Y.-f. Yang, *Phys. Rev. B* **109**, L081105 (2024).
- [12] Q.-G. Yang, D. Wang, and Q.-H. Wang, *Phys. Rev. B* **108**, L140505 (2023).
- [13] H. Sakakibara, N. Kitamine, M. Ochi, and K. Kuroki, *Phys. Rev. Lett.* **132**, 106002 (2024).
- [14] R. Jiang, J. Hou, Z. Fan, Z.-J. Lang, and W. Ku, *Phys. Rev. Lett.* **132**, 126503 (2024).
- [15] L. C. Rhodes and P. Wahl, *Phys. Rev. Mater.* **8**, 044801 (2024).
- [16] Y. Zhang, L.-F. Lin, A. Moreo, T. A. Maier, and E. Dagotto, *Phys. Rev. B* **108**, 165141 (2023).
- [17] B. Geisler, J. J. Hamlin, G. R. Stewart, R. G. Hennig, and P. J. Hirschfeld, *npj Quantum Materials* **9**, 38 (2024).
- [18] Y.-B. Liu, J.-W. Mei, F. Ye, W.-Q. Chen, and F. Yang, *Phys. Rev. Lett.* **131**, 236002 (2023).
- [19] H. LaBollita, V. Pardo, M. R. Norman, and A. S. Botana, *Electronic structure and magnetic properties of  $\text{La}_3\text{Ni}_2\text{O}_7$  under pressure* (2023), arXiv:2309.17279 [cond-mat].
- [20] H. Sakakibara, M. Ochi, H. Nagata, Y. Ueki, H. Sakurai, R. Matsumoto, K. Terashima, K. Hirose, H. Ohta, M. Kato, Y. Takano, and K. Kuroki, *Phys. Rev. B* **109**, 144511 (2024).
- [21] Y. Zhang, L.-F. Lin, A. Moreo, T. A. Maier, and E. Dagotto, *Nature Communications* **15**, 2470 (2024).
- [22] H. Oh and Y.-H. Zhang, *Phys. Rev. B* **108**, 174511 (2023).
- [23] Z. Liao, L. Chen, G. Duan, Y. Wang, C. Liu, R. Yu, and Q. Si, *Phys. Rev. B* **108**, 214522 (2023).
- [24] Q. Qin and Y.-f. Yang, *Phys. Rev. B* **108**, L140504 (2023).
- [25] C. Lu, Z. Pan, F. Yang, and C. Wu, *Phys. Rev. Lett.* **132**, 146002 (2024).
- [26] Y.-H. Tian, Y. Chen, J.-M. Wang, R.-Q. He, and Z.-Y. Lu, *Phys. Rev. B* **109**, 165154 (2024).
- [27] D.-C. Lu, M. Li, Z.-Y. Zeng, W. Hou, J. Wang, F. Yang, and Y.-Z. You, *Superconductivity from Doping Symmetric Mass Generation Insulators: Application to  $\text{La}_3\text{Ni}_2\text{O}_7$  under Pressure* (2023), arXiv:2308.11195 [cond-mat].
- [28] H. Lange, L. Homeier, E. Demler, U. Schollwöck, F. Grusdt, and A. Bohrdt, *Feshbach resonance in a strongly repulsive bilayer model: a possible scenario for bilayer nickelate superconductors* (2023), arXiv:2309.15843 [cond-mat].
- [29] W. Wú, Z. Luo, D.-X. Yao, and M. Wang, *Science China Physics, Mechanics & Astronomy* **67**, 117402 (2024).
- [30] A. I. Lichtenstein and M. I. Katsnelson, *Physical Review B* **62**, R9283 (2000).
- [31] G. Kotliar, S. Y. Savrasov, G. Pálsson, and G. Biroli, *Physical Review Letters* **87**, 186401 (2001), publisher: American Physical Society.
- [32] T. Maier, M. Jarrell, T. Pruschke, and M. H. Hettler, *Reviews of Modern Physics* **77**, 1027 (2005).
- [33] K. Momma and F. Izumi, *Journal of Applied Crystallography*

- 44**, 1272 (2011).
- [34] V. Christiansson, F. Petocchi, and P. Werner, *Phys. Rev. Lett.* **131**, 206501 (2023).
- [35] See Supplemental Material for additional data and discussion, which includes Refs. [1, 6–11, 13, 16–19, 21, 34, 36, 50–61, 63–83].
- [36] E. Gull, A. J. Millis, A. I. Lichtenstein, A. N. Rubtsov, M. Troyer, and P. Werner, *Rev. Mod. Phys.* **83**, 349 (2011).
- [37] C. Melnick, P. Sémon, K. Yu, N. D’Imperio, A.-M. Tremblay, and G. Kotliar, *Computer Physics Communications* **267**, 108075 (2021).
- [38] A. Georges, G. Kotliar, W. Krauth, and M. J. Rozenberg, *Rev. Mod. Phys.* **68**, 13 (1996).
- [39] M. Jarrell and J. Gubernatis, *Physics Reports* **269**, 133 (1996).
- [40] D. Bergeron and A.-M. S. Tremblay, *Phys. Rev. E* **94**, 023303 (2016).
- [41] S. Biermann, A. Poteryaev, A. I. Lichtenstein, and A. Georges, *Physical Review Letters* **94**, 026404 (2005), publisher: American Physical Society.
- [42] J. M. Tomczak, F. Aryasetiawan, and S. Biermann, *Physical Review B* **78**, 115103 (2008), publisher: American Physical Society.
- [43] W. Brito, M. Aguiar, K. Haule, and G. Kotliar, *Physical Review Letters* **117**, 056402 (2016), publisher: American Physical Society.
- [44] Z. Zhang, M. Greenblatt, and J. B. Goodenough, *Journal of Solid State Chemistry* **108**, 402 (1994).
- [45] S. Taniguchi, T. Nishikawa, Y. Yasui, Y. Kobayashi, J. Takeda, S.-i. Shamoto, and M. Sato, *Journal of the Physical Society of Japan* **64**, 1644 (1995), publisher: The Physical Society of Japan.
- [46] G. Wu, J. J. Neumeier, and M. F. Hundley, *Physical Review B* **63**, 245120 (2001), publisher: American Physical Society.
- [47] C. D. Ling, D. N. Argyriou, G. Wu, and J. J. Neumeier, *Journal of Solid State Chemistry* **152**, 517 (2000).
- [48] Z. Liu, H. Sun, M. Huo, X. Ma, Y. Ji, E. Yi, L. Li, H. Liu, J. Yu, Z. Zhang, Z. Chen, F. Liang, H. Dong, H. Guo, D. Zhong, B. Shen, S. Li, and M. Wang, *Science China Physics, Mechanics & Astronomy* **66**, 217411 (2022).
- [49] K. Chen, X. Liu, J. Jiao, M. Zou, C. Jiang, X. Li, Y. Luo, Q. Wu, N. Zhang, Y. Guo, and L. Shu, *Phys. Rev. Lett.* **132**, 256503 (2024).
- [50] Z. Dan, Y. Zhou, M. Huo, Y. Wang, L. Nie, M. Wang, T. Wu, and X. Chen, Spin-density-wave transition in double-layer nickelate  $\text{La}_3\text{Ni}_2\text{O}_7$  (2024), [arXiv:2402.03952](https://arxiv.org/abs/2402.03952) [cond-mat.supr-con].
- [51] X. Chen, J. Choi, Z. Jiang, J. Mei, K. Jiang, J. Li, S. Agrestini, M. Garcia-Fernandez, X. Huang, H. Sun, D. Shen, M. Wang, J. Hu, Y. Lu, K.-J. Zhou, and D. Feng, Electronic and magnetic excitations in  $\text{La}_3\text{Ni}_2\text{O}_7$  (2024), [arXiv:2401.12657](https://arxiv.org/abs/2401.12657) [cond-mat.supr-con].
- [52] N. E. Bickers, in *Theoretical Methods for Strongly Correlated Electrons*, CRM Series in Mathematical Physics, edited by D. Sénéchal, A.-M. Tremblay, and C. Bourbonnais (Springer, New York, NY, 2004) pp. 237–296.
- [53] G. Rohringer, H. Hafermann, A. Toschi, A. Katanin, A. Antipov, M. Katsnelson, A. Lichtenstein, A. Rubtsov, and K. Held, *Reviews of Modern Physics* **90**, 025003 (2018), publisher: American Physical Society.
- [54] T. A. Maier, M. Jarrell, and D. J. Scalapino, *Physical Review B* **75**, 134519 (2007), publisher: American Physical Society.
- [55] R. Nourafkan, G. Kotliar, and A.-M. Tremblay, *Physical Review Letters* **117**, 137001 (2016), publisher: American Physical Society.
- [56] O. Gingras, R. Nourafkan, A.-M. S. Tremblay, and M. Côté, *Physical Review Letters* **123**, 217005 (2019), publisher: American Physical Society.
- [57] S. Käser, H. U. R. Strand, N. Wentzell, A. Georges, O. Parcollet, and P. Hansmann, *Physical Review B* **105**, 155101 (2022), publisher: American Physical Society.
- [58] L. Wang, Y. Li, S. Xie, F. Liu, H. Sun, C. Huang, Y. Gao, T. Nakagawa, B. Fu, B. Dong, Z. Cao, R. Yu, S. I. Kawaguchi, H. Kadobayashi, M. Wang, C. Jin, H. kwang Mao, and H. Liu, Structure responsible for the superconducting state in  $\text{La}_3\text{Ni}_2\text{O}_7$  at high pressure and low temperature conditions (2023), [arXiv:2311.09186](https://arxiv.org/abs/2311.09186) [cond-mat.supr-con].
- [59] J. Yang, H. Sun, X. Hu, Y. Xie, T. Miao, H. Luo, H. Chen, B. Liang, W. Zhu, G. Qu, C.-Q. Chen, M. Huo, Y. Huang, S. Zhang, F. Zhang, F. Yang, Z. Wang, Q. Peng, H. Mao, G. Liu, Z. Xu, T. Qian, D.-X. Yao, M. Wang, L. Zhao, and X. J. Zhou, *Nature Communications* **15**, 4373 (2024).
- [60] H. Li, X. Zhou, T. Nummy, J. Zhang, V. Pardo, W. E. Pickett, J. F. Mitchell, and D. S. Dessau, *Nature Communications* **8**, 704 (2017).
- [61] X. Du, Y. D. Li, Y. T. Cao, C. Y. Pei, M. X. Zhang, W. X. Zhao, K. Y. Zhai, R. Z. Xu, Z. K. Liu, Z. W. Li, J. K. Zhao, G. Li, Y. L. Chen, Y. P. Qi, H. J. Guo, and L. X. Yang, Correlated electronic structure and density-wave gap in trilayer nickelate  $\text{La}_4\text{Ni}_3\text{O}_{10}$  (2024), [arXiv:2405.19853](https://arxiv.org/abs/2405.19853) [cond-mat.supr-con].
- [62] Y. Zhou, J. Guo, S. Cai, H. Sun, P. Wang, J. Zhao, J. Han, X. Chen, Q. Wu, Y. Ding, M. Wang, T. Xiang, H. kwang Mao, and L. Sun, Evidence of filamentary superconductivity in pressurized  $\text{La}_3\text{Ni}_2\text{O}_7$  single crystals (2023), [arXiv:2311.12361](https://arxiv.org/abs/2311.12361) [cond-mat.supr-con].
- [63] Z. Liu, M. Huo, J. Li, Q. Li, Y. Liu, Y. Dai, X. Zhou, J. Hao, Y. Lu, M. Wang, and H.-H. Wen, *Electronic correlations and energy gap in the bilayer nickelate  $\text{La}_3\text{Ni}_2\text{O}_7$*  (2023), [arXiv:2307.02950](https://arxiv.org/abs/2307.02950) [cond-mat].
- [64] J. Mravlje, M. Aichhorn, T. Miyake, K. Haule, G. Kotliar, and A. Georges, *Physical Review Letters* **106**, 096401 (2011), publisher: American Physical Society.
- [65] S. Rye, M. J. Han, and S. Choi, *Physical Review Letters* **126**, 206401 (2021), publisher: American Physical Society.
- [66] S. Rye, S. Choi, and M. J. Han, *Physical Review Research* **5**, 033134 (2023), publisher: American Physical Society.
- [67] T. Ayril, S. Biermann, and P. Werner, *Physical Review B* **87**, 125149 (2013), publisher: American Physical Society.
- [68] M. Schüler, M. Rösner, T. O. Wehling, A. I. Lichtenstein, and M. I. Katsnelson, *Physical Review Letters* **111**, 036601 (2013), publisher: American Physical Society.
- [69] E. G. C. P. van Loon, M. Schüler, M. I. Katsnelson, and T. O. Wehling, *Physical Review B* **94**, 165141 (2016), publisher: American Physical Society.
- [70] F. Nilsson, L. Boehnke, P. Werner, and F. Aryasetiawan, *Physical Review Materials* **1**, 043803 (2017), publisher: American Physical Society.
- [71] S. Rye, P. Sémon, M. J. Han, and S. Choi, *npj Quantum Materials* **5**, 1 (2020), number: 1 Publisher: Nature Publishing Group.
- [72] A. H. Nevidomskyy and P. Coleman, *Physical Review Letters* **103**, 147205 (2009), publisher: American Physical Society.
- [73] Z. P. Yin, K. Haule, and G. Kotliar, *Physical Review B* **86**, 195141 (2012), publisher: American Physical Society.
- [74] A. Georges, L. d. Medici, and J. Mravlje, *Annual Review of Condensed Matter Physics* **4**, 137 (2013).
- [75] C. Aron and G. Kotliar, *Physical Review B* **91**, 041110 (2015), publisher: American Physical Society.
- [76] S. Rye and T. O. Wehling, *Nano Letters* **23**, 573 (2023),

- <https://doi.org/10.1021/acs.nanolett.2c04169>.
- [77] J. Li, M. Wallerberger, N. Chikano, C.-N. Yeh, E. Gull, and H. Shinaoka, *Phys. Rev. B* **101**, 035144 (2020), [arxiv:1908.07575](https://arxiv.org/abs/1908.07575).
- [78] N. Witt, E. G. C. P. van Loon, T. Nomoto, R. Arita, and T. O. Wehling, *Physical Review B* **103**, 205148 (2021), publisher: American Physical Society.
- [79] N. Witt, J. M. Pizarro, J. Berges, T. Nomoto, R. Arita, and T. O. Wehling, *Physical Review B* **105**, L241109 (2022).
- [80] N. Witt, L. Si, J. M. Tomczak, K. Held, and T. O. Wehling, *SciPost Phys.* **15**, 197 (2023).
- [81] H. Shinaoka, J. Otsuki, M. Ohzeki, and K. Yoshimi, *Physical Review B* **96**, 035147 (2017).
- [82] H. Shinaoka, N. Chikano, E. Gull, J. Li, T. Nomoto, J. Otsuki, M. Wallerberger, T. Wang, and K. Yoshimi, *SciPost Physics Lecture Notes* **10.21468/scipostphyslectnotes.63** (2022).
- [83] M. Wallerberger, S. Badr, S. Hoshino, S. Huber, F. Kakizawa, T. Koretsune, Y. Nagai, K. Nogaki, T. Nomoto, H. Mori, J. Otsuki, S. Ozaki, T. Plaikner, R. Sakurai, C. Vogel, N. Witt, K. Yoshimi, and H. Shinaoka, *SoftwareX* **21**, 101266 (2023).

# Supplemental Material for “Quenched pair breaking by interlayer correlations as a key to superconductivity in $\text{La}_3\text{Ni}_2\text{O}_7$ ”

Siheon Ryee,<sup>1,\*</sup> Niklas Witt,<sup>1,2</sup> and Tim O. Wehling<sup>1,2</sup>

<sup>1</sup>*Institute of Theoretical Physics, University of Hamburg, Notkestrasse 9, 22607 Hamburg, Germany*

<sup>2</sup>*The Hamburg Centre for Ultrafast Imaging, Luruper Chaussee 149, 22761 Hamburg, Germany*

## CONTENTS

SM1. Microscopic model	S2
SM2. Imaginary part of the CDMFT self-energy	S2
SM3. Influence of different onsite interaction parameters on the Fermi surface	S2
SM4. Influence of interlayer density-density interaction $V$	S3
SM5. Influence of Hund’s coupling $J$	S4
SM6. Mimicking charge-self-consistent DFT+(C)DMFT	S5
SM7. Why the $\beta$ Fermi-surface pocket becomes more diamond-shaped with pressure	S5
SM8. The low-pressure Fermi surface	S7
SM9. How nesting of the $\beta$ Fermi-surface pocket is affected by interlayer correlations	S8
SM10. Gap equation	S9
A. Pairing interactions	S9
B. Approximations for the pairing interactions and the resulting gap equation	S10
C. Solving the gap equation using the intermediate representation basis	S11
SM11. Mapping of interaction values to Stoner enhancement factors	S11
SM12. Spin susceptibility	S12
SM13. Additional data: Structure of pairing vertex and the $s_{\pm}$ -wave gap function	S13
SM14. Additional data: The critical role of FM $\chi_{z_+z_+z_+z_+}^0(q)$ in the singlet pairing	S15
References	S16

---

\* [sryee@physnet.uni-hamburg.de](mailto:sryee@physnet.uni-hamburg.de)

### SM1. MICROSCOPIC MODEL

We consider a Hamiltonian on the bilayer square lattice:  $\mathcal{H} = H_0 + H_{\text{int}}$ . Here,  $H_0$  is a tight-binding term describing the noninteracting band structure, which reads

$$H_0 = \sum_{il,jm,\sigma} t_{il,jm} d_{il\sigma}^\dagger d_{jm,\sigma}, \quad (\text{S1})$$

where  $d_{il,\sigma}^\dagger$  ( $d_{jm,\sigma}$ ) is the electron creation (annihilation) operator for site  $i, j$  of the bilayer square lattice, spin  $\sigma \in \{\uparrow, \downarrow\}$ , and orbital  $l, m \in \{\bar{\eta}, \eta\}$  where  $\bar{\eta}$  and  $\eta$  represent Ni- $e_g$  orbitals  $\eta \in \{x^2 - y^2, z^2\}$  in the top and bottom layers, respectively. We simply denote  $x^2 - y^2$  by  $x$  and  $z^2$  by  $z$ .  $\{t_{il,jm}\}$  are the hopping amplitudes for which we use values obtained from the maximally localized Wannier function (MLWF) description of the DFT result for  $\text{La}_3\text{Ni}_2\text{O}_7$  under high pressure (29.5 GPa) [S1]. Note in particular that  $t_{\perp}^\eta \equiv t_{i\bar{\eta},i\eta} = t_{i\eta,i\bar{\eta}}$  with  $t_{\perp}^x = -0.049$  eV and  $t_{\perp}^z = -0.628$  eV [S1]. The band dispersion of  $H_0$  is presented in Fig. 2(c) in the main text.  $H_{\text{int}}$  is the onsite interaction term given by the standard Kanamori form

$$H_{\text{int}} = \frac{1}{2} \sum_{i,l,m',m',\sigma,\sigma'} U_{lm'm'l}^{\sigma\sigma'} d_{il\sigma}^\dagger d_{il'\sigma'}^\dagger d_{im'\sigma'} d_{im\sigma}, \quad (\text{S2})$$

where  $l, l', m, m' \in \{\bar{x}, \bar{z}, \underline{x}, \underline{z}\}$ .  $U_{lm'm'l}^{\sigma\sigma'}$  is nonzero only for  $U \equiv U_{\bar{\eta}\bar{\eta}\bar{\eta}\bar{\eta}}^{\sigma\sigma} = U_{\bar{\eta}\bar{\eta}\bar{\eta}\bar{\eta}}^{\sigma-\sigma} = U_{\eta\eta\eta\eta}^{\sigma\sigma} = U_{\eta\eta\eta\eta}^{\sigma-\sigma}$ ,  $U' \equiv U_{\bar{\eta}\bar{\eta}'\bar{\eta}\bar{\eta}'}^{\sigma\sigma} = U_{\bar{\eta}\bar{\eta}'\bar{\eta}\bar{\eta}'}^{\sigma-\sigma} = U_{\eta\eta'\eta'\eta}^{\sigma\sigma} = U_{\eta\eta'\eta'\eta}^{\sigma-\sigma}$ , and  $J \equiv U_{\bar{\eta}\bar{\eta}'\bar{\eta}'\bar{\eta}}^{\sigma\sigma} = U_{\bar{\eta}\bar{\eta}'\bar{\eta}'\bar{\eta}}^{\sigma-\sigma} = U_{\eta\eta'\eta'\eta'}^{\sigma\sigma} = U_{\eta\eta'\eta'\eta'}^{\sigma-\sigma} = U_{\eta\eta'\eta'\eta}^{\sigma\sigma} = U_{\eta\eta'\eta'\eta}^{\sigma-\sigma} = U_{\eta\eta\eta'\eta'}^{\sigma\sigma} = U_{\eta\eta\eta'\eta'}^{\sigma-\sigma}$  ( $\eta \neq \eta'$ ). We take  $U = 3.7$ ,  $J = 0.6$  eV, and  $U' = U - 2J$  by taking *ab initio* estimates for the  $e_g$  MLWF model [S2].

To mitigate the Monte Carlo sign problem of the two-site cluster impurity, we solve the model in a bonding-antibonding (BA) basis in which the electron annihilation operator  $\tilde{d}_{i\eta\pm\sigma}$  is defined as the symmetric (+) and antisymmetric (−) combinations of the top and bottom layer  $e_g$  orbital operators:

$$\begin{pmatrix} \tilde{d}_{i\bar{x}+\sigma} \\ \tilde{d}_{i\bar{z}+\sigma} \\ \tilde{d}_{i\underline{x}-\sigma} \\ \tilde{d}_{i\underline{z}-\sigma} \end{pmatrix} = \mathbf{A} \begin{pmatrix} d_{i\bar{x}\sigma} \\ d_{i\bar{z}\sigma} \\ d_{i\underline{x}\sigma} \\ d_{i\underline{z}\sigma} \end{pmatrix} = \frac{1}{\sqrt{2}} \begin{pmatrix} 1 & 0 & 1 & 0 \\ 0 & 1 & 0 & 1 \\ 1 & 0 & -1 & 0 \\ 0 & 1 & 0 & -1 \end{pmatrix} \begin{pmatrix} d_{i\bar{x}\sigma} \\ d_{i\bar{z}\sigma} \\ d_{i\underline{x}\sigma} \\ d_{i\underline{z}\sigma} \end{pmatrix}, \quad \text{where } \mathbf{A} = \frac{1}{\sqrt{2}} \begin{pmatrix} 1 & 0 & 1 & 0 \\ 0 & 1 & 0 & 1 \\ 1 & 0 & -1 & 0 \\ 0 & 1 & 0 & -1 \end{pmatrix}. \quad (\text{S3})$$

Under this basis transformation,  $H_0$  and  $H_{\text{int}}$  are rewritten as

$$H_0 = \sum_{il,jm,\sigma} \left( \sum_{l_1,m_1} t_{il_1,jm_1} A_{l_1 l} A_{m_1 m}^* \right) \tilde{d}_{il\sigma}^\dagger \tilde{d}_{jm,\sigma}, \quad (\text{S4})$$

$$H_{\text{int}} = \frac{1}{2} \sum_{i,l,m',m',\sigma,\sigma'} \left( \sum_{l_1,m_2,m_1,l_2} U_{l_1 m_2 m_1 l_2}^{\sigma\sigma'} A_{l_1 l} A_{l_2 l'} A_{m_1 m}^* A_{m_2 m'}^* \right) \tilde{d}_{il\sigma}^\dagger \tilde{d}_{il'\sigma'}^\dagger \tilde{d}_{im'\sigma'} \tilde{d}_{im\sigma}. \quad (\text{S5})$$

The transformed Coulomb interaction tensor to the BA basis, namely  $\tilde{U}_{lm'm'l}^{\sigma\sigma'} = \sum_{l_1 m_2 m_1 l_2} U_{l_1 m_2 m_1 l_2}^{\sigma\sigma'} A_{l_1 l} A_{l_2 l'} A_{m_1 m}^* A_{m_2 m'}^*$ , has in general nonzero four-index elements. While the four-index terms cause the Monte Carlo sign problem, it is actually largely alleviated in the BA basis compared to the  $e_g$  basis thanks to the orbital-diagonal hybridization function.

### SM2. IMAGINARY PART OF THE CDMFT SELF-ENERGY

The imaginary part of the CDMFT self-energy,  $\Im\Sigma_l(i\omega_n)$  is presented in Fig. S1. Noticeable is the strong orbital dependence of  $\Im\Sigma_l(i\omega_n)$ : the  $z_{\pm}$  components are more correlated than the  $x_{\pm}$ , i.e.,  $|\Im\Sigma_{z_{\pm}}(i\omega_n)| > |\Im\Sigma_{x_{\pm}}(i\omega_n)|$ . The result is qualitatively consistent with the available experimental data on the ambient-pressure structure of  $\text{La}_3\text{Ni}_2\text{O}_7$  [S3, S4]. The origin is traced back to the resulting electron occupation of the  $\bar{z}$  and  $\underline{z}$  orbitals ( $\langle n_{\bar{z}} \rangle = \langle n_{\underline{z}} \rangle \simeq 0.93$ ) being much closer to half filling than the  $\bar{x}$  and  $\underline{x}$  ( $\langle n_{\bar{x}} \rangle = \langle n_{\underline{x}} \rangle \simeq 0.57$ ). The IECs between  $\bar{z}$  and  $\underline{z}$  orbitals further differentiate  $z_+$  and  $z_-$ , namely  $|\Im\Sigma_{z_-}(i\omega_n)| > |\Im\Sigma_{z_+}(i\omega_n)|$ , leading to a larger mass enhancement  $m^*/m_{\text{DFT}}$  ( $m_{\text{DFT}}$  is the bare DFT mass) in the  $z_-$  component. The mass enhancements directly extracted from  $\Im\Sigma_l(i\omega_n)$  using fourth-order polynomial fitting [S5–S7] are  $m^*/m_{\text{DFT}} \simeq 2.8$  for  $z_+$  and 5.1 for  $z_-$ . On the other hand,  $m^*/m_{\text{DFT}} \simeq 2$  for both weaker-correlated  $x_+$  and  $x_-$  orbitals.

### SM3. INFLUENCE OF DIFFERENT ONSITE INTERACTION PARAMETERS ON THE SURFACE

We have used *ab initio* estimate of  $U$  ( $U = 3.7$  eV) and  $J$  ( $J = 0.6$  eV) obtained from the constrained random phase approximation (cRPA) [S2] for our presentation in the main text. Since we have neglected i) frequency dependence of  $U$  and

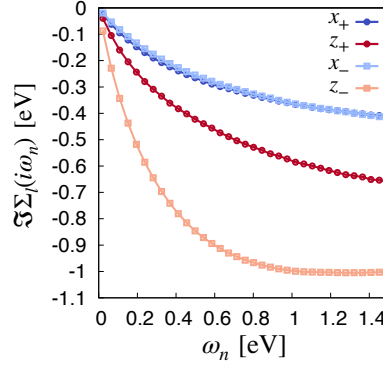


FIG. S1. The imaginary part of the CDMFT self-energy on the Matsubara frequency axis.

$J$  by using their static limits and ii) spatially long-ranged Coulomb tails by taking only onsite values, it would be necessary to check how the low-energy electronic structure is affected by different values of  $U$  and  $J$ . Here, we change  $U$  and keep the ratio  $J/U$  fixed.

We present the calculated FSs in Fig. S2. As is expected, the strength of IECs increases with  $U$  and  $J$ . Namely, the  $\gamma$  pocket at the  $M$  point gets suppressed and the  $\beta$  pocket becomes more diamond-shaped with increasing  $U$  and  $J$  in CDMFT results. On the other hand, we find no appreciable change within DMFT in which only onsite electronic correlations are taken into account. In any case, we find that in a reasonable range around the cRPA estimates IECs significantly modify the FS making the  $\gamma$  pocket largely suppressed.

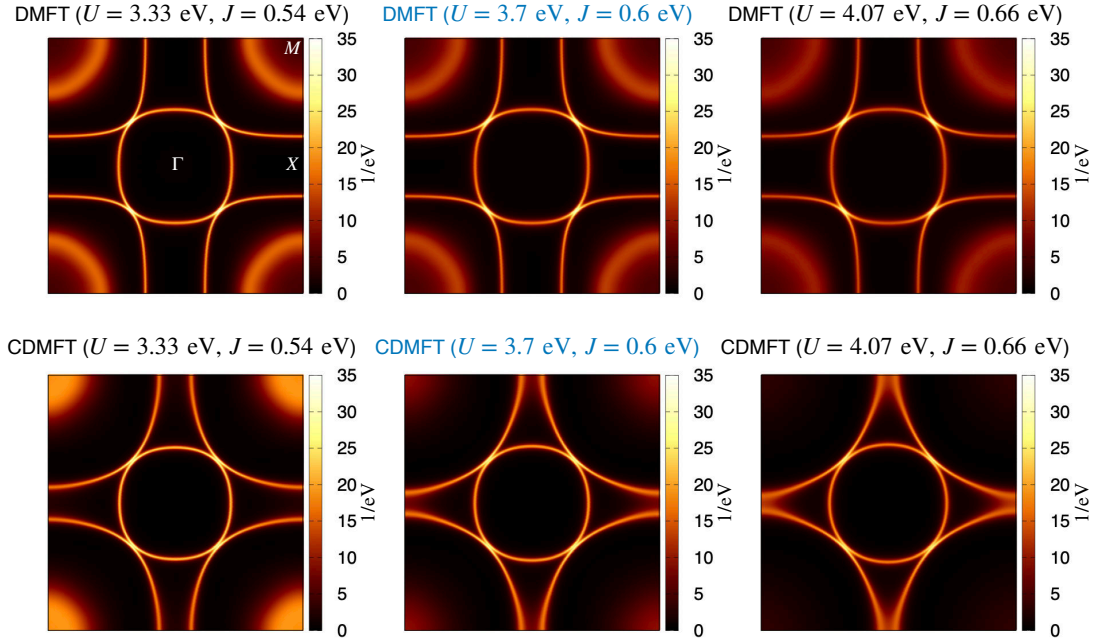


FIG. S2. The calculated FSs by DMFT (top panels) and CDMFT (bottom panel) for different interaction parameters. The FSs are approximated to  $-\sum_{lm} \delta_{lm} \Im G_{lm}(\mathbf{k}, i\omega_0)$  where  $l, m \in \{x_+, z_+, x_-, z_-\}$ . The FSs in the middle panels are obtained from the *ab initio* interaction parameters as discussed in the main text.  $U' = U - 2J$  for all the sets.

#### SM4. INFLUENCE OF INTERLAYER DENSITY-DENSITY INTERACTION $V$

Using the BA basis for CDMFT calculations, the nearest-neighbor interlayer interactions can be addressed on the same footing as onsite interactions ( $U$  and  $J$ ) without invoking further computational complexity. In light of this, we here consider the effects

of density-density interaction  $V$  within CDMFT by introducing an additional term  $H_V$  to our Hamiltonian.  $H_V$  reads

$$\begin{aligned}
 H_V &= \sum_{\eta, \eta' \in \{x, z\}}^{i\sigma\sigma'} V d_{i\eta\sigma}^\dagger d_{i\eta'\sigma'}^\dagger d_{i\eta'\sigma} d_{i\eta\sigma} \quad (e_g \text{ basis}) \\
 &= \sum_{l, m \in \{x_+, z_+, x_-, z_-\}}^{i\sigma\sigma'} \left( \sum_{\eta, \eta' \in \{x, z\}} V A_{\eta l} A_{\eta' m} A_{\eta l}^* A_{\eta' m}^* \right) \tilde{d}_{i l \sigma}^\dagger \tilde{d}_{i m \sigma'}^\dagger \tilde{d}_{i m \sigma'} \tilde{d}_{i l \sigma} \quad (\text{BA basis}).
 \end{aligned} \tag{S6}$$

We use the cRPA estimate of  $V$ :  $V = 0.5$  eV [S2].

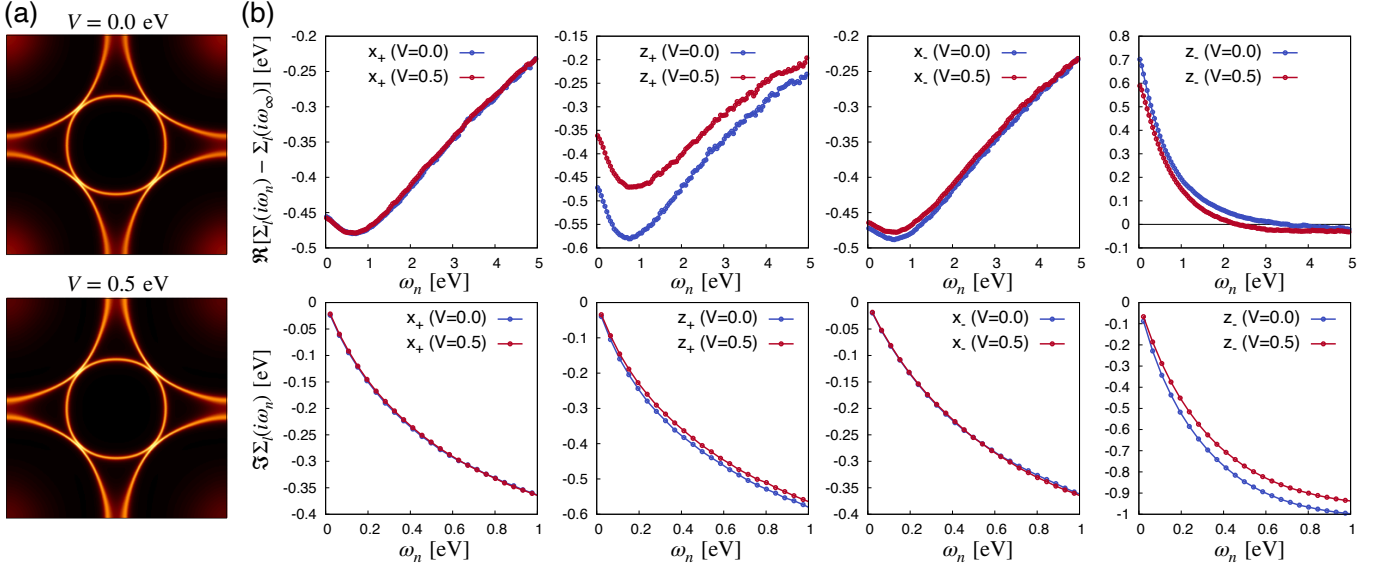


FIG. S3. (a) The calculated FSs by CDMFT for  $V = 0$  (top) and  $V = 0.5$  eV (bottom). (b) The real (top) and imaginary (bottom) parts of the CDMFT self-energies.  $U = 3.7$  eV,  $J = 0.6$  eV, and  $U' = U - 2J = 2.5$  eV.

Figure S3 presents the FS and the self-energy calculated by CDMFT with  $V = 0.5$  eV. For comparison, we also show the results with  $V = 0$ . We first find that the FS is basically unaffected by  $V$ , although  $V$  slightly suppresses the  $\gamma$  pocket at the  $M$  point. This minor difference can be traced back to the small difference in the real part of the self-energy [upper panels in Fig. S3(b)]. For all orbital characters, the effect of  $V$  induces at most a  $\sim 0.1$  eV decrease in the magnitude of the real part. Note that for comparison of the two cases on the same footing, we subtracted the infinite-frequency Hartree-Fock self-energy from the real part. We also find basically negligible modifications in the imaginary part of the self-energy [lower panels in Fig. S3(b)], albeit them being systematically decreased in magnitude by  $V$ . We can ascribe these suppressed real and imaginary parts of the self-energy in the finite  $V$  case to the generic effect of  $V$  which reduces the “effective” onsite interaction strength by screening [S8–S12]. At any rate, these small changes in the FS and the self-energy legitimately allow us to employ only onsite interactions as we did in the present paper.

### SM5. INFLUENCE OF HUND’S COUPLING $J$

Since  $\text{La}_3\text{Ni}_2\text{O}_7$  realizes a multiorbital system, it would be informative to investigate how Hund’s coupling  $J$  affects the low-energy physics. Figure S4 presents the effect of  $J$  on the imaginary part of the CDMFT self-energy. Interestingly, the magnitude of  $\Im\Sigma_l(i\omega_n)$  increases for all the orbital character once we turn on  $J$ . Thus, the system becomes more correlated by  $J$ , which in this sense can be identified as a “Hund’s metal” [S13]. This is because the formation of large local spin moments promoted by Hund’s coupling suppresses Kondo screening, thereby prohibiting the emergence of long-lived quasiparticles [S7, S13–S17]. We also find a strong orbital dependence of  $\Im\Sigma_l(i\omega_n)$  for both  $J = 0$  and  $J = 0.6$  eV (the *ab initio* estimate) due to the fact that the electron occupation of the  $\bar{z}$  and  $\underline{z}$  orbitals is much closer to half filling than that of the  $\bar{x}$  and  $\underline{x}$  orbitals in both cases. The redistribution of electron filling by turning on  $J$  is found to be almost negligible in this system.



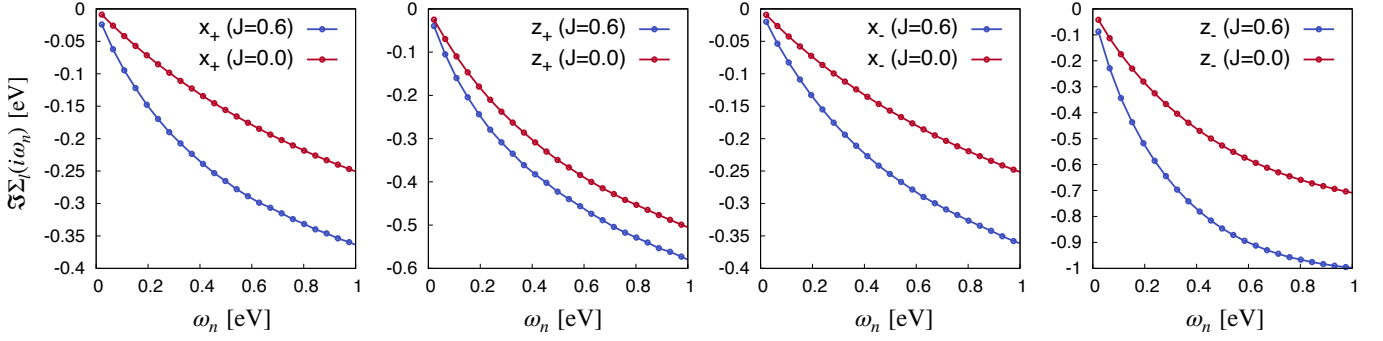


FIG. S4. The imaginary parts of the CDMFT self-energies for  $J = 0.6$  eV (blue) and  $J = 0.0$  (red).  $U = 3.7$  eV and  $U' = U - 2J$  for both cases.

### SM6. MIMICKING CHARGE-SELF-CONSISTENT DFT+(C)DMFT

In this paper, we have addressed the (C)DMFT results to the *ab initio* lattice model derived from DFT as defined in Sec. SM1. We here argue that charge self-consistency in the spirit of DFT+(C)DMFT may not affect the findings of our paper.

To mimic the charge self-consistency in the low-energy lattice model  $\mathcal{H} = H_0 + H_{\text{int}}$ , we here resort to a strategy by noting that a redistribution of electrons by (C)DMFT modifies a charge-density profile  $\rho(\mathbf{r})$  and the resulting local electron occupation, from which the subsequent DFT would result in new on-site energy levels of  $x$  and  $z$  orbitals for the kinetic part  $H_0$ . In short, we iterate (C)DMFT calculations for the updated  $H_0$ , which we call  $\tilde{H}_0$  in which the on-site energy levels ( $\varepsilon_{x/z}$ ) are adjusted such that the noninteracting electron occupation ( $\langle n_{x/z} \rangle_0$ ) is equal to the self-consistently determined (C)DMFT occupation ( $\langle n_{x/z} \rangle_{(\text{C})\text{DMFT}}$ ) of the previous iteration; see Fig. S5(a).

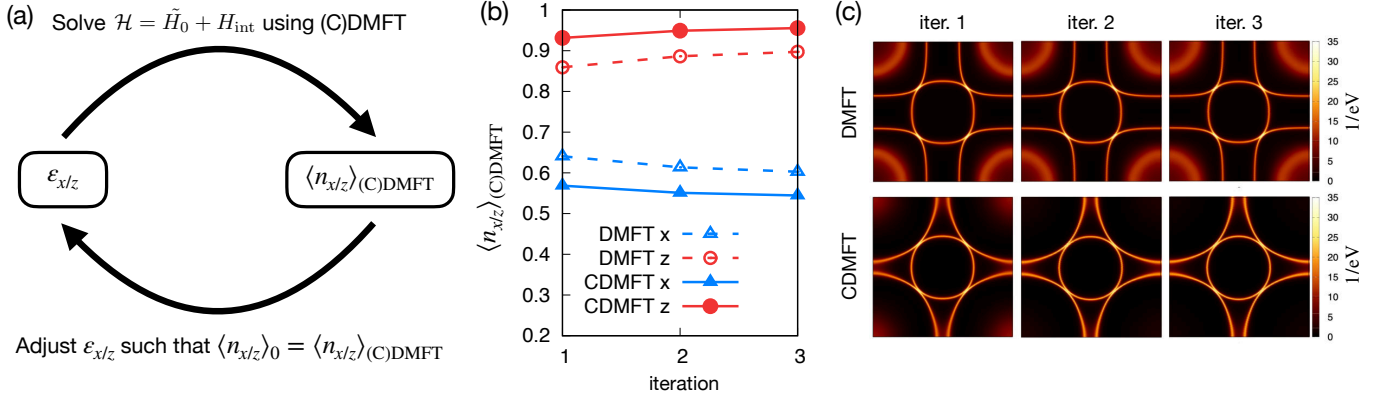


FIG. S5. (a) Schematic of mimicking DFT+(C)DMFT charge self-consistency by adjusting the on-site energy levels ( $\varepsilon_{x/z}$ ) for top and bottom layer  $x$  and  $z$  orbitals. (b) The (C)DMFT electron occupation  $\langle n_{x/z} \rangle_{(\text{C})\text{DMFT}}$  as a function of iteration steps. (c) The resulting (C)DMFT FSs for each iteration step. The FSs in Iteration 1 correspond to the (C)DMFT results presented throughout this paper.

Figure S5(b) presents  $\langle n_{x/z} \rangle_{(\text{C})\text{DMFT}}$  as a function of the iteration step. Note that iteration 1 corresponds to the (C)DMFT result which we have discussed throughout the paper. We find that  $\langle n_{x/z} \rangle_{(\text{C})\text{DMFT}}$  almost converges at the third iteration, albeit  $\langle n_{x/z} \rangle_{(\text{C})\text{DMFT}}$  does not change significantly during the iteration. Most importantly, FS remains almost unchanged [Fig. S5(c)], which validates (C)DMFT approach employed in this paper. Indeed, our DMFT FS is consistent with the charge-self-consistent DFT+DMFT results reported in Refs. [S18, S19].

### SM7. WHY THE $\beta$ FERMI-SURFACE POCKET BECOMES MORE DIAMOND-SHAPED WITH PRESSURE

To model lower pressure cases, we look at a recent experimental study on the evolution of Ni-O bond length as a function of pressure [S20]. Here, it is reported that pressure mainly shrinks the out-of-plane Ni-O bond length while the in-plane one is very weakly affected [S20]. Thus, the main effect of pressure can be addressed with the change in the magnitude of  $t_{\perp}^z$  which is sensitive to the out-of-plane Ni-O bond length. Since  $t_{\perp}^z \simeq -0.63$  eV at 29.5 GPa under which superconductivity emerges,

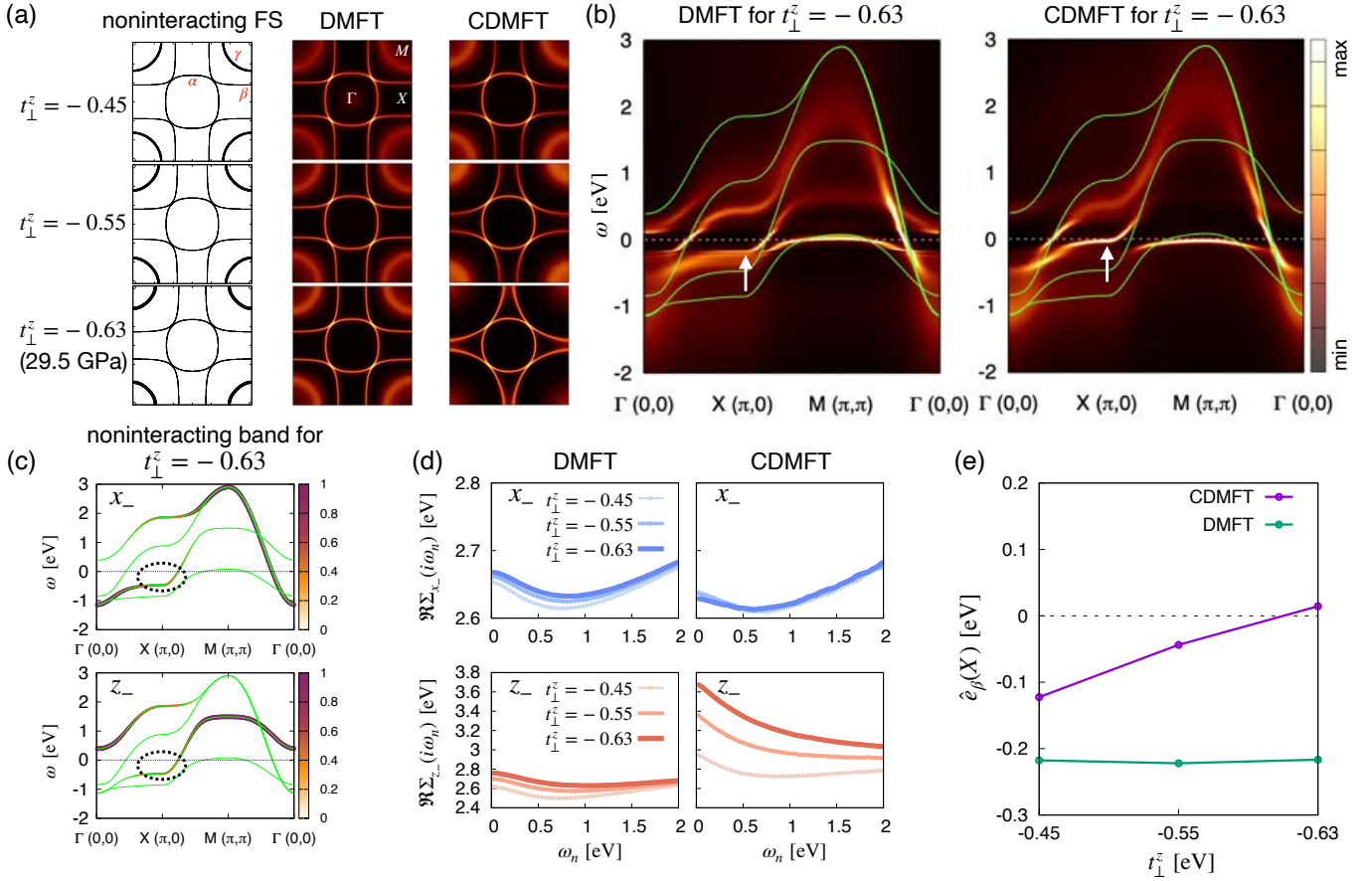


FIG. S6. (a) Fermi surfaces obtained from the noninteracting Hamiltonian (left panels), DMFT (middle panels), and CDMFT (right panels) for the three different values of  $t_{\perp}^z$  (in units of eV). (b) The momentum-dependent spectral function obtained from DMFT (left panel) and CDMFT (right panel) for  $t_{\perp}^z = -0.63$  eV. The green solid lines indicate the DFT bands. The Fermi level is at  $\omega = 0$ . (c) The weight of  $x_{-}$  (top panel) and  $z_{-}$  (bottom panel) orbitals in the DFT band structure at the high-pressure phase where  $t_{\perp}^z = -0.63$  eV. (d) The real part of the DMFT and CDMFT self-energies for  $x_{-}$  (top panels) and  $z_{-}$  (bottom panels) on the Matsubara frequency axis for the same values of  $t_{\perp}^z$ . (e) The calculated  $\hat{e}_{\beta}(X)$  according to Eq. (S14).

Figure S6(a) presents Fermi surfaces (FSs) for three different values of  $t_{\perp}^z$ . DFT-like noninteracting FS remains almost unchanged albeit the  $\gamma$  pocket gets slightly suppressed as  $|t_{\perp}^z|$  increases (or, equivalently as the applied pressure increases). In CDMFT, FS is also basically the same as the noninteracting FS for the lowest pressure case in which  $t_{\perp}^z = -0.45$  eV. Interestingly, however, as  $|t_{\perp}^z|$  increases, the  $\beta$  pocket becomes more diamond-shaped in CDMFT. The shape change of the  $\beta$  FS pocket in CDMFT is traced back to the upward energy shift of the spectral weight near the  $X$  point of the Brillouin zone in the CDMFT spectral function compared to the DMFT as highlighted with white arrows in Fig. S6(b). Furthermore, the shape change of the  $\beta$  FS pocket with  $|t_{\perp}^z|$  presented in Fig. S6(a) implies that the spectral weight near the  $X$  point gets pushed upward in CDMFT with  $|t_{\perp}^z|$ .

The reason for such change of the  $\beta$  pocket is two-fold: i) the  $\beta$  pocket contains the  $z_{-}$  orbital character near the  $X$  point as highlighted with black dotted ovals in Fig. S6(c) and ii) the real part of the CDMFT  $z_{-}$ -orbital self-energy  $\Re\Sigma_{z_{-}}$  increases with pressure as presented in Fig. S6(d). For a more quantitative understanding of this argument, let us now investigate in detail how the energy level at the  $X$  point is modified in DMFT and CDMFT. To this end, we first write down the interacting Green's function which reads

$$\mathbf{G}^{-1}(\mathbf{k}, \omega) = (\omega + \mu)\mathbf{I} - \mathbf{H}_0(\mathbf{k}) - \Sigma(\omega), \quad (\text{S7})$$

where  $\omega$  is real frequency,  $\mathbf{k}$  the crystal momentum,  $\mu$  a chemical potential. A bold capital letter represents a  $4 \times 4$  matrix in the space of BA orbital  $l$  ( $l \in \{x_{+}, z_{+}, x_{-}, z_{-}\}$ ).  $\mathbf{I}$  is the identity matrix.  $\mathbf{H}_0(\mathbf{k})$  is a one-particle Hamiltonian derived from DFT, and  $\Sigma(\omega)$  a self-energy calculated by DMFT or CDMFT. We are interested in how the poles of  $\mathbf{G}(\mathbf{k}, \omega)$  are shifted by electronic

correlations, so it is useful to investigate the quasiparticle energies which are the solutions  $\omega(\mathbf{k})$  of

$$\text{Det}[(\omega + \mu)\mathbf{I} - \mathbf{H}_0(\mathbf{k}) - \Re\Sigma(\omega)] = 0. \quad (\text{S8})$$

Near the Fermi level ( $\omega = 0$ ),  $\Re\Sigma(\omega)$  can be expanded to the linear order in  $\omega$ :

$$\Re\Sigma(\omega) \simeq \Re\Sigma(0) + \omega(\mathbf{I} - \mathbf{Z}^{-1}) \simeq \Re\Sigma(i\omega_0) + \omega(\mathbf{I} - \mathbf{Z}^{-1}), \quad (\text{S9})$$

where  $\mathbf{Z}^{-1} = (\mathbf{I} - \partial\Re\Sigma(\omega)/\partial\omega)|_{\omega=0} = (\mathbf{I} - \partial\Im\Sigma(i\omega_n)/\partial\omega_n)|_{\omega_n=0}$  is the inverse of the quasiparticle weight  $\mathbf{Z}$ . In practice, we evaluate  $\mathbf{Z}$  using  $\Im\Sigma(i\omega_n)$  defined in the Matsubara frequency space  $\omega_n$  by employing the fourth-order polynomial fitting [S5–S7].  $\Re\Sigma(i\omega_0)$  is the real-part of the self-energy at the lowest Matsubara frequency, which approximates  $\Re\Sigma(\omega = 0)$ . We then express  $\mathbf{Z}^{-1}$  as a symmetrical product:

$$\mathbf{Z}^{-1} = \mathbf{Z}^{-1/2} \mathbf{Z}^{-1/2}. \quad (\text{S10})$$

By plugging Eq. (S9) in Eq. (S8) we arrive at

$$\text{Det}[\omega\mathbf{I} - \sqrt{\mathbf{Z}}\{\mathbf{H}_0(\mathbf{k}) - \mu\mathbf{I} + \Re\Sigma(i\omega_0)\}\sqrt{\mathbf{Z}}] = 0. \quad (\text{S11})$$

One can identify a Hermitian matrix  $\sqrt{\mathbf{Z}}\{\mathbf{H}_0(\mathbf{k}) - \mu\mathbf{I} + \Re\Sigma(i\omega_0)\}\sqrt{\mathbf{Z}}$  as the quasiparticle Hamiltonian whose eigenvalues at each  $\mathbf{k}$  correspond to the quasiparticle energies. A useful insight can be obtained from the change of basis of Eq. (S11) to the ‘‘band basis’’ by which  $\mathbf{H}_0(\mathbf{k})$  becomes diagonal:

$$\sqrt{\mathbf{Z}}\{\mathbf{H}_0(\mathbf{k}) - \mu\mathbf{I} + \Re\Sigma(i\omega_0)\}\sqrt{\mathbf{Z}} \xrightarrow{\text{band basis}} \hat{\sqrt{\mathbf{Z}}}\{\hat{\mathbf{H}}_0(\mathbf{k}) - \mu\hat{\mathbf{I}} + \Re\hat{\Sigma}(i\omega_0)\}\hat{\sqrt{\mathbf{Z}}}, \quad (\text{S12})$$

where bold capital letters with hat represent  $4 \times 4$  matrices in the band basis.  $\hat{\mathbf{H}}_0(\mathbf{k})$  is the diagonal matrix whose elements  $e_n(\mathbf{k})$  ( $n$ : band index) are the band energies. We find that off-diagonal elements of  $\hat{\sqrt{\mathbf{Z}}}$  and  $\Re\hat{\Sigma}(i\omega_0)$  are much smaller than the diagonal elements. Thus the band energy  $e_n(\mathbf{k})$  approximately turns into a quasiparticle energy  $\hat{e}_n(\mathbf{k})$ :

$$e_n(\mathbf{k}) \rightarrow \hat{e}_n(\mathbf{k}) \equiv \hat{\sqrt{\mathbf{Z}}}_{nn}\{e_n(\mathbf{k}) - \mu + \Re\hat{\Sigma}(i\omega_0)_{nn}\}\hat{\sqrt{\mathbf{Z}}}_{nn}, \quad (\text{S13})$$

where  $\hat{\sqrt{\mathbf{Z}}}_{nn}$  and  $\Re\hat{\Sigma}(i\omega_0)_{nn}$  are the  $n$ -th diagonal elements, respectively, of  $\hat{\sqrt{\mathbf{Z}}}$  and  $\Re\hat{\Sigma}(i\omega_0)$ . Equation (S13) allows us to trace how  $e_n(\mathbf{k})$  is shifted in energy due to electronic correlations. Evaluating Eq. (S13) at  $\mathbf{k} = X$  for the  $\beta$  pocket ( $n = \beta$ ) yields the approximate quasiparticle energy  $\hat{e}_\beta(X)$  which reads

$$\begin{aligned} \hat{e}_\beta(X) = & \{|c_{x_-}|^2\sqrt{\mathbf{Z}}_{x_-} + |c_{z_-}|^2\sqrt{\mathbf{Z}}_{z_-}\}\{e_\beta(X) - \mu + |c_{x_-}|^2\Re\Sigma_{x_-}(i\omega_0) + |c_{z_-}|^2\Re\Sigma_{z_-}(i\omega_0)\} \\ & \times \{|c_{x_-}|^2\sqrt{\mathbf{Z}}_{x_-} + |c_{z_-}|^2\sqrt{\mathbf{Z}}_{z_-}\}, \end{aligned} \quad (\text{S14})$$

where  $\sqrt{\mathbf{Z}}_l$  and  $\Re\Sigma_l(i\omega_0)$  are the diagonal elements corresponding to the orbital  $l$  of  $\sqrt{\mathbf{Z}}$  and  $\Re\Sigma(i\omega_0)$ , respectively.  $|c_l|^2$  is the weight of the Wannier function  $|\tilde{d}_l\rangle$  in the  $\beta$  pocket eigenstate  $|\psi_\beta(\mathbf{k})\rangle$  of  $\mathbf{H}_0(\mathbf{k})$  at  $\mathbf{k} = X$ ;  $|\psi_\beta(\mathbf{k} = X)\rangle = \sum_l c_l|\tilde{d}_l\rangle$ . We find that  $c_{x_+} = c_{z_+} = 0$  in this case. Furthermore, near the  $X$  point of the  $\beta$  pocket  $x_-$  and  $z_-$  orbitals have almost equal weight as highlighted with dotted black ovals in Fig. S6(c), so  $|c_{x_-}|^2 \simeq |c_{z_-}|^2 \simeq 0.5$ . Thus, Eq. (S14) implies that the electronic correlations emerging from  $x_-$  and  $z_-$  orbital components influence  $\hat{e}_\beta(X)$  as a weighted average.

Now, let us see the result of our analysis. Figure S6(e) presents how  $\hat{e}_\beta(X)$  changes with  $t_\perp^z$  according to Eq. (S13). Indeed,  $\hat{e}_\beta(X)$  increases with  $|t_\perp^z|$  in CDMFT, which is consistent with how the  $\beta$  pocket changes with  $|t_\perp^z|$  in Fig. S6(a). The reason for this increase of  $\hat{e}_\beta(X)$  is because  $\Re\Sigma_{z_-}(i\omega_0)$  is enhanced significantly with  $t_\perp^z$  in CDMFT as presented in Fig. S6(d), in contrast to the other terms of Eq. (S13) which are found to vary only weakly with  $t_\perp^z$ . Thus, how  $\hat{e}_\beta(X)$  changes with pressure is almost entirely dependent on how  $\Re\Sigma_{z_-}(i\omega_0)$  changes with  $t_\perp^z$ . In this respect, it is useful to examine  $\hat{e}_\beta(X)$  in DMFT since  $\Re\Sigma_{z_-}(i\omega_0)$  weakly changes with  $t_\perp^z$  in DMFT; see Fig. S6(d). Indeed,  $\hat{e}_\beta(X)$  remains almost unchanged with  $t_\perp^z$  in DMFT as shown in Fig. S6(e), which also explains why the  $\beta$  pocket in DMFT remains almost intact.

## SM8. THE LOW-PRESSURE FERMI SURFACE

Figure S7 summarizes which theoretical method results in which FS pockets. We once again clarify here that, to simulate the high-pressure phase, we have employed DMFT and CDMFT for the *ab initio* model with one-body part of the Hamiltonian being derived from DFT (dubbed ‘‘DFT  $H_0$ ’’), as highlighted in Fig. S7.

Method	low pressure	high pressure
DFT	$\alpha, \beta, \gamma$	$\alpha, \beta, \gamma$
DFT+U	$\alpha, \beta$	$\alpha, \beta, \gamma$
DMFT	$\alpha, \beta, \gamma$ (model $H_0$ )	$\alpha, \beta, \gamma$ (DFT $H_0$ )
CDMFT	$\alpha, \beta, \gamma$ (model $H_0$ )	$\alpha, \beta$ (DFT $H_0$ )
ARPES (Yang et al.)	$\alpha, \beta$	

Quenched  $\gamma$  pocket promotes SC.

Drop of  $R_H$  and emergence of SC

FIG. S7. The table summarizes which method results in which FS pockets at the low-pressure and high-pressure phases of  $\text{La}_3\text{Ni}_2\text{O}_7$ . Here “model  $H_0$ ” indicates the  $H_0$  obtained from DFT in the high pressure phase with  $t_{\perp}^z$  being tuned to mimic the low-pressure phase. The ARPES FS by Yang et al. [S3] for the ambient-pressure phase is composed of the  $\alpha$  and the  $\beta$  pockets. For the low-pressure DFT FS, see, e.g., Refs. [S21, S22]. For the high-pressure DFT FS, see, e.g., Refs. [S1, S21–S28]. For both the low-pressure and the high-pressure DFT+U FSs, see, e.g., Refs. [S29, S30]. Our high-pressure DMFT FS is also consistent with that in Refs. [S18, S19].

Having established the role of the interlayer correlations for the high-pressure phase, it is tempting to reach out to a picture also commenting on the low-pressure phase. To this end, we have used a simplified model, where we have only rescaled  $t_{\perp}^z$  of DFT  $H_0$  (dubbed “model  $H_0$ ” in Fig. S7). With this model we could possibly explain the evolution of  $R_H$  [S31] and the emergence of superconductivity by comparing high- and low-pressure phases; see Fig. S7. Furthermore, the calculated CDMFT spin susceptibility for the low-pressure “model” is close to the spin-density wave (SDW) ordering vector reported by experiments [S32, S33] as discussed in the main text and Sec. SM12.

The  $\gamma$  pocket is absent in the available ARPES data [S3], which is not consistent with our “low-pressure” phase results; see also Fig. S7. Drawing a definite conclusion would be premature at the moment, however, considering the delicacy of ARPES experiment on nickelates due to the oxygen vacancies (which are prevalent in the actual  $\text{La}_3\text{Ni}_2\text{O}_7$  samples), the sample-to-sample variation of  $\text{NiO}_6$ -plane stacking in  $\text{La}_3\text{Ni}_2\text{O}_7$  (trilayer–monolayer vs. bilayer–bilayer), and surface effects. In this regard, it is noteworthy that there is a discrepancy exactly on the fermiology even between the two experiments on  $\text{La}_4\text{Ni}_3\text{O}_{10}$ . Namely, while Du et al. [S34] reported that the  $\gamma$  pocket constitutes the FS and its position remains unchanged with temperature (presumably down to  $\sim 20$  K), a previous ARPES study by Li et al. [S35] reported in contrast that this  $\gamma$  pocket is gapped out at a low temperature ( $\sim 30$  K), thereby being disappeared from the FS. Further theoretical as well as experimental study is requested to establish the fermiology of the ambient-pressure phase.

### SM9. HOW NESTING OF THE $\beta$ FERMI-SURFACE POCKET IS AFFECTED BY INTERLAYER CORRELATIONS

The  $\beta$  Fermi surface pocket is also modified by the interlayer electronic correlations (IECs) in CDMFT as discussed in the previous section. This change is beneficial for the nesting of the irreducible susceptibility  $\chi_{x_-x_-x_-x_-}^0(\mathbf{q}, i\nu_0)$  as shown in Fig. S8.

In Fig. S8(a) and Fig. S8(b), we present the DMFT and CDMFT  $\beta$  pockets and their associated orbital character. Since the shape of the  $\beta$  pocket becomes more “diamond-shaped” in CDMFT, the FS sectors in which the  $x_-$  orbital occupies the entire weight, as highlighted with dotted white ovals in Fig. S8(a) and Fig. S8(b), become less curved. In addition to the shape change, spectral weight of  $x_-$  orbital near the  $X$  point gets enhanced in CDMFT. These changes in CDMFT result in i) an overall enhancement of  $\chi_{x_-x_-x_-x_-}^0(\mathbf{q}, i\nu_0)$  and ii) a better-nesting for the nesting vectors connecting the two dotted white ovals facing each other along the zone diagonal direction; see, e.g.,  $\mathbf{Q}_{\text{DMFT}}$  and  $\mathbf{Q}_{\text{CDMFT}}$ , as can be confirmed from Fig. S8(c).

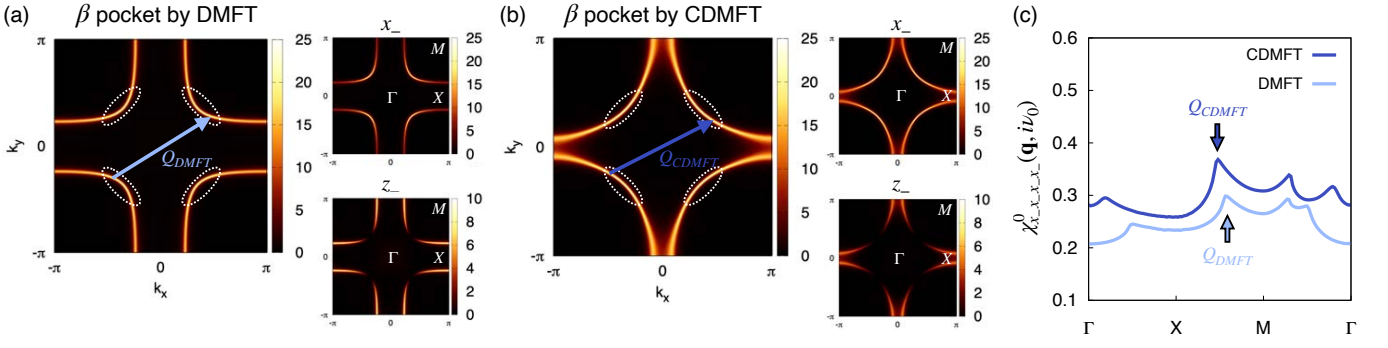


FIG. S8. The  $\beta$  Fermi surface pockets obtained from (a) DMFT and (b) CDMFT. The  $\beta$  pocket consists of both  $x_-$  and  $z_-$  orbital character as presented in the right panels. The nesting vector  $\mathbf{Q}$  is highlighted by  $\mathbf{Q}_{(C)DMFT}$ . (c)  $\chi_{x-x-x-x}^0(\mathbf{q}, i\nu_0)$  calculated using DMFT and CDMFT Green's functions.  $\mathbf{Q}_{(C)DMFT}$  and the associated values of  $\chi_{x-x-x-x}^0(\mathbf{q}, i\nu_0)$  are highlighted with colored arrows.

## SM10. GAP EQUATION

### A. Pairing interactions

To obtain the effective singlet and triplet pairing interactions, we begin with the spin and charge irreducible vertices in the particle-hole channel, which read

$$\Gamma^{\text{sp/ch}}(q, k, k')_{l_1 l_2 l_3 l_4} = \Gamma_{\text{ph}}(q, k, k')_{l_1 l_2 l_3 l_4}^{\uparrow\uparrow\downarrow\downarrow} \mp \Gamma_{\text{ph}}(q, k, k')_{l_1 l_2 l_3 l_4}^{\uparrow\uparrow\uparrow\uparrow}. \quad (\text{S15})$$

$\Gamma_{\text{ph}}(q, k, k')_{l_1 l_2 l_3 l_4}^{\sigma_1 \sigma_2 \sigma_3 \sigma_4}$  is displayed in Fig. S9.  $k \equiv (\mathbf{k}, i\omega_n)$  and  $q \equiv (\mathbf{q}, i\nu_n)$ . The spin and charge susceptibilities are obtained

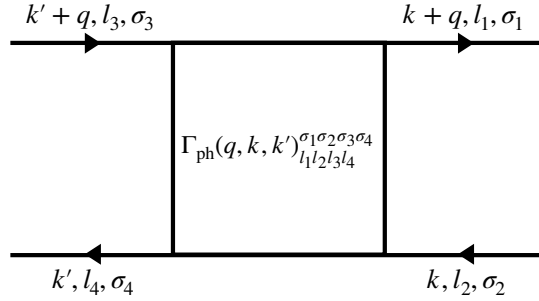


FIG. S9. The particle-hole irreducible vertex.

using these vertices from the Bethe-Salpeter equation:

$$\chi^{\text{sp/ch}}(q)_{kk'}^{l_1 l_2 l_7 l_8} = \chi^0(q)_{kk'}^{l_1 l_2 l_7 l_8} \pm \frac{T^2}{N^2} \chi^{\text{sp/ch}}(q)_{kk_1}^{l_1 l_2 l_3 l_4} \Gamma^{\text{sp/ch}}(q, k_1, k_2)_{l_3 l_4 l_5 l_6} \chi^0(q)_{k_2 k'}^{l_5 l_6 l_7 l_8}, \quad (\text{S16})$$

where  $\chi^0(q)_{kk'}^{lml'm'} = -\frac{N}{T} G_{ll'}(k+q) G_{m'm}(k') \delta_{kk'}$ . Here indices repeated twice should be summed over. We below keep this summation convention. By employing the parquet equations, one can formally express the singlet (s) and triplet (t) pairing interactions using  $\Gamma^{\text{sp/ch}}$  and  $\chi^{\text{sp/ch}}$  as [S36, S37]

$$\Gamma_{l_1 l_4 l_3 l_2}^{\text{s}}(k, k') = \Lambda^{\text{irr,s}}(k, k')_{l_1 l_4 l_3 l_2} + \frac{3}{2} \Phi^{\text{sp}}(-k + k', -k', k)_{l_2 l_4 l_3 l_1} - \frac{1}{2} \Phi^{\text{ch}}(-k + k', -k', k)_{l_2 l_4 l_3 l_1} + \frac{3}{2} \Phi^{\text{sp}}(k + k', -k', -k)_{l_1 l_4 l_3 l_2} - \frac{1}{2} \Phi^{\text{ch}}(k + k', -k', -k)_{l_1 l_4 l_3 l_2}, \quad (\text{S17})$$

$$\Gamma_{l_1 l_4 l_3 l_2}^{\text{t}}(k, k') = \Lambda^{\text{irr,t}}(k, k')_{l_1 l_4 l_3 l_2} - \frac{1}{2} \Phi^{\text{sp}}(-k + k', -k', k)_{l_2 l_4 l_3 l_1} - \frac{1}{2} \Phi^{\text{ch}}(-k + k', -k', k)_{l_2 l_4 l_3 l_1} - \frac{1}{2} \Phi^{\text{sp}}(k + k', -k', -k)_{l_1 l_4 l_3 l_2} - \frac{1}{2} \Phi^{\text{ch}}(k + k', -k', -k)_{l_1 l_4 l_3 l_2}, \quad (\text{S18})$$

where ladder vertices  $\Phi^{\text{sp/ch}}(q, k, k')_{l_1 l_2 l_7 l_8} = \frac{T^2}{N^2} \Gamma^{\text{sp/ch}}(q, k, k_1)_{l_1 l_2 l_3 l_4} \chi^{\text{sp/ch}}(q)_{k_1 k_2}^{l_3 l_4 l_5 l_6} \Gamma^{\text{sp/ch}}(q, k_2, k')_{l_5 l_6 l_7 l_8} \cdot \Lambda^{\text{irr,s/t}}(k, k')_{l_1 l_4 l_3 l_2}$  are the fully irreducible vertices in the singlet (s) and triplet (t) channels. The bare constant terms of  $\Lambda^{\text{irr,s/t}}$ , namely  $\Lambda^{0,\text{s/t}}$ , are linear combinations of bare spin and charge interaction tensors  $\mathcal{U}^{\text{sp/ch}}$ :  $\Lambda_{l_1 l_4 l_3 l_2}^{0,\text{s}} = \frac{1}{2} [3\mathcal{U}^{\text{sp}} + \mathcal{U}^{\text{ch}}]_{l_1 l_4 l_3 l_2}$  and  $\Lambda_{l_1 l_4 l_3 l_2}^{0,\text{t}} = -\frac{1}{2} [\mathcal{U}^{\text{sp}} - \mathcal{U}^{\text{ch}}]_{l_1 l_4 l_3 l_2}$ . Since the interaction tensor  $H_{\text{int}}$  [Eq. (S2)] is more sparse in the original  $e_g$ -orbital basis than the BA basis, so are the resulting  $\mathcal{U}^{\text{sp/ch}}$  which are given by  $\mathcal{U}_{l_1 l_4 l_3 l_2}^{\text{sp/ch}} = \mathcal{U}_{l_1 l_3 l_4 l_2}^{\uparrow\downarrow} \mp (\mathcal{U}_{l_1 l_3 l_4 l_2}^{\uparrow\uparrow} - \mathcal{U}_{l_1 l_4 l_3 l_2}^{\uparrow\uparrow})$ . In the  $e_g$ -orbital basis, elements of  $\mathcal{U}^{\text{sp/ch}}$  read

$$\mathcal{U}_{l_1 l_4 l_3 l_2}^{\text{sp}} = \begin{cases} U \\ U' \\ J \\ J \end{cases}, \quad \mathcal{U}_{l_1 l_4 l_3 l_2}^{\text{ch}} = \begin{cases} U & \text{if } l_1 = l_2 = l_3 = l_4, \\ -U' + 2J & \text{if } l_1 = l_3 \neq l_2 = l_4, \\ 2U' - J & \text{if } l_1 = l_4 \neq l_2 = l_3, \\ J & \text{if } l_1 = l_2 \neq l_3 = l_4, \end{cases} \quad (\text{S19})$$

for the Kanamori interaction with  $U' = U - 2J$ . Using above formulas, a superconducting instability can be formulated in terms of a non-Hermitian eigenvalue problem, namely the gap equation, which reads

$$\lambda_{\text{sc}} \Delta_{l_1 l_2}(k) = -\frac{T}{2N} \sum_{k', l_3 l_4 l_5 l_6} \Gamma_{l_1 l_4 l_3 l_2}^{\text{s/t}}(k, k') G_{l_4 l_5}(k') G_{l_3 l_6}(-k') \Delta_{l_5 l_6}(k'), \quad (\text{S20})$$

where  $\lambda_{\text{sc}}$  is the eigenvalue,  $G_{lm}(k)$  the (C)DMFT Green's function, and  $\Delta_{lm}(k)$  the anomalous self-energy (gap function). The transition temperature  $T_c$  corresponds to the temperature at which the maximum (leading) eigenvalue  $\lambda_{\text{sc}}$  reaches unity.

## B. Approximations for the pairing interactions and the resulting gap equation

Evaluating Eqs. (S17) and (S18) for the full vertex is a formidable task, it thus requires some approximations. First, we employ the well-known parquet approximation, which approximates  $\Lambda^{\text{irr,s/t}}$  by  $\Lambda^{0,\text{s/t}}$ . Within DMFT and CDMFT for our model,  $\Gamma^{\text{sp/ch}}(q, k, k')_{l_1 l_2 l_3 l_4}$  can be approximated by the momentum-independent impurity vertices  $\Gamma_{\text{imp}}^{\text{sp/ch}}(i\nu_m, i\omega_n, i\omega_{n'})_{l_1 l_2 l_3 l_4}$ , which are in principle feasible to be numerically evaluated using the continuous-time quantum Monte Carlo methods [S38]. However, for multiorbital systems huge stochastic noise prohibits us from using the measured  $\Gamma_{\text{imp}}^{\text{sp/ch}}(i\nu_m, i\omega_n, i\omega_{n'})_{l_1 l_2 l_3 l_4}$  in practice. Following an idea employed in Refs. [S39–S42], we parametrize  $\Gamma^{\text{sp/ch}}$  using effective screened Coulomb interaction  $\bar{U}$  and Hund's coupling  $\bar{J}$ , i.e., we substitute  $\Gamma^{\text{sp/ch}} \rightarrow \bar{\Gamma}^{\text{sp/ch}}(\bar{U}, \bar{J})$ . As we used for the bare interaction, the effective screened interorbital Coulomb interaction  $\bar{U}'$  obeys  $\bar{U}' = \bar{U} - 2\bar{J}$ . Note that  $\bar{U}$  and  $\bar{J}$  are generally different from bare  $U$  and  $J$  which enter  $\Lambda^{0,\text{s/t}}$ . In the  $e_g$ -orbital basis,  $\bar{\Gamma}^{\text{sp/ch}}(\bar{U}, \bar{J})$  are then given by

$$\bar{\Gamma}_{l_1 l_4 l_3 l_2}^{\text{sp}} = \begin{cases} \bar{U} \\ \bar{U}' \\ \bar{J} \\ \bar{J} \end{cases}, \quad \bar{\Gamma}_{l_1 l_4 l_3 l_2}^{\text{ch}} = \begin{cases} \bar{U} & \text{if } l_1 = l_2 = l_3 = l_4, \\ -\bar{U}' + 2\bar{J} & \text{if } l_1 = l_3 \neq l_2 = l_4, \\ 2\bar{U}' - \bar{J} & \text{if } l_1 = l_4 \neq l_2 = l_3, \\ \bar{J} & \text{if } l_1 = l_2 \neq l_3 = l_4, \end{cases} \quad (\text{S21})$$

Using this approximation,

$$\Phi^{\text{sp/ch}}(q, k, k')_{l_1 l_2 l_7 l_8} \rightarrow \bar{\Phi}^{\text{sp/ch}}(q)_{l_1 l_2 l_7 l_8} = \bar{\Gamma}_{l_1 l_2 l_3 l_4}^{\text{sp/ch}} \chi^{\text{sp/ch}}(q)_{l_3 l_4 l_5 l_6} \bar{\Gamma}_{l_5 l_6 l_7 l_8}^{\text{sp/ch}}. \quad (\text{S22})$$

Here  $\chi^{\text{sp/ch}}(q)_{l_1 l_2 l_3 l_4} \equiv \frac{T^2}{N^2} \sum_{kk'} \chi^{\text{sp/ch}}(q)_{kk'}^{l_1 l_2 l_3 l_4}$  obtained from using  $\bar{\Gamma}^{\text{sp/ch}}(\bar{U}, \bar{J})$  for the irreducible vertices in Eq. (S16):

$$\begin{aligned} \chi^{\text{sp/ch}}(q)_{l_1 l_2 l_3 l_4} &\equiv \frac{T^2}{N^2} \sum_{kk'} \chi^{\text{sp/ch}}(q)_{kk'}^{l_1 l_2 l_3 l_4} = \chi^0(q)_{l_1 l_2 l_7 l_8} \pm \chi^{\text{sp/ch}}(q)_{l_1 l_2 l_3 l_4} \bar{\Gamma}_{l_3 l_4 l_5 l_6}^{\text{sp/ch}} \chi^0(q)_{l_5 l_6 l_7 l_8}, \\ &= [\chi^0(q) [\mathbf{1} \mp \bar{\Gamma}^{\text{sp/ch}} \chi^0(q)]^{-1}]_{l_1 l_2 l_3 l_4}, \end{aligned} \quad (\text{S23})$$

where  $\chi^0(q)_{l_1 l_2 l_3 l_4} \equiv \frac{T^2}{N^2} \sum_{kk'} \chi^0(q)_{kk'}^{l_1 l_2 l_3 l_4} = -\frac{T}{N} \sum_k G_{l_1 l_3}(k+q) G_{l_4 l_2}(k)$  and  $\mathbf{1}$  is identity matrix in orbital space. We finally arrive at the gap equation presented in the main text

$$\lambda_{\text{sc}} \Delta_{l_1 l_2}(k) = -\frac{T}{2N} \sum_{k', l_3 l_4 l_5 l_6} \Gamma_{l_1 l_4 l_3 l_2}^{\text{s/t}}(k-k') G_{l_4 l_5}(k') G_{l_3 l_6}(-k') \Delta_{l_5 l_6}(k'). \quad (\text{S24})$$

Using the symmetry relations of singlet and triplet gap functions [S41, S42] the effective singlet and triplet pairing interactions  $\Gamma^{s/t}$  in Eq. (S24) are given by

$$\begin{aligned}\Gamma^s(k-k')_{l_1 l_4 l_3 l_2} &= \Lambda_{l_1 l_4 l_3 l_2}^{0,s} + 3\overline{\Phi}^{\text{sp}}(k-k')_{l_1 l_4 l_3 l_2} - \overline{\Phi}^{\text{ch}}(k-k')_{l_1 l_4 l_3 l_2}, \\ &= \Lambda_{l_1 l_4 l_3 l_2}^{0,s} + 3[\overline{\Gamma}^{\text{sp}}\chi^{\text{sp}}(k-k')\overline{\Gamma}^{\text{sp}}]_{l_1 l_4 l_3 l_2} - [\overline{\Gamma}^{\text{ch}}\chi^{\text{ch}}(k-k')\overline{\Gamma}^{\text{ch}}]_{l_1 l_4 l_3 l_2},\end{aligned}\quad (\text{S25})$$

$$\begin{aligned}\Gamma^t(k-k')_{l_1 l_4 l_3 l_2} &= \Lambda_{l_1 l_4 l_3 l_2}^{0,t} - \overline{\Phi}^{\text{sp}}(k-k')_{l_1 l_4 l_3 l_2} - \overline{\Phi}^{\text{ch}}(k-k')_{l_1 l_4 l_3 l_2}, \\ &= \Lambda_{l_1 l_4 l_3 l_2}^{0,t} - [\overline{\Gamma}^{\text{sp}}\chi^{\text{sp}}(k-k')\overline{\Gamma}^{\text{sp}}]_{l_1 l_4 l_3 l_2} - [\overline{\Gamma}^{\text{ch}}\chi^{\text{ch}}(k-k')\overline{\Gamma}^{\text{ch}}]_{l_1 l_4 l_3 l_2}.\end{aligned}\quad (\text{S26})$$

### C. Solving the gap equation using the intermediate representation basis

We solve the gap equation [Eq. (S24)] on a  $96 \times 96$   $\mathbf{k}$ -mesh using the power iteration method. We converge up to a tolerance of  $5 \cdot 10^{-5}$  for the eigenvalue  $\lambda_{\text{sc}}$  of the dominant gap function. In order to efficiently solve this self-consistent problem, we use the sparse-sampling approach [S43–S46] of the intermediate representation (IR) basis [S47, S48] and its python library `sparse-ir` [S49] for efficient data compression. To set up the IR basis functions, we use the IR basis parameter  $\Lambda_{\text{IR}} = \beta\omega_{\text{max}} = 1450$  with inverse temperature  $\beta = 145 \text{ eV}^{-1} \simeq 80 \text{ K}$  and cutoff frequency  $\omega_{\text{max}} = 10 \text{ eV}$ . We transform the (C)DMFT lattice Green's function  $G(\mathbf{k}, i\omega_n) = [(i\omega_n + \mu)\mathbb{1} - H_0(\mathbf{k}) - \Sigma(i\omega_n)]^{-1}$  data ( $\mathbb{1}$  is unity matrix in orbital space and  $\mu$  the chemical potential) on its full and equidistantly sampled frequency mesh ( $N_{\omega_n} = 1846$  for  $\omega_n > 0$ ) to the IR basis functions  $U_l$  from the expansion

$$G(i\omega_n) = \sum_{l=0}^{l_{\text{max}}} G_l U_l(i\omega_n) \quad (\text{S27})$$

via least-square fitting. We set the truncation error to  $\delta_{\text{IR}} = 10^{-5}$  to not overfit the statistical noise from the quantum Monte Carlo (QMC) simulations. This corresponds to using  $N_{\text{IR}} = l_{\text{max}} - 1 = 31$  basis coefficients. Note, that we here use the notation  $ab$  instead of  $lm$  for orbital indices  $\{\bar{x}, \bar{z}, \underline{x}, \underline{z}\}$  in the  $e_g$  basis to prevent confusion with the IR basis index  $l$ . We set the basis size from analyzing the decay of the local (C)DMFT Green's function expansion coefficients  $G_l^{\text{loc}}$  [Fig. S10(a)]. Beyond  $l_{\text{max}}$  (gray shaded area), the coefficients do not decay anymore and become larger than the exponentially decaying singular values  $S_l/S_0$  (red dashed line) of the IR basis kernel due to fitting of QMC noise. The singular values approximately set the truncation error [S49]. By taking coefficients larger than the singular values into account, the conditioning of the transformation between IR basis and Matsubara frequency/imaginary time becomes bad, i.e., the numerical error can potentially amplify in an uncontrolled manner during calculation. Fig. S10(b) shows the corresponding reconstructed Green function data on a sparsely sampled frequency grid with  $N_{\omega_n}^{\text{IR}} = l_{\text{max}} = 32$  frequency points.

## SM11. MAPPING OF INTERACTION VALUES TO STONER ENHANCEMENT FACTORS

Throughout the paper, we discuss the superconducting phase diagram in terms of the Stoner enhancement factor  $\alpha_{\text{sp}}$ . It is a proxy for the system's tendency towards a magnetic instability that we obtain from analyzing where the spin susceptibility  $\chi^{\text{sp}}$  [Eq. (S23)] diverges, i.e., where the denominator becomes zero. This is true, if the largest eigenvalue  $\alpha_{\text{sp}} = \max_q \{\overline{\Gamma}^{\text{sp}}\chi^0(q)\}$  reaches unity. Here, we comment further on the Stoner enhancement of the (C)DMFT calculations.

For a given  $\chi^0(q)$ ,  $\alpha_{\text{sp}}$  is a function of the effective Hund's coupling  $\overline{J}$  and the effective intraorbital Coulomb interaction  $\overline{U}$ . By fixing the value of  $\overline{J}/\overline{U}$ , the ratio  $\alpha_{\text{sp}}/\overline{U}$  is uniquely determined, as we show in Fig. S11(a). This function exhibits a kink around  $\overline{J}/\overline{U} \approx 0.05 - 0.06$  which is manifested as a kink in the superconducting phase boundary ( $\lambda_{\text{sc}} = 1$ ) shown in Fig. 3(a) of the main text and Fig. (S16). The kink originates from two different wave vectors  $\mathbf{Q}$  at which the eigenvalue of  $\overline{\Gamma}^{\text{sp}}\chi^0(\mathbf{Q}, i\nu_0)$  has its maximal value: around the X point  $\mathbf{Q} \approx (\pi, 0)$  for  $\overline{J}/\overline{U} \lesssim 0.06$  and an incommensurate wave vector around the M point for  $\overline{J}/\overline{U} \gtrsim 0.06$  which we here denote by  $\mathbf{Q} \approx (\kappa\pi, \kappa\pi)$  with  $\kappa < 1$ . The change between these two dominant momenta  $\mathbf{Q}$  depends on the momentum structure of  $\chi^0(q)$  [c.f. Fig. 3(b) of the main text and Fig. S14 in Sec. SM13] and on how  $\overline{J}$ ,  $\overline{U}$  mix different orbital components of  $\chi^0(q)$ . The exact location of the kink is, hence, different for the DMFT and CDMFT irreducible susceptibilities. It is noticeable that  $\alpha_{\text{sp}}/\overline{U}$  of the DMFT calculation is generally larger than that of the CDMFT calculation.

For completeness, we mention that an identical analysis of possible charge instabilities can be made. Here, the charge Stoner enhancement  $\alpha_{\text{ch}} = \max_q \{-\overline{\Gamma}^{\text{ch}}\chi^0(q)\}$  needs to be analyzed [Fig. S11(b)]. This system, however, does not host any charge instability because  $\alpha_{\text{ch}}$  is too small.

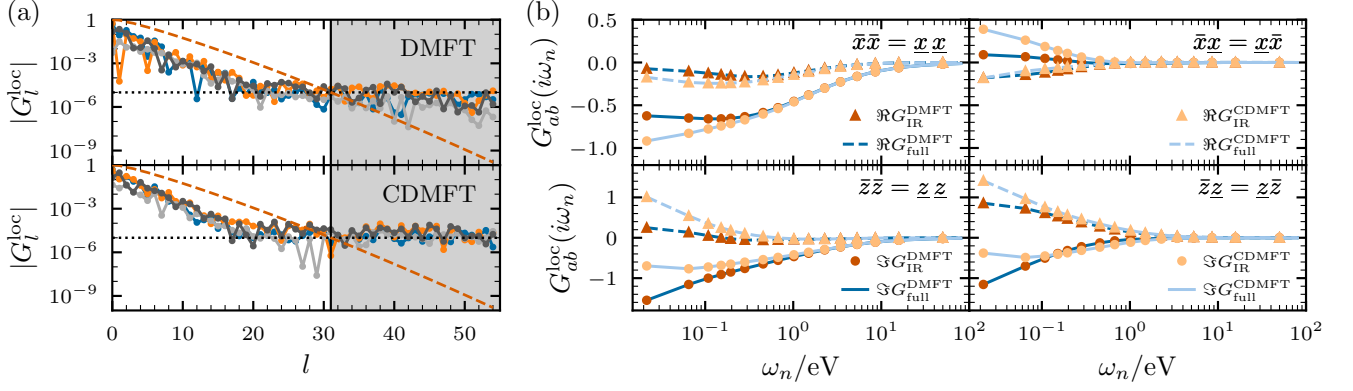


FIG. S10. Representation of local (C)DMFT Green's functions  $G_l^{\text{loc}} = \frac{1}{N_k} \sum_{\mathbf{k}} G_l(\mathbf{k})$  in the IR basis. (a) Expansion coefficients  $G_l$  as a function of expansion order  $l$ . Colored lines with dots correspond to coefficients for different orbital components in the  $e_g$  basis. The red dashed line corresponds to the truncation error set by the singular values. We cut the expansion after  $l_{\text{max}} = 31$  coefficients (vertical solid line) with a truncation error of  $\delta_{\text{IR}} = 10^{-5}$  (horizontal dotted line), such that the coefficients in the gray shaded area are disregarded. (b) Reconstruction of the (C)DMFT Green's function orbital components ( $a, b \in \{\bar{x}, \bar{z}, \underline{x}, \underline{z}\}$ ) on a sparse frequency grid from the IR basis. Markers and lines represent data on the sparse IR grid and full equidistant grid, respectively. Note the logarithmic frequency axis.

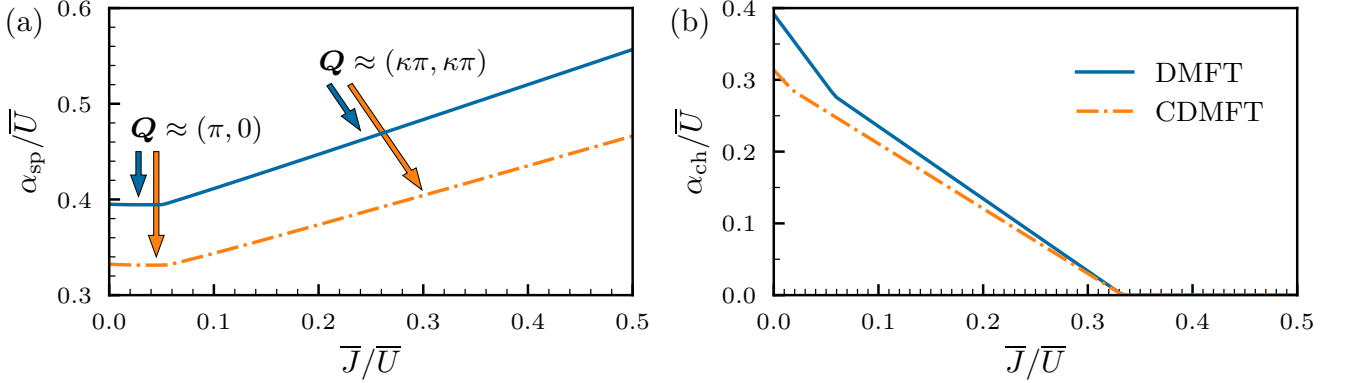


FIG. S11. Stoner enhancement factor in the (a) magnetic and (b) charge channel for the irreducible susceptibility of the (C)DMFT as a function of interaction ratio  $\bar{J}/\bar{U}$ . The kink around  $\bar{J}/\bar{U} \approx 0.05-0.06$  originates from different  $\mathbf{Q}$  vectors contributing to the maximal eigenvalue of  $\bar{\Gamma}^{\text{sp}} \chi^0(\mathbf{Q}, i\nu_0)$  as indicated by arrows.

## SM12. SPIN SUSCEPTIBILITY

While the  $\gamma$  pocket gives rise to strong ferromagnetic fluctuations, the actual magnetic transition occurs at a finite transfer momentum as shown in Fig. S12. Figure S12 presents the calculated maximum eigenvalue of the spin susceptibility at each  $\mathbf{q}$ ,  $\chi_{\text{max}}^{\text{sp}}(\mathbf{q}, i\nu_0)$ . A peak of  $\chi_{\text{max}}^{\text{sp}}(\mathbf{q}, i\nu_0)$  at  $\mathbf{q} = \mathbf{Q}$  would result in a spin-density wave (SDW) with the ordering vector  $\mathbf{Q}$ .

For  $t_{\perp}^z = -0.45$  eV,  $\chi_{\text{max}}^{\text{sp}}(\mathbf{q}, i\nu_0)$  shows a peak at  $\mathbf{Q}_{\text{SDW}}$  which is different from but close to the SDW ordering wave vector  $\mathbf{Q}_{\text{SDW}}^{\text{exp}} = (0.5, 0.5)\pi$  (or  $\mathbf{Q}_{\text{SDW}}^{\text{exp}} = (0.25, 0.25)$  if we follow the notation of Ref. [S32]) reported by experiments under ambient pressure [S32, S33]. On the other hand, in the high-pressure phase ( $t_{\perp}^z = -0.63$  eV)  $\chi_{\text{max}}^{\text{sp}}(\mathbf{q}, i\nu_0)$  forms an arc not a peak; see the rightmost panels in Fig. S12. The strong ferromagnetic fluctuation by the  $\gamma$  pocket is captured in Fig. S12 in that depressurizing the system (by reducing the magnitude of  $t_{\perp}^z$ ) enhances  $\chi_{\text{max}}^{\text{sp}}(\mathbf{q}, i\nu_0)$  at  $\mathbf{q} = 0$ , in accordance with the evolution of the Fermi surface in Fig. 4(b) of the main text.

Importantly, the aforementioned peak of  $\chi_{\text{max}}^{\text{sp}}(\mathbf{q}, i\nu_0)$  at  $\mathbf{q} = \mathbf{Q}_{\text{SDW}}$  in the low-pressure phase is not driven by the  $\gamma$  pocket, but by the  $\alpha$ - $\beta$  nesting. To see this, we present in Fig. S13 the orbital-resolved spin susceptibilities,  $\chi_{lmml}^{\text{sp}}(\mathbf{q}, i\nu_0)$  and  $\chi_{lmml}^{\text{sp}}(\mathbf{q}, i\nu_0)$  for both the smallest and the largest  $t_{\perp}^z$  we used. For simplicity we hereafter use indices 1, 2, 3, and 4 for  $x_+$ ,  $z_+$ ,  $x_-$ , and  $z_-$  orbitals, respectively. Interestingly, the left panel in Fig. S13 shows that  $\chi_{2222}^{\text{sp}}(\mathbf{q}, i\nu_0)$  is the largest element for  $t_{\perp}^z = -0.45$  eV and exhibits the maximum at  $\mathbf{q} = 0$  because of the  $\gamma$  pocket crossing the Fermi level. It looks first at odds with  $\chi_{\text{max}}^{\text{sp}}(\mathbf{q}, i\nu_0)$  presented in Fig. S12, where  $\mathbf{q}$  shows a peak at  $\mathbf{Q}_{\text{SDW}}$ , not at  $\mathbf{q} = 0$ . It should be noted that the two sublead-



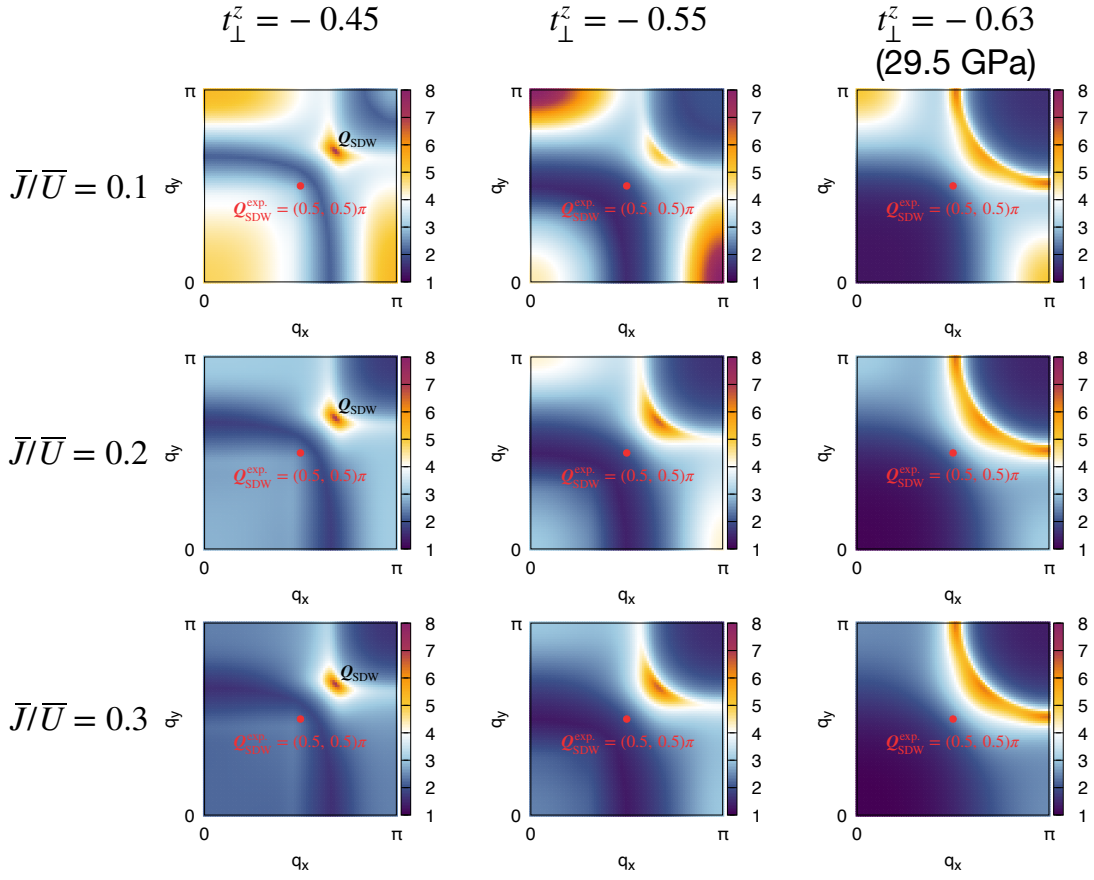


FIG. S12.  $\chi_{\max}^{\text{sp}}(\mathbf{q}, i\nu_0)$  at  $\alpha_{\text{sp}} = 0.95$ . The suggested magnetic ordering vector under ambient pressure in experiments,  $\mathbf{Q}_{\text{SDW}}^{\text{exp}}$  [S32, S33], is highlighted with red circles in each panel.

ing elements, namely  $\chi_{3131}^{\text{sp}}(\mathbf{q}, i\nu_0)$  and  $\chi_{4242}^{\text{sp}}(\mathbf{q}, i\nu_0)$  show the peak at  $\mathbf{q} = \mathbf{Q}_{\text{SDW}}$ . Thus these two elements dominate over  $\chi_{2222}^{\text{sp}}(\mathbf{q}, i\nu_0)$ , giving rise to the largest value of  $\chi_{\max}^{\text{sp}}(\mathbf{q}, i\nu_0)$  at  $\mathbf{q} = \mathbf{Q}_{\text{SDW}}$ . The  $\mathbf{Q}_{\text{SDW}}$  corresponds to the vector connecting the  $\alpha$  and the  $\beta$  FS pockets as depicted in Fig. 4(b) of the main text. The discrepancy between the  $\mathbf{Q}_{\text{SDW}}^{\text{exp}}$  and  $\mathbf{Q}_{\text{SDW}}$  can be attributed to the size of the  $\alpha$  and  $\beta$  pockets in simulating the low-pressure phases for which we neglected the change of in-plane hoppings due to the octahedral distortions present in the ambient-pressure structure.

In the high-pressure phase ( $t_{\perp}^z = -0.63$  eV)  $\chi_{\max}^{\text{sp}}(\mathbf{q}, i\nu_0)$  is quenched due to the disappearance of the  $\gamma$  pocket; see the right panel in Fig. S13. Here  $\chi_{3131}^{\text{sp}}(\mathbf{q}, i\nu_0)$  and  $\chi_{4242}^{\text{sp}}(\mathbf{q}, i\nu_0)$  are the largest elements which lead to the strong pair scattering between the bonding  $\alpha$  and the antibonding  $\beta$  pockets in line with the  $s_{\pm}$ -wave gap symmetry.

### SM13. ADDITIONAL DATA: STRUCTURE OF PAIRING VERTEX AND THE $s_{\pm}$ -WAVE GAP FUNCTION

In the main text, we discuss the dominant pairing symmetry which is the intraorbital  $s$ -wave/interorbital  $d_{x^2-y^2}$ -wave pairing in the original  $e_g$ -orbital basis, which corresponds to the  $s_{\pm}$ -wave symmetry by projecting it to the noninteracting FS. Apart from this symmetry, we checked many possible trial gap functions with different sign combinations of spin ( $S$ ), parity ( $P$ ), orbital ( $O$ ), and time-reversal ( $T$ ) symmetry which are in line with the  $D_{4h}$  symmetry of the model. Importantly, throughout the whole  $\alpha_{\text{sp}} - \bar{J}/\bar{U}$  plane, none of these pairing channels have an eigenvalue larger than that of the  $s_{\pm}$ -wave symmetry. Only a subleading channel with intraorbital  $d_{x^2-y^2}$ /interorbital  $s$ -wave pairing reaches for the CDMFT electronic structure an eigenvalue  $\lambda_{\text{sc}}$  of unity in the region of  $\alpha_{\text{sp}} \gtrsim 0.96$  and  $\bar{J}/\bar{U} \gtrsim 0.06$ .

Here, we discuss the full orbital and momentum structure of the dominant gap function  $\Delta_{lm}(\mathbf{k}, i\omega_0)$  and dominant matrix elements of the singlet pairing vertex  $\Gamma_{llmm}^{\text{s}}(\mathbf{q}, i\nu_0)$  obtained from the CDMFT electronic structure. We show those in Fig. S14 for  $\bar{J}/\bar{U} = 0.04$  and  $0.2$  at  $\alpha_{\text{sp}} = 0.95$  in the  $e_g$ -orbital basis; see Fig. S15 for the corresponding gap functions projected to the noninteracting FS, which shows clearly the  $s_{\pm}$ -wave symmetry. The vertex generally has an orbital block structure with intralayer components being positive and interlayer components being negative which originates from the interlayer AFM fluctuations. The different dominant pairing vectors  $\mathbf{Q}$  discussed in the main text and in Sec. SM11 can be easily distinguished

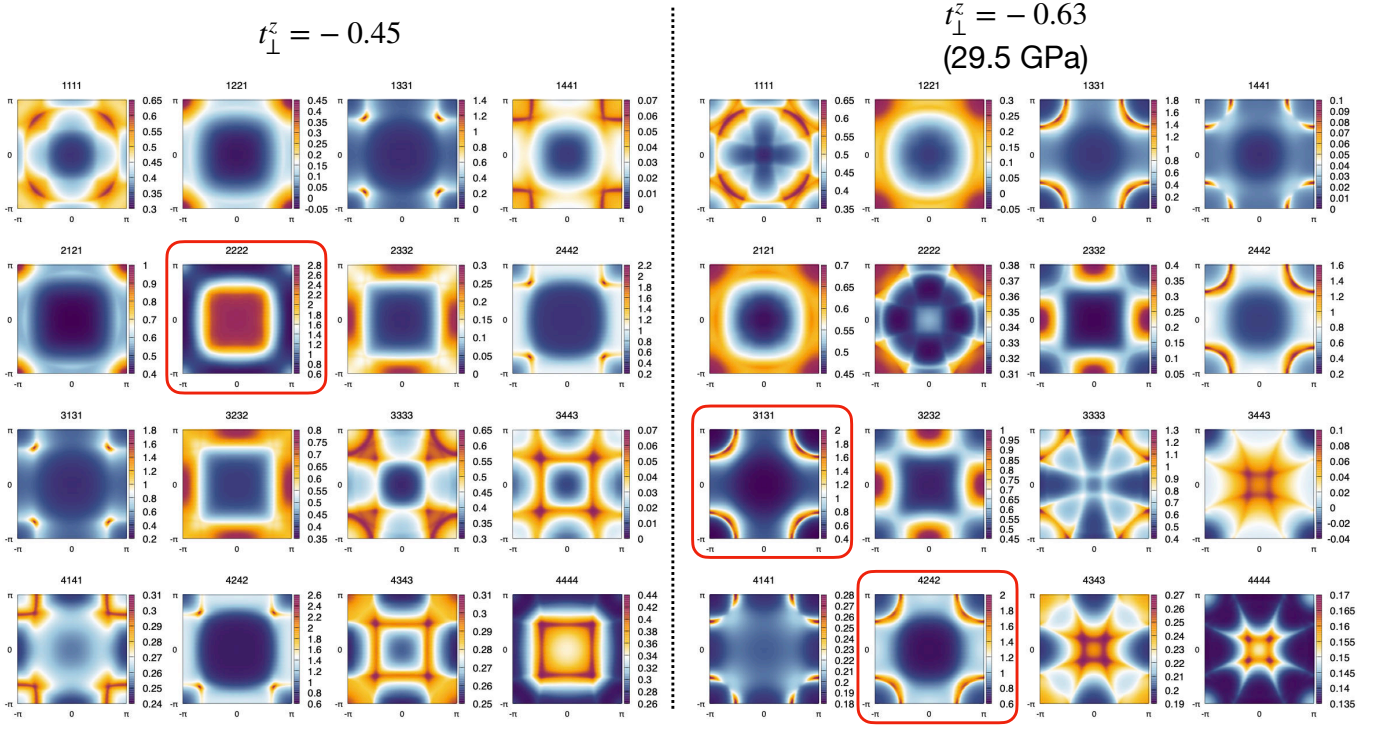


FIG. S13. The orbital-resolved spin susceptibility  $\chi_{lmm}^{\text{SP}}(\mathbf{q}, i\nu_0)$  and  $\chi_{lmlm}^{\text{SP}}(\mathbf{q}, i\nu_0)$  at  $\alpha_{\text{SP}} = 0.95$  and  $\bar{J}/\bar{U} = 0.2$ . Indices 1, 2, 3, and 4 correspond to  $x_+$ ,  $z_+$ ,  $x_-$ , and  $z_-$  orbitals, respectively. The matrix elements highlighted with red boxes correspond to the largest elements for each  $t_{\perp}^z$ .

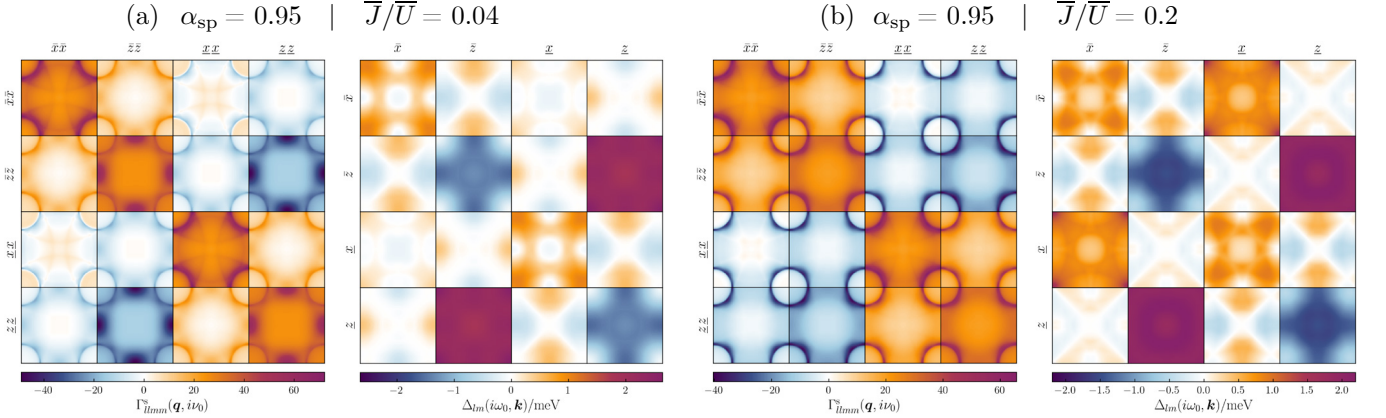


FIG. S14. Orbital and momentum space structure of the dominant singlet pairing vertex components  $\Gamma_{llmm}^{\text{s}}(\mathbf{q}, i\nu_0)$  and gap function  $\Delta_{lm}(\mathbf{k}, i\nu_0)$  for  $\alpha_{\text{SP}} = 0.95$  and two values of the interaction ratio  $\bar{J}/\bar{U} = 0.04$  (a) and  $0.2$  (b). Note that the quantities are presented in the  $e_g$ -orbital basis.

by comparing panels (a) and (b). However, increasing  $\bar{J}/\bar{U}$  does not only change the dominant  $\mathbf{Q}$  vector, but it also changes the relative weight of the orbital components. Namely, for small  $\bar{J}/\bar{U}$  mostly intraorbital components  $\Gamma_{lll}^{\text{s}}$  and the interlayer  $z$  components  $\Gamma_{zzz}^{\text{s}}$  play a role, whereas for larger  $\bar{J}/\bar{U}$  the magnitude of the components increases and evens out. This, in turn, affects the orbital structure of the dominant gap. By increasing  $\bar{J}/\bar{U}$ , the gap function gains more weight in the interlayer  $x$ -component  $\Delta_{\bar{x}\bar{x}}$ , i.e., the gap opening on the FS pockets with  $x_{\pm}$  character is enhanced.

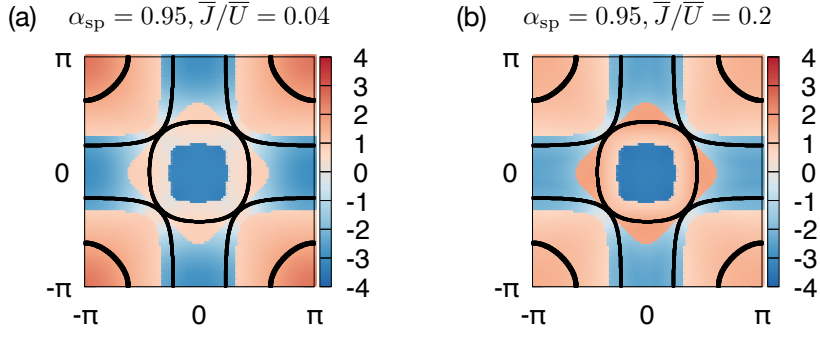


FIG. S15. Gap functions  $\hat{\Delta}_n(\mathbf{k}, i\omega_0)$  (in meV) obtained by projecting  $\Delta_{lm}(\mathbf{k}, i\omega_0)$  at each  $\mathbf{k}$  to the band  $n$  closest to the Fermi level.  $\hat{\Delta}_n(\mathbf{k}, i\omega_0) = \sum_{lm} P_{nl}^{-1} \Delta_{lm}(\mathbf{k}, i\omega_0) P_{mn}$  where  $P_{mn}$  ( $P_{nl}^{-1}$ ) is the basis-transformation matrix from the  $e_g$ -orbital  $m$  ( $l$ ) to the band  $n$  closest to the Fermi level. The black solid lines indicate the noninteracting FS obtained from DFT.

#### SM14. ADDITIONAL DATA: THE CRITICAL ROLE OF FM $\chi_{z_+z_+z_+z_+}^0(q)$ IN THE SINGLET PAIRING

As we have discussed in the main text, the disappearance of the  $\gamma$  pocket from the FS due to IECs within CDMFT results leads to the suppression of the FM fluctuation arising from  $\chi_{z_+z_+z_+z_+}^0(q, i\nu_0)$ . In the singlet channel, this FM fluctuation is directly manifested by a repulsive (rather than attractive) interaction  $\Gamma_{\bar{z}\bar{z}\bar{z}\bar{z}}^s(q=0)$ . Quenching of the FM  $\chi_{z_+z_+z_+z_+}^0$  as in CDMFT yields the attractive pairing interaction  $\Gamma_{\bar{z}\bar{z}\bar{z}\bar{z}}^s(q=0)$  between top and bottom layer  $z$  orbitals as clearly shown in Fig. S16(b–d) for three distinct  $\bar{J}/\bar{U}$  values. This, in turn, promotes the singlet pairing as evidenced by the enhanced superconducting instabilities in CDMFT [Fig. S16(a)].

To further corroborate this argument, we analyze how the DMFT superconducting instabilities are affected by the FM fluctuation by introducing a scaling factor  $\zeta$  for  $\chi_{z_+z_+z_+z_+}^0(q)$ . Namely,  $\chi_{z_+z_+z_+z_+}^0(q)$  is rescaled to  $\zeta\chi_{z_+z_+z_+z_+}^0(q)$  before constructing  $\chi^{\text{sp/ch}}$  and  $\Gamma^s$ , and then we monitor how  $\lambda_{\text{sc}}$  behaves due to this change.

Interestingly, indeed,  $\lambda_{\text{sc}}$  increases with decreasing  $\zeta$  for all the  $\bar{J}/\bar{U}$  values we investigated. Looking into the related spin susceptibilities, the components involving solely  $\bar{z}$  or  $z$  characters are found to be most affected by the rescaled  $\chi_{z_+z_+z_+z_+}^0(q)$  as expected. In effect, as presented in Fig. S16(b–d), the interlayer FM spin susceptibility  $\chi_{\bar{z}\bar{z}\bar{z}\bar{z}}^{\text{sp}}(q=0)$  at  $\zeta=1$  becomes AFM with decreasing  $\zeta$ . Through Eq. (S25)  $\chi_{\bar{z}\bar{z}\bar{z}\bar{z}}^{\text{sp}}(q)$  directly affects the corresponding pairing interaction  $\Gamma_{\bar{z}\bar{z}\bar{z}\bar{z}}^s(q)$ , whereby it should faithfully follow the behavior of  $\chi_{\bar{z}\bar{z}\bar{z}\bar{z}}^{\text{sp}}(q)$ . As such, the repulsive pairing interaction  $\Gamma_{\bar{z}\bar{z}\bar{z}\bar{z}}^s(q=0)$  at  $\zeta=1$  turns attractive below  $\zeta \simeq 0.9$  (for all the  $\bar{J}/\bar{U}$  values) at which  $\chi_{\bar{z}\bar{z}\bar{z}\bar{z}}^{\text{sp}}(q=0)$  changes its sign; see orange lines in the lower panels of Fig. S16(b–d).

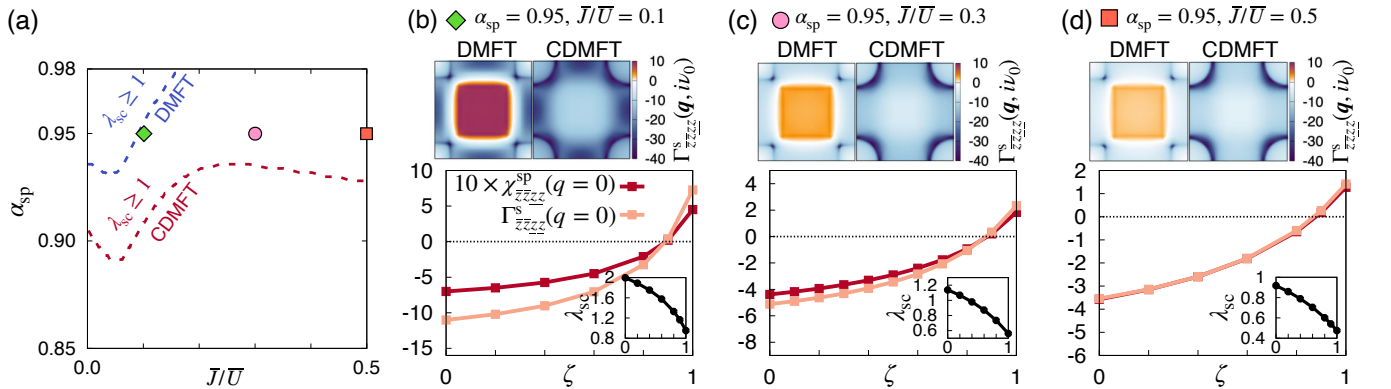


FIG. S16. (a) Superconducting phase diagram in the  $\alpha_{\text{sp}}-\bar{J}/\bar{U}$  space at  $T = 1/145$  eV  $\simeq 80$  K. The superconductivity sets in (i.e.,  $\lambda_{\text{sc}} \geq 1$ ) in the regions above the dashed lines; blue for the DMFT and red for the CDMFT. (b–d) Upper panel: the spin-singlet pairing interaction  $\Gamma_{\bar{z}\bar{z}\bar{z}\bar{z}}^s(\mathbf{q}, i\nu_0)$  between top and bottom layer  $z$  orbitals in the FBZ. Lower panel:  $\chi_{\bar{z}\bar{z}\bar{z}\bar{z}}^{\text{sp}}(q=0)$ ,  $\Gamma_{\bar{z}\bar{z}\bar{z}\bar{z}}^s(q=0)$ , and  $\lambda_{\text{sc}}$  (inset) as a function of scaling factor  $\zeta$  for DMFT  $\chi_{z_+z_+z_+z_+}^0(q)$ .

- [S1] Y. Gu, C. Le, Z. Yang, X. Wu, and J. Hu, **Effective model and pairing tendency in bilayer Ni-based superconductor  $\text{La}_3\text{Ni}_2\text{O}_7$**  (2023), arXiv:2306.07275 [cond-mat].
- [S2] V. Christiansson, F. Petocchi, and P. Werner, **Phys. Rev. Lett.** **131**, 206501 (2023).
- [S3] J. Yang, H. Sun, X. Hu, Y. Xie, T. Miao, H. Luo, H. Chen, B. Liang, W. Zhu, G. Qu, C.-Q. Chen, M. Huo, Y. Huang, S. Zhang, F. Zhang, F. Yang, Z. Wang, Q. Peng, H. Mao, G. Liu, Z. Xu, T. Qian, D.-X. Yao, M. Wang, L. Zhao, and X. J. Zhou, **Nature Communications** **15**, 4373 (2024).
- [S4] Z. Liu, M. Huo, J. Li, Q. Li, Y. Liu, Y. Dai, X. Zhou, J. Hao, Y. Lu, M. Wang, and H.-H. Wen, **Electronic correlations and energy gap in the bilayer nickelate  $\text{La}_3\text{Ni}_2\text{O}_7$**  (2023), arXiv:2307.02950 [cond-mat].
- [S5] J. Mravlje, M. Aichhorn, T. Miyake, K. Haule, G. Kotliar, and A. Georges, **Physical Review Letters** **106**, 096401 (2011), publisher: American Physical Society.
- [S6] S. Ryee, M. J. Han, and S. Choi, **Physical Review Letters** **126**, 206401 (2021), publisher: American Physical Society.
- [S7] S. Ryee, S. Choi, and M. J. Han, **Physical Review Research** **5**, 033134 (2023), publisher: American Physical Society.
- [S8] T. Ayral, S. Biermann, and P. Werner, **Physical Review B** **87**, 125149 (2013), publisher: American Physical Society.
- [S9] M. Schüler, M. Rösner, T. O. Wehling, A. I. Lichtenstein, and M. I. Katsnelson, **Physical Review Letters** **111**, 036601 (2013), publisher: American Physical Society.
- [S10] E. G. C. P. van Loon, M. Schüler, M. I. Katsnelson, and T. O. Wehling, **Physical Review B** **94**, 165141 (2016), publisher: American Physical Society.
- [S11] F. Nilsson, L. Boehnke, P. Werner, and F. Aryasetiawan, **Physical Review Materials** **1**, 043803 (2017), publisher: American Physical Society.
- [S12] S. Ryee, P. Sémon, M. J. Han, and S. Choi, **npj Quantum Materials** **5**, 1 (2020), number: 1 Publisher: Nature Publishing Group.
- [S13] A. Georges, L. d. Medici, and J. Mravlje, **Annual Review of Condensed Matter Physics** **4**, 137 (2013).
- [S14] A. H. Nevidomskyy and P. Coleman, **Physical Review Letters** **103**, 147205 (2009), publisher: American Physical Society.
- [S15] Z. P. Yin, K. Haule, and G. Kotliar, **Physical Review B** **86**, 195141 (2012), publisher: American Physical Society.
- [S16] C. Aron and G. Kotliar, **Physical Review B** **91**, 041110 (2015), publisher: American Physical Society.
- [S17] S. Ryee and T. O. Wehling, **Nano Letters** **23**, 573 (2023), <https://doi.org/10.1021/acs.nanolett.2c04169>.
- [S18] D. A. Shilenko and I. V. Leonov, **Physical Review B** **108**, 125105 (2023), publisher: American Physical Society.
- [S19] F. Lechermann, J. Gondolf, S. Bötzel, and I. M. Eremin, **Phys. Rev. B** **108**, L201121 (2023).
- [S20] L. Wang, Y. Li, S. Xie, F. Liu, H. Sun, C. Huang, Y. Gao, T. Nakagawa, B. Fu, B. Dong, Z. Cao, R. Yu, S. I. Kawaguchi, H. Kadobayashi, M. Wang, C. Jin, H. Kwang Mao, and H. Liu, Structure responsible for the superconducting state in  $\text{La}_3\text{Ni}_2\text{O}_7$  at high pressure and low temperature conditions (2023), arXiv:2311.09186 [cond-mat.supr-con].
- [S21] H. LaBollita, V. Pardo, M. R. Norman, and A. S. Botana, **Electronic structure and magnetic properties of  $\text{La}_3\text{Ni}_2\text{O}_7$  under pressure** (2023), arXiv:2309.17279 [cond-mat].
- [S22] Y. Zhang, L.-F. Lin, A. Moreo, T. A. Maier, and E. Dagotto, **Nature Communications** **15**, 2470 (2024).
- [S23] Z. Luo, X. Hu, M. Wang, W. Wú, and D.-X. Yao, **Physical Review Letters** **131**, 126001 (2023), publisher: American Physical Society.
- [S24] Y. Zhang, L.-F. Lin, A. Moreo, and E. Dagotto, **Phys. Rev. B** **108**, L180510 (2023).
- [S25] Y. Cao and Y.-f. Yang, **Phys. Rev. B** **109**, L081105 (2024).
- [S26] H. Sakakibara, N. Kitamine, M. Ochi, and K. Kuroki, **Phys. Rev. Lett.** **132**, 106002 (2024).
- [S27] Y.-B. Liu, J.-W. Mei, F. Ye, W.-Q. Chen, and F. Yang, **Phys. Rev. Lett.** **131**, 236002 (2023).
- [S28] Y. Zhang, L.-F. Lin, A. Moreo, T. A. Maier, and E. Dagotto, **Phys. Rev. B** **108**, 165141 (2023).
- [S29] H. Sun, M. Huo, X. Hu, J. Li, Z. Liu, Y. Han, L. Tang, Z. Mao, P. Yang, B. Wang, J. Cheng, D.-X. Yao, G.-M. Zhang, and M. Wang, **Nature** **621**, 493 (2023), number: 7979 Publisher: Nature Publishing Group.
- [S30] B. Geisler, J. J. Hamlin, G. R. Stewart, R. G. Hennig, and P. J. Hirschfeld, **npj Quantum Materials** **9**, 38 (2024).
- [S31] Y. Zhou, J. Guo, S. Cai, H. Sun, P. Wang, J. Zhao, J. Han, X. Chen, Q. Wu, Y. Ding, M. Wang, T. Xiang, H. Kwang Mao, and L. Sun, Evidence of filamentary superconductivity in pressurized  $\text{La}_3\text{Ni}_2\text{O}_7$  single crystals (2023), arXiv:2311.12361 [cond-mat.supr-con].
- [S32] X. Chen, J. Choi, Z. Jiang, J. Mei, K. Jiang, J. Li, S. Agrestini, M. Garcia-Fernandez, X. Huang, H. Sun, D. Shen, M. Wang, J. Hu, Y. Lu, K.-J. Zhou, and D. Feng, Electronic and magnetic excitations in  $\text{La}_3\text{Ni}_2\text{O}_7$  (2024), arXiv:2401.12657 [cond-mat.supr-con].
- [S33] Z. Dan, Y. Zhou, M. Huo, Y. Wang, L. Nie, M. Wang, T. Wu, and X. Chen, Spin-density-wave transition in double-layer nickelate  $\text{La}_3\text{Ni}_2\text{O}_7$  (2024), arXiv:2402.03952 [cond-mat.supr-con].
- [S34] X. Du, Y. D. Li, Y. T. Cao, C. Y. Pei, M. X. Zhang, W. X. Zhao, K. Y. Zhai, R. Z. Xu, Z. K. Liu, Z. W. Li, J. K. Zhao, G. Li, Y. L. Chen, Y. P. Qi, H. J. Guo, and L. X. Yang, Correlated electronic structure and density-wave gap in trilayer nickelate  $\text{La}_4\text{Ni}_3\text{O}_{10}$  (2024), arXiv:2405.19853 [cond-mat.supr-con].
- [S35] H. Li, X. Zhou, T. Nummy, J. Zhang, V. Pardo, W. E. Pickett, J. F. Mitchell, and D. S. Dessau, **Nature Communications** **8**, 704 (2017).
- [S36] N. E. Bickers, in **Theoretical Methods for Strongly Correlated Electrons**, CRM Series in Mathematical Physics, edited by D. Sénéchal, A.-M. Tremblay, and C. Bourbonnais (Springer, New York, NY, 2004) pp. 237–296.
- [S37] G. Rohringer, H. Hafermann, A. Toschi, A. Katanin, A. Antipov, M. Katsnelson, A. Lichtenstein, A. Rubtsov, and K. Held, **Reviews of Modern Physics** **90**, 025003 (2018), publisher: American Physical Society.
- [S38] E. Gull, A. J. Millis, A. I. Lichtenstein, A. N. Rubtsov, M. Troyer, and P. Werner, **Rev. Mod. Phys.** **83**, 349 (2011).
- [S39] T. A. Maier, M. Jarrell, and D. J. Scalapino, **Physical Review B** **75**, 134519 (2007), publisher: American Physical Society.
- [S40] R. Nourafkan, G. Kotliar, and A.-M. Tremblay, **Physical Review Letters** **117**, 137001 (2016), publisher: American Physical Society.
- [S41] O. Gingras, R. Nourafkan, A.-M. S. Tremblay, and M. Côté, **Physical Review Letters** **123**, 217005 (2019), publisher: American Physical Society.

- [S42] S. Käser, H. U. R. Strand, N. Wentzell, A. Georges, O. Parcollet, and P. Hansmann, *Physical Review B* **105**, 155101 (2022), publisher: American Physical Society.
- [S43] J. Li, M. Wallerberger, N. Chikano, C.-N. Yeh, E. Gull, and H. Shinaoka, *Phys. Rev. B* **101**, 035144 (2020), [arxiv:1908.07575](https://arxiv.org/abs/1908.07575).
- [S44] N. Witt, E. G. C. P. van Loon, T. Nomoto, R. Arita, and T. O. Wehling, *Physical Review B* **103**, 205148 (2021), publisher: American Physical Society.
- [S45] N. Witt, J. M. Pizarro, J. Berges, T. Nomoto, R. Arita, and T. O. Wehling, *Physical Review B* **105**, L241109 (2022).
- [S46] N. Witt, L. Si, J. M. Tomczak, K. Held, and T. O. Wehling, *SciPost Phys.* **15**, 197 (2023).
- [S47] H. Shinaoka, J. Otsuki, M. Ohzeki, and K. Yoshimi, *Physical Review B* **96**, 035147 (2017).
- [S48] H. Shinaoka, N. Chikano, E. Gull, J. Li, T. Nomoto, J. Otsuki, M. Wallerberger, T. Wang, and K. Yoshimi, *SciPost Physics Lecture Notes* [10.21468/scipostphyslectnotes.63](https://doi.org/10.21468/scipostphyslectnotes.63) (2022).
- [S49] M. Wallerberger, S. Badr, S. Hoshino, S. Huber, F. Kakizawa, T. Koretsune, Y. Nagai, K. Nogaki, T. Nomoto, H. Mori, J. Otsuki, S. Ozaki, T. Plaikner, R. Sakurai, C. Vogel, N. Witt, K. Yoshimi, and H. Shinaoka, *SoftwareX* **21**, 101266 (2023).

### 4.3 Moiré materials

Two-dimensional vdW materials and their functionalization in heterostructures represent one of the most versatile platforms for studying, tuning, and simulating emergent quantum phenomena [22, 158, 162]. These materials offer a high degree of (non-invasive) control over key system parameters, such as the electron density through electrostatic doping from gate voltage or chemical doping via adatoms [69, 77, 162], interaction strength modified by environmental screening [163, 630–632], and responses to electromagnetic fields [74, 75, 633].

In this context, moiré materials serve as a new quantum platform that took over the condensed matter community in the past six years [21–24]. These materials are formed either by rotational misalignment of identical two-dimensional atomic crystals or by lattice mismatch of dissimilar ones, as depicted in Figure 4.4(a,d). Such incommensurability results in long-wavelength interference patterns between the two constituent atomic lattices, forming an enlarged moiré superlattice with lattice constant  $\lambda_M$  on the order of  $O(10 \text{ nm})$ . The emergence of this additional length scale effectively enables the decoupling of low-energy physics, governed by  $\lambda_M$ , from the high-energy physics, dictated by the original lattice spacing  $a$ .

The moiré pattern creates a periodic potential with periodicity  $\lambda_M$ , which leads to a modulation of electronic properties, such as the emergence of flat bands and correlated electronic phases [24, 77, 163, 634]. A simple scaling argument illustrates the flattening of electronic bands and tuning of correlation strength in twisted materials: The emergent moiré length scale as a function of twist angle  $\theta$  is given by  $\lambda_M(\theta) = a/(2 \sin(\theta/2)) \sim \theta^{-1}$  [635]. Assuming free electrons (parabolic dispersion), the kinetic energy  $W$  and Coulomb interaction  $U$  scale with the twist angle as

$$\left. \begin{aligned} W &= \frac{\hbar^2}{2m} \frac{1}{\lambda_M^2} \propto \theta^2 \\ U &= \frac{e^2}{\kappa} \frac{1}{\lambda_M} \propto \theta \end{aligned} \right\} \Rightarrow \frac{U}{W} \propto \frac{1}{\theta}. \quad (4.1)$$

Thus, by adjusting the twist angle and the screening environment (represented by the dielectric constant  $\kappa$ ), one can fine-tune the degree of correlation strength (cf. supplemental Fig. SM5(b) of publication IV).

The experimental breakthrough of moiré materials began with the successful synthesis of magic-angle twisted bilayer graphene (MATBG) [77, 163], which itself hosts a wide array of correlated and topological phases (see Figures 1.1c and 4.4b). Since then, a plethora of moiré materials have been experimentally discovered and theoretically suggested [21–24], giving rise to complex and rich phase diagrams filled with correlated electronic and topologically protected states, as illustrated in Figure 4.4 for MATBG and different TMDC-based moiré materials. The high

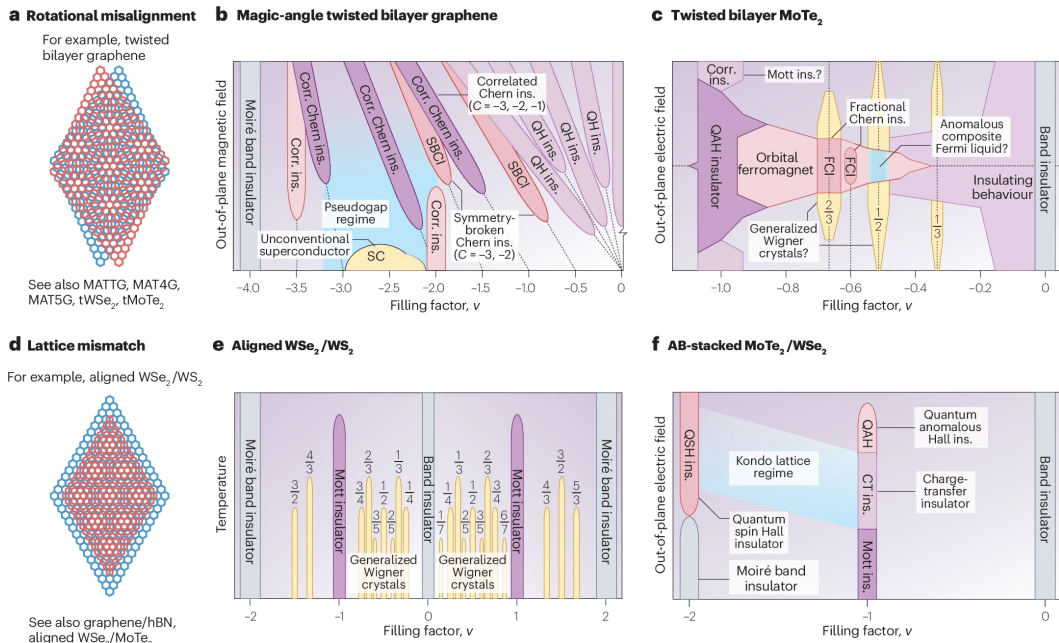


**Figure 4.4 – Phase diagrams of moiré materials.** Schematic of moiré structures created from (a) rotational misalignment or (d) a lattice mismatch. Panels b, c, e, and f show schematic phase diagrams of different moiré materials as a function of out-of-plane magnetic or electric fields, temperature, and filling factor  $\nu$ . They host different correlated and topological states including unconventional superconductivity (SC), a high-field pseudogap regime, correlated Mott or charge-transfer insulators (corr. ins.), different types of quantum Hall insulators (QH ins.), different types of Chern insulators (CI), magnetic phases, or generalized Wigner crystal states. Further abbreviations: symmetry-broken CI (SBCI), fractional CI (fCI), quantum anomalous Hall (QAH), quantum spin Hall (QSH). Reprinted from [24] with permission from © 2024 Springer Nature. Not covered by the CC BY 4.0 license.

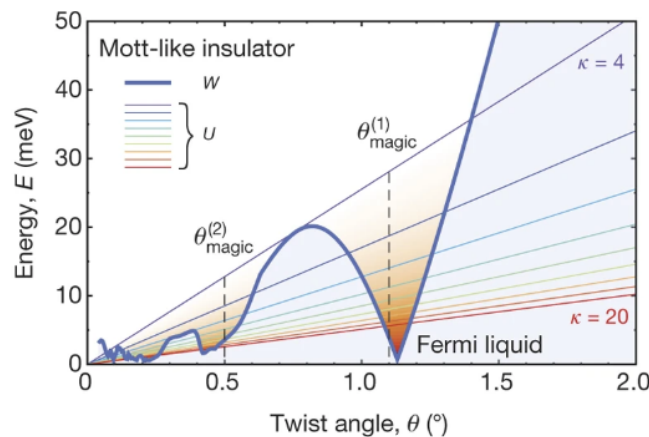


**Figure 4.5 – Angle-dependent correlation strength in twisted bilayer graphene.** Comparison of bandwidth  $W$  of the flat band in twisted bilayer graphene and on-site energy  $U$  (screened as indicated by colored lines for different values of  $\kappa$ , cf. Eq. (4.1)) as a function of twist angle  $\theta$ . The correlation strength  $U/W$  is tuned by  $\theta$  and the magic angles emerge in regions of  $U > W$ . Reprinted from [163] with permission from © 2024 Springer Nature. Not covered by the CC BY 4.0 license.

tunability of system parameters allows for characterizing these phase diagrams in great detail, thus making moiré material an excellent platform for studying quantum phenomena.

Superconductivity, in particular, has only been observed in twisted graphene-based systems and more recently also in twisted WSe<sub>2</sub>, as discussed below. The graphene-based superconductors are specifically MATBG [163] and magic-angle twisted trilayer graphene (MATTG) [78], where superconductivity occurs at characteristic “magic angles” of approximately 1.1° and 1.6°, respectively. The reason for the existence of magic angles is related to the vanishing of the moiré Bloch bands’ renormalized Fermi velocity as a function of twist angle [634] which originates from the linear dispersion of the original Dirac cones. The corresponding twist-angle dependence of the bandwidth  $W$  leads to a different scaling of correlation strength as that in Eq. (4.1) which is illustrated in Figure 4.5 for MATBG.

The superconducting phases in MATBG and MATTG are far from being understood.<sup>5</sup> Discussing the theoretical proposals and experimental evidence regarding the nature and pairing mechanism of these systems is beyond the scope of this thesis.<sup>6</sup> Instead, we refer interested readers to recent comprehensive reviews [24, 536, 635, 639]; see also the references in Ref. [638] for MATBG specifically. Nonetheless, we want to highlight a few important properties of superconductivity in these materials: For instance, the superconducting phase occurs at exceptionally low electron densities on the order of  $10^{11}$  cm<sup>-2</sup>, the ratio of critical temperature ( $T_C$ ) to Fermi temperature ( $T_F$ ) is notably high (on the order of 0.1, cf. Uemura plot in Figure 6.1), and the superconducting condensate has a short coherence length on the order of a few moiré lattice spacings [77, 78, 639]. In addition, different studies have revealed the importance of quantum geometric contributions to the superconducting stiffness [450, 451, 536, 543, 544, 582], which would otherwise vanish in the limit of flat bands and thus hinder superconductivity.

### 4.3.1 Twisted transition metal dichalcogenides

A different class of two-dimensional vdW materials is given by transition metal dichalcogenides (TMDCs). Even without twisting, these materials host a range of correlated phases, such as superconductivity [69–73], charge density waves [70, 229], or insulating states [640, 641]. Depending on the specific transition metal and chalcogen elements, the electronic structure of TMDCs can vary from metallic to insulating behavior [158]. Here, we will focus on the class of twisted semi-conducting TMDCs ( $MX_2$ ,  $M=Mo, We$  and  $X=S, Se$ ), which have a characteristic

---

<sup>5</sup>Many of MATBG’s non-superconducting, correlated low-energy phases can be understood within an effective heavy fermion model of MATBG [636] from the interplay of correlation effects, symmetry-broken phases, and reshuffling of electronic charges [637, 638].

<sup>6</sup>This topic could easily form the basis for one or more PhD projects.



layer-dependent bandgap that becomes direct in the monolayer case. TMDCs show a few important differences to graphene-based moiré materials which include the absence of a magic-angle condition, interaction strengths that can be up to ten times larger than in graphene, and the possibility of spin-valley locking when inversion symmetry is broken in conjunction with SOC, unlike degenerate spin and valley degrees of freedom in twisted graphene systems. For a comprehensive overview of semiconducting moiré materials, we refer to the review by Mak and Shan [23].

Moiré structures of TMDCs can be created both from homobilayers and heterobilayers. The crucial difference is the dependence on twist angles: homobilayers exhibit a strong dependence, whereas heterobilayers show negligible sensitivity. Recently, superconductivity in twisted homobilayer WSe<sub>2</sub> has been reported by two independent groups at 220 mK for a twist angle of 3.65° [79] and up to 426 mK at 5° [80]. These studies highlight the proximity of the superconducting phase to insulating and antiferromagnetic states. An earlier experimental work from 2020 already suggested the presence of a superconducting state [165] up to 3 K for a twist angle of  $\theta = 5.1^\circ$  adjacent to an insulating state, but the robustness of superconductivity was not conclusively established.<sup>7</sup> Understanding the superconductivity in twisted WSe<sub>2</sub> and its interplay with possible other correlated states is an open question for future research.

Twisted homobilayer WSe<sub>2</sub> has a more complex moiré valence low-energy electronic structure than the other semiconducting TMDCs, namely MoS<sub>2</sub>, MoSe<sub>2</sub>, and WS<sub>2</sub>. A good description for the electronic structure is a continuum model of the valley that the moiré valence band structure originates from, i.e., the maximum of the monolayer valence band.<sup>8</sup> In case of WSe<sub>2</sub>, the moiré band structure is formed by the states at the band maxima located at the K and K' points of the individual layers. As the K point hosts large SOC, this results in a spin-valley locking of the moiré valence band structure [643]. The resulting low-energy electronic structure hosts a variety of correlated phases depending on environmental conditions [120, 644–646]. In contrast, the low-energy states in the other TMDCs originate from the  $\Gamma$  valley, thereby simplifying the electronic structure. Within the continuum model of  $\Gamma$ -valley twisted TMDCs [647], the lowest energy bands can be characterized by a simple honeycomb lattice using an *s*-orbital tight-binding model with higher-energy bands being described by a *p*-orbital model. These bands only begin to mix at larger twist angles exceeding 5°.

In the embedded publication below, we study superconductivity in  $\Gamma$ -valley twisted TMDCs by constructing a Wannier model of the of the continuum model's low energy bands [647]. We investigate spin-fluctuation-driven superconductivity

<sup>7</sup>One reason for the difficulty in observing superconductivity in various moiré systems is given by the challenges associated with fabricating high-quality experimental samples [23, 642].

<sup>8</sup>As we are discussing the valence band, “lower” and “higher” energy states refer to the viewpoint of hole carriers in the following.

using the FLEX approximation and compare it to conventional phonon-mediated mechanisms. Notably, the improvement of the IR-based FLEX implementation allowed us to access  $T_c$  and to perform a full characterization of the phase diagram of the underlying honeycomb lattice model, which has not been possible in earlier calculations [648, 649]. Our findings reveal for spin-fluctuation-mediated pairing a dome-shaped critical temperature structure as a function of doping, reaching temperatures  $T_c \sim \mathcal{O}(1 \text{ K})$ . We identify the non-trivial doping dependence to arise from the interplay of the density of states and the spatial profile of spin fluctuations. This contrasts with phonon-mediated superconductivity which primarily depends on the available density of states. To gauge the strength of conventional superconductivity, we estimate the effective pairing potential strength for different moiré phonon modes.

We note that our modeling approach has been extended to address the lower-lying multi-orbital bands of the continuum model [650].

Niklas Witt, José M. Pizarro, Jan Berges, Takuya Nomoto, Ryotaro Arita, Tim O. Wehling

**Key points summary**







- Explorative study of superconductivity in  $\Gamma$ -valley twisted homobilayer TMDCs ( $WS_2, MoS_2, MoSe_2$ ) tunable by electrostatic doping and twist angle. Discussion of how to distinguish pairing mechanisms by their characteristic doping dependence in experimental studies.
- Spin-fluctuation-mediated pairing reveals critical temperatures on the order of 0.1 – 1 K with non-trivial dome-shaped dependence on doping, which can be traced back to an interplay of the density of states, the spatial profile of the spin fluctuations, and retardation effects.
- Comparison to conventional phonon-mediated pairing for different models of electron-phonon coupling displays distinct  $T_c$  doping profile, which, irrespective of the phonon model, is predominantly determined by the density of states.

**Author Contributions**

I performed and analyzed the FLEX calculations to study spin-mediated superconductivity based on the continuum model wannierization by J. M. Pizarro. I prepared the figures in the main text (except panel 1(a)) with data input by J. M. Pizarro for Fig. 1. I wrote the initial manuscript together with J. M. Pizarro where I particularly contributed to the presentation of results, their discussion, and the interpretation. In the supplemental material, I prepared sections S5 to S8 and S10 with the corresponding figures S4 to S9 and S11. The project was conceived by J. M. Pizarro, T. Wehling, and myself. All authors commented on the text and participated in the discussion of the results. I was responsible for handling the paper submission and communication with editor and referees.

**Copyright Notice**

Reprinted with permission from N. Witt et al., Physical Review B **105**, L241109 (2022). Copyright © 2022 by the American Physical Society. This is the accepted and published version of the article available at doi: [10.1103/PhysRevB.105.L241109](https://doi.org/10.1103/PhysRevB.105.L241109).

**Doping fingerprints of spin and lattice fluctuations in moiré superlattice systems**Niklas Witt <sup>1,2,3,\*</sup>, José M. Pizarro <sup>1,4,†</sup>, Jan Berges <sup>1</sup>, Takuya Nomoto <sup>5</sup>, Ryotaro Arita <sup>5,6</sup> and Tim O. Wehling <sup>1,2,3,‡</sup><sup>1</sup>*Institute of Theoretical Physics, Bremen Center for Computational Materials Science, and MAPEX Center for Materials and Processes, University of Bremen, Otto-Hahn-Allee 1, 28359 Bremen, Germany*<sup>2</sup>*I. Institute of Theoretical Physics, University of Hamburg, Notkestraße 9, 22607 Hamburg, Germany*<sup>3</sup>*The Hamburg Centre for Ultrafast Imaging, Luruper Chaussee 149, 22761, Hamburg, Germany*<sup>4</sup>*Max Planck Institute for the Structure and Dynamics of Matter, Luruper Chaussee 149, 22671 Hamburg, Germany*<sup>5</sup>*Department of Applied Physics, The University of Tokyo, 7-3-1 Hongo, Bunkyo-ku, Tokyo 113-8656, Japan*<sup>6</sup>*RIKEN Center for Emergent Matter Science, 2-1 Hirosawa, Wako, Saitama 351-0198, Japan*

(Received 12 August 2021; revised 18 March 2022; accepted 26 May 2022; published 13 June 2022)

Twisted Van der Waals systems offer the unprecedented possibility to tune different states of correlated quantum matter with external noninvasive electrostatic doping. The nature of the superconducting order presents a recurring open question in this context. In this work, we assess quantitatively the case of spin-fluctuation-mediated pairing for  $\Gamma$ -valley twisted transition metal dichalcogenide homobilayers. We calculate self-consistently and dynamically the doping-dependent superconducting transition temperature  $T_c$  revealing a superconducting dome with a maximal  $T_c \approx 0.1$ –1 K depending on twist angle. We compare our results with conventional phonon-mediated superconductivity, and we identify clear fingerprints in the doping dependence of  $T_c$ , which enable experiments to distinguish between different pairing mechanisms.

DOI: [10.1103/PhysRevB.105.L241109](https://doi.org/10.1103/PhysRevB.105.L241109)

**Introduction.** Twisting layers of two-dimensional (2D) materials leads to a moiré pattern, where flat bands can emerge close to the Fermi level [1–3]. The associated quenching of the kinetic energy leads to strong electronic correlations, which often interplay with topology [4–6]. Among these effects are Mott and topological Chern insulators, and different kinds of magnetic, nematic, and superconducting ordered states [7–28]. One can precisely tune between these states and change the filling of the flat bands from completely empty to filled by electrostatic doping [29], which is special in the domain of correlated materials.

The nature of superconducting states in twisted 2D systems is highly controversial. On the one hand, unconventional pairing mechanisms based on spin, orbital, and/or nematic fluctuations are regularly hypothesized [27,30–34]. The reasons are that superconductivity emerges next to a strongly correlated state [8,9,20,27,35] and that the ratio of critical temperature  $T_c$  and Fermi temperature  $T_F$  fits within the boundary of other unconventional superconductors [8,24,36]. On the other hand, recent experiments in magic-angle twisted bilayer graphene (MATBG) showed that the strongly correlated states and superconductivity are affected differently by the dielectric environment [17,18,28], which might point to a conventional origin, i.e., electron-phonon coupling.

Twisted 2D systems can be classified according to the symmetry of the low-energy Hamiltonian associated with the moiré pattern [37]. Honeycomb twisted 2D systems hold promise for hosting correlated Dirac fermions and topological

$d + id$  chiral superconductivity [30,38,39]. Examples of honeycomb systems are MATBG [3,40], twisted double bilayer graphene [41–43], magic-angle twisted trilayer graphene (MATTG) [44–46], and twisted transition metal dichalcogenides (TMDCs) [47–49]. Most of the experimental and theoretical work has been focused on graphite-based systems. However, their complicated low-energy electronic structure makes theoretical many-body studies difficult [42–46,50–52]. The low-energy electronic structure of twisted TMDC homobilayers is simpler than that of twisted graphitic systems since it can be described by an effective single-orbital model (see below) and it does not show topological obstruction preventing simple Wannier constructions [40,53]. As such, they are good candidates for establishing a link between experiments and theoretical many-body modeling. Recently, a zero-resistance state has been reported in a twisted TMDC homobilayer [20], the nature of which remains to be understood.

In this Letter we provide a quantitative study of the critical temperature  $T_c$  due to spin-fluctuation-mediated pairing in  $\Gamma$ -valley twisted TMDCs in terms of doping and twisting, which we obtain dynamically by means of the fluctuation exchange approximation (FLEX) [54,55]. We additionally provide a qualitative understanding of spin fluctuations versus electron-phonon coupling, and we propose that experimental measurements on the doping-dependent  $T_c$  can help to unveil the nature of the superconducting states.

**Band Structures, Wannierization and Hartree Potential Effect.** We consider the twisting of TMDC homobilayers with respect to the untwisted ( $\theta = 0^\circ$ ) situation. In Fig. 1(a) we show the emergent moiré pattern, where the AA regions form a triangular superlattice surrounded by AB and BA regions arranged in a honeycomb pattern. We focus on the so-called  $\Gamma$ -valley twisted TMDCs ( $\text{WS}_2$ ,  $\text{MoS}_2$ , and  $\text{MoSe}_2$ )

\*niklas.witt@physik.uni-hamburg.de

†jose.pizarro@mpsd.mpg.de

‡tim.wehling@physik.uni-hamburg.de

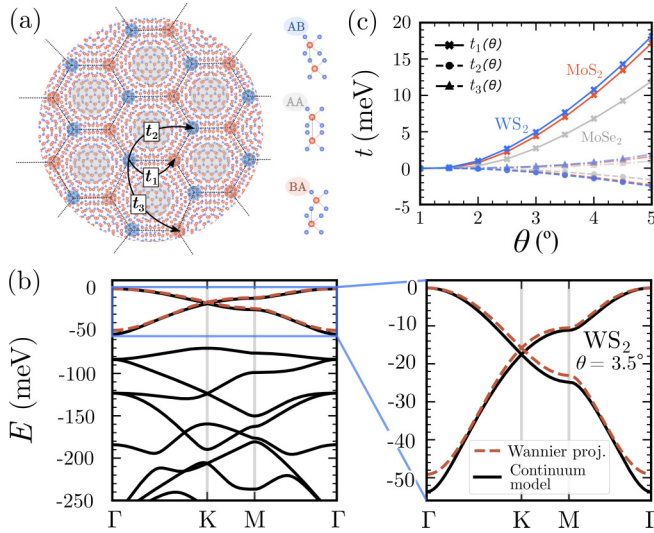


FIG. 1.  $\Gamma$ -valley twisted TMDCs. (a) Moiré pattern of twisted TMDCs. AA (gray shaded), AB (blue shaded), and BA (red shaded) regions in the moiré pattern correspond to different stackings of the two layers, as shown on the right side. Dashed black lines serve as a guide to the eye to identify the honeycomb superlattice. The most relevant hopping processes are sketched with black arrows. (b) Continuum model for  $\text{WS}_2$  at a twist angle of  $\theta = 3.5^\circ$  (black solid line) with a third-nearest-neighbor hopping tight-binding model (red dashed line) of the highest valence bands. The effective honeycomb lattice is formed by the AB and BA moiré sites. The right panel shows a zoom of the flat Dirac bands. (c) Twist-angle dependence of the hopping parameters for different  $\Gamma$ -valley twisted TMDCs,  $\text{WS}_2$ ,  $\text{MoS}_2$ , and  $\text{MoSe}_2$  obtained via Wannier projection.

[49,56,57], in which the valence band maximum of the untwisted homobilayer is located at the center of the Brillouin zone  $\Gamma$  due to the hybridization between the transition metal  $d$  and chalcogen  $p$  orbitals. The valence band maximum is an antibonding state energetically separated from its bonding counterpart by hundreds of meV. Also the conduction band is separated from the valence band maximum by more than an eV [58,59]. Based on this observation, Angeli and MacDonald constructed a low-energy continuum model in which only the antibonding state is included [49]. The emergent symmetry of these moiré valence bands is that of a 2D honeycomb lattice.

In the plane-wave basis defined by the moiré vectors  $\mathbf{G} = m\mathbf{G}_1^M + n\mathbf{G}_2^M$ , with integers  $m, n$  and  $\mathbf{G}_{1,2}^M$  spanning the reciprocal lattice, the Hamiltonian of the continuum model takes the form

$$H = -\frac{\hbar^2|\mathbf{k} + \mathbf{G}|^2}{2m^*}\delta_{\mathbf{G},\mathbf{G}'} + V_M(\mathbf{G} - \mathbf{G}'), \quad (1)$$

where  $\mathbf{k}$  are the reciprocal vectors defined in the mini Brillouin zone,  $m^*$  is the effective mass, and  $V_M(\mathbf{G})$  is the Fourier transformation of the moiré potential [60]. This Hamiltonian is expanded up to a plane-wave cutoff  $G_c = 5G^M$ , where  $G^M = |\mathbf{G}_{1,2}^M|$ .

The low-energy electronic structure of  $\Gamma$ -valley twisted TMDCs shows 2D honeycomb Dirac bands for the highest valence band; see Fig. 1(b). The Dirac point can be accessed by hole doping and the Dirac bands are well isolated from higher energy bands for twist angles  $1^\circ < \theta < 5^\circ$ . In this

twist angle range, the bandwidth of the flat Dirac bands varies between 0.5 and 100 meV [60].

We next construct a tight-binding Hamiltonian to describe the flat Dirac bands with one orbital per honeycomb superlattice site. Here, the AB and BA regions play the role of the A and B sublattice degrees of freedom in the honeycomb lattice. We include up to three nearest-neighbor hoppings  $t_1, t_2, t_3$  in our model, which we obtain by Wannier projection [60]. The tight-binding and continuum model band structure agree very well in the twist angle range  $1^\circ < \theta < 5^\circ$  [60]. We observe that, when comparing among different  $\Gamma$ -valley twisted TMDCs, the transition metal does not influence the hopping amplitudes significantly, while the chalcogen atoms do. We also find dominant nearest-neighbor hopping  $t_1 \gg t_2, t_3$ , and that  $t_1 \sim \alpha \sin^2(\theta) \approx \alpha\theta^2$  with  $\alpha \approx 2 \text{ eV/rad}^2$ .

In other twisted 2D systems, such as MATBG [61–64] or MATTG [34], the effect of the purely electrostatic and long-range (Hartree) potential in doped flat bands is important. Thus, we also consider its influence in our model [60]. We find that, contrary to MATBG and MATTG, the flat Dirac bands remain unaffected. Therefore, we disregard doping-dependent long-range Coulomb reconstructions on the flat bands from now on.

*Doping- and Interaction-dependent Spin Fluctuations.* Since the nearest-neighbor hopping  $t_1(\theta)$  dominates over  $t_2$  and  $t_3$  for twist angles  $1^\circ < \theta < 5^\circ$ , we neglect  $t_2$  and  $t_3$  here. We discuss their influence in the Supplemental Material [60]. We study the Hubbard Hamiltonian

$$H_U = - \sum_{\langle im, jn \rangle, \sigma} t(c_{im\sigma}^\dagger c_{jn\sigma} + \text{H.c.}) + U \sum_{im} n_{im\uparrow} n_{im\downarrow}, \quad (2)$$

where the hopping amplitude  $t \equiv t_1(\theta)$  sets the energy scale, and  $\langle im, jn \rangle$  denotes that the sum is limited to neighboring lattice sites of a moiré unit cell  $i, j$  and sublattice  $m, n$ .  $c_{im\sigma}^\dagger$  ( $c_{im\sigma}$ ) creates (annihilates) an electron with spin  $\sigma$ , and  $U$  is the local Coulomb repulsion between electrons on the same lattice site. In the simplified tight-binding model, the system is particle-hole symmetric with respect to the Dirac point and has a logarithmically diverging density of states (DOS) at the Van Hove singularities (VHS) that are present in the  $M$  points of the Brillouin zone [65]. We redefine our zero-doping level  $\delta = 0$  to correspond to a Fermi energy at the Dirac point; see Fig. 1(b). Then, the VHS are at  $\delta = 0.25$ .

The Hubbard model for the honeycomb lattice has previously been studied, indicating a rich phase diagram of competing many-body instabilities [39,66–72]. The emergence of spin-density waves (SDWs) and superconductivity in close proximity suggests an unconventional pairing mechanism mediated by spin fluctuations. Following this premise, we study the magnetic and superconducting excitations using FLEX [60] in the model described above [73–75] as a representation of spin-fluctuation-mediated pairing in  $\Gamma$ -valley twisted TMDCs. A recently developed sparse sampling method [76,77] enabled us to perform the numerically demanding calculations at low temperatures.

In FLEX, the exchange of spin and charge fluctuations is treated dynamically and self-consistently with an effective electron-electron interaction of a random phase approximation (RPA) type. Estimates of the Hubbard interaction

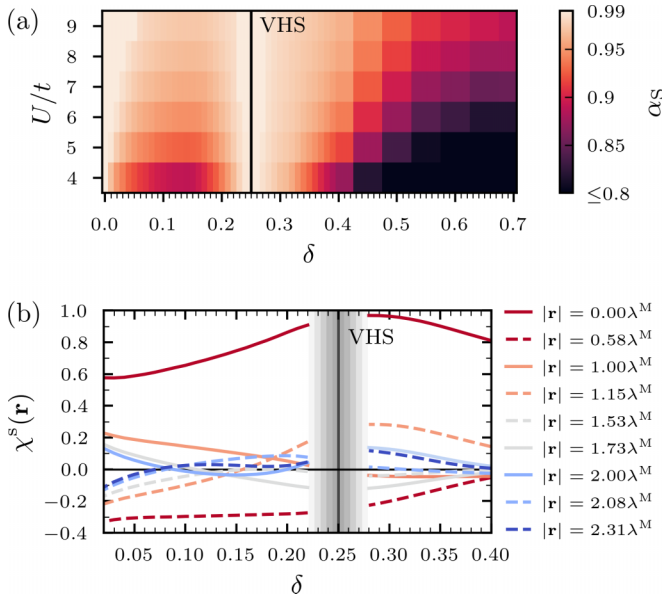


FIG. 2. Spin fluctuation characteristics of  $\Gamma$ -valley twisted TMDs at  $T/t = 0.003$ . (a) Leading Stoner enhancement factor  $\alpha_S = \max_{\mathbf{q}}\{U\chi^0(\mathbf{q})\}$  for different Coulomb interaction strengths  $U/t$  and dopings  $\delta$  with respect to the Dirac point as obtained from FLEX. A transition to a quasiordered magnetic state is assumed for  $\alpha_S \geq 0.99$ . (b) Real-space components of the static spin susceptibility  $\chi^s(\mathbf{r})$  for  $U/t = 6$ . Up to eighth-nearest-neighbor components are shown, with  $|\mathbf{r}|$  denoting the distance between two spins in terms of the moiré unit length  $\lambda^M$ . Solid (dashed) lines correspond to the AA (AB) components of  $\chi^s$ , i.e., correlations between same (different) sublattice sites. The area around the Van Hove singularities (VHS) is not accessible because of too strong fluctuations; it is marked by a gray shaded area [cf. panel (a)].

parameter given in the Supplemental Material [60] show that  $U$  is highly tunable via twist angle and the dielectric environment [17,18,28,78–84]. For example, for  $\theta = 5^\circ$ , the interaction strength is tunable in the range  $4 < U/t < 8$  [60]. In addition, vertex corrections that are neglected in FLEX could contribute to further screening [85–87]. In what follows, we treat  $U$  as a free parameter.

We analyze the emergence of magnetic fluctuations by inspecting the leading Stoner enhancement factor  $\alpha_S = \max_{\mathbf{q}}\{U\chi^0(\mathbf{q})\}$  with the static irreducible susceptibility  $\chi^0(\mathbf{q})$ ; see Fig. 2(a). If  $\alpha_S \geq 0.99$ , the transition to a quasiordered magnetic phase is assumed [60]. This situation occurs in two locations of the phase diagram: at the Dirac point ( $\delta = 0$ ) and in the vicinity of the VHS ( $\delta = 0.25$ ). Between these two points,  $\alpha_S$  is strong but does not reach the quasiordering criterion. When doping beyond the VHS ( $\delta \gtrsim 0.3$ ), the relative spin fluctuation strength decreases rapidly and the system stays paramagnetic. Increasing the interaction strength amplifies  $\alpha_S$ , but the doping dependence remains largely unaffected.

The presence of strong spin fluctuations can induce an effective electron-electron interaction with nonlocal attractive regions, which gives rise to superconducting pairing [88,89]. FLEX captures this effect with the dominant contribution to the effective interaction coming from the spin susceptibility  $\chi^s$ . Optimal pairing conditions can be inferred from

its real-space profile. In Fig. 2(b), we show the doping dependence of up to eighth-nearest-neighbor components of  $\chi^s(\mathbf{r})$  for  $U/t = 6$ . For doping levels in the vicinity of the Dirac point, antiferromagnetic fluctuations with respect to the sublattices A and B emerge, i.e., the AB (intersublattice) components have a negative sign, whereas the AA (intrasublattice) components are positive. Upon doping, initially the longest range and successively the more short-range components of  $\chi^s$  change their sign. Hence, antiferromagnetic fluctuations are suppressed, and an admixture of ferromagnetic components to  $\chi^s$  is triggered away from the Dirac point. Beyond the VHS, fluctuations turn increasingly ferromagnetic and their relative strength weakens. Further insight into the emerging SDWs and their origin from nesting conditions can be gained by inspecting the momentum-resolved structure of  $\chi^s$  [60].

To investigate the dominant superconducting pairing symmetry and transition temperature  $T_c$ , we solve the linearized Eliashberg equation for different possible order parameters. In all our calculations, the degenerate singlet  $d$ -wave pairings ( $d_{xy}, d_{x^2-y^2}$ ) emerge as the dominant pairing symmetries [60]. This is in agreement with the antiferromagnetic fluctuations as they favor singlet-pairing symmetries. Below  $T_c$ , the order parameter forms a time-reversal symmetry-broken chiral  $d + id$  pairing state [38,39,69].

In Fig. 3(a), we show the doping dependence of  $T_c$  for different  $U/t$ . We find a superconducting dome that is characterized by a nonmonotonous behavior with a maximal value  $T_c^{\max}$  at an optimal doping  $\delta_{\text{opt}}$ . The existence of such a maximum results from the interplay of the pairing interaction pattern and the electronic DOS at the Fermi level [60]. Doping away from the Dirac point increases the DOS at the Fermi level, which supports  $d$ -wave pairing via antiferromagnetic spin fluctuations. As the doping level increases further, however, an increasing amount of pair-breaking ferromagnetic spin fluctuations emerges [cf. Fig. 2(b)]. Thus, we reach a situation of optimal doping around  $\delta_{\text{opt}} = 0.06$  and a decrease in  $T_c$  upon further doping.

We obtain increasing  $T_c$  with increasing interaction  $U$  until the highest  $T_c$  curve for  $U/t = 8$  with a maximal value of  $T_c^{\max}/t = 4.8 \times 10^{-3}$  at  $\delta_{\text{opt}} = 0.06$  is reached. For larger interactions  $U/t \gtrsim 9$ , the superconducting transition temperatures decrease again.

Near the VHS, possible superconducting order [39,67,68,90] is masked by magnetic fluctuations in FLEX, that is,  $\alpha_S$  exceeds 0.99. As the spin fluctuations turn ferromagnetic towards and beyond the VHS doping, singlet-pairing emerging from antiferromagnetic spin fluctuation exchange is strongly suppressed. In addition, triplet superconductivity does not arise for any temperature  $T/t > 10^{-3}$  due to the weakened fluctuation strength [60]. The material and twist-angle-dependent hopping amplitudes given in Fig. 1(c) set the temperature scale.  $T_c$  takes values on the order of 0.1–1 K, which is in agreement with reports on other twisted 2D systems [8,9,20,27].

*Spin Fluctuations Versus Electron-phonon Coupling.* The previous discussion showed that superconductivity arising from a spin-fluctuation-mediated pairing mechanism exhibits a characteristic doping-dependent transition line with a clear maximum near Dirac filling. To contrast this pairing scenario,

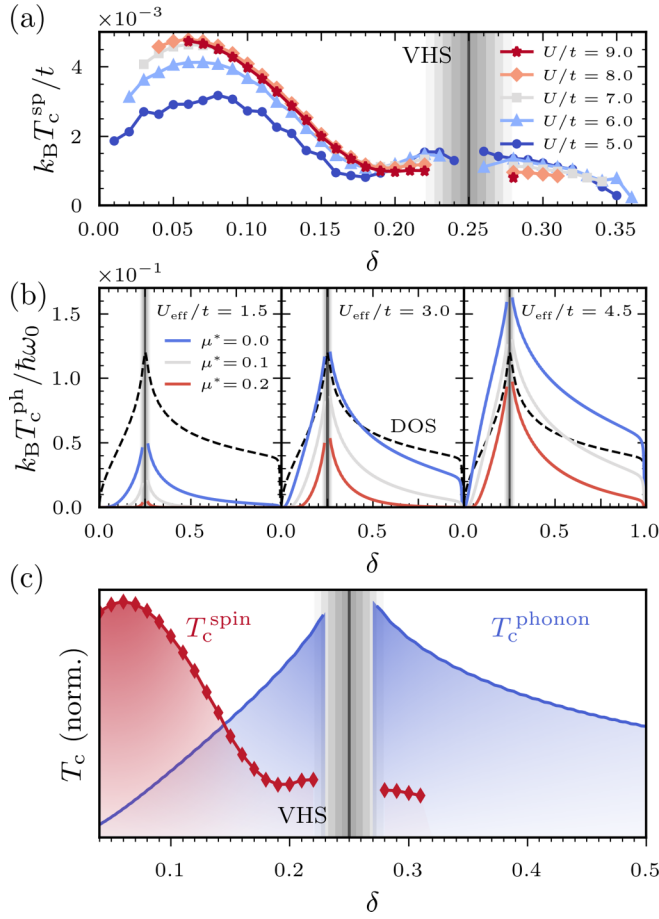


FIG. 3. Doping dependence of the superconducting transition temperature  $T_c$  in  $\Gamma$ -valley twisted TMDCs. (a) Phase diagram for spin-fluctuation-mediated pairing for different local Coulomb interaction strengths  $U/t$  from FLEX calculations. The critical temperature  $T_c/t$  belongs to the dominant singlet  $d$ -wave pairing symmetry. (b) Phonon-mediated  $T_c$  for an Einstein-Holstein phonon mode  $\omega_0$  and for different Coulomb pseudopotentials  $\mu^* = 0.0$  (blue),  $0.1$  (gray), and  $0.2$  (red). From left to right, the effective attractive interaction  $U_{\text{eff}}$  from electron-phonon coupling is increased. The trend of the density of states (DOS) is indicated by black dashed lines. (c) Comparison of the doping-dependent phase diagram of the maximum  $T_c$  obtained for spin fluctuations and phonons. This phase diagram holds qualitatively for all  $\Gamma$ -valley twisted TMDCs.

we assess how the doping characteristics appear in the conventional case of phonon-mediated superconductivity.

We estimate the transition temperature  $T_c^{\text{ph}}$  by means of McMillan's formula [91,92]

$$T_c^{\text{ph}} = \frac{\hbar\langle\omega\rangle}{1.20 k_B} \exp \left\{ \frac{-1.04(1 + \lambda)}{\lambda - 0.62\lambda\mu^* - \mu^*} \right\}, \quad (3)$$

where  $\langle\omega\rangle$  is an effective phonon frequency,  $\lambda$  denotes the effective pairing strength, and  $\mu^*$  is the Tolmachev-Morel-Anderson Coulomb pseudopotential [93,94].  $\langle\omega\rangle$  and  $\lambda$  are generally obtained from the phonon spectral function  $\alpha^2F(\omega)$ . Here, we consider the limiting case of an Einstein-Holstein phonon mode, i.e., with a constant electron-phonon coupling  $g$  and a constant phonon frequency  $\omega_0$ . We discuss the opposite

limit of nonlocal Peierls coupling with dispersive phonons in the Supplemental Material [60].

When discussing phonon-mediated superconductivity, it is simplest to do so in terms of a BCS-like effective attractive interaction  $U_{\text{eff}}$  such that  $\lambda = U_{\text{eff}}N(\delta)$  with the DOS  $N(\delta)$  per spin and unit cell for a particular doping  $\delta$ . In the Einstein-Holstein model, we explicitly have  $U_{\text{eff}} = 2g^2/\hbar\omega_0$  and  $\langle\omega\rangle = \omega_0$ . The exact values of  $\omega_0$ ,  $U_{\text{eff}}$ , and  $\mu^*$  are material-specific and they depend on factors such as twist angle or external screening [95–101]. Twisted TMDCs display phonon modes at energies on the order of a few 10 meV as in the bulk and in addition feature moiré phonons in the range 2–5 meV [100–102]. We estimate  $U_{\text{eff}}$  to be in the large range of  $0.05$ – $8t$  [60], and typical values of  $\mu^*$  are in the range  $0.0$ – $0.2$  [94].

The key observation is that the generic doping dependence of  $T_c^{\text{ph}}$  derives mainly from the DOS. To illustrate this point, we show in Fig. 3(b) results for  $T_c^{\text{ph}}$  in units of  $\omega_0$  for different  $U_{\text{eff}}$  and  $\mu^*$  together with the DOS. We tune  $U_{\text{eff}}$  to yield weak to intermediate coupling strengths ( $\lambda \lesssim 1$ ). Increasing  $\mu^*$  suppresses  $T_c^{\text{ph}}$ , while increasing  $U_{\text{eff}}$  has the opposite effect. The quantitative details may vary, but the qualitative shape of the  $T_c^{\text{ph}}$  curve is unaffected in both cases, mainly following  $N(\delta)$ . Our findings for nonlocal coupling [60] support the robustness of the doping dependence of  $T_c^{\text{ph}}$ : A peaked structure emerges around the VHS and extends over the whole range of dopings  $\delta \in [0, 1]$ , i.e., in particular also beyond the VHS in the region of  $\delta > 0.25$ . The relevant temperature scale is set by  $\omega_0$ , with  $T_c^{\text{ph}}$  taking values on the order of  $0.1$ – $10$  K. Note that we excluded the immediate region around the VHS in our discussion since the competition of different instabilities complicates the determination of the doping dependence [103–105].

A direct comparison of the doping-dependent superconducting phase diagram obtained for the different pairing mechanisms—spin fluctuations and phonons—is given in Fig. 3(c). We use the normalized results of Fig. 3(a) for  $U/t = 8$  and those of Fig. 3(b) for  $U_{\text{eff}}/t = 3$  and  $\mu^* = 0.0$ . Each pairing mechanism shows unique fingerprints for which we identify two key differences. First, phonon-mediated superconductivity shows a clear increase towards the VHS, whereas for spin-fluctuation-mediated pairing, a global maximum appears close to the Dirac point at  $\delta_{\text{opt}}$ . Second, phonon-induced superconductivity persists over a wider doping range and is closely linked to the DOS, while spin-fluctuation-mediated superconductivity is confined to a narrow doping region near an antiferromagnetic instability, which diminishes rapidly after the VHS due to the emergence of pair-breaking ferromagnetic fluctuations.

*Summary and Outlook.* We have shown that the superconducting response to doping in  $\Gamma$ -valley twisted TMDCs depends decisively on the quantum nature of the pairing fluctuations. Superconducting pairing mechanisms and their experimental determination present a major open problem in twisted 2D systems. Thus, the question is, are there simple experimental ways to discern different pairing mechanisms?

Our analysis demonstrates that different pairing mechanisms can be distinguished by simple doping-dependent

transport experiments of  $T_c$ . Fingerprints unique to the particular microscopic mechanism can be found with respect to the doping levels of maximal  $T_c$  or the doping extent over which superconductivity persists.

This possibility has not been explored in other unconventional superconductors [106] because of the difficulties of performing systematic doping-dependent studies. The consideration of multiple local and nonlocal electron-phonon coupling profiles [60] indicates that the distinct doping dependence between  $T_c^{\text{sp}}$  and  $T_c^{\text{ph}}$  is generic. Hence, our conclusions are not only valid for the  $\Gamma$ -valley twisted TMDCs, but they can help to elucidate pairing mechanisms in other twisted 2D Van der Waals materials, such as MATBG or MATTG.

*Acknowledgments.* We acknowledge support and funding by the Deutsche Forschungsgemeinschaft (DFG) via RTG 2247 (QM<sup>3</sup>) (Project No. 286518848), via the priority program SPP 2244 (Project No. 422707584), via EXC 2077 (University Allowance, University of Bremen, Project No. 390741603), and via the Cluster of Excellence ‘CUI: Advanced Imaging of Matter’ – EXC 2056 (Project No. 390715994). Funding from the European Commission via the Graphene Flagship Core Project 3 (Grant Agreement ID: 881603) and computing time at the HLRN facilities (Berlin and Göttingen) are acknowledged. This work was supported by a Grant-in-Aid for Scientific Research (No. 19H05825) by MEXT and by JST PRESTO (No. JP-MJPR20L7), Japan.

- [1] E. Suárez Morell, J. D. Correa, P. Vargas, M. Pacheco, and Z. Barticevic, Flat bands in slightly twisted bilayer graphene: Tight-binding calculations, *Phys. Rev. B* **82**, 121407(R) (2010).
- [2] R. Bistritzer and A. H. MacDonald, Moiré bands in twisted double-layer graphene, *Proc. Natl. Acad. Sci. (USA)* **108**, 12233 (2011).
- [3] M. Koshino, N. F. Q. Yuan, T. Koretsune, M. Ochi, K. Kuroki, and L. Fu, Maximally Localized Wannier Orbitals and the Extended Hubbard Model for Twisted Bilayer Graphene, *Phys. Rev. X* **8**, 031087 (2018).
- [4] A. Marrazzo, M. Gibertini, D. Campi, N. Mounet, and N. Marzari, Prediction of a Large-Gap and Switchable Kane-Mele Quantum Spin Hall Insulator, *Phys. Rev. Lett.* **120**, 117701 (2018).
- [5] X. Wu, M. Fink, W. Hanke, R. Thomale, and D. Di Sante, Unconventional superconductivity in a doped quantum spin Hall insulator, *Phys. Rev. B* **100**, 041117(R) (2019).
- [6] J. M. Pizarro, S. Adler, K. Zantout, T. Mertz, P. Barone, R. Valentí, G. Sangiovanni, and T. O. Wehling, Deconfinement of Mott localized electrons into topological and spin-orbit-coupled Dirac fermions, *npj Quantum Mater.* **5**, 79 (2020).
- [7] Y. Cao, V. Fatemi, A. Demir, S. Fang, S. L. Tomarken, J. Y. Luo, J. D. Sanchez-Yamagishi, K. Watanabe, T. Taniguchi, E. Kaxiras, R. C. Ashoori, and P. Jarillo-Herrero, Correlated insulator behaviour at half-filling in magic-angle graphene superlattices, *Nature (London)* **556**, 80 (2018).
- [8] Y. Cao, V. Fatemi, S. Fang, K. Watanabe, T. Taniguchi, E. Kaxiras, and P. Jarillo-Herrero, Unconventional superconductivity in magic-angle graphene superlattices, *Nature (London)* **556**, 43 (2018).
- [9] M. Yankowitz, S. Chen, H. Polshyn, Y. Zhang, K. Watanabe, T. Taniguchi, D. Graf, A. F. Young, and C. R. Dean, Tuning superconductivity in twisted bilayer graphene, *Science* **363**, 1059 (2019).
- [10] G. Chen, L. Jiang, S. Wu, B. Lyu, H. Li, B. L. Chittari, K. Watanabe, T. Taniguchi, Z. Shi, J. Jung, Y. Zhang, and F. Wang, Evidence of a gate-tunable Mott insulator in a trilayer graphene moiré superlattice, *Nat. Phys.* **15**, 237 (2019).
- [11] A. L. Sharpe, E. J. Fox, A. W. Barnard, J. Finney, K. Watanabe, T. Taniguchi, M. A. Kastner, and D. Goldhaber-Gordon, Emergent ferromagnetism near three-quarters filling in twisted bilayer graphene, *Science* **365**, 605 (2019).
- [12] X. Lu, P. Stepanov, W. Yang, M. Xie, M. A. Aamir, I. Das, C. Urgell, K. Watanabe, T. Taniguchi, G. Zhang, A. Bachtold, A. H. MacDonald, and D. K. Efetov, Superconductors, orbital magnets and correlated states in magic-angle bilayer graphene, *Nature (London)* **574**, 653 (2019).
- [13] G. W. Burg, J. Zhu, T. Taniguchi, K. Watanabe, A. H. MacDonald, and E. Tutuc, Correlated Insulating States in Twisted Double Bilayer Graphene, *Phys. Rev. Lett.* **123**, 197702 (2019).
- [14] E. C. Regan, D. Wang, C. Jin, M. I. Bakti Utama, B. Gao, X. Wei, S. Zhao, W. Zhao, Z. Zhang, K. Yumigeta, M. Blei, J. D. Carlström, K. Watanabe, T. Taniguchi, S. Tongay, M. Crommie, A. Zettl, and F. Wang, Mott and generalized Wigner crystal states in WSe<sub>2</sub>/WS<sub>2</sub> moiré superlattices, *Nature (London)* **579**, 359 (2020).
- [15] Y. Tang, L. Li, T. Li, Y. Xu, S. Liu, K. Barmak, K. Watanabe, T. Taniguchi, A. H. MacDonald, J. Shan, and K. F. Mak, Simulation of Hubbard model physics in WSe<sub>2</sub>/WS<sub>2</sub> moiré superlattices, *Nature (London)* **579**, 353 (2020).
- [16] C. Shen, Y. Chu, Q. Wu, N. Li, S. Wang, Y. Zhao, J. Tang, J. Liu, J. Tian, K. Watanabe, T. Taniguchi, R. Yang, Z. Y. Meng, D. Shi, O. V. Yazyev, and G. Zhang, Correlated states in twisted double bilayer graphene, *Nat. Phys.* **16**, 520 (2020).
- [17] P. Stepanov, I. Das, X. Lu, A. Fahimniya, K. Watanabe, T. Taniguchi, F. H. L. Koppens, J. Lischner, L. Levitov, and D. K. Efetov, Untying the insulating and superconducting orders in magic-angle graphene, *Nature (London)* **583**, 375 (2020).
- [18] Y. Saito, J. Ge, K. Watanabe, T. Taniguchi, and A. F. Young, Independent superconductors and correlated insulators in twisted bilayer graphene, *Nat. Phys.* **16**, 926 (2020).
- [19] Y. Cao, D. Rodan-Legrain, O. Rubies-Bigorda, J. M. Park, K. Watanabe, T. Taniguchi, and P. Jarillo-Herrero, Tunable correlated states and spin-polarized phases in twisted bilayer-bilayer graphene, *Nature (London)* **583**, 215 (2020).
- [20] L. Wang, E.-M. Shih, A. Ghiotto, L. Xian, D. A. Rhodes, C. Tan, M. Claassen, D. M. Kennes, Y. Bai, B. Kim, K. Watanabe, T. Taniguchi, X. Zhu, J. Hone, A. Rubio, A. N. Pasupathy, and C. R. Dean, Correlated electronic phases in twisted bilayer transition metal dichalcogenides, *Nat. Mater.* **19**, 861 (2020).



- [21] S. Chen, M. He, Y.-H. Zhang, V. Hsieh, Z. Fei, K. Watanabe, T. Taniguchi, D. H. Cobden, X. Xu, C. R. Dean, and M. Yankowitz, Electrically tunable correlated and topological states in twisted monolayer–bilayer graphene, *Nat. Phys.* **17**, 374 (2021).
- [22] H. Polshyn, J. Zhu, M. A. Kumar, Y. Zhang, F. Yang, C. L. Tschirhart, M. Serlin, K. Watanabe, T. Taniguchi, A. H. MacDonald, and A. F. Young, Electrical switching of magnetic order in an orbital Chern insulator, *Nature (London)* **588**, 66 (2020).
- [23] K. P. Nuckolls, M. Oh, D. Wong, B. Lian, K. Watanabe, T. Taniguchi, B. A. Bernevig, and A. Yazdani, Strongly correlated Chern insulators in magic-angle twisted bilayer graphene, *Nature (London)* **588**, 610 (2020).
- [24] J. M. Park, Y. Cao, K. Watanabe, T. Taniguchi, and P. Jarillo-Herrero, Tunable strongly coupled superconductivity in magic-angle twisted trilayer graphene, *Nature (London)* **590**, 249 (2021).
- [25] S. Wu, Z. Zhang, K. Watanabe, T. Taniguchi, and E. Y. Andrei, Chern insulators, van Hove singularities and topological flat bands in magic-angle twisted bilayer graphene, *Nat. Mater.* **20**, 488 (2021).
- [26] S. Xu, M. M. Al Ezzi, N. Balakrishnan, A. Garcia-Ruiz, B. Tsim, C. Mullan, J. Barrier, N. Xin, B. A. Piot, T. Taniguchi, K. Watanabe, A. Carvalho, A. Mishchenko, A. K. Geim, V. I. Fal'ko, S. Adam, A. H. C. Neto, K. S. Novoselov, and Y. Shi, Tunable van Hove singularities and correlated states in twisted monolayer-bilayer graphene, *Nat. Phys.* **17**, 619 (2021).
- [27] Y. Cao, D. Rodan-Legrain, J. M. Park, N. F. Q. Yuan, K. Watanabe, T. Taniguchi, R. M. Fernandes, L. Fu, and P. Jarillo-Herrero, Nematicity and competing orders in superconducting magic-angle graphene, *Science* **372**, 264 (2021).
- [28] X. Liu, Z. Wang, K. Watanabe, T. Taniguchi, O. Vafek, and J. I. A. Li, Tuning electron correlation in magic-angle twisted bilayer graphene using Coulomb screening, *Science* **371**, 1261 (2021).
- [29] Y. Cao, J. Y. Luo, V. Fatemi, S. Fang, J. D. Sanchez-Yamagishi, K. Watanabe, T. Taniguchi, E. Kaxiras, and P. Jarillo-Herrero, Superlattice-Induced Insulating States and Valley-Protected Orbits in Twisted Bilayer Graphene, *Phys. Rev. Lett.* **117**, 116804 (2016).
- [30] C.-C. Liu, L.-D. Zhang, W.-Q. Chen, and F. Yang, Chiral Spin Density Wave and  $d + id$  Superconductivity in the Magic-Angle-Twisted Bilayer Graphene, *Phys. Rev. Lett.* **121**, 217001 (2018).
- [31] Y.-Z. You and A. Vishwanath, Superconductivity from valley fluctuations and approximate  $SO(4)$  symmetry in a weak coupling theory of twisted bilayer graphene, *npj Quantum Mater.* **4**, 16 (2019).
- [32] L. Klebl and C. Honerkamp, Inherited and flatband-induced ordering in twisted graphene bilayers, *Phys. Rev. B* **100**, 155145 (2019).
- [33] A. Fischer, L. Klebl, C. Honerkamp, and D. M. Kennes, Spin-fluctuation-induced pairing in twisted bilayer graphene, *Phys. Rev. B* **103**, L041103 (2021).
- [34] A. Fischer, Z. A. H. Goodwin, A. A. Mostofi, J. Lischner, D. M. Kennes, and L. Klebl, Unconventional superconductivity in magic-angle twisted trilayer graphene, *npj Quantum Mater.* **7**, 5 (2022).
- [35] M. Oh, K. P. Nuckolls, D. Wong, R. L. Lee, X. Liu, K. Watanabe, T. Taniguchi, and A. Yazdani, Evidence for unconventional superconductivity in twisted bilayer graphene, *Nature (London)* **600**, 240 (2021).
- [36] E. F. Talantsev, R. C. Maitra, and W. P. Crump, Classifying superconductivity in moiré graphene superlattices, *Sci. Rep.* **10**, 212 (2020).
- [37] D. M. Kennes, M. Claassen, L. Xian, A. Georges, A. J. Millis, J. Hone, C. R. Dean, D. N. Basov, A. N. Pasupathy, and A. Rubio, Moiré heterostructures as a condensed-matter quantum simulator, *Nat. Phys.* **17**, 155 (2021).
- [38] Z. Kuznetsova and V. Barzykin, Pairing state in multicomponent superconductors, *Europhys. Lett.* **72**, 437 (2005).
- [39] A. M. Black-Schaffer and C. Honerkamp, Chiral  $d$ -wave superconductivity in doped graphene, *J. Phys.: Condens. Matter* **26**, 423201 (2014).
- [40] H. C. Po, L. Zou, A. Vishwanath, and T. Senthil, Origin of Mott Insulating Behavior and Superconductivity in Twisted Bilayer Graphene, *Phys. Rev. X* **8**, 031089 (2018).
- [41] J. Y. Lee, E. Khalaf, S. Liu, X. Liu, Z. Hao, P. Kim, and A. Vishwanath, Theory of correlated insulating behaviour and spin-triplet superconductivity in twisted double bilayer graphene, *Nat. Commun.* **10**, 5333 (2019).
- [42] F. Haddadi, Q. Wu, A. J. Kruchkov, and O. V. Yazyev, Moiré flat bands in twisted double bilayer graphene, *Nano Lett.* **20**, 2410 (2020).
- [43] X. Liang, Z. A. H. Goodwin, V. Vitale, F. Corsetti, A. A. Mostofi, and J. Lischner, Effect of bilayer stacking on the atomic and electronic structure of twisted double bilayer graphene, *Phys. Rev. B* **102**, 155146 (2020).
- [44] S. Carr, C. Li, Z. Zhu, E. Kaxiras, S. Sachdev, and A. Kruchkov, Ultraheavy and ultrarelativistic Dirac quasiparticles in sandwiched graphenes, *Nano Lett.* **20**, 3030 (2020).
- [45] Z. Wu, Z. Zhan, and S. Yuan, Lattice relaxation, mirror symmetry and magnetic field effects on ultraflat bands in twisted trilayer graphene, *Sci. China Phys. Mech. Astron.* **64**, 267811 (2021).
- [46] A. Lopez-Bezanilla and J. L. Lado, Electrical band flattening, valley flux, and superconductivity in twisted trilayer graphene, *Phys. Rev. Res.* **2**, 033357 (2020).
- [47] L. Xian, D. M. Kennes, N. Tancogne-Dejean, M. Altarelli, and A. Rubio, Multiflat bands and strong correlations in twisted bilayer boron nitride: Doping-induced correlated insulator and superconductor, *Nano Lett.* **19**, 4934 (2019).
- [48] L. Xian, M. Claassen, D. Kiese, M. M. Scherer, S. Trebst, D. M. Kennes, and A. Rubio, Realization of nearly dispersionless bands with strong orbital anisotropy from destructive interference in twisted bilayer  $MoS_2$ , *Nat. Commun.* **12**, 5644 (2021).
- [49] M. Angeli and A. H. MacDonald,  $\Gamma$  valley transition metal dichalcogenide moiré bands, *Proc. Natl. Acad. Sci. (USA)* **118**, e2021826118 (2021).
- [50] H. C. Po, L. Zou, T. Senthil, and A. Vishwanath, Faithful tight-binding models and fragile topology of magic-angle bilayer graphene, *Phys. Rev. B* **99**, 195455 (2019).
- [51] S. Carr, S. Fang, Z. Zhu, and E. Kaxiras, Exact continuum model for low-energy electronic states of twisted bilayer graphene, *Phys. Rev. Res.* **1**, 013001 (2019).

- [52] V. o. T. Phong and E. J. Mele, Obstruction and Interference in Low-Energy Models for Twisted Bilayer Graphene, *Phys. Rev. Lett.* **125**, 176404 (2020).
- [53] L. Zou, H. C. Po, A. Vishwanath, and T. Senthil, Band structure of twisted bilayer graphene: Emergent symmetries, commensurate approximants, and Wannier obstructions, *Phys. Rev. B* **98**, 085435 (2018).
- [54] N. E. Bickers, D. J. Scalapino, and S. R. White, Conserving Approximations for Strongly Correlated Electron Systems: Bethe-Salpeter Equation and Dynamics for the Two-Dimensional Hubbard Model, *Phys. Rev. Lett.* **62**, 961 (1989).
- [55] N. E. Bickers and D. J. Scalapino, Conserving approximations for strongly fluctuating electron systems. I. Formalism and calculational approach, *Ann. Phys.* **193**, 206 (1989).
- [56] Y. Zhang, N. F. Q. Yuan, and L. Fu, Moiré quantum chemistry: Charge transfer in transition metal dichalcogenide superlattices, *Phys. Rev. B* **102**, 201115(R) (2020).
- [57] Y. Zhang, T. Liu, and L. Fu, Electronic structures, charge transfer, and charge order in twisted transition metal dichalcogenide bilayers, *Phys. Rev. B* **103**, 155142 (2021).
- [58] F. A. Rasmussen and K. S. Thygesen, Computational 2D materials database: Electronic structure of transition-metal dichalcogenides and oxides, *J. Phys. Chem. C* **119**, 13169 (2015).
- [59] A. Chaves, J. G. Azadani, H. Alsalman, D. R. da Costa, R. Frisenda, A. J. Chaves, S. H. Song, Y. D. Kim, D. He, J. Zhou, A. Castellanos-Gomez, F. M. Peeters, Z. Liu, C. L. Hinkle, S.-H. Oh, P. D. Ye, S. J. Koester, Y. H. Lee, P. Avouris, X. Wang *et al.*, Bandgap engineering of two-dimensional semiconductor materials, *npj 2D Mater. Appl.* **4**, 29 (2020).
- [60] See Supplemental Material at <http://link.aps.org/supplemental/10.1103/PhysRevB.105.L241109> for details on the low-energy continuum model of the electronic bands in  $\Gamma$ -valley twisted TMDCs, for the construction of the Wannier orbitals in the 2D honeycomb moiré pattern, for a study of the electrostatic and long-range Hartree potential in the flat Dirac bands, for an estimation of the on-site and nearest-neighbor Coulomb interaction, for numerical details on the FLEX calculations, for a discussion on the nature of magnetic ordering, for an in-depth discussion of the spin susceptibility structure, for the temperature dependence of the  $d$ - and  $f$ -wave superconducting eigenvalues and order parameters, for a discussion of the influence of band asymmetry as induced by long-range hopping, for a study of superconductivity arising from nonlocal dispersive phonons, and for an estimation of the phonon-induced attractive interaction  $U_{\text{eff}}$  and it includes Refs. [17,18,28,34,38,39,49,54,55,61–64,68,69,73–77,80,81,83,91,104,107–137].
- [61] F. Guinea and N. R. Walet, Electrostatic effects, band distortions, and superconductivity in twisted graphene bilayers, *Proc. Natl. Acad. Sci. (USA)* **115**, 13174 (2018).
- [62] T. Cea, N. R. Walet, and F. Guinea, Electronic band structure and pinning of Fermi energy to Van Hove singularities in twisted bilayer graphene: A self-consistent approach, *Phys. Rev. B* **100**, 205113 (2019).
- [63] T. Cea and F. Guinea, Band structure and insulating states driven by Coulomb interaction in twisted bilayer graphene, *Phys. Rev. B* **102**, 045107 (2020).
- [64] M. J. Calderón and E. Bascones, Interactions in the 8-orbital model for twisted bilayer graphene, *Phys. Rev. B* **102**, 155149 (2020).
- [65] A. H. Castro Neto, F. Guinea, N. M. R. Peres, K. S. Novoselov, and A. K. Geim, The electronic properties of graphene, *Rev. Mod. Phys.* **81**, 109 (2009).
- [66] F. F. Assaad and I. F. Herbut, Pinning the Order: The Nature of Quantum Criticality in the Hubbard Model on Honeycomb Lattice, *Phys. Rev. X* **3**, 031010 (2013).
- [67] M. L. Kiesel, C. Platt, W. Hanke, D. A. Abanin, and R. Thomale, Competing many-body instabilities and unconventional superconductivity in graphene, *Phys. Rev. B* **86**, 020507(R) (2012).
- [68] W.-S. Wang, Y.-Y. Xiang, Q.-H. Wang, F. Wang, F. Yang, and D.-H. Lee, Functional renormalization group and variational Monte Carlo studies of the electronic instabilities in graphene near  $\frac{1}{4}$  doping, *Phys. Rev. B* **85**, 035414 (2012).
- [69] R. Nandkishore, L. S. Levitov, and A. V. Chubukov, Chiral superconductivity from repulsive interactions in doped graphene, *Nat. Phys.* **8**, 158 (2012).
- [70] X. Y. Xu, S. Wessel, and Z. Y. Meng, Competing pairing channels in the doped honeycomb lattice Hubbard model, *Phys. Rev. B* **94**, 115105 (2016).
- [71] M. Raczkowski, R. Peters, T. T. Phùng, N. Takemori, F. F. Assaad, A. Honecker, and J. Vahedi, Hubbard model on the honeycomb lattice: From static and dynamical mean-field theories to lattice quantum Monte Carlo simulations, *Phys. Rev. B* **101**, 125103 (2020).
- [72] N. C. Costa, K. Seki, and S. Sorella, Magnetism and Charge Order in the Honeycomb Lattice, *Phys. Rev. Lett.* **126**, 107205 (2021).
- [73] K. Kuroki and R. Arita, Spin-triplet superconductivity in repulsive Hubbard models with disconnected Fermi surfaces: A case study on triangular and honeycomb lattices, *Phys. Rev. B* **63**, 174507 (2001).
- [74] S. Onari, K. Kuroki, R. Arita, and H. Aoki, Superconductivity induced by interband nesting in the three-dimensional honeycomb lattice, *Phys. Rev. B* **65**, 184525 (2002).
- [75] K. Kuroki, Spin-fluctuation-mediated  $d + id'$  pairing mechanism in doped  $\beta$ -MnCl ( $M=\text{Hf,Zr}$ ) superconductors, *Phys. Rev. B* **81**, 104502 (2010).
- [76] J. Li, M. Wallerberger, N. Chikano, C.-N. Yeh, E. Gull, and H. Shinaoka, Sparse sampling approach to efficient ab initio calculations at finite temperature, *Phys. Rev. B* **101**, 035144 (2020).
- [77] N. Witt, E. G. C. P. van Loon, T. Nomoto, R. Arita, and T. O. Wehling, Efficient fluctuation-exchange approach to low-temperature spin fluctuations and superconductivity: From the Hubbard model to  $\text{Na}_x\text{CoO}_2 \cdot y\text{H}_2\text{O}$ , *Phys. Rev. B* **103**, 205148 (2021).
- [78] M. Rösner, C. Steinke, M. Lorke, C. Gies, F. Jahnke, and T. O. Wehling, Two-dimensional heterojunctions from nonlocal manipulations of the interactions, *Nano Lett.* **16**, 2322 (2016).
- [79] A. Raja, A. Chaves, J. Yu, G. Arefe, H. M. Hill, A. F. Rigosi, T. C. Berkelbach, P. Nagler, C. Schüller, T. Korn, C. Nuckolls, J. Hone, L. E. Brus, T. F. Heinz, D. R. Reichman, and A. Chernikov, Coulomb engineering of the bandgap and excitons in two-dimensional materials, *Nat. Commun.* **8**, 15251 (2017).
- [80] J. M. Pizarro, M. Rösner, R. Thomale, R. Valentí, and T. O. Wehling, Internal screening and dielectric engineering

- in magic-angle twisted bilayer graphene, *Phys. Rev. B* **100**, 161102(R) (2019).
- [81] Z. A. H. Goodwin, F. Corsetti, A. A. Mostofi, and J. Lischner, Twist-angle sensitivity of electron correlations in moiré graphene bilayers, *Phys. Rev. B* **100**, 121106(R) (2019).
- [82] Z. A. H. Goodwin, V. Vitale, F. Corsetti, D. K. Efetov, A. A. Mostofi, and J. Lischner, Critical role of device geometry for the phase diagram of twisted bilayer graphene, *Phys. Rev. B* **101**, 165110 (2020).
- [83] H. S. Arora, R. Polski, Y. Zhang, A. Thomson, Y. Choi, H. Kim, Z. Lin, I. Z. Wilson, X. Xu, J.-H. Chu, K. Watanabe, T. Taniguchi, J. Alicea, and S. Nadj-Perge, Superconductivity in metallic twisted bilayer graphene stabilized by WSe<sub>2</sub>, *Nature (London)* **583**, 379 (2020).
- [84] M. Kim, S. G. Xu, A. I. Berdyugin, A. Principi, S. Slizovskiy, N. Xin, P. Kumaravadeivel, W. Kuang, M. Hamer, R. K. Kumar, R. V. Gorbachev, K. Watanabe, T. Taniguchi, I. V. Grigorieva, V. I. Fal'ko, M. Polini, and A. K. Geim, Control of electron-electron interaction in graphene by proximity screening, *Nat. Commun.* **11**, 2339 (2020).
- [85] N. Bulut, D. J. Scalapino, and S. R. White, Comparison of Monte Carlo and diagrammatic calculations for the two-dimensional Hubbard model, *Phys. Rev. B* **47**, 2742 (1993).
- [86] N. Bulut, D. J. Scalapino, and S. R. White, Effective electron-electron interaction in the two-dimensional Hubbard model, *Phys. Rev. B* **50**, 9623 (1994).
- [87] J. Zhang, R. Sknepnek, R. M. Fernandes, and J. Schmalian, Orbital coupling and superconductivity in the iron pnictides, *Phys. Rev. B* **79**, 220502(R) (2009).
- [88] T. Moriya and K. Ueda, Antiferromagnetic spin fluctuation and superconductivity, *Rep. Prog. Phys.* **66**, 1299 (2003).
- [89] D. J. Scalapino, A common thread: The pairing interaction for unconventional superconductors, *Rev. Mod. Phys.* **84**, 1383 (2012).
- [90] T. Ying and S. Wessel, Pairing and chiral spin density wave instabilities on the honeycomb lattice: A comparative quantum Monte Carlo study, *Phys. Rev. B* **97**, 075127 (2018).
- [91] W. L. McMillan, Transition temperature of strong-coupled superconductors, *Phys. Rev.* **167**, 331 (1968).
- [92] R. Dynes, McMillan's equation and the  $T_c$  of superconductors, *Solid State Commun.* **10**, 615 (1972).
- [93] V. V. Tolmachev, Logarithmic criterion for superconductivity, *Dokl. Akad. Nauk SSSR* **140**, 563 (1961).
- [94] P. Morel and P. W. Anderson, Calculation of the superconducting state parameters with retarded electron-phonon interaction, *Phys. Rev.* **125**, 1263 (1962).
- [95] F. Wu, A. H. MacDonald, and I. Martin, Theory of Phonon-Mediated Superconductivity in Twisted Bilayer Graphene, *Phys. Rev. Lett.* **121**, 257001 (2018).
- [96] M.-L. Lin, Q.-H. Tan, J.-B. Wu, X.-S. Chen, J.-H. Wang, Y.-H. Pan, X. Zhang, X. Cong, J. Zhang, W. Ji, P.-A. Hu, K.-H. Liu, and P.-H. Tan, Moiré phonons in twisted bilayer MoS<sub>2</sub>, *ACS Nano Nano* **12**, 8770 (2018).
- [97] Y. W. Choi and H. J. Choi, Strong electron-phonon coupling, electron-hole asymmetry, and nonadiabaticity in magic-angle twisted bilayer graphene, *Phys. Rev. B* **98**, 241412(R) (2018).
- [98] B. Lian, Z. Wang, and B. A. Bernevig, Twisted Bilayer Graphene: A Phonon-Driven Superconductor, *Phys. Rev. Lett.* **122**, 257002 (2019).
- [99] R. Debnath, I. Maity, R. Biswas, V. Raghunathan, M. Jain, and A. Ghosh, Evolution of high-frequency Raman modes and their doping dependence in twisted bilayer MoS<sub>2</sub>, *Nanoscale* **12**, 17272 (2020).
- [100] K.-Q. Lin, J. Holler, J. M. Bauer, P. Parzefall, M. Scheuck, B. Peng, T. Korn, S. Bange, J. M. Lupton, and C. Schüller, Large-scale mapping of moiré superlattices by hyperspectral Raman imaging, *Adv. Mater.* **33**, 2008333 (2021).
- [101] P. Parzefall, J. Holler, M. Scheuck, A. Beer, K.-Q. Lin, B. Peng, B. Monserrat, P. Nagler, M. Kempf, T. Korn, and C. Schüller, Moiré phonons in twisted MoSe<sub>2</sub>-WSe<sub>2</sub> heterobilayers and their correlation with interlayer excitons, *2D Mater.* **8**, 035030 (2021).
- [102] J. Quan, L. Linhart, M.-L. Lin, D. Lee, J. Zhu, C.-Y. Wang, W.-T. Hsu, J. Choi, J. Embley, C. Young, T. Taniguchi, K. Watanabe, C.-K. Shih, K. Lai, A. H. MacDonald, P.-H. Tan, F. Libisch, and X. Li, Phonon renormalization in reconstructed MoS<sub>2</sub> moiré superlattices, *Nat. Mater.* **20**, 1100 (2021).
- [103] T. M. Rice and G. K. Scott, New Mechanism for a Charge-Density-Wave Instability, *Phys. Rev. Lett.* **35**, 120 (1975).
- [104] S. Jiang, A. Meszaros, and Y. Ran, Chiral Spin-Density Wave, Spin-Charge-Chern Liquid, and  $d + id$  Superconductivity in 1/4-Doped Correlated Electronic Systems on the Honeycomb Lattice, *Phys. Rev. X* **4**, 031040 (2014).
- [105] J. Berges, E. G. C. P. van Loon, A. Schobert, M. Rösner, and T. O. Wehling, *Ab initio* phonon self-energies and fluctuation diagnostics of phonon anomalies: Lattice instabilities from Dirac pseudospin physics in transition metal dichalcogenides, *Phys. Rev. B* **101**, 155107 (2020).
- [106] B. Keimer, S. A. Kivelson, M. R. Norman, S. Uchida, and J. Zaanen, From quantum matter to high-temperature superconductivity in copper oxides, *Nature (London)* **518**, 179 (2015).
- [107] D. Xiao, G.-B. Liu, W. Feng, X. Xu, and W. Yao, Coupled Spin and Valley Physics in Monolayers of MoS<sub>2</sub> and Other Group-VI Dichalcogenides, *Phys. Rev. Lett.* **108**, 196802 (2012).
- [108] S. Venkateswarlu, A. Honecker, and G. Trambly de Laissardière, Electronic localization in twisted bilayer mos<sub>2</sub> with small rotation angle, *Phys. Rev. B* **102**, 081103(R) (2020).
- [109] N. Marzari, A. A. Mostofi, J. R. Yates, I. Souza, and D. Vanderbilt, Maximally localized Wannier functions: Theory and applications, *Rev. Mod. Phys.* **84**, 1419 (2012).
- [110] N. F. Q. Yuan, H. Isobe, and L. Fu, Magic of high-order van Hove singularity, *Nat. Commun.* **10**, 5769 (2019).
- [111] L. Classen, A. V. Chubukov, C. Honerkamp, and M. M. Scherer, Competing orders at higher-order Van Hove points, *Phys. Rev. B* **102**, 125141 (2020).
- [112] G. P. Kerker, Efficient iteration scheme for self-consistent pseudopotential calculations, *Phys. Rev. B* **23**, 3082 (1981).
- [113] E. G. C. P. van Loon, M. Schüler, M. I. Katsnelson, and T. O. Wehling, Capturing nonlocal interaction effects in the Hubbard model: Optimal mappings and limits of applicability, *Phys. Rev. B* **94**, 165141 (2016).
- [114] K. Ohno, Some remarks on the Pariser-Parr-Pople method, *Theor. Chim. Acta* **2**, 219 (1964).
- [115] T. Cea and F. Guinea, Coulomb interaction, phonons, and superconductivity in twisted bilayer graphene, *Proc. Natl. Acad. Sci. (USA)* **118**, e2107874118 (2021).
- [116] A. Laturia, M. L. Van de Put, and W. G. Vandenberghe, Dielectric properties of hexagonal boron nitride and transition metal

- dichalcogenides: from monolayer to bulk, *npj 2D Mater. Appl.* **2**, 6 (2018).
- [117] A. Weston, Y. Zou, V. Enaldiev, A. Summerfield, N. Clark, V. Zólyomi, A. Graham, C. Yelgel, S. Magorrian, M. Zhou, J. Zultak, D. Hopkinson, A. Barinov, T. H. Bointon, A. Kretinin, N. R. Wilson, P. H. Beton, V. I. Fal'ko, S. J. Haigh, and R. Gorbachev, Atomic reconstruction in twisted bilayers of transition metal dichalcogenides, *Nat. Nanotechnol.* **15**, 592 (2020).
- [118] H. Kontani and K. Ueda, Electronic Properties of the Trellis-Lattice Hubbard Model: Pseudogap and Superconductivity, *Phys. Rev. Lett.* **80**, 5619 (1998).
- [119] S. Koikegami, S. Fujimoto, and K. Yamada, Electronic structure and transition temperature of the  $d$ - $p$  model, *J. Phys. Soc. Jpn.* **66**, 1438 (1997).
- [120] H. Shinaoka, N. Chikano, E. Gull, J. Li, T. Nomoto, J. Otsuki, M. Wallerberger, T. Wang, and K. Yoshimi, [arXiv:2106.12685](https://arxiv.org/abs/2106.12685).
- [121] H. Shinaoka, J. Otsuki, M. Ohzeki, and K. Yoshimi, Compressing Green's function using intermediate representation between imaginary-time and real-frequency domains, *Phys. Rev. B* **96**, 035147 (2017).
- [122] N. Chikano, K. Yoshimi, J. Otsuki, and H. Shinaoka, irbasis: Open-source database and software for intermediate-representation basis functions of imaginary-time Green's function, *Comput. Phys. Commun.* **240**, 181 (2019).
- [123] M. Sigrist and K. Ueda, Phenomenological theory of unconventional superconductivity, *Rev. Mod. Phys.* **63**, 239 (1991).
- [124] N. D. Mermin and H. Wagner, Absence of Ferromagnetism or Antiferromagnetism in One- or Two-Dimensional Isotropic Heisenberg Models, *Phys. Rev. Lett.* **17**, 1307 (1966).
- [125] H. Kontani and M. Ohno, Effect of a nonmagnetic impurity in a nearly antiferromagnetic Fermi liquid: Magnetic correlations and transport phenomena, *Phys. Rev. B* **74**, 014406 (2006).
- [126] H. Kino and H. Kontani, Phase diagram of superconductivity on the anisotropic triangular lattice Hubbard model: An effective model of  $\kappa$ -(BEDT-TTF) salts, *J. Phys. Soc. Jpn.* **67**, 3691 (1998).
- [127] M. Kitatani, N. Tsuji, and H. Aoki, FLEX+DMFT approach to the  $d$ -wave superconducting phase diagram of the two-dimensional Hubbard model, *Phys. Rev. B* **92**, 085104 (2015).
- [128] W. A. Harrison, *Elementary Electronic Structure*, rev. ed. (World Scientific, Singapore, 2004).
- [129] P. B. Allen and R. C. Dynes, Transition temperature of strongly-coupled superconductors reanalyzed, *Phys. Rev. B* **12**, 905 (1975).
- [130] M. Rösner, S. Haas, and T. O. Wehling, Phase diagram of electron-doped dichalcogenides, *Phys. Rev. B* **90**, 245105 (2014).
- [131] G. Schönhoff, M. Rösner, R. E. Groenewald, S. Haas, and T. O. Wehling, Interplay of screening and superconductivity in low-dimensional materials, *Phys. Rev. B* **94**, 134504 (2016).
- [132] G. D. Mahan, *Many-Particle Physics*, 3rd ed. (Springer, US, 2000).
- [133] J. L. Feldman, Elastic constants of 2H-MoS<sub>2</sub> and 2H-NbSe<sub>2</sub> extracted from measured dispersion curves and linear compressibilities, *J. Phys. Chem. Solids* **37**, 1141 (1976).
- [134] Y. Zhao, X. Luo, H. Li, J. Zhang, P. T. Araujo, C. K. Gan, J. Wu, H. Zhang, S. Y. Quek, M. S. Dresselhaus, and Q. Xiong, Interlayer breathing and shear modes in few-trilayer MoS<sub>2</sub> and WSe<sub>2</sub>, *Nano Lett.* **13**, 1007 (2013).
- [135] L. D. Landau and E. M. Lifshitz, *Theory of Elasticity*, 2nd ed. (Pergamon, Oxford, 1970), Vol. 7.
- [136] D. Çakır, F. M. Peeters, and C. Sevik, Mechanical and thermal properties of h-MX<sub>2</sub> (M=Cr, Mo, W; X=O, S, Se, Te) monolayers: A comparative study, *Appl. Phys. Lett.* **104**, 203110 (2014).
- [137] K. Liu, Q. Yan, M. Chen, W. Fan, Y. Sun, J. Suh, D. Fu, S. Lee, J. Zhou, S. Tongay, J. Ji, J. B. Neaton, and J. Wu, Elastic properties of chemical-vapor-deposited monolayer MoS<sub>2</sub>, WS<sub>2</sub>, and their bilayer heterostructures, *Nano Lett.* **14**, 5097 (2014).

# Supplemental Material: Doping fingerprints of spin and lattice fluctuations in moiré superlattice systems

Niklas Witt,<sup>1,2,\*</sup> José M. Pizarro,<sup>1,3,†</sup> Jan Berges,<sup>1</sup> Takuya Nomoto,<sup>4</sup> Ryotaro Arita,<sup>4,5</sup> and Tim O. Wehling<sup>1,2</sup>

<sup>1</sup>*Institute of Theoretical Physics, Bremen Center for Computational Materials Science, and MAPEX Center for Materials and Processes, University of Bremen, Otto-Hahn-Allee 1, 28359 Bremen, Germany*

<sup>2</sup>*I. Institute of Theoretical Physics, University of Hamburg, Notkestraße 9, 22607 Hamburg, Germany*

<sup>3</sup>*Max Planck Institute for the Structure and Dynamics of Matter, Luruper Chaussee 149, 22671 Hamburg, Germany*

<sup>4</sup>*Department of Applied Physics, The University of Tokyo, 7-3-1 Hongo, Bunkyo-ku, Tokyo 113-8656, Japan*

<sup>5</sup>*RIKEN Center for Emergent Matter Science, 2-1 Hirosawa, Wako, Saitama 351-0198, Japan*

In Section S1 of this Supplemental Material, we give a short description of the low-energy continuum model developed in Ref. [S1] for  $\Gamma$ -valley twisted transition metal dichalcogenides (TMDCs) which we employed here. We show the band structure for all  $\Gamma$ -valley twisted TMDCs,  $\text{WS}_2$ ,  $\text{MoS}_2$ , and  $\text{MoSe}_2$ , at different twist angles  $\theta$ . In Section S2, we present the Wannier construction for the two top-most superlattice valence bands in a twist angle range of  $1^\circ < \theta < 5^\circ$ . In Section S3, we discuss the effect of the long-range Coulomb interactions on the low-energy flat bands in presence of doping in the Hartree approximation. We follow the procedure from Refs. [S2, S3] for magic-angle twisted bilayer graphene (MATBG). Section S4 gives estimations of the of the electronic Coulomb interaction strength, in particular the on-site and nearest-neighbor interaction parameters  $U$  and  $V$ . In Section S5, we explain the calculations in the fluctuation exchange (FLEX) approximation [S4, S5]. In Section S6, we discuss the nature of magnetic ordering, analyze the momentum dependence of the static spin susceptibility at different dopings  $\delta$  and temperatures  $T/t$ , and show its real space profile. In Section S7, we investigate the leading superconducting order parameter and possible pairing symmetries in the honeycomb Hubbard model at various dopings and temperatures. Section S8 discusses the influence of longer-ranged hopping terms on spin fluctuations and superconductivity. In Section S9 we investigate the influence of non-local electron-phonon coupling as well as dispersive phonon frequencies on the doping dependence of phonon-mediated superconductivity. In Section S10 we provide an estimation of the effective electron-phonon interaction  $U_{\text{eff}}$  used for the Holstein model calculations in the main text and for the non-local Peierls coupling employed in Section S9.

## S1. LOW-ENERGY CONTINUUM MODEL FOR $\Gamma$ -VALLEY TWISTED TMDCS

We outline here the low-energy continuum model which we used for the description of the moiré valence band structure of  $\Gamma$ -valley twisted TMDCs. The model was introduced in Ref. [S1], from where we outline here the main points. In this continuum model, only the valence antibonding state at the  $\Gamma$  point is considered, which is isolated from other bands by hundreds of meV because of the interlayer coupling. Since the bands around the  $\Gamma$ -point are mainly of transition metal  $d_{z^2}$ -character, spin-orbit coupling effects are small and can be neglected. Because of this, the description of these  $\Gamma$ -valley twisted TMDCs is easier than other TMDC systems like homobilayer  $\text{WSe}_2$ , where the valence band maximum is at the  $K$ -point with strong spin-orbit coupling [S6]. The low-energy Hamiltonian of the continuum model can be written as

$$H = -\frac{\hbar^2 k^2}{2m^*} + V_{\text{M}}(\mathbf{r}), \quad (\text{S1})$$

where  $m^*$  is the effective mass and  $V_{\text{M}}(\mathbf{r})$  is the moiré potential felt by the holes at the valence band maximum in  $\Gamma$ . The moiré potential has the following expression in real space:

$$V_{\text{M}}(\mathbf{r}) = \sum_{s=1}^3 \sum_{j=1}^6 V^s e^{i(\mathbf{g}_j^s \cdot \mathbf{r} + \phi^s)}. \quad (\text{S2})$$

Here,  $s$  is the  $s$ -th shell of six moiré reciprocal lattice vectors  $\mathbf{g}_j^s = \mathcal{R}_{(j-1)\pi/3} \mathbf{G}^s$  ( $j = 1, \dots, 6$ ) with  $\mathcal{R}_\alpha$  being the two-dimensional (2D) rotation matrix about an angle  $\alpha$ . We choose reciprocal lattice vectors pointing to the  $s$ -th

---

\* niklas.witt@physik.uni-hamburg.de

† jose.pizarro@mpsd.mpg.de

Table S1. Continuum model parameters for  $\Gamma$ -valley twisted TMDCs.  $a_0$  is the lattice constant in  $\text{\AA}$ ,  $m^*$  is the effective mass in bare electron mass units, and  $V^s$  are in meV. Data taken from Ref. [S1].

	WS <sub>2</sub>	MoS <sub>2</sub>	MoSe <sub>2</sub>
$a_0$	3.18	3.182	3.295
$m^*$	0.87	0.9	1.17
$V^1$	33.5	39.45	36.8
$V^2$	4.0	6.5	8.4
$V^3$	5.5	10.0	10.2
$\phi^{1,2,3}$	$\pi$	$\pi$	$\pi$

shell as  $\mathbf{G}^1 = \mathbf{G}_2^M$ ,  $\mathbf{G}^2 = \mathbf{G}_1^M + \mathbf{G}_2^M$ , and  $\mathbf{G}^3 = 2\mathbf{G}_2^M$ , where  $\mathbf{G}_{1,2}^M$  span the reciprocal moiré lattice. The phase factors  $\phi^s$  are constrained by the  $C_{6z}$  symmetry of the moiré lattice to be either 0 or  $\pi$ .

The continuum model parameters ( $m^*$ ,  $V^s$ ,  $\phi^s$ ) were obtained from the *ab initio* calculation of the fully relaxed twisted bilayers, and they are given in Table S1 for the different  $\Gamma$ -valley twisted TMDCs, WS<sub>2</sub>, MoS<sub>2</sub>, and MoSe<sub>2</sub> [S1]. The maximum of the moiré potential of Eq. (S2) felt by the holes in the valence band maximum is found in the AB/BA regions (see Fig. 1B of Ref. [S1]), so that the low-energy physics of the  $\Gamma$ -valley twisted TMDCs is controlled by orbitals sitting in the honeycomb AB/BA regions.

The diagonalization of  $H$  is performed in reciprocal space, where the Hamiltonian of Eq. (S1) is given by (see Eq. (1) in the main text)

$$H = -\frac{\hbar^2|\mathbf{k} + \mathbf{G}|^2}{2m^*}\delta_{\mathbf{G},\mathbf{G}'} + V_M(\mathbf{G} - \mathbf{G}'). \quad (\text{S3})$$

$\mathbf{k}$  and  $\mathbf{G}$  denote moiré crystal momentum and vectors from the moiré reciprocal lattice, respectively.  $V_M(\mathbf{G} - \mathbf{G}')$  is the Fourier transformation of  $V_M(\mathbf{r})$ . This Hamiltonian is expanded up to a plane-wave cutoff  $G_c$  for a given twist angle  $\theta$ . In Fig. S1 we show the band structures for  $\Gamma$ -valley twisted TMDCs at twist angles in the range  $1^\circ < \theta < 5^\circ$ . The zero energy is defined as the top of the valence band. For this twist angle range it is sufficient to use  $G_c = 4-5 G^M$ , where  $G^M = |\mathbf{G}_{1,2}^M|$ .

From the valence band edge, two flat bands emerge which touch at a Dirac point in the corner of the Brillouin zone and at a certain negative energy. We refer to these bands as "flat Dirac bands" for brevity. These bands are well isolated from other higher energy bands for  $\theta < 5^\circ$ . The bandwidth of the flat Dirac bands continuously increases approximately quadratically with the twist angle.

Another approach to calculate band structures is the derivation of atomistic tight-binding models, which, for instance, has been done in Ref. [S7] for MoS<sub>2</sub>. This approach yields the same results and reproduces ab-initio calculations consistently.

## S2. WANNIER PROJECTION OF FLAT DIRAC BANDS

Based on our observations in the previous section, we construct a tight-binding Hamiltonian for the isolated flat Dirac bands via Wannier projection with one orbital per sublattice site. The AB and BA regions play the role of the A and B sublattice sites in a honeycomb lattice. The eigenstates of the low-energy continuum model are

$$\Phi_{\mathbf{k}}^\alpha(\mathbf{r}) \equiv |\Phi_{\mathbf{k}}^\alpha\rangle = \sum_{\mathbf{G}} c_{\mathbf{k}\mathbf{G}}^\alpha e^{i(\mathbf{k}+\mathbf{G})\cdot\mathbf{r}}, \quad (\text{S4})$$

where  $\alpha$  is the band index and  $c_{\mathbf{k}\mathbf{G}}^\alpha$  are the plane-wave coefficients obtained from the diagonalization of the Hamiltonian from Eq. (S3). We set  $G_c = 5G^M$  and use a  $\mathbf{k}$ -mesh of  $15 \times 15$ . We consider Gaussian functions centered on A and B sites as the trial orbitals  $|g_{\mathbf{k}}^m\rangle$ , whose plane-wave expansion coefficients are given by

$$g_{\mathbf{k}\mathbf{G}}^m = e^{-(\Delta\mathbf{K})^2/2} e^{-i\mathbf{K}\cdot\mathbf{l}_m}. \quad (\text{S5})$$

Here,  $m \in \{A, B\}$  is the sublattice (orbital) index,  $\mathbf{K} = \mathbf{k} + \mathbf{G}$ , and  $\mathbf{l}_A = \mathbf{L}_1^M/3 + 2\mathbf{L}_2^M/3$  and  $\mathbf{l}_B = 2\mathbf{L}_1^M/3 + \mathbf{L}_2^M/3$  are vectors pointing from the moiré unit cell origin to A and B sites, respectively.  $\mathbf{L}_{1,2}^M$  are the moiré lattice vectors,  $\lambda^M = |\mathbf{L}_{1,2}^M|$ , and  $\Delta = \lambda^M/3$  is the extent of the trial orbitals. These trial orbitals are then projected onto the

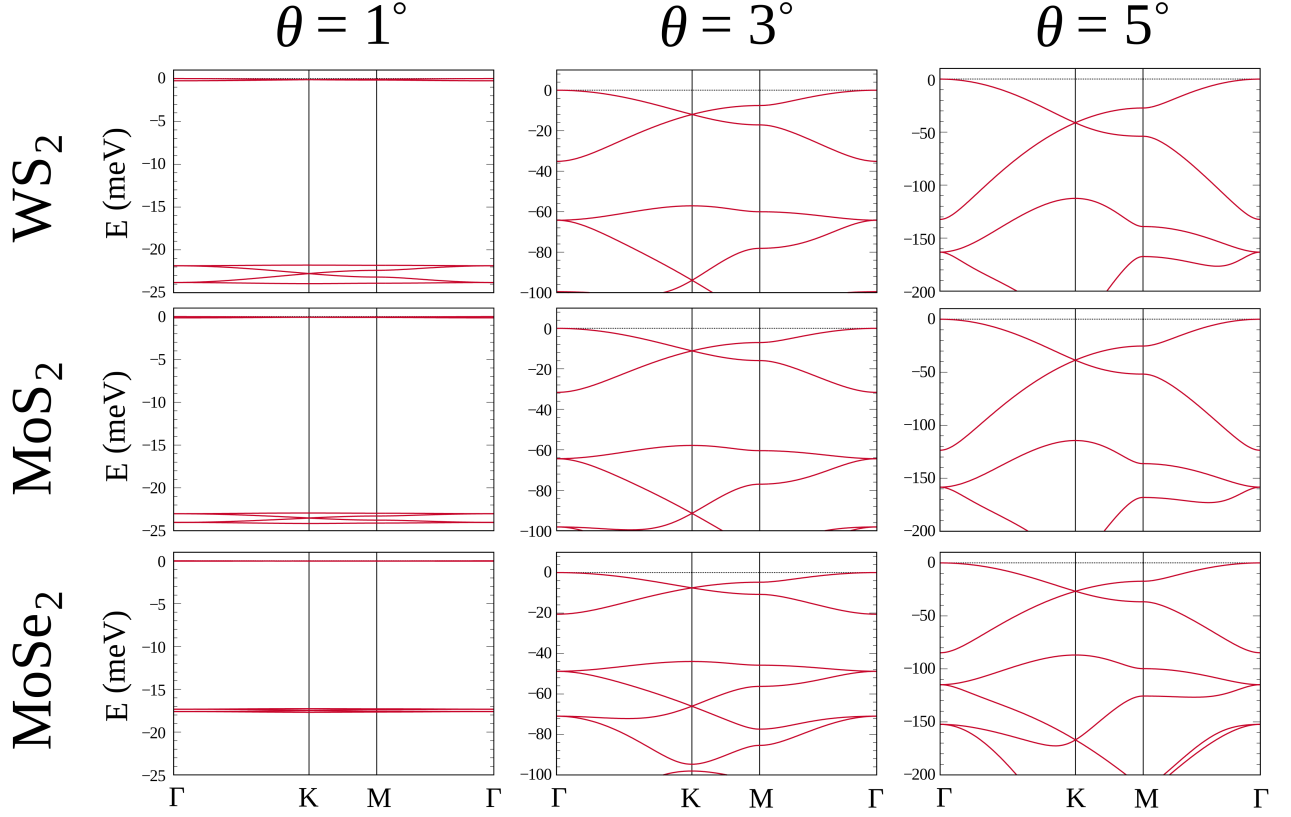


Figure S1. (Color online) Band structures for the  $\Gamma$ -valley twisted TMDCs,  $\text{WS}_2$  (top row),  $\text{MoS}_2$  (middle row), and  $\text{MoSe}_2$  (bottom row). We show the low-energy band evolution for the twist angle range  $1^\circ < \theta < 5^\circ$ .

eigenstates manifold of the low energy Dirac bands  $|\phi_{\mathbf{k}}^m\rangle = \sum_{\alpha} \langle \Phi_{\mathbf{k}}^{\alpha} | g_{\mathbf{k}}^m \rangle |\Phi_{\mathbf{k}}^{\alpha}\rangle$ , which yields the corresponding plane-wave expansion coefficients of the state  $|\phi_{\mathbf{k}}^m\rangle$  [S8]

$$\phi_{\mathbf{k}\mathbf{G}}^m = \sum_{\alpha} c_{\mathbf{k}\mathbf{G}}^{\alpha} P_{\mathbf{k}}^{\alpha m}. \quad (\text{S6})$$

The projection matrix  $P_{\mathbf{k}}^{\alpha m} = \langle \Phi_{\mathbf{k}}^{\alpha} | g_{\mathbf{k}}^m \rangle \equiv \sum_{\mathbf{G}} (c_{\mathbf{k}\mathbf{G}}^{\alpha})^{\dagger} g_{\mathbf{k}\mathbf{G}}^m$  allows to calculate the overlap matrix as

$$S_{\mathbf{k}}^{mn} = \langle \phi_{\mathbf{k}}^m | \phi_{\mathbf{k}}^n \rangle = (P_{\mathbf{k}}^{\dagger} P_{\mathbf{k}})^{mn}. \quad (\text{S7})$$

Eqs. (S6) and (S7) are used to calculate the so-called smooth gauge plane-wave expansion coefficients of the smooth gauge Bloch states  $|\tilde{\Phi}_{\mathbf{k}}^m\rangle$

$$\tilde{c}_{\mathbf{k}\mathbf{G}}^m = \sum_n \phi_{\mathbf{k}\mathbf{G}}^n \cdot (S_{\mathbf{k}}^{-1/2})^{nm}. \quad (\text{S8})$$

The resulting set of well-localized Wannier orbitals can be constructed in real space as

$$\mathcal{W}_{\mathbf{R}m}(\mathbf{r}) = \frac{1}{N_{\mathbf{k}} \sqrt{A_M}} \sum_{\mathbf{k}} \sum_{\mathbf{G}} \tilde{c}_{\mathbf{k}\mathbf{G}}^m e^{i\mathbf{K} \cdot (\mathbf{r} - \mathbf{R})}, \quad (\text{S9})$$

where  $A_M = \sqrt{3}\lambda^M/2$  is the moiré unit cell size,  $\mathbf{r}$  denotes the real space coordinates, and  $\mathbf{R}$  describes the Bravais lattice. In Fig. S2(a) we show the real-space probability density  $|\mathcal{W}|^2$  for the two Wannier orbitals  $m$  from the unit cell at the origin of the Bravais lattice obtained from the flat Dirac bands.

Now, the Hamiltonian in the Wannier orbital basis can be calculated by projecting the continuum Hamiltonian onto the smooth gauge Bloch states  $|\tilde{\Phi}_{\mathbf{k}}^m\rangle$

$$\tilde{H}_{\mathbf{k}}^{mn} = \langle \tilde{\Phi}_{\mathbf{k}}^m | H | \tilde{\Phi}_{\mathbf{k}}^n \rangle \equiv \sum_{\mathbf{G}, \mathbf{G}'} (\tilde{c}_{\mathbf{k}\mathbf{G}}^m)^{\dagger} \tilde{c}_{\mathbf{k}\mathbf{G}'}^n H_{\mathbf{k}\mathbf{G}\mathbf{G}'}, \quad (\text{S10})$$

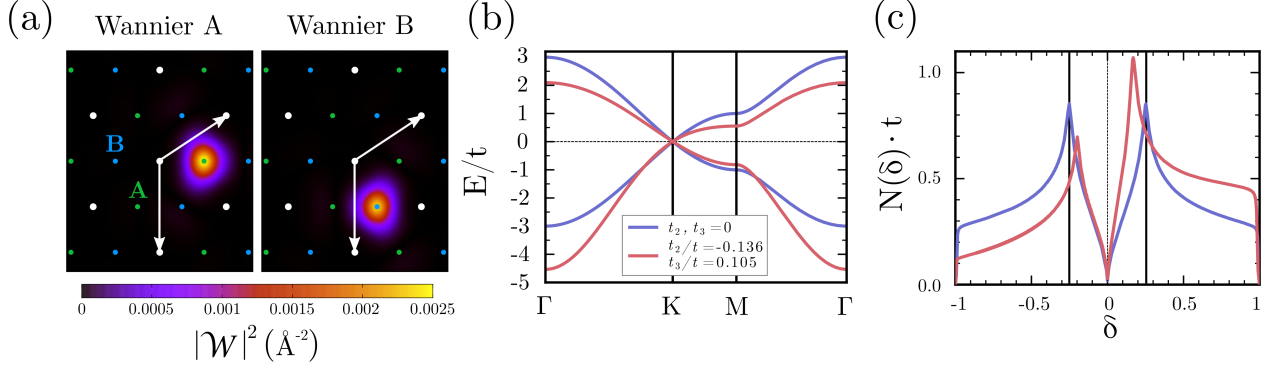


Figure S2. (Color online) Wannier tight-binding model for twisted  $\text{WS}_2$  at  $3.5^\circ$ . (a) Wannier densities  $|\mathcal{W}_m|^2$  for each orbital centered in the sublattices A (green dots) and B (blue dots). White dots denote the Bravais lattice  $\mathbf{R}$  and white arrows are the moiré lattice vectors  $\mathbf{L}_{1,2}^M$ . (b) Band structure and (c) density of states  $N(\delta)$  per spin and unit cell of the honeycomb tight-binding model with nearest-neighbor hopping only ( $t_2, t_3 = 0$ , blue line) and including also longer-ranged hopping terms ( $t_2/t_1 = -0.136, t_3/t_1 = 0.105$ , red line). The doping  $\delta$  is counted relative to the Dirac point. Van Hove singularities (VHS) appear at the  $M$ -points in the Brillouin zone, corresponding to a doping of  $\delta = \pm 0.25$  ( $\delta \approx -0.2, 0.17$ ) in the particle-hole symmetric (asymmetric) case.

where  $H_{\mathbf{k}\mathbf{G}\mathbf{G}'}$  are the matrix elements of the Hamiltonian in Eq. (S3). Fourier transformation of Eq. (S10) gives the real space Wannier Hamiltonian  $\tilde{H}_{\mathbf{r}}^{mn}$  whose matrix elements  $m, n$  are the hopping integrals entering the tight-binding model used in the main text. We find that including up to three nearest-neighbor hoppings is sufficient to describe the band structures found by the continuum model in the twist angle range  $1^\circ < \theta < 5^\circ$ , as shown in Fig. 1(b) of the main text for  $\text{WS}_2$  at  $\theta = 3.5^\circ$ . The angle dependence of the hopping amplitudes is shown in Fig. 1(c) of the main text.

The resulting honeycomb tight-binding model is

$$H_0(\mathbf{k}) = \begin{pmatrix} H_{AA}(\mathbf{k}) & H_{AB}(\mathbf{k}) \\ H_{BA}(\mathbf{k}) & H_{BB}(\mathbf{k}) \end{pmatrix} \quad \text{with} \quad (\text{S11})$$

$$H_{AA}(\mathbf{k}) = H_{BB}(\mathbf{k}) = 2t_2 [\cos(\mathbf{k} \cdot \mathbf{L}_1^M) + \cos(\mathbf{k} \cdot \mathbf{L}_2^M) + \cos(\mathbf{k} \cdot (\mathbf{L}_1^M + \mathbf{L}_2^M))] ,$$

$$H_{AB}(\mathbf{k}) = H_{BA}^*(\mathbf{k}) = t_1 [1 + e^{i\mathbf{k} \cdot \mathbf{L}_1^M} + e^{i\mathbf{k} \cdot (\mathbf{L}_1^M + \mathbf{L}_2^M)}] + t_3 [2 \cos(\mathbf{k} \cdot \mathbf{L}_2^M) e^{i\mathbf{k} \cdot (2\mathbf{L}_1^M + \mathbf{L}_2^M)}] .$$

The corresponding band structure and density of states (DOS) per spin and unit cell can be found in Figs. S2(b) and (c), respectively. The DOS is shown as a function of doping  $\delta$  that is counted relative to the Dirac point. We show the third nearest-neighbor hopping model with  $t_2/t_1 = -0.136$  and  $t_3/t_1 = 0.105$  for  $\text{WS}_2$  at  $\theta = 5^\circ$  using  $t \equiv t_1$  as unit of energy. It reveals a slight particle-hole asymmetry around the Dirac point. We also show a simplified model which only accounts for nearest-neighbor hopping and which is particle-hole symmetric. In both cases there are Van Hove singularities (VHS) emerging at the  $M$  points of the moiré Brillouin zone.

Since  $t_1 \gg t_2, t_3$ , the character of the VHS does not change to higher order VHS [S9, S10] and the qualitative physics occurring in the system are not expected to change significantly (c.f. Section S8 for an explicit demonstration). Therefore, we neglect  $t_2$  and  $t_3$  and consider the particle-hole symmetric model with nearest-neighbor hopping  $t_1 \equiv t$  only in the main text.

### S3. LONG-RANGE COULOMB INTERACTIONS

Several twisted 2D systems are known to show a strong reconstruction of their band structure upon doping caused by the Hartree potential resulting from the long-range Coulomb interaction [S2, S3, S11–S13]. Here, we study the effect of the Hartree potential in  $\Gamma$ -valley twisted TMDCs. We follow the method developed in Ref. [S2]. The Hartree potential contribution to the total Hamiltonian of Eq. (S1) is given by

$$V_H(\mathbf{r}) = \int d^2\mathbf{r}' V_C(\mathbf{r} - \mathbf{r}') \delta\rho(\mathbf{r}'), \quad (\text{S12})$$



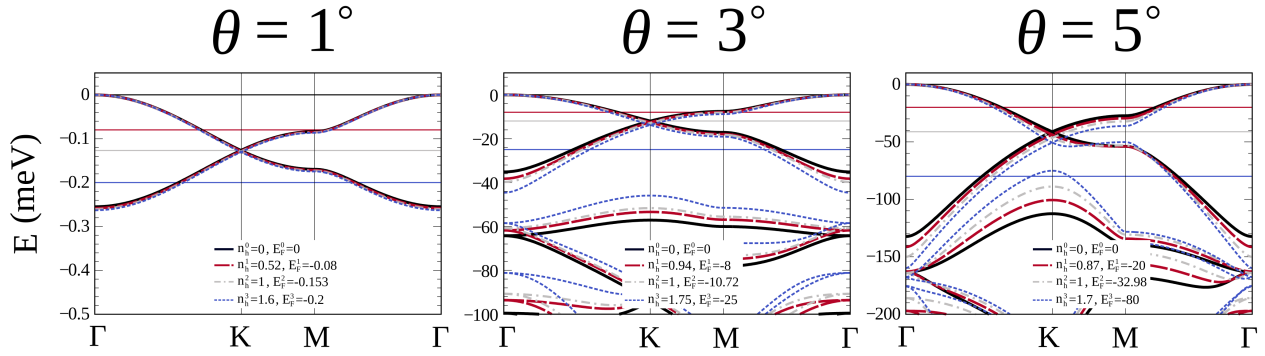


Figure S3. (Color online) Hartree potential effect in the doped band structures of twisted WS<sub>2</sub>. From left to right, we show results for different twist angles  $\theta$ . The undoped bands are shown with black solid lines. Band structures corresponding to Fermi levels  $E_F^i$  and hole doping  $n_h^i$  set between the undoped valence band maximum and the Dirac point (dashed red,  $i = 1$ ), at the Dirac point (dashed gray,  $i = 2$ ), and between the Dirac point and the bottom of the flat Dirac bands (dashed blue,  $i = 3$ ). The solid horizontal lines represent the corresponding Fermi energies. Calculations were performed at  $T = 0$ .

where  $V_C(\mathbf{r}) = \frac{e^2}{\epsilon|\mathbf{r}|}$  is the Coulomb potential,  $\epsilon = 4.5$  is the dielectric constant of the environment as produced by hBN, and  $\delta\rho(\mathbf{r})$  is the deviation of the charge density from charge neutrality.  $\delta\rho = 0$  corresponds to the undoped continuum model, i.e., when the Fermi level is at the top of the flat Dirac bands. We can then write

$$\delta\rho(\mathbf{r}) = \frac{1}{A_M} \sum_{\mathbf{G}} \delta\rho(\mathbf{G}) e^{i\mathbf{G}\cdot\mathbf{r}}. \quad (\text{S13})$$

The Fourier components  $\delta\rho(\mathbf{G})$  are given by

$$\delta\rho(\mathbf{G}) = -\frac{2}{N_{\mathbf{k}}} \sum_{\mathbf{k}, \mathbf{G}'} \sum_{\alpha'} \left( c_{\mathbf{k}\mathbf{G}'}^{\alpha'} \right)^\dagger c_{\mathbf{k}\mathbf{G}'+\mathbf{G}}^{\alpha'}, \quad (\text{S14})$$

where the sum over  $\alpha'$  runs over the unoccupied states in the valence band, so it depends on the doping level  $E_F$ , the factor 2 accounts for the spin degeneracy, and the minus sign refers to hole doping. Due to the  $D_6$  symmetry of the lattice,  $\delta\rho(\mathbf{G})$  are equally weighted in the same  $s$  shell of  $\mathbf{g}_j^s$  vectors, so we can write  $\delta\rho_s \equiv \delta\rho(\mathbf{g}_j^s)$  for any  $j$ . We also checked that it is enough to consider the first and second shells  $s = 1, 2$  to correctly address the effect of the Hartree potential. Under these assumptions, we can write the Hartree potential as

$$V_H(\mathbf{r}) = \sum_s V_0^s \delta\rho_s \sum_j e^{i\mathbf{g}_j^s \cdot \mathbf{r}}, \quad (\text{S15})$$

where  $V_0^s = \frac{2\pi e^2}{\epsilon A_M |\mathbf{G}^s|}$ .  $\delta\rho_s$  are the amplitudes which define the Hartree potential and have to be determined self-consistently. By Fourier transforming Eq. (S15), we can introduce the Hartree potential in Eq. (S3) and solve the total Hamiltonian  $H + V_H$  in the reciprocal space.

The self-consistent procedure is as follows:

- We consider various doping levels with respect to the top of the valence band  $n_h$  (number of holes per spin). Here  $n_h = 0$  corresponds to the undoped system,  $n_h = 1$  to the hole doping to the Dirac point, and  $n_h = 2$  to completely empty flat Dirac bands. We consider  $n_h^1$  between the undoped level and the Dirac point,  $n_h^2$  at the Dirac point, and  $n_h^3$  between the Dirac point and the bottom of the flat Dirac bands. We obtain the plane-wave coefficients  $c_{\mathbf{k}\mathbf{G}}^\alpha$  from diagonalizing  $H + V_H$ .
- Using Eq. (S14), we calculate the new charges  $\delta\rho_s^{\text{new}}$ .
- In each iteration step, the self-consistent convergence is checked by  $|\delta\rho_s^{\text{old}} - \delta\rho_s^{\text{new}}| < 10^{-6}$ . If the convergence criterion is fulfilled, we finish the code and calculate the new and renormalized band structures.
- If the convergence criterion is not fulfilled, then we update  $\delta\rho_s$  using a Kerker mixing procedure [S14], where  $\delta\rho_s = \delta\rho_s^{\text{old}} + \alpha \frac{G_s^2}{G_s^2 + \beta^2} (\delta\rho_s^{\text{new}} - \delta\rho_s^{\text{old}})$ . We set  $\alpha = 0.1$ ,  $\beta = 0.9$ , and  $G_s \equiv |\mathbf{G}^s|$ . A simple straight mixing is obtained if  $\beta$  is set to a very small value. We find that the charges are usually converged after less than 30 iterations depending on the chosen twist angle  $\theta$  and the doping level  $n_h^i$ .

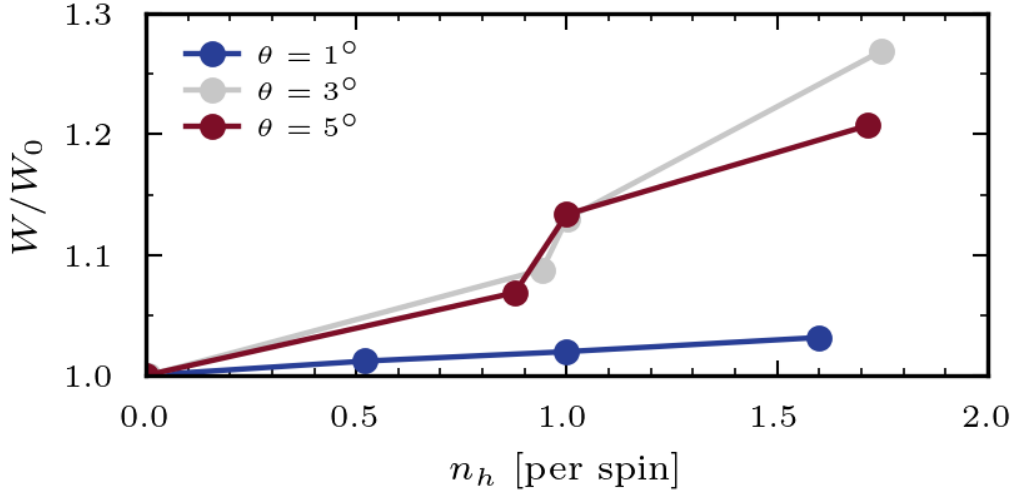


Figure S4. (Color online) Relative change in the bandwidth with respect to the undoped case  $W/W_0$  due to the Hartree potential in twisted  $\text{WS}_2$ . The change is larger for large hole dopings and non-monotonous in terms of the twist angle. The largest relative change for  $\theta = 3^\circ$  at  $n_h \approx 1.75$  is approximately 27%.

We show in Fig. S3 the effect of the Hartree potential for  $\text{WS}_2$  at different twist angles  $\theta$  and different Fermi energies  $E_F^i$  corresponding to respective hole dopings  $n_h^i$ . The Hartree potential mainly shifts the bands as a whole and increases the bandwidth. Only for larger twist angles  $\theta \geq 5^\circ$  and dopings  $n_h^3$ , the flat Dirac bands start to be reconstructed, with the higher energy bands below the flat Dirac bands even being partially filled. This is in contrast to graphene-based systems, where the entangled multiorbital nature of the flat bands facilitate strong renormalization of the bands.

The bandwidth renormalization can be easily visualized when plotting the relative change of the bandwidth with respect to the undoped case  $W/W_0$ , see Fig. S4, where the change is larger for larger dopings. The change is non-monotonic when changing the twist angle. From these results, we conclude that  $\theta \leq 5^\circ$  is the limit of applicability of our calculations. In any case and for the purpose of our FLEX calculations, we can assume that the doping  $\delta = 1 - n_h$  used in the main text occurs between the valence band maximum and the Dirac point, where the bands are essentially unaffected by the Hartree potential.

#### S4. ESTIMATION OF THE COULOMB INTERACTION STRENGTH

From the definition of the Wannier orbitals in Eq. (S9), we estimate the value of the screened Coulomb interaction matrix elements  $W_{\mathbf{R},mn}$ . The local and nearest-neighbor Coulomb interactions can be then calculated as the matrix elements  $U \equiv W_{\mathbf{0},AA}$  and  $V \equiv W_{\mathbf{0},AB}$ . The resulting extended Hubbard model can be mapped onto a local Hubbard model by making the assumption  $U^* = U - V$  [S15]. We estimate the upper and lower bounds by projecting an effective interaction  $V_{\text{eff}}(\mathbf{r})$  onto the Wannier functions in two limiting dielectric environment cases: free-standing twisted bilayers, for which the external screening is minimal, and a metallic gate in direct contact with the twisted bilayers, for which the external screening is maximal [S16]. The screened Coulomb interaction matrix is given by

$$W_{\mathbf{R},mn} = \iint d^2\mathbf{r} d^2\mathbf{r}' V_{\text{eff}}(\mathbf{r} - \mathbf{r}') \rho_{\mathbf{R}m}(\mathbf{r}) \rho_{\mathbf{0}n}(\mathbf{r}'), \quad (\text{S16})$$

with  $\rho_{\mathbf{R}m}(\mathbf{r}) = |\mathcal{W}_{\mathbf{R}m}(\mathbf{r})|^2$ .  $V_{\text{eff}}(\mathbf{r})$  is the Coulomb interaction screened by the TMDC bilayer in its undoped state and the dielectric environment. We start from an Ohno potential [S17]

$$V_{\text{Ohno}}(\mathbf{r}) = \frac{e^2}{\sqrt{r^2 + \xi^2}} \quad (\text{S17})$$

that regularizes the bare Coulomb interaction  $e^2/r$  at a short wavelength cut-off  $\xi = 1 \text{ \AA}$ , which is set by the spacial extent of the  $W$   $d$ -orbitals. The effect of screening is easily included in reciprocal space, so the effective interaction is

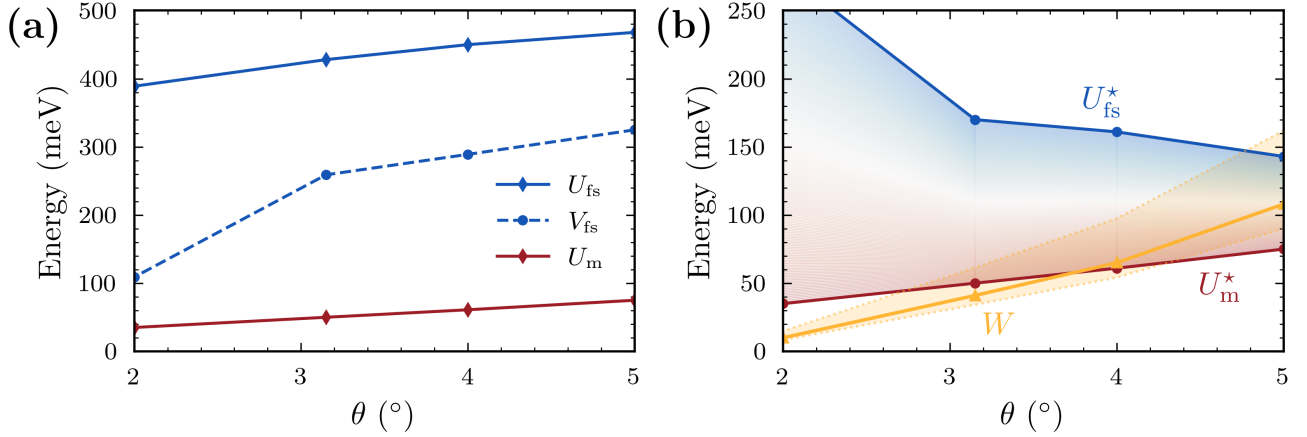


Figure S5. (Color online) Estimated Coulomb interactions in different dielectric environments for WS<sub>2</sub>. (a) Local and nearest-neighbor Coulomb interaction  $U$  and  $V$  in two dielectric environments, free-standing twisted bilayer (‘fs’, red line) and metallic gate in direct contact with the twisted bilayer (‘m’, blue line). (b) Effective local Hubbard interactions  $U^* = U - V$  and bandwidth  $W$  (orange line). The blue-red shaded region describes the possible values that  $U^*$  can take depending on the dielectric environmental setup. The orange-shaded region indicates interaction values we use in the FLEX calculations ( $U^*/t \sim 5-9$ ).

$V_{\text{eff}}(\mathbf{r})$  then calculated from the inverse Fourier transformation of

$$V_{\text{eff}}(\mathbf{q}) = \frac{V_{\text{Ohno}}(\mathbf{q})}{\epsilon(\mathbf{q})} = \frac{2\pi e^2}{\epsilon(\mathbf{q})q} e^{-q\xi}, \quad (\text{S18})$$

where  $\epsilon(\mathbf{q})$  is the dielectric function that encodes the environmental screening effect. For our two limiting cases, free-standing (‘fs’) and metal in direct contact (‘m’), we use the effective dielectric functions [S16, S18]:

$$\begin{aligned} \epsilon_{\text{fs}}(\mathbf{q}) &= \kappa \frac{1 - \tilde{\kappa} e^{-qh}}{1 + \tilde{\kappa} e^{-qh}}, \\ \epsilon_{\text{m}}(\mathbf{q}) &= \kappa \coth \frac{qh}{2}. \end{aligned} \quad (\text{S19})$$

Here,  $\kappa \approx 10$  is the internal screening of the twisted TMDC,  $h \approx 13 \text{ \AA}$  is the bilayer height [S19, S20], and  $\tilde{\kappa} = (\kappa - 1)/(\kappa + 1)$ . In Fig. S5(a) we plot the on-site and nearest-neighbor interactions  $U$  and  $V$  at different twist angles  $\theta$  for the two limiting cases for WS<sub>2</sub>. Since the nearest-neighbor interaction with a metal gate contact  $V_m$  is on the order of 1 meV, we did not include it in the plot. Fig. S5(b) shows the effective local Hubbard interaction  $U^*$  and the bandwidth  $W$ . A realistic value for  $U^*$  in  $\Gamma$ -valley twisted TMDCs will fall inside the shaded regions between the limiting cases  $U_{\text{fs}}^*$  and  $U_{\text{m}}^*$  which depends on the experimental setup and which can be tuned by changing the dielectric environment [S16, S21–S25]. For our FLEX calculations, we use  $U^*/t = 5-9$  (where we assume an effective Hubbard model with  $U \equiv U^*$ ) which is indicated by an orange-shaded region, since  $W \approx 6t$ . These interaction values correspond to experimentally accessible interaction strengths in a twist angle range of  $3-5^\circ$ .

## S5. NUMERICAL DETAILS OF FLEX CALCULATIONS

We summarize the calculation steps performed in the FLEX approximation [S4, S5] and give details on the numerical parameters used. In the FLEX approximation, one solves the Dyson equation

$$\hat{G}(k)^{-1} = \hat{G}^0(k)^{-1} - \hat{\Sigma}(k), \quad (\text{S20})$$

with the dressed (bare) Green function  $G$  ( $G^0$ ), self-energy  $\Sigma$ , and the four-momentum  $k = (i\omega_n, \mathbf{k})$ .  $\mathbf{k}$  is the crystal momentum and  $\omega_n = (2n + 1)\pi k_B T$  are the Matsubara frequencies at a temperature  $T$ . In case of the single-orbital honeycomb model, all quantities are given by  $2 \times 2$  matrices in terms of sublattice indices A and B [S26, S27] which is denoted by a hat  $G_{\alpha\beta} \equiv (\hat{G})_{\alpha\beta}$ . The non-interacting Green function is given by

$$\hat{G}^0(k) = \left[ i\omega_n \mathbf{1} - (\hat{H}_0(\mathbf{k}) - \mu \mathbf{1}) \right]^{-1}, \quad (\text{S21})$$

where  $H_0$  is the non-interacting Hamiltonian given in Eq. (S11),  $\mathbf{1}$  denotes the  $2 \times 2$  identity matrix, and  $\mu$  is the chemical potential of the doping level  $\delta$ . The self-energy  $\Sigma$  mainly consists of contributions from spin and charge fluctuations and is calculated from

$$\Sigma_{\alpha\beta}(k) = \frac{T}{N_{\mathbf{k}}} \sum_q G_{\alpha\beta}(k-q) \left\{ U^2 \left[ \frac{3}{2} \hat{\chi}^s(q) + \frac{1}{2} \hat{\chi}^c(q) - \hat{\chi}^0(q) \right] + \mathbf{1}U \right\}_{\alpha\beta}, \quad (\text{S22})$$

with the number of sites  $N_{\mathbf{k}}$ , and the Hubbard interaction  $U$  as given in Eq. (2) of the main text. The charge and spin susceptibility entering Eq. (S22) are defined by

$$\hat{\chi}^{c,s}(q) = \hat{\chi}^0(q) [\mathbf{1} \pm U \hat{\chi}^0(q)]^{-1}, \quad (\text{S23})$$

where the irreducible susceptibility is

$$\chi_{\alpha\beta}^0(q) = -\frac{T}{N_{\mathbf{k}}} \sum_k G_{\alpha\beta}(k+q) G_{\beta\alpha}(k). \quad (\text{S24})$$

Eqs. (S20) – (S24) are solved self-consistently. The calculations are initialized using only the bare Green function  $G^0$  with  $\Sigma = 0$ , i.e., starting from free electrons, and in each iteration step the chemical potential  $\mu$  needs to be adjusted to keep the doping  $\delta$  fixed. We employ a linear mixing  $G = \kappa G^{\text{new}} + (1 - \kappa) G^{\text{old}}$  with  $\kappa = 0.2$ . We then defined self-consistency for a relative difference of  $10^{-4}$  between the self-energy of two iteration steps. In all calculations, we used a  $\mathbf{k}$ -mesh resolution of  $120 \times 120$ . For the Matsubara frequencies we used the sparse-sampling approach [S28–S30] of the intermediate representation (IR) basis [S31, S32] with an IR parameter  $\Lambda = 10^4$  and a basis cutoff  $\delta_{\text{IR}} = 10^{-8}$ . Since the numerical cost of FLEX calculations for  $T = \mathcal{O}(0.001t)$  is quite expensive, this formalism is crucial. For instance, older works studying honeycomb models [S33–S35] could not determine the transition temperature  $T_c$ . Details on the implementation can be found in Ref. [S29].

To study the superconducting phase transition driven by spin fluctuations, we consider the linearized gap equation

$$\lambda \Delta_{\alpha\beta}^S(k) = -\frac{T}{N_{\mathbf{k}}} \sum_q \sum_{\alpha',\beta'} V_{\alpha\beta}^S(q) G_{\alpha\alpha'}(k-q) G_{\beta\beta'}(q-k) \Delta_{\alpha'\beta'}^S(k-q), \quad (\text{S25})$$

for the pairing potential or gap function  $\Delta$  on sublattice  $\alpha$  and with spin orientation  $S$ . This equation represents an eigenvalue problem for  $\Delta$  where the eigenvalue  $\lambda$  can be understood as the relative pairing strength of a certain pairing channel. The dominant pairing symmetry of the gap function has the largest eigenvalue  $\lambda$  and the transition temperature is found if  $\lambda$  reaches unity. Since we do not consider spin-orbit coupling, the linearized gap equation (S25) is diagonal in the spin singlet- and triplet-pairing channel ( $S = 0, 1$ ) with the respective interactions due to the exchange of spin and charge fluctuations

$$\hat{V}^{S=0}(q) = \frac{3}{2} U^2 \hat{\chi}^s(q) - \frac{1}{2} U^2 \hat{\chi}^c(q) + \mathbf{1}U, \quad \hat{V}^{S=1}(q) = -\frac{1}{2} U^2 \hat{\chi}^s(q) - \frac{1}{2} U^2 \hat{\chi}^c(q). \quad (\text{S26})$$

We solve Eqs. (S25) and (S26) by using the power iteration method with a relative error of  $10^{-4}$  for convergence. As an input serve the converged Green function of the normal state calculations and a trial gap function  $\Delta_0$ , which is set up according to the irreducible representations of the  $D_6$  symmetry group [S36].

## S6. MAGNETIC QUASIORDER AND SPIN FLUCTUATIONS IN THE HONEYCOMB HUBBARD MODEL

In two dimensions, the Mermin-Wagner theorem [S37] prevents the formation of (genuine) long-range order at finite temperature as obeyed by the FLEX approximation [S38]. However, tendencies towards magnetic quasi-order can be read off from the Stoner enhancement factor  $U\chi^0(\mathbf{q})$ , which enters the denominator of the static spin susceptibility  $\chi^s(i\nu_0 = 0, \mathbf{q})$  (c.f. Eq. (S23)). Thus, possible formation of spin density waves (SDWs) can be investigated in FLEX by inspecting the instabilities of  $\chi^s(i\nu_0, \mathbf{q})$ . When the Stoner enhancement approaches unity [ $U\chi^0 \sim \mathcal{O}(0.99)$ ],  $\chi^s$  diverges and the transition to a quasi-ordered magnetic state is assumed [S4, S39, S40]. At this point, the FLEX calculations turn unstable and do not converge anymore. A discussion of the leading Stoner enhancement, indicating regions of strong magnetic fluctuations, is given in the main text.

While the real-space profile of the magnetic fluctuations is discussed in the main text, Fig. 2(b), further insight into the emerging SDWs can be gained by inspecting the momentum-space structure of  $\chi^s(i\nu_0, \mathbf{q})$ . In Fig. S6, we show the

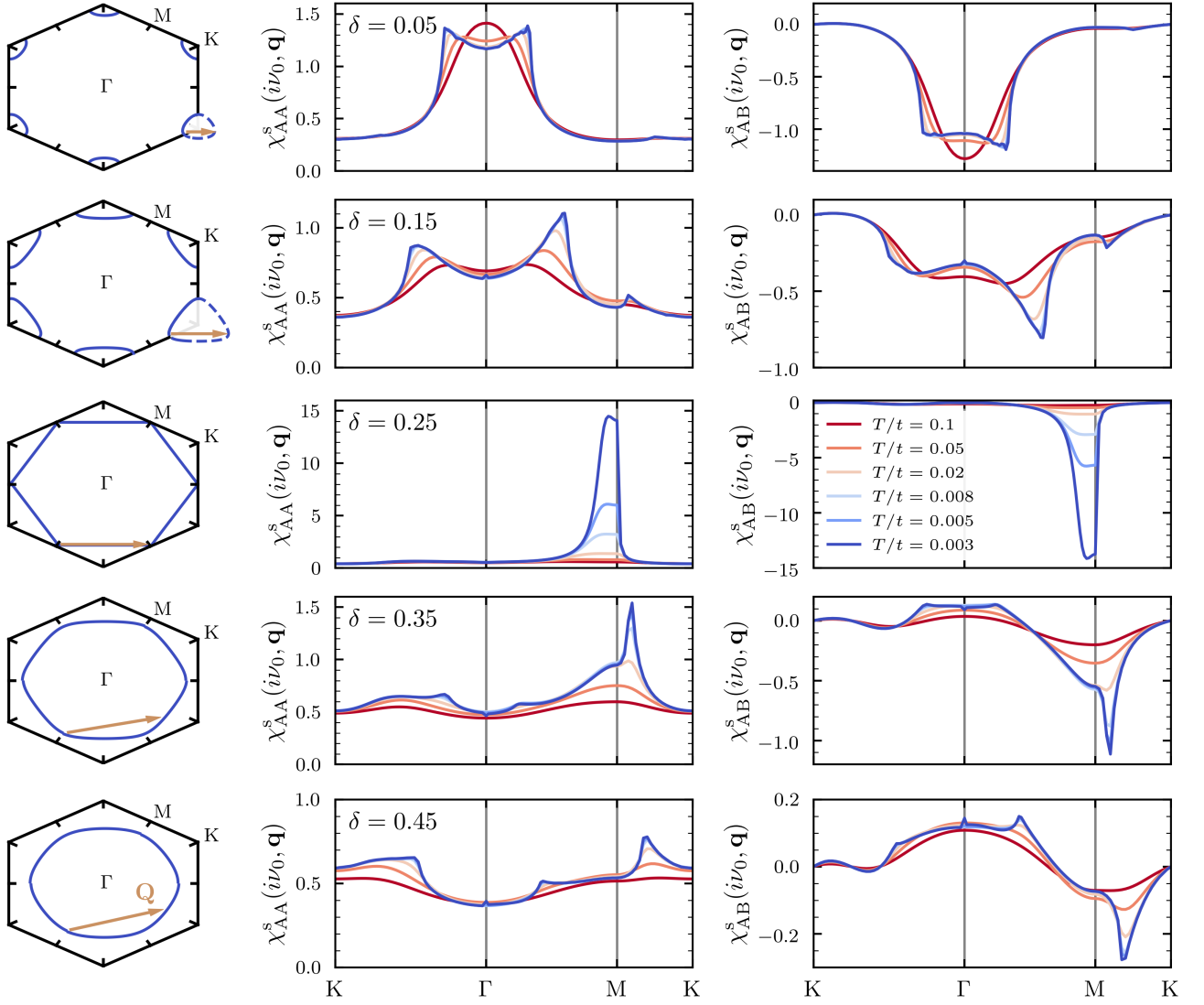


Figure S6. (Color online) Momentum dependent static spin susceptibility calculated in FLEX for different temperatures  $T/t$  and dopings  $\delta$  (rows) at fixed interaction  $U/t = 4$ . The left column contains the non-interacting Fermi surfaces at the respective doping levels and the dominant nesting vectors  $\mathbf{Q}$  associated with the largest peak of  $\chi^s(i\nu_0, \mathbf{q})$ . Middle and right column show the momentum resolved real part of the spin susceptibility within (AA-component) and between (AB-component) sublattices, respectively.

intra-sublattice (AA) and inter-sublattice (AB) components of  $\chi^s(i\nu_0, \mathbf{q})$  along high-symmetry paths of the Brillouin zone for different  $\delta$  and  $T$  at an intermediate interaction of  $U/t = 4$ . Additionally, we included the Fermi surfaces of the non-interacting system associated with each doping level.

In the doping range between the Dirac point and VHS, the AA- and AB-components of  $\chi^s$  carry predominantly a different sign signaling antiferromagnetic fluctuations with respect to the A and B sublattices. Beyond the VHS, ferromagnetic fluctuations with respect to the sublattice index emerge and the relative fluctuation strength decreases. In each sublattice, the peak structure of  $\chi^s$  changes significantly depending on the Fermi surface shape and becomes more pronounced for lower temperatures. That is, because the spin fluctuations emerge from the nesting conditions of the Fermi surface, i.e., possible intra-pocket electron scattering. To illustrate this, we also draw the nesting vector  $\mathbf{Q}$  belonging to the dominant peak of  $\chi^s$  between Fermi surface sheets.

Near Dirac doping ( $\delta = 0.05$ ), the Fermi surface is formed by small, almost circular pockets around the K point so that long-wavelength SDWs emerge, since  $\chi^s$  peaks close to the  $\Gamma$  point. This situation corresponds to an almost ferromagnetic ordering in each sublattice, but antiferromagnetic fluctuations between the sublattices. Increasing the doping ( $\delta = 0.15$ ) deforms the Fermi surface to an equilateral shape whereby the spin fluctuations assume shorter wavelengths, as the peak in  $\chi^s$  shifts from the  $\Gamma$  point to the M point. At the VHS ( $\delta = 0.25$ ), the system undergoes

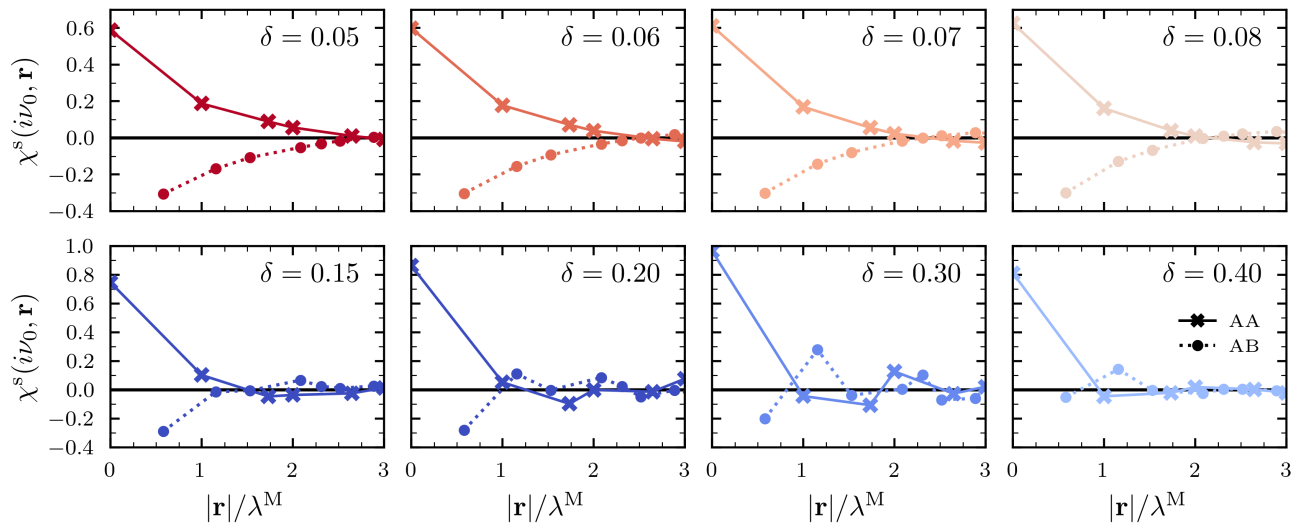


Figure S7. (Color online) Real space profile of the static spin susceptibility calculated in FLEX for different dopings  $\delta$  at  $T/t = 0.003$  and  $U/t = 6$ . The distance  $|\mathbf{r}|$  of two lattice sites is given in units of the moiré length  $\lambda^M$ . Correlations between spins on equal (different) sublattice sites are marked by solid lines with crosses (dotted lines with circles), corresponding to the AA (AB) component of  $\chi^s$ .

a Lifshitz transition and the Fermi surface turns hexagonal with perfect nesting conditions. This causes strong fluctuations with a chiral spin profile on each sublattice [S41, S42]. Beyond the VHS ( $\delta = 0.35, 0.45$ ), the Fermi surface contracts around the  $\Gamma$  point with decreasing relative fluctuation strength. Increasing the interaction  $U$  enhances the fluctuation strength, but does not affect the general structure of  $\chi^s$ .

Spin fluctuations can mediate an effective electron-electron interaction, as described by Eq. (S26). This interaction has non-local attractive regions which can pair spatially correlated electrons as they avoid occupying the same site. Thus, the real space profile  $\chi^s(i\nu_0, \mathbf{r})$  provides information on the pairing potential for electrons. In Fig. S7, we show  $\chi^s(i\nu_0, \mathbf{r})$  for different dopings at  $T/t = 0.003$  and  $U/t = 6$ . In accordance with the previous discussion of the momentum space structure, antiferromagnetic correlations between different sublattice sites occur for doping levels in the vicinity of the Dirac point ( $\delta \lesssim 0.15$ ) which turn ferromagnetic for larger dopings. By increasing the doping, the AA and AB components of  $\chi^s$  change sign on a shorter length scale, so that regions with antiferromagnetic correlations shrink. This reduces the attractive regions ( $V^S \sim \chi^s < 0$ ) leading to a less optimal pairing situation since the pair electrons need to move closer while the Coulomb repulsion pushes them apart.

In the main text, we discuss that an optimal pairing condition with maximal transition temperature  $T_c^{\max}$  arises. This can be understood from the structure of  $\chi^s(i\nu_0, \mathbf{r})$  and DOS. Considering  $U/t = 6$ ,  $T_c^{\max}$  is located around  $\delta_{\text{opt}} \sim 0.06 - 0.07$ . The top row of Fig. S7 shows that the fourth- and fifth-nearest-neighbor component of  $\chi_{AB}^s$  change sign in this doping region. Up to this point,  $T_c$  increases with doping driven by the increase in the DOS at the Fermi level (c.f. Fig. S1(c)). As the attractive region shrinks beyond  $\delta_{\text{opt}}$ , pairing conditions deteriorate and  $T_c$  decreases. The optimal situation appears where these two counteracting trends are balanced.

## S7. LEADING SUPERCONDUCTING INSTABILITY

The possible pairing symmetries of the superconducting order can be classified according to the irreducible representation of the point group symmetry of the system [S36]. The honeycomb lattice is of  $D_6$  symmetry which can possibly host singlet extended  $s$ -wave, or degenerate  $d$ -wave ( $d_{xy}, d_{x^2-y^2}$ ) as well as triplet degenerate  $p$ -wave ( $p_x, p_y$ ),  $f_{x(x^2-3y^2)}$ -wave, or  $f_{y(3x^2-y^2)}$ -wave pairing. The dominant pairing symmetry emerges with the largest eigenvalue  $\lambda$  of the linearized gap equation (S25).

In Fig. S8(a), we compare  $\lambda$  of the  $d$ -wave and  $f \equiv f_{x(x^2-3y^2)}$ -wave pairing symmetry for different dopings  $\delta$  between the Dirac point and VHS. These two pairings emerge as the dominant pairing symmetries in the singlet and triplet pairing channel, respectively. The momentum dependence of the corresponding intra-sublattice order parameters at lowest Matsubara frequency  $\Delta_{AA}(i\omega_1, \mathbf{k})$  is shown in Fig. S8(b). By comparing the superconducting eigenvalues, it can be seen that singlet pairing is favored over triplet pairing. This is, in fact, consistent with the observed antiferromagnetic fluctuations as they support singlet pairing. Clearly, the  $d$ -wave pairing is the dominant

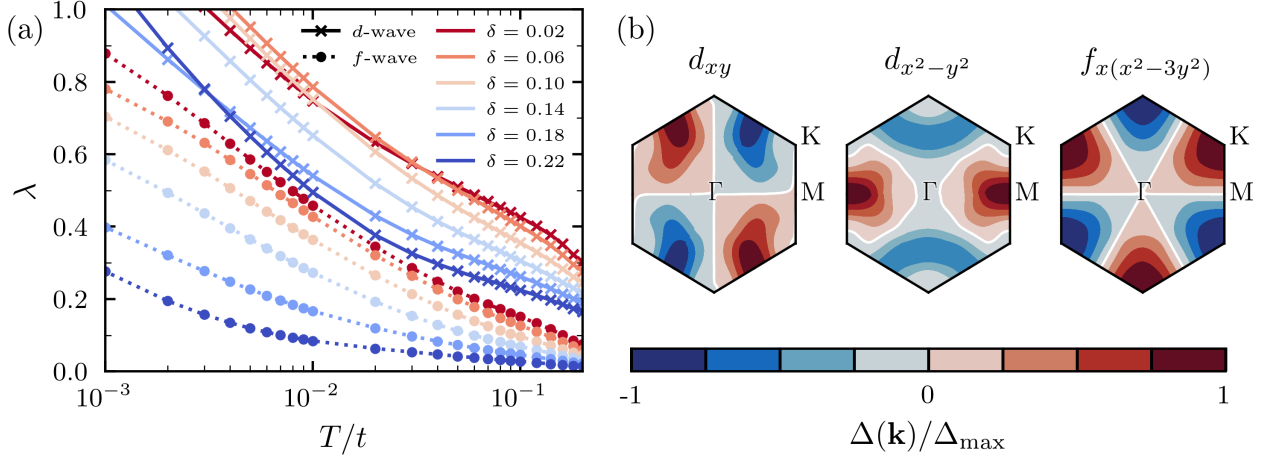


Figure S8. (Color online) Singlet vs. triplet superconductivity in the honeycomb Hubbard model. (a) Eigenvalues  $\lambda$  of the linearized Eliashberg equation for the degenerate  $d$ -wave (solid lines) and the  $f \equiv f_{x(x^2-3y^2)}$ -wave (dotted lines) pairing symmetries. Shown is the temperature dependence of  $\lambda$  for different dopings  $\delta$  at  $U/t = 6$ . Note that the temperature scale is logarithmic. (b) Momentum-space structure of the order character for the  $d$ -wave and  $f$ -wave pairing symmetries. Shown are the normalized diagonal elements of the gap function  $\Delta_{AA}$  at lowest Matsubara frequency for converged calculations at  $T/t = 0.005$ ,  $U/t = 6$ , and  $\delta = 0.1$ . The nodes of the gap are indicated by white lines.

superconducting instability for which the critical temperature  $T_c$  is read off for  $\lambda_d \rightarrow 1$ . The values of  $\lambda_f$ , on the other hand, do not reach unity in the studied temperature region indicating that a possible transition would occur at considerably lower temperatures.

For the dominant  $d$ -wave pairing, we find that the pairing mainly takes place between different sublattices since we observe  $|\Delta_{AB}| > |\Delta_{AA}|$ . This is also in agreement with the antiferromagnetic alignment of the spins between the sublattices. Because of this, the triplet pairing instability can be enhanced and even dominate over the singlet pairing by introducing a staggered potential between the A and B sublattice sites [S33].

Below  $T_c$ , a linear combination of the degenerate  $d$ -wave states forms as the superconducting ground state. The exact realization depends on the free energy with the possibility of a chiral or nematic states [S36]. For the simple honeycomb lattice, the chiral  $d+id$  state is the preferred solution with the lowest free energy [S43–S45], as the number of nodes in the quasiparticle spectrum is minimized in this case.

### S8. INFLUENCE OF PARTICLE-HOLE ASYMMETRY ON SPIN-FLUCTUATION-MEDIATED SUPERCONDUCTIVITY

In Section S1, we discussed the influence of longer-ranged hopping terms on the band structure and DOS of the honeycomb lattice tight-binding model (c.f. Fig. S1(b) and (c)). Here, we assess the change of the spin-fluctuation-mediated superconducting phase transition line due to the resulting particle-hole asymmetry. We use the same parameters  $t_2/t = -0.136$  and  $t_3/t = 0.105$  as in Section S1. To describe the asymmetry, we need to compare each side of the Dirac point. We calculate the critical temperature  $T_c^{\text{SP}}$  for one Hubbard parameter  $U/t = 6$ .

A comparison of the doping dependence of  $T_c$  for the particle-hole symmetric and asymmetric model is shown in Fig. S9. In accordance with the band structure and DOS asymmetry, an asymmetry in the doping dependence of  $T_c^{\text{SP}}$  emerges. On the left side of the Dirac point, superconductivity is slightly enhanced, while it is suppressed on the other side. This might be contrary to expectations, since the enhancement/suppression of the DOS is opposite. The reason for this is a change in the shape of the Fermi surface and hence nesting conditions caused by the additional hopping terms. Near the Dirac point, the triangular parts of the Fermi surface become flatter and the spin fluctuation strength increases due to better nesting. At the VHS, the hexagonal shape of the Fermi surface becomes rounder causing weaker spin fluctuations. The extent to which this happens, is different for each side of the Dirac point resulting in two different curves. For instance, on the left side the DOS of both cases is similar, but  $T_c^{\text{SP}}$  of the asymmetric model is slightly increased due to stronger spin fluctuations. The different nesting conditions also cause the VHS to be less detrimental to the calculations, since the Stoner enhancement does not diverge as strongly.

Even though quantitative aspects of  $T_c^{\text{SP}}(\delta)$  change by the presence of long-range contributions to the single-particle

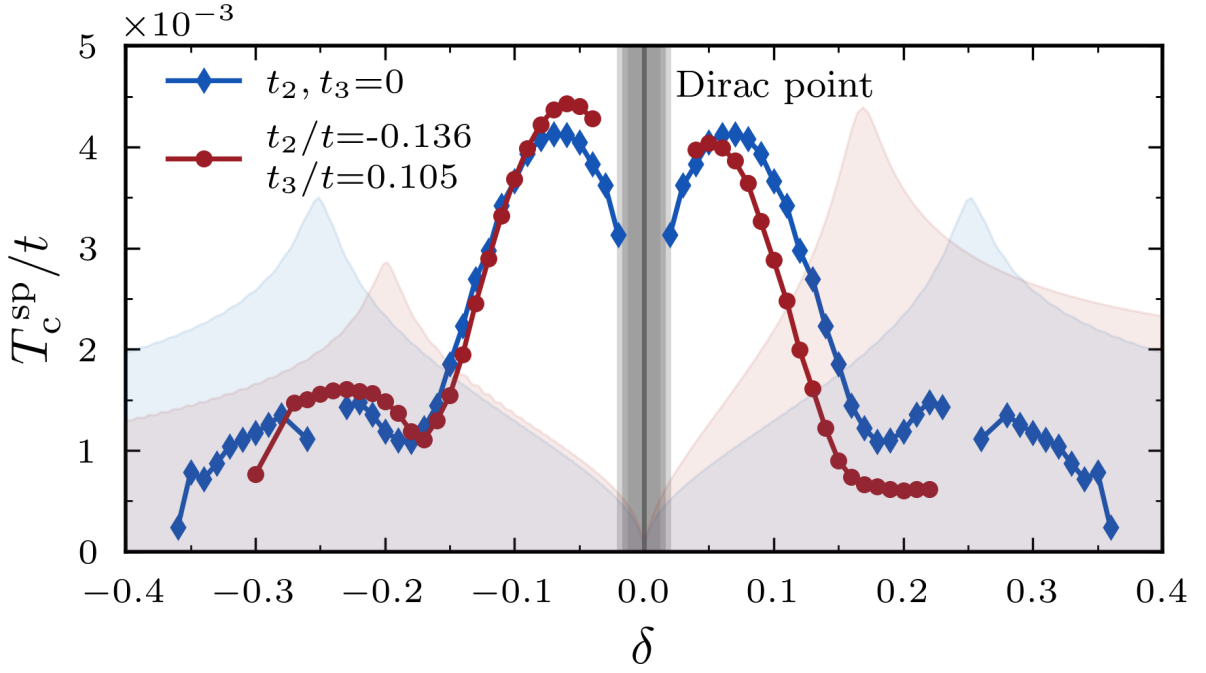


Figure S9. (Color online) Comparison of the doping dependence of the spin-fluctuation-driven superconducting transition line  $T_c^{\text{sp}}$  for the particle-hole symmetric ( $t_2, t_3 = 0$ , blue line with diamonds) and asymmetric ( $t_2/t = -0.136$ ,  $t_3/t = 0.105$ , red line with circles) honeycomb lattice model. The density of states for each model is drawn by a shaded area to indicate the position of the Van Hove singularities (VHS) in each case and how the phononic transition line  $T_c^{\text{ph}}$  would differ qualitatively. The Dirac point and its vicinity are indicated by a gray shaded area.

dispersion, the general qualitative behavior remains unchanged. A clear maximum of  $T_c^{\text{sp}}$  exists on both sides of the Dirac point, while superconductivity is suppressed by doping away from that region. Still ferromagnetic fluctuations form beyond the VHS which lead to the absence of superconductivity.

## S9. SUPERCONDUCTIVITY FROM NON-LOCAL ELECTRON-PHONON INTERACTION

In the main text, we have stated that conventional superconductivity driven by the electron–phonon interaction persists over a larger doping range and peaks at different levels than unconventional superconductivity driven by spin fluctuations. More precisely, using the approximations of a single Einstein phonon mode and a constant Holstein electron–phonon coupling, we have shown that the critical temperature closely follows the electronic DOS. Here, we will demonstrate that these observations remain valid for more general momentum-dependent phonon frequencies and Peierls electron–phonon coupling.

We describe the electrons and phonons of the moiré superlattice using nearest-neighbor-only tight-binding and mass–spring models on a honeycomb lattice. The tight-binding Hamiltonian is equivalent to the nearest-neighbor part of Eq. (S11), except that we change the orientation of the two electronic sublattices A, B and the primitive moiré lattice vectors  $\mathbf{L}_{1,2}^M$  for the sake of notational simplicity, see Fig. S10 (a). Using reciprocal lattice units  $k_{1,2} = \mathbf{k} \cdot \mathbf{L}_{1,2}^M$ , the tight-binding Hamiltonian can then be defined as

$$H_{\mathbf{k}AB} = t(1 + e^{ik_1} + e^{-ik_2}), \quad H_{\mathbf{k}BA} = H_{\mathbf{k}AB}^*, \quad H_{\mathbf{k}AA} = H_{\mathbf{k}BB} = 0, \quad (\text{S27})$$

where  $t \equiv t_1$  and the asterisk denotes the complex conjugate. The corresponding electron dispersion relation (see Fig. S2 (b)) reads

$$E_{\mathbf{k}\pm} = \pm t \sqrt{3 + 2 \cos(k_1) + 2 \cos(k_2) + 2 \cos(k_1 + k_2)}. \quad (\text{S28})$$

For the phonons, we use a mass–spring model with an isotropic nearest-neighbor force constant. Using reciprocal lattice units  $q_{1,2} = \mathbf{q} \cdot \mathbf{L}_{1,2}^M$ , the dynamical matrix can be defined as

$$D_{\mathbf{q}AB} = -\mathbb{1} \frac{k}{M} (1 + e^{iq_1} + e^{-iq_2}), \quad D_{\mathbf{q}BA} = D_{\mathbf{q}AB}^*, \quad D_{\mathbf{q}AA} = D_{\mathbf{q}BB} = \mathbb{1} \frac{3k}{M}, \quad (\text{S29})$$



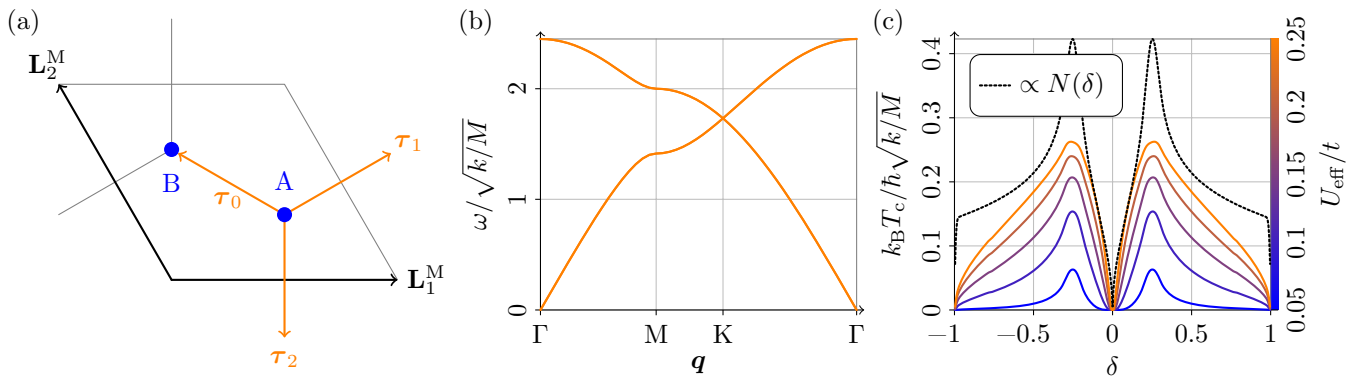


Figure S10. (Color online) Non-local electron-phonon interactions. (a) Honeycomb lattice with primitive lattice vectors  $\mathbf{L}_{1,2}^M$ , bond vectors  $\tau_{0,1,2}$ , and sublattices A, B. (b) Phonon dispersion  $\omega_{\mathbf{q}\pm}$  in units of  $\sqrt{k/M}$  with force constant  $k$  and mass  $M$ . (c) Critical temperature  $T_c$  in units of  $\sqrt{k/M}$  and density of states  $N$  in arbitrary units as a function of the doping level  $\delta$  for different strengths of the effective interaction  $U_{\text{eff}}$  in units of the hopping  $t$ .

where  $k$  and  $M$  are the effective force constant and a mass, respectively. The force constant and mass have to be understood as effective quantities related to the moiré unit cell and not referring to the primitive unit cell or individual atoms.  $\mathbb{1}$  denotes the unit matrix in the space of Cartesian displacement directions.

We show in Fig. S10 (b) the corresponding phonon dispersion which consists of two branches, whose degeneracy is the number of spatial dimensions, and reads  $\omega_{\mathbf{q}\pm} = \sqrt{k_{\mathbf{q}\pm}/M}$  with

$$k_{\mathbf{q}\pm} = k[3 \pm \sqrt{3 + 2 \cos(q_1) + 2 \cos(q_2) + 2 \cos(q_1 + q_2)}]. \quad (\text{S30})$$

Finally, modeling the dependence of the hopping  $t$  on the bond length  $\tau$  as  $t/t_0 = (\tau/\tau_0)^{-\beta}$  [S46] and labeling the sublattices of the ionic displacements as  $A', B'$ , the deformation-potential matrix element can be defined as

$$\mathbf{d}_{\mathbf{q}A'\mathbf{k}AB} = \frac{\beta t}{\tau} (\hat{\tau}_0 + \hat{\tau}_1 e^{ik_1} + \hat{\tau}_2 e^{-ik_2}), \quad \mathbf{d}_{\mathbf{q}A'\mathbf{k}BA} = \mathbf{d}_{\mathbf{q}A'\mathbf{k}+qAB}^*, \quad \mathbf{d}_{\mathbf{q}B'\mathbf{k}ij} = -\mathbf{d}_{\mathbf{q}A'\mathbf{k}ji}^*, \quad (\text{S31})$$

where  $\hat{\tau}_{0,1,2}$  are the normalized nearest-neighbor bond directions (Fig. S10 (a)) and  $i, j \in A, B$ .  $d_{\mathbf{q}x\mathbf{k}ij}$  quantifies the scattering of an electron from  $\mathbf{k}, j$  to  $\mathbf{k} + \mathbf{q}, i$  due to a  $\mathbf{q}, x$  displacement. Using the eigenvectors  $\psi$  and  $\mathbf{e}$  of the tight-binding Hamiltonian and the dynamical matrix, the deformation-potential matrix element can be transformed to the band basis via

$$d_{\mathbf{q}\nu\mathbf{k}mn} = \sum_{xij} e_{\mathbf{q}x\nu} \psi_{\mathbf{k}+\mathbf{q}im}^* \psi_{\mathbf{k}jn} d_{\mathbf{q}x\mathbf{k}ij}, \quad (\text{S32})$$

where  $\nu$  denotes the phonon branch and  $m, n$  the electronic band. The index  $x$  combines  $A', B'$  and Cartesian directions. With this, we have everything needed to calculate the effective electron-phonon coupling strength

$$\lambda(\mu) = N(\mu) \frac{\sum_{\mathbf{q}\nu\mathbf{k}mn} \delta(\epsilon_{\mathbf{k}+\mathbf{q}m} - \mu) \delta(\epsilon_{\mathbf{k}n} - \mu) U_{\mathbf{q}\nu\mathbf{k}mn}^{\text{eff}}}{\sum_{\mathbf{q}\mathbf{k}mn} \delta(\epsilon_{\mathbf{k}+\mathbf{q}m} - \mu) \delta(\epsilon_{\mathbf{k}n} - \mu)}, \quad (\text{S33})$$

where we have defined the effective attractive interaction  $U_{\mathbf{q}\nu\mathbf{k}mn}^{\text{eff}} = |d_{\mathbf{q}\nu\mathbf{k}mn}|^2 / k_{\mathbf{q}\nu}$ , and the logarithmic average of the phonon energy

$$\omega_{\log}(\mu) = \exp \left[ \frac{\sum_{\mathbf{q}\nu\mathbf{k}mn} \delta(\epsilon_{\mathbf{k}+\mathbf{q}m} - \mu) \delta(\epsilon_{\mathbf{k}n} - \mu) U_{\mathbf{q}\nu\mathbf{k}mn}^{\text{eff}} \log(\omega_{\mathbf{q}\nu})}{\sum_{\mathbf{q}\nu\mathbf{k}mn} \delta(\epsilon_{\mathbf{k}+\mathbf{q}m} - \mu) \delta(\epsilon_{\mathbf{k}n} - \mu) U_{\mathbf{q}\nu\mathbf{k}mn}^{\text{eff}}} \right] \quad (\text{S34})$$

as a function of the chemical potential  $\mu$  [S47]. Here,  $N(\mu)$  is the DOS per spin direction and unit cell, see Fig. S2(c) for the DOS as a function of the doping level  $\delta$ . Both  $\lambda$  and  $\omega_{\log}$  are double Fermi-surface averages; the  $\delta$  functions ensure that both in- and outgoing states  $\mathbf{k}, n$  and  $\mathbf{k} + \mathbf{q}, m$  are on the Fermi surface. Note that the shape of  $\lambda$  and  $\omega_{\log}$  as a function of  $\mu$  for our model is fixed and their magnitude depends solely on the prefactors  $U_{\text{eff}}/t = \beta^2 t / \tau^2 k$  and  $\sqrt{k/M}$ , respectively.

We calculate the critical temperature  $T_c$  using McMillan's formula [S47, S48] (Eq. (3) of the main text) for different values of  $U_{\text{eff}}$  covering the entire range from weak to strong coupling, i.e.,  $0 < \lambda \lesssim 2$ , as a function of the doping  $\delta$ . For simplicity, we set the Coulomb pseudopotential  $\mu^* = 0$ , while finite  $\mu^*$  do not change the picture qualitatively. We sample the Brillouin zone using  $96 \times 96 \times 1$   $\mathbf{q}$  and  $\mathbf{k}$  points in combination with a Gaussian broadening of  $0.05t$ . In all cases,  $T_c$  approximately follows the DOS, see Fig. S10 (c). Depending on the value of  $U_{\text{eff}}$ , the maxima at the VHS are more or less pronounced.

### S10. ESTIMATION OF EFFECTIVE ELECTRON-PHONON INTERACTION PARAMETER $U_{\text{eff}}$

In the main text and in Section S9 we used McMillan's formula to show that superconductivity arising from electron-phonon coupling reveals generic and robust doping fingerprints by  $T_c$  following the DOS. The quantitative details of the superconducting transition are then determined by the material properties. Here, we give an estimation on the order of magnitude for the effective BCS-like interaction  $U_{\text{eff}}$  entering the pairing strength  $\lambda = U_{\text{eff}}N(E_F)$  for  $\Gamma$ -valley twisted TMDCs.

The simplest estimation for the pairing strength  $\lambda$  for twisted moiré systems is to extrapolate from calculations for the untwisted material. In homobilayer TMDCs,  $\lambda$  can take values up to 8 [S49] depending on the doping with the DOS varying between  $0.4 \text{ eV}^{-1}$  and  $2 \text{ eV}^{-1}$  [S50]. Hence, the effective interaction strength is  $U_{\text{eff}} = \lambda/N(E_F) \approx 4-12 \text{ eV}$  per unit cell. This value needs to be scaled to the moiré unit cell which contains approximately  $(\lambda^M/a_0)^2 = 1/\sin^2\theta \approx \theta^{-2}$  single unit cells with lattice constant  $a_0$  (c.f. Table S1) for small  $\theta$ , i.e., the effective interaction is twist-angle dependent  $U_{\text{eff}}(\theta) \approx 4-12\theta^2 \text{ eV}$ . Using our observation  $t \propto \theta^2$  (c.f. Fig. 1(c) of the main text), we can express  $U_{\text{eff}}$  in units of  $t$ . For instance, for twisted MoS<sub>2</sub> bilayer we can write  $t \approx 2 \text{ eV} \cdot \theta^2 = \alpha\theta^2$  with  $\theta$  in radians. Thus, we estimate an interaction strength of  $U_{\text{eff}}/t = 2-6$ .

We also discuss moiré phonon modes, where we obtain  $U_{\text{eff}} = d^2/k$  from elastic properties of the bilayer TMDCs. Instead of using the microscopic electron-phonon coupling  $g$  and the averaged ("typical") phonon frequency  $\langle\omega\rangle$ , we express  $U_{\text{eff}}$  in terms of an effective moiré deformation potential  $d$  and an effective moiré force constant  $k$ . They are related by

$$U_{\text{eff}} = \frac{2g^2}{\hbar\langle\omega\rangle} = \frac{2}{\hbar\langle\omega\rangle} \frac{\hbar d^2}{2M\langle\omega\rangle} = \frac{d^2}{k}, \quad (\text{S35})$$

since  $g = \sqrt{\frac{\hbar}{2M\langle\omega\rangle}}d$  [S51] and  $\langle\omega\rangle = \sqrt{k/M}$  with mass  $M$ . It shows that the attractive phonon-mediated interaction can be interpreted as a classical quantity, as all  $\hbar$  cancel out.

First, we consider a case which corresponds to a purely local mode with Holstein-type coupling, which results from an interlayer breathing mode, see Fig. S11(a). In this case, a restoring force  $F = k\Delta h$  is induced when the interlayer distance is changed by an amount  $\Delta h$ . The response of the system is also encoded in the elastic constant in out-of-plane direction

$$C_{33} = \frac{\sigma}{\varepsilon} = \frac{F/A}{\Delta h/h} = \frac{Fh}{A\Delta h} \quad (\text{S36})$$

with the tensile stress  $\sigma$  of the lifted area  $A$  and strain  $\varepsilon$  of the equilibrium layer distance  $h$ . Thus, the force constant can be calculated from

$$k = \frac{F}{\Delta h} = \frac{AC_{33}}{h}. \quad (\text{S37})$$

We assume that only a fraction  $p < 1$  (the AB, BA regions) of the moiré unit cell needs to be lifted, so that  $A = p\frac{\sqrt{3}}{2}(\lambda^M)^2 \approx p\frac{\sqrt{3}}{2}a_0^2\theta^{-2}$ . The magnitude of the deformation potential is given in Eq. (S31) and for a single mode it simplifies to

$$d = \frac{\beta t_{\perp}}{h} \quad (\text{S38})$$

with the interlayer hopping  $t_{\perp}$ . The attractive interaction in Eq. (S35) then takes the form

$$U_{\text{eff}}^{\text{Holst.}} = \frac{d^2}{k} = \left(\frac{\beta t_{\perp}}{h}\right)^2 \cdot \frac{h}{AC_{33}} \approx \frac{\beta^2 t_{\perp}^2}{\frac{\sqrt{3}}{2}pa_0^2\theta^{-2}hC_{33}}. \quad (\text{S39})$$

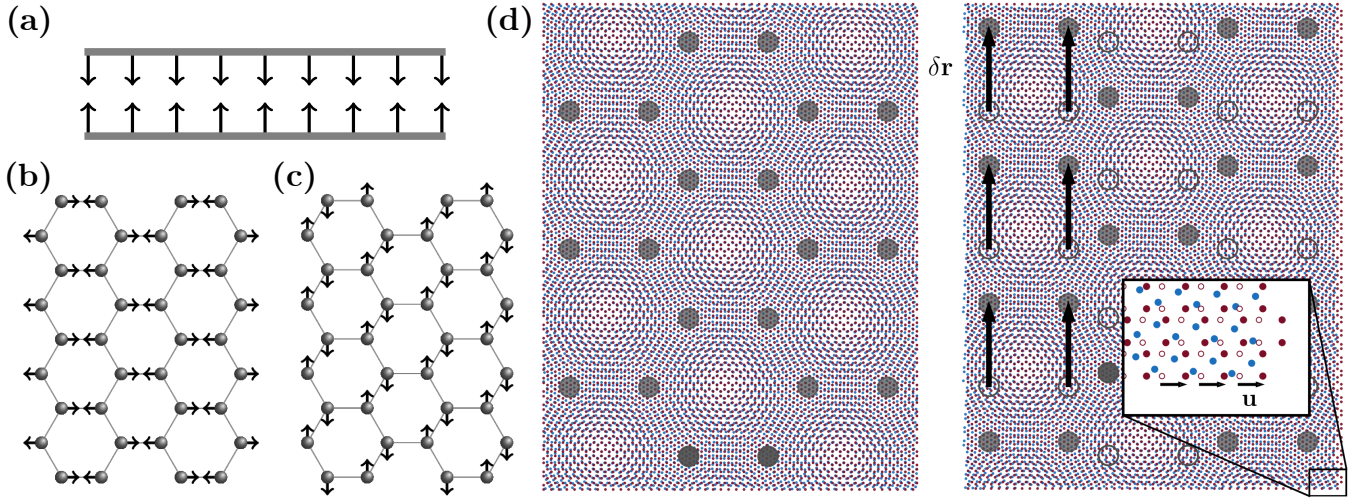


Figure S11. (Color online) Moiré phonon modes. (a) Layer-breathing mode (“Holstein” coupling). (b, c) Optical in-plane modes of a honeycomb lattice at  $\Gamma$  (“Peierls” coupling). (d) Effect of TMDC layer displacement. The left panel shows the unshifted lattice, while in the right panel the red TMDC lattice was displaced to the right by  $\mathbf{u}$ , so that the moiré superlattice is shifted to the top by  $\delta\mathbf{r}$ . Empty circles denote the unshifted atom positions.

Expressing  $U_{\text{eff}}^{\text{Holst.}}$  in units of the moiré honeycomblattice hopping  $t \approx \alpha\theta^2$  yields

$$U_{\text{eff}}^{\text{Holst.}} \approx \frac{2}{\sqrt{3}} \frac{\beta^2 t_{\perp}^2}{\alpha p a_0^2 h C_{33}} t. \quad (\text{S40})$$

We can estimate  $U_{\text{eff}}^{\text{Holst.}}$  to be in the range of  $0.05 - 1.4 t$  by assuming  $\beta = 4 - 5$  [S46],  $a_0 = 3.18 \text{ \AA}$  [S50],  $C_{33} = 52 \text{ GPa}$  [S52, S53],  $t_{\perp} = 0.3 - 0.4 \text{ eV}$  [S1],  $h = 3 - 6 \text{ \AA}$ ,  $\alpha = 2 \text{ eV}$ , and  $p = 0.167 - 0.5$ . In our simplified approach, we thus get interactions that can induce superconductivity (c.f. Fig. S3(b) of the main text) since the pairing strength  $\lambda = U_{\text{eff}}/t \cdot N(E_{\text{F}})t$  reaches values up to  $\lambda \approx 0.5$  (c.f. Fig. S2(c)).

Now, we consider an interlayer shear mode with the two layers being moved in opposite directions and opposite shearing profile in the AB and BA regions of the moiré. This effectively modulates the bond lengths in the moiré honeycomb superlattice, i.e., we estimate the effective interaction arising from the Peierls coupling discussed in Section S9. Two equivalent shear modes exist, see Fig. S11(b,c), for which the potential energy is given by the optical  $\mathbf{q} = \mathbf{0}$  eigenmode (c.f. Eq. (S30)) of the spring model in Section S9. The displacement  $\delta r_0$  of a Wannier center with respect to the origin at an AB/BA site thus has the elastic energy

$$E_{\text{el}} = \frac{1}{2} k_{\mathbf{q}=\mathbf{0},+} \delta r_0^2 = 3k \delta r_0^2. \quad (\text{S41})$$

On the other hand, we can estimate the equivalent displacement energy [S54]

$$E = \frac{1}{2} \int_{A_{\text{M}}} d^2r \sum_{\alpha} \lambda_{\text{L}} u_{\alpha\alpha}^2 + \sum_{\alpha\beta} 2\mu_{\text{L}} u_{\alpha\beta}^2 \quad (\text{S42})$$

associated with the displacement field  $\mathbf{u}$  of a single layer. Here,  $u_{\alpha\beta} = \frac{1}{2} (\frac{\partial u_{\alpha}}{\partial x_{\beta}} + \frac{\partial u_{\beta}}{\partial x_{\alpha}} + \sum_{\gamma} \frac{\partial u_{\gamma}}{\partial x_{\alpha}} \frac{\partial u_{\gamma}}{\partial x_{\beta}})$  is the strain tensor and  $\lambda_{\text{L}}$ ,  $\mu_{\text{L}}$  are the Lamé constants which are linked to the Young’s modulus  $Y$  and Poisson ratio  $\nu$  via

$$\lambda_{\text{L}} = \frac{\nu}{1 - 2\nu} \frac{1}{1 + \nu} Y, \quad \mu_{\text{L}} = \frac{1}{2(1 + \nu)} Y \quad (\text{S43})$$

with  $Y \approx 150 \text{ N/m}$  and  $\nu \approx 0.22$  for TMDC homobilayers [S55, S56]. The shear displacement  $\mathbf{u}$  of the TMDC layers induces a perpendicular shift  $\delta\mathbf{r}$  of the Wannier center with respect to the origin at an AB site as shown Fig. S11(d). They are linked by

$$\mathbf{u}_{\pm} = [\mathcal{R}_{\pm\theta/2} - \mathbb{1}_{2 \times 2}] \delta\mathbf{r} \approx \begin{pmatrix} 0 & \pm \frac{\theta}{2} \\ \mp \frac{\theta}{2} & 0 \end{pmatrix} \delta\mathbf{r}, \quad (\text{S44})$$

for small twist angles where the upper and lower TMDC layer carry a different sign. For each mode the displacement field  $\delta\mathbf{r}_{(b,c)} = \delta r(\mathbf{r})\mathbf{e}_{x,y}$  can be described by the leading Fourier components

$$\delta r(\mathbf{r}) = \frac{2\delta r_0}{3\sqrt{3}} \left( \sin(\mathbf{G}_1^M \mathbf{r}) + \sin([\mathbf{G}_2^M - \mathbf{G}_1^M] \mathbf{r}) - \sin(\mathbf{G}_2^M \mathbf{r}) \right). \quad (\text{S45})$$

Since the shear modes (and displacement energies) are equivalent, we focus on the mode in Fig. S11(b) in the following. For this mode, we have the stress tensor components

$$\begin{aligned} u_{xx} &= 0, \\ u_{xy} &= u_{yx} = \frac{1}{2} \frac{\partial u_y}{\partial x} = \pm \frac{\theta \delta r_0}{12} G^M \left( \cos(\mathbf{G}_1^M \mathbf{r}) + \cos([\mathbf{G}_2^M - \mathbf{G}_1^M] \mathbf{r}) \right), \\ u_{yy} &= \frac{\partial u_y}{\partial y} = \pm \frac{\theta \delta r_0}{6\sqrt{3}} G^M \left( \cos(\mathbf{G}_1^M \mathbf{r}) + \cos([\mathbf{G}_2^M - \mathbf{G}_1^M] \mathbf{r}) - 2 \cos(\mathbf{G}_2^M \mathbf{r}) \right) \end{aligned} \quad (\text{S46})$$

where the higher order terms of the offdiagonal components were neglected for small displacements and  $G^M = |\mathbf{G}_{1,2}^M| = 2\pi/\lambda^M$ . Inserting Eq. (S46) into Eq. (S42) and integrating over the moiré unit cell area, the displacement energy for one layer yields

$$E = \frac{1}{2} \frac{\theta^2 \delta r_0^2}{36} (G^M)^2 A_M (\lambda_L + 3\mu_L). \quad (\text{S47})$$

We obtain the force constant by equating the displacement energy for both layers with twice (due to two layers) the elastic energy in Eq. (S41) and using Eq. (S43) as

$$k = \frac{2}{3\delta r_0^2} E_{\text{el}} = \frac{1}{108} (G^M)^2 A_M (\lambda_L + 3\mu_L) \theta^2 = \frac{\sqrt{3}\pi^2}{108} \frac{3 - 4\nu}{(1 - 2\nu)(1 + \nu)} Y \theta^2 = k_0 \theta^2 \quad (\text{S48})$$

with  $k_0 \approx 5.6 \text{ eV}/\text{\AA}^2$ . The deformation potential is as in Eq. (S38) with  $t_\perp$  and  $h$  being replaced by  $t$  and  $\lambda^M/3$  (Wannier orbital extent), respectively. The effective potential takes the form

$$U_{\text{eff}}^{\text{Peierls}} \approx \frac{(\beta t \frac{3}{\lambda^M})^2}{k_0 \theta^2} \approx \frac{9\beta^2 t^2 \left(\frac{\theta}{a_0}\right)^2}{k_0 \theta^2} = \frac{9\beta^2}{a_0^2 k_0} t^2 = \frac{9\alpha\beta^2}{a_0^2 k_0} \theta^2 \cdot t. \quad (\text{S49})$$

Since  $U_{\text{eff}}^{\text{Peierls}}/t \propto t \propto \theta^2$  with the prefactor  $\frac{9\alpha\beta^2}{a_0^2 k_0} \approx 5-8$ , the effective interaction and hence pairing strength is very small. From our estimation we conclude that superconductivity from moiré Peierls coupling will not be realized in the real material system.

- 
- [S1] M. Angeli and A. H. MacDonald,  $\Gamma$  valley transition metal dichalcogenide moiré bands, *Proc. Natl. Acad. Sci.* **118**, e2021826118 (2021), [arXiv:2008.01735](https://arxiv.org/abs/2008.01735).
- [S2] T. Cea, N. R. Walet, and F. Guinea, Electronic band structure and pinning of Fermi energy to Van Hove singularities in twisted bilayer graphene: A self-consistent approach, *Phys. Rev. B* **100**, 205113 (2019).
- [S3] T. Cea and F. Guinea, Band structure and insulating states driven by Coulomb interaction in twisted bilayer graphene, *Phys. Rev. B* **102**, 045107 (2020).
- [S4] N. E. Bickers, D. J. Scalapino, and S. R. White, Conserving Approximations for Strongly Correlated Electron Systems: Bethe-Salpeter Equation and Dynamics for the Two-Dimensional Hubbard Model, *Phys. Rev. Lett.* **62**, 961 (1989).
- [S5] N. E. Bickers and D. J. Scalapino, Conserving approximations for strongly fluctuating electron systems. I. Formalism and calculational approach, *Ann. Phys. (NY)* **193**, 206 (1989).
- [S6] D. Xiao, G.-B. Liu, W. Feng, X. Xu, and W. Yao, Coupled Spin and Valley Physics in Monolayers of MoS<sub>2</sub> and Other Group-VI Dichalcogenides, *Phys. Rev. Lett.* **108**, 196802 (2012).
- [S7] S. Venkateswarlu, A. Honecker, and G. Trambly de Laissardière, Electronic localization in twisted bilayer mos<sub>2</sub> with small rotation angle, *Phys. Rev. B* **102**, 081103 (2020).
- [S8] N. Marzari, A. A. Mostofi, J. R. Yates, I. Souza, and D. Vanderbilt, Maximally localized Wannier functions: Theory and applications, *Rev. Mod. Phys.* **84**, 1419 (2012).
- [S9] N. F. Q. Yuan, H. Isobe, and L. Fu, Magic of high-order van Hove singularity, *Nat Commun.* **10**, 5769 (2019).
- [S10] L. Classen, A. V. Chubukov, C. Honerkamp, and M. M. Scherer, Competing orders at higher-order Van Hove points, *Phys. Rev. B* **102**, 125141 (2020).

- [S11] F. Guinea and N. R. Walet, Electrostatic effects, band distortions, and superconductivity in twisted graphene bilayers, *Proc. Natl. Acad. Sci.* **115**, 13174 (2018).
- [S12] M. J. Calderón and E. Bascones, Interactions in the 8-orbital model for twisted bilayer graphene, *Phys. Rev. B* **102**, 155149 (2020).
- [S13] A. Fischer, Z. A. H. Goodwin, A. A. Mostofi, J. Lischner, D. M. Kennes, and L. Klebl, Unconventional superconductivity in magic-angle twisted trilayer graphene, *npj Quantum Mater.* **7**, 5 (2022).
- [S14] G. P. Kerker, Efficient iteration scheme for self-consistent pseudopotential calculations, *Phys. Rev. B* **23**, 3082 (1981).
- [S15] E. G. C. P. van Loon, M. Schüler, M. I. Katsnelson, and T. O. Wehling, Capturing nonlocal interaction effects in the Hubbard model: Optimal mappings and limits of applicability, *Phys. Rev. B* **94**, 165141 (2016).
- [S16] J. M. Pizarro, M. Rösner, R. Thomale, R. Valentí, and T. O. Wehling, Internal screening and dielectric engineering in magic-angle twisted bilayer graphene, *Phys. Rev. B* **100**, 161102 (2019).
- [S17] K. Ohno, Some remarks on the Pariser-Parr-Pople method, *Theoretica chimica acta* **2**, 219 (1964).
- [S18] T. Cea and F. Guinea, Coulomb interaction, phonons, and superconductivity in twisted bilayer graphene, *Proc. Natl. Acad. Sci.* **118**, e2107874118 (2021).
- [S19] A. Laturia, M. L. Van de Put, and W. G. Vandenberghe, Dielectric properties of hexagonal boron nitride and transition metal dichalcogenides: from monolayer to bulk, *npj 2D Mater. Appl.* **2**, 6 (2018).
- [S20] A. Weston, Y. Zou, V. Enaldiev, A. Summerfield, N. Clark, V. Zólyomi, A. Graham, C. Yelgel, S. Magorrian, M. Zhou, J. Zultak, D. Hopkinson, A. Barinov, T. H. Bointon, A. Kretinin, N. R. Wilson, P. H. Beton, V. I. Fal'ko, S. J. Haigh, and R. Gorbachev, Atomic reconstruction in twisted bilayers of transition metal dichalcogenides, *Nat. Nanotechnol.* **15**, 592 (2020).
- [S21] Z. A. H. Goodwin, F. Corsetti, A. A. Mostofi, and J. Lischner, Twist-angle sensitivity of electron correlations in moiré graphene bilayers, *Phys. Rev. B* **100**, 121106 (2019).
- [S22] P. Stepanov, I. Das, X. Lu, A. Fahimniya, K. Watanabe, T. Taniguchi, F. H. L. Koppens, J. Lischner, L. Levitov, and D. K. Efetov, Untying the insulating and superconducting orders in magic-angle graphene, *Nature* **583**, 375 (2020).
- [S23] Y. Saito, J. Ge, K. Watanabe, T. Taniguchi, and A. F. Young, Independent superconductors and correlated insulators in twisted bilayer graphene, *Nat. Phys.* **16**, 926 (2020).
- [S24] H. S. Arora, R. Polski, Y. Zhang, A. Thomson, Y. Choi, H. Kim, Z. Lin, I. Z. Wilson, X. Xu, J.-H. Chu, K. Watanabe, T. Taniguchi, J. Alicea, and S. Nadj-Perge, Superconductivity in metallic twisted bilayer graphene stabilized by WSe<sub>2</sub>, *Nature* **583**, 379 (2020).
- [S25] X. Liu, Z. Wang, K. Watanabe, T. Taniguchi, O. Vafek, and J. I. A. Li, Tuning electron correlation in magic-angle twisted bilayer graphene using Coulomb screening, *Science* **371**, 1261 (2021).
- [S26] H. Kontani and K. Ueda, Electronic Properties of the Trellis-Lattice Hubbard Model: Pseudogap and Superconductivity, *Phys. Rev. Lett.* **80**, 5619 (1998).
- [S27] S. Koikegami, S. Fujimoto, and K. Yamada, Electronic Structure and Transition Temperature of the *d-p* Model, *J. Phys. Soc. Jpn.* **66**, 1438 (1997).
- [S28] J. Li, M. Wallerberger, N. Chikano, C.-N. Yeh, E. Gull, and H. Shinaoka, Sparse sampling approach to efficient ab initio calculations at finite temperature, *Phys. Rev. B* **101**, 035144 (2020), [arxiv:1908.07575](https://arxiv.org/abs/1908.07575).
- [S29] N. Witt, E. G. C. P. van Loon, T. Nomoto, R. Arita, and T. O. Wehling, Efficient fluctuation-exchange approach to low-temperature spin fluctuations and superconductivity: From the Hubbard model to Na<sub>x</sub>CoO<sub>2</sub>·yH<sub>2</sub>O, *Phys. Rev. B* **103**, 205148 (2021), [arXiv:2012.04562](https://arxiv.org/abs/2012.04562).
- [S30] H. Shinaoka, N. Chikano, E. Gull, J. Li, T. Nomoto, J. Otsuki, M. Wallerberger, T. Wang, and K. Yoshimi, Efficient ab initio many-body calculations based on sparse modeling of Matsubara Green's function, [2106.12685](https://arxiv.org/abs/2106.12685).
- [S31] H. Shinaoka, J. Otsuki, M. Ohzeki, and K. Yoshimi, Compressing Green's function using intermediate representation between imaginary-time and real-frequency domains, *Phys. Rev. B* **96**, 035147 (2017), [arxiv:1702.03054](https://arxiv.org/abs/1702.03054).
- [S32] N. Chikano, K. Yoshimi, J. Otsuki, and H. Shinaoka, irbasis: Open-source database and software for intermediate-representation basis functions of imaginary-time Green's function, *Comput. Phys. Commun.* **240**, 181 (2019), [arXiv:1807.05237](https://arxiv.org/abs/1807.05237).
- [S33] K. Kuroki and R. Arita, Spin-triplet superconductivity in repulsive Hubbard models with disconnected Fermi surfaces: A case study on triangular and honeycomb lattices, *Phys. Rev. B* **63**, 174507 (2001).
- [S34] S. Onari, K. Kuroki, R. Arita, and H. Aoki, Superconductivity induced by interband nesting in the three-dimensional honeycomb lattice, *Phys. Rev. B* **65**, 184525 (2002).
- [S35] K. Kuroki, Spin-fluctuation-mediated *d+id'* pairing mechanism in doped  $\beta$ -MnCl(M=Hf,Zr)superconductors, *Phys. Rev. B* **81**, 104502 (2010).
- [S36] M. Sgrist and K. Ueda, Phenomenological theory of unconventional superconductivity, *Rev. Mod. Phys.* **63**, 239 (1991).
- [S37] N. D. Mermin and H. Wagner, Absence of Ferromagnetism or Antiferromagnetism in One- or Two-Dimensional Isotropic Heisenberg Models, *Phys. Rev. Lett.* **17**, 1307 (1966).
- [S38] H. Kontani and M. Ohno, Effect of a nonmagnetic impurity in a nearly antiferromagnetic Fermi liquid: Magnetic correlations and transport phenomena, *Phys. Rev. B* **74**, 014406 (2006).
- [S39] H. Kino and H. Kontani, Phase Diagram of Superconductivity on the Anisotropic Triangular Lattice Hubbard Model: An Effective Model of  $\kappa$ -(BEDT-TTF) Salts, *J. Phys. Soc. Jpn.* **67**, 3691 (1998), [arxiv:cond-mat/9807147](https://arxiv.org/abs/cond-mat/9807147).
- [S40] M. Kitatani, N. Tsuji, and H. Aoki, FLEX+DMFT approach to the *d*-wave superconducting phase diagram of the two-dimensional Hubbard model, *Phys. Rev. B* **92**, 085104 (2015), [arxiv:1505.04865](https://arxiv.org/abs/1505.04865).
- [S41] W.-S. Wang, Y.-Y. Xiang, Q.-H. Wang, F. Wang, F. Yang, and D.-H. Lee, Functional renormalization group and variational Monte Carlo studies of the electronic instabilities in graphene near  $\frac{1}{4}$  doping, *Phys. Rev. B* **85**, 035414 (2012).

- [S42] S. Jiang, A. Mesaros, and Y. Ran, Chiral Spin-Density Wave, Spin-Charge-Chern Liquid, and  $d + id$  Superconductivity in 1/4-Doped Correlated Electronic Systems on the Honeycomb Lattice, *Phys. Rev. X* **4**, 031040 (2014).
- [S43] Z. Kuznetsova and V. Barzykin, Pairing state in multicomponent superconductors, *Europhys. Lett.* **72**, 437 (2005).
- [S44] R. Nandkishore, L. S. Levitov, and A. V. Chubukov, Chiral superconductivity from repulsive interactions in doped graphene, *Nat. Phys.* **8**, 158 (2012).
- [S45] A. M. Black-Schaffer and C. Honerkamp, Chiral  $d$ -wave superconductivity in doped graphene, *J. Phys.: Condens. Matter* **26**, 423201 (2014), arxiv:1406.0101.
- [S46] W. A. Harrison, *Elementary Electronic Structure*, rev. ed. (World Scientific, Singapore, 2004).
- [S47] P. B. Allen and R. C. Dynes, Transition temperature of strong-coupled superconductors reanalyzed, *Phys. Rev. B* **12**, 905 (1975).
- [S48] W. L. McMillan, Transition Temperature of Strong-Coupled Superconductors, *Phys. Rev.* **167**, 331 (1968).
- [S49] M. Rösner, S. Haas, and T. O. Wehling, Phase diagram of electron-doped dichalcogenides, *Phys. Rev. B* **90**, 245105 (2014).
- [S50] G. Schönhoff, M. Rösner, R. E. Groenewald, S. Haas, and T. O. Wehling, Interplay of screening and superconductivity in low-dimensional materials, *Phys. Rev. B* **94**, 134504 (2016).
- [S51] G. D. Mahan, *Many-Particle Physics*, 3rd ed. (Springer US, 2000).
- [S52] J. L. Feldman, Elastic constants of 2H-MoS<sub>2</sub> and 2H-NbSe<sub>2</sub> extracted from measured dispersion curves and linear compressibilities, *J. Phys. Chem. Solids* **37**, 1141 (1976).
- [S53] Y. Zhao, X. Luo, H. Li, J. Zhang, P. T. Araujo, C. K. Gan, J. Wu, H. Zhang, S. Y. Quek, M. S. Dresselhaus, and Q. Xiong, Interlayer Breathing and Shear Modes in Few-Trilayer MoS<sub>2</sub> and WSe<sub>2</sub>, *Nano Lett.* **13**, 1007 (2013).
- [S54] L. D. Landau and E. M. Lifshitz, *Theory of Elasticity*, 2nd ed., Vol. 7 (Oxford: Pergamon, 1970).
- [S55] D. Çakır, F. M. Peeters, and C. Sevik, Mechanical and thermal properties of h-MX<sub>2</sub> (M=Cr, Mo, W; X=O, S, Se, Te) monolayers: A comparative study, *Appl. Phys. Lett.* **104**, 203110 (2014).
- [S56] K. Liu, Q. Yan, M. Chen, W. Fan, Y. Sun, J. Suh, D. Fu, S. Lee, J. Zhou, S. Tongay, J. Ji, J. B. Neaton, and J. Wu, Elastic Properties of Chemical-Vapor-Deposited Monolayer MoS<sub>2</sub>, WS<sub>2</sub>, and Their Bilayer Heterostructures, *Nano Lett.* **14**, 5097 (2014).

# Absence of room-temperature superconductivity

# 5

*In theory there is no difference between theory and practice. In practice there is.*

— Benjamin Brewster

Much of the research effort on classifying, understanding, and optimizing superconductivity is targeted towards the quest of potentially discovering a superconducting material operable under ambient conditions. Achieving this tantalizing goal could have an unpredictable transformative impact on our technological society, akin to the invention of transistors and their enabling of computer technology. The prospects of an *ideal* ambient-condition superconductor<sup>1</sup> are vast: They include the development of more efficient power grids and energy storage systems, more powerful and affordable electromagnets for scientific, medical, and transportation uses, as well as ultrafast switches for classical computing or novel quantum computing architecture.

Research often focuses on achieving a transition temperature ( $T_c$ ) to be at or above room temperature. Yet, for practical applications, a generally large critical surface (cf. Fig. 3.3) with appreciable critical current densities and critical magnetic fields is paramount. An example of this conflict is given by cuprate HTSCs which exhibit an enhanced  $T_c$  on the order of 100 K. Hence, superconductivity can be sustained in these materials using liquid nitrogen for cooling. Despite this, the effective operating temperature for high-field applications is typically between 30–50 K for ReBCO (rare earth barium copper oxide) superconductors or even below 20 K for  $\text{Bi}_2\text{Sr}_2\text{CaCu}_2\text{O}_{8+\delta}$  (Bi2212) [4, 651]. Consequently, the initial advantage of a  $T_c$  high enough to be cooled by liquid nitrogen becomes impractical, as more expensive cooling methods, such as liquid hydrogen or cryocoolers, are still necessary.

Nonetheless, the discovery of room-temperature superconductivity would present a tremendous advancement in physics [652]. Hydride materials present a promising avenue toward achieving this goal [98, 653], albeit under extremely high pressure on the order of gigapascals (GPa). The circumstances surrounding the retraction of

---

<sup>1</sup>Such an idealized material would not only show excellent electromagnetic properties but should possess good mechanical properties that allow for flexibility and versatility in applications.

possibly fraudulent publications on hydride materials claiming very high  $T_c = 15\text{--}25\text{ }^\circ\text{C}$  [654, 655] demonstrate the level of scrutiny any potential discovery in this area will face from the scientific community [433, 656–659]. In the following, we discuss another purported room-temperature superconductor that has undergone similar scientific scrutiny.

### 5.1 Copper-doped lead apatite – $\text{Pb}_{10-x}\text{Cu}_x(\text{PO}_4)_6\text{O}$

In the summer of 2023, Lee et al. [660–662] claimed to have found ambient-pressure, room-temperature superconductivity in modified lead apatite,  $\text{Pb}_{10-x}\text{Cu}_x(\text{PO}_4)_6\text{O}$  ( $0.9 < x < 1.1$ ), also known as LK-99. The authors argued for superconductivity occurring above  $100\text{ }^\circ\text{C}$ , supported by an observed sharp resistivity drop and the (half-)levitation of an LK-99 sample flake [661, 662]. Additionally, a prior study [660] reported a peak in the specific heat capacity which was interpreted as a  $\lambda$ -transition characteristic of superconductors and superfluids [44]. The announcement of the purported room-temperature superconductor generated significant public interest and brought the compound  $\text{Pb}_{10-x}\text{Cu}_x(\text{PO}_4)_6\text{O}$  into the focus of solid-state research. Subsequent to the claim, replication efforts were promptly initiated by various research teams [663–670], facilitated by the affordable cost of materials and the rather simple synthesis procedure [661, 663, 666, 669].

To date, superconductivity in  $\text{Pb}_{10-x}\text{Cu}_x(\text{PO}_4)_6\text{O}$  has not been replicated in almost all reported experiments, for example, Refs. [617, 663, 664, 666–668, 670–677]. Although (half-)levitation was indeed observed in some instances [666, 667, 671, 678], the electromagnetic properties varied significantly among samples synthesized by different research groups [661, 662, 664–667, 670, 671, 675, 677, 678]. One reason for this variation is that LK-99 is a polycrystalline material of which the precise composition is difficult to determine. The structural ambiguity allows for the persistence of disorder effects, the influence of magnetic impurities, and coexistence of different phases or superstructures [672, 679–684].

In later studies, it was determined that a structural phase transition of contaminating  $\text{Cu}_2\text{S}$ , a byproduct of the synthesis, was responsible for the observed resistivity drop at the alleged superconducting critical temperature above  $100\text{ }^\circ\text{C}$  [668, 674, 676, 685, 686]. Notably, the sharp reduction in resistivity does not reach zero indicating that LK-99 has very low conductivity. The synthesis of pure single crystals supported this finding, determining  $\text{Pb}_{10-x}\text{Cu}_x(\text{PO}_4)_6\text{O}$  to be a non-magnetic insulator that is optically transparent [673]. Conversely, the (half-)levitation could be attributed to ferromagnetism within the composite material [667, 669, 678, 687].

Alongside with experimental reproduction efforts, also theoretical characterizations were conducted. Electronic structure calculations employing DFT+U [672, 680, 682, 688–692] as well as DFT+DMFT [682, 693–695] identified  $\text{Pb}_{10-x}\text{Cu}_x(\text{PO}_4)_6\text{O}$  to



be a Mott or charge transfer insulator for all Cu concentrations  $x$ . The corresponding gap opening is in agreement with the transparent single crystals [673]. In the stoichiometric compound  $Pb_9Cu_1(PO_4)_6O$ , a Pb atom of the lead apatite structure is replaced by Cu due to which two very flat bands (bandwidth  $W \approx 140$  meV) crossing the Fermi energy emerge from the Cu- $e_g$  orbitals (see Fig. 1 of publication V). Below these, slightly more dispersive O bands are located. Estimations and cRPA calculations for the local Hubbard interaction  $U$  find that  $U/W \sim O(10)$  [V, 694, 695], classifying  $Pb_9Cu_1(PO_4)_6O$  as a strongly correlated material that turns insulating from dominating electronic interactions. Upon doping, Weyl points emerge close to the Fermi surface [696, 697], relevant for topologically protected surface states [698].

Initially, it was unclear whether further doping could also potentially turn the material superconducting [694]. This idea was inspired by the similarity to cuprates which belong to the same class of charge transfer insulators with relevant contributions from Cu and O to the low-energy electronic structure [10, 31, 34]. Based on this premise, we studied the possibility of electronically-induced superconductivity from exchange of spin and orbital fluctuations upon doping in publication V. Our analysis based on a minimal two-orbital model of the Cu- $e_g$  orbitals has not shown any evidence of superconductivity down to 20 K. At the time of preparing the work [V], our results gave an important indication for the absence of room-temperature superconductivity in  $Pb_{10-x}Cu_x(PO_4)_6O$  since the experimental picture was not as clear as it is nowadays.

Besides observing the lack of superconducting behavior in LK-99, our work yields two broader insights. Asking for the reasons that prevent superconductivity to emerge, allows for identifying potential pathways to achieve superconductivity under different conditions.  $Pb_9Cu_1(PO_4)_6O$  is a triangular lattice system that can be compared to other triangular lattice superconductors such as organic salts or sodium cobaltate (see section 4.1.1). This comparison reveals two major drawbacks preventing superconductivity. First, the flat bands are too small to host spin fluctuations with a sufficient energy spread to mediate superconductivity [32, 34]. Second, the system's three-dimensionality is unfavorable because only a small fraction of the phase space participates in pairing [339], and the competition between ferromagnetic and antiferromagnetic fluctuations is enhanced [699].

The second insight addresses the methods for investigating electronic superconductivity. In our study, we utilized two approaches: unrenormalized RPA and fully self-consistent FLEX calculations. While we did not find electronic superconductivity within the FLEX approximation, we could induce a superconducting response in the RPA treatment by positioning the material close enough to a magnetic instability. This comparison underscores the importance of caution in applying unrenormalized weak-coupling approaches.

Niklas Witt, Liang Si, Jan M. Tomczak, Karsten Held, Tim O. Wehling

### Key points summary

- Timely investigation of possible superconductivity under ambient conditions in copper-doped lead apatite ( $\text{Pb}_9\text{Cu}_1(\text{PO}_4)_6\text{O}$ ).
- Absence of spin- and orbital-fluctuation-driven superconducting pairing at room temperature and lower temperatures down to 20 K, excluding the possibility of superconductivity in the studied two-band model.
- Discussion of possible reasons for the absence of superconductivity, e.g., from comparison to other triangular lattice superconductors .
- Demonstrating importance of self-consistency as the superconducting instability always present in RPA is removed in self-consistent FLEX.

### Author Contributions

I performed and analyzed the RPA and FLEX calculations based on the wannierized two-orbital model by L. Si and cRPA calculations by J. M. Tomczak. I prepared Figs. 2 and 3. The project was conceived by K. Held, T. Wehling, and myself. All authors contributed to writing of the text and participated in the discussion of the results and their implications. I was responsible for handling the paper submission and communication with editor and referees.

### Copyright Notice

This work is licensed under the Creative Commons Attribution 4.0 International License (CC-BY), which permits unrestricted use, distribution, and reproduction in any medium, provided the original work is properly cited:

N. Witt et al., SciPost Physics 15, 197 (2023).

Copyright © 2023 The Authors. This is an accepted version of the article published by the SciPost Foundation at doi: [10.21468/SciPostPhys.15.5.197](https://doi.org/10.21468/SciPostPhys.15.5.197).

# No superconductivity in $\text{Pb}_9\text{Cu}_1(\text{PO}_4)_6\text{O}$ found in orbital and spin fluctuation exchange calculations

 Niklas Witt<sup>1,2\*</sup>,  Liang Si<sup>3,4</sup>,  Jan M. Tomczak<sup>4,5</sup>,  
 Karsten Held<sup>4°</sup> and  Tim O. Wehling<sup>1,2†°</sup>

1 I. Institute for Theoretical Physics, University of Hamburg,  
Notkestraße 9-11, 22607 Hamburg, Germany

2 The Hamburg Centre for Ultrafast Imaging,  
Luruper Chaussee 149, 22607 Hamburg, Germany

3 School of Physics, Northwest University, Xi'an 710127, China

4 Institute of Solid State Physics, TU Wien, 1040 Vienna, Austria

5 Department of Physics, King's College London, Strand, London WC2R 2LS, United Kingdom

\* [niklas.witt@physik.uni-hamburg.de](mailto:niklas.witt@physik.uni-hamburg.de), † [tim.wehling@physik.uni-hamburg.de](mailto:tim.wehling@physik.uni-hamburg.de)

## Abstract

Finding a material that turns superconducting under ambient conditions has been the goal of over a century of research, and recently  $\text{Pb}_{10-x}\text{Cu}_x(\text{PO}_4)_6\text{O}$  aka LK-99 has been put forward as a possible contestant. In this work, we study the possibility of electronically driven superconductivity in LK-99 also allowing for electron or hole doping. We use an *ab initio* derived two-band model of the Cu  $e_g$  orbitals for which we determine interaction values from the constrained random phase approximation (cRPA). For this two-band model we perform calculations in the fluctuation exchange (FLEX) approach to assess the strength of orbital and spin fluctuations. We scan over a broad range of parameters and enforce no magnetic or orbital symmetry breaking. Even under optimized conditions for superconductivity, spin and orbital fluctuations turn out to be too weak for superconductivity anywhere near to room-temperature. We contrast this finding to non-self-consistent RPA, where it is possible to induce spin singlet  $d$ -wave superconductivity at  $T_c \geq 300$  K if the system is put close enough to a magnetic instability.



Copyright N. Witt *et al.*

This work is licensed under the Creative Commons

[Attribution 4.0 International License](https://creativecommons.org/licenses/by/4.0/).

Published by the SciPost Foundation.

Received 05-09-2023

Accepted 06-11-2023

Published 21-11-2023

doi:[10.21468/SciPostPhys.15.5.197](https://doi.org/10.21468/SciPostPhys.15.5.197)



Check for updates

---

## Contents

<b>1</b>	<b>Introduction</b>	<b>2</b>
<b>2</b>	<b>Results</b>	<b>3</b>
<b>3</b>	<b>Discussion and conclusion</b>	<b>5</b>

<sup>°</sup> These authors contributed equally to this work.

<b>A Methods</b>	<b>7</b>
A.1 Electronic structure	7
A.2 Constrained random phase approximation	8
A.3 Fluctuation exchange approach	8
<b>References</b>	<b>9</b>

---

## 1 Introduction

The recent papers by Lee *et al.* [1, 2] reporting that  $\text{Pb}_{10-x}\text{Cu}_x(\text{PO}_4)_6\text{O}$  with  $0.9 < x < 1.1$  (aka LK-99) is a room-temperature superconductor at ambient-pressure have been followed by extraordinary experimental and theoretical efforts. It even caught the attention of major news outlets and went viral on social media.

Experimental efforts to reproduce these measurements have led to mixed results. Some experiments confirm a jump in the conductivity as in the original work [1–3], albeit at a different temperature [4] or at a similar temperature but with an insulating resistivity at lower temperatures [5]. Also the levitation of Lee, Kim, *et al.* [2] or their diamagnetic response has been reproduced by other groups [6–8].

In stark contrast, other experiments find an insulator [4, 9, 10] and a paramagnetic behavior [9, 10]. Most experiments show a gray-black color, but a recent one reported transparency [11]. Matters become even more complicated, since –to the best of our knowledge– hitherto no single phase sample has been synthesized, as evidenced by x-ray diffraction (XRD) [2, 4, 10] — not to speak of a single crystal. How can one make sense of these seemingly contradictory results?

Based on the observation that the Coulomb interaction  $U$  dominates over the kinetic energy or bandwidth  $W$ , with  $U/W$  of  $\mathcal{O}(10)$ , two of us [12] concluded that LK-99 must be a Mott or charge transfer insulator irrespective of  $x$ . This has been confirmed in independent calculations [13–15] using density functional theory (DFT) in combination with dynamical mean-field theory (DMFT) [16–19]. Likewise, DFT+ $U$  calculations [13, 20–24] show a splitting into Hubbard bands. However, here a magnetic symmetry breaking (ordering) and a crystal structure or distortion that lifts the degeneracy of the two Cu  $e_g$  orbitals crossing the Fermi energy is required. All of this confirms: Pure LK-99 is a Mott or charge transfer insulator. Thus, simultaneous to experimental efforts, theoretical simulations explain the insulating and paramagnetic behavior.

At the same time, the metallic (and potentially also the superconducting) behavior could be explained if LK-99 is electron or hole-doped, e.g.,  $\text{Pb}_{10-x}\text{Cu}_x(\text{P}_{1-y}\text{S}_y\text{O}_4)_6\text{O}_{1+z}$  with  $y > 0$  and  $z \neq 0$ . At least metallic behavior and a gray-black or similar color [2, 4, 10] are then to be expected. A noteworthy other explanation has been put forward by Zhu *et al.* [25] and Jain [26]: the resistivity jump and  $\lambda$ -like feature in the specific heat could be simply caused by  $\text{Cu}_2\text{S}$  which is clearly present as a secondary phase in XRD measurements [2, 4, 10, 25].

The most important question however remains open: Is electron or hole doped LK-99 superconducting? Here, experiment is inconclusive and calculations have so-far been very limited: Enforcing superconductivity with a Bardeen, Cooper and Schrieffer (BCS) [27] Hamiltonian, Tavakol *et al.* [28] find  $f$ -wave pairing. Oh and Zhang [29] obtain a self-consistently determined  $s$ -wave pairing in an effective  $t - J$  model at zero temperature.

In this paper, we aim at giving a more definite answer regarding superconductivity. Based on an *ab initio* derived two-band model [13],<sup>1</sup> which suffices for a Mott insulator, we employ

<sup>1</sup>A first tight-binding parametrization mimicking the DFT dispersion was derived in Ref. [30] purely from sym-

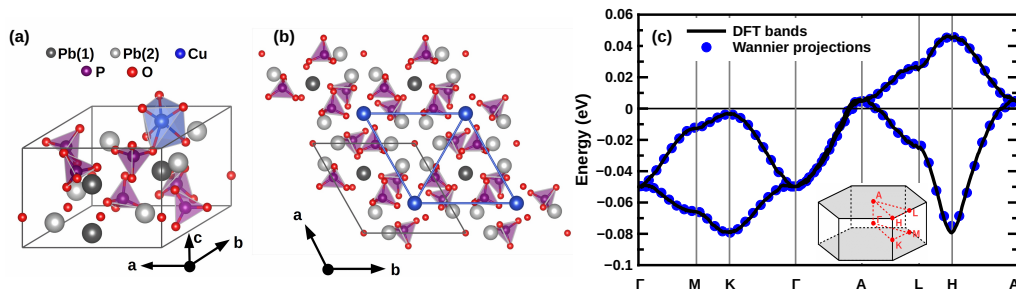


Figure 1: **Crystal structure and electronic bands of LK-99.** (a) DFT-relaxed structure of  $\text{Pb}_9\text{Cu}(\text{PO}_4)_6\text{O}$ ; (b) View along  $z$ -direction for the  $2 \times 2 \times 1$  supercell of (a); (c) DFT and Wannier band structures, the inset shows the  $k$ -path selected for band plotting. The DFT and Wannier projection data are adopted from Ref. [13].

the fluctuation exchange (FLEX) [31–33] approach. Our results are very clear: we can exclude superconductivity — at least superconductivity based on orbital and spin fluctuations in the two-band model of LK-99.

## 2 Results

For the structure of LK-99 shown in Fig. 1(a,b), where the Cu atoms form a triangular sublattice, DFT calculations [12,22,34,35] yield the low-energy *ab initio* band structure shown in Fig. 1(c). The two lowest-energy bands are well captured by the Wannier functions projected onto the  $d_{yz}$  and  $d_{xz}$  orbitals in the energy window of  $[-0.1, 0.1]$  eV. These bands disperse over a bandwidth of the order of  $\sim 120$  meV. External pressure is expected to enlarge the hopping and bandwidth by reducing the lattice constants and distance between Cu cations. Calculations of the Coulomb interaction tensor in the constrained random phase approximation (cRPA) yield local intra-orbital Hubbard repulsion  $U_{\text{cRPA}} = 1.8$  eV, an inter-orbital  $U'_{\text{cRPA}} = 1.14$  eV, and a Hund’s exchange  $J_{\text{cRPA}} = 0.33$  eV (c.f. section A.2). These interactions exceed the electronic bandwidth by far and put LK-99 – with or without pressure – into the regime of strong electron correlations — in line with recent DMFT [13–15] and DFT+ $U$  studies [13,20–24].

Here, our goal is to establish an *upper boundary* for spin- and orbital-fluctuation-driven superconductivity (SC) in LK-99. To this end, we resort to a RPA and FLEX analysis. Fig. 2 compares the static momentum ( $\mathbf{q}$ )-dependent non-interacting susceptibility  $\chi^0(\mathbf{q})$  (left column) to the spin susceptibility  $\chi^s(\mathbf{q})$  as obtained from RPA and FLEX for an interaction with an  $U/J$  ratio as in cRPA. First, we study the system for a scaled-down overall magnitude of the interaction matrix elements with  $U = 0.115$  eV. This regime is close to the RPA’s magnetic instability, where we expect the strongest tendencies towards spin-fluctuation-driven superconductivity. We consider two different dopings: the nominal filling of  $n = 3$  electrons per unit cell (upper panel) and hole doping to  $n = 2.7$ . At both doping levels, the RPA spin susceptibility exceeds the non-interacting susceptibility by factors of 4 to 20, respectively, signaling a correspondingly strong Stoner enhancement. Indeed, this strong Stoner enhancement confirms that our scaled down interaction ( $U = 0.115$  eV) is close to the RPA Stoner instability and thus also in the vicinity of the region, where we potentially expect the strongest tendency for spin- or orbital-fluctuation-driven superconductivity.

Indeed, we find magnetic instabilities over a wide range of fillings  $2 < n < 3.3$  in RPA that set in already for interactions of the order of the bandwidth,  $U \approx 0.12$  eV  $\ll U_{\text{cRPA}}$ . RPA therefore puts LK-99 deeply into a magnetically ordered state.

metry considerations.

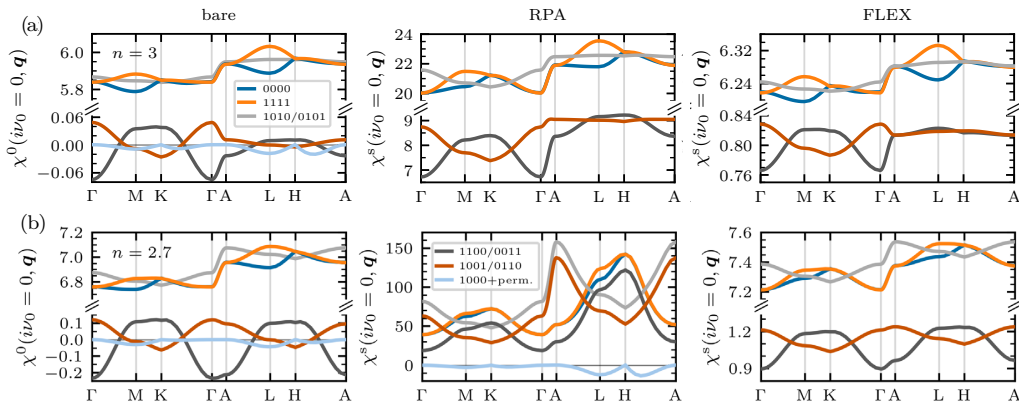


**Figure 2: Susceptibilities and spin fluctuations.** Plots of the static non-interacting susceptibility  $\chi^0$  (left column), RPA (middle column) and FLEX spin susceptibility  $\chi^s$  (right column) components as function of momentum  $\mathbf{q}$  obtained at temperature  $T = 300$  K for (a) the nominal filling of LK-99 ( $n = 3$ ) and (b) in a hole-doped case ( $n = 2.7$ ). The RPA and FLEX calculations assumed the ratio  $U/J = 0.183$  as in cRPA, but the interaction magnitude tuned to  $U = 0.115$  eV, which is in RPA near the magnetic instability and thus in the vicinity of the point of maximal spin fluctuations. Note the very different scales of the spin susceptibilities in RPA and FLEX.

However, care must be taken since renormalization effects and vertex corrections can decisively impact phase diagrams and could hypothetically suppress magnetic order. The FLEX method takes into account renormalization effects stemming from the scattering of electrons with spin, orbital and charge fluctuations in terms of a diagrammatic ladder resummation. The resultant FLEX spin susceptibilities (Fig. 2 right columns) are indeed much smaller than their RPA counterparts and show much weaker Stoner enhancement. A further increase of the Hubbard  $U$  leads to a *reduced* spin susceptibility in FLEX related to a reduction of the electronic quasiparticle weight.

Scattering of electrons off spin and orbital fluctuations can mediate superconductivity [36, 37]. Within RPA and FLEX, the resultant pairing interactions in the singlet and triplet channel, cf. Eq. (A.10), are controlled by the spin and charge susceptibilities and grow as  $\chi^{s,c}$  increase. A transition into a superconducting state is indicated by the leading eigenvalue,  $\lambda_{SC}$ , of the linearized Eliashberg equation, see Eq. (A.9) below, reaching unity. Fig. 3 shows  $\lambda_{SC}$  as obtained from RPA for different doping levels and ratios  $J/U^2$  as a function of interaction strength  $U$  at a temperature of  $T = 300$  K. We see that essentially at any hole-doping level in the range of  $2.1 < n < 3$  fine tuning of the interaction seemingly leads to a superconducting instability even at 300 K. The resultant dominant order parameter in RPA is visualized in Fig. 3(f). This order parameter is in the spin singlet channel and involves significant inter-orbital pairing as well as sign changes between different momentum or orbital components. Electron doping ( $n = 3.3$ ), on the contrary, is detrimental to the formation of SC pairing even within RPA.

Analyzing the RPA results more closely, we find that the superconducting tendencies exclusively occur when closely approaching a Stoner instability, where the effective interaction strength [see Eq. (A.10) below] becomes unphysically large.

Indeed, renormalization effects strongly limit the maximal strength of the effective pairing interaction: This effect manifests dramatically in the Eliashberg eigenvalues  $\lambda_{SC}$  achievable in FLEX. Scanning a wide range of interaction strengths and dopings, we obtain the temperature

<sup>2</sup>The ratio  $J/U = 0.183$  stems from our cRPA simulations; the interaction estimate by Si *et al.* [13] leads to  $J/U = 0.22$ , whereas the cRPA calculations by Yue *et al.* [15] fall in-between with  $J/U = 0.207$ .

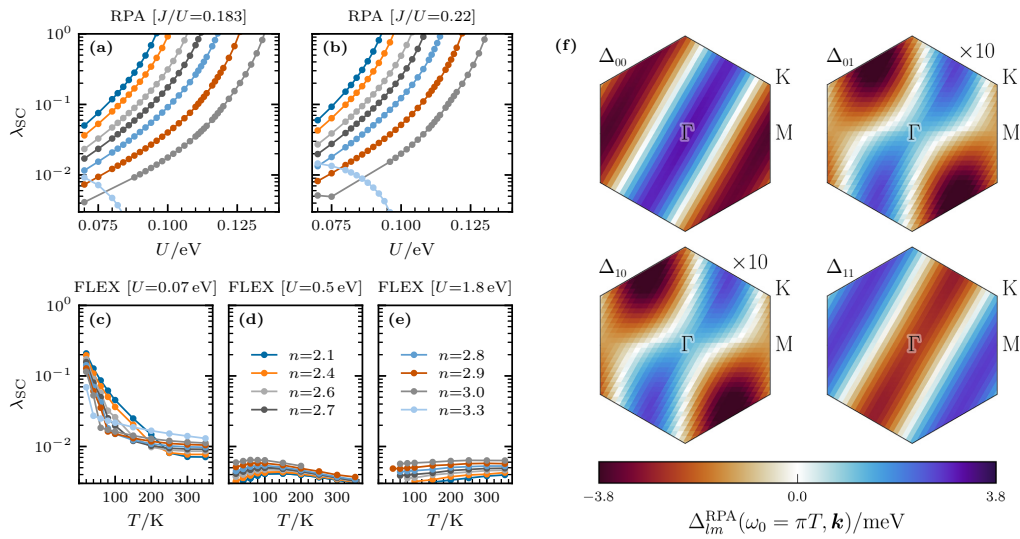


**Figure 3: Superconductivity and SC order parameters in RPA and FLEX.** Eigenvalues of the leading SC instability in linearized Eliashberg equation as obtained in (a,b) RPA and (c-e) FLEX for different dopings  $n$ . In RPA,  $\lambda_{SC}$  is shown as function of interaction strength  $U$  at temperature  $T = 300$  K for different ratios  $J/U = 0.183$  (a) and  $0.22$  (b). Whenever a generalized Stoner instability is approached the SC eigenvalue reaches up to order  $\lambda_{SC} \approx 1$  in RPA seemingly signaling an SC instability of the system. The associated gap function  $\Delta$  is shown in panel (f), where the momentum dependence of each matrix element  $\Delta_{lm}$  is shown in the  $k_z = 0$  plane (note that the off-diagonal components  $\Delta_{01/10}$  are enlarged by a factor 10). FLEX calculations kept the ratio  $J/U = 0.183$  fixed, and show  $\lambda_{SC}$  as a function of temperature  $T$  for different interaction strengths  $U = 0.07$  eV (c),  $U = 0.5$  eV (d), and  $U = 1.8$  eV (e). At room temperature we have  $\lambda_{SC} \ll 10^{-1}$  ruling out any SC instabilities at this temperature.

dependent  $\lambda_{SC}$  in FLEX shown in Fig. 3(c-e). Anywhere close to room temperature we have  $\lambda_{SC}$  merely of the order of  $10^{-2}$ , which is far away from any superconducting instability. Even if we go down in temperature to 20 K,  $\lambda_{SC}$  at best reaches values on the order of  $10^{-1}$ . If Coulomb interaction mediated spin- or orbital-fluctuation-driven superconductivity sets in, it could only do so at significantly reduced temperatures.

The stark contrast between non-self-consistent RPA, where it is possible to seemingly find SC states with  $T_c \geq 300$  K, and FLEX where SC is absent anywhere close to room temperature shows that the loss of electronic coherence due to scattering between electrons and spin fluctuations, which is missing in RPA, is responsible for the absence of superconductivity in the two-band model of LK-99.

### 3 Discussion and conclusion

Our FLEX simulations do not find any superconducting instability in an *ab initio* derived two-band description of LK-99 — despite of a large range of dopings and interactions being considered. How unlikely does this render spin- or orbital-fluctuation-driven superconductivity in LK-99?

It is clear that also FLEX is an approximate method with shortcomings in the regime of strong correlations, including the failure to describe Hubbard bands correctly. Importantly,

however, previous comparisons of FLEX against DMFT-based treatments of strongly correlated superconductivity for the one-band Hubbard model [33] showed that achievable critical temperatures  $T_c$  have the same magnitude in both approaches. Thus, within the two-band model considered here, room temperature superconductivity appears out of reach.

Still, two loopholes related to the two-band model by itself remain in principle open: First, the model considered here, assumes a periodic crystal with minimal unit cell comprising one idealized chemical composition  $\text{Pb}_{10-x}\text{Cu}_x(\text{P}_{1-y}\text{S}_y\text{O}_4)_6\text{O}_{1+z}$  with  $x = 1$ ,  $y = 0$ ,  $z = 0$  and optimized O and Cu positions [12]. This implies a triangular lattice of the Cu sites. However, several structures with different O and Cu positions are very close in energy [12,21] such that a disordered arrangement as suggested also by the XRD experiments [2,4,10] can be expected. While we cannot exclude disorder-enhanced superconductivity, it is not clear how a sufficient stiffness of the SC order parameter and a sufficient pairing strength to boost  $T_c$  by more than an order of magnitude should be achievable here. Further, electron and hole doping of LK-99, corresponding to  $y \neq 0$  and/or  $z \neq 0$ , is merely treated by changing the chemical potential in a rigid band approach.

Second, FLEX does not describe Hubbard bands. For a doped Mott insulator, however, we have quasiparticle renormalized Cu- $d$  bands crossing the Fermi energy. This situation and potentially arising superconducting instabilities *can* be described by FLEX. Qualitatively, we are thus on the safe side, since we committed ourselves to analyzing a broad range of parameters with largely different quasiparticle renormalizations. Still, a hole-doped charge transfer insulator, where the oxygen  $p$  bands cross the Fermi energy and the lower copper  $d$  Hubbard band lies just below, cf. Ref. [13], cannot be described. At least for hole-doped cuprate superconductors, which are charge transfer insulators, O  $p$  and Cu  $d$  orbitals form a strongly hybridized single band — a situation [63,64] which, then again, is in reach of FLEX. For electron doping, the Pb  $p$  orbitals are too high in energy ( $\geq 3$  eV) [12] for a charge-transfer arrangement with the upper Hubbard band.

Our results also invite a comparison to other triangular lattice materials where (unconventional) SC has been observed experimentally, for instance in organic salts [38–41], water intercalated sodium cobalt oxide ( $\text{Na}_x\text{CoO}_2 \cdot y\text{H}_2\text{O}$ ) [42,43] or certain 5d transition-metal compounds [44–47]. In particular, various FLEX studies found superconductivity in single- and multi-orbital models on a triangular lattice [33,48–54] as well as related honeycomb and Kagome systems [55–59]. However, some decisive differences to doped lead-apatite exist: A major distinction is the very small hopping amplitude in the two-band model due to the large distance between Cu ions. This allows for only a small energy spread of spin fluctuations on which  $T_c$  is considered to depend on [36,37,60]. On another note, most of the triangular lattice superconductors constitute (quasi-)two-dimensional systems which are suggested to be more favorable than three-dimensional systems such as LK-99 for spin-fluctuation-mediated superconductivity. This is because a larger fraction of the phase space volume contributes to pairing via the interaction kernel [56,60–62].

Taken together, our study puts strong constraints on superconductivity in LK-99 and in particular excludes spin- and orbital-fluctuation-driven room temperature superconductivity in the two-band model of LK-99.

*Note added* — When completing this manuscript, a first single crystal of LK-99 has been synthesized and shows a non-magnetic insulating and transparent behavior [65], consistent with a Mott or charge transfer insulator [12–15].



## Acknowledgments

For the purpose of open access, the authors have applied a CC BY public copyright license to any Author Accepted Manuscript version arising from this submission.

**Author contributions** N.W. performed RPA and FLEX calculations. L.S. performed DFT calculations and the Wannierization. J.M.T. performed the cRPA calculations. N.W. and T.W. analyzed the RPA and FLEX results. N.W., K.H. and T.W. conceived the project. All authors discussed the results, physical implications and remaining caveats, and contributed to writing the manuscript.

**Funding information** We, in particular, acknowledge funding via the Research Unit ‘QUAST’ by the Deutsche Forschungsgemeinschaft (DFG; project ID FOR5249, Project No. 449872909) and Austrian Science Fund (FWF, project ID I 5868). N. W. and T. W. further gratefully acknowledge funding by the Cluster of Excellence ‘CUI: Advanced Imaging of Matter’ of the DFG (EXC 2056, Project ID 390715994). K. H. has received additional funding through the FWF projects I 5398, P 36213, SFB Q-M&S (FWF project ID F86). L. S. is thankful for the starting funds from Northwest University and FWF project I-5398. J. T. acknowledges financial support through joint project I 6142 of FWF and the French National Research Agency (ANR). The RPA and FLEX calculations have been performed on the supercomputer Lise at NHR@ZIB as part of the NHR infrastructure; cRPA calculations have been done on the Vienna Scientific Cluster (VSC).

**Data availability** The DFT and Wannierization data are available from the NOMAD repository doi:[10.17172/NOMAD/2023.10.12-1](https://doi.org/10.17172/NOMAD/2023.10.12-1). The cRPA, RPA and FLEX data sets analyzed during the current study are available via doi:[10.5281/zenodo.10014333](https://doi.org/10.5281/zenodo.10014333). Simulation data are available from the corresponding authors on request.

**Code availability** VASP and Wien2K, used as the starting point of the relaxation and Wannierization, respectively, are commercial codes. The code for the Wannierization itself is publicly available at <https://github.com/wien2wannier/wien2wannier>. The computer code to perform FLEX calculations using the IR basis is publicly available under [https://github.com/nikwitt/FLEX\\_IR](https://github.com/nikwitt/FLEX_IR).

**Competing interests** The authors declare no competing interests.

## A Methods

### A.1 Electronic structure

For a realistic simulation of putative superconducting properties in LK-99, we set up an effective low-energy theory via a Hamiltonian  $\mathcal{H}=\mathcal{H}^0+\mathcal{H}_{\text{int}}$ . For the non-interacting part,  $\mathcal{H}^0$ , we use the *ab initio* derived two-orbital Wannier model of Si *et al.* [13]. It is given by

$$\mathcal{H}^0 = \sum_{i,j} \sum_{m,n} \sum_{\sigma} t_{im,jn} c_{im\sigma}^{\dagger} c_{jn\sigma}, \quad (\text{A.1})$$

where  $c_{im\sigma}^{\dagger}$  ( $c_{im\sigma}$ ) are the creation (annihilation) operators; and  $i, j$  indicate unit cells, while  $m, n$  are orbital indices, and  $\sigma$  is the spin index. The full two-orbital hopping parameters  $t_{im,jn}$  yield Fig. 1(c) and a truncated set of these is tabulated in Ref. [13].

## A.2 Constrained random phase approximation

We here compute the interacting part of the Hamiltonian from first principles. Specifically, we consider

$$\mathcal{H}_{\text{int}} = \frac{1}{4} \sum_i \sum_{\alpha_1 \alpha_2 \alpha_3 \alpha_4} \Gamma_{\alpha_1 \alpha_4, \alpha_3 \alpha_2}^0 c_{i\alpha_1}^\dagger c_{i\alpha_2}^\dagger c_{i\alpha_3} c_{i\alpha_4}, \quad (\text{A.2})$$

where  $i$  is a lattice site and the indices  $\alpha_m = (\sigma, m)$  combine spin and orbital information. The bare vertex  $\Gamma^0$  is expressed as

$$\Gamma_{\alpha_1 \alpha_4, \alpha_3 \alpha_2}^0 = -\frac{1}{2} U_{m_1 m_4, m_3 m_2}^s \boldsymbol{\sigma}_{\sigma_1 \sigma_4} \cdot \boldsymbol{\sigma}_{\sigma_2 \sigma_3} + \frac{1}{2} U_{m_1 m_4, m_3 m_2}^c \delta_{\sigma_1 \sigma_4} \delta_{\sigma_2 \sigma_3}, \quad (\text{A.3})$$

with the interaction matrices

$$U_{ll', nn'}^s = \begin{cases} U & (l = l' = n = n') \\ U' & (l = n \neq n' = l') \\ J & (l = l' \neq n' = n) \\ J & (l = n' \neq n = l') \end{cases}, \quad U_{ll', nn'}^c = \begin{cases} U & (l = l' = n = n') \\ -U' + 2J & (l = n \neq n' = l') \\ 2U' - J & (l = l' \neq n' = n) \\ J & (l = n' \neq n = l') \end{cases},$$

in the spin (s) and charge (c) channel. The static matrix elements  $U$ ,  $U'$  and  $J$  of the screened Coulomb interaction have then been computed with the constrained random phase approximation (cRPA) in the maximally localized Wannier basis [66], using  $3 \times 3 \times 3$  reducible  $\mathbf{k}$ -points, and including screening from orbitals up to  $l = 3$  (2) for Pb, Cu (O, P). For the above two-orbital model, we find an intra-orbital Hubbard repulsion  $U = 1.8$  eV, an inter-orbital  $U' = 1.14$  eV and a Hund's exchange  $J = 0.33$  eV that are found to verify the symmetry relation  $U' = U - 2J$ . The reduction from the bare interactions  $V = 12.7$  eV,  $V' = 11.6$  eV and  $J_0 = 0.56$  eV, respectively, is larger than in the recent Refs. [11, 15], possibly owing to our inclusion of more high-energy orbitals.

## A.3 Fluctuation exchange approach

To study the possibility of electronically-driven superconductivity, we employ the multi-orbital FLEX approximation [31, 32]. FLEX is a conserving approximation that self-consistently incorporates spin and charge fluctuations by an infinite resummation of closed bubble and ladder diagrams. Although FLEX cannot capture strong-coupling physics like the Mott-insulator transition, it works well in the presence of strong spin fluctuations.

We consider the multi-orbital formulation of FLEX without spin-orbit coupling [33, 67, 68] where we consider a local interaction Hamiltonian. In the FLEX approximation, one solves the Dyson equation

$$\hat{G}(k)^{-1} = i\omega_n \mathbb{1} - (\hat{H}_0(k) - \mu \mathbb{1}) - \hat{\Sigma}(k), \quad (\text{A.4})$$

with the dressed Green function  $G$ , non-interacting Hamiltonian  $H_0$ , self-energy  $\Sigma$ , chemical potential  $\mu$  and the four-momentum  $k = (i\omega_n, \mathbf{k})$  containing crystal momentum  $\mathbf{k}$  and Matsubara frequencies  $\omega_n = (2n + 1)\pi k_B T$ . The hat denotes a matrix in orbital space, where  $\mathbb{1}$  is the identity matrix. The interaction  $V$  that enters the self-energy  $\Sigma$  via

$$\Sigma_{lm}(k) = \frac{T}{N_{\mathbf{k}}} \sum_{q, l', m'} V_{ll', mm'}(q) G_{l'm'}(k - q), \quad (\text{A.5})$$

consists of scattering off of spin and charge fluctuations given by

$$\hat{V}(q) = \frac{3}{2} \hat{U}^s \left[ \hat{\chi}^s(q) - \frac{1}{2} \hat{\chi}^0(q) \right] \hat{U}^s + \frac{1}{2} \hat{U}^c \left[ \hat{\chi}^c(q) - \frac{1}{2} \hat{\chi}^0(q) \right] \hat{U}^c, \quad (\text{A.6})$$

neglecting the constant Hartree-Fock term. The charge and spin susceptibility entering Eq. (A.5) are defined by

$$\hat{\chi}^{s,c}(q) = \hat{\chi}^0(q) [\mathbb{1} \mp \hat{U}^{s,c} \hat{\chi}^0(q)]^{-1}, \quad (\text{A.7})$$

with the irreducible susceptibility

$$\chi_{ll',mm'}^0(q) = -\frac{T}{N_{\mathbf{k}}} \sum_{\mathbf{k}} G_{lm}(k+q) G_{m'l'}(k). \quad (\text{A.8})$$

These equations are solved self-consistently with adjusting  $\mu$  at every iteration to keep the electron filling fixed. We employ a linear mixing  $G = \kappa G^{\text{new}} + (1 - \kappa) G^{\text{old}}$  with  $\kappa = 0.2$  and defined self-consistency for a relative difference of  $10^{-4}$  between the self-energy of two iteration steps. In all calculations, we used a  $\mathbf{k}$ -mesh resolution of  $30 \times 30 \times 30$ . For the imaginary-time and Matsubara frequency grids we applied the sparse-sampling approach [33, 69, 70] in combination with the intermediate representation (IR) basis [71–73], where we used an IR parameter of  $\Lambda = 10^4$  and a basis cutoff of  $\delta_{\text{IR}} = 10^{-15}$ .

To study the superconducting phase transition driven by spin fluctuations, we consider the linearized gap equation

$$\lambda_{\text{SC}} \Delta_{lm}^S(k) = \frac{T}{N_{\mathbf{k}}} \sum_{q,l',m'} V_{ll',m'm}^S(q) F_{l'm'}^S(k-q), \quad (\text{A.9})$$

for the gap function  $\Delta$  with anomalous Green function  $F(k) = -G(k)\Delta(k)G^T(-k)$  in the spin singlet ( $S = 0$ ) or spin triplet pairing channel ( $S = 1$ ) with the respective interactions

$$\begin{aligned} \hat{V}^{S=0}(q) &= \frac{3}{2} \hat{U}^s \hat{\chi}^s(q) \hat{U}^s - \frac{1}{2} \hat{U}^c \hat{\chi}^c(q) \hat{U}^c, \\ \hat{V}^{S=1}(q) &= -\frac{1}{2} \hat{U}^s \hat{\chi}^s(q) \hat{U}^s - \frac{1}{2} \hat{U}^c \hat{\chi}^c(q) \hat{U}^c. \end{aligned} \quad (\text{A.10})$$

Constant terms  $\sim \hat{U}^{s,c}$  were neglected as they did not influence the dominant pairing symmetry. The gap equation represents an eigenvalue problem for  $\Delta$  where the eigenvalue  $\lambda_{\text{SC}}$  can be understood as the relative pairing strength of a certain pairing channel. The dominant pairing symmetry of the gap function has the largest eigenvalue  $\lambda_{\text{SC}}$  and the transition temperature is found if  $\lambda_{\text{SC}}$  reaches unity.

## References

- [1] S. Lee, J. Kim and Y.-W. Kwon, *The first room-temperature ambient-pressure superconductor*, (arXiv preprint) doi:[10.48550/arXiv.2307.12008](https://doi.org/10.48550/arXiv.2307.12008).
- [2] S. Lee, J. Kim, H.-T. Kim, S. Im, S. An and K. H. Auh, *Superconductor  $\text{Pb}_{10-x}\text{Cu}_x(\text{PO}_4)_6\text{O}$  showing levitation at room temperature and atmospheric pressure and mechanism*, (arXiv preprint) doi:[10.48550/arXiv.2307.12037](https://doi.org/10.48550/arXiv.2307.12037).
- [3] S. Lee, J. Kim, S. Im, S. An, Y.-W. Kwon and K. H. Auh, *Consideration for the development of room-temperature ambient-pressure superconductor (LK-99)*, J. Korean Cryst. Growth Cryst. Technol. **33**, 61 (2023), doi:[10.6111/JKCGCT.2023.33.2.061](https://doi.org/10.6111/JKCGCT.2023.33.2.061).
- [4] Q. Hou, W. Wei, X. Zhou, Y. Sun and Z. Shi, *Observation of zero resistance above 100° K in  $\text{Pb}_{10-x}\text{Cu}_x(\text{PO}_4)_6\text{O}$* , (arXiv preprint) doi:[10.48550/arXiv.2308.01192](https://doi.org/10.48550/arXiv.2308.01192).

- [5] H. Wu, L. Yang, J. Yu, G. Zhang, B. Xiao and H. Chang, *Observation of abnormal resistance-temperature behavior along with diamagnetic transition in  $Pb_{10-x}Cu_x(PO_4)_6O$ -based composite*, (arXiv preprint) doi:[10.48550/arXiv.2308.05001](https://doi.org/10.48550/arXiv.2308.05001).
- [6] H. Wu, L. Yang, B. Xiao and H. Chang, *Successful growth and room temperature ambient-pressure magnetic levitation of LK-99*, (arXiv preprint) doi:[10.48550/arXiv.2308.01516](https://doi.org/10.48550/arXiv.2308.01516).
- [7] K. Guo, Y. Li and S. Jia, *Ferromagnetic half levitation of LK-99-like synthetic samples*, *Sci. China Phys. Mech. Astron.* **66**, 107411 (2023), doi:[10.1007/s11433-023-2201-9](https://doi.org/10.1007/s11433-023-2201-9).
- [8] K. Kumar, N. K. Karn, Y. Kumar and V. P. S. Awana, *Absence of superconductivity in LK-99 at ambient conditions*, *ACS Omega* **8**, 41737 (2023), doi:[10.1021/acsomega.3c06096](https://doi.org/10.1021/acsomega.3c06096).
- [9] K. Kumar, N. K. Karn and V. P. S. Awana, *Synthesis of possible room temperature superconductor LK-99:  $Pb_9Cu(PO_4)_6O$* , *Supercond. Sci. Technol.* **36**, 10LT02 (2023), doi:[10.1088/1361-6668/acf002](https://doi.org/10.1088/1361-6668/acf002).
- [10] L. Liu, Z. Meng, X. Wang, H. Chen, Z. Duan, X. Zhou, H. Yan, P. Qin and Z. Liu, *Semiconducting transport in  $Pb_{10-x}Cu_x(PO_4)_6O$  sintered from  $Pb_2SO_5$  and  $Cu_3P$* , *Adv. Funct. Mater.* 2308938 (2023), doi:[10.1002/adfm.202308938](https://doi.org/10.1002/adfm.202308938).
- [11] Y. Jiang et al.,  *$Pb_9Cu(PO_4)_6(OH)_2$ : Phonon bands, localized flat band magnetism, models, and chemical analysis*, (arXiv preprint) doi:[10.48550/arXiv.2308.05143](https://doi.org/10.48550/arXiv.2308.05143).
- [12] L. Si and K. Held, *Electronic structure of the putative room-temperature superconductor  $Pb_9Cu(PO_4)_6O$* , *Phys. Rev. B* **108**, L121110 (2023), doi:[10.1103/PhysRevB.108.L121110](https://doi.org/10.1103/PhysRevB.108.L121110).
- [13] L. Si, M. Wallerberger, A. Smolyanyuk, S. di Cataldo, J. M. Tomczak and K. Held,  *$Pb_{10-x}Cu_x(PO_4)_6O$ : A Mott or charge transfer insulator in need of further doping for (super)conductivity*, *J. Phys.: Condens. Matter* **36**, 065601 (2023), doi:[10.1088/1361-648X/ad0673](https://doi.org/10.1088/1361-648X/ad0673).
- [14] D. M. Korotin, D. Y. Novoselov, A. O. Shorikov, V. I. Anisimov and A. R. Oganov, *Electronic correlations in promising room-temperature superconductor  $Pb_9Cu(PO_4)_6O$ : A DFT+DMFT study*, (arXiv preprint) doi:[10.48550/arXiv.2308.04301](https://doi.org/10.48550/arXiv.2308.04301).
- [15] C. Yue, V. Christiansson and P. Werner, *Correlated electronic structure of  $Pb_{10-x}Cu_x(PO_4)_6O$* , (arXiv preprint) doi:[10.48550/arXiv.2308.04976](https://doi.org/10.48550/arXiv.2308.04976).
- [16] V. I. Anisimov, A. I. Poteryaev, M. A. Korotin, A. O. Anokhin and G. Kotliar, *First-principles calculations of the electronic structure and spectra of strongly correlated systems: Dynamical mean-field theory*, *J. Phys.: Condens. Matter* **9**, 7359 (1997), doi:[10.1088/0953-8984/9/35/010](https://doi.org/10.1088/0953-8984/9/35/010).
- [17] A. I. Lichtenstein and M. I. Katsnelson, *Ab initio calculations of quasiparticle band structure in correlated systems: LDA++ approach*, *Phys. Rev. B* **57**, 6884 (1998), doi:[10.1103/PhysRevB.57.6884](https://doi.org/10.1103/PhysRevB.57.6884).
- [18] K. Held, *Electronic structure calculations using dynamical mean field theory*, *Adv. Phys.* **56**, 829 (2007), doi:[10.1080/00018730701619647](https://doi.org/10.1080/00018730701619647).
- [19] G. Kotliar, S. Y. Savrasov, K. Haule, V. S. Oudovenko, O. Parcollet and C. A. Marianetti, *Electronic structure calculations with dynamical mean-field theory*, *Rev. Mod. Phys.* **78**, 865 (2006), doi:[10.1103/RevModPhys.78.865](https://doi.org/10.1103/RevModPhys.78.865).

- [20] H. Bai, L. Gao and C. Zeng, *Magnetic properties and spin-orbit coupling induced semiconductivity in LK-99*, (arXiv preprint) doi:[10.48550/arXiv.2308.05134](https://doi.org/10.48550/arXiv.2308.05134).
- [21] J. Liu, T. Yu, J. Li, J. Wang, J. Lai, Y. Sun, X.-Q. Chen and P. Liu, *Symmetry breaking induced insulating electronic state in  $Pb_9Cu_x(PO_4)_6O$* , Phys. Rev. B **108**, L161101 (2023), doi:[10.1103/physrevb.108.l161101](https://doi.org/10.1103/physrevb.108.l161101).
- [22] J. Lai, J. Li, P. Liu, Y. Sun and X.-Q. Chen, *First-principles study on the electronic structure of  $Pb_{10-x}Cu_x(PO_4)_6O$  ( $x = 0, 1$ )*, J. Mater. Sci. Technol. **171**, 66 (2024), doi:[10.1016/j.jmst.2023.08.001](https://doi.org/10.1016/j.jmst.2023.08.001).
- [23] Y. Sun, K.-M. Ho and V. Antropov, *Metallization and spin fluctuations in cu-doped lead apatite*, (arXiv preprint) doi:[10.48550/arXiv.2308.03454](https://doi.org/10.48550/arXiv.2308.03454).
- [24] J. Zhang, H. Li, M. Yan, M. Gao, F. Ma, X.-W. Yan and Z. Xie, *Structural, electronic, magnetic properties of Cu-doped lead-apatite  $Pb_{10-x}Cu_x(PO_4)_6O$* , (arXiv preprint) doi:[10.48550/arXiv.2308.04344](https://doi.org/10.48550/arXiv.2308.04344).
- [25] S. Zhu, W. Wu, Z. Li and J. Luo, *First order transition in  $Pb_{10-x}Cu_x(PO_4)_6O$  ( $0.9 < x < 1.1$ ) containing  $Cu_2S$* , (arXiv preprint) doi:[10.48550/arXiv.2308.04353](https://doi.org/10.48550/arXiv.2308.04353).
- [26] P. K. Jain, *Superionic phase transition of copper(i) sulfide and its implication for purported superconductivity of LK-99*, J. Phys. Chem. C **127**, 18253 (2023), doi:[10.1021/acs.jpcc.3c05684](https://doi.org/10.1021/acs.jpcc.3c05684).
- [27] J. Bardeen, L. N. Cooper and J. R. Schrieffer, *Microscopic theory of superconductivity*, Phys. Rev. **106**, 162 (1957), doi:[10.1103/PhysRev.106.162](https://doi.org/10.1103/PhysRev.106.162).
- [28] O. Tavakol and T. Scaffidi, *Minimal model for the flat bands in copper-substituted lead phosphate apatite*, (arXiv preprint) doi:[10.48550/arXiv.2308.01315](https://doi.org/10.48550/arXiv.2308.01315).
- [29] H. Oh and Y.-H. Zhang, *s-wave pairing in a two-orbital t-J model on triangular lattice: Possible application to  $Pb_{10-x}Cu_x(PO_4)_6O$* , (arXiv preprint) doi:[10.48550/arXiv.2308.02469](https://doi.org/10.48550/arXiv.2308.02469).
- [30] M. M. Hirschmann and J. Mitscherling, *Tight-binding models for SG 143 (P3) and application to recent DFT results on copper-doped lead apatite*, (arXiv preprint) doi:[10.48550/arXiv.2308.03751](https://doi.org/10.48550/arXiv.2308.03751).
- [31] N. E. Bickers, D. J. Scalapino and S. R. White, *Conserving approximations for strongly correlated electron systems: Bethe-Salpeter equation and dynamics for the two-dimensional Hubbard model*, Phys. Rev. Lett. **62**, 961 (1989), doi:[10.1103/physrevlett.62.961](https://doi.org/10.1103/physrevlett.62.961).
- [32] N. E. Bickers and D. J. Scalapino, *Conserving approximations for strongly fluctuating electron systems. I. Formalism and calculational approach*, Ann. Phys. **193**, 206 (1989), doi:[10.1016/0003-4916\(89\)90359-x](https://doi.org/10.1016/0003-4916(89)90359-x).
- [33] N. Witt, E. G. C. P. van Loon, T. Nomoto, R. Arita and T. O. Wehling, *Efficient fluctuation-exchange approach to low-temperature spin fluctuations and superconductivity: From the Hubbard model to  $Na_xCoO_2 \cdot yH_2O$* , Phys. Rev. B **103**, 205148 (2021), doi:[10.1103/physrevb.103.205148](https://doi.org/10.1103/physrevb.103.205148).
- [34] S. M. Griffin, *Origin of correlated isolated flat bands in copper-substituted lead phosphate apatite*, (arXiv preprint) doi:[10.48550/arXiv.2307.16892](https://doi.org/10.48550/arXiv.2307.16892).
- [35] R. Kurlito, S. Lany, D. Pashov, S. Acharya, M. van Schilfgaarde and D. S. Dessau, *Pb-apatite framework as a generator of novel flat-band CuO based physics, including possible room temperature superconductivity*, (arXiv preprint) doi:[10.48550/arXiv.2308.00698](https://doi.org/10.48550/arXiv.2308.00698).

- [36] T. Moriya and K. Ueda, *Antiferromagnetic spin fluctuation and superconductivity*, Rep. Prog. Phys. **66**, 1299 (2003), doi:[10.1088/0034-4885/66/8/202](https://doi.org/10.1088/0034-4885/66/8/202).
- [37] D. J. Scalapino, *A common thread: The pairing interaction for unconventional superconductors*, Rev. Mod. Phys. **84**, 1383 (2012), doi:[10.1103/RevModPhys.84.1383](https://doi.org/10.1103/RevModPhys.84.1383).
- [38] R. H. McKenzie, *Similarities between organic and cuprate superconductors*, Science **278**, 820 (1997), doi:[10.1126/science.278.5339.820](https://doi.org/10.1126/science.278.5339.820).
- [39] Y. Kurosaki, Y. Shimizu, K. Miyagawa, K. Kanoda and G. Saito, *Mott transition from a spin liquid to a Fermi liquid in the spin-frustrated organic conductor  $\kappa$ -(ET)<sub>2</sub>Cu<sub>2</sub>(CN)<sub>3</sub>*, Phys. Rev. Lett. **95**, 177001 (2005), doi:[10.1103/physrevlett.95.177001](https://doi.org/10.1103/physrevlett.95.177001).
- [40] S. E. Brown, *Organic superconductors: The Bechgaard salts and relatives*, Phys. C: Supercond. Appl. **514**, 279 (2015), doi:[10.1016/j.physc.2015.02.030](https://doi.org/10.1016/j.physc.2015.02.030).
- [41] M. Buzzi et al., *Phase diagram for light-induced superconductivity in  $\kappa$ -(ET)<sub>2</sub>-X*, Phys. Rev. Lett. **127**, 197002 (2021), doi:[10.1103/physrevlett.127.197002](https://doi.org/10.1103/physrevlett.127.197002).
- [42] K. Takada, H. Sakurai, E. Takayama-Muromachi, F. Izumi, R. A. Dilanian and T. Sasaki, *Superconductivity in two-dimensional CoO<sub>2</sub> layers*, Nature **422**, 53 (2003), doi:[10.1038/nature01450](https://doi.org/10.1038/nature01450).
- [43] H. Sakurai, Y. Ihara and K. Takada, *Superconductivity of cobalt oxide hydrate, Na<sub>x</sub>(H<sub>3</sub>O)<sub>z</sub>CoO<sub>2</sub>·yH<sub>2</sub>O*, Phys. C: Supercond. Appl. **514**, 378 (2015), doi:[10.1016/j.physc.2015.02.010](https://doi.org/10.1016/j.physc.2015.02.010).
- [44] S. Pyon, K. Kudo and M. Nohara, *Superconductivity induced by bond breaking in the triangular lattice of IrTe<sub>2</sub>*, J. Phys. Soc. Jpn. **81**, 053701 (2012), doi:[10.1143/jpsj.81.053701](https://doi.org/10.1143/jpsj.81.053701).
- [45] D. Ootsuki et al., *Important roles of Te 5p and Ir 5d spin-orbit interactions on the multi-band electronic structure of triangular lattice superconductor Ir<sub>1-x</sub>Pt<sub>x</sub>Te<sub>2</sub>*, J. Phys. Soc. Jpn. **83**, 033704 (2014), doi:[10.7566/jpsj.83.033704](https://doi.org/10.7566/jpsj.83.033704).
- [46] D. Hirai, R. Kawakami, O. V. Magdysyuk, R. E. Dinnebier, A. Yaresko and H. Takagi, *Superconductivity at 3.7 K in ternary silicide Li<sub>2</sub>IrSi<sub>3</sub>*, J. Phys. Soc. Jpn. **83**, 103703 (2014), doi:[10.7566/jpsj.83.103703](https://doi.org/10.7566/jpsj.83.103703).
- [47] K. Horigane et al., *Superconductivity in a new layered triangular-lattice system Li<sub>2</sub>IrSi<sub>2</sub>*, New J. Phys. **21**, 093056 (2019), doi:[10.1088/1367-2630/ab4159](https://doi.org/10.1088/1367-2630/ab4159).
- [48] H. Kino and H. Kontani, *Phase diagram of superconductivity on the anisotropic triangular lattice Hubbard model: An effective model of  $\kappa$ -(BEDT-TTF) salts*, J. Phys. Soc. Jpn. **67**, 3691 (1998), doi:[10.1143/jpsj.67.3691](https://doi.org/10.1143/jpsj.67.3691).
- [49] J. Schmalian, *Pairing due to spin fluctuations in layered organic superconductors*, Phys. Rev. Lett. **81**, 4232 (1998), doi:[10.1103/physrevlett.81.4232](https://doi.org/10.1103/physrevlett.81.4232).
- [50] K. Kuroki and R. Arita, *Spin-triplet superconductivity in repulsive Hubbard models with disconnected Fermi surfaces: A case study on triangular and honeycomb lattices*, Phys. Rev. B **63**, 174507 (2001), doi:[10.1103/physrevb.63.174507](https://doi.org/10.1103/physrevb.63.174507).
- [51] H. Kondo and T. Moriya, *Superconductivity in organic compounds with pseudo-triangular lattice*, J. Phys. Soc. Jpn. **73**, 812 (2004), doi:[10.1143/jpsj.73.812](https://doi.org/10.1143/jpsj.73.812).

- [52] M. Mochizuki, Y. Yanase and M. Ogata, *Ferromagnetic fluctuation and possible triplet superconductivity in  $\text{Na}_x\text{CoO}_2 \cdot y\text{H}_2\text{O}$ : Fluctuation-exchange study of the multiorbital Hubbard model*, Phys. Rev. Lett. **94**, 147005 (2005), doi:[10.1103/physrevlett.94.147005](https://doi.org/10.1103/physrevlett.94.147005).
- [53] M. Ogata, *A new triangular system:  $\text{Na}_x\text{CoO}_2$* , J. Phys.: Condens. Matter **19**, 145282 (2007), doi:[10.1088/0953-8984/19/14/145282](https://doi.org/10.1088/0953-8984/19/14/145282).
- [54] H. Kimura, S. Onari and Y. Tanaka, *Spin-triplet superconductivity induced by off-site Coulomb interaction in a triangular lattice*, J. Phys. Chem. Solids **69**, 3310 (2008), doi:[10.1016/j.jpcs.2008.06.134](https://doi.org/10.1016/j.jpcs.2008.06.134).
- [55] S. Onari, K. Kuroki, R. Arita and H. Aoki, *Superconductivity induced by interband nesting in the three-dimensional honeycomb lattice*, Phys. Rev. B **65**, 184525 (2002), doi:[10.1103/physrevb.65.184525](https://doi.org/10.1103/physrevb.65.184525).
- [56] S. Onari, R. Arita, K. Kuroki and H. Aoki, *Superconductivity in repulsive electron systems with three-dimensional disconnected Fermi surfaces*, Phys. Rev. B **68**, 024525 (2003), doi:[10.1103/physrevb.68.024525](https://doi.org/10.1103/physrevb.68.024525).
- [57] K. Kuroki, *Spin-fluctuation-mediated  $d + id'$  pairing mechanism in doped  $\beta\text{-MNCl}$  ( $M = \text{Hf}, \text{Zr}$ ) superconductors*, Phys. Rev. B **81**, 104502 (2010), doi:[10.1103/physrevb.81.104502](https://doi.org/10.1103/physrevb.81.104502).
- [58] J. Kang, S.-L. Yu, Z.-J. Yao and J.-X. Li, *Spin-fluctuation-mediated pairing symmetry on the metallic Kagome lattice*, J. Phys.: Condens. Matter **23**, 175702 (2011), doi:[10.1088/0953-8984/23/17/175702](https://doi.org/10.1088/0953-8984/23/17/175702).
- [59] N. Witt, J. M. Pizarro, J. Berges, T. Nomoto, R. Arita and T. O. Wehling, *Doping fingerprints of spin and lattice fluctuations in moiré superlattice systems*, Phys. Rev. B **105**, L241109 (2022), doi:[10.1103/physrevb.105.l241109](https://doi.org/10.1103/physrevb.105.l241109).
- [60] R. Arita, K. Kuroki and H. Aoki, *Magnetic-field induced triplet superconductivity in the repulsive Hubbard model on the triangular lattice*, J. Phys. Soc. Jpn. **73**, 533 (2004), doi:[10.1143/jpsj.73.533](https://doi.org/10.1143/jpsj.73.533).
- [61] R. Arita, K. Kuroki and H. Aoki,  *$d$ - and  $p$ -wave superconductivity mediated by spin fluctuations in two- and three-dimensional single-band repulsive Hubbard model*, J. Phys. Soc. Jpn. **69**, 1181 (2000), doi:[10.1143/jpsj.69.1181](https://doi.org/10.1143/jpsj.69.1181).
- [62] P. Monthoux and G. G. Lonzarich, *Magnetically mediated superconductivity in quasi-two and three dimensions*, Phys. Rev. B **63**, 054529 (2001), doi:[10.1103/physrevb.63.054529](https://doi.org/10.1103/physrevb.63.054529).
- [63] O. K. Andersen, A. I. Liechtenstein, O. Jepsen and F. Paulsen, *LDA energy bands, low-energy Hamiltonians,  $t'$ ,  $t''$ ,  $t_{\perp}(k)$ , and  $J_{\perp}$* , J. Phys. Chem. Solids **56**, 1573 (1995), doi:[10.1016/0022-3697\(95\)00269-3](https://doi.org/10.1016/0022-3697(95)00269-3).
- [64] P. A. Lee, N. Nagaosa and X.-G. Wen, *Doping a Mott insulator: Physics of high-temperature superconductivity*, Rev. Mod. Phys. **78**, 17 (2006), doi:[10.1103/RevModPhys.78.17](https://doi.org/10.1103/RevModPhys.78.17).
- [65] P. Puphal, M. Y. P. Akbar, M. Hepting, E. Goering, M. Isobe, A. A. Nugroho and B. Keimer, *Single crystal synthesis, structure, and magnetism of  $\text{Pb}_{10-x}\text{Cu}_x(\text{PO}_4)_6\text{O}$* , APL Mater. **11**, 101128 (2023), doi:[10.1063/5.0172755](https://doi.org/10.1063/5.0172755).
- [66] T. Miyake and F. Aryasetiawan, *Screened Coulomb interaction in the maximally localized Wannier basis*, Phys. Rev. B **77**, 085122 (2008), doi:[10.1103/PhysRevB.77.085122](https://doi.org/10.1103/PhysRevB.77.085122).

- [67] T. Takimoto, T. Hotta and K. Ueda, *Strong-coupling theory of superconductivity in a degenerate Hubbard model*, Phys. Rev. B **69**, 104504 (2004), doi:[10.1103/physrevb.69.104504](https://doi.org/10.1103/physrevb.69.104504).
- [68] K. Kubo, *Pairing symmetry in a two-orbital Hubbard model on a square lattice*, Phys. Rev. B **75**, 224509 (2007), doi:[10.1103/physrevb.75.224509](https://doi.org/10.1103/physrevb.75.224509).
- [69] J. Li, M. Wallerberger, N. Chikano, C.-N. Yeh, E. Gull and H. Shinaoka, *Sparse sampling approach to efficient ab initio calculations at finite temperature*, Phys. Rev. B **101**, 035144 (2020), doi:[10.1103/physrevb.101.035144](https://doi.org/10.1103/physrevb.101.035144).
- [70] H. Shinaoka, N. Chikano, E. Gull, J. Li, T. Nomoto, J. Otsuki, M. Wallerberger, T. Wang and K. Yoshimi, *Efficient ab initio many-body calculations based on sparse modeling of Matsubara Green's function*, SciPost Phys. Lect. Notes **63** (2022), doi:[10.21468/scipostphyslectnotes.63](https://doi.org/10.21468/scipostphyslectnotes.63).
- [71] H. Shinaoka, J. Otsuki, M. Ohzeki and K. Yoshimi, *Compressing Green's function using intermediate representation between imaginary-time and real-frequency domains*, Phys. Rev. B **96**, 035147 (2017), doi:[10.1103/physrevb.96.035147](https://doi.org/10.1103/physrevb.96.035147).
- [72] N. Chikano, K. Yoshimi, J. Otsuki and H. Shinaoka, *irbasis: Open-source database and software for intermediate-representation basis functions of imaginary-time Green's function*, Comput. Phys. Commun. **240**, 181 (2019), doi:[10.1016/j.cpc.2019.02.006](https://doi.org/10.1016/j.cpc.2019.02.006).
- [73] M. Wallerberger et al., *sparse-ir: Optimal compression and sparse sampling of many-body propagators*, SoftwareX **21**, 101266 (2023), doi:[10.1016/j.softx.2022.101266](https://doi.org/10.1016/j.softx.2022.101266).



# Towards high-performance superconductivity

# 6

為せば成る、為さねば成らぬ、何事も。  
成らぬは人の為さぬなりけり。<sup>1</sup>

— 上杉鷹山 (Uesugi Yōzan)

Discovering new and possibly high-temperature superconductors is often a matter of serendipity, even when actively sought. These circumstances highlight the inherent difficulty of achieving high-temperature superconductivity and present a conundrum for both experimental and theoretical research. A major challenge in achieving robust high-temperature superconductivity lies in balancing the two intrinsic energy scales of a superconductor: the pairing amplitude (superconducting gap) and the phase coherence (stiffness), cf. chapter 3. These energies often compete and thereby limit the accessible critical temperatures [198, 453–455]. Understanding such constraints on superconductivity is crucial for identifying pathways toward optimizing superconducting materials [VI, 204].

A pivotal example of the limitations imposed by the trade-off between superconducting energy scales is observed when tuning the pairing interaction or coupling strength  $U$  of a single-band superconductor. This process is well described by the BCS–BEC crossover phenomenology, which we briefly outline here and discuss in more detail in section 6.1.2 and publication VI. As the pairing interaction increases, the nature of electron pairs shifts from weakly-bound, overlapping pairs in the weak-coupling BCS (Bardeen–Cooper–Schrieffer) limit to tightly-bound pairs in the strong-coupling BEC (Bose–Einstein Condensate) limit (cf. Fig. 1 in publication VI). In this crossover, the pair binding energy depending on the QP gap  $\Delta$  is enhanced by increasing  $U$ . However, the phase stiffness  $D_s$  is suppressed in the strong-coupling limit, where tightly-bound pairs with large effective masses dominate, i.e., kinetic energy is quenched. Consequently, phase fluctuations can readily compromise the weak phase coherence, which constrains the achievable critical temperature  $T_c$  despite high pair binding energies at large interactions. The character of the strong

<sup>1</sup>*Nasebanaru, nasaneba naranu, nanigoto mo. Naranu ha hito no nasanunarikeri* — You can accomplish anything by simply doing it. Nothing will get done unless you do it. If something was not accomplished, that's because no one did it.

coupling state crucially depends on the kinetic energy degrees of freedom of the underlying fermionic model [575, 700], as discussed further below.

In publication VI, we demonstrate how this conventional constraint on critical temperatures in the strong coupling limit can be overcome by leveraging multi-orbital physics. Specifically, in a model of alkali-doped fullerenes ( $A_3C_{60}$ ), we identify a strong-coupling superconducting state characterized by localized coherence length but with robust stiffness, for which  $T_c$  is substantially enhanced through increased pairing interaction. This strengthened superconducting state is sustained by a persistent mixed-valence metallic phase at higher temperatures, which emerges from the competition of different local multi-orbital interaction scales. Consequently, our results are unattainable within the confines of a single-band model, where a singular local interaction ( $U < 0$ ) influences both pairing and phase coherence (through kinetic energy) in conflicting manners.

In our study, the detailed characterization of the superconducting phase diagram hinges on quantifying the aforementioned superconducting energy scales. These are equivalently specified by the intrinsic length scales, the coherence length  $\xi_0$  and the London penetration depth  $\lambda_L$ , as introduced in chapter 3. While weak-coupling BCS theory offers straightforward expressions for the length or energy scales (cf. Eqs. (3.14) and (3.125)), their applicability to strongly correlated superconductors is uncertain. To address this, we introduce a theoretical framework in publication VI based on finite-momentum pairing within the Nambu-Gor'kov formalism, which facilitates the calculation of  $\xi_0$  and  $\lambda_L$  from microscopic models and *ab initio* approaches, particularly also in the presence of strong correlations.

To set the stage for the discussion in publication VI, we provide a more detailed analysis of heuristic and rigorous bounds on  $T_c$  arising from competing energy scales in section 6.1. In particular, we introduce pairing and phase ordering temperatures [453] and we discuss how several unconventional superconductors are limited by the phase ordering temperature, as empirically captured in the Uemura plot classification scheme [197, 701–703] (cf. Figure 6.1). In this context, we briefly review the BCS–BEC crossover phenomenology and the analogy to magnetism found in the half-filled Hubbard model. Following this, section 6.2 introduces the material family of  $A_3C_{60}$  and their superconducting phase diagram.

### 6.1 Constraints on superconductivity

Understanding the physics that dictate critical temperatures is a highly non-trivial task, making it equally challenging to predict optimal superconducting materials. To find routes for elevating  $T_c$ , it is a valid strategy to first identify and analyze constraints that limit these temperatures. A common approach involves focusing on key aspects essential to the formation of the superconducting state and establishing

heuristic or rigorous bounds on achievable critical temperatures [45, 169, 196–203, 588]. Although these bounds are commonly respected due to their solid physical motivation, counter examples can be found – either through clever system design [204] or unprecedented insights, such as the discovery of high-temperature superconductivity in cuprates, which ‘violated’ the Cohen–Anderson limit and challenged Matthias’ rules [28].

Here, we focus on constraints arising from the competition of the energy scales that determine particle pairing (gap  $\Delta$ ) and condensation through the onset of phase coherence (stiffness  $D_s$ ). To illustrate this consideration, we follow an argument made by Emery and Kivelson [453], who formulated it to describe the dome-shaped doping dependence of the critical temperature in cuprate materials. The argument centers around the question of when superconducting order breaks down due to thermal fluctuations. The answer depends strongly on the robustness of phase coherence. We can quantify this by the phase-ordering temperature  $k_B T_\varphi \simeq D_s(T=0) = \hbar^2 n_s / 4m^*$  (cf. Eq. (3.44)). In three dimensions, an additional length scale  $L$  needs to be added, which in case of layered materials can be taken as the mean spacing between layers, see the discussion in section 3.1.3. If  $T_c \ll T_\varphi$ , as is the case for large densities  $n_s$ , particle pairing and the onset of macroscopic phase coherence appear at the same temperature  $T_c \sim T_P$ , where  $T_P$  is the temperature above which pairs break up. In BCS theory, this is simply  $k_B T_P = \Delta_0 / 2 \approx k_B T_c (= \Delta_0 / 1.76)$  with the zero-temperature gap  $\Delta_0$ . However, in the case of  $T_c \approx T_\varphi$ , phase fluctuations have a significant influence and  $T_c$  is limited by  $T_\varphi$ , as superconducting long-range order cannot be sustained above  $T_\varphi$ .

For most conventional metals,  $T_\varphi$  is much larger than  $T_c$  and particle pairing determines the onset of superconductivity. In many unconventional superconductors, the phase ordering energy scale is the dominant factor. The similarity in size of  $T_c$  and  $T_\varphi$  can be estimated from material parameters of unconventional superconductors [453, 454]. More importantly, strong empirical evidence for this relationship is provided by the Uemura relation, shown and discussed in Figure 6.1 below. Before addressing that point, we want to emphasize the importance of the phase stiffness as a general limiting factor for superconductivity. This applies in particular to (quasi-)two-dimensional systems, where the influence of phase fluctuations is more pronounced and the BKT transition needs to be considered. As discussed in section 3.1.5, the transition temperature  $T_{\text{BKT}}$  is constrained by  $D_s(T_{\text{BKT}})$  via the Nelson–Kosterlitz criterion (3.59). Building on this premise, Refs. [198–200] derived rigorous upper bounds for  $D_s(0) \geq D_s(T_{\text{BKT}})$  based on optical sum rules and even tighter constraints obtained from a renormalization group analysis of the stiffness. One important result is the boundary  $T_{\text{BKT}} \leq T_F / 8$  for free fermions with a parabolic dispersion, where  $T_F = E_F / k_B$  is the Fermi temperature. Furthermore,

lower bounds for topologically non-trivial systems can be formulated based on contributions from the quantum geometric tensor of the Bloch bands [536, 543, 544].

As discussed in Ref. [198], deriving general rigorous bounds for three-dimensional systems is more challenging. Nonetheless, a scaling law can be established near a quantum critical point as [198]

$$T_c \sim [D_s(T = 0)]^{\frac{z}{z+d-2}} \quad (6.1)$$

with dimension  $d$  and the dynamical critical exponent  $z$ , relating correlation time  $t$  and correlation length  $\xi$  via  $t \sim \xi^z$ . In two dimensions, we find the expected linear scaling relationship between  $T_c$  and  $D_s$ , but for three dimensions, we have  $T_c \sim D_s^{z/(z+1)}$  close to the quantum critical point. Since  $z > 0$ , this implies that the suppression of  $T_c$  with respect to the stiffness is weakened due to sublinear scaling. For example, the case  $z = 1$  corresponding to  $T_c \sim \sqrt{D_s}$  fits well to experimental observations in cuprate superconductors [198].

This strong dependence on dimensionality is intriguing in light of a recent study by Sobirey et al. [704]. They observed a universal scaling of  $\Delta_0/E_F$  with the dimensionless pair size  $\xi k_F$ , applicable to both two- and three-dimensional superconductors. The authors concluded that correlation effects are more important for the stability of the superconducting state than the dimensionality. This observation is in qualitative agreement with measurements on monolayer and bulk forms of  $\text{Bi}_2\text{Sr}_2\text{CaCu}_2\text{O}_{8+\delta}$ , which displayed similar superconducting properties across the structural phases [705]. Furthermore, a recent theoretical study of various cuprate systems suggests that variations in the Hubbard interaction strength  $U$  are primarily responsible for the material dependence of critical temperatures [110], emphasizing the dominant role of electron correlations. It presents an interesting question for future research to understand how the strong dependence of many unconventional superconductors on the phase ordering scale  $T_\varphi$  – most pronounced in (quasi-)two-dimensional systems – aligns with the observed insensitivity to dimensionality.

### 6.1.1 Uemura relation

The superconducting stiffness  $D_s$  can be directly obtained from measurements of quantities like the London penetration depth  $\lambda_L$  (cf. Eq. (3.44)) or the imaginary part of the low-frequency optical conductivity [204]. In a series of papers, Uemura and coworkers used  $\lambda_L$  data obtained from  $\mu\text{SR}$  relaxation rates to establish an important classification scheme for superconducting materials [197, 701–703, 706, 707]. While the original study [701] compared critical temperatures  $T_c$  to the stiffness  $D_s \propto \lambda_L^{-2}$ , subsequent works used the connection of penetration depth and stiffness to the ratio of condensate density  $n_s$  and effective mass  $m^*$  ( $\lambda_L^{-2} \propto D_s \propto n_s/m^*$ ) at low

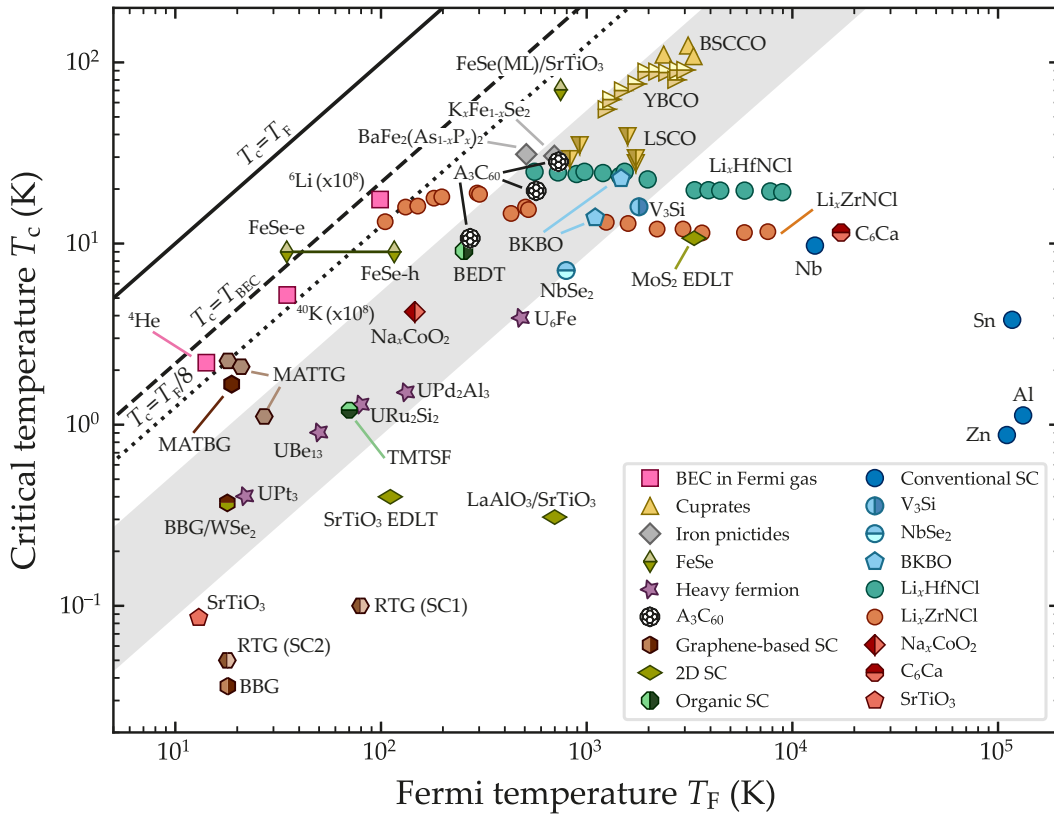


**Figure 6.1 – Uemura plot.** Comparison of critical temperature  $T_c$  and Fermi temperature  $T_F$  for various superconductors in a logarithmic plot. The solid line corresponds to  $T_c = T_F$ , the dashed line indicates the critical temperature of a non-interacting BEC in 3D with  $T_{BEC} = T_F/4.16$  [266], and the dotted line represents the upper limit for the BKT transition of free electrons in two dimensions with  $T_c = T_F/8$  [198]. The gray shaded area indicates where most unconventional superconductors are located (here drawn from  $T_c = 0.04 T_{BEC}$  to  $0.25 T_{BEC}$ ). The data points of the semiconducting materials  $Li_xZrNCl$  and  $Li_xHfNCl$  indicate different doping concentrations  $x$ , and  $FeSe$ -e/h denote the estimated  $T_F$  of the small electron and hole Fermi pockets of  $FeSe$ , respectively. Data provided by [708] and additional data taken from Refs. [197, 639].

temperatures  $T \rightarrow 0$  to determine an effective Fermi temperature  $T_F$ , representing the (available kinetic) energy scale of superconducting charge carriers.

The comparison of  $T_c$  and  $T_F$  (or  $n_s/\lambda_L^{-2}$ ) is referred to as “Uemura plot”, which we show in Figure 6.1 for various different superconducting materials and BECs in Fermi gases.<sup>2</sup> We additionally draw lines indicating the upper bound for paired electrons with parabolic dispersion in two dimensions,  $T_c = T_F/8$ , as well as the condensation

<sup>2</sup>We stress that the more common representation depending on  $T_F$  includes highly processed experimental data and a series of assumptions to calculate  $T_F$ . Typically, the relation of non-interacting fermions is used, which in (quasi)-two-dimensional materials yields the direct relation  $E_F^{2D} = \hbar^2 \pi n_s^2 / m^* \propto \lambda_L^{-2}$ . In three dimensions, however,  $E_F^{3D} \propto n_s^{3/2} / m^*$  depends on a different power of  $n_s$ , necessitating the inclusion of an additional quantity to calculate  $E_F$ . For instance, the Sommerfeld constant, Pauli susceptibility, or coherence length have been used to determine data shown in Figure 6.1 [702, 706, 707].

temperature  $T_{\text{BEC}} = T_{\text{F}}/4.6$  of a three-dimensional, non-interacting BEC with density  $n_{\text{B}} = n_{\text{s}}/2$  and mass  $m_{\text{B}} = 2m^*$ , which describes the idealized scenario of all electrons condensing into a dilute gas of tightly-bound pairs. Within the Uemura classification, most unconventional superconductors fall into a limited region of  $T_{\text{c}}/T_{\text{F}} \sim 0.01 - 0.06$  and display linear scaling  $T_{\text{c}} \propto T_{\text{F}}$  across material families [197]. This evidences the previously discussed comparable scales of  $T_{\text{c}}$  and the phase-ordering temperature, for which we can roughly associate  $T_{\phi} \sim T_{\text{F}}$ . In contrast, conventional superconductors described by BCS theory have comparably high  $T_{\text{F}}$  and low  $T_{\text{c}}$  since only a small fraction of electrons condenses into pairs. Notably, the variation of  $T_{\text{c}}$  with carrier density is weak for conventional superconductors, rather indicating the dependence on the pairing energy with  $T_{\text{P}} \sim \Delta_0 \sim \omega_{\text{D}}$  in BCS theory.

From the Uemura plot,  $T_{\text{BEC}}$  emerges as an empirical upper bound to  $T_{\text{c}}$ . However, most superconducting materials, including cuprate materials with the highest known  $T_{\text{c}}$  at ambient conditions, are not even close to this boundary. Exceptions are twisted graphene-based systems, monolayer iron-selenide, and doped two-dimensional semiconductors, which all come close to the simple two-dimensional boundary of  $T_{\text{F}}/8$ . We further address these observations in publication VI, for which Figure 6.1 can serve as a graphical reference. For an extended discussion of specific material families, the relation of the Uemura plot to other experimental observables such as the Nernst coefficient, and its connection to light-induced superconductivity, we refer to Ref. [197].

The Uemura plot suggests that the critical temperature of many superconducting materials appears to depend linearly on a single parameter  $T_{\text{F}} \propto n_{\text{s}}$ . This observation has encouraged discussions about the potential of a BCS–BEC crossover description for unconventional superconductivity. Recent experiments on doped two-dimensional semiconductors have studied the BCS–BEC crossover, demonstrating how  $T_{\text{F}}$  and, consequently,  $T_{\text{c}}$  can be tuned across the Uemura plot through doping. In these studies,  $T_{\text{c}}$  approaches the two-dimensional constraint of  $T_{\text{F}}/8$  in the dilute limit [708]. However, for many superconducting materials, the applicability of a BCS–BEC crossover description remains uncertain [VI, 700, 709, 710]. Nonetheless, the BCS–BEC crossover phenomenology offers a qualitative understanding of critical temperature limitations as discussed in the next section. These constraints explain the absence of a straight upward trend in the Uemura plot.

### 6.1.2 The BCS–BEC crossover

In section 3.1, our general symmetry considerations of the superconducting and superfluid condensate demonstrated that their wave functions are similarly described by coherent states. While we pointed out in section 3.2.1 that electronic Cooper pairs are not proper bosons, we also demonstrated that the pairing operators  $b \sim cc$  [Eq. (3.83)] effectively acquire bosonic properties in the dilute and/or localized

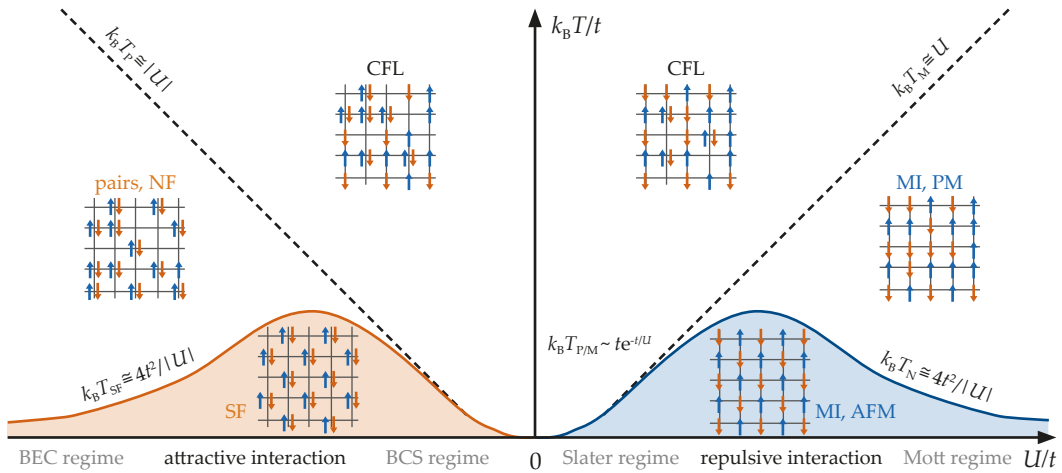


**Figure 6.2 – Phase diagram of the Hubbard model at half-filling for a three-dimensional cubic lattice.** The temperature  $T$  and interaction  $U$  phase diagram in units of electronic hopping  $t$  is symmetric with respect to the non-interacting fermionic lattice model ( $U = 0$ ) due to particle-hole symmetry. For attractive interactions  $U < 0$ , a second-order transition between normal fluid (NF) and  $s$ -wave superfluid (SF) phase emerges, which is characterized by the BCS–BEC crossover with distinct scaling of the transition temperature  $T_{\text{SF}}$  in the weak and strong coupling regimes. While phase coherence is lost above  $T_{\text{SF}}$ , incoherent pairing fluctuations remain up to the pairing temperature  $T_{\text{P}}$ , which determines the crossover to the correlated Fermi liquid (CFL). For repulsive interactions  $U > 0$ , the superconducting phase is mapped onto an antiferromagnetic (AFM) and Mott-insulating (MI) phase. The Néel temperature  $T_{\text{N}}$  describes the transition to magnetic order. Above  $T_{\text{N}}$ , the Mott temperature  $T_{\text{M}}$  separates the charge sector transition between paramagnetic (PM) and CFL phases. Adapted from Ref. [266].

limit. Indeed, the ground state wave functions used in the mean-field descriptions of the BCS condensate and the BEC can be continuously connected by tuning the density or interaction strength, as demonstrated in the pioneering works of Leggett [574], and Nozières and Schmitt-Rink [575]. This connection forms the basis of the BCS–BEC crossover, allowing for a smooth transition between the BCS regime of weakly-bound, overlapping pairs in momentum space and BEC regime of strongly localized, molecule-like pairs in real space, with corresponding changes in physical quantities such as transition temperatures.

A comprehensive overview on the BCS–BEC crossover is given in publication VI, which we do not repeat here (see also reviews such as Refs. [266, 700] and further references in VI). Instead, we aim to build on the previous discussion and illustrate how the hierarchy between superconducting energy scales,  $\Delta$  and  $D_s$ , evolves during the BCS–BEC crossover. To this end, we consider the specific realization of the BCS–BEC crossover in the attractive Hubbard model [Eq. (2.14) with  $U < 0$ ], which characterizes the crossover by a change from potential-energy to kinetic-energy-driven pairing [455, 711, 712]. Figure 6.2 shows the phase diagram for the half-filled Hubbard model, where the BCS–BEC crossover can be tuned by changing the ratio  $|U|/t$  for  $U < 0$ . Due to particle-hole symmetry, we can map the superconducting

phase of the attractive Hubbard model onto antiferromagnetism in the repulsive Hubbard model ( $U > 0$ ) [711]. This makes the BCS–BEC crossover analogous to the transition between weak-coupling, itinerant Slater magnetism and strong-coupling, localized Heisenberg magnetism.

In the BCS limit,  $T_c$  increases exponentially with  $|U|$  and is governed by the pairing energy scale  $k_B T_P \propto |U|$ .<sup>3</sup> The transition to the superconducting state is primarily stabilized by the gain in potential energy  $E_{\text{pot}} = -|U| \sum_i \langle n_{i\uparrow} n_{i\downarrow} \rangle$  determined by the local density of double occupancies [455]. As the interaction strength increases, the system transitions to the strong-coupling BEC regime, where pairing becomes driven by kinetic energy rather than potential energy [455, 712]. In this regime, pair mobility (necessary for phase coherence) is reduced because pair hopping in the lattice requires fermion pairs to break apart and perform virtual fermionic hopping, cf. Fig. 1b in publication VI. This behavior is captured in an effective model of hardcore bosons with bosonic hopping  $t_B = 4t^2/|U|$ .<sup>4</sup> As electron pairs become increasingly localized in the BEC regime, the effective pair mass is enhanced ( $m_P \propto t_B^{-1} \propto |U|$ ), which impedes pair hopping and reduces phase coherence ( $D_s \propto m_P^{-1}$ ). Consequently, the transition temperature  $k_B T_c \simeq t_B \propto 1/|U|$  is suppressed in the strong coupling limit and approaches zero for  $|U| \rightarrow \infty$ .

In conclusion, the dominant energy scale that limits  $T_c$  switches by increasing the interaction strength  $|U|$ : from the pairing energy  $\Delta \propto |U|$  in the BCS regime to the phase coherence energy  $D_s \propto 1/m_P \propto 1/|U|$  in the BEC limit. As a result, a characteristic  $T_c$  dome emerges with a maximum in the intermediate coupling regime. From this discussion, we can formulate two approaches to optimize critical temperatures. One viable option is to tune the system to be at the optimal  $T_c$  in the intermediate regime of the crossover. Another option, in line with our previous discussion, is to search for possibilities to achieve a sufficiently high stiffness in the strong coupling regime by evading the suppressing constraints. The high degrees of freedom in multi-orbital systems provide a good playground for exploring this idea. For example, one can try to separate the processes of particle pairing and achieving phase coherence into different electronic bands, where a sufficient hybridization of the two bands can lead to enhanced superconductivity [454]. On the other hand, the quantum geometric contributions to the stiffness can be sufficient to facilitate superconductivity [450–452, 536, 543, 544]. In publication VI, we showcase an alternative approach where a robust stiffness derives from an interaction-resilient metallic parent state.

<sup>3</sup>The attractive Hubbard interaction Hamiltonian is identical to the BCS interaction by restricting electron scattering to pairs of equal momenta and zero center-of-mass momentum.

<sup>4</sup>This is derived by integrating out the fermionic degrees of freedom in the strong coupling regime. It is analogous to the effective antiferromagnetic exchange coupling  $J = -4t^2/U$  obtained from mapping the Hubbard model to the Heisenberg or  $t$ - $J$  model at large repulsive interactions.



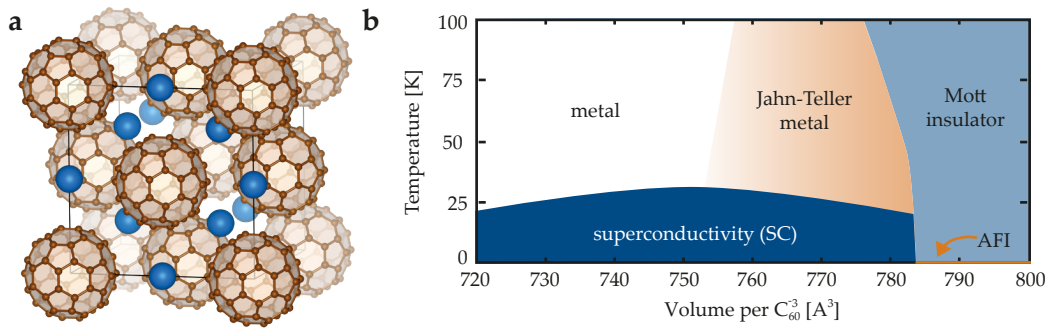


**Figure 6.3 – Structure and phase diagram of alkali-doped fullerides.** (a) Crystal structure of fcc  $A_3C_{60}$  ( $A=K, Rb, Cs$ ) drawn using VESTA [714]. (b) Schematic phase diagram of equilibrium  $A_3C_{60}$  as a function of temperature and volume per  $C_{60}$  molecule. It contains  $s$ -wave superconductivity (SC) up to a Mott insulating (MI) phase, which becomes an antiferromagnetic insulator (AFI) at low temperature. A Jahn-Teller metallic phase emerges between the SC and MI regions. Phase diagram adapted from Ref. [119].

## 6.2 Resilient superconductivity from multi-orbital physics in $A_3C_{60}$

In publication VI, we study the material family of alkali-doped fullerides ( $A_3C_{60}$ ,  $A=K, Rb, Cs$ ), which consist of  $C_{60}$  molecules arranged on a fcc or A15 lattice structure and turn superconducting upon doping with alkali atoms. We here focus on the fcc structure and summarize the key features of their phase diagram, see Figure 6.3. General reviews on these materials and details on the superconducting mechanisms can be found in Refs. [128, 129, 713]; see also references in publication VI.

Alkali-doped fullerides have the highest critical temperatures among organic superconductors, reaching up to 38 K under pressure. The critical temperature displays a dome-shaped dependence on the unit cell volume determined by the size of the alkali atom dopant. The superconducting phase is an isotropic  $s$ -wave, which emerges in proximity to a Mott-insulating phase. Those superconducting and insulating states are connected by the Jahn-Teller metallic phase, which is characterized by the coexistence of localized Jahn-Teller-active electrons and itinerant electrons. In addition, antiferromagnetism is found at temperatures below 2 K in the Mott-insulating phase.

A fully *ab initio* study was able to closely reproduce the phase diagram of  $A_3C_{60}$  [232]. Superconducting pairing in  $A_3C_{60}$  is induced by an interplay of strong electron-phonon coupling and purely electronic correlation effects. The coupling to Jahn-Teller phonon modes induces an effectively negative Hund's coupling  $J < 0$ , which then facilitates Cooper pairing [128]. Recently, the discovery of light-induced superconductivity in  $A_3C_{60}$  [182–188] shifted these materials back into the focus of research.

Niklas Witt, Yusuke Nomura, Sergey Brener, Ryotaro Arita,  
Alexander I. Lichtenstein, Tim O. Wehling

### Key points summary

- Development of framework to calculate coherence length  $\xi_0$ , London penetration depth  $\lambda_L$ , and depairing current  $j_{dp}$  from microscopic theories and first principles in presence of strong electron correlations based on Nambu–Gor’kov Green’s function formalism with finite-momentum pairing (FMP).
- Application to alkali-doped fullerenes ( $A_3C_{60}$ ) showing good agreement with experimental measurements of  $\xi_0$  and  $\lambda_L$ , and revealing two distinct localized superconducting regimes tunable by local interactions.
- Strong coupling superconductivity for increased inverted Hund’s coupling  $J < 0$  demonstrates short coherence length, but resiliently high stiffness and enhanced critical temperature  $T_c$  beyond expectations of lattice BCS–BEC crossover phenomenology. Results are discussed in the context of limitations on critical temperatures and possibilities of  $T_c$ -enhancement through multi-orbital physics.






### Author Contributions

I performed and analyzed the calculations, prepared the figures, and wrote the manuscript with input from all authors. A. I. Lichtenstein and I modified the DMFT code provided by Y. Nomura and R. Arita to include FMP, and I developed the post-processing routines to extract  $\xi_0$ ,  $\lambda_L$ , and  $j_{dp}$ . S. Brener and I analyzed the FMP Ginzburg–Landau formalism. T. Wehling, A. I. Lichtenstein, and I conceived the project. All authors discussed the results and their interpretation. I was responsible for handling the paper submission and communication with editor and reviewers.

### Copyright Notice

This manuscript has been published as [N. Witt et al., npj Quantum Mater. 9, 100 \(2024\)](#). In the following, a preliminary version from the review process is embedded, which was uploaded as a preprint to the arXiv servers under the identifier [2310.09063v3](#).

# Bypassing the lattice BCS-BEC crossover in strongly correlated superconductors through multiorbital physics

Niklas Witt <sup>1,2,\*</sup> Yusuke Nomura <sup>3</sup> Sergey Brener,<sup>1</sup> Ryotaro Arita <sup>4,5</sup> Alexander I. Lichtenstein <sup>1,2</sup> and Tim O. Wehling <sup>1,2</sup>

<sup>1</sup>*Institute of Theoretical Physics, University of Hamburg, Notkestraße 9-11, 22607 Hamburg, Germany*

<sup>2</sup>*The Hamburg Centre for Ultrafast Imaging, Luruper Chaussee 149, 22607 Hamburg, Germany*

<sup>3</sup>*Institute for Materials Research (IMR), Tohoku University, 2-1-1 Katahira, Aoba-ku, Sendai 980-8577, Japan*

<sup>4</sup>*Research Center for Advanced Science and Technology,*

*The University of Tokyo, 4-6-1 Komaba, Meguro-ku, Tokyo 153-8904, Japan*

<sup>5</sup>*RIKEN Center for Emergent Matter Science (CEMS), 2-1 Hirosawa, Wako, Saitama 351-0198, Japan*

(Dated: August 11, 2024)

Superconductivity emerges from the spatial coherence of a macroscopic condensate of Cooper pairs. Increasingly strong binding and localization of electrons into these pairs compromises the condensate's phase stiffness, thereby limiting critical temperatures – a phenomenon known as the BCS-BEC crossover in lattice systems. In this study, we demonstrate enhanced superconductivity in a multiorbital model of alkali-doped fullerenes ( $A_3C_{60}$ ) that goes beyond the limits of the lattice BCS-BEC crossover. We identify that the interplay of strong correlations and multiorbital effects results in a localized superconducting state characterized by a short coherence length but robust stiffness and a domeless rise in critical temperature with increasing pairing interaction. To derive these insights, we introduce a new theoretical framework allowing us to calculate the fundamental length scales of superconductors, namely the coherence length ( $\xi_0$ ) and the London penetration depth ( $\lambda_L$ ), even in presence of strong electron correlations.

## INTRODUCTION

The collective and phase coherent condensation of electrons into bound Cooper pairs leads to the emergence of superconductivity. This macroscopic coherence enables dissipationless charge currents, perfect diamagnetism, fluxoid quantization and technical applications<sup>1,2</sup> ranging from electromagnets in particle accelerators to quantum computing hardware. Often, superconducting (SC) functionality is controlled by the critical surface spanned by critical magnetic fields, currents, and temperatures which a SC condensate can tolerate. Fundamentally, these are determined by the characteristic length scales of a superconductor – the London penetration depth,  $\lambda_L$ , and the coherence length,  $\xi_0$ .

$\lambda_L$  and  $\xi_0$  quantify different aspects of the SC condensate: The penetration depth is the length associated with the mass term that the vector potential gains through the Anderson-Higgs mechanism<sup>3</sup>. In consequence, magnetic fields decay exponentially over a distance  $\lambda_L$  inside a superconductor. Through this,  $\lambda_L$  is connected to the energy cost of order parameter (OP) phase variations and hence the SC stiffness  $D_s$ . The coherence length, on the other hand, is the intrinsic length scale of OP amplitude variations and is associated with the amplitude Higgs mode.  $\xi_0$  sets the scale below which amplitude and phase modes significantly couple such that spatial variations of the OP's phase reduce its amplitude<sup>3,4</sup>.

In addition to influencing the macroscopic properties of superconductors,  $\lambda_L$  and  $\xi_0$  play an important role to understand strongly correlated superconductors, as is epitomized in the Uemura plot<sup>5-8</sup>. For instance, the interplay of  $\lambda_L$  and  $\xi_0$  impacts critical temperatures<sup>9</sup>, it is relevant for the pseu-

dogap formation<sup>10-13</sup>, it influences magneto-thermal transport properties like the Nernst effect<sup>8,14,15</sup>, and it might underlie the light-enhancement of superconductivity<sup>15-19</sup>. An important concept in this context is the BCS-BEC crossover phenomenology<sup>20-24</sup>. It continuously connects the two limiting cases of weak-coupling Bardeen-Cooper-Schrieffer (BCS) superconductivity with weakly-bound and largely overlapping Cooper pairs to tightly-bound molecule-like pairs in the strong-coupling Bose-Einstein condensate (BEC) as the interaction strength or the density is varied (Fig. 1).

The BCS-BEC crossover has been studied in ultracold Fermi gases<sup>23</sup>, low-density doped semiconductors<sup>25</sup>, and is under debate for several unconventional superconductors<sup>6,8,24,26-30</sup>. However, quasi-continuous systems, for instance Fermi gases, and strongly correlated superconducting solids show a crucially different behavior of how their SC properties, most importantly the critical temperature  $T_c$ , change towards the strong coupling BEC limit. While  $T_c$  converges to a constant temperature  $T_{BEC}$  for Fermi gases in a continuum<sup>31</sup> (Fig. 1a),  $T_c$  can become arbitrarily small in strongly correlated lattice systems due to the quenching of kinetic energy (Fig. 1b). Since the movement of electron pairs, i.e., bosonic hopping, necessitates intermediate fermionic hopping, it becomes increasingly unfavorable for strong attractions. Thus, as Cooper pairs become localized on the scale of the lattice constant, the condensate's stiffness and hence  $T_c$  are compromised<sup>21,24</sup>. Fig. 1 contrasts this generic BCS-BEC crossover picture for Fermi gases and correlated lattice systems in terms of the change of  $T_c$  and the pair size  $\xi_p$  as a function of pairing strength. Due to the decrease of  $T_c$  in the BCS and BEC limits, a prominent dome-shape of  $T_c$  can be expected in the crossover region for solid materials. Because of this, recent experimental efforts to increase  $T_c$  concentrate on stabilizing SC materials in this region<sup>24,25,27,30</sup>.

In this work, we demonstrate how multiorbital effects can

\* niklas.witt@physik.uni-hamburg.de

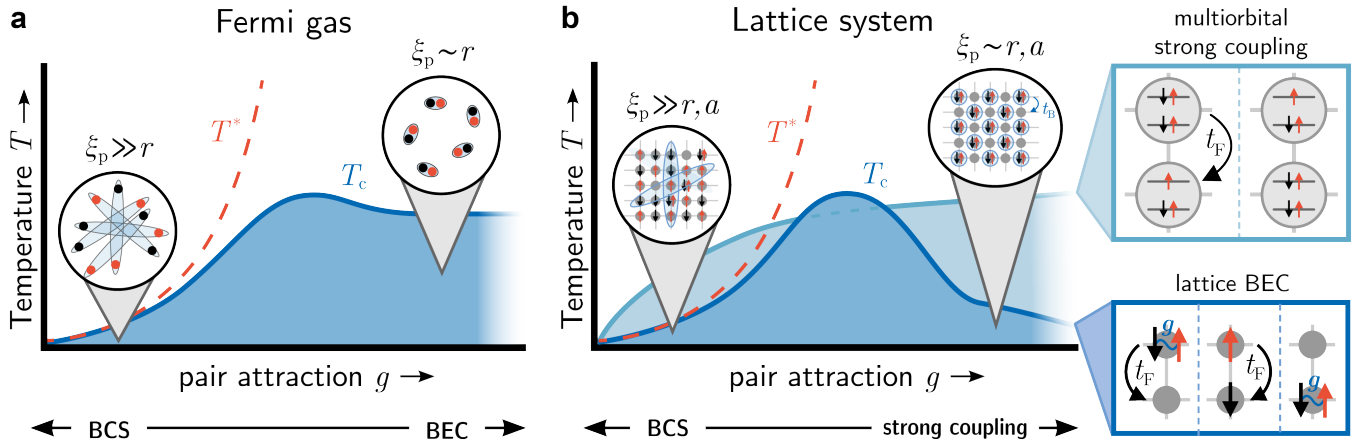


**Fig. 1 | BCS-BEC crossover in Fermi gases vs. lattice systems.** Evolution of the critical temperature  $T_c$  and Cooper pair size  $\xi_p$  in the BCS-BEC crossover (dark blue line) for (a) Fermi gases and (b) lattice systems. Both cases display a dome-shaped behavior of  $T_c$  in the intermediate crossover regime but behave qualitatively different in the strong coupling BEC phase:  $T_c$  remains finite in the Fermi gas (a)<sup>31</sup> but approaches zero in the lattice case (b). During the crossover,  $\xi_p$  is reduced to the order of interparticle spacing  $r$  (a & b) and lattice constant  $a$  (b). For the lattice system, we contrast the evolution towards the multiorbital strong coupling phase (light blue line) discussed in this article. Here, the localization of pairs differently affects the Bosonic hopping  $t_B$ , as drawn in the insets on the right. In the lattice BEC limit, Bosonic hopping relies on a second-order process involving two fermionic hoppings,  $t_F$ , and a virtual intermediate state with broken pairs that is inhibited by the strong attraction  $g < 0$ . Consequently, this process and also  $T_c \propto t_B = t_F^2/|g|$  are quenched at large  $|g|$ <sup>21,24</sup>. In the multiorbital strong coupling case, the local coexistence of paired and unpaired electrons fluctuating between different orbitals enables Bosonic hopping  $t_B$  as a first order process in  $t_F$  without any intermediate broken pair states. A second temperature scale  $T^*$  is drawn in both panels as its splitting from  $T_c$  (corresponding to the opening of a pseudogap) marks the beginning of the crossover regime<sup>24</sup>.

enhance superconductivity beyond the expectations of the lattice BCS-BEC crossover phenomenology (as contrasted in Fig. 1b) with a model inspired by alkali-doped fullerenes ( $A_3C_{60}$  with  $A=K, Rb, Cs$ ). The material family of  $A_3C_{60}$  hosts exotic  $s$ -wave superconductivity of critical temperatures up to  $T_c = 38$  K, being the highest temperatures among molecular superconductors<sup>32–35</sup>, and they possibly reach photo-induced SC at even higher temperatures<sup>15,17,18,36</sup>. In order to theoretically characterize the SC state, the knowledge of the intrinsic SC length scales is essential. While BCS theory and Eliashberg theory provide a microscopic description of  $\lambda_L$  and  $\xi_0$  for weakly correlated materials<sup>37–39</sup>, their validity is unclear for superconductors with strong electron correlations. To the best of our knowledge,  $\xi_0$  is generally not known from theory in strongly correlated materials. Only approaches to determine  $\lambda_L$  exist where an approximate, microscopic assessment of the SC stiffness from locally exact theories has been established, albeit neglecting vertex corrections<sup>40–45</sup>.

For this reason, we introduce a novel theoretical framework to microscopically access  $\lambda_L$  and  $\xi_0$  from the tolerance of SC pairing to spatial OP variations. Central to our approach are calculations in the superconducting state under a constraint of finite-momentum pairing (FMP). Via Nambu-Gor'kov Green functions we get direct access to the superconducting OP and the depairing current  $j_{dp}$  which in turn yield  $\xi_0$  and  $\lambda_L$ . The FMP constraint is the SC analog to planar spin spirals applied to magnetic systems<sup>46–48</sup>. As in magnetism, a generalized Bloch theorem holds that allows us to consider FMP without supercells; see Supplementary Note 2 for a proof. As a result, our approach can be easily embedded in microscopic

theories and *ab initio* approaches to tackle material-realistic calculations.

In this work, we implement FMP in Dynamical Mean-Field theory (DMFT)<sup>49</sup> to treat strongly correlated superconductivity. In DMFT, the interacting many-body problem is solved by self-consistently mapping the lattice model onto a local impurity problem. By this, local correlations are treated exactly. We apply the FMP-constrained DMFT to  $A_3C_{60}$  where we find  $\xi_0$  and  $\lambda_L$  in line with experiment for model parameter ranges derived from *ab initio* estimates, validating our approach. For enhanced pairing interaction, we then reveal a multiorbital strong coupling SC state with minimal  $\xi_0$  on the order of only 2–3 lattice constants, but with robust stiffness  $D_s$  and high  $T_c$  which increases with the pair interaction strength without a dome shape. This strong coupling SC state is distinct to the lattice BCS-BEC crossover phenomenology showing promising routes to optimize superconductors with higher critical temperatures. We discuss this possibility in-depth after the presentation of our results.

The remaining paper is organized as follows: First, we motivate how the FMP constraint is linked to  $\lambda_L$  and  $\xi_0$  from phenomenological Ginzburg-Landau theory after which we summarize the microscopic approach from Green function methods. Technical details are available in the Supplementary Information as cross-referenced at relevant points. Subsequently, we discuss our results for the multiorbital model of  $A_3C_{60}$ . Readers primarily interested in the analysis of these results might skip the first part on the physical motivation for obtaining superconducting length scales from the FMP constraint.

## RESULTS

### Extracting superconducting length scales from the constraint of finite-momentum pairing

In most SC materials, Cooper pairs do not carry a finite center-of-mass momentum  $\mathbf{q} = \mathbf{0}$ . Yet, in presence of external fields, coexisting magnetism, or even spontaneously SC states with FMP, i.e.,  $\mathbf{q} \neq \mathbf{0}$ , might arise<sup>50–54</sup> as originally conjectured in Fulde-Ferrel-Larkin-Ovchinnikov (FFLO) theory<sup>55–57</sup>. Here, we introduce a method to access the characteristic SC length scales  $\xi_0$  and  $\lambda_L$  of strongly correlated materials through the calculation of FMP states with a manually constrained pair center-of-mass momentum  $\mathbf{q}$ . For this, we enforce the OP to be of the FMP form  $\Psi_{\mathbf{q}}(\mathbf{r}) = |\Psi_{\mathbf{q}}|e^{i\mathbf{q}\mathbf{r}}$  corresponding to FF-type pairing<sup>55</sup>, which is to be differentiated from pair density waves with amplitude modulations<sup>56–58</sup>. We contrast the OP for zero and finite momentum in real and momentum space in the top panel of Fig. 2. For FMP, the OP's phase is a helix winding around the direction of  $\mathbf{q}$ , while the OP for zero momentum pairing is simply a constant.

Before turning to the implementation in microscopic approaches, we motivate how the FMP constraint relates to  $\lambda_L$  and  $\xi_0$ . The Ginzburg-Landau (GL) framework provides an intuitive picture to this connection which we summarize here and discuss in detail in Supplementary Note 1. The GL low-order expansion of the free energy density  $f_{\text{GL}}$  in terms of the FMP-constrained OP reads

$$f_{\text{GL}}[\Psi_{\mathbf{q}}] = \alpha|\Psi_{\mathbf{q}}|^2 + \frac{b}{2}|\Psi_{\mathbf{q}}|^4 + \frac{\hbar^2}{2m^*}q^2|\Psi_{\mathbf{q}}|^2 \quad (1)$$

with  $q = |\mathbf{q}|$ .  $\alpha$ ,  $b$ , and  $m^*$  are the material and temperature dependent GL parameters. Here, the temperature-dependent (GL) correlation length  $\xi(T)$  appears as the natural length scale of the amplitude mode ( $\propto |\alpha|$ ) and the kinetic energy term

$$\xi(T) = \sqrt{\frac{\hbar^2}{2m^*|\alpha|}} = \xi_0 \left(1 - \frac{T}{T_c}\right)^{-\frac{1}{2}} \quad (2)$$

with its zero-temperature value  $\xi_0$  being the coherence length<sup>4</sup>. The stationary point of Eq. (1) shows that the  $q$ -dependent OP amplitude  $|\Psi_{\mathbf{q}}| = |\Psi_0| \sqrt{1 - \xi^2 q^2}$  ( $T$ -dependence suppressed) decreases with increasing momentum  $q$ . For large enough  $q$ , SC order breaks down (i.e.,  $\Psi_{\mathbf{q}} \rightarrow 0$ ) as the kinetic energy from phase modulations becomes comparable to the gain in energy from pairing. The length scale associated with this breakdown is  $\xi(T)$  and can, therefore, be inferred from the  $q$ -dependent OP suppression. We employ, here, the criterion  $\xi(T) = 1/(\sqrt{2}|Q|)$  with  $Q$  such that  $|\Psi_Q(T)/\Psi_0(T)| = 1/\sqrt{2}$  for fixed  $T$  (see Supplementary Note 5-A for more information).

The finite center-of-mass momentum of the Cooper pairs entails a charge supercurrent  $\mathbf{j}_{\mathbf{q}} \propto |\Psi_{\mathbf{q}}|^2 \mathbf{q}$ , c.f. Eq. (8) in Supplementary Note 1. This current density is a non-monotonous function of  $q$  with a maximum called depairing current density  $j_{\text{dp}}$ . It provides a theoretical upper bound to critical current

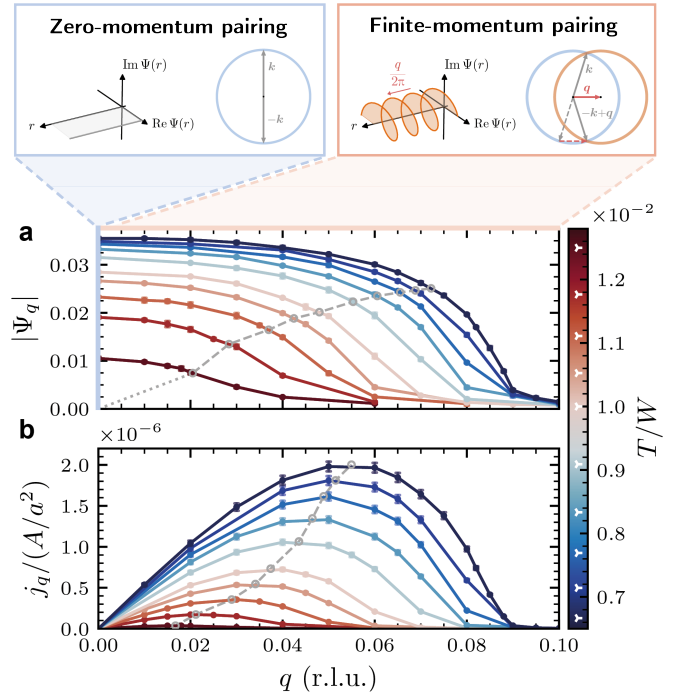


**Fig. 2 | Influence of finite-momentum pairing (FMP) constraint on the superconducting condensate.** The top panel insets sketch the position and momentum space representation of the order parameter (OP)  $\Psi_{\mathbf{q}}(\mathbf{r}) = |\Psi_{\mathbf{q}}|e^{i\mathbf{q}\mathbf{r}}$  in the zero-momentum (left,  $q = 0$ ) and finite-momentum pairing states (right,  $q > 0$ ). The main panels show (a) the momentum dependence of the OP modulus and (b) the supercurrent density  $j_{\mathbf{q}} = |\mathbf{j}_{\mathbf{q}}|$  as function of Cooper pair momentum  $q = |\mathbf{q}|$  in reciprocal lattice units (r.l.u.). Gray lines indicate the points of extracting  $\xi$  and  $j_{\text{dp}}$  (see text). The data shown are results for the  $A_3C_{60}$  model (c.f. Eq. (7)) with lattice constant  $a$  and interaction parameters  $U/W = 1.4$ ,  $J/W = -0.04$  evaluated at different temperatures  $T$  (color coded; see color bar with white triangular markers).

densities,  $j_c$ , measured in experiment. We note that careful design of SC samples is necessary for  $j_c$  reaching  $j_{\text{dp}}$  as its value crucially depends on sample geometry and defect densities<sup>38,59</sup>.  $j_{\text{dp}}$  is related to the London penetration depth  $\lambda_L$  in GL theory via

$$\lambda_L(T) = \sqrt{\frac{\Phi_0}{3\sqrt{3}\pi\mu_0\xi(T)j_{\text{dp}}(T)}} = \lambda_{L,0} \left(1 - \left(\frac{T}{T_c}\right)^4\right)^{-\frac{1}{2}} \quad (3)$$

with the magnetic flux quantum  $\Phi_0 = h/2e$ . The temperature dependence with the quartic power stated here is empirical<sup>37,38</sup> and we find that it describes our calculations better than the linearized GL expectation as discussed in Supplementary Note 5-B. Note that taking the  $q \rightarrow 0$  limit in our approach is related to linear-response-based methods to calculate  $\lambda_L$  or, equivalently, the stiffness  $D_s$ <sup>45,60</sup>.

The GL analysis shows that the OP suppression and supercurrent induced by the FMP constraint connect to  $\xi_0$  and  $\lambda_L$ . In a microscopic description, we acquire the OP and supercurrent

density from the Nambu-Gor'kov Green function

$$\begin{aligned} \mathcal{G}_q(\tau, \mathbf{k}) &= -\langle T_\tau \psi_{\mathbf{k},q}(\tau) \psi_{\mathbf{k},q}^\dagger \rangle \\ &= \begin{pmatrix} G_q(\tau, \mathbf{k}) & F_q(\tau, \mathbf{k}) \\ F_q^*(\tau, \mathbf{k}) & \bar{G}_q(\tau, -\mathbf{k}) \end{pmatrix} \end{aligned} \quad (4)$$

where  $\psi_{\mathbf{k},q}^\dagger = \left( c_{\mathbf{k}+\frac{q}{2}\uparrow}^\dagger \ c_{-\mathbf{k}+\frac{q}{2}\downarrow}^\dagger \right)$  (orbital indices suppressed) are Nambu spinors that carry an additional dependence on  $q$  due to the FMP constraint.  $G$  ( $F$ ) denotes the normal (anomalous) Green function component for electrons ( $G$ ) and holes ( $\bar{G}$ ) in imaginary time  $\tau$ . For  $s$ -wave superconductivity as in  $A_3C_{60}$ <sup>61–64</sup>, we use the orbital-diagonal, local anomalous Green function as the OP

$$|\Psi_q\rangle \equiv [F_q^{\text{loc}}(\tau = 0^-)]_{\alpha\alpha} = \sum_{\mathbf{k}} \langle c_{\alpha\mathbf{k}+\frac{q}{2}\uparrow} c_{\alpha-\mathbf{k}+\frac{q}{2}\downarrow} \rangle, \quad (5)$$

which is the same for all orbitals  $\alpha$ . This allows us to work with a single-component OP. The current density can be calculated via (c.f. Eq. (26) in the Supplementary Information)

$$\mathbf{j}_q = \frac{2e}{N_{\mathbf{k}}} \sum_{\mathbf{k}} \text{Tr}_\alpha \left[ \underline{\mathbf{v}}(\mathbf{k}) \underline{G}_q \left( \tau = 0^-, \mathbf{k} - \frac{\mathbf{q}}{2} \right) \right] \quad (6)$$

where  $\hbar\mathbf{v} = \nabla_{\mathbf{k}} \underline{h}(\mathbf{k})$  is the group velocity obtained from the one-electron Hamiltonian  $\underline{h}(\mathbf{k})$  and the trace runs over the orbital indices of  $\underline{\mathbf{v}}$  and  $\underline{G}_q$ . Underlined quantities indicate matrices in orbital space,  $N_{\mathbf{k}}$  is the number of momentum points and  $e$  is the elementary charge. See Methods and Supplementary Note 4 for details on the DMFT-based implementation and Supplementary Notes 3 for a derivation and discussion of Eq. (6).

The bottom panels of Fig. 2 show an example of our DMFT calculations which illustrates the  $q$ -dependence of the OP amplitude and current density for different temperatures  $T$ . Throughout the paper, we choose  $q$  parallel to a reciprocal lattice vector  $q = qb_1$ . We find a monotonous suppression of the OP with increasing  $q$ . The supercurrent initially grows linearly with  $q$ , reaches its maximum  $j_{\text{dp}}$  and then collapses upon further increase of  $q$ . Thus, both  $|\Psi_q|$  and  $j_q$  behave qualitatively as expected from the GL description. For decreasing temperature, the point where the OP gets significantly suppressed moves towards larger momenta  $q$  (smaller length scales  $\xi(T)$ ), while  $j_{\text{dp}}(T)$  increases. We indicate the points where we extract  $\xi(T)$  and  $j_{\text{dp}}(T)$  with gray circles connected by dashed lines.

### Superconducting coherence in alkali-doped fullerenes

We apply FMP superconductivity to study a degenerate three-orbital model  $H = H_{\text{kin}} + H_{\text{int}}$ , where  $H_{\text{kin}}$  is the kinetic energy and the electron-electron interaction is described by a local Kanamori-Hubbard interaction<sup>65</sup>

$$H_{\text{int}} = (U - 3J) \frac{\hat{N}(\hat{N} - 1)}{2} - J \left( 2\hat{S}^2 + \frac{1}{2}\hat{L}^2 - \frac{5}{2}\hat{N} \right) \quad (7)$$

with total number  $\hat{N}$ , spin  $\hat{S}$ , and angular momentum operator  $\hat{L}$ . The independent interactions are the intraorbital Hubbard term  $U$  and Hund exchange  $J$ , as we use the rotational  $SU(2) \times SO(3)$  symmetric parametrization. This model is often discussed in the context of Hund's metal physics relevant to, e.g., transition-metal oxides like ruthenates with partially filled  $t_{2g}$  shells<sup>65,66</sup>. In the special case of negative exchange energy  $J < 0$ , it has been introduced to explain superconductivity in  $A_3C_{60}$  materials<sup>61–64</sup>. In fullerides, exotic  $s$ -wave superconductivity exists in proximity to a Mott-insulating (MI)<sup>33,34,67</sup> and a Jahn-Teller metallic phase<sup>34,68–70</sup>. The influence of strong correlation effects and inverted Hund's coupling were shown to be essential for the SC pairing<sup>61–64,71</sup> utilizing orbital fluctuations<sup>72</sup> in a Suhl-Kondo mechanism<sup>68</sup>.

The inversion of  $J$  seems unusual from the standpoint of atomic physics, where it dictates the filling of atomic shells via Hund's rules. In  $A_3C_{60}$ , a negative  $J$  is induced by the electronic system coupling to intramolecular Jahn-Teller phonon modes<sup>64,71,73,74</sup>. As a result, Hund's rules are inverted such that states which minimize first spin  $S$  and then angular momentum  $L$  are energetically most favorable, see the second term of Eq. (7) for  $J < 0$ .

We connect the model to  $A_3C_{60}$  by using an *ab initio* derived model for the kinetic energy<sup>75</sup>

$$H_{\text{kin}} = \sum_{ij} \sum_{\alpha\gamma\sigma} t_{\alpha\gamma}(\mathbf{R}_{ij}) c_{i\alpha\sigma}^\dagger c_{j\gamma\sigma} \quad (8)$$

where  $t_{\alpha\gamma}(\mathbf{R}_{ij})$  is the hopping amplitude between half-filled  $t_{1u}$  orbitals ( $\alpha, \gamma = 1, 2, 3$ ) of  $C_{60}$  molecules on sites connected by lattice vector  $\mathbf{R}_{ij}$ . We take the bandwidth  $W$  as the unit of energy ( $W \approx 0.3 - 0.5$  eV for Cs to K based  $A_3C_{60}$ )<sup>64,75</sup>, see Supplemental Note 4-D for further details. For the interaction, we take the first principles' estimates of fixed  $J/W = -0.04$  and varying  $U/W$ <sup>61–64,69</sup> to emulate unit cell volumes as resulting from the size of different alkali dopants. We solve this Hamiltonian using DMFT, which explicitly takes into account superconducting order. Through the momentum dependence of  $|\Psi_q(T)|$  and  $\mathbf{j}_q(T)$ ,  $\xi(T)$  and  $\lambda_L(T)$  can be extracted as discussed in the previous subsection. We show the derived temperature dependence of  $|\Psi_{q=0}(T)|$ ,  $\xi(T)$ , and  $\lambda_L(T)$  for different  $U/W$  in Fig. 3.

Close to the transition point, the OP vanishes and the critical temperature  $T_c$  can be extracted from  $|\Psi_0(T)|^2 \propto T - T_c$ . We find that  $T_c$  increases with  $U$ , contrary to the expectation that a repulsive interaction should be detrimental to electron pairing. This behavior is well understood in the picture of strongly correlated superconductivity. As the correlations quench the mobility of carriers, the effective pairing interaction  $\sim J/ZW$  increases due to a reduction of the quasiparticle weight  $Z$ <sup>61,63</sup>. The trend of increasing  $T_c$  is broken by a first-order SC to MI phase transition for critical  $U \sim 2W$  which is indicated by a dotted line. Upon approaching the MI phase, the magnitude of  $|\Psi_0|$  behaves in a dome-like shape. The  $T_c$  values of  $0.8 - 1.4 \times 10^{-2} W$  that we obtain from DMFT correspond to 49 – 85 K which is on the order of but quantitatively higher than the experimentally observed values. The reason for this is that we approximate the interaction to be instantaneous as well as that we neglect disorder effects and non-local correlations

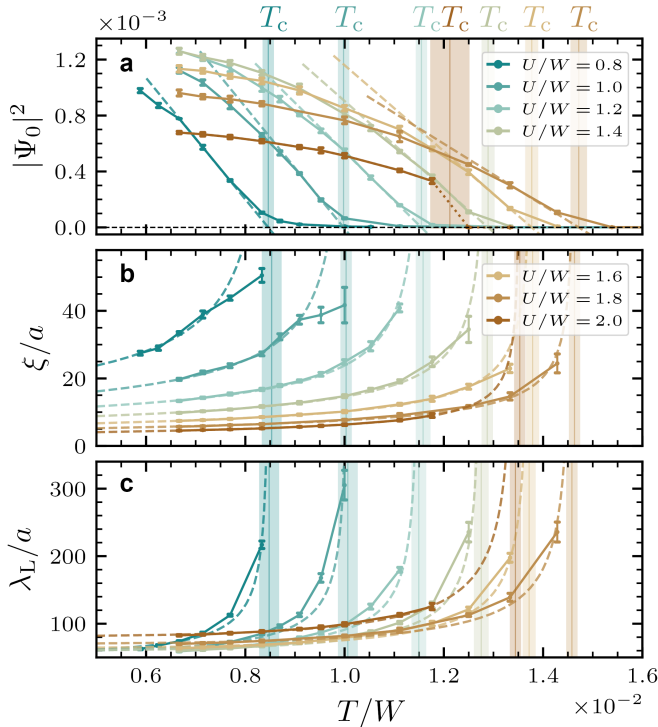


**Fig. 3 | Order parameter, correlation length, and penetration depth in  $A_3C_{60}$ .** The temperature dependence of (a) the zero-momentum order parameter  $|\Psi_0|$ , (b) the correlation length  $\xi$ , and (c) the London penetration depth  $\lambda_L$  are shown for different ratios  $U/W$ . The data were obtained for fixed  $J/W = -0.04$  as estimated from *ab initio* data. Length scales are given in units of the lattice constant  $a$ . Fits to extract critical temperatures  $T_c$  and zero-temperature values  $\xi_0$  and  $\lambda_{L,0}$  are shown by dashed lines. The region of uncertainty to fit  $T_c$  is indicated by shaded regions.

which reduce  $T_c$ <sup>63,64</sup>. The same effects could mitigate the dominance of the MI phase which prevents us from observing the experimental  $T_c$ -dome<sup>34,64</sup>.

Turning to the correlation length, we observe that, away from  $T_c$ ,  $\xi(T)$  is strongly reduced to only a few lattice constants ( $a \sim 14.2\text{--}14.5 \text{ \AA}$ ) by increasing  $U$ , i.e., pairing becomes very localized. At the same time,  $\lambda_L(T)$  is enlarged. Hence, the condensate becomes much softer as there is a reduction of the SC stiffness  $D_s \propto \lambda_L^{-2}$  upon increasing  $U$ . Fitting Eqs. (2) and (3) to our data, we obtain zero-temperature values of  $\xi_0 = 3\text{--}10 \text{ nm}$  and  $\lambda_{L,0} = 80\text{--}120 \text{ nm}$ . Comparing our results with experimental values of  $\xi_0 \sim 2\text{--}4.5 \text{ nm}$  and  $\lambda_L \sim 200\text{--}800 \text{ nm}$ <sup>6,7,35,76,77</sup>, we see an almost quantitative match for  $\xi_0$  and a qualitative match for  $\lambda_L$ . Both experiment and theory consistently classify  $A_3C_{60}$  as type II superconductors ( $\lambda_L \gg \xi_0$ )<sup>35,77</sup>.

We speculate that disorder and spontaneous orbital-symmetry breaking<sup>70</sup> in the vicinity of the Mott state could lead to a further reduction of  $\xi_0$  as well as an increase of  $\lambda_L$  beyond what is found here for the pure system. This could bring our calculations with minimal  $\xi_0 = 3 \text{ nm}$  closer to the experimental minimal coherence length of  $2 \text{ nm}$  revealed by measurements of large upper critical fields reaching up to a

maximal  $H_{c2} = 90 \text{ T}$  in Ref.<sup>76</sup> using  $H_{c2} = \Phi_0/(2\pi\xi_0)$  with the flux quant  $\Phi_0$ .

### Circumvention of the lattice BCS-BEC crossover upon boosting inverted Hund's coupling

The inverted Hund's coupling is crucial for superconductivity in  $A_3C_{60}$ . This premise motivates us to explore in Fig. 4 the nature of the SC state in the interaction  $(U, J)$  phase space for  $J < 0$  beyond *ab initio* estimates.

As long as  $|J| < U/2$ , we find that strengthening the negative Hund's coupling enhances the SC critical temperature with an increase up to  $T_c \approx 5 \times 10^{-2} W$ , i.e., by a factor of seven compared to the *ab initio* motivated case of  $J/W = -0.04$ . There is, however, a change in the role that  $U$  plays in the formation of superconductivity. While  $U$  was supportive for small magnitudes  $|J| \lesssim 0.05 W$ , it increasingly becomes unfavorable for  $|J| > 0.05 W$  where  $T_c$  is reduced with increasing  $U$ . The effect is largest close to the MI phase where superconductivity is strongly suppressed. We indicate this proximity region by a dashed line (c.f. Supplementary Note 5-C).

The impact of  $U$  on the SC state can be understood from the  $U$ -dependence of the London penetration depth:  $\lambda_L$  grows monotonously with  $U$  and reaches its maximum close to the MI phase. Hence, the condensate is softest in the region where Mott physics is important and it becomes stiffer at smaller  $U$ . We find that this fits to the behavior of the effective bandwidth  $W_{\text{eff}} = ZW \propto D_s$  where the quasiparticle weight  $Z$  is suppressed upon approaching the Mott phase. The behavior of  $Z$  shown in Fig. 4a confirms the qualitative connection  $\lambda_L \propto D_s^{-1/2} \propto 1/\sqrt{Z}$  for  $|J| > 0.05 W$ . The  $J$ -dependence of  $\lambda_L$  is much weaker than the  $U$ -dependence, as can be seen in Fig. 4a and the corresponding line-cuts in Fig. 5.

$\xi_0$ , in contrast, depends strongly on  $J$ . By just slightly increasing  $|J|$  above the *ab initio* estimate of  $|J|$ , the SC state becomes strongly localized with a short coherence length on the order of  $2\text{--}3 a$ . Remarkably, the small value of  $\xi_0$  is independent of  $U$  and thus the proximity to the MI phase. The localization of the condensate with  $\xi_0$  on the order of the lattice constant is reminiscent of a crossover to the BEC-type SC state. However, the dome-shaped behavior, characteristic of the lattice BCS-BEC crossover<sup>27,29</sup>, with decreasing  $T_c$  in the strong coupling limit is notably absent here. Instead,  $T_c$  still grows inside the plateau of minimal  $\xi_0$  when increasing the effective pairing strength proportional to  $|J|$  for fixed  $U/W$  (c.f. Fig. 5a). Only by diagonally traversing the  $(U, J)$  phase space, it is possible to suppress  $T_c$  inside the short  $\xi_0$  plateau with a dome structure as shown, e.g., in Ref.<sup>69</sup>.

The reason for this circumvention of the lattice BCS-BEC phenomenology can be understood from an analysis of the local density matrix weights  $\rho_{|\phi_n\rangle}$ , where  $|\phi_n\rangle$  refers to the eigenstates of the local Hamiltonian of our DMFT auxiliary impurity problem. We show  $\rho_{|\phi_n\rangle}$  of four different points in the interaction phase space in Fig. 4b. In the region of short  $\xi_0$ , the local density matrix is dominated by only eight states (red and blue bars) given by the ‘‘inverted Hund's rule’’ ground states  $|\phi_0\rangle$  of the charge sectors with  $N = 2, 3, 4$  particles that

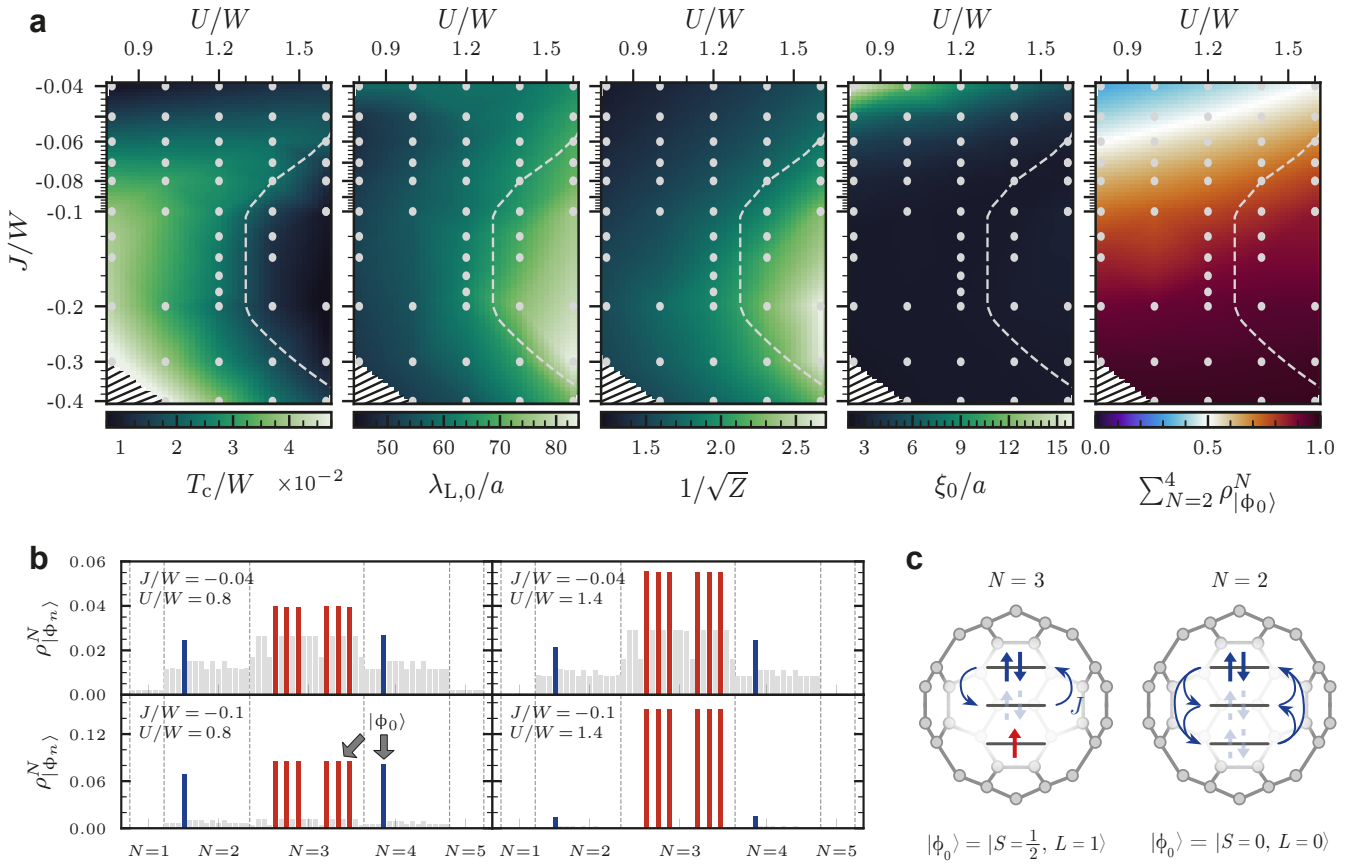


**Fig. 4 | Superconducting state of the  $A_3C_{60}$  model in the  $(U, J)$ -interaction space.** (a) Critical temperature  $T_c$ , zero temperature penetration depth  $\lambda_{L,0}$ , inverse square root of quasiparticle weight  $Z$ , coherence length  $\xi_0$ , and the statistical weight  $\rho_{|\phi_0\rangle}^N$  of the local lowest energy states  $|\phi_0\rangle$  of the  $N = 2, 3, 4$  particle sectors obeying inverted Hund's rules as a function of  $U$  and  $J$ . Gray dots show original data points used for interpolation and the dashed line indicates a region where the proximity to the Mott state leads to a suppression of the superconducting state. There is no data point at the charge degeneracy line  $U = 2|J|$  in the lower left corner as marked by black 'canceling' lines. (b) Distribution of statistical weights  $\rho_{|\phi_0\rangle}^N$  at four different interaction values  $U$  and  $J$ . (See Supplementary Note 7 for a listing of the eigenstates  $|\phi_0\rangle$  and their respective local eigenenergies  $E_n^N$ ). Red (blue) bars denote the density matrix weight of ground states in the  $N = 3$  ( $N = 2, 4$ ) particle sector, the sum of which is plotted in the last panel of a. (c) Exemplary depiction of representative lowest inverted Hund's rule eigenstates. A delocalized doublon (electron pair) fluctuates between different orbitals due to correlated pair hopping  $J$ .

are sketched in Fig. 4c. This can be seen in the last panel of Fig. 4a as the total weight of these eight states approaches one when entering the plateau of short  $\xi_0$ .

By increasing  $|J|$ , the system is driven into a strong coupling phase where local singlets are formed as Cooper pair precursors<sup>73</sup> while electronic hopping is *not* inhibited. On the contrary, hopping between the  $N = 2, 3, 4$  ground states is even facilitated via large negative  $J$ . It does so by affecting two different energy scales: Enhancing  $J < 0$  reduces the atomic gap  $\Delta_{\text{at}} = E_0^{N=4} + E_0^{N=2} - 2E_0^{N=3} = U - 2|J|$ <sup>65</sup> relevant to charge excitations and thereby supports hopping. A higher negative Hund's exchange simultaneously increases the energy  $\Delta E = 2|J|$  necessary to break up the orbital singlets within a fixed charge sector. As a result, unpaired electrons in the  $N = 3$  state become more itinerant while the local Cooper pair binding strength increases. Since the hopping is not reduced, the SC stiffness is not compromised by larger  $|J|$ . This two-faced role or Janus effect of negative Hund's exchange,

that localizes Cooper pairs but delocalizes electrons, can be understood as a competition of a Mott and a charge disproportionated insulator giving way for a mixed-valence metallic state in between<sup>78</sup>.

Correspondingly, as the superconducting state at  $-J/W > 0.05$  relies on direct transitions between the local inverted Hund's ground states from filling  $N = 3$  to  $N = 2$  and  $N = 4$ , the local Hubbard repulsion  $U$  has to fulfill two requirements for superconductivity with appreciable critical temperatures. First, significant occupation of the  $N = 2$  and  $4$  states at half-filling requires that  $U$  is not too large. Otherwise, the system turns Mott insulating (around  $U/W \gtrsim 1.6$  for enhanced  $|J|$ ) and the SC phase stiffness is reduced upon increasing  $U$  towards the Mott limit. At the same time, a significant amount of statistical weight of the  $N = 3$  states demands that  $U$  must not be too small either. We find that  $\Delta_{\text{at}} > 0$  and thus  $U > 2|J|$  is necessary for robust SC pairing. At  $\Delta_{\text{at}} < 0$  there is a predominance of  $N = 2$  and  $4$  states, which couple kinetically



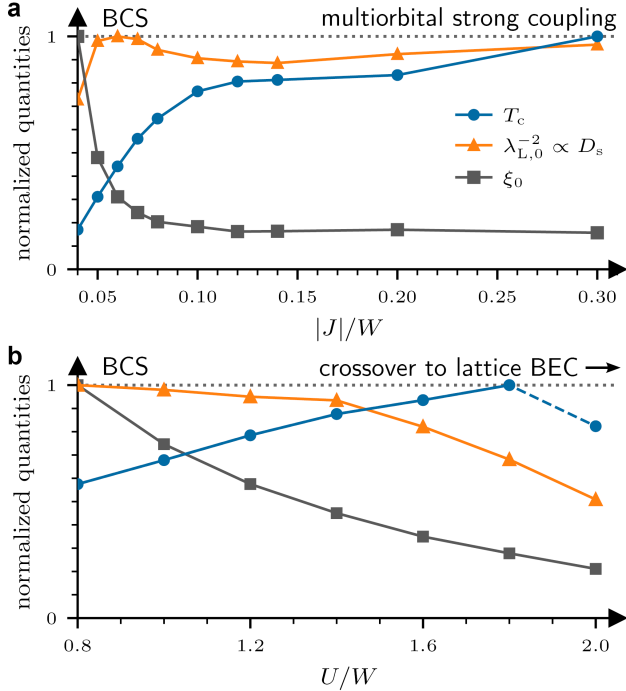


**Fig. 5 | Crossover of superconducting properties between different interaction regimes in the  $A_3C_{60}$  model.** Critical temperature  $T_c$ , coherence length  $\xi_0$ , and stiffness  $D_s \propto \lambda_{L,0}^{-2}$  when approaching the multiorbital strong coupling state as function of  $|J|/W$  at fixed  $U/W = 0.8$  (a) and when approaching the Mott insulating state as function of  $U/W$  at fixed  $J/W = -0.04$  (b). To indicate a general trend, each quantity is normalized to its maximal value within the line cut. The phenomenology of the SC regimes resembles the BCS to lattice BEC crossover in the latter case (b), which is distinct from the multiorbital strong coupling case (a) (c.f. summary listed in Table 1). Note that the  $T_c$  at  $U/W = 2$  in (b) corresponds to the transition from a Mott insulating state instead of a metallic phase, as visually differentiated by a dashed connecting line.

only in second-order processes and which are susceptible to charge disproportionation<sup>78</sup>. Our analysis shows that a sweet spot for a robust SC state with high phase stiffness and large  $T_c$  exists for  $|J|$  approaching  $U/2$ .

## DISCUSSION

We summarize the overall change from a weak-coupling BCS state to the multiorbital strong coupling SC state characterized by  $T_c$ ,  $\xi_0$  and  $D_s \propto \lambda_{L,0}^{-2}$  upon enhancing  $|J|$  in Fig. 5a and contrast it with the lattice BCS-BEC phenomenology in Table 1. Behavior as in the lattice BCS-BEC crossover can be found upon approaching the MI state (Fig. 5b), where strong local repulsion  $U$  decreases  $\xi_0$  and superconductivity compromises stiffness. As discussed above, we cannot observe a proper  $T_c$  dome that is seen in the experimental phase diagram due to the MI state dominating over the SC state in our calculations for fixed  $J/W = -0.04$ <sup>34,63,64</sup>. However, an additional analysis of the SC gap  $\Delta$  and coupling strength in Supple-

mentary Note 6 indicates that our calculations are indeed in the vicinity of the crossover region. Diagonally traversing the  $(U, J)$  interaction plane by increasing  $U$  for  $J = -\gamma U$  ( $\gamma \leq 0.5$ ) leads to a similar conclusion, although a  $T_c$  dome can emerge more easily<sup>69</sup> as charge excitations controlled by  $\Delta_{at}$  are suppressed at a slower pace.

Thus, two distinct localized SC states exist in the multiorbital model  $A_3C_{60}$  – one facilitated by local Hubbard repulsion  $U$  and the other by enhanced inverted Hund’s coupling  $|J|$ . One might speculate under which conditions THz driving or more generally photoexcitation<sup>15,17,18,36</sup> could enhance  $|J|$  and steer  $A_3C_{60}$  into this high- $T_c$  and short- $\xi_0$  strong coupling region, e.g., via quasiparticle trapping or displacive metastability<sup>79</sup>. Further experimental characterization via observables susceptible to changes in  $\xi_0$  and  $\lambda_L$ , like critical fields, currents (see Supplementary Note 1-B) or thermoelectric and thermal transport coefficients<sup>8,14</sup>, can lash down the possibility of this scenario. Twisted bilayer graphene might be another platform to host the mechanism proposed in this work as an inverted Hund’s pairing similar to that in  $A_3C_{60}$  is currently under discussion<sup>80–82</sup>.

On general grounds, the bypassing of the usual lattice BCS-BEC scenario via multiorbital physics is promising for optimization of superconducting materials to achieve higher critical currents or temperatures. Generally, limits of accessible  $T_c$  are unknown with so far only a rigorous boundary existing for two-dimensional (2D) systems<sup>83,84</sup>. An empirical upper bound to  $T_c$  emerges from the Uemura classification<sup>5–8</sup> which compares  $T_c$  to the Fermi temperature  $T_F = E_F/k_B \propto D_s$ : the temperature  $T_{BEC}^{3D} = T_F/4.6$  of a three-dimensional (3D) non-interacting BEC. Most superconducting materials, including cuprate materials with the highest known  $T_c$  at ambient conditions, however, are not even close to this boundary; typically,  $T_c/T_{BEC} = 0.1–0.2$  for unconventional superconductors. Notable exceptions are monolayer FeSe<sup>85</sup> ( $T_c/T_{BEC} = 0.43$ ), twisted graphitic systems<sup>26,80</sup> ( $T_c/T_{BEC} \sim 0.37–0.57$ ), and 2D semiconductors at low carrier densities<sup>25</sup> ( $T_c/T_{BEC} \sim 0.36–0.56$ ) which all reach close to the 2D boundary  $T_{c,lim}^{2D}/T_{BEC}^{3D} \approx 0.575$ <sup>83</sup>. Only ultracold Fermi gases can be tuned very close to the optimal  $T_{BEC}$ <sup>23,24</sup>.

The empirical limitations of  $T_c$  in most unconventional superconductors with rather high densities make sense from the standpoint and constraints of the lattice BCS-BEC crossover. In this picture, high densities seem favorable for reaching high  $T_c$  as electrons can reach high intrinsic energy scales. Yet, lattice effects and their negative impact on the kinetic energy of superconducting carriers become also more pronounced, preventing  $T_c$  to reach  $T_{BEC}$ . Possible routes to evade these constraints include quantum geometric and hybridization related band structure effects<sup>86–94</sup> as well as the multiorbital Hund’s interaction effects triggering substantial localized stiffness uncovered here.

We emphasize that the framework to calculate the coherence length  $\xi_0$  and the London penetration depth  $\lambda_L$  introduced in this work can be implemented in any Green function or density functional based approach to superconductivity without significant increase of the numerical complexity. Thus, our work opens the gate for “in silico” superconducting materi-

**Table 1 | Characteristics of the BCS, crossover to lattice BEC, and multiorbital strong coupling limits.** Behavior of the critical temperature  $T_c$ , coherence length  $\xi_0$ , superconducting stiffness  $D_s$ , and the ratio of superconducting gap  $\Delta$  to the Fermi energy  $E_F$  (coupling strength) in the BCS, crossover to lattice BEC<sup>24</sup> and “multiorbital strong coupling” limit. We indicate in the last row where we can find the respective behavior in the interaction plane of the  $A_3C_{60}$  model. We do not observe the deep BEC limit for large  $U/W$  and small  $J/W$ , but signatures indicating the onset of the BCS-BEC crossover (c.f. Figs. 4a and 5 as well as Supplementary Note 6).

	<b>BCS limit</b>	<b>Crossover to lattice BEC limit</b>	<b>Multiorbital strong coupling</b>
$T_c$	Increase with pairing interaction, $T_c \propto \Delta(T=0)$	Decrease with pairing interaction, $T_c \propto D_s$	Increase with pairing interaction, $T_c \propto \Delta, D_s$
$\xi_0$	Long ( $\xi_0 \gg a$ )	Short ( $\xi_0 \gtrsim a$ ) increasing in (deep) BEC limit	Short ( $\xi_0 \sim a$ ) constant with pairing interaction
$D_s \propto \lambda_L^{-2}$	Constant with pairing interaction	Decreasing with pairing interaction	Increasing/constant with pairing interaction
$\Delta/E_F$	Small value ( $\Delta/E_F \ll 1$ )	Large value ( $\Delta/E_F \gtrsim 1$ )	Intermediate value ( $\Delta/E_F \sim O(0.1)$ )
<b>Corresponding (<math>U, J</math>) region</b>	$\sim$ small $U/W$ $\sim$ small $ J /W$	Onset at $\sim$ large $U/W$	$\sim$ small to intermediate $U/W$ $\sim$ large $ J /W,  J /U < 1/2$

als’ optimization targeting not only  $T_c$  but also  $\xi_0$  and  $\lambda_L$ . On a more fundamental level, availability of  $\xi_0$  and  $\lambda_L$  rather than  $T_c$  alone can provide more constraints on possible pairing mechanisms through more rigorous theory-experiment comparisons, particularly in the domain of superconductors with strong electronic correlations.

## METHODS

### Dynamical mean-field theory under the constraint of finite-momentum pairing

We study the multiorbital interacting model  $H_{\text{kin}} + H_{\text{int}}$  of  $A_3C_{60}$  using Dynamical Mean-Field theory (DMFT) in Nambu space under the constraint of finite-momentum pairing (FMP). In DMFT, the lattice model is mapped onto a single Anderson impurity problem with a self-consistent electronic bath that can be solved numerically exactly. The self-energy becomes purely local  $\Sigma_{ij}(i\omega_n) = \delta_{ij}\Sigma(i\omega_n)$  capturing all local correlation effects. To this end, we have to solve the following set of self-consistent equations

$$\left\{ \begin{array}{l} \underline{G}_{\text{loc}}(i\omega_n) = \frac{1}{N_{\mathbf{k}}} \sum_{\mathbf{k}} \underline{G}_{\mathbf{k}}(i\omega_n) \\ \quad = \frac{1}{N_{\mathbf{k}}} \sum_{\mathbf{k}} \left[ (i\omega_n + \mu)\mathbb{1} - \underline{h}(\mathbf{k}) - \underline{\Sigma}(i\omega_n) \right]^{-1} \\ \underline{G}_{\text{W}}^{-1}(i\omega_n) = \underline{G}_{\text{loc}}^{-1}(i\omega_n) + \underline{\Sigma}(i\omega_n) \\ \underline{\Sigma}(i\omega_n) = \underline{G}_{\text{W}}^{-1}(i\omega_n) - \underline{G}_{\text{imp}}^{-1}(i\omega_n) \end{array} \right. \quad (9)$$

in DMFT<sup>49</sup>. Here, the local Green function  $G_{\text{loc}}$  is obtained from the lattice Green function  $G_{\mathbf{k}}$  (first line) in order to construct the impurity problem by calculating the Weiss field  $G_{\text{W}}$  (second line). Solving the impurity problem yields the impurity Green function  $G_{\text{imp}}$  from which the self-energy  $\Sigma$  is derived (third line). Underlined quantities denote matrices with respect to orbital indices ( $\alpha$ ),  $\mathbb{1}$  is the unit matrix in orbital space,  $\omega_n = (2n+1)\pi T$  denote Matsubara frequencies,  $h_{\alpha\gamma}(\mathbf{k}) = \sum_j t_{\alpha\gamma}(\mathbf{R}_j) e^{ik\mathbf{R}_j}$  is the Fourier transform of the hopping matrix in Eq. (8),  $\mu$  indicates the chemical potential, and  $N_{\mathbf{k}}$  is the number of  $\mathbf{k}$ -points in the momentum mesh. Convergence of the self-consistency problem is reached when the equality  $\underline{G}_{\text{loc}}(i\omega_n) = \underline{G}_{\text{imp}}(i\omega_n)$  holds.

We can study superconductivity directly in the symmetry-broken phase by extending the formalism to Nambu-Gor’kov space. The Nambu-Gor’kov function under the constraint of FMP (c.f. Eq. (4)) on Matsubara frequencies

$$\left[ \underline{\mathcal{G}}_{\mathbf{q}}(i\omega_n, \mathbf{k}) \right]^{-1} = \begin{pmatrix} (i\omega_n + \mu)\mathbb{1} - \underline{h}(\mathbf{k} + \frac{\mathbf{q}}{2}) - \underline{\Sigma}^{\text{N}}(i\omega_n) & -\underline{\Sigma}^{\text{AN}}(i\omega_n) \\ -\underline{\Sigma}^{\text{AN}}(i\omega_n) & (i\omega_n - \mu)\mathbb{1} + \underline{h}(-\mathbf{k} + \frac{\mathbf{q}}{2}) + [\underline{\Sigma}^{\text{N}}]^*(i\omega_n) \end{pmatrix} \quad (10)$$

then takes the place of the lattice Green function  $\underline{G}_{\mathbf{k}}(i\omega_n) \mapsto \underline{\mathcal{G}}_q(i\omega_n, \mathbf{k})$  in the self-consistency cycle in Eq. (9). In addition to the normal component  $\Sigma^N \equiv \Sigma$ , the self-energy gains an anomalous matrix element  $\Sigma^{\text{AN}}$  for which the gauge is chosen such that it is real-valued.

We use a  $35 \times 35 \times 35$   $\mathbf{k}$ -mesh and 43200 Matsubara frequencies to set up the lattice Green function in the DMFT loop. In order to solve the local impurity problem, we use a continuous-time quantum Monte Carlo (CT-QMC) solver<sup>95</sup> based on the strong coupling expansion in the hybridization function (CT-HYB)<sup>96</sup>. Details on the implementation can be found in Refs.<sup>63,64</sup>. Depending on calculation parameters ( $T, U, J$ ) and proximity to the superconducting transition, we perform between  $2.4 \times 10^6$  up to  $19.2 \times 10^6$  Monte Carlo sweeps and use a Legendre expansion with 50 up to 80 basis functions. Some calculations very close to the onset of the superconducting phase transition (depending on  $T$  or  $q$ ) needed more than 200 DMFT iterations until convergence. We average 10 or more converged DMFT iterations and calculate the mean value and standard deviation in order to estimate the uncertainty of the order parameter originating from the statistical noise of the QMC simulation.

Further details on code implementation are given in Supplementary Note 4. It entails a comparison of finite-momentum pairing to the zero-momentum case<sup>49</sup> in the Nambu-Gor'kov formalism, an explanation on the readjustment of the chemical potential  $\mu$  to fix the electron filling, and a simplification of the Matsubara sum for calculating  $\hat{j}_q$  in Eq. (6).

#### ACKNOWLEDGMENTS

We thank M. Capone, A. Cavalleri, M. Eckstein, M. Katnelson, Y. Iwasa, L. Mathey, T. Nomoto, G. Rai, S. Ryee,

A. Toschi, and P. Werner for fruitful discussions.

N.W., A.I.L., and T.W. acknowledge funding by the Cluster of Excellence ‘CUI: Advanced Imaging of Matter’ of the Deutsche Forschungsgemeinschaft (DFG) (EXC 2056, Project ID 390715994) and the DFG research unit FOR 5249 (‘QUAST’, Project No. 449872909). Y.N. is grateful to funding via JSPS KAKENHI (No. JP23H04869 and JP21H01041). R.A. acknowledges funding by JSPS KAKENHI (No. JP24H00190). A.I.L. is supported by the European Research Council via Synergy Grant 854843 - FAST-CORR. The authors gratefully acknowledge the computing time granted by the Resource Allocation Board under the project hhp00056 and provided on the supercomputer Lise at NHR@ZIB as part of the NHR infrastructure. Additional calculations were performed on the Physnet cluster at the University of Hamburg.

**Author contributions:** N.W. performed the calculations, prepared the figures and wrote the manuscript with input from all authors. Y.N. and R.A. provided the code for the DMFT calculations of the  $A_3C_{60}$  model which A.I.L. and N.W. modified to include FMP. N.W. and S.B. analyzed the GL formulation of the FMP constraint. All authors discussed the results and physical implications. T.W., A.I.L., and N.W. conceived the project. T.W. supervised the project.

**Competing interests:** All authors declare that they have no competing interests.

**Data availability:** The data that support the findings of this study are available from the corresponding author upon reasonable request.

- 
1. Y. Tokura, M. Kawasaki, and N. Nagaosa, Emergent functions of quantum materials, *Nature Physics* **13**, 1056 (2017).
  2. C. Yao and Y. Ma, Superconducting materials: Challenges and opportunities for large-scale applications, *iScience* **24**, 102541 (2021).
  3. R. Shimano and N. Tsuji, Higgs Mode in Superconductors, *Annual Review of Condensed Matter Physics* **11**, 103 (2020).
  4. P. Coleman, *Introduction to Many-Body Physics* (Cambridge University Press, 2008).
  5. Y. J. Uemura, G. M. Luke, B. J. Sternlieb, J. H. Brewer, J. F. Carolan, W. N. Hardy, R. Kadono, J. R. Kempton, R. F. Kiefl, S. R. Kretzman, P. Mulhern, T. M. Riseman, D. L. Williams, B. X. Yang, S. Uchida, H. Takagi, J. Gopalakrishnan, A. W. Sleight, M. A. Subramanian, C. L. Chien, M. Z. Cieplak, G. Xiao, V. Y. Lee, B. W. Statt, C. E. Stronach, W. J. Kossler, and X. H. Yu, Universal Correlations between  $T_c$  and  $n_s/m^*$  (Carrier Density over Effective Mass) in High- $T_c$  Cuprate Superconductors, *Physical Review Letters* **62**, 2317 (1989).
  6. Y. J. Uemura, L. P. Le, G. M. Luke, B. J. Sternlieb, W. D. Wu, J. H. Brewer, T. M. Riseman, C. L. Seaman, M. B. Maple, M. Ishikawa, D. G. Hinks, J. D. Jorgensen, G. Saito, and H. Yamochi, Basic similarities among cuprate, bismuthate, organic, Chevrel-phase, and heavy-fermion superconductors shown by penetration-depth measurements, *Physical Review Letters* **66**, 2665 (1991).
  7. Y. J. Uemura, A. Keren, L. P. Le, G. M. Luke, B. J. Sternlieb, W. D. Wu, J. H. Brewer, R. L. Whetten, S. M. Huang, S. Lin, R. B. Kaner, F. Diederich, S. Donovan, G. Grüner, and K. Holczner, Magnetic-field penetration depth in  $K_3C_{60}$  measured by muon spin relaxation, *Nature* **352**, 605 (1991).
  8. Y. J. Uemura, Dynamic superconductivity responses in photoexcited optical conductivity and Nernst effect, *Physical Review Materials* **3**, 104801 (2019).
  9. V. J. Emery and S. A. Kivelson, Importance of phase fluctuations in superconductors with small superfluid density, *Nature* **374**, 434 (1995).
  10. T. Timusk and B. Statt, The pseudogap in high-temperature superconductors: an experimental survey, *Reports on Progress in Physics* **62**, 61 (1999).
  11. M. R. Norman, D. Pines, and C. Kallin, The pseudogap: friend or foe of high  $T_c$ ?, *Advances in Physics* **54**, 715 (2005).
  12. P. A. Lee, N. Nagaosa, and X.-G. Wen, Doping a Mott insulator: Physics of high-temperature superconductivity, *Reviews of Modern Physics* **78**, 17 (2006).

13. O. Gunnarsson, T. Schäfer, J. LeBlanc, E. Gull, J. Merino, G. Sangiovanni, G. Rohringer, and A. Toschi, Fluctuation Diagnostics of the Electron Self-Energy: Origin of the Pseudogap Physics, *Physical Review Letters* **114**, 236402 (2015).
14. I. Ussishkin, S. L. Sondhi, and D. A. Huse, Gaussian Superconducting Fluctuations, Thermal Transport, and the Nernst Effect, *Physical Review Letters* **89**, 287001 (2002).
15. G. Jotzu, G. Meier, A. Cantaluppi, A. Cavalleri, D. Pontiroli, M. Riccò, A. Ardavan, and M.-S. Nam, Superconducting Fluctuations Observed Far above  $T_C$  in the Isotropic Superconductor  $K_3C_{60}$ , *Physical Review X* **13**, 021008 (2023).
16. D. Fausti, R. I. Tobey, N. Dean, S. Kaiser, A. Dienst, M. C. Hoffmann, S. Pyon, T. Takayama, H. Takagi, and A. Cavalleri, Light-Induced Superconductivity in a Stripe-Ordered Cuprate, *Science* **331**, 189 (2011).
17. M. Mitrano, A. Cantaluppi, D. Nicoletti, S. Kaiser, A. Perucchi, S. Lupi, P. D. Pietro, D. Pontiroli, M. Riccò, S. R. Clark, D. Jaksch, and A. Cavalleri, Possible light-induced superconductivity in  $K_3C_{60}$  at high temperature, *Nature* **530**, 461 (2016).
18. E. Rowe, B. Yuan, M. Buzzi, G. Jotzu, Y. Zhu, M. Fechner, M. Först, B. Liu, D. Pontiroli, M. Riccò, and A. Cavalleri, Resonant enhancement of photo-induced superconductivity in  $K_3C_{60}$ , *Nature Physics* **19**, 1821 (2023).
19. A. Cavalleri, Photo-induced superconductivity, *Contemporary Physics* **59**, 31 (2017).
20. A. J. Leggett, Diatomic molecules and cooper pairs, in *Modern Trends in the Theory of Condensed Matter*, Lecture Notes in Physics, Vol. 115, edited by J. A. P. Andrzej Pękalski (Springer Berlin Heidelberg, 1980) pp. 13–27.
21. P. Nozières and S. Schmitt-Rink, Bose condensation in an attractive fermion gas: From weak to strong coupling superconductivity, *Journal of Low Temperature Physics* **59**, 195 (1985).
22. C. A. R. Sá de Melo, When fermions become bosons: Pairing in ultracold gases, *Physics Today* **61**, 45 (2008).
23. M. Randeria and E. Taylor, Crossover from Bardeen-Cooper-Schrieffer to Bose-Einstein Condensation and the Unitary Fermi Gas, *Annual Review of Condensed Matter Physics* **5**, 209 (2014).
24. Q. Chen, Z. Wang, R. Boyack, S. Yang, and K. Levin, When superconductivity crosses over: From BCS to BEC, *Reviews of Modern Physics* **96**, 025002 (2024).
25. Y. Nakagawa, Y. Kasahara, T. Nomoto, R. Arita, T. Nojima, and Y. Iwasa, Gate-controlled BCS-BEC crossover in a two-dimensional superconductor, *Science* **372**, 190 (2021).
26. J. M. Park, Y. Cao, K. Watanabe, T. Taniguchi, and P. Jarillo-Herrero, Tunable strongly coupled superconductivity in magic-angle twisted trilayer graphene, *Nature* **590**, 249 (2021).
27. Y. Suzuki, K. Wakamatsu, J. Ibuka, H. Oike, T. Fujii, K. Miyagawa, H. Taniguchi, and K. Kanoda, Mott-Driven BEC-BCS Crossover in a Doped Spin Liquid Candidate  $\kappa$ -(BEDT-TTF) $_4$ Hg $_{2.89}$ Br $_8$ , *Physical Review X* **12**, 011016 (2022).
28. J. Sous, Y. He, and S. A. Kivelson, Absence of a BCS-BEC crossover in the cuprate superconductors, *npj Quantum Materials* **8**, 25 (2023).
29. Q. Chen, Z. Wang, R. Boyack, and K. Levin, Test for BCS-BEC crossover in the cuprate superconductors, *npj Quantum Materials* **9**, 27 (2024).
30. Y. Mizukami, M. Haze, O. Tanaka, K. Matsuura, D. Sano, J. Böker, I. Eremin, S. Kasahara, Y. Matsuda, and T. Shibauchi, Unusual crossover from Bardeen-Cooper-Schrieffer to Bose-Einstein-condensate superconductivity in iron chalcogenides, *Communications Physics* **6**, 183 (2023).
31. C. A. R. Sá de Melo, M. Randeria, and J. R. Engelbrecht, Crossover from BCS to Bose superconductivity: Transition temperature and time-dependent Ginzburg-Landau theory, *Physical Review Letters* **71**, 3202 (1993).
32. A. F. Hebard, M. J. Rosseinsky, R. C. Haddon, D. W. Murphy, S. H. Glarum, T. T. M. Palstra, A. P. Ramirez, and A. R. Kortan, Superconductivity at 18 K in potassium-doped  $C_{60}$ , *Nature* **350**, 600 (1991).
33. A. Y. Ganin, Y. Takabayashi, P. Jeglič, D. Arčon, A. Potočnik, P. J. Baker, Y. Ohishi, M. T. McDonald, M. D. Tzirakis, A. McLennan, G. R. Darling, M. Takata, M. J. Rosseinsky, and K. Prassides, Polymorphism control of superconductivity and magnetism in  $Cs_3C_{60}$  close to the Mott transition, *Nature* **466**, 221 (2010).
34. R. H. Zadik, Y. Takabayashi, G. Klupp, R. H. Colman, A. Y. Ganin, A. Potočnik, P. Jeglič, D. Arčon, P. Matus, K. Kamarás, Y. Kasahara, Y. Iwasa, A. N. Fitch, Y. Ohishi, G. Garbarino, K. Kato, M. J. Rosseinsky, and K. Prassides, Optimized unconventional superconductivity in a molecular Jahn-Teller metal, *Science Advances* **1**, e150005 (2015).
35. A. P. Ramirez, Superconductivity in alkali-doped  $C_{60}$ , *Physica C: Superconductivity and its Applications* **514**, 166 (2015).
36. M. Budden, T. Gebert, M. Buzzi, G. Jotzu, E. Wang, T. Matsuyama, G. Meier, Y. Laplace, D. Pontiroli, M. Riccò, F. Schlawin, D. Jaksch, and A. Cavalleri, Evidence for metastable photo-induced superconductivity in  $K_3C_{60}$ , *Nature Physics* **17**, 611 (2021).
37. J. Bardeen, L. N. Cooper, and J. R. Schrieffer, Theory of Superconductivity, *Physical Review* **108**, 1175 (1957).
38. M. Tinkham, *Introduction to superconductivity*, 2nd ed. (Dover Publications, 2004).
39. P. B. Allen, Theory of superconducting transition temperature, pair susceptibility, and coherence length, in *Modern Trends in the Theory of Condensed Matter*, edited by A. Pękalski and J. A. Przystawa (Springer Berlin Heidelberg, 2008) pp. 388–413.
40. A. Toschi, M. Capone, and C. Castellani, Energetic balance of the superconducting transition across the BCS—Bose Einstein crossover in the attractive Hubbard model, *Physical Review B* **72**, 235118 (2005).
41. C. Yue, S. Hoshino, A. Koga, and P. Werner, Unconventional pairing from local orbital fluctuations in strongly correlated  $A_3C_{60}$ , *Physical Review B* **104**, 075107 (2021).
42. E. Gull and A. J. Millis, Superconducting and pseudogap effects on the interplane conductivity and Raman scattering cross section in the two-dimensional Hubbard model, *Physical Review B* **88**, 075127 (2013).
43. O. Simard, C.-D. Hébert, A. Foley, D. Sénéchal, and A.-M. S. Tremblay, Superfluid stiffness in cuprates: Effect of Mott transition and phase competition, *Physical Review B* **100**, 094506 (2019).
44. M. Harland, S. Brener, A. I. Lichtenstein, and M. I. Katsnelson, Josephson lattice model for phase fluctuations of local pairs in copper oxide superconductors, *Physical Review B* **100**, 024510 (2019).
45. L. Liang, T. I. Vanhala, S. Peotta, T. Siro, A. Harju, and P. Törmä, Band geometry, Berry curvature, and superfluid weight, *Physical Review B* **95**, 024515 (2017).
46. A. I. Lichtenstein, M. I. Katsnelson, and V. A. Gubanov, Exchange interactions and spin-wave stiffness in ferromagnetic metals, *Journal of Physics F: Metal Physics* **14**, L125 (1984).
47. M. Fleck, A. I. Lichtenstein, A. M. Oleś, L. Hedin, and V. I. Anisimov, Dynamical Mean-Field Theory for Doped Antiferromagnets, *Physical Review Letters* **80**, 2393 (1998).
48. L. M. Sandratskii, Noncollinear magnetism in itinerant-electron systems: Theory and applications, *Advances in Physics* **47**, 91 (1998).

49. A. Georges, G. Kotliar, W. Krauth, and M. J. Rozenberg, Dynamical mean-field theory of strongly correlated fermion systems and the limit of infinite dimensions, *Reviews of Modern Physics* **68**, 13 (1996).
50. A. Q. Chen, M. J. Park, S. T. Gill, Y. Xiao, D. Reig-i Plessis, G. J. MacDougall, M. J. Gilbert, and N. Mason, Finite momentum Cooper pairing in three-dimensional topological insulator Josephson junctions, *Nature Communications* **9**, 3478 (2018).
51. D. Zhao, L. Debbeler, M. Kühne, S. Fecher, N. Gross, and J. Smet, Evidence of finite-momentum pairing in a centrosymmetric bilayer, *Nature Physics* **19**, 1599 (2023).
52. P. Wan, O. Zheliuk, N. F. Q. Yuan, X. Peng, L. Zhang, M. Liang, U. Zeitler, S. Wiedmann, N. E. Hussey, T. T. M. Palstra, and J. Ye, Orbital Fulde-Ferrell-Larkin-Ovchinnikov state in an Ising superconductor, *Nature* **619**, 46 (2023).
53. N. F. Q. Yuan and L. Fu, Supercurrent diode effect and finite-momentum superconductors, *Proceedings of the National Academy of Sciences* **119**, e2119548119 (2022).
54. S.-B. Zhang, L.-H. Hu, and T. Neupert, Finite-momentum Cooper pairing in proximitized altermagnets, *Nature Communications* **15**, 1801 (2024).
55. P. Fulde and R. A. Ferrell, Superconductivity in a Strong Spin-Exchange Field, *Physical Review* **135**, A550 (1964).
56. A. I. Larkin and Y. N. Ovchinnikov, Nonuniform state of superconductors, *Zh. Eksp. Teor. Fiz.* **47**, 1136 (1964).
57. J. J. Kinnunen, J. E. Baarsma, J.-P. Martikainen, and P. Törmä, The Fulde-Ferrell-Larkin-Ovchinnikov state for ultracold fermions in lattice and harmonic potentials: a review, *Reports on Progress in Physics* **81**, 046401 (2018).
58. D. F. Agterberg, J. S. Davis, S. D. Edkins, E. Fradkin, D. J. V. Harlingen, S. A. Kivelson, P. A. Lee, L. Radzihovsky, J. M. Tranquada, and Y. Wang, The Physics of Pair-Density Waves: Cuprate Superconductors and Beyond, *Annual Review of Condensed Matter Physics* **11**, 231 (2020).
59. K. Xu, P. Cao, and J. R. Heath, Achieving the Theoretical Depairing Current Limit in Superconducting Nanomesh Films, *Nano Letters* **10**, 4206 (2010).
60. M. E. Fisher, M. N. Barber, and D. Jasnow, Helicity Modulus, Superfluidity, and Scaling in Isotropic Systems, *Physical Review A* **8**, 1111 (1973).
61. M. Capone, M. Fabrizio, C. Castellani, and E. Tosatti, Strongly Correlated Superconductivity, *Science* **296**, 2364 (2002).
62. M. Capone, M. Fabrizio, C. Castellani, and E. Tosatti, Colloquium: Modeling the unconventional superconducting properties of expanded  $A_3C_{60}$  fullerides, *Reviews of Modern Physics* **81**, 943 (2009).
63. Y. Nomura, S. Sakai, M. Capone, and R. Arita, Unified understanding of superconductivity and Mott transition in alkali-doped fullerides from first principles, *Science Advances* **1**, e1500568 (2015).
64. Y. Nomura, S. Sakai, M. Capone, and R. Arita, Exotic *s*-wave superconductivity in alkali-doped fullerides, *Journal of Physics: Condensed Matter* **28**, 153001 (2016).
65. A. Georges, L. de' Medici, and J. Mravlje, Strong Correlations from Hund's Coupling, *Annual Review of Condensed Matter Physics* **4**, 137 (2013).
66. L. de' Medici, Hund's coupling and its key role in tuning multiorbital correlations, *Physical Review B* **83**, 205112 (2011).
67. Y. Ihara, H. Alloul, P. Wzietek, D. Pontiroli, M. Mazzani, and M. Riccò, NMR study of the mott transitions to superconductivity in the two  $Cs_3C_{60}$ , *Physical Review Letters* **104**, 256402 (2010).
68. S. Suzuki, S. Okada, and K. Nakao, Theoretical Study on the Superconductivity Induced by the Dynamic Jahn-Teller Effect in Alkali-Metal-Doped  $C_{60}$ , *Journal of the Physical Society of Japan* **69**, 2615 (2000).
69. S. Hoshino and P. Werner, Spontaneous Orbital-Selective Mott Transitions and the Jahn-Teller Metal of  $A_3C_{60}$ , *Physical Review Letters* **118**, 177002 (2017).
70. S. Hoshino, P. Werner, and R. Arita, Unconventional orbital ordering and emergent dimensional reduction in fulleride superconductors, *Physical Review B* **99**, 235133 (2019).
71. M. Capone, M. Fabrizio, and E. Tosatti, Direct transition between a Singlet Mott Insulator and a Superconductor, *Physical Review Letters* **86**, 5361 (2001).
72. A. Koga and P. Werner, Superconductivity in the two-band Hubbard model, *Physical Review B* **91**, 085108 (2015).
73. J. E. Han, O. Gunnarsson, and V. H. Crespi, Strong Superconductivity with Local Jahn-Teller Phonons in  $C_{60}$  Solids, *Physical Review Letters* **90**, 167006 (2003).
74. Y. Nomura and R. Arita, *Ab initio* downfolding for electron-phonon-coupled systems: Constrained density-functional perturbation theory, *Physical Review B* **92**, 245108 (2015).
75. Y. Nomura, K. Nakamura, and R. Arita, *Ab initio* derivation of electronic low-energy models for  $C_{60}$  and aromatic compounds, *Physical Review B* **85**, 155452 (2012).
76. Y. Kasahara, Y. Takeuchi, R. H. Zadik, Y. Takabayashi, R. H. Colman, R. D. McDonald, M. J. Rosseinsky, K. Prassides, and Y. Iwasa, Upper critical field reaches 90 tesla near the Mott transition in fulleride superconductors, *Nature Communications* **8**, 14467 (2017).
77. O. Gunnarsson, Superconductivity in fullerides, *Reviews of Modern Physics* **69**, 575 (1997).
78. A. Isidori, M. Berović, L. Fanfarillo, L. de' Medici, M. Fabrizio, and M. Capone, Charge Disproportionation, Mixed Valence, and Janus Effect in Multiorbital Systems: A Tale of Two Insulators, *Physical Review Letters* **122**, 186401 (2019).
79. S. Chattopadhyay, C. J. Eckhardt, D. M. Kennes, M. A. Sentef, D. Shin, A. Rubio, A. Cavalleri, E. A. Demler, and M. H. Michael, Mechanisms for Long-Lived, Photo-Induced Superconductivity, (2023), arXiv:2303.15355.
80. Y. Cao, V. Fatemi, S. Fang, K. Watanabe, T. Taniguchi, E. Kaxiras, and P. Jarillo-Herrero, Unconventional superconductivity in magic-angle graphene superlattices, *Nature* **556**, 43 (2018).
81. J. F. Dodaro, S. A. Kivelson, Y. Schattner, X. Q. Sun, and C. Wang, Phases of a phenomenological model of twisted bilayer graphene, *Physical Review B* **98**, 075154 (2018).
82. Y.-J. Wang, G.-D. Zhou, S.-Y. Peng, B. Lian, and Z.-D. Song, Molecular Pairing in Twisted Bilayer Graphene Superconductivity, (2024), arXiv:2402.00869.
83. T. Hazra, N. Verma, and M. Randeria, Bounds on the Superconducting Transition Temperature: Applications to Twisted Bilayer Graphene and Cold Atoms, *Physical Review X* **9**, 031049 (2019).
84. T. Shi, W. Zhang, and C. A. R. S. de Melo, Tighter upper bounds on the critical temperature of two-dimensional superconductors and superfluids from the BCS to the Bose regime, (2023), arXiv:2303.10939.
85. Q.-Y. Wang, Z. Li, W.-H. Zhang, Z.-C. Zhang, J.-S. Zhang, W. Li, H. Ding, Y.-B. Ou, P. Deng, K. Chang, J. Wen, C.-L. Song, K. He, J.-F. Jia, S.-H. Ji, Y.-Y. Wang, L.-L. Wang, X. Chen, X.-C. Ma, and Q.-K. Xue, Interface-Induced High-Temperature Superconductivity in Single Unit-Cell FeSe Films on  $SrTiO_3$ , *Chinese Physics Letters* **29**, 037402 (2012).
86. P. Törmä, S. Peotta, and B. A. Bernevig, Superconductivity, superfluidity and quantum geometry in twisted multilayer systems, *Nature Reviews Physics* **4**, 528 (2022).
87. J. S. Hofmann, D. Chowdhury, S. A. Kivelson, and E. Berg,

- Heuristic bounds on superconductivity and how to exceed them, *npj Quantum Materials* **7**, 10.1038/s41535-022-00491-1 (2022).
88. K. Kuroki, T. Higashida, and R. Arita, High- $T_c$  superconductivity due to coexisting wide and narrow bands: A fluctuation exchange study of the Hubbard ladder as a test case, *Physical Review B* **72**, 212509 (2005).
  89. L. Salasnich, A. A. Shanenko, A. Vagov, J. A. Aguiar, and A. Perali, Screening of pair fluctuations in superconductors with coupled shallow and deep bands: A route to higher-temperature superconductivity, *Physical Review B* **100**, 064510 (2019).
  90. A. A. Shanenko, T. T. Saraiva, A. Vagov, A. S. Vasenko, and A. Perali, Suppression of fluctuations in a two-band superconductor with a quasi-one-dimensional band, *Physical Review B* **105**, 214527 (2022).
  91. C. Yue, H. Aoki, and P. Werner, Superconductivity enhanced by pair fluctuations between wide and narrow bands, *Physical Review B* **106**, L180506 (2022).
  92. M. V. M. A. P. Sathish Kumar Paramasivam, Shakhil Ponnarassery Gangadharan, High- $T_c$  Berezinskii-Kosterlitz-Thouless transition in 2D superconducting systems with coupled deep and quasi-flat electronic bands with van Hove singularities, (2023), arXiv:2312.09017.
  93. M. Nakata, D. Ogura, H. Usui, and K. Kuroki, Finite-energy spin fluctuations as a pairing glue in systems with coexisting electron and hole bands, *Physical Review B* **95**, 214509 (2017).
  94. S. Ryee, N. Witt, and T. O. Wehling, Quenched pair breaking by interlayer correlations as a key to superconductivity in  $\text{La}_3\text{Ni}_2\text{O}_7$ , (2023), arXiv:2310.17465.
  95. E. Gull, A. J. Millis, A. I. Lichtenstein, A. N. Rubtsov, M. Troyer, and P. Werner, Continuous-time Monte Carlo methods for quantum impurity models, *Reviews of Modern Physics* **83**, 349 (2011).
  96. P. Werner, A. Comanac, L. de' Medici, M. Troyer, and A. J. Millis, Continuous-Time Solver for Quantum Impurity Models, *Physical Review Letters* **97**, 076405 (2006).
  97. D.-H. Kim, J. J. Kinnunen, J.-P. Martikainen, and P. Törmä, Exotic Superfluid States of Lattice Fermions in Elongated Traps, *Physical Review Letters* **106**, 095301 (2011).
  98. M. Heikkinen, D.-H. Kim, M. Troyer, and P. Törmä, Nonlocal Quantum Fluctuations and Fermionic Superfluidity in the Imbalanced Attractive Hubbard Model, *Physical Review Letters* **113**, 185301 (2014).
  99. A. A. Abrikosov, L. P. Gorkov, and I. E. Dzyaloshinski, *Methods of quantum field theory in statistical physics* (Dover Publications, 1975) p. 352.
  100. E. Gull and A. J. Millis, Pairing glue in the two-dimensional Hubbard model, *Physical Review B* **90**, 041110 (2014).

*Supplementary Information:*  
**Bypassing the lattice BCS-BEC crossover in  
strongly correlated superconductors through multiorbital physics**

Niklas Witt\*, Yusuke Nomura, Sergey Brener, Ryotaro Arita,  
Alexander I. Lichtenstein, Tim O. Wehling

\*Corresponding author: niklas.witt@physik.uni-hamburg.de

## Contents

<b>1</b>	<b>Phenomenological Ginzburg-Landau theory with finite-momentum pairing</b>	<b>1</b>
1-A	Order parameter and supercurrent density . . . . .	1
1-B	Relation to experimental observables . . . . .	4
<b>2</b>	<b>Generalized Bloch theorem in Nambu space</b>	<b>4</b>
<b>3</b>	<b>Derivation of the supercurrent density</b>	<b>6</b>
<b>4</b>	<b>Numerical implementation of DMFT with FMP constraint</b>	<b>8</b>
4-A	Nambu-Gor'kov formalism with finite-momentum pairing . . . . .	8
4-B	Determination of chemical potential . . . . .	11
4-C	Handling the Matsubara summation in the calculation of the current density . .	11
4-D	Lattice model details and current direction . . . . .	13
<b>5</b>	<b>Details on the calculation of <math> \Psi_q </math>, <math>\xi_0</math>, <math>j_{dp}</math>, and <math>\lambda_L</math> from DMFT</b>	<b>15</b>
5-A	Order parameter and coherence length . . . . .	15
5-B	Current density and penetration depth . . . . .	17
5-C	Proximity region to the Mott transition . . . . .	18
<b>6</b>	<b>Analysis of superconducting gap and coupling strength</b>	<b>20</b>
<b>7</b>	<b>Atomic limit of three-orbital model with inverted Hund's coupling</b>	<b>22</b>

# Supplementary Note 1: Phenomenological Ginzburg-Landau theory with finite-momentum pairing

The Ginzburg-Landau (GL) framework is a phenomenological (macroscopic) approach to the superconducting phase transition. Here, we illustrate with GL theory how introducing a FMP constraint gives access to the London penetration depth  $\lambda_L$ , coherence length  $\xi_0$ , and also the depairing current  $j_{dp}$ . The GL description with FMP has been discussed in other contexts like the superconducting diode effect [53] and Fulde-Ferrel-Larkin-Ovchinnikov (FFLO) theory [57]. Note that, as mentioned in the main text, we use the term ‘FMP’ to refer exclusively to the order parameter with a helical phase variation and constant amplitude, whereas it is sometimes also used in the context of pair density waves [56, 58] which imprint an amplitude modulation on the superconducting gap.

## 1-A Order parameter and supercurrent density

We start from the GL expansion of the free energy of the symmetry-broken state in terms of the complex superconducting order parameter (OP)  $\Psi(\mathbf{r}) = |\Psi(\mathbf{r})|e^{i\varphi(\mathbf{r})}$  close to the phase transition point  $T_c$  which reads

$$\mathcal{F}[\Psi] = \mathcal{F}_N + \int d^3r \left[ \alpha(T)|\Psi(\mathbf{r})|^2 + \frac{b}{2}|\Psi(\mathbf{r})|^4 + \frac{\hbar^2}{2m^*}|\nabla\Psi(\mathbf{r})|^2 \right] \quad (1)$$

where  $\mathcal{F}_N$  is the free energy of the normal state and  $\alpha(T) = \alpha_0(T - T_c)$  ( $\alpha_0 > 0$ ),  $b > 0$ , and  $m^*$  are the material dependent GL parameters. The GL functional encodes the two types of collective modes that emerge in the symmetry-broken state: fluctuations of the amplitude (Higgs mode) and the phase (Nambu-Goldstone mode) of the OP. The constraint of FMP means that we require the Cooper pairs to carry a finite fixed momentum  $\mathbf{q}$ , which translates to the requirement for the OP to be of the form  $\Psi_{\mathbf{q}}(\mathbf{r}) = |\Psi_{\mathbf{q}}|e^{i\mathbf{q}\cdot\mathbf{r}}$ . Then, the GL free energy density becomes

$$f_{GL}[\Psi_{\mathbf{q}}] = (\mathcal{F}[\Psi_{\mathbf{q}}] - \mathcal{F}_N)/V = \alpha|\Psi_{\mathbf{q}}|^2 + \frac{b}{2}|\Psi_{\mathbf{q}}|^4 + \frac{\hbar^2 q^2}{2m^*}|\Psi_{\mathbf{q}}|^2 \quad (2)$$

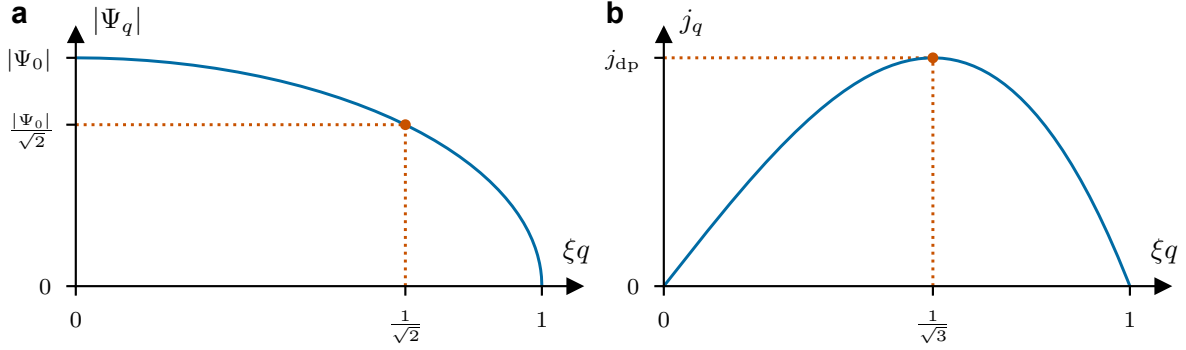
The gradient term in this expression has an associated length scale which is the temperature-dependent correlation length  $\xi(T)$  given by

$$\xi(T) = \sqrt{\frac{\hbar^2}{2m^*|\alpha|}} = \xi_0 \left(1 - \frac{T}{T_c}\right)^{-\frac{1}{2}} \quad (3)$$

with the coherence length  $\xi_0 = \hbar/\sqrt{\alpha_0 m^* T_c}$  at  $T = 0$  [4]. The system’s stationary point is calculated from

$$\frac{\delta f_{GL}}{\delta \Psi_{\mathbf{q}}^*} = 2\Psi_{\mathbf{q}} \left[ \alpha(1 - \xi^2 q^2) + b|\Psi_{\mathbf{q}}|^2 \right] \stackrel{!}{=} 0 \quad (4)$$





**Supplementary Figure 1 | Ginzburg-Landau solution for finite-momentum pairing.** Ginzburg-Landau expectation of the momentum ( $q$ )-dependent (a) order parameter modulus  $|\Psi_q|$  and (b) the concomitant supercurrent density  $j_q$  of a system under the constraint of finite-momentum pairing superconductivity in units of the correlation length  $\xi$ . We marked the characteristic length scale on which the order parameter is reduced and the point of the depairing current density  $j_{dp}$ .

which results in the  $q$ -dependence of the OP given by

$$|\Psi_q(T)|^2 = |\Psi_0(T)|^2(1 - \xi(T)^2 q^2) \quad (5)$$

with the homogeneous OP  $|\Psi_0(T)|^2 = -\alpha(T)/b \propto T - T_c$ . We plot this relation in Fig. 1a. It shows that the OP amplitude is reduced compared to the zero-momentum pairing case for any finite  $q = |q| > 0$ . This suppression is induced by the nonlinear coupling of the Higgs mode to the phase mode [3]. For some critical momentum value  $q_c$ , superconducting order breaks down completely ( $\Psi_{q_c} = 0$ ) because the kinetic energy from phase modulations exceeds the gain in energy from pairing. In GL theory, this value is given exactly by  $q_c = \xi(T)^{-1}$  (c.f. Eq. (5)). The temperature dependence of the OP and extracted  $\xi(T)$  gives access to the coherence length  $\xi_0$  via Eq. (3) (c.f. Note 5-A).

The  $q$ -dependence of the OP also connects to  $j_{dp}$ . To see this, we derive the current density in the superconducting state. For this purpose, we (briefly) introduce a vector potential  $\mathbf{A}$  via minimal coupling to the free energy [4, 53]

$$\begin{aligned} f_{GL}[\Psi_q] &= \alpha|\Psi_q|^2 + \frac{b}{2}|\Psi_q|^4 + \frac{1}{2m^*}|(i\hbar\nabla + e^*\mathbf{A})\Psi_q(\mathbf{r})|^2 \\ &= \alpha|\Psi_q|^2 + \frac{b}{2}|\Psi_q|^4 + \frac{1}{2m^*}|(\hbar^2 q^2 - 4\hbar e\mathbf{q} \cdot \mathbf{A} + 4e^2 A^2)|\Psi_q|^2 \end{aligned} \quad (6)$$

where we choose the Coulomb-gauge  $\nabla \cdot \mathbf{A} = 0$  and use  $e^* = 2e$ . We can explicitly set  $e^*$  and, in this regard, treat the charge differently to the mass  $m^*$  because  $e^*$  and  $(e^*)^2$  couple the same way to the OP, i.e., the charge of the Cooper pair is not renormalized. We obtain the steady-state

current density from the first derivative with respect to the vector potential

$$\mathbf{j} = -\left. \frac{\delta f_{\text{GL}}}{\delta \mathbf{A}} \right|_{\mathbf{A}=0} = \frac{2\hbar e}{m^*} |\Psi_q|^2 \left( \mathbf{q} - \frac{2\pi}{\Phi_0} \mathbf{A} \right) \Big|_{\mathbf{A}=0} = \frac{2\hbar e}{m^*} |\Psi_q|^2 \mathbf{q} \quad (7)$$

with the magnetic flux quantum  $\Phi_0 = h/(2e) = \pi\hbar/e$ . By inserting the OP from Eq. (5), we obtain a  $\mathbf{q}$ -dependent expression for the current density ( $T$ -dependence suppressed)

$$\mathbf{j}_q = \frac{2\hbar e}{m^*} |\Psi_0|^2 (1 - \xi^2 q^2) q \hat{\mathbf{q}} \quad (8)$$

that directly shows how the Cooper pairs carry the supercurrent with their finite center-of-mass momentum along the direction  $\hat{\mathbf{q}} = \mathbf{q}/q$ . The current density,  $j_q = |\mathbf{j}_q|$ , is a non-monotonous function of  $q$  that exhibits a maximum called depairing current,  $j_{\text{dp}}$  (c.f. Fig. 1b).  $j_{\text{dp}}$  can be explicitly calculated from  $\partial j_q / \partial q = 0$  which yields  $q_{\text{max}} = 1/(\sqrt{3}\xi)$  and

$$j_{\text{dp}} \equiv j_{q_{\text{max}}} = \frac{4}{3\sqrt{3}} \frac{\hbar e |\Psi_0|^2}{m^* \xi} \quad (9)$$

Since the supercurrent  $\mathbf{j}$  is directly related to the vector potential  $\mathbf{A}$ , it is possible to derive the London equation within GL theory. We obtain the second London equation by taking the curl of Eq. (7) with  $\mathbf{q} = 0$  such that

$$\frac{1}{\mu_0 \lambda_L^2} \mathbf{B} = -\nabla \times \mathbf{j} = \frac{4\pi\hbar e |\Psi_0|^2}{m^* \Phi_0} \nabla \times \mathbf{A} = \frac{4e^2 |\Psi_0|^2}{m^*} \mathbf{B} \quad (10)$$

Here, the London penetration depth  $\lambda_L$  is introduced which, in turn, can be reformulated to depend on the correlation length and depairing current:

$$\lambda_L(T) = \sqrt{\frac{m^*}{4\mu_0 e^2 |\Psi_0(T)|^2}} \stackrel{\text{Eq. (9)}}{=} \sqrt{\frac{\Phi_0}{3\sqrt{3}\pi\mu_0 \xi(T) j_{\text{dp}}(T)}} = \lambda_{L,0} \left( 1 - \left( \frac{T}{T_c} \right)^4 \right)^{-\frac{1}{2}} \quad (11)$$

The temperature dependence with the quartic power stated here is empirical (derived from the Gorter-Casimir model) and often used to fit experimental data [37, 38]. In Note 5-B, we show that this temperature dependence models our DMFT data better than a linear power law as assumed in GL theory.

To summarize, we obtain the correlation length  $\xi(T)$  and depairing current  $j_{\text{dp}}(T)$  from analyzing the OP  $\Psi_q(\mathbf{r}) = |\Psi_q| e^{i\mathbf{q}\cdot\mathbf{r}}$  subject to the FMP constraint. In a second step, we can derive the London penetration depth  $\lambda_L(T)$  from these two quantities. This connection also holds in microscopic theories, where we calculate the OP and current density from the Nambu-Gor'kov Green function (see main text and Note 5). Lastly, we want to note that the analysis of length scales  $\xi(T)$  and  $\lambda_L(T)$  as done in this work is equivalent to discussing energy scales of Higgs and Nambu-Goldstone modes [.

## 1-B Relation to experimental observables

$\xi$ ,  $\lambda_L$ , and  $j_{dp}$  link to several experimental observables [38] where we suppress the  $T$ -dependence for brevity.  $j_{dp}$  constitutes an upper theoretical bound to the critical current density,  $j_c$ , that limits the maximal current which the superconducting state of a material can endure and which is the observable measured in experiment. The value of  $j_c$  crucially depends on sample geometry and defect densities as a current only flows near the surface shell of thickness  $\sim \lambda_L$ .

$\xi$  and  $\lambda_L$  are used to distinguish type I ( $\xi/\lambda_L > \sqrt{2}$ ) and type II ( $\xi/\lambda_L < \sqrt{2}$ ) superconductors and they relate to the critical magnetic fields: The first critical magnetic field

$$H_{c1} = \frac{\Phi_0}{4\pi\mu_0\lambda_L^2} \ln \frac{\lambda_L}{\xi} \quad (12)$$

that separates the Meissner and Abrikosov vortex lattice phases, the second critical magnetic field

$$H_{c2} = \frac{\Phi_0}{2\pi\mu_0\xi^2} \quad (13)$$

that determines the magnetic field strength boundary at which the superconductor becomes a normal metal, and the thermodynamic critical field

$$H_{c,th} = \frac{\Phi_0}{2\sqrt{2}\pi\mu_0\xi\lambda} = \sqrt{\frac{\alpha^2}{b\mu_0}} = \sqrt{\frac{2}{\mu_0}(f_N - f_{SC})|_{\min,q=0}} \quad (14)$$

## Supplementary Note 2: Generalized Bloch theorem in Nambu space

Crystal momentum  $\mathbf{k}$  is in general not a good quantum number for systems with spatial inhomogeneity. This applies to the situation of an arbitrary spatially varying superconducting gap  $\Delta(\mathbf{r}) = |\Delta(\mathbf{r})|e^{i\varphi(\mathbf{r})}$ . In the special case of FMP with an OP of Fulde-Ferrel-type [55], i.e., with helical phase  $\varphi(\mathbf{r}) = \mathbf{q} \cdot \mathbf{r}$  and constant amplitude  $|\Delta(\mathbf{r})| = |\Delta|$ , however, a generalized lattice translation symmetry exists in Nambu space that implies a generalized Bloch theorem: We define a generalized translation operator  $\mathcal{T}_n$  that acts on the Nambu spinor  $\underline{\psi}^\dagger = (\psi_\uparrow^\dagger, \psi_\downarrow)$  of field operators  $\psi^{(\dagger)}(\mathbf{r})$ :

$$\mathcal{T}_n \underline{\psi}(\mathbf{r}) = \mathcal{T}_n \begin{pmatrix} \psi_\uparrow(\mathbf{r}) \\ \psi_\downarrow(\mathbf{r}) \end{pmatrix} = \begin{pmatrix} e^{i\phi_n/2} \psi_\uparrow(\mathbf{r} + \mathbf{R}_n) \\ e^{-i\phi_n/2} \psi_\downarrow(\mathbf{r} + \mathbf{R}_n) \end{pmatrix} = e^{i\phi_n\sigma_z/2} \underline{\psi}(\mathbf{r} + \mathbf{R}_n) \quad (15)$$

Here, the spinor is not only shifted by a Bravais lattice vector  $\mathbf{R}_n$  but it is also rotated by the angle  $\phi_n = \mathbf{q} \cdot \mathbf{R}_n$  about the  $z$ -axis on the Bloch sphere with  $\sigma_z$  being a Pauli matrix.

In the following, we show that the translation defined by Eq. (15) leaves the Hamiltonian  $H = H_0 + H_{\text{SC}}$  of a superconducting system consisting of lattice ( $H_0$ ) and pairing ( $H_{\text{SC}}$ ) term invariant, i.e., that it obeys a generalized Bloch theorem. In Nambu space, the Hamiltonian takes in  $d$  dimensions the form

$$\begin{aligned}
H_0 + H_{\text{SC}} &= \int d^d r \left[ \sum_{\sigma} \{h(\mathbf{r})\psi_{\sigma}^{\dagger}(\mathbf{r})\psi_{\sigma}(\mathbf{r})\} + \Delta_{\mathbf{q}}^*(\mathbf{r})\psi_{\uparrow}^{\dagger}(\mathbf{r})\psi_{\downarrow}^{\dagger}(\mathbf{r}) + \Delta_{\mathbf{q}}(\mathbf{r})\psi_{\downarrow}(\mathbf{r})\psi_{\uparrow}(\mathbf{r}) \right] \\
&= \int d^d r \left[ \underline{\psi}^{\dagger}(\mathbf{r}) \begin{pmatrix} h(\mathbf{r}) & \Delta_{\mathbf{q}}^*(\mathbf{r}) \\ \Delta_{\mathbf{q}}(\mathbf{r}) & -h(\mathbf{r}) \end{pmatrix} \underline{\psi}(\mathbf{r}) \right] \\
&= \int d^d r \left[ \underline{\psi}^{\dagger}(\mathbf{r}) \left( h(\mathbf{r})\sigma_z + \text{Re} \{ \Delta_{\mathbf{q}}(\mathbf{r}) \} \sigma_x + \text{Im} \{ \Delta_{\mathbf{q}}(\mathbf{r}) \} \sigma_y \right) \underline{\psi}(\mathbf{r}) \right] \quad (16)
\end{aligned}$$

with the single-particle Hamiltonian  $h(\mathbf{r}) = -\frac{\hbar^2}{2m}\nabla^2 + V(\mathbf{r})$  containing the lattice periodic potential  $V(\mathbf{r}) = V(\mathbf{r} + \mathbf{R}_n)$  and with the FMP pairing potential or gap function  $\Delta_{\mathbf{q}}(\mathbf{r}) = |\Delta|e^{i\mathbf{q}\cdot\mathbf{r}}$ . Since  $\Delta \propto \Psi$ , the superconducting gap carries over the phase dependence of the order parameter under the FMP constraint. From the last line of Eq. (16), it is immediately clear that  $H_0$  is invariant under translation  $\mathcal{T}_n$  in Nambu space, as  $\mathcal{T}_n$  trivially commutes with  $h(\mathbf{r})\sigma_z$ . The invariance of  $H_{\text{SC}}$  follows from the phase shift of the pairing field  $\Delta_{\mathbf{q}}(\mathbf{r} + \mathbf{R}_n) = \Delta_{\mathbf{q}}(\mathbf{r})e^{i\phi_n}$  associated with

$$\begin{aligned}
H_{\text{SC}} &= \int d^d r \left[ \underline{\psi}^{\dagger}(\mathbf{r}) \begin{pmatrix} 0 & \Delta_{\mathbf{q}}^*(\mathbf{r}) \\ \Delta_{\mathbf{q}}(\mathbf{r}) & 0 \end{pmatrix} \underline{\psi}(\mathbf{r}) \right] \\
&= \int d^d r \left[ \underline{\psi}^{\dagger}(\mathbf{r} + \mathbf{R}_n) \begin{pmatrix} 0 & \Delta_{\mathbf{q}}^*(\mathbf{r} + \mathbf{R}_n) \\ \Delta_{\mathbf{q}}(\mathbf{r} + \mathbf{R}_n) & 0 \end{pmatrix} \underline{\psi}(\mathbf{r} + \mathbf{R}_n) \right] \\
&= \int d^d r \left[ \underline{\psi}^{\dagger}(\mathbf{r} + \mathbf{R}_n) \begin{pmatrix} 0 & \Delta_{\mathbf{q}}^*(\mathbf{r})e^{-i\phi_n} \\ \Delta_{\mathbf{q}}(\mathbf{r})e^{i\phi_n} & 0 \end{pmatrix} \underline{\psi}(\mathbf{r} + \mathbf{R}_n) \right] \\
&= \int d^d r \left[ \underline{\psi}^{\dagger}(\mathbf{r} + \mathbf{R}_n) e^{-i\phi_n\sigma_z/2} \begin{pmatrix} 0 & \Delta_{\mathbf{q}}^*(\mathbf{r}) \\ \Delta_{\mathbf{q}}(\mathbf{r}) & 0 \end{pmatrix} e^{i\phi_n\sigma_z/2} \underline{\psi}(\mathbf{r} + \mathbf{R}_n) \right] \\
&= \int d^d r \left[ \underline{\psi}^{\dagger}(\mathbf{r})\mathcal{T}_n^{\dagger} \begin{pmatrix} 0 & \Delta_{\mathbf{q}}^*(\mathbf{r}) \\ \Delta_{\mathbf{q}}(\mathbf{r}) & 0 \end{pmatrix} \mathcal{T}_n \underline{\psi}(\mathbf{r}) \right]
\end{aligned}$$

Thus, the generalized translation in Eq. (15) is a symmetry of the system and (generalized) crystal momentum  $\mathbf{k}$  constitutes a good quantum number in the case of FMP superconductivity. Note, though, that this is not true for pair density waves or generally speaking more complex FFLO-type pairings which also modulate the amplitude of the OP. In this case, methods employing supercells to accommodate for the extent of the OP modulation are necessary as was done, e.g., in Refs. [97, 98].

## Supplementary Note 3: Derivation of the supercurrent density

In this section, we will derive how to calculate the charge supercurrent associated with the finite center-of-mass momentum of Cooper pairs under the FMP constraint. We start with the definition of the current operator  $\hat{\mathbf{j}}$ . Generally, a current  $\mathbf{j}$  in a system is induced by the change of the local polarization  $\mathbf{P}$ . The polarization operator is given by

$$\hat{\mathbf{P}} = e \sum_i \mathbf{R}_i c_i^\dagger c_i = e \sum_i \mathbf{R}_i n_i \quad (17)$$

for electrons of charge  $e$  sitting at a lattice site  $i$  (we suppress orbital and spin indices for now). The current is given by the time derivative (von-Neumann equation) of the polarization operator

$$\hat{\mathbf{j}} = \dot{\hat{\mathbf{P}}} = \frac{i}{\hbar} [\hat{\mathbf{P}}, H] \quad (18)$$

We want to study the Hamiltonian with a superconducting pairing field  $\Delta_{ij}$ , where we here recast Eq. (16)

$$H = \underbrace{\sum_{ij} t_{ij} c_i^\dagger c_j}_{H_N \equiv H_0} + \underbrace{\sum_{ij} \Delta_{ij} c_i c_j + \Delta_{ij}^* c_j^\dagger c_i^\dagger}_{H_{AN} \equiv H_{SC}} \quad (19)$$

for discrete lattice sites  $i$  instead of the continuous positions  $\mathbf{r}$ . To evaluate expression (18), we have to solve three kinds of commutators

$$\begin{aligned} [n_m, c_i^\dagger c_j] &= c_i^\dagger [n_m, c_j] + [n_m, c_i^\dagger] c_j = (\delta_{mi} - \delta_{mj}) c_i^\dagger c_j \\ [n_m, c_i c_j] &= c_i [n_m, c_j] + [n_m, c_i] c_j = -(\delta_{mi} + \delta_{mj}) c_i c_j \\ [n_m, c_i^\dagger c_j^\dagger] &= c_i^\dagger [n_m, c_j^\dagger] + [n_m, c_i^\dagger] c_j^\dagger = (\delta_{mi} + \delta_{mj}) c_i^\dagger c_j^\dagger \end{aligned}$$

where we used  $[A, BC] = B[A, C] + [A, B]C$  and  $[n_m, c_i^\dagger] = \delta_{im} c_i^\dagger$  ( $[n_m, c_i] = -\delta_{im} c_i$ ). We inspect the normal and anomalous component separately ( $\hat{\mathbf{j}} = \hat{\mathbf{j}}_N + \hat{\mathbf{j}}_{AN}$ ):

$$\begin{aligned} \hat{\mathbf{j}}_N &= \frac{i}{\hbar} [\hat{\mathbf{P}}, H_N] = i \frac{e}{\hbar} \sum_{ijm} \mathbf{R}_m t_{ij} [n_m, c_i^\dagger c_j] = i \frac{e}{\hbar} \sum_{ijm} \mathbf{R}_m t_{ij} (\delta_{mi} - \delta_{mj}) c_i^\dagger c_j \\ &= i \frac{e}{\hbar} \sum_{ij} (\mathbf{R}_i - \mathbf{R}_j) t_{ij} c_i^\dagger c_j \end{aligned} \quad (20)$$

$$\begin{aligned} \hat{\mathbf{j}}_{AN} &= \frac{i}{\hbar} [\hat{\mathbf{P}}, H_{AN}] = i \frac{e}{\hbar} \sum_{ijm} \mathbf{R}_m (\Delta_{ij} [n_m, c_i c_j] + \Delta_{ij}^* [n_m, c_j^\dagger c_i^\dagger]) \\ &= -i \frac{e}{\hbar} \sum_{ijm} \mathbf{R}_m (\delta_{mi} + \delta_{mj}) (\Delta_{ij} c_i c_j - \Delta_{ij}^* c_j^\dagger c_i^\dagger) \\ &= -i \frac{e}{\hbar} \sum_{ij} (\mathbf{R}_i + \mathbf{R}_j) (\Delta_{ij} c_i c_j - \Delta_{ij}^* c_j^\dagger c_i^\dagger) \end{aligned} \quad (21)$$

For calculating the current density  $\mathbf{j} = \langle \hat{\mathbf{j}} \rangle$  we can make simplifications using the fact that we have local  $s$ -wave pairing in our system, i.e.,  $\Delta_{ij} \equiv \delta_{ij} \Delta e^{iqR_i}$ . Since  $\langle c_i c_j \rangle = -\langle c_j c_i \rangle$  and  $\Delta_{ij} = \Delta_{ji}$ , the expectation value of the anomalous part  $\langle \hat{\mathbf{j}}_{\text{AN}} \rangle$  vanishes then.

Since the anomalous part does not contribute, we only have to evaluate the normal component (20) of the current. For this purpose, we will assume that the states at site  $i$  represent Wannier orbitals  $i \rightarrow (\mathbf{R}_i, \alpha_i, \sigma_i)$  (orbital  $\alpha$ , spin  $\sigma$ ) which are centered on the unit cell center as is the case in the  $A_3C_{60}$  model (c.f. Note 4-D). Then, we can insert the Fourier transform of the creation and annihilation operators

$$c_i = \frac{1}{N_{\mathbf{k}}} \sum_{\mathbf{k}} \langle i | \mathbf{k} \rangle c_{\mathbf{k}} = \sum_{\mathbf{k}} e^{-i\mathbf{k}\mathbf{R}_i} \delta_{\alpha_i, \alpha_{\mathbf{k}}} \delta_{\sigma_i, \sigma_{\mathbf{k}}} c_{\mathbf{k}}, \quad c_i^\dagger = \frac{1}{N_{\mathbf{k}}} \sum_{\mathbf{k}} e^{i\mathbf{k}\mathbf{R}_i} \delta_{\alpha_i, \alpha_{\mathbf{k}}} \delta_{\sigma_i, \sigma_{\mathbf{k}}} c_{\mathbf{k}}^\dagger \quad (22)$$

to yield

$$\begin{aligned} \hat{\mathbf{j}} &= \hat{\mathbf{j}}_{\text{N}} = i \frac{e}{\hbar} \frac{1}{N_{\mathbf{k}}^2} \sum_{i,j,k,k'} \delta_{\sigma_i, \sigma} \delta_{\sigma_j, \sigma'} \delta_{\alpha_i, \alpha} \delta_{\alpha_j, \alpha'} \delta_{\sigma_i, \sigma_j} [\mathbf{R}_i - \mathbf{R}_j] t_{\alpha_i \alpha_j}(\mathbf{R}_i - \mathbf{R}_j) e^{i(\mathbf{k}\mathbf{R}_i - \mathbf{k}'\mathbf{R}_j)} c_{\mathbf{k}\alpha\sigma}^\dagger c_{\mathbf{k}'\alpha'\sigma'} \\ &\stackrel{\mathbf{R}_i \mapsto \mathbf{R}_i + \mathbf{R}_j}{=} i \frac{e}{\hbar} \frac{1}{N_{\mathbf{k}}} \sum_{\substack{\mathbf{R}_i k k' \\ \alpha \alpha' \sigma}} \mathbf{R}_i t_{\alpha \alpha'}(\mathbf{R}_i) e^{i\mathbf{k}\mathbf{R}_i} \underbrace{\frac{1}{N_{\mathbf{k}}} \sum_{\mathbf{R}_j} e^{i(\mathbf{k} - \mathbf{k}')\mathbf{R}_j}}_{\delta_{\mathbf{k}\mathbf{k}'}} c_{\mathbf{k}\alpha\sigma}^\dagger c_{\mathbf{k}'\alpha'\sigma} \\ &= \frac{e}{\hbar} \frac{1}{N_{\mathbf{k}}} \sum_{\mathbf{k}\alpha\alpha'\sigma} i \underbrace{\sum_{\mathbf{R}_i} \mathbf{R}_i t_{\alpha \alpha'}(\mathbf{R}_i) e^{i\mathbf{k}\mathbf{R}_i}}_{=(\nabla_{\mathbf{k}} h(\mathbf{k}))_{\alpha \alpha'}} c_{\mathbf{k}\alpha\sigma}^\dagger c_{\mathbf{k}\alpha'\sigma} = \frac{e}{N_{\mathbf{k}}} \sum_{\mathbf{k}\alpha\alpha'\sigma} \mathbf{v}_{\alpha \alpha'}(\mathbf{k}) c_{\mathbf{k}\alpha\sigma}^\dagger c_{\mathbf{k}\alpha'\sigma} \end{aligned} \quad (23)$$

with the velocity  $\mathbf{v}(\mathbf{k}) = \frac{1}{\hbar} \nabla_{\mathbf{k}} h(\mathbf{k})$ . Thus, the current density is given by

$$\mathbf{j}_{\mathbf{q}} = \langle \hat{\mathbf{j}} \rangle_{\mathbf{q}} = \frac{e}{N_{\mathbf{k}}} \sum_{\mathbf{k}\alpha\gamma\sigma} \mathbf{v}_{\alpha\gamma}(\mathbf{k}) \langle c_{\mathbf{k}\alpha\sigma}^\dagger c_{\mathbf{k}\gamma\sigma} \rangle_{\mathbf{q}} = \frac{2e}{N_{\mathbf{k}}} \sum_{\mathbf{k}\alpha\gamma} \mathbf{v}_{\alpha\gamma}(\mathbf{k}) \langle c_{\mathbf{k}\alpha\uparrow}^\dagger c_{\mathbf{k}\gamma\uparrow} \rangle_{\mathbf{q}} \quad (24)$$

where we introduced the index  $\mathbf{q}$  to the expectation value  $\langle \dots \rangle_{\mathbf{q}}$  to stress that the reduced density matrix  $\langle c_{\mathbf{k}\alpha\uparrow}^\dagger c_{\mathbf{k}\gamma\uparrow} \rangle_{\mathbf{q}}$  is evaluated for the FMP constraint imposed on the gap and order parameter, i.e.,  $\Delta e^{iqR_n}$ . We connect to Green function theories by writing

$$\langle c_{\mathbf{k}\alpha\uparrow}^\dagger c_{\mathbf{k}\gamma\uparrow} \rangle_{\mathbf{q}} = \langle c_{\mathbf{k} - \frac{\mathbf{q}}{2} + \frac{\mathbf{q}}{2}\alpha\uparrow}^\dagger c_{\mathbf{k} - \frac{\mathbf{q}}{2} + \frac{\mathbf{q}}{2}\gamma\uparrow} \rangle_{\mathbf{q}} = \left[ \underline{\mathcal{G}}_{\mathbf{q}} \left( \tau = 0^-, \mathbf{k} - \frac{\mathbf{q}}{2} \right) \right]_{\gamma\alpha} = \left[ \underline{\mathcal{G}}_{\mathbf{q}}^{\uparrow\uparrow} \left( \tau = 0^-, \mathbf{k} - \frac{\mathbf{q}}{2} \right) \right]_{\gamma\alpha} \quad (25)$$

We want to stress that the velocity  $\mathbf{v}(\mathbf{K})$  and the reduced density matrix  $\langle c_{\mathbf{K}\sigma}^\dagger c_{\mathbf{K}\sigma} \rangle$  have to carry the same momentum label  $\mathbf{K}$  to fulfill Eq. (24) (here  $\mathbf{K} = \mathbf{k}$ ). The expression in terms of a Green function then depends decisively on the notation used for FMP in the Nambu-Gor'kov

formalism. To match the definition given in Eq. (34) (and Eq. (4) of the main text) necessitates a shift of the  $\mathbf{k}$  argument.

Thus, we obtain an expression for the current density derived from the Nambu-Gor'kov Green function as stated in Eq. (6) of the main text:

$$\mathbf{j}_q = \frac{2e}{N_k} \sum_{k\alpha\gamma} v_{\alpha\gamma}(\mathbf{k}) \left[ \underline{G}_q \left( \tau = 0^-, \mathbf{k} - \frac{\mathbf{q}}{2} \right) \right]_{\gamma\alpha} = \frac{2e}{N_k} \sum_k \text{Tr}_\alpha \left[ \underline{v}(\mathbf{k}) \underline{G}_q \left( \tau = 0^-, \mathbf{k} - \frac{\mathbf{q}}{2} \right) \right] \quad (26)$$

In practical calculations, however, we use Eq. (40) as this shows better convergence with respect to the Matsubara summation associated with obtaining  $G(\tau = 0^-)$ . For details, see Note 4-C. We note that our approach reduces to linear-response-based approaches to calculate the stiffness  $D_s \propto \lambda_L^{-2}$  in the limit of  $q \rightarrow 0$ . In this limit, one finds  $\mathbf{j} = -D_s \mathbf{A}$  by introducing a small  $\mathbf{A}$  via Peierls-substitution [45] which is gauge-equivalent to the FMP constraint with small  $\mathbf{q}$ . We, however, explicitly account for finite  $q$  in our calculations inside the superconducting phase and determine the depairing current  $j_{dp}$  for the evaluation of  $\lambda_L$  (see Note 5-B). We stress that one also needs the full  $q$ -dependence encoded in the order parameter to evaluate the correlation length  $\xi(T)$ .

We want to note that a similar expression to Eq. (26) is given above Eq. (38.13) in the book by Abrikosov, Gor'kov, and Dzyaloshinski [99] as well as in Eq. (14.245) in the book by Coleman [4]. In both cases, however, it is discussed in the context of an external magnetic field  $\mathbf{A}$  similar to the implementation in Ref. [45].

## Supplementary Note 4: Numerical implementation of DMFT with FMP constraint

### 4-A Nambu-Gor'kov formalism with finite-momentum pairing

We want to comment on the Dynamical Mean-Field theory (DMFT) calculations in Nambu space under the constraint of finite-momentum pairing (FMP). First, we summarize the description of superconductivity within DMFT using the Nambu-Gor'kov formalism entering explicitly the superconducting state for zero-momentum pairing [49]. Afterwards, we detail how the FMP constraint can be incorporated into the superconducting Nambu Gor'kov DMFT formalism.

To extend the normal state DMFT formalism to Nambu-Gor'kov space [49], we perform a particle-hole transformation of the spin-down sector  $c_{k\alpha\downarrow}^\dagger \mapsto c_{-k\alpha\downarrow}$  and introduce Nambu spinors

$$\psi_{k,\alpha}^\dagger = \begin{pmatrix} c_{k\alpha\uparrow}^\dagger & c_{-k\alpha\downarrow} \end{pmatrix}, \quad \psi_{k,\alpha} = \begin{pmatrix} c_{k\alpha\uparrow} \\ c_{-k\alpha\downarrow}^\dagger \end{pmatrix} \quad (27)$$

The corresponding single-particle Green function (Nambu-Gor'kov Green function) becomes a  $2 \times 2$  matrix in Nambu space

$$\begin{aligned} \mathcal{G}_{\alpha\gamma}(\tau, \mathbf{k}) &= -\langle T_\tau \psi_{\mathbf{k},\alpha}(\tau) \psi_{\mathbf{k},\gamma}^\dagger \rangle = \begin{pmatrix} -\langle T_\tau c_{\mathbf{k}\alpha\uparrow}(\tau) c_{\mathbf{k}\gamma\uparrow}^\dagger \rangle & -\langle T_\tau c_{\mathbf{k}\alpha\uparrow}(\tau) c_{-\mathbf{k}\gamma\downarrow} \rangle \\ -\langle T_\tau c_{-\mathbf{k}\alpha\downarrow}^\dagger(\tau) c_{\mathbf{k}\gamma\uparrow}^\dagger \rangle & -\langle T_\tau c_{-\mathbf{k}\alpha\downarrow}^\dagger(\tau) c_{-\mathbf{k}\gamma\downarrow} \rangle \end{pmatrix} \\ &= \begin{pmatrix} G_{\alpha\gamma}(\tau, \mathbf{k}) & F_{\alpha\gamma}(\tau, \mathbf{k}) \\ F_{\alpha\gamma}^\dagger(\tau, \mathbf{k}) & \bar{G}_{\alpha\gamma}(\tau, -\mathbf{k}) \end{pmatrix} = \begin{pmatrix} G_{\alpha\gamma}(\tau, \mathbf{k}) & F_{\alpha\gamma}(\tau, \mathbf{k}) \\ F_{\alpha\gamma}^\dagger(\tau, \mathbf{k}) & -G_{\alpha\gamma}(-\tau, -\mathbf{k}) \end{pmatrix} \equiv \begin{pmatrix} \mathcal{G}_{\alpha\gamma}^{\uparrow\uparrow} & \mathcal{G}_{\alpha\gamma}^{\uparrow\downarrow} \\ \mathcal{G}_{\alpha\gamma}^{\downarrow\uparrow} & \mathcal{G}_{\alpha\gamma}^{\downarrow\downarrow} \end{pmatrix} \end{aligned} \quad (28)$$

where we used  $\bar{G}(\tau, -\mathbf{k}) = -G(-\tau, -\mathbf{k})$  for the hole propagator and  $F$  denotes the anomalous (Gor'kov) Green function. The Nambu-Gor'kov Green function is determined from a Dyson equation where the non-interacting Green function

$$[\underline{\mathcal{G}}^0(i\omega_n, \mathbf{k})]^{-1} = \begin{pmatrix} (i\omega_n + \mu)\mathbb{1} - \underline{h}(\mathbf{k}) & 0 \\ 0 & (i\omega_n - \mu)\mathbb{1} + \underline{h}(-\mathbf{k}) \end{pmatrix} \equiv i\omega_n \mathbb{1} \cdot \sigma_0 - [\underline{h}(\mathbf{k}) - \mu \mathbb{1}] \cdot \sigma_z \quad (29)$$

and self-energy

$$\underline{\mathcal{S}}(i\omega_n) = \begin{pmatrix} \underline{\Sigma}^N(i\omega_n) & \underline{\Sigma}^{\text{AN}}(i\omega_n) \\ \underline{\Sigma}^{\text{AN}}(i\omega_n) & -[\underline{\Sigma}^N]^*(i\omega_n) \end{pmatrix} \equiv \Re \underline{\Sigma}^N(i\omega_n) \cdot \sigma_z + i \Im \underline{\Sigma}^N(i\omega_n) \cdot \sigma_0 + \underline{\Sigma}^{\text{AN}}(i\omega_n) \cdot \sigma_x \quad (30)$$

also become matrices in Nambu space which can be expressed by Pauli matrices  $\sigma_i$  ( $i = 0, x, y, z$ ) for inversion symmetry  $h(\mathbf{k}) = h(-\mathbf{k})$ . The self-energy  $\mathcal{S}$  is obtained from solving the appropriate impurity problem defined by the Weiss field  $\mathcal{G}_W$  in Nambu space and the particle-hole-transformed interaction Hamiltonion. In addition to the normal component  $\Sigma^N \equiv \Sigma$ , the self-energy gains an anomalous matrix element  $\Sigma^{\text{AN}}$  for which the gauge is chosen such that it is real-valued, i.e., only  $\sigma_x$  is involved in constructing  $\mathcal{S}$ . Thus, the lattice Green function in Nambu-Gor'kov space is given by

$$\begin{aligned} [\underline{\mathcal{G}}(i\omega_n, \mathbf{k})]^{-1} &= [\underline{\mathcal{G}}^0(i\omega_n, \mathbf{k})]^{-1} - \underline{\mathcal{S}}(i\omega_n) \\ &= \begin{pmatrix} (i\omega_n + \mu)\mathbb{1} - \underline{h}(\mathbf{k}) - \underline{\Sigma}^N(i\omega_n) & -\underline{\Sigma}^{\text{AN}}(i\omega_n) \\ -\underline{\Sigma}^{\text{AN}}(i\omega_n) & (i\omega_n - \mu)\mathbb{1} + \underline{h}(-\mathbf{k}) + [\underline{\Sigma}^N]^*(i\omega_n) \end{pmatrix} \end{aligned} \quad (31)$$

The self-consistency circle of DMFT (Eq. (9) in the Methods section) generally becomes a matrix formulation in Nambu space where the lattice Green function is replaced by the Nambu-Gor'kov Green function  $\underline{G}_k(i\omega_n) \mapsto \underline{\mathcal{G}}(i\omega_n, \mathbf{k})$ . We can restate the DMFT self-consistency problem in the superconducting state using calligraphic letters

$$\begin{cases} \underline{\mathcal{G}}_{\text{loc}}(i\omega_n) = \frac{1}{N_k} \sum_{\mathbf{k}} \underline{\mathcal{G}}(i\omega_n, \mathbf{k}) \\ \underline{\mathcal{G}}_W^{-1}(i\omega_n) = \underline{\mathcal{G}}_{\text{loc}}^{-1}(i\omega_n) + \underline{\mathcal{S}}(i\omega_n) \\ \underline{\mathcal{S}}(i\omega_n) = \underline{\mathcal{G}}_W^{-1}(i\omega_n) - \underline{\mathcal{G}}_{\text{imp}}^{-1}(i\omega_n) \end{cases} \quad (32)$$



We now want to incorporate the FMP constraint into the Nambu-Gor'kov formalism. To treat the phase  $e^{iq\mathbf{r}}$  of the OP and gap in the framework of DMFT, several possibilities exist. For the simplest implementation, we introduce a phase gauge shift that cancels the momentum dependence of the order parameter  $\Psi_{\mathbf{q}}(\mathbf{R}_i) = |\Psi|e^{iq\mathbf{R}_i} = \langle c_{i\uparrow}c_{i\downarrow} \rangle$  at site  $\mathbf{R}_i$ . By applying the transformation  $c_{i\alpha\sigma} \mapsto c_{i\alpha\sigma}e^{iq\mathbf{R}_i/2}$  ( $c_{i,\sigma}^\dagger \mapsto c_{i,\sigma}^\dagger e^{-iq\mathbf{R}_i/2}$ ), the hopping amplitudes  $t(\mathbf{R}_{ij})$  are modified to yield  $\tilde{t}(\mathbf{R}_{ij}) = t(\mathbf{R}_{ij})e^{iq\mathbf{R}_{ij}/2}$  such that the dispersion  $\underline{\varepsilon}_{\mathbf{k}}$  obtained from diagonalizing  $\underline{h}(\mathbf{k})$  is effectively replaced by  $\underline{\varepsilon}_{\mathbf{k}\pm\mathbf{q}/2}$ , i.e., the dispersion for up and down spins gets shifted by  $\pm\mathbf{q}/2$ , respectively. This shows that the introduction of FMP breaks time-reversal symmetry. The advantage of completely transferring the  $\mathbf{q}$ -dependence to the hopping matrix is that we keep the gauge freedom to choose the anomalous self-energy to be a real-valued function.

To this end, we recast Eqs. (27) to (31) including the FMP momentum  $\mathbf{q}$ . Through the gauge transform, the Fourier transformed creation and annihilation operators pick up the  $\pm\mathbf{q}/2$  momentum shift such that the Nambu spinors obtain an additional parametric dependence

$$\psi_{\mathbf{k},\mathbf{q},\alpha}^\dagger = \begin{pmatrix} c_{\mathbf{k}+\frac{\mathbf{q}}{2}\alpha\uparrow}^\dagger & c_{-\mathbf{k}+\frac{\mathbf{q}}{2}\alpha\downarrow} \end{pmatrix}, \quad \psi_{\mathbf{k}+\frac{\mathbf{q}}{2},\alpha} = \begin{pmatrix} c_{\mathbf{k}+\frac{\mathbf{q}}{2}\alpha\uparrow} \\ c_{-\mathbf{k}+\frac{\mathbf{q}}{2}\alpha\downarrow}^\dagger \end{pmatrix} \quad (33)$$

The Nambu-Gor'kov Green function consequently is parametrized by  $\mathbf{q}$  as well

$$\begin{aligned} \left[ \underline{\mathcal{G}}_{\mathbf{q}}(\tau, \mathbf{k}) \right]_{\alpha\gamma} &= -\langle T_\tau \psi_{\mathbf{k},\mathbf{q},\alpha}(\tau) \psi_{\mathbf{k},\mathbf{q},\gamma}^\dagger \rangle = \begin{pmatrix} -\langle T_\tau c_{\mathbf{k}+\frac{\mathbf{q}}{2}\alpha\uparrow}(\tau) c_{\mathbf{k}+\frac{\mathbf{q}}{2}\gamma\uparrow}^\dagger \rangle & -\langle T_\tau c_{\mathbf{k}+\frac{\mathbf{q}}{2}\alpha\uparrow}(\tau) c_{-\mathbf{k}+\frac{\mathbf{q}}{2}\gamma\downarrow} \rangle \\ -\langle T_\tau c_{-\mathbf{k}+\frac{\mathbf{q}}{2}\alpha\downarrow}^\dagger(\tau) c_{\mathbf{k}+\frac{\mathbf{q}}{2}\gamma\uparrow} \rangle & -\langle T_\tau c_{-\mathbf{k}+\frac{\mathbf{q}}{2}\alpha\downarrow}^\dagger(\tau) c_{-\mathbf{k}+\frac{\mathbf{q}}{2}\gamma\downarrow} \rangle \end{pmatrix} \\ &= \begin{pmatrix} \left[ \underline{G}_{\mathbf{q}}(\tau, \mathbf{k}) \right]_{\alpha\gamma} & \left[ \underline{F}_{\mathbf{q}}(\tau, \mathbf{k}) \right]_{\alpha\gamma} \\ \left[ \underline{F}_{\mathbf{q}}^\dagger(\tau, \mathbf{k}) \right]_{\alpha\gamma} & \left[ \underline{G}_{\mathbf{q}}(\tau, -\mathbf{k}) \right]_{\alpha\gamma} \end{pmatrix} \equiv \begin{pmatrix} \left[ \underline{\mathcal{G}}_{\mathbf{q}}^{\uparrow\uparrow}(\tau, \mathbf{k}) \right]_{\alpha\gamma} & \left[ \underline{\mathcal{G}}_{\mathbf{q}}^{\downarrow\downarrow}(\tau, \mathbf{k}) \right]_{\alpha\gamma} \\ \left[ \underline{\mathcal{G}}_{\mathbf{q}}^{\downarrow\uparrow}(\tau, \mathbf{k}) \right]_{\alpha\gamma} & \left[ \underline{\mathcal{G}}_{\mathbf{q}}^{\uparrow\downarrow}(\tau, \mathbf{k}) \right]_{\alpha\gamma} \end{pmatrix} \quad (34) \end{aligned}$$

Generally, it holds that  $\underline{\mathcal{G}}_{\mathbf{q}}^{\uparrow\uparrow}(\tau, \mathbf{k}) \neq -\underline{\mathcal{G}}_{\mathbf{q}}^{\downarrow\downarrow}(-\tau, -\mathbf{k})$  for arbitrary, finite  $\mathbf{q}$  due to the time-reversal symmetry breaking. Note that it is possible to define the Fourier transform of  $c_i^{(\dagger)}$  differently such that the pairing is non-symmetric with respect to  $\mathbf{q}$ . Another often employed notation describes Cooper pairs with electrons of momenta  $\mathbf{k}$  (in  $\underline{\mathcal{G}}^{\uparrow\uparrow}$ ) and  $-\mathbf{k} + \mathbf{q}$  (in  $\underline{\mathcal{G}}^{\downarrow\downarrow}$ ) (as depicted in Fig. 2 of the main text). We here choose the symmetric notation by putting  $-\frac{\mathbf{q}}{2}$  to both diagonal components.

On Matsubara frequencies, the Nambu-Gor'kov Green function is set up via (c.f. Eq. (10) in the main text)

$$\left[ \underline{\mathcal{G}}_{\mathbf{q}}(i\omega_n, \mathbf{k}) \right]^{-1} = \begin{pmatrix} (i\omega_n + \mu)\mathbb{1} - \underline{h}(\mathbf{k} + \frac{\mathbf{q}}{2}) - \underline{\Sigma}^{\text{N}}(i\omega_n) & -\underline{\Sigma}^{\text{AN}}(i\omega_n) \\ -\underline{\Sigma}^{\text{AN}}(i\omega_n) & (i\omega_n - \mu)\mathbb{1} + \underline{h}(-\mathbf{k} + \frac{\mathbf{q}}{2}) + [\underline{\Sigma}^{\text{N}}]^*(i\omega_n) \end{pmatrix} \quad (35)$$

We note that the approach outlined here does not require the computationally more demanding use of supercells as, e.g., implemented in Refs. [97, 98] and discussed in the review by Kinnunen et al. [57] to study FFLO-type superconductivity.

To induce symmetry-breaking in our calculations, we add a small pairing field  $\eta = 0.1$  meV on the off-diagonal of the Nambu-Gor'kov Green function throughout the calculation. We keep it for the whole superconducting DMFT loop because it helps stabilizing the calculations. We checked that the presence of the small, but finite  $\eta$  does not change the results. In this work, we always choose  $\mathbf{q} = q\mathbf{b}_1$  along the direction of a reciprocal lattice vector  $\mathbf{b}_1$  (c.f. Note 4-D). The calculations with finite  $q$  are performed in practice as in the case of  $q = 0$ , but with  $q$  becoming an additional input parameter. Calculations can be sped up by first converging the DMFT loop for  $q = 0$  and then using the result as a starting point for finite  $q > 0$  values.

## 4-B Determination of chemical potential

In our calculations, we adjust the chemical potential  $\mu$  in each DMFT iteration in order to keep the filling of the system fixed to  $\langle n \rangle_q = N_{\text{orb}} = 3$ , i.e., the  $t_{1u}$  bands of  $A_3C_{60}$  are half-filled. The code implementation was done in Ref. [63] (see also Ref. [64]) for DMFT in the Nambu-Gor'kov formalism with  $q = 0$ , but it can also be used for finite momenta. To determine the chemical potential, we solve the following equation

$$\begin{aligned}
\langle n \rangle_q &= \frac{1}{N_k} \sum_{k\alpha\sigma} \langle c_{k+\frac{q}{2}\alpha\sigma}^\dagger c_{k+\frac{q}{2}\alpha\sigma} \rangle = \frac{1}{N_k} \sum_{k\alpha} \langle c_{k+\frac{q}{2}\alpha\uparrow}^\dagger c_{k+\frac{q}{2}\alpha\uparrow} \rangle + \langle c_{-k+\frac{q}{2}\alpha\downarrow}^\dagger c_{-k+\frac{q}{2}\alpha\downarrow} \rangle \\
&= \frac{1}{N_k} \sum_{k\alpha} \langle 1 - c_{k+\frac{q}{2}\alpha\uparrow} c_{k+\frac{q}{2}\alpha\uparrow}^\dagger \rangle + \langle c_{-k+\frac{q}{2}\alpha\downarrow}^\dagger c_{-k+\frac{q}{2}\alpha\downarrow} \rangle \\
&= N_{\text{orb}} + \frac{1}{N_k} \sum_{k\alpha} [G_q(\tau = 0^+, \mathbf{k}) - \bar{G}_q(\tau = 0^+, -\mathbf{k})]_{\alpha\alpha} \\
&= N_{\text{orb}} + \frac{1}{N_k} \sum_{k\omega_n} \text{Tr}_\alpha [\mathcal{G}_q^{\uparrow\uparrow} - \mathcal{G}_q^{\downarrow\downarrow}] (i\omega_n, \mathbf{k}) e^{i\omega_n 0^+} \tag{36}
\end{aligned}$$

In the second step, we relabeled momentum  $\mathbf{k} \mapsto \mathbf{k} + \mathbf{q}$  for the spin down sector. Taking the difference  $\mathcal{G}_q^{\uparrow\uparrow} - \mathcal{G}_q^{\downarrow\downarrow}$  helps with the convergence of the Matsubara sum to evaluate the Green functions at  $\tau = 0^+$  since the frequency tail becomes  $\mathcal{O}(1/(i\omega_n)^2)$ .

## 4-C Handling the Matsubara summation in the calculation of the current density

The expression for the current density, Eq. (26), contains a Matsubara sum of the spin-up Nambu-Gor'kov Green function component  $\mathcal{G}^{\uparrow\uparrow} = G$  to compute the reduced density matrix

$\langle c_{k\alpha\uparrow}^\dagger c_{k\gamma\uparrow} \rangle_{\mathbf{q}}$  (c.f. Eq. (25)). The Green function typically has slow convergence of Matsubara frequencies due to the  $1/(i\omega_n)$ -tail at large frequencies. We can achieve better convergence by including the inverse of the diagonal part of the Nambu Gor'kov Green function, i.e., the inverse of the non-interacting Green function plus the normal self-energy. Generally, we can expand the full Nambu Gor'kov Green function from Eq. (35) in the isospin space in terms of Pauli matrices

$$\underline{\mathcal{G}}^{-1} = \underline{g}_0 \sigma_0 + \underline{g}_z \sigma_z + \underline{g}_x \sigma_x \quad (37)$$

We now define

$$\underline{\mathcal{G}}_{\text{N}}^{-1} = \underline{g}_0 \sigma_0 + \underline{g}_z \sigma_z \quad \text{and} \quad \underline{\mathcal{G}}_{\Delta}^{-1} = \underline{g}_x \sigma_x \quad (38)$$

Since  $\mathcal{G}_{\text{N}}$  describes a time-reversal symmetric system, the following term

$$\sum_{\mathbf{k}} \text{Tr}_{\alpha} \left[ \underline{\mathbf{v}}(\mathbf{k}) \underline{\mathcal{G}}_{\text{N}}^{\uparrow\uparrow} \left( \tau = 0^-, \mathbf{k} - \frac{\mathbf{q}}{2} \right) \right] = 0 \quad (39)$$

has to vanish. Eq. (39) essentially states that the charge supercurrent is induced by the superconducting condensate which only contributes to the full Nambu Green function  $\mathcal{G}$  via the anomalous self-energy contained in  $\mathcal{G}_{\Delta}^{-1}$  since  $\underline{g}_x \equiv \underline{\Sigma}_{\text{AN}}$ . Thus, we can subtract Eq. (39) from the current to obtain

$$\mathbf{j} = \frac{2e}{N_k} \sum_{\mathbf{k}} \text{Tr}_{\alpha} \left[ \underline{\mathbf{v}}(\mathbf{k}) \left\{ \underline{\mathcal{G}} - \underline{\mathcal{G}}_{\text{N}} \right\}^{\uparrow\uparrow} \left( \tau = 0^-, \mathbf{k} - \frac{\mathbf{q}}{2} \right) \right] = \frac{2e}{N_k} \sum_{\mathbf{k}} \text{Tr}_{\alpha} \left[ \underline{\mathbf{v}}(\mathbf{k}) \delta \underline{\mathcal{G}}^{\uparrow\uparrow} \left( \tau = 0^-, \mathbf{k} - \frac{\mathbf{q}}{2} \right) \right] \quad (40)$$

which has a better convergence with respect to Matsubara frequencies, since  $\delta \mathcal{G}^{\uparrow\uparrow} \propto 1/(i\omega_n)^3$  at large frequencies. To see the convergence behavior, we do a Taylor expansion where we focus on the isospin dependence only:

$$\begin{aligned} \delta \mathcal{G} &= \mathcal{G} - \mathcal{G}_{\text{N}} = (\mathcal{G}_{\text{N}}^{-1} + G_{\Delta}^{-1})^{-1} - \mathcal{G}_{\text{N}} = \mathcal{G}_{\text{N}} (\sigma_0 + \mathcal{G}_{\Delta}^{-1} \mathcal{G}_{\text{N}})^{-1} - \mathcal{G}_{\text{N}} \\ &= \mathcal{G}_{\text{N}} (\sigma_0 + \mathcal{G}_{\Delta}^{-1} \mathcal{G}_{\text{N}} + \mathcal{G}_{\Delta}^{-1} \mathcal{G}_{\text{N}} \mathcal{G}_{\Delta}^{-1} \mathcal{G}_{\text{N}} + \dots) - \mathcal{G}_{\text{N}} \\ &= \mathcal{G}_{\text{N}} \mathcal{G}_{\Delta}^{-1} \mathcal{G}_{\text{N}} + \mathcal{G}_{\text{N}} \mathcal{G}_{\Delta}^{-1} \mathcal{G}_{\text{N}} \mathcal{G}_{\Delta}^{-1} \mathcal{G}_{\text{N}} + \dots \end{aligned}$$

The first term of the last line does not have any diagonal components since  $\mathcal{G}_{\text{N}} = 1/\mathcal{G}_{\text{N}}^{-1} \propto \dots \sigma_0 + \dots \sigma_z$  and  $\mathcal{G}_{\Delta}^{-1} \propto \sigma_x$  such that their product

$$\mathcal{G}_{\text{N}} \mathcal{G}_{\Delta}^{-1} \mathcal{G}_{\text{N}} \propto \dots \sigma_0 \sigma_x + \dots \sigma_x \sigma_z \propto \dots \sigma_x + \dots \sigma_y \quad (41)$$

has only off-diagonal components. Hence, the lowest order term contributing to the  $\uparrow\uparrow$  component of  $\delta \mathcal{G}$  is  $O(\mathcal{G}_{\text{N}}^3 \mathcal{G}_{\Delta}^2)$  which has a  $1/(i\omega_n)^3$ -tail from  $\mathcal{G}_{\text{N}}^3$ . The Taylor expansion shows

that  $\mathcal{G}_N$  is the zero-order term that causes the overall  $1/(i\omega_n)$ -tail of  $\mathcal{G}$  which we mitigate with Eq. (40). An approximate expression for the current utilizing the Taylor expansion up to lowest order can be found in Eq. (38.13) in the book by Abrikosov, Gor'kov, and Dzyaloshinski [99].

We compute the momentum and Matsubara summation occurring in the expression of the supercurrent density  $\mathbf{j}_q$  (c.f. Eq. (26) in Note 4) using a  $35^3$   $\mathbf{k}$ -mesh and 200 Matsubara frequencies.

#### 4-D Lattice model details and current direction

We here give further details on the lattice model of  $A_3C_{60}$  materials derived in Ref. [75]. In this model, the  $C_{60}$  molecules reside on a fcc lattice for which we construct Bravais lattice vectors and momenta as

$$\mathbf{R}_i = \sum_{j=1}^3 n_j \mathbf{a}_j \quad , \quad \mathbf{k} = \sum_{j=1}^3 k_j \mathbf{b}_j \quad (42)$$

with  $i \equiv (n_1, n_2, n_3)$ . We choose the lattice and corresponding reciprocal lattice vectors to be

$$\mathbf{a}_1 = \frac{a}{2}(\hat{x} + \hat{y}) \quad , \quad \mathbf{a}_2 = \frac{a}{2}(\hat{y} + \hat{z}) \quad , \quad \mathbf{a}_3 = \frac{a}{2}(\hat{x} + \hat{z}) \quad (43)$$

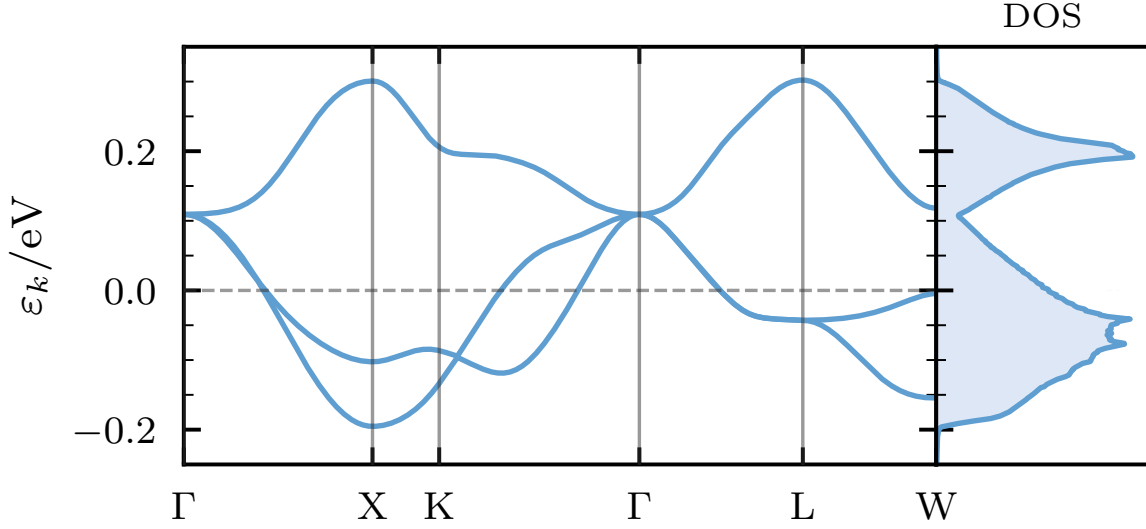
$$\mathbf{b}_1 = \frac{2\pi}{a}(\hat{x} + \hat{y} - \hat{z}) \quad , \quad \mathbf{b}_2 = \frac{2\pi}{a}(-\hat{x} + \hat{y} + \hat{z}) \quad , \quad \mathbf{b}_3 = \frac{2\pi}{a}(\hat{x} - \hat{y} + \hat{z}) \quad (44)$$

with lattice constant  $a \sim 14.2 - 14.5 \text{ \AA}$ .  $\hat{x}$ ,  $\hat{y}$ , and  $\hat{z}$  are the Cartesian unit vectors. We restate the lattice model from Eq. (8) in the main text

$$H_{\text{kin}} = \sum_{ij} \sum_{\alpha\gamma\sigma} t_{\alpha\gamma}(\mathbf{R}_{ij}) c_{i\alpha\sigma}^\dagger c_{j\gamma\sigma} = \sum_{\mathbf{k}} \sum_{\alpha\gamma\sigma} h_{\alpha\gamma}(\mathbf{k}) c_{\mathbf{k}\alpha\sigma}^\dagger c_{\mathbf{k}\gamma\sigma} \quad (45)$$

where we inserted the Fourier transformation (22) of creation and annihilation operators with  $h_{\alpha\gamma}(\mathbf{k}) = \sum_j t_{\alpha\gamma}(\mathbf{R}_j) e^{i\mathbf{k}\mathbf{R}_j}$ . We here specify the hopping terms  $t_{\alpha\gamma}(\mathbf{R}_{ij})$  connecting electrons of spin  $\sigma$  on sites  $i, j$  and molecular (Wannier) orbitals  $\alpha, \gamma$  via  $\mathbf{R}_{ij} = \mathbf{R}_i - \mathbf{R}_j$ . The Wannier orbitals labeled  $\alpha = 1, 2, 3$  describe degenerate  $p_x$ -,  $p_y$ -, and  $p_z$ -like orbitals. For the 12 nearest-neighbor (NN) distances, the hopping matrices are given by

$$\begin{aligned} & \begin{pmatrix} t_1 & t_2 & 0 \\ t_2 & t_3 & 0 \\ 0 & 0 & t_4 \end{pmatrix} \text{ for } \mathbf{R} = (0.5, 0.5, 0.0), & \begin{pmatrix} t_1 & -t_2 & 0 \\ -t_2 & t_3 & 0 \\ 0 & 0 & t_4 \end{pmatrix} \text{ for } \mathbf{R} = (0.5, -0.5, 0.0), \\ & \begin{pmatrix} t_4 & 0 & 0 \\ 0 & t_1 & t_2 \\ 0 & t_2 & t_3 \end{pmatrix} \text{ for } \mathbf{R} = (0, 0, 0.5, 0.5), & \begin{pmatrix} t_4 & 0 & 0 \\ 0 & t_1 & -t_2 \\ 0 & -t_2 & t_3 \end{pmatrix} \text{ for } \mathbf{R} = (0.0, 0.5, -0.5), \\ & \begin{pmatrix} t_3 & 0 & t_2 \\ 0 & t_4 & 0 \\ t_2 & 0 & t_1 \end{pmatrix} \text{ for } \mathbf{R} = (0.5, 0.0, 0.5), & \begin{pmatrix} t_3 & 0 & -t_2 \\ 0 & t_4 & 0 \\ -t_2 & 0 & t_1 \end{pmatrix} \text{ for } \mathbf{R} = (-0.5, 0.0, 0.5) \end{aligned}$$



**Supplementary Figure 2 | Electronic structure of fullerenes.** Band structure  $\varepsilon_k$  and density of states (DOS) of the degenerate half-filled  $t_{1u}$  bands using hopping parameters for  $K_3C_{60}$ .

where the connecting lattice vectors in Cartesian coordinates  $\mathbf{R}_{ij} \equiv \mathbf{R} = (R_x, R_y, R_z)$  are in units of the lattice constant  $a$ . Hopping matrices for transfer processes to the 6 next-nearest-neighbor (NNN) sites of a  $C_{60}$  molecule are

$$\begin{pmatrix} t_5 & 0 & 0 \\ 0 & t_6 & 0 \\ 0 & 0 & t_7 \end{pmatrix} \text{ for } \mathbf{R} = (1, 0, 0), \quad \begin{pmatrix} t_7 & 0 & 0 \\ 0 & t_5 & 0 \\ 0 & 0 & t_6 \end{pmatrix} \text{ for } \mathbf{R} = (0, 1, 0), \quad \begin{pmatrix} t_6 & 0 & 0 \\ 0 & t_7 & 0 \\ 0 & 0 & t_5 \end{pmatrix} \text{ for } \mathbf{R} = (0, 0, 1)$$

The remaining NN and NNN hopping matrices can be generated from inversion symmetry  $t_{\alpha\gamma}(\mathbf{R}) = t_{\alpha\gamma}(-\mathbf{R})$ . In this work, we employ the Wannier construction for  $K_3C_{60}$  for which the numerical values are (in meV):  $t_1 = -4$ ,  $t_2 = -33.9$ ,  $t_3 = 42.1$ ,  $t_4 = -18.7$ ,  $t_5 = -9.3$ ,  $t_6 = -1.4$ ,  $t_7 = -0.2$ . The onsite energy  $t_{\alpha\alpha}(\mathbf{R}_{ij} = \mathbf{0})$  is set to zero. We show the corresponding band structure (bandwidth  $W \approx 0.5$  eV) and density of states for the non-interacting model in Fig. 2. The main difference between different  $A_3C_{60}$  compounds is the bandwidth  $W$  and effective electronic interaction strength  $U$  [64, 75]. One can approximate the volume effect induced by different alkali dopands by changing the ratio  $U/W$ . The interaction Hamiltonian  $H_{\text{int}}$  is discussed in more detail in Note 7.

We also comment on the direction of the current. In all calculations, we put the FMP momentum  $\mathbf{q}$  parallel to one of the reciprocal lattice vectors:  $\mathbf{q} = q\mathbf{b}_1 = \frac{2\pi q}{a}(\hat{x} + \hat{y} - \hat{z})$  such that in Cartesian coordinates  $q_x = q_y = -q_z$ . By this, we can employ an analytical expression

for the velocity

$$\hbar \underline{v}(\mathbf{k}) = \nabla_{\mathbf{k}} \underline{h}(\mathbf{k}) = \nabla_{\mathbf{k}} \sum_{\mathbf{R}} \underline{t}(\mathbf{R}) e^{i\mathbf{k}\mathbf{R}} = i \sum_{\mathbf{R}} \mathbf{R} \underline{t}(\mathbf{R}) e^{i\mathbf{k}\mathbf{R}} \quad (46)$$

instead of numerically evaluating the gradient of  $h(\mathbf{k})$  in Eq. (40). The direction of the velocity and, hence, the supercurrent can be used as an internal consistency check of the code. The condition of  $\mathbf{j} \parallel \mathbf{q}$  demands that

$$\mathbf{j} = j_1 \mathbf{a}_1 + j_2 \mathbf{a}_2 + j_3 \mathbf{a}_3 \stackrel{!}{=} j(\mathbf{x} + \mathbf{y} - \mathbf{z}) \quad (47)$$

$$= a(j_1 + j_3) \hat{\mathbf{x}} + a(j_1 + j_2) \hat{\mathbf{y}} + a(j_2 + j_3) \hat{\mathbf{z}} \quad (48)$$

$$\Leftrightarrow j_3 = j_2 = -\frac{1}{3} j_1 \quad (49)$$

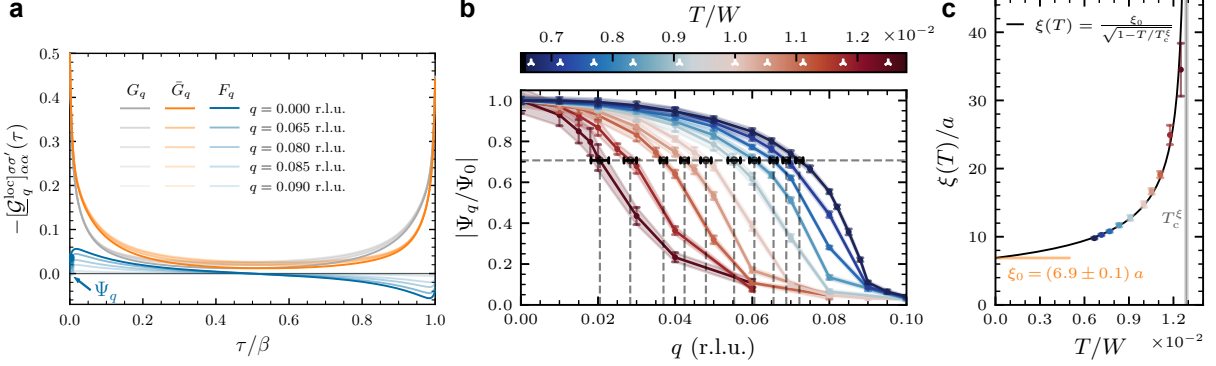
To have the correct sign of the direction, we need  $j_1 > 0$  (i.e.,  $j_2, j_3 < 0$ ). Since the fcc lattice has a very high symmetry, we can approximately treat the system to be isotropic. Because of this, we discuss in Fig. 2 of the main text and in Note 5-B only the absolute value of the current given by  $|\mathbf{j}| = 2\sqrt{3}ax$  with  $x = |j_2| = |j_3| = j_1/3$ .

## Supplementary Note 5: Details on the calculation of $|\Psi_q|$ , $\xi_0$ , $j_{\text{dp}}$ , and $\lambda_L$ from DMFT

In this section, we illustrate how the order parameter  $|\Psi_q|$  and concomitantly the coherence length  $\xi_0$  (c.f. 5-A) as well as the depairing current  $j_{\text{dp}}$  and London penetration depth  $\lambda_L$  (c.f. 5-B) are obtained from the  $\mathbf{q}$ - and  $T$ -dependence of the Nambu-Gor'kov Green function in practice. Furthermore, we elaborate on how the critical temperature extracted from the temperature dependence of  $\xi(T)$  and  $\lambda_L(T)$  can be used to scrutinize the proximity region of the Mott insulating phase and how it impacts the superconducting region (c.f. Note 5-C and Fig. 4A of the main text).

### 5-A Order parameter and coherence length

Generally, the superconducting order parameter carries an orbital dependence. The superconducting pairing in  $A_3C_{60}$ , however, is orbital diagonal. Because of this, we perform an orbital average over the self-energy components  $\Sigma^N$  and  $\Sigma^{AN}$  in each iteration step of the DMFT loop such that they are diagonal matrices in orbital space with degenerate entries ( $\Sigma_{\alpha\gamma}^{(A)N} = \delta_{\alpha\gamma} \Sigma^{(A)N}$ ). As a result, we explicitly prevent spontaneous orbital symmetry breaking in the self-energy [69] and the anomalous Green function  $F$  also becomes a degenerate, diagonal matrix in orbital space.



**Supplementary Figure 3 | Order parameter  $|\Psi_q|$  and coherence length  $\xi_0$  from the local anomalous Green function  $F^{\text{loc}}$ .** (a) Normal (particle  $G_q = \mathcal{G}_q^{\uparrow\uparrow}$ , hole  $\bar{G}_q = \mathcal{G}_q^{\downarrow\downarrow}$ ) and anomalous ( $F_q = \mathcal{G}_q^{\uparrow\downarrow}$ ) components of the local Nambu-Gor'kov Green function  $\mathcal{G}_q^{\text{loc}} = \sum_{\mathbf{k}} \mathcal{G}_q(\mathbf{k})$  for different values of  $q$  at fixed  $T/W = 6.7 \times 10^{-3}$ . The OP is taken at  $\tau = 0$  which we indicate by an arrow. (b) Momentum dependence of the OP normalized to the  $q = 0$  value for various  $T$  values. The condition  $|\Psi_Q(T)/\Psi_0(T)| = 1/\sqrt{2}$  to determine the correlation length via  $\xi(T) = 1/(\sqrt{2}Q)$  for fixed  $T$  is drawn with dashed lines. Different temperatures  $T$  are indicated in the color bar by white triangular markers and the shaded areas for each  $T$  show the range spanned by the uncertainty  $\delta|\Psi_q|$  which we use for spline fitting to determine an error for  $\xi(T)$ . (c) Temperature dependence of  $\xi(T)$  as obtained from panel b with the same coloring for each temperature. The fit of Eq. (3) (Eq. (2) in the main text) to extract  $\xi_0$  is plotted with a solid black line. Shown data are results of the DMFT calculations for  $U/W = 1.4$  and  $J/W = -0.04$ , equal to the content of Figs. 2 and 3 of the main text.

This allows us to work with a single-component OP for which we take the local anomalous Green function (c.f. Eq. (5) of the main text)

$$|\Psi_q| \equiv [F_q^{\text{loc}}(\tau = 0^-)]_{\alpha\alpha} = \sum_{\mathbf{k}} \langle c_{\alpha\mathbf{k}+\frac{q}{2}\uparrow} c_{\alpha-\mathbf{k}+\frac{q}{2}\downarrow} \rangle \quad (50)$$

Another option to define the OP is the superconducting gap  $\Delta$ , c.f. Note 6. Since, here,  $F$  and  $\Delta$  are orbital diagonal, they can be equivalently used for defining the OP as they have the same  $q$ - and  $T$ -dependence. Taking  $\Delta$  as the OP would change the relative scaling of the GL free energy because of  $\Delta \approx \mathcal{U}_{\text{eff}} F$  with an effective pairing potential  $\mathcal{U}_{\text{eff}}$  which is not of importance for determining  $\xi(T)$  from the OP.

In Fig. 3a, we show the normal ( $G$ ,  $\bar{G}$ ) and anomalous ( $F$ ) Green functions on imaginary time for different values of  $q = |q|$  where we also indicate the point of taking  $|\Psi_q|$  at  $\tau = 0^+$ . The amplitude of  $F$  is reduced by increasing  $q$ , whereas  $G$  and  $\bar{G}$  change only slightly. Interestingly, the anomalous Green function is a non-monotonous function of  $\tau$ .

In the main text, we discuss the momentum-dependence of the OP obtained in DMFT calculations under the constraint of FMP. Here, we want to further elaborate on how  $\xi(T)$  is

obtained from  $\Psi_q(T)$ . In GL theory, we found that  $\xi(T) = q_c^{-1}$  for  $\lim_{q \rightarrow q_c} \Psi_q(T) = 0$ . Since the point where  $\Psi_q$  goes to zero is difficult to evaluate numerically, we use in our DMFT calculations the criterion  $|\Psi_Q(T)/\Psi_0(T)| = 1/\sqrt{2}$  deriving from Eq. (5) such that  $\xi(T) = 1/(\sqrt{2}|Q|)$  for fixed  $T$ . In Fig. 3b, we illustrate how this criterion is applied to the DMFT results. Since our microscopic calculations include higher order terms of the free energy, the exact momentum dependence of  $\Psi_q$  differs from the GL expectation (Eq. (5)). Note that we take  $\xi(T)$  to be isotropic due to the high symmetry of the fcc lattice. In principle, it is possible to apply FMP with  $q$  in different directions in order to consider anisotropic behavior of  $\xi(T)$ .

Fig. 3 in the main text and Fig. 3 here in the Supplementary Information show error bars for  $\xi(T)$  which result from propagating the statistical QMC error of the OP to  $\xi(T)$ . The uncertainty in  $\xi(T)$  has been estimated as follows: For every dataset  $|\Psi_q(T)|$  we perform a series of spline fits where we randomly vary for each  $q$  the values to be fit in the range of  $[|\Psi_q| - \delta|\Psi_q|, |\Psi_q| + \delta|\Psi_q|]$  spanned by the uncertainty  $\delta|\Psi_q|$  of the OP. We indicate this range by color-shaded areas in Fig. 3b. Based on each spline interpolation, we obtain a value for  $Q$ . The error in  $Q$  is then estimated as the standard deviation of  $Q$  values in the so-obtained ensemble.

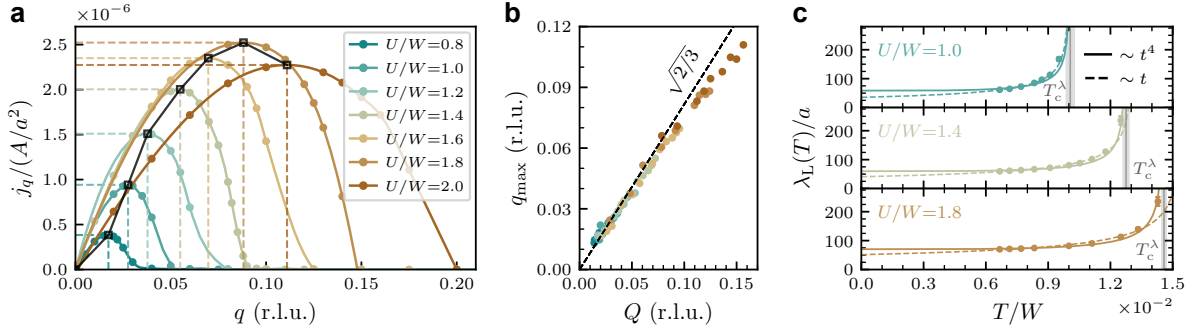
The temperature dependence of extracted  $\xi(T)$  and their uncertainty is plotted in panel C of Fig. 3. As expected from GL theory, the correlation length diverges towards the critical temperature  $T_c$  and decays to a finite value  $\xi_0$  for  $T \rightarrow 0$ . By fitting Eq. (3) to the data, we can extract the coherence length  $\xi_0$  and also obtain a value for the critical temperature  $T_c$ . We discuss the utility of extracting  $T_c$  this way in Note 5-C.

## 5-B Current density and penetration depth

We derived in Note 3 an expression for the current density  $j_q$  (Eq. (26)) where we in practice employ the modified Eq. (40) to ensure better convergence of the Matsubara summations. We show results of  $j_q = |j_q|$  depending on the interaction value  $U/W$  for the *ab initio* estimated Hund's coupling value  $J/W = -0.04$  and fixed  $T/W = 6.7 \times 10^{-2}$  in Fig. 4a.  $j_q$  exhibits a maximum, the depairing current  $j_{dp}$ , that we obtain by using a spline interpolation of the calculated data. By increasing  $U/W$ ,  $j_{dp}$  exhibits a dome shape which is similar to the OP but different to  $T_c$ . We note that the momenta  $q_{max}$  where  $j_{dp} = j_{q_{max}}$  correlate with the momenta  $Q$  used to calculate  $\xi(T)$  from the OP suppression as can be seen in panel B. A line of slope  $\sqrt{\frac{2}{3}}$  fits the data well suggesting  $q_{max} = \sqrt{\frac{2}{3}}Q$  as expected from the GL description. Only for large  $U$ , i.e., large values of  $Q$  and  $q_{max}$ , deviations can be seen which arise from the fact that our DMFT calculations include higher order terms which are not accounted for in the GL expansion in Eq. (4).

From combining the depairing current and the coherence length, we obtain the London



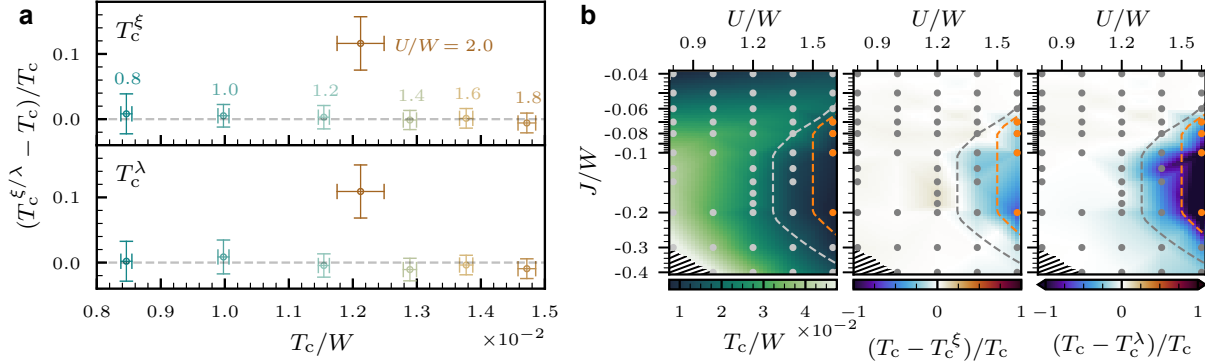


**Supplementary Figure 4 | Evaluation of supercurrent density  $j_q = |j_q|$  and London penetration depth  $\lambda_L$ .** (a) Momentum-dependence of the current density for different interaction ratios  $U/W$  with  $J/W = -0.04$  similar to Fig. 3 of the main text and fixed  $T/W = 6.7 \times 10^{-2}$ . The depairing current density  $j_{dp}$  (maximal  $j_q$ ) and corresponding momentum  $q_{max}$  are marked by dotted lines which are extracted from a spline interpolation drawn with a solid line connecting data points. The dome-shape behavior of  $j_{dp}$  as a function of  $U/W$  is marked by a black solid line. (b) Correlation between the momentum  $Q$  used to calculate  $\xi(T)$  from the suppression of the OP (c.f. Note 5-A) and the momentum  $q_{max}$  of maximal current density  $j_{dp}$ . Data points of the same color correspond to different temperatures for the same  $U/W$  where the coloring is the same as in panel a. A linear function with slope  $\sqrt{2}/3$  indicated by a dashed black line fits the data well. (c) Temperature dependence of the London penetration depth  $\lambda_L$  for different  $U/W$  and  $J/W = -0.04$ . We plot the fit according to Eq. (11) (Eq. (3) in the main text) with the quartic temperature dependence with a solid line and the fit with a linear temperature dependence with a dashed line ( $t = T/T_c$ ).

penetration depth  $\lambda_L(T)$ . In GL theory, the  $T$ -dependence of  $\lambda_L$  is linearized to depend on  $t = T/T_c$ . However, our calculations are better described by using the empirical quartic power law  $t^4$  as stated in Eq. (11) (Eq. (3) of the main text). We show exemplary results of  $\lambda_L(T)$  for different  $U/W$  and  $J/W = -0.04$  in Fig. 4c. At small  $U$ , the  $t$  and  $t^4$  dependence both match the data points quite well but the  $t$ -fit yields smaller values for the zero-temperature limit  $\lambda_{L,0}$ . Close to the Mott state for large  $U$ , the agreement becomes worse and only the  $t^4$  dependence fits the data well. We observed the same behavior also in the strong coupling region for increased values of  $|J|$ .

### 5-C Proximity region to the Mott transition

From our analysis of the  $T$ -dependence of the zero-momentum OP  $|\Psi_0|$ , correlation length  $\xi(T)$ , and London penetration depth  $\lambda_L$ , we are able to obtain different values of the superconducting transition temperature  $T_c$ . In this section, we discuss how they compare and use the notation of  $T_c^{\xi,\lambda}$  to differentiate the critical temperatures obtained by fitting  $\xi(T)$  and  $\lambda_L(T)$  from the  $T_c$



**Supplementary Figure 5 | Influence of proximity to the Mott insulating region on the superconducting state.** (a) Relative difference of critical temperature  $T_c^{(\xi,\lambda)}$  computed from fitting  $\xi(T)$  and  $\lambda_L(T)$  versus  $T_c$  as obtained from the OP  $|\Psi_0\rangle$  for the data at  $J/W = -0.04$  and different  $U/W$  as plotted in Fig. 3 of the main text. (b)  $T_c$  and relative difference to  $T_c^{(\xi,\lambda)}$  as a function of interactions  $U$  and  $J$ . Orange (gray) dots indicate data points where the critical temperature describes a transition from superconducting to Mott insulating (metallic) phase. Dashed lines are a guide to the eye separating the regions where the proximity to the Mott phase suppresses superconductivity characterized by  $T_c^{(\xi,\lambda)} < T_c$ . The  $T_c$  plot is the same as in Fig. 4A of the main text.

derived via  $|\Psi_0|^2 \sim T - T_c$ .

A first understanding can be gained by analyzing Fig. 3 of the main text. We summarize the respective critical temperatures in Fig. 5a. Generally, the critical temperature values obtained in all three methods agree well. Only in the special case of the first-order transition from the superconducting to the Mott-insulating phase for  $U/W = 2$ , we obtain higher values for  $T_c^{\xi,\lambda}$ . We conjecture that these temperatures describe a second-order transition to a metallic state hidden by the Mott insulating phase. We can utilize this fact to gauge the influence of the Mott state to reveal a suppression of superconductivity.

In Fig. 5b, we show the critical temperature  $T_c$  and the relative difference to  $T_c^{\xi,\lambda}$  in the  $(U, J)$ -plane analogous to Fig. 4A of the main text. Dots indicate original data points where orange dots (not shown in Fig. 4A) denote a critical temperature for a first-order transition from superconductor to Mott insulator. At these points, both  $T_c^\xi$  and  $T_c^\lambda$  are clearly larger than the critical temperature obtained from  $|\Psi_0|^2$  which is inline with the observation at  $J/W = -0.04$ . However, the suppression of  $T_c$  extends to the nearby region of the direct superconductor-Mott transition. The dashed lines, of which we also draw the gray line in Fig. 4A of the main text, are a guide to the eye to separate the region where proximity to Mott insulating states leads to a suppression of the critical temperature – even for a transition to the metallic state.

## Supplementary Note 6: Analysis of superconducting gap and coupling strength

In this section, we analyze the superconducting gap  $\Delta$  to further characterize the different superconducting regimes found in the  $A_3C_{60}$  model. The gap is given by [100]

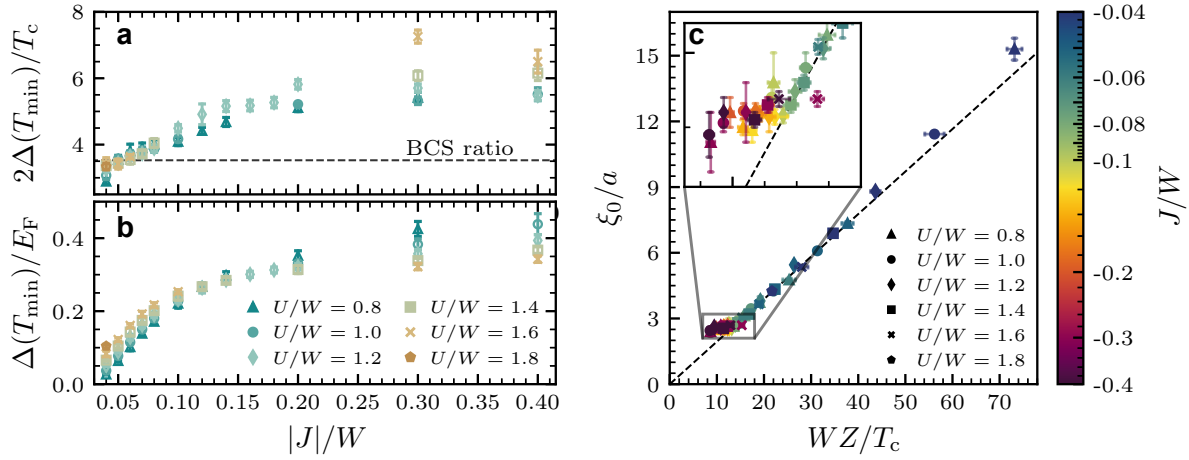
$$\Delta(i\omega_n) = \frac{\text{Re}\Sigma^{\text{AN}}(i\omega_n)}{\mathbb{1} - \frac{\text{Im}\Sigma^{\text{N}}(i\omega_n)}{\omega_n}} \equiv Z\Sigma^{\text{AN}} \quad (51)$$

with the quasiparticle weight  $Z^{-1} = \mathbb{1} - \text{Im}\Sigma^{\text{N}}(i\omega_0)/\omega_0$  and anomalous self-energy  $\Sigma^{\text{AN}}$  as we evaluate the gap on the lowest Matsubara frequency  $\Delta \equiv \Delta(i\omega_0)$ . We note that in the (deep) BEC limit, the quasiparticle gap is not given by  $\Delta$  due to the appearance of bound bosonic states. Instead, one needs to analyze  $\sqrt{\Delta^2 + \mu^2}$  with the chemical potential  $\mu$ .

In order to characterize the superconducting state, we analyze two different criteria: The first is the BCS ratio of the gap to the critical temperature  $T_c$  which in weak-coupling BCS theory has the universal value  $2\Delta_0/T_c = 3.53$  for the zero-temperature gap  $\Delta_0 = \Delta(T = 0)$ . In our calculations, we cannot reach zero temperature because of which we consider the gap for the lowest temperature  $T_{\text{min}}$  available for each interaction parameter set  $(U, J)$ . This is important for interpreting results for small Hund's coupling  $J/W \lesssim -0.1$  where we could not calculate far below  $T_c$ , i.e., the gap is far from saturating towards the zero-temperature value. Hence,  $\Delta(T_{\text{min}})$  only yields a lower bound.

We show the BCS ratio in Fig. 6a as a function of inverted Hund's coupling strength  $J < 0$  for different  $U/W$ . For small magnitudes  $|J|/W \lesssim 0.05$ , our results show good agreement with the BCS value. This is in disagreement with experimental measurements [34, 76] which observe the Cs and Rb compounds to have a ratio  $2\Delta/T_c$  much larger than the BCS value. We speculate that the discrepancy to our data arises for two reasons: First, we cannot get close to the zero-temperature value of the gap in our calculations, i.e.,  $T_{\text{min}}$  is rather close to  $T_c$  and the ratio is likely to be underestimated by this lower bound. Second, the overestimation of  $T_c$  in DMFT can additionally lead to an underestimation of the BCS ratio. Taking into account dynamical interactions give results that are in better agreement with experiment [63, 64]. Nonetheless, the qualitative trend of increasing  $2\Delta/T_c$  for larger  $U/W$  fits to experimental observation. A pronounced deviation from the BCS value can be found for large inverted Hund's coupling  $|J|/W > 0.05$ . Although  $T_c$  and  $\Delta$  both increase in the ‘‘multiorbital strong coupling’’ region for enhanced  $J < 0$ , superconductivity here is distinct to weak-coupling BCS theory. Note that we do not show  $T_c$  of a transition to the Mott insulating state.

The second criterion that we analyze is the ratio of the gap to the Fermi energy  $E_F$ . This ratio  $\Delta/E_F$  can be interpreted as a dimensionless coupling strength [25] which is small in the



**Supplementary Figure 6 | Characterization of superconducting regions in the model of  $A_3C_{60}$ .** (a) Ratio of the superconducting gap  $\Delta$  at the lowest available temperature  $T_{\min}$  and critical temperature  $T_c$  as a function of inverted Hund's coupling  $J < 0$ . The BCS ratio  $\Delta_0/T_c = 3.53$  is drawn with a dashed line. (b) Coupling strength characterized by the ratio of  $\Delta$  against the Fermi energy  $E_F$ . (c) Scaling of the coherence length  $\xi_0$  with the ratio of quasiparticle weight  $Z$  and  $T_c$ . Note that the color scale used to mark Hund's coupling  $J < 0$  is logarithmic. A linear fit is drawn as a guide to the eye where the zoom-in shows deviations for large  $J < 0$ . We note that  $T_c$  shown in panels a and c are only for the superconductor-metal transition, not for a first-order transition to the Mott phase.

weak-coupling region but grows to the order of 0.1–1 in the crossover and strong-coupling regime [24]. We note, however, that the theoretical determination of  $E_F$  is not trivial. To gauge the order of magnitude, we here resort to the non-interacting, renormalized definition

$$E_F = k_B T_F = \frac{\hbar^2 k_F^2}{2m^*} = \frac{\hbar^2}{2m^*} (3\pi^2 n)^{\frac{2}{3}} = \frac{(3\pi^2)^{\frac{2}{3}} \hbar^2}{2m_e} \cdot Z n^{\frac{2}{3}} \quad (52)$$

where we inserted the quasiparticle weight  $Z = m^*/m_e$ . The density is  $n = 3/(a/4)^3$  for the half-filled  $t_{1u}$  bands. We show the results in Fig. 6b. For small  $|J|$ , the coupling strength is weak as  $\Delta/E_F < 0.1$ . Towards the Mott regime, the couplings strengths grows to  $\sim 0.1$ , i.e., increasing  $U/W$  brings the system towards the BCS-BEC crossover regime. However, increasing  $|J|$  has a much stronger effect of driving the system into a strong coupling phase with  $\Delta/E_F > 0.1$ . Interestingly, larger  $U$  here quenches the coupling strength.

Lastly, we want to characterize the superconducting regimes via the coherence length  $\xi_0$ . In BCS theory and Eliashberg theory, the scaling  $\xi_0 \sim v_F^*/T_c \propto Z/T_c$  in terms of a renormalized Fermi velocity  $v_F^* = Z v_F$  can be established [37–39]. We investigate this relation in Fig. 6c. The scaling  $\xi_0 \sim Z/T_c$  as in BCS and Eliashberg theory holds for most interaction values up to  $J/W \sim -0.1$ , even towards the Mott insulating region. It, however, deviates in the localized

multiorbital strong coupling region for large  $|J|/W > 0.1$ , where  $\xi_0$  is not further reduced and  $Z$  stays almost constant but  $T_c$  still increases. Thus, the multiorbital strong coupling phase is to be differentiated from a (strongly) renormalized Eliashberg system as which one might be able to describe the system in the vicinity of the Mott insulating phase.

## Supplementary Note 7: Atomic limit of three-orbital model with inverted Hund's coupling

In the main text, we found that Cooper pairs become very localized with a short coherence length  $\xi_0 \sim O(2 - 3a)$  by increasing the inverted Hund's coupling  $J < 0$ . It suggests that local physics become increasingly important for the formation of superconducting pairing. Indeed, this was confirmed through the analysis of local density matrix weights in the main text. Here, we want to complement the discussion of the main text with discussing the atomic limit of the interacting impurity problem.

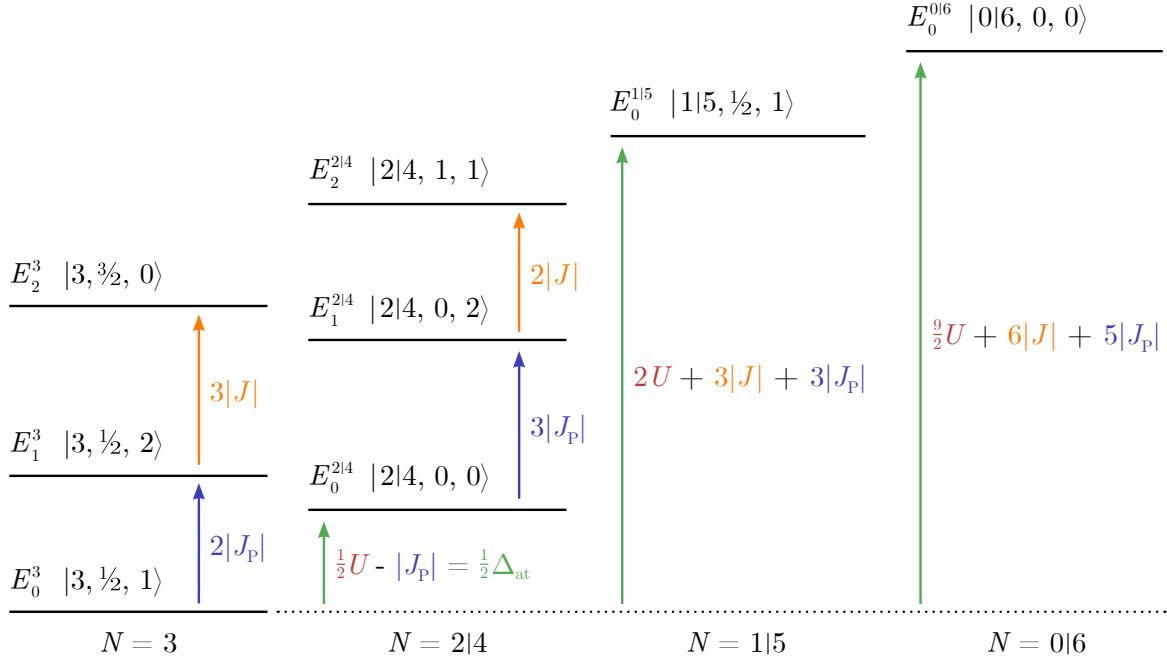
To this end, we want to solve the Kanamori-Hubbard interaction Hamiltonian as given in Eq. (7) of the main text without hopping processes. The form of the interaction given in the main text is convenient to read-off the (inverted) Hund's rules. We, here, restate the Kanamori-Hubbard Hamiltonian in its generalized formulation that indicates the different electronic interaction processes more clearly:

$$\begin{aligned}
H_{\text{int}} = & \sum_{\alpha} U n_{\alpha\uparrow} n_{\alpha\downarrow} + \sum_{\alpha < \gamma, \sigma\sigma'} (U' - \delta_{\sigma\sigma'} J) n_{\alpha\sigma} n_{\gamma\sigma'} \\
& - \sum_{\alpha \neq \gamma} J_X c_{\alpha\uparrow}^{\dagger} c_{\alpha\downarrow} c_{\gamma\downarrow}^{\dagger} c_{\gamma\uparrow} + \sum_{\alpha \neq \gamma} J_P c_{\alpha\uparrow}^{\dagger} c_{\alpha\downarrow}^{\dagger} c_{\gamma\downarrow} c_{\gamma\uparrow}
\end{aligned} \quad (53)$$

It consists of intraorbital interaction  $U$ , interorbital interaction  $U'$ , Hund's coupling  $J$ , spin-exchange  $J_X$ , and correlated pair hopping  $J_P$ . Yet, not all coupling constants are independent. We assume  $SU(2) \times SO(3)$  symmetry implying  $J_X = J$  and  $J_P = U - U' - J$  [65]. In the physical system and our calculations, we have in addition  $J_P = J$  resulting in  $U' = U - 2J$ . In the following discussion, we will emphasize the contribution of  $J_P$  since the low-energy excitations for inverted Hund's coupling  $J < 0$  are only governed by  $J_P$ . It is instructive to rewrite Eq. (53) in the same way as Eq. (7) of the main text (c.f. Eq. 5 in Ref. [65]) to see the role of  $J_P$ :

$$H_{\text{int}} = \frac{1}{4}(2U - 3J - 3J_P)\hat{N}(\hat{N} - 1) - (J + J_P)\hat{S}^2 - \frac{1}{2}J_P\hat{L}^2 + \frac{1}{4}(3J + 7J_P)\hat{N} \quad (54)$$

The pair hopping term, most notably, dictates the energy gain from high orbital angular momentum  $L^2$  and partially that of the total spin  $S^2$  of a given eigenstate for this Hamiltonian. We detail the spectrum in Tab. 1 for the case of negative  $J$ ,  $J_P < 0$  and half-filled orbitals where we add a



**Supplementary Figure 7 | Spectrum of the three-orbital Hubbard-Kanamori model.** The energies  $E_n^N$  and states  $|\phi_n^N\rangle \equiv |N, S, L\rangle$  of the three-orbital atom with Hubbard-Kanamori interaction (Eq. (54) at half-filling correspond to the notation used in Tab. 1. The relative positions of energies are drawn for the case of  $U > 2|J_P|$ , such that the ground state lies in the  $N = 3$  sector given by  $E_0^{N=3}$  and  $|N = 3, S = \frac{1}{2}, L = 1\rangle$ .

chemical potential  $\mu$  to ensure particle-hole symmetry. The chemical potential at half-filling is given by  $\mu = \frac{1}{2}U + \frac{N-1}{2}(2U' - J) = \frac{5}{2}U - 3J - 2J_P$  with  $N = 3$  and  $U' = U - J - J_P$ , as can be inferred from particle-hole transforming Eq. (54). The dimension of the complete Fock space is  $\dim \mathcal{H}_{\text{Fock}} = 2^6 = 64$ . Fig. 4B in the main text shows the statistical occupation of these 64 states during the QMC calculation in DMFT.

In case of half-filling, the atomic gap of the system is  $\Delta_{\text{at}} = E_0^{N=4} - E_0^{N=3} - (E_0^{N=3} - E_0^{N=2}) = U + 2J_P = U - 2|J_P|$ . For  $\Delta_{\text{at}} > 0$ , i.e.,  $U > 2|J_P|$ , the lowest energy state lies in the  $N = 3$  particle sector and is given by  $E_0^{N=3}$ . We sketch the energy spectrum for this case in Fig. 7. The lowest energy excitations from the ground state  $E_0^{N=3}$  are charge excitation to the  $N = 2$  and  $N = 4$  particle sectors with  $\Delta E_{\text{ch}} = \frac{1}{2}U + J_P = \frac{1}{2}U - |J_P| \equiv \frac{1}{2}\Delta_{\text{at}}$  as well as spin reconfiguration with  $\Delta E_{\text{sp}} = -2J_P = 2|J_P|$  within the  $N = 3$  charge sector which breaks up orbital singlets and increases the orbital angular momentum from  $L = 1$  to  $L = 2$ . Thus, the low-energy physics is governed by correlated pair hopping  $J_P$  and onsite repulsion  $U$ . The results presented in Fig. 4 of the main text can be understood from this local limit by addition of the kinetic hopping.

**Supplementary Table 1 | Spectrum of the local Kanamori-Hubbard Hamiltonian for a three-orbital system at half-filling.** The eigenenergies  $E_n^N$  are sorted in descending order in each charge sector of particle number  $N$  for  $J < 0$  where the contribution of the correlated pair hopping  $J_P$  ( $J_P \equiv J$  in our calculations) is explicitly stated. Each state is characterized by total spin  $S$ , orbital angular momentum  $L$ , and respective degeneracy  $(2S+1)(2L+1)$  with  $X = \langle \hat{X} \rangle$  ( $X = N, S, L$ ). The corresponding eigenstates  $|\phi_n^N\rangle$  are given for  $N \leq 3$  since the  $N \geq 4$  states can be constructed from particle-hole symmetry. The eigenstates in blue color are those depicted in Fig. 4C of the main text.

Energy $E_n^N$	$N$	$S$	$L$	Degeneracy ( $2S+1)(2L+1$ )	Eigenstates $ \phi_n^N\rangle$ ( $N \leq 3$ )
$E_0^{0[6]} = 0$	0[6]	0	0	1	$ 0, 0, 0\rangle$
$E_0^{1[5]} = -\frac{5}{2}U + 3J + 2J_P$	1[5]	1/2	1	6	$ \uparrow, 0, 0\rangle,  0, \uparrow, 0\rangle,  0, 0, \uparrow\rangle,$ $ \downarrow, 0, 0\rangle,  0, \downarrow, 0\rangle,  0, 0, \downarrow\rangle$
$E_2^{2[4]} = -4U + 4J + 3J_P$	2[4]	1	1	9	$ \uparrow, \uparrow, 0\rangle,  0, \uparrow, \uparrow\rangle,  \uparrow, 0, \uparrow\rangle,  \downarrow, 0, \downarrow\rangle,  0, \downarrow, \downarrow\rangle,  \downarrow, 0, \downarrow\rangle,$ $\frac{1}{\sqrt{2}}( \uparrow, 0, \downarrow\rangle -  \downarrow, 0, \uparrow\rangle), \frac{1}{\sqrt{2}}( 0, \uparrow, \downarrow\rangle -  0, \downarrow, \uparrow\rangle), \frac{1}{\sqrt{2}}( \uparrow, \downarrow, 0\rangle -  \downarrow, \uparrow, 0\rangle)$
$E_1^{2[4]} = -4U + 6J + 3J_P$	2[4]	0	2	5	$\frac{1}{\sqrt{2}}( \uparrow, 0, \downarrow\rangle +  \downarrow, 0, \uparrow\rangle), \frac{1}{\sqrt{2}}( 0, \uparrow, \downarrow\rangle +  0, \downarrow, \uparrow\rangle), \frac{1}{\sqrt{2}}( \uparrow, \downarrow, 0\rangle +  \downarrow, \uparrow, 0\rangle)$ $\frac{1}{\sqrt{2}}( \uparrow, \downarrow, 0, 0\rangle -  0, \uparrow, \downarrow, 0\rangle), \frac{1}{\sqrt{2}}( \uparrow, \downarrow, 0, 0\rangle -  0, 0, \uparrow, \downarrow\rangle)$
$E_0^{2[4]} = -4U + 6J + 6J_P$	2[4]	0	0	1	$\frac{1}{\sqrt{3}}( \uparrow, \downarrow, 0, 0\rangle +  0, \uparrow, \downarrow, 0\rangle +  0, 0, \uparrow, \downarrow\rangle)$
$E_2^3 = -\frac{9}{2}U + 3J + 3J_P$	3	3/2	0	4	$ \uparrow, \uparrow, \uparrow\rangle, \frac{1}{\sqrt{3}}( \uparrow, \downarrow, \downarrow\rangle +  \downarrow, \uparrow, \downarrow\rangle +  \downarrow, \downarrow, \uparrow\rangle),$ $ \downarrow, \downarrow, \downarrow\rangle, \frac{1}{\sqrt{3}}( \downarrow, \uparrow, \uparrow\rangle +  \uparrow, \downarrow, \uparrow\rangle +  \uparrow, \uparrow, \downarrow\rangle)$
$E_1^3 = -\frac{9}{2}U + 6J + 3J_P$	3	1/2	2	10	$\frac{1}{\sqrt{2}}( \uparrow, \downarrow, \downarrow\rangle -  \downarrow, \uparrow, \downarrow\rangle), \frac{1}{\sqrt{2}}( \uparrow, \downarrow, \downarrow\rangle -  \downarrow, \downarrow, \uparrow\rangle),$ $\frac{1}{\sqrt{2}}( \uparrow, \uparrow, 0\rangle -  \uparrow, 0, \uparrow\rangle), \frac{1}{\sqrt{2}}( \uparrow, \downarrow, \uparrow, 0\rangle -  0, \uparrow, \uparrow\rangle), \frac{1}{\sqrt{2}}( \uparrow, \downarrow, 0, \uparrow\rangle -  0, \uparrow, \downarrow\rangle),$ $\frac{1}{\sqrt{2}}( \downarrow, \uparrow, 0\rangle -  \downarrow, 0, \uparrow\rangle), \frac{1}{\sqrt{2}}( \uparrow, \downarrow, \downarrow, 0\rangle -  0, \downarrow, \uparrow\rangle), \frac{1}{\sqrt{2}}( \uparrow, \downarrow, 0, \downarrow\rangle -  0, \uparrow, \downarrow\rangle),$ $\frac{1}{\sqrt{2}}( \downarrow, \uparrow, \uparrow\rangle -  \uparrow, \downarrow, \uparrow\rangle), \frac{1}{\sqrt{2}}( \downarrow, \uparrow, \uparrow\rangle -  \uparrow, \uparrow, \downarrow\rangle)$
$E_0^3 = -\frac{9}{2}U + 6J + 5J_P$	3	1/2	1	6	$\frac{1}{\sqrt{2}}( \uparrow, \uparrow, \downarrow, 0\rangle +  \uparrow, 0, \uparrow, \downarrow\rangle), \frac{1}{\sqrt{2}}( \uparrow, \downarrow, \uparrow, 0\rangle +  0, \uparrow, \uparrow, \downarrow\rangle), \frac{1}{\sqrt{2}}( \uparrow, \downarrow, 0, \uparrow\rangle +  0, \uparrow, \downarrow\rangle),$ $\frac{1}{\sqrt{2}}( \downarrow, \uparrow, \downarrow, 0\rangle +  \downarrow, 0, \uparrow, \downarrow\rangle), \frac{1}{\sqrt{2}}( \uparrow, \downarrow, \downarrow, 0\rangle +  0, \downarrow, \uparrow, \downarrow\rangle), \frac{1}{\sqrt{2}}( \uparrow, \downarrow, 0, \downarrow\rangle +  0, \uparrow, \downarrow\rangle)$





# Concluding remarks

*It is important to draw wisdom from many different places.  
If you take it from only one place, it becomes rigid and stale.*

— Iroh

In this thesis, we have conducted material-realistic studies on the interplay between electron correlations and unconventional superconductivity in different materials. To this end, we developed and applied new computational tools that enhance both efficiency and capability of many-body methods. Those developments empowered the numerical investigation of previously inaccessible parameter regions and material properties. In the following, we summarize the achievements of this thesis in relation to the overarching questions in superconductivity research discussed in section 1.3. Furthermore, we give an outlook on possible future research directions.

## Improving the efficiency of computational many-body methods

We have enhanced the numerical efficiency of many-body methods by utilizing low-rank representations of Matsubara Green's functions in conjunction with sparse modeling techniques. Specifically, we employed the IR basis for optimal data compression, which derives from the singular value decomposition of the spectral representation kernel. This integrated approach effectively addresses computational bottlenecks associated with the linear scaling of Matsubara frequencies with inverse temperature, enabling material-realistic calculations at low-temperatures.

To facilitate this improvement, we have developed the standalone code library `sparse-ir`, which we introduced in publication I. This library provides the IR basis functions and evaluation utilities, allowing for efficient implementation of many-body methods. Its simple architecture enables seamless integration into both existing codebases and new applications. Alongside the library, we have created extensive tutorials that illustrate the code's capabilities, while also serving as a reference for implementations of common many-body approaches.

The improvements provided by the IR basis were utilized in several applications studying spin-fluctuation-driven superconductivity. In our benchmark study of water-intercalated sodium cobalt oxide in publication II, the FLEX+IR implementation showcased the enhanced numerical efficiency: We could perform calculations

at very low temperatures down to the order of  $10^{-4}$  in units of the bandwidth. Through this low-temperature analysis, we identified the predominance of the triplet  $f_{y(x^2-3y^2)}$ -wave pairing symmetry by examining the superconducting eigenvalue of the linearized gap equation. However, contrary to previous expectations based on higher-temperature calculations, we did not observe a transition to the superconducting phase at the scale of experimental  $T_c = 4.5$  K, with the superconducting eigenvalue reaching up to only 0.7 at 2 K. To conclusively determine the potential for spin-fluctuation-mediated triplet superconductivity, the influence of doping in the actual experimental compound  $\text{Na}_x(\text{H}_3\text{O})_z\text{CoO}_2 \cdot y\text{H}_2\text{O}$  needs to be explored in future studies.

The ability to perform calculations at previously inaccessible temperatures enabled us to compute critical temperatures for spin-fluctuation-driven superconductivity in the nearest-neighbor tight-binding model of a honeycomb lattice pertinent to  $\Gamma$ -valley twisted TMDCs. This progress allowed us to draw a comprehensive doping-dependent phase diagram in publication IV, which we contrasted to that of conventional superconductivity mediated by moiré phonons. An extension of our study to K-valley twisted  $\text{WSe}_2$  could help in elucidating the recent experimental reports on possibly unconventional superconductivity in that material [79, 80, 165].

Furthermore, in publication III, we highlighted the critical role of inter-layer correlations in the formation of superconductivity in bilayer nickelates. Through CDMFT calculations, we observed a Lifshitz transition characterized by the disappearance of the  $\gamma$  pocket from the Fermi surface. The concomitant suppression of ferromagnetic fluctuations enhances superconductivity, as shown by comparisons to DMFT calculations that lack inter-layer correlations. Transforming the (C)DMFT data into the IR basis facilitated the calculation of the superconducting phase. Notably, the sparse-ir library enabled a straightforward interoperability of Green's functions data and allowed for precise error control of the noise from the QMC simulations in (C)DMFT. Given the young stage of research on  $\text{La}_3\text{Ni}_2\text{O}_7$ , many open questions regarding its normal state and superconducting properties exist as detailed in section 4.2.1. Another intriguing question is why, in particular, the bilayer variant of the Ruddlesden-Poppers nickelates exhibits such a high critical temperature compared to other layer numbers.

### Optimized conditions for superconductivity

In chapter 6, we examined the limitations of superconductivity arising from the competition between energy scales of particle pairing and phase stiffness. To raise critical temperatures, it is generally necessary to increase the energy scale for particle pairing. For conventional phonon-mediated superconductivity, BCS and Migdal-Eliashberg theory suggest that this can be achieved by optimizing the phonon energy scale  $\omega_D$ , the interaction strength  $U$ , or the density of states. We reaffirmed this

---

principle in publication IV, where we found that the doping dependence of the critical temperature in moiré phonon-mediated pairing is primarily determined by the electronic density of states.

In contrast, the optimal conditions for spin-fluctuation-mediated pairing are more complex, as shown in publications II, III, IV, and V. This complexity arises from factors such as the spatial and orbital structure of spin fluctuations, the presence of competing and possibly pair breaking spin fluctuations, as well as the available electronic density of states. In particular, the absence of superconductivity in copper-substituted lead apatite showed that the bandwidth needs to be sufficiently large to facilitate strong enough spin fluctuations. Comparing this material to other studied systems underscores the preference for (quasi-)two-dimensional systems in facilitating strong superconductivity driven by spin fluctuations.

Nonetheless, the formation of a resilient superconducting condensate also requires sufficiently large phase stiffness. Our discussion of the Uemura relation and the BCS–BEC crossover in section 6.1 indicates that a viable route to enhance superconductivity is to focus on achieving a high stiffness. For alkali-doped fullerenes, we demonstrated enhanced strong-coupling superconductivity that is effectively enabled by an interaction-resilient metallic phase of mixed valence at higher temperatures. This mixed-valence state, created from the interplay of multi-orbital interaction scales, supports a high phase stiffness and allows critical temperatures to be elevated by increasing the pairing interaction. Remarkably, the mechanism revealed in this work leads to a simultaneous increase or preservation of both pairing and phase coherence energy scales for electrons of the same (degenerate) electronic bands. This approach contrasts with the strategy of enhancing superconductivity through hybridization effects, such as coupling a flat band to a dispersive band. In this scenario, the flat band hosts strong pairing and large energy gaps, while the mobile electrons from the dispersive band establish phase stiffness [454]. Identifying systems with a similar mechanism to that found in  $A_3C_{60}$  is an interesting future research direction.

### Extended characterization of superconducting materials

We have introduced a generic method to calculate key superconducting parameters: the correlation length  $\xi$ , the London penetration depth  $\lambda_L$ , and the depairing current (density)  $j_{dp}$ . Our approach is based on the Nambu–Gor’kov Green’s function formalism incorporating finite-momentum pairing (FMP). By applying this method to  $A_3C_{60}$ , we demonstrated good agreement with experimental values for the length scales  $\xi$  and  $\lambda_L$ , thereby validating our approach.

Access to the superconducting length scales and the depairing current extends the theoretical and computational characterization of superconductors, which is commonly focused only on critical temperatures and gap functions. In particular, critical

magnetic fields  $H_c$  and critical currents  $j_c$  can be obtained from  $\xi$  and  $\lambda_L$ , which is crucial for applications of superconducting materials. Therefore, our method significantly broadens the scope of computational modeling of superconducting matter, opening up many opportunities for future research. One important aspect is that access to  $\xi$  and  $\lambda_L$  allows for a more rigorous comparison between experimental results and theoretical modeling, potentially helping to unveil the unresolved pairing mechanisms, e.g., in heavy fermion compounds, MATBG, or  $\text{Sr}_2\text{RuO}_4$ .

In publication VI, we applied the FMP framework to describe strongly correlated  $s$ -wave superconductivity in a model of  $\text{A}_3\text{C}_{60}$  using DMFT. However, our approach can be generalized to other pairing symmetries and it can be integrated into any Green's function-based method in order to characterize superconductivity across a variety of materials. Importantly, this method bridges a significant gap in the analysis of strongly correlated superconductors, offering unprecedented access to both superconducting length scales. For instance, extending our approach to the  $d$ -wave superconductivity in cuprates could provide insights on the relation of the superconducting dome and the BCS–BEC crossover phenomenology, a topic under long-standing debate [197, 703, 709, 710]. Recently, Chen et al. [710] emphasized that experimental access to  $\xi$  can aid in scrutinizing the role of the BCS–BEC crossover in cuprate physics. We suggest that a complementary analysis through microscopic calculations is also valuable for illuminating this scenario.

The recent progress in computational methods has advanced the accuracy of non-empirical calculations of critical temperatures [96, 119, 155, 432, 715]. In this context, implementing the FMP constraint for non-empirical calculations of  $\xi$ ,  $\lambda_L$ , and  $j_{dp}$  (hence also  $H_c$  and  $j_c$ ), could provide a comprehensive characterization of the superconducting critical surface. This opens pathways for in-situ computational optimization of superconducting material, which can potentially be enhanced by machine learning techniques.

# Bibliography

- [I] M. Wallerberger et al., “sparse-ir: Optimal compression and sparse sampling of many-body propagators”, *SoftwareX* **21**, 101266 (2023), included on p. 49 et sqq. (*Cit. on pp. 30, 45, 46, 105*).
- [II] N. Witt, E. G. C. P. van Loon, T. Nomoto, R. Arita, and T. O. Wehling, “Efficient fluctuation-exchange approach to low-temperature spin fluctuations and superconductivity: From the Hubbard model to  $\text{Na}_x\text{CoO}_2 \cdot y\text{H}_2\text{O}$ ”, *Phys. Rev. B* **103**, 205148 (2021), [arXiv:2012.04562](#), included on p. 114 et sqq. (*Cit. on pp. 23, 36, 46, 58, 84, 106*).
- [III] S. Ryee, N. Witt, and T. O. Wehling, “Quenched Pair Breaking by Interlayer Correlations as a Key to Superconductivity in  $\text{La}_3\text{Ni}_2\text{O}_7$ ”, *Phys. Rev. Lett.* **133**, 096002 (2024), [arXiv:2310.17465](#) (*cit. on pp. 46, 58, 84, 106*).
- [IV] N. Witt, J. M. Pizarro, J. Berges, T. Nomoto, R. Arita, and T. O. Wehling, “Doping fingerprints of spin and lattice fluctuations in moiré superlattice systems”, *Phys. Rev. B* **105**, L241109 (2022), [arXiv:2108.01121](#), included on p. 161 et sqq. (*Cit. on pp. 46, 58, 84, 106*).
- [V] N. Witt, L. Si, J. M. Tomczak, K. Held, and T. O. Wehling, “No superconductivity in  $\text{Pb}_9\text{Cu}_1(\text{PO}_4)_6\text{O}$  found in orbital and spin fluctuation exchange calculations”, *SciPost Phys.* **15**, 197 (2023), included on p. 192 et sqq. (*Cit. on pp. 46, 58, 64, 84, 106, 191*).
- [VI] N. Witt, Y. Nomura, S. Brener, R. Arita, A. I. Lichtenstein, and T. O. Wehling, “Bypassing the lattice BCS–BEC crossover in strongly correlated superconductors through multiorbital physics”, *npj Quantum Mater.* **9**, 100 (2024), [arXiv:2310.09063](#) (*cit. on pp. 12, 207, 212*).
- [1] D. Castelvetti, “Why superconductor research is in a ‘golden age’ — despite controversy”, *Nature*, **10**. 1038 / d41586 - 023 - 03551 - z (2023) (*cit. on p. xi*).
- [2] B. Keimer and J. E. Moore, “The physics of quantum materials”, *Nat. Phys.* **13**, 1045 (2017) (*cit. on pp. 1, 15*).
- [3] Y. Tokura, M. Kawasaki, and N. Nagaosa, “Emergent functions of quantum materials”, *Nat. Phys.* **13**, 1056 (2017) (*cit. on pp. 1, 6*).
- [4] C. Yao and Y. Ma, “Superconducting materials: Challenges and opportunities for large-scale applications”, *iScience* **24**, 102541 (2021), [arXiv:2106.02825](#) (*cit. on pp. 1, 3, 6, 70, 189*).

- [5] M. Kjaergaard, M. E. Schwartz, J. Braumüller, P. Krantz, J. I.-J. Wang, S. Gustavsson, and W. D. Oliver, “Superconducting Qubits: Current State of Play”, *Annu. Rev. Condens. Matter Phys.* **11**, 369 (2020), [arXiv:1905.13641](#) (*cit. on p. 1*).
- [6] N. Samarth, “Quantum materials discovery from a synthesis perspective”, *Nat. Mater.* **16**, 1068 (2017) (*cit. on pp. 1, 6, 109*).
- [7] D. N. Basov, R. D. Averitt, and D. Hsieh, “Towards properties on demand in quantum materials”, *Nat. Mater.* **16**, 1077 (2017) (*cit. on pp. 1, 6, 10*).
- [8] F. Giustino et al., “The 2021 quantum materials roadmap”, *J. Phys. Mater.* **3**, 042006 (2020), [arXiv:2102.02644](#) (*cit. on pp. 1, 8*).
- [9] N. F. Mott, “Metal-Insulator Transition”, *Rev. Mod. Phys.* **40**, 677 (1968) (*cit. on pp. 1, 17, 36, 39, 40*).
- [10] M. Imada, A. Fujimori, and Y. Tokura, “Metal-insulator transitions”, *Rev. Mod. Phys.* **70**, 1039 (1998) (*cit. on pp. 1, 17, 39, 110, 191*).
- [11] K. v. Klitzing, G. Dorda, and M. Pepper, “New Method for High-Accuracy Determination of the Fine-Structure Constant Based on Quantized Hall Resistance”, *Phys. Rev. Lett.* **45**, 494 (1980) (*cit. on p. 1*).
- [12] C.-Z. Chang, C.-X. Liu, and A. H. MacDonald, “Colloquium : Quantum anomalous Hall effect”, *Rev. Mod. Phys.* **95**, 011002 (2023) (*cit. on p. 1*).
- [13] M. Z. Hasan and C. L. Kane, “Colloquium: Topological insulators”, *Rev. Mod. Phys.* **82**, 3045 (2010), [arXiv:1002.3895](#) (*cit. on p. 1*).
- [14] X.-L. Qi and S.-C. Zhang, “Topological insulators and superconductors”, *Rev. Mod. Phys.* **83**, 1057 (2011), [arXiv:1008.2026](#) (*cit. on p. 1*).
- [15] L. Savary and L. Balents, “Quantum spin liquids: a review”, *Rep. Prog. Phys.* **80**, 016502 (2016), [arXiv:1601.03742](#) (*cit. on p. 1*).
- [16] L. Šmejkal, J. Sinova, and T. Jungwirth, “Beyond Conventional Ferromagnetism and Antiferromagnetism: A Phase with Nonrelativistic Spin and Crystal Rotation Symmetry”, *Phys. Rev. X* **12**, 031042 (2022), [arXiv:2105.05820](#) (*cit. on p. 1*).
- [17] L. Šmejkal, J. Sinova, and T. Jungwirth, “Emerging Research Landscape of Altermagnetism”, *Phys. Rev. X* **12**, 040501 (2022), [arXiv:2204.10844](#) (*cit. on p. 1*).
- [18] C.-W. Chen, J. Choe, and E. Morosan, “Charge density waves in strongly correlated electron systems”, *Rep. Prog. Phys.* **79**, 084505 (2016) (*cit. on p. 1*).
- [19] M. Fiebig, T. Lottermoser, D. Meier, and M. Trassin, “The evolution of multiferroics”, *Nat. Rev. Mater.* **1**, 16046 (2016) (*cit. on p. 1*).
- [20] N. A. Spaldin and R. Ramesh, “Advances in magnetoelectric multiferroics”, *Nat. Mater.* **18**, 203 (2019) (*cit. on p. 1*).
- [21] L. Balents, C. R. Dean, D. K. Efetov, and A. F. Young, “Superconductivity and strong correlations in moiré flat bands”, *Nat. Phys.* **16**, 725 (2020) (*cit. on pp. 1, 8, 156*).

- [22] D. M. Kennes, M. Claassen, L. Xian, A. Georges, A. J. Millis, J. Hone, C. R. Dean, D. N. Basov, A. N. Pasupathy, and A. Rubio, “Moiré heterostructures as a condensed-matter quantum simulator”, *Nat. Phys.* **17**, 155 (2021), [arXiv:2011.12638](#) (cit. on pp. 1, 8, 109, 156).
- [23] K. F. Mak and J. Shan, “Semiconductor moiré materials”, *Nat. Nanotechnol.* **17**, 686 (2022) (cit. on pp. 1, 8, 156, 159).
- [24] K. P. Nuckolls and A. Yazdani, “A microscopic perspective on moiré materials”, *Nat. Rev. Mater.* **9**, 460 (2024), [arXiv:2404.08044](#) (cit. on pp. 1, 2, 8, 109, 156–158).
- [25] A. Cavalleri, “Photo-induced superconductivity”, *Contemp. Phys.* **59**, 31 (2017) (cit. on pp. 1, 11).
- [26] A. de la Torre, D. M. Kennes, M. Claassen, S. Gerber, J. W. McIver, and M. A. Sentef, “Colloquium: Nonthermal pathways to ultrafast control in quantum materials”, *Rev. Mod. Phys.* **93**, 041002 (2021), [arXiv:2103.14888](#) (cit. on p. 1).
- [27] J. G. Bednorz and K. A. Müller, “Possible high  $T_c$  superconductivity in the Ba-La-Cu-O system”, *Z. Phys. B Condens. Matter* **64**, 189 (1986) (cit. on pp. 1, 5, 9).
- [28] B. Keimer, S. A. Kivelson, M. R. Norman, S. Uchida, and J. Zaanen, “From quantum matter to high-temperature superconductivity in copper oxides”, *Nature* **518**, 179 (2015) (cit. on pp. 1, 2, 6, 9, 10, 88, 109, 110, 209).
- [29] G. R. Stewart, “Unconventional superconductivity”, *Adv. Phys.* **66**, 75 (2017), [arXiv:1705.05593](#) (cit. on p. 2).
- [30] A. V. Narlikar, *Superconductors* (Oxford University Press, Incorporated, Oxford, 2014) (cit. on pp. 2, 3, 9, 57, 70, 72).
- [31] P. A. Lee, N. Nagaosa, and X.-G. Wen, “Doping a Mott insulator: Physics of high-temperature superconductivity”, *Rev. Mod. Phys.* **78**, 17 (2006), [arXiv:cond-mat/0410445](#) (cit. on pp. 2, 6, 191).
- [32] T. Moriya and K. Ueda, “Antiferromagnetic spin fluctuation and superconductivity”, *Rep. Prog. Phys.* **66**, 1299 (2003) (cit. on pp. 2, 6, 58, 105, 106, 191).
- [33] Y. Yanase, T. Jujo, T. Nomura, H. Ikeda, T. Hotta, and K. Yamada, “Theory of superconductivity in strongly correlated electron systems”, *Phys. Rep.* **387**, 1 (2003), [arXiv:cond-mat/0309094](#) (cit. on pp. 2, 6, 36, 38, 58, 105, 106).
- [34] D. J. Scalapino, “A common thread: The pairing interaction for unconventional superconductors”, *Rev. Mod. Phys.* **84**, 1383 (2012), [arXiv:1207.4093](#) (cit. on pp. 2, 6, 22, 43, 58, 105, 106, 191).
- [35] R. M. Fernandes, A. I. Coldea, H. Ding, I. R. Fisher, P. J. Hirschfeld, and G. Kotliar, “Iron pnictides and chalcogenides: a new paradigm for superconductivity”, *Nature* **601**, 35 (2022), [arXiv:2201.02095](#) (cit. on pp. 2, 7).
- [36] P. W. Phillips, N. E. Hussey, and P. Abbamonte, “Stranger than metals”, *Science* **377**, 6602 (2022), [arXiv:2205.12979](#) (cit. on pp. 2, 11, 31, 129).

- [37] A. Damascelli, Z. Hussain, and Z.-X. Shen, "Angle-resolved photoemission studies of the cuprate superconductors", *Rev. Mod. Phys.* **75**, 473 (2003), [arXiv:cond-mat/0208504](#) (cit. on p. 2).
- [38] X. Lu et al., "Superconductors, orbital magnets and correlated states in magic-angle bilayer graphene", *Nature* **574**, 653 (2019), [arXiv:1903.06513](#) (cit. on pp. 2, 8).
- [39] H. K. Onnes, *Commun. Phys. Lab. Univ. Leiden* 120b, 122b, 124c (1911) (cit. on p. 3).
- [40] D. van Delft and P. Kes, "The discovery of superconductivity", *Phys. Today* **63**, 38 (2010) (cit. on p. 3).
- [41] J. Bardeen, L. N. Cooper, and J. R. Schrieffer, "Theory of Superconductivity", *Phys. Rev.* **108**, 1175 (1957) (cit. on pp. 3, 67, 89–92, 96).
- [42] K.-H. Bennemann and J. B. Ketterson, *Superconductivity*, Vol. 1 (Springer-Verlag GmbH, 2008) (cit. on pp. 3, 10, 57).
- [43] A. A. Abrikosov, L. P. Gorkov, and I. E. Dzyaloshinski, *Methods of quantum field theory in statistical physics* (Dover Publications, New York, 1975) (cit. on pp. 3, 23, 27, 37).
- [44] P. Coleman, *Introduction to Many-Body Physics* (Cambridge University Press, Cambridge, 2015) (cit. on pp. 3, 16, 23, 24, 27–29, 31, 32, 41, 59, 60, 62, 64–66, 68–70, 75, 78–80, 91, 93, 94, 96, 98, 100–102, 190).
- [45] B. T. Matthias, "Chapter V Superconductivity in the Periodic System", in *Progress in low temperature physics* (Elsevier, 1957), pp. 138–150 (cit. on pp. 3, 209).
- [46] I. I. Mazin, "Superconductivity gets an iron boost", *Nature* **464**, 183 (2010) (cit. on p. 3).
- [47] N. Witt, "A multi-orbital Fluctuation Exchange Approach to Models and Materials within the Intermediate Representation Basis", MA thesis (Institute for Theoretical Physics, University of Bremen, 2020) (cit. on pp. 4, 29, 37, 106, 114).
- [48] P. J. Ray, "Structural investigation of  $\text{La}_{2-x}\text{Sr}_x\text{CuO}_{4+y}$  - Following staging as a function of temperature", MA thesis (Niels Bohr Institute, Faculty of Science, University of Copenhagen, 2015) (cit. on p. 4).
- [49] D. Li, K. Lee, B. Y. Wang, M. Osada, S. Crossley, H. R. Lee, Y. Cui, Y. Hikita, and H. Y. Hwang, "Superconductivity in an infinite-layer nickelate", *Nature* **572**, 624 (2019) (cit. on pp. 4, 7, 127, 128).
- [50] M. Osada, B. Y. Wang, K. Lee, D. Li, and H. Y. Hwang, "Phase diagram of infinite layer praseodymium nickelate  $\text{Pr}_{1-x}\text{Sr}_x\text{NiO}_2$  thin films", *Phys. Rev. Materials* **4**, 121801 (2020), [arXiv:2010.16101](#) (cit. on pp. 4, 127).



- [51] M. Osada, B. Y. Wang, B. H. Goodge, S. P. Harvey, K. Lee, D. Li, L. F. Kourkoutis, and H. Y. Hwang, "Nickelate Superconductivity without Rare-Earth Magnetism: (La,Sr)NiO<sub>2</sub>", *Adv. Mater.* **33**, 2104083 (2021), [arXiv:2105.13494](#) (cit. on pp. 4, 127).
- [52] S. Zeng et al., "Superconductivity in infinite-layer nickelate La<sub>1-x</sub>Ca<sub>x</sub>NiO<sub>2</sub> thin films", *Sci. Adv.* **8**, eabl9927 (2022), [arXiv:2105.13492](#) (cit. on pp. 4, 127).
- [53] G. A. Pan et al., "Superconductivity in a quintuple-layer square-planar nickelate", *Nat. Mater.* **21**, 160 (2021), [arXiv:2109.09726](#) (cit. on pp. 4, 127, 128).
- [54] N. N. Wang et al., "Pressure-induced monotonic enhancement of T<sub>c</sub> to over 30 k in superconducting Pr<sub>0.82</sub>Sr<sub>0.18</sub>NiO<sub>2</sub> thin films", *Nat. Commun.* **13**, 4367 (2022), [arXiv:2109.12811](#) (cit. on pp. 4, 127).
- [55] K. Lee et al., "Linear-in-temperature resistivity for optimally superconducting (Nd,Sr)NiO<sub>2</sub>", *Nature* **619**, 288 (2023) (cit. on pp. 4, 127, 128).
- [56] H. Sun et al., "Signatures of superconductivity near 80 K in a nickelate under high pressure", *Nature* **621**, 493 (2023), [arXiv:2305.09586](#) (cit. on pp. 4, 7, 127, 129).
- [57] Y. Zhu et al., "Superconductivity in pressurized trilayer La<sub>4</sub>Ni<sub>3</sub>O<sub>10-δ</sub> single crystals", *Nature* **631**, 531 (2024), [arXiv:2311.07353](#) (cit. on pp. 4, 127).
- [58] B. D. White, J. D. Thompson, and M. B. Maple, "Unconventional superconductivity in heavy-fermion compounds", *Phys. C: Supercond. Appl.* **514**, 246 (2015) (cit. on pp. 4, 5).
- [59] S. Ran et al., "Nearly ferromagnetic spin-triplet superconductivity", *Science* **365**, 684 (2019) (cit. on pp. 4, 5, 72).
- [60] B. T. Matthias, H. Suhl, and E. Corenzwit, "Ferromagnetic superconductors", *Phys. Rev. Lett.* **1**, 449 (1958) (cit. on p. 4).
- [61] H. Barz, "New ternary superconductors with silicon", *Mater. Res. Bull.* **15**, 1489 (1980) (cit. on p. 4).
- [62] B. R. Ortiz et al., "CsV<sub>3</sub>Sb<sub>5</sub>: A Z<sub>2</sub> Topological Kagome Metal with a Superconducting Ground State", *Phys. Rev. Lett.* **125**, 247002 (2020), [arXiv:2011.06745](#) (cit. on pp. 4, 6).
- [63] Q. Yin, Z. Tu, C. Gong, Y. Fu, S. Yan, and H. Lei, "Superconductivity and Normal-State Properties of Kagome Metal RbV<sub>3</sub>Sb<sub>5</sub> Single Crystals", *Chinese Phys. Lett.* **38**, 037403 (2021), [arXiv:2101.10193](#) (cit. on pp. 4, 6).
- [64] B. R. Ortiz, P. M. Sarte, E. M. Kenney, M. J. Graf, S. M. L. Teicher, R. Seshadri, and S. D. Wilson, "Superconductivity in the Z<sub>2</sub> kagome metal KV<sub>3</sub>Sb<sub>5</sub>", *Phys. Rev. Materials* **5**, 034801 (2021), [arXiv:2012.09097](#) (cit. on pp. 4, 6).
- [65] K. Y. Chen et al., "Double Superconducting Dome and Triple Enhancement of T<sub>c</sub> in the Kagome Superconductor CsV<sub>3</sub>Sb<sub>5</sub> under High Pressure", *Phys. Rev. Lett.* **126**, 247001 (2021), [arXiv:2102.09328](#) (cit. on pp. 4, 6).

- [66] E. Revolinsky, G. A. Spiering, and D. J. Beerntsen, "Superconductivity in the niobium-selenium system", *J. Phys. Chem. Solids* **26**, 1029 (1965) (*cit. on pp. 4, 8*).
- [67] B. Sipos, A. F. Kusmartseva, A. Akrap, H. Berger, L. Forró, and E. Tutiš, "From Mott state to superconductivity in 1T-TaS<sub>2</sub>", *Nat. Mater.* **7**, 960 (2008) (*cit. on p. 4*).
- [68] A. F. Kusmartseva, B. Sipos, H. Berger, L. Forró, and E. Tutiš, "Pressure Induced Superconductivity in Pristine 1T-TiSe<sub>2</sub>", *Phys. Rev. Lett.* **103**, 236401 (2009) (*cit. on p. 4*).
- [69] J. T. Ye, Y. J. Zhang, R. Akashi, M. S. Bahramy, R. Arita, and Y. Iwasa, "Superconducting Dome in a Gate-Tuned Band Insulator", *Science* **338**, 1193 (2012) (*cit. on pp. 4, 8, 156, 158*).
- [70] W. Shi, J. Ye, Y. Zhang, R. Suzuki, M. Yoshida, J. Miyazaki, N. Inoue, Y. Saito, and Y. Iwasa, "Superconductivity Series in Transition Metal Dichalcogenides by Ionic Gating", *Sci. Rep.* **5**, 12534 (2015) (*cit. on pp. 4, 8, 158*).
- [71] X. Xi, L. Zhao, Z. Wang, H. Berger, L. Forró, J. Shan, and K. F. Mak, "Strongly enhanced charge-density-wave order in monolayer NbSe<sub>2</sub>", *Nat. Nanotechnol.* **10**, 765 (2015), [arXiv:1507.05595](https://arxiv.org/abs/1507.05595) (*cit. on pp. 4, 8, 158*).
- [72] Y. Qi et al., "Superconductivity in Weyl semimetal candidate MoTe<sub>2</sub>", *Nat. Commun.* **7**, 11038 (2016), [arXiv:1508.03502](https://arxiv.org/abs/1508.03502) (*cit. on pp. 4, 158*).
- [73] S. C. de la Barrera et al., "Tuning Ising superconductivity with layer and spin-orbit coupling in two-dimensional transition-metal dichalcogenides", *Nat. Commun.* **9**, 1427 (2018), [arXiv:1711.00468](https://arxiv.org/abs/1711.00468) (*cit. on pp. 4, 8, 72, 158*).
- [74] H. Zhou, T. Xie, T. Taniguchi, K. Watanabe, and A. F. Young, "Superconductivity in rhombohedral trilayer graphene", *Nature* **598**, 434 (2021), [arXiv:2106.07640](https://arxiv.org/abs/2106.07640) (*cit. on pp. 4, 8, 156*).
- [75] H. Zhou, L. Holleis, Y. Saito, L. Cohen, W. Huynh, C. L. Patterson, F. Yang, T. Taniguchi, K. Watanabe, and A. F. Young, "Isospin magnetism and spin-polarized superconductivity in Bernal bilayer graphene", *Science* **375**, 774 (2022), [arXiv:2110.11317](https://arxiv.org/abs/2110.11317) (*cit. on pp. 4, 8, 156*).
- [76] R. Niu, J. Li, W. Zhen, F. Xu, S. Weng, Z. Yue, X. Meng, J. Xia, N. Hao, and C. Zhang, "Enhanced Superconductivity and Critical Current Density Due to the Interaction of InSe<sub>2</sub> Bonded Layer in (InSe<sub>2</sub>)<sub>0.12</sub>NbSe<sub>2</sub>", *JACS* **146**, 1244 (2024) (*cit. on pp. 4, 8*).
- [77] Y. Cao, V. Fatemi, S. Fang, K. Watanabe, T. Taniguchi, E. Kaxiras, and P. Jarillo-Herrero, "Unconventional superconductivity in magic-angle graphene superlattices", *Nature* **556**, 43 (2018), [arXiv:1803.02342](https://arxiv.org/abs/1803.02342) (*cit. on pp. 4, 8, 156, 158*).
- [78] J. M. Park, Y. Cao, K. Watanabe, T. Taniguchi, and P. Jarillo-Herrero, "Tunable strongly coupled superconductivity in magic-angle twisted trilayer graphene", *Nature* **590**, 249 (2021), [arXiv:2012.01434](https://arxiv.org/abs/2012.01434) (*cit. on pp. 4, 8, 72, 158*).

- [79] Y. Xia, Z. Han, K. Watanabe, T. Taniguchi, J. Shan, and K. F. Mak, "Unconventional superconductivity in twisted bilayer  $\text{WSe}_2$ ", arXiv preprint (2024), [arXiv:2405.14784](https://arxiv.org/abs/2405.14784) (cit. on pp. 4, 8, 159, 256).
- [80] Y. Guo et al., "Superconductivity in twisted bilayer  $\text{WSe}_2$ ", arXiv preprint (2024), [arXiv:2406.03418](https://arxiv.org/abs/2406.03418) (cit. on pp. 4, 8, 159, 256).
- [81] M. N. Gastiasoro, J. Ruhman, and R. M. Fernandes, "Superconductivity in dilute  $\text{SrTiO}_3$ : A review", *Ann. Phys.* **417**, 168107 (2020), [arXiv:1912.01509](https://arxiv.org/abs/1912.01509) (cit. on p. 4).
- [82] T. Watanabe, H. Yanagi, T. Kamiya, Y. Kamihara, H. Hiramatsu, M. Hirano, and H. Hosono, "Nickel-Based Oxyphosphide Superconductor with a Layered Crystal Structure,  $\text{LaNiOP}$ ", *Inorg. Chem.* **46**, 7719 (2007) (cit. on p. 4).
- [83] H. Kim et al., "Nodal superconductivity in miassite  $\text{Rh}_{17}\text{S}_{15}$ ", *Commun. Mater.* **5**, 17 (2024) (cit. on p. 4).
- [84] J. Cheng et al., "Superconductivity in a Layered Cobalt Oxychalcogenide  $\text{Na}_2\text{CoSe}_2\text{O}$  with a Triangular Lattice", *JACS* **146**, 5908 (2024), [arXiv:2310.17464](https://arxiv.org/abs/2310.17464) (cit. on pp. 4, 7, 18).
- [85] J. A. Flores-Livas, L. Boeri, A. Sanna, G. Profeta, R. Arita, and M. Eremets, "A perspective on conventional high-temperature superconductors at high pressure: Methods and materials", *Phys. Rep.* **856**, 1 (2020), [arXiv:1905.06693](https://arxiv.org/abs/1905.06693) (cit. on pp. 5–9, 103, 104).
- [86] M. R. Koblishka and A. Koblishka-Veneva, "Calculation of  $T_c$  of Superconducting Elements with the Roeser–Huber Formalism", *Metals* **12**, 337 (2022) (cit. on p. 5).
- [87] J. Song, G. Fabbris, W. Bi, D. Haskel, and J. S. Schilling, "Pressure-Induced Superconductivity in Elemental Ytterbium Metal", *Phys. Rev. Lett.* **121**, 037004 (2018), [arXiv:1801.03630](https://arxiv.org/abs/1801.03630) (cit. on p. 5).
- [88] F. Steglich, J. Aarts, C. D. Bredl, W. Lieke, D. Meschede, W. Franz, and H. Schäfer, "Superconductivity in the Presence of Strong Pauli Paramagnetism:  $\text{CeCu}_2\text{Si}_2$ ", *Phys. Rev. Lett.* **43**, 1892 (1979) (cit. on p. 5).
- [89] D. Aoki, J.-P. Brison, J. Flouquet, K. Ishida, G. Knebel, Y. Tokunaga, and Y. Yanase, "Unconventional superconductivity in  $\text{UTe}_2$ ", *J. Phys. Condens. Matter* **34**, 243002 (2022), [arXiv:2110.10451](https://arxiv.org/abs/2110.10451) (cit. on pp. 5, 72).
- [90] D. Aoki and J. Flouquet, "Ferromagnetism and Superconductivity in Uranium Compounds", *J. Phys. Soc. Jpn.* **81**, 011003 (2012), [arXiv:1108.4807](https://arxiv.org/abs/1108.4807) (cit. on pp. 5, 72).
- [91] A. Schilling, M. Cantoni, J. D. Guo, and H. R. Ott, "Superconductivity above 130 K in the Hg–Ba–Ca–Cu–O system", *Nature* **363**, 56 (1993) (cit. on p. 5).
- [92] L. Gao, Y. Y. Xue, F. Chen, Q. Xiong, R. L. Meng, D. Ramirez, C. W. Chu, J. H. Eggert, and H. K. Mao, "Superconductivity up to 164 K in  $\text{HgBa}_2\text{Ca}_{m-1}\text{Cu}_m\text{O}_{2m+2+\delta}$  ( $m=1, 2$ , and 3) under quasihydrostatic pressures", *Phys. Rev. B* **50**, 4260 (1994) (cit. on p. 5).

- [93] X. Dong, E. Gull, and A. J. Millis, “Quantifying the role of antiferromagnetic fluctuations in the superconductivity of the doped Hubbard model”, *Nat. Phys.* **18**, 1293 (2022), [arXiv:2202.10577](#) (cit. on pp. 6, 22, 43).
- [94] X. Dong, L. Del Re, A. Toschi, and E. Gull, “Mechanism of superconductivity in the Hubbard model at intermediate interaction strength”, *PNAS* **119**, e2205048119 (2022), [arXiv:2205.06286](#) (cit. on pp. 6, 43).
- [95] N. Singh, “Leading theories of the cuprate superconductivity: A critique”, *Phys. C: Supercond. Appl.* **580**, 1353782 (2021), [arXiv:2006.06335](#) (cit. on pp. 6, 10, 106).
- [96] R. Arita, T. Koretsune, S. Sakai, R. Akashi, Y. Nomura, and W. Sano, “Nonempirical Calculation of Superconducting Transition Temperatures in Light-Element Superconductors”, *Adv. Mater.* **29**, 1602421 (2017) (cit. on pp. 6, 8, 9, 103–105, 258).
- [97] F. Giustino, “Electron-phonon interactions from first principles”, *Rev. Mod. Phys.* **89**, 015003 (2017), [arXiv:1603.06965](#) (cit. on pp. 6, 103–105, 109).
- [98] L. Boeri et al., “The 2021 room-temperature superconductivity roadmap”, *J. Phys. Condens. Matter* **34**, 183002 (2022) (cit. on pp. 6, 7, 189).
- [99] L. N. Oliveira, E. K. U. Gross, and W. Kohn, “Density-Functional Theory for Superconductors”, *Phys. Rev. Lett.* **60**, 2430 (1988) (cit. on p. 6).
- [100] M. Lüders, M. A. L. Marques, N. N. Lathiotakis, A. Floris, G. Profeta, L. Fast, A. Continenza, S. Massidda, and E. K. U. Gross, “Ab initio theory of superconductivity. I. Density functional formalism and approximate functionals”, *Phys. Rev. B* **72**, 024545 (2005), [arXiv:cond-mat/0408685](#) (cit. on p. 6).
- [101] R. Akashi and R. Arita, “Development of Density-Functional Theory for a Plasmon-Assisted Superconducting State: Application to Lithium Under High Pressures”, *Phys. Rev. Lett.* **111**, 057006 (2013), [arXiv:1303.5152](#) (cit. on pp. 6, 104).
- [102] F. Essenberg, A. Sanna, A. Linscheid, F. Tandetky, G. Profeta, P. Cudazzo, and E. K. U. Gross, “Superconducting pairing mediated by spin fluctuations from first principles”, *Phys. Rev. B* **90**, 214504 (2014), [arXiv:1409.7968](#) (cit. on pp. 6, 104).
- [103] A. Davydov, A. Sanna, C. Pellegrini, J. K. Dewhurst, S. Sharma, and E. K. U. Gross, “Ab initio theory of plasmonic superconductivity within the Eliashberg and density-functional formalisms”, *Phys. Rev. B* **102**, 214508 (2020), [arXiv:2007.12886](#) (cit. on pp. 6, 104).
- [104] A. Sanna, C. Pellegrini, and E. K. U. Gross, “Combining Eliashberg Theory with Density Functional Theory for the Accurate Prediction of Superconducting Transition Temperatures and Gap Functions”, *Phys. Rev. Lett.* **125**, 057001 (2020) (cit. on p. 6).
- [105] C. Pellegrini and A. Sanna, “Ab initio methods for superconductivity”, *Nat. Rev. Phys.*, 509 (2024) (cit. on pp. 6, 8).

- [106] N. Marzari, A. A. Mostofi, J. R. Yates, I. Souza, and D. Vanderbilt, “Maximally localized Wannier functions: Theory and applications”, *Rev. Mod. Phys.* **84**, 1419 (2012), [arXiv:1112.5411](#) (*cit. on pp. 6, 18–20*).
- [107] M. Imada and T. Miyake, “Electronic Structure Calculation by First Principles for Strongly Correlated Electron Systems”, *J. Phys. Soc. Jpn.* **79**, 112001 (2010), [arXiv:1009.3851](#) (*cit. on pp. 6, 18*).
- [108] H. Ikeda, R. Arita, and J. Kuneš, “Phase diagram and gap anisotropy in iron-pnictide superconductors”, *Phys. Rev. B* **81**, 054502 (2010), [arXiv:0912.1893](#) (*cit. on pp. 6, 36, 84*).
- [109] H. Sakakibara, H. Usui, K. Suzuki, T. Kotani, H. Aoki, and K. Kuroki, “Model Construction and a Possibility of Cupratelike Pairing in a New  $d^9$  Nickelate Superconductor (Nd,Sr)NiO<sub>2</sub>”, *Phys. Rev. Lett.* **125**, 077003 (2020), [arXiv:1909.00060](#) (*cit. on pp. 6, 36, 128*).
- [110] M. T. Schmid, J.-B. Morée, R. Kaneko, Y. Yamaji, and M. Imada, “Superconductivity Studied by Solving Ab Initio Low-Energy Effective Hamiltonians for Carrier Doped CaCuO<sub>2</sub>, Bi<sub>2</sub>Sr<sub>2</sub>CuO<sub>6</sub>, Bi<sub>2</sub>Sr<sub>2</sub>CaCu<sub>2</sub>O<sub>8</sub>, and HgBa<sub>2</sub>CuO<sub>4</sub>”, *Phys. Rev. X* **13**, 041036 (2023), [arXiv:2303.06672](#) (*cit. on pp. 6, 22, 210*).
- [111] A. Georges, G. Kotliar, W. Krauth, and M. J. Rozenberg, “Dynamical mean-field theory of strongly correlated fermion systems and the limit of infinite dimensions”, *Rev. Mod. Phys.* **68**, 13 (1996) (*cit. on pp. 6, 39–42*).
- [112] T. Maier, M. Jarrell, T. Pruschke, and M. H. Hettler, “Quantum cluster theories”, *Rev. Mod. Phys.* **77**, 1027 (2005), [arXiv:cond-mat/0404055](#) (*cit. on pp. 6, 43*).
- [113] G. Rohringer, H. Hafermann, A. Toschi, A. A. Katanin, A. E. Antipov, M. I. Katsnelson, A. I. Lichtenstein, A. N. Rubtsov, and K. Held, “Diagrammatic routes to nonlocal correlations beyond dynamical mean field theory”, *Rev. Mod. Phys.* **90**, 025003 (2018), [arXiv:1705.00024](#) (*cit. on pp. 6, 35, 43*).
- [114] G. Kotliar, S. Y. Savrasov, K. Haule, V. S. Oudovenko, O. Parcollet, and C. A. Marianetti, “Electronic structure calculations with dynamical mean-field theory”, *Rev. Mod. Phys.* **78**, 865 (2006), [arXiv:cond-mat/0511085](#) (*cit. on pp. 6, 18, 39–41*).
- [115] K. Held, “Electronic structure calculations using dynamical mean field theory”, *Adv. Phys.* **56**, 829 (2007), [arXiv:cond-mat/0511293](#) (*cit. on pp. 6, 18, 39–41*).
- [116] A. Paul and T. Birol, “Applications of DFT+DMFT in Materials Science”, *Annu. Rev. Mater. Res.* **49**, 31 (2019), [arXiv:1809.09246](#) (*cit. on p. 6*).
- [117] M. Kitatani, R. Arita, T. Schäfer, and K. Held, “Strongly correlated superconductivity with long-range spatial fluctuations”, *J. Phys. Mater.* **5**, 034005 (2022), [arXiv:2203.12844](#) (*cit. on pp. 6, 43, 58, 64, 105, 106*).
- [118] E. Gull, O. Parcollet, and A. J. Millis, “Superconductivity and the Pseudogap in the Two-Dimensional Hubbard Model”, *Phys. Rev. Lett.* **110**, 216405 (2013), [arXiv:1207.2490](#) (*cit. on pp. 6, 22, 43*).

- [119] Y. Nomura, S. Sakai, M. Capone, and R. Arita, “Unified understanding of superconductivity and Mott transition in alkali-doped fullerenes from first principles”, *Sci. Adv.* **1**, e1500568 (2015), [arXiv:1505.05849](#) (*cit. on pp. 6, 9, 215, 258*).
- [120] S. Ryee and T. O. Wehling, “Switching between Mott-Hubbard and Hund Physics in Moiré Quantum Simulators”, *Nano Lett.* **23**, 573 (2023) (*cit. on pp. 6, 159*).
- [121] J. Singleton and C. Mielke, “Quasi-two-dimensional organic superconductors: A review”, *Contemp. Phys.* **43**, 63 (2002), [arXiv:cond-mat/0202442](#) (*cit. on p. 6*).
- [122] S. E. Brown, “Organic superconductors: The Bechgaard salts and relatives”, *Phys. C: Supercond. Appl.* **514**, 279 (2015) (*cit. on p. 6*).
- [123] J. Nagamatsu, N. Nakagawa, T. Muranaka, Y. Zenitani, and J. Akimitsu, “Superconductivity at 39 K in magnesium diboride”, *Nature* **410**, 63 (2001) (*cit. on p. 6*).
- [124] M. Hanna, H. Fang, Y. X. Zhou, M. Alessandrini, P. T. Putman, and K. Salama, “Mechanical properties of superconducting MgB<sub>2</sub> wire”, *J. Mater. Process. Tech.* **181**, 44 (2007) (*cit. on p. 6*).
- [125] Y. Jiang and Y. Liang, “Enhancing mechanical properties of MgB<sub>2</sub> superconductors through Nb substitution: a first-principles study”, *Phys. B: Condens. Matter* **683**, 415931 (2024) (*cit. on p. 6*).
- [126] A. F. Hebard, M. J. Rosseinsky, R. C. Haddon, D. W. Murphy, S. H. Glarum, T. T. M. Palstra, A. P. Ramirez, and A. R. Kortan, “Superconductivity at 18 K in potassium-doped C<sub>60</sub>”, *Nature* **350**, 600 (1991) (*cit. on p. 6*).
- [127] M. J. Rosseinsky, A. P. Ramirez, S. H. Glarum, D. W. Murphy, R. C. Haddon, A. F. Hebard, T. T. M. Palstra, A. R. Kortan, S. M. Zahurak, and A. V. Makhija, “Superconductivity at 28 K in Rb<sub>x</sub>C<sub>60</sub>”, *Phys. Rev. Lett.* **66**, 2830 (1991) (*cit. on p. 6*).
- [128] M. Capone, M. Fabrizio, C. Castellani, and E. Tosatti, “Colloquium: Modeling the unconventional superconducting properties of expanded A<sub>3</sub>C<sub>60</sub> fullerenes”, *Rev. Mod. Phys.* **81**, 943 (2009), [arXiv:0809.0910](#) (*cit. on pp. 6, 9, 215*).
- [129] Y. Nomura, S. Sakai, M. Capone, and R. Arita, “Exotic s-wave superconductivity in alkali-doped fullerenes”, *J. Phys. Condens. Matter* **28**, 153001 (2016), [arXiv:1512.05755](#) (*cit. on pp. 6, 215*).
- [130] Y. Maeno, H. Hashimoto, K. Yoshida, S. Nishizaki, T. Fujita, J. G. Bednorz, and F. Lichtenberg, “Superconductivity in a layered perovskite without copper”, *Nature* **372**, 532 (1994) (*cit. on p. 6*).
- [131] Y. Maeno, S. Yonezawa, and A. Ramirez, “Still Mystery after All These Years—Unconventional Superconductivity of Sr<sub>2</sub>RuO<sub>4</sub>—”, *J. Phys. Soc. Jpn.* **93**, 062001 (2024), [arXiv:2402.12117](#) (*cit. on pp. 6, 11, 12, 110*).

- [132] K. Takada, H. Sakurai, E. Takayama-Muromachi, F. Izumi, R. A. Dilanian, and T. Sasaki, "Superconductivity in two-dimensional  $\text{CoO}_2$  layers", *Nature* **422**, 53 (2003) (*cit. on pp. 6, 110*).
- [133] M. Ogata, "A new triangular system:  $\text{Na}_x\text{CoO}_2$ ", *J. Phys. Condens. Matter* **19**, 145282 (2007) (*cit. on pp. 6, 111, 112*).
- [134] H. Sakurai, Y. Ihara, and K. Takada, "Superconductivity of cobalt oxide hydrate,  $\text{Na}_x(\text{H}_3\text{O})_z\text{CoO}_2 \cdot y\text{H}_2\text{O}$ ", *Phys. C: Supercond. Appl.* **514**, 378 (2015) (*cit. on pp. 6, 111–113*).
- [135] H. Hosono and K. Kuroki, "Iron-based superconductors: Current status of materials and pairing mechanism", *Phys. C: Supercond. Appl.* **514**, 399 (2015), [arXiv:1504.04919](https://arxiv.org/abs/1504.04919) (*cit. on p. 7*).
- [136] Q. Si and N. E. Hussey, "Iron-based superconductors: Teenage, complex, challenging", *Phys. Today* **76**, 34 (2023), [arXiv:2305.03035](https://arxiv.org/abs/2305.03035) (*cit. on p. 7*).
- [137] Y. Kamihara, H. Hiramatsu, M. Hirano, R. Kawamura, H. Yanagi, T. Kamiya, and H. Hosono, "Iron-Based Layered Superconductor:  $\text{LaOFeP}$ ", *JACS* **128**, 10012 (2006) (*cit. on p. 7*).
- [138] Y. Kamihara, T. Watanabe, M. Hirano, and H. Hosono, "Iron-Based Layered Superconductor  $\text{La}[\text{O}_{1-x}\text{F}_x]\text{FeAs}$  ( $x = 0.05\text{--}0.12$ ) with  $T_c = 26\text{ K}$ ", *JACS* **130**, 3296 (2008) (*cit. on p. 7*).
- [139] J.-F. Ge, Z.-L. Liu, C. Liu, C.-L. Gao, D. Qian, Q.-K. Xue, Y. Liu, and J.-F. Jia, "Superconductivity above 100 K in single-layer  $\text{FeSe}$  films on doped  $\text{SrTiO}_3$ ", *Nat. Mater.* **14**, 285 (2014), [arXiv:1406.3435](https://arxiv.org/abs/1406.3435) (*cit. on p. 7*).
- [140] A. Georges, L. de' Medici, and J. Mravlje, "Strong Correlations from Hund's Coupling", *Annu. Rev. Condens. Matter Phys.* **4**, 137 (2013), [arXiv:1207.3033](https://arxiv.org/abs/1207.3033) (*cit. on pp. 7, 15, 21, 22*).
- [141] R. Yu and Q. Si, "Orbital-Selective Mott Phase in Multiorbital Models for Alkaline Iron Selenides  $\text{K}_{1-x}\text{Fe}_{2-y}\text{Se}_2$ ", *Phys. Rev. Lett.* **110**, 146402 (2013), [arXiv:1208.5547](https://arxiv.org/abs/1208.5547) (*cit. on p. 7*).
- [142] L. de' Medici, G. Giovannetti, and M. Capone, "Selective Mott Physics as a Key to Iron Superconductors", *Phys. Rev. Lett.* **112**, 177001 (2014), [arXiv:1212.3966](https://arxiv.org/abs/1212.3966) (*cit. on p. 7*).
- [143] M. Kim, S. Choi, W. H. Brito, and G. Kotliar, "Orbital-Selective Mott Transition Effects and Nontrivial Topology of Iron Chalcogenide", *Phys. Rev. Lett.* **132**, 136504 (2024), [arXiv:2304.05002](https://arxiv.org/abs/2304.05002) (*cit. on p. 7*).
- [144] Y. Nomura and R. Arita, "Superconductivity in infinite-layer nickelates", *Rep. Prog. Phys.* **85**, 052501 (2022), [arXiv:2107.12923](https://arxiv.org/abs/2107.12923) (*cit. on pp. 7, 127, 128*).
- [145] L. Si, P. Worm, and K. Held, "Fingerprints of Topotactic Hydrogen in Nickelate Superconductors", *Crystals* **12**, 656 (2022) (*cit. on p. 7*).
- [146] B. Y. Wang, K. Lee, and B. H. Goodge, "Experimental Progress in Superconducting Nickelates", *Annu. Rev. Condens. Matter Phys.* **15**, 305 (2024) (*cit. on pp. 7, 127, 129*).

- [147] W. Zhao, X. Huang, Z. Zhang, S. Chen, M. Du, D. Duan, and T. Cui, "Superconducting ternary hydrides: progress and challenges", *Natl. Sci. Rev.* **11**, nwad307 (2023), [arXiv:2308.03544](#) (cit. on pp. 7, 8).
- [148] N. W. Ashcroft, "Metallic Hydrogen: A High-Temperature Superconductor?", *Phys. Rev. Lett.* **21**, 1748 (1968) (cit. on p. 7).
- [149] N. W. Ashcroft, "Hydrogen Dominant Metallic Alloys: High Temperature Superconductors?", *Phys. Rev. Lett.* **92**, 187002 (2004) (cit. on p. 7).
- [150] Y. Li, J. Hao, H. Liu, Y. Li, and Y. Ma, "The metallization and superconductivity of dense hydrogen sulfide", *J. Chem. Phys.* **140**, 174712 (2014), [arXiv:1402.2721](#) (cit. on p. 7).
- [151] D. Duan, Y. Liu, F. Tian, D. Li, X. Huang, Z. Zhao, H. Yu, B. Liu, W. Tian, and T. Cui, "Pressure-induced metallization of dense  $(\text{H}_2\text{S})_2\text{H}_2$  with high- $T_c$  superconductivity", *Sci. Rep.* **4**, 6968 (2014) (cit. on p. 7).
- [152] A. P. Drozdov, M. I. Erements, I. A. Troyan, V. Ksenofontov, and S. I. Shylin, "Conventional superconductivity at 203 kelvin at high pressures in the sulfur hydride system", *Nature* **525**, 73 (2015), [arXiv:1506.08190](#) (cit. on p. 8).
- [153] A. P. Drozdov et al., "Superconductivity at 250 K in lanthanum hydride under high pressures", *Nature* **569**, 528 (2019), [arXiv:1812.01561](#) (cit. on p. 8).
- [154] M. Somayazulu, M. Ahart, A. K. Mishra, Z. M. Geballe, M. Baldini, Y. Meng, V. V. Struzhkin, and R. J. Hemley, "Evidence for Superconductivity above 260 K in Lanthanum Superhydride at Megabar Pressures", *Phys. Rev. Lett.* **122**, 027001 (2019), [arXiv:1808.07695](#) (cit. on p. 8).
- [155] T. F. T. Cerqueira, A. Sanna, and M. A. L. Marques, "Sampling the Materials Space for Conventional Superconducting Compounds", *Adv. Mater.* **36**, 2307085 (2023), [arXiv:2307.10728](#) (cit. on pp. 8, 258).
- [156] A. Sanna, T. F. T. Cerqueira, Y.-W. Fang, I. Errea, A. Ludwig, and M. A. L. Marques, "Prediction of ambient pressure conventional superconductivity above 80 K in hydride compounds", *npj Comput. Mater.* **10**, 44 (2024), [arXiv:2310.06804](#) (cit. on p. 8).
- [157] K. S. Novoselov, A. K. Geim, S. V. Morozov, D. Jiang, Y. Zhang, S. V. Dubonos, I. V. Grigorieva, and A. A. Firsov, "Electric Field Effect in Atomically Thin Carbon Films", *Science* **306**, 666 (2004), [arXiv:cond-mat/0410550](#) (cit. on p. 8).
- [158] A. K. Geim and I. V. Grigorieva, "Van der Waals heterostructures", *Nature* **499**, 419 (2013), [arXiv:1307.6718](#) (cit. on pp. 8, 109, 156, 158).
- [159] N. Mounet et al., "Two-dimensional materials from high-throughput computational exfoliation of experimentally known compounds", *Nat. Nanotechnol.* **13**, 246 (2018), [arXiv:1611.05234](#) (cit. on p. 8).
- [160] Y. Lei et al., "Graphene and Beyond: Recent Advances in Two-Dimensional Materials Synthesis, Properties, and Devices", *ACS Nanoscience Au* **2**, 450 (2022) (cit. on p. 8).



- [161] M. Zeng, Y. Xiao, J. Liu, K. Yang, and L. Fu, "Exploring Two-Dimensional Materials toward the Next-Generation Circuits: From Monomer Design to Assembly Control", *Chem. Rev.* **118**, 6236 (2018) (*cit. on p. 8*).
- [162] D. Qiu, C. Gong, S. Wang, M. Zhang, C. Yang, X. Wang, and J. Xiong, "Recent Advances in 2D Superconductors", *Adv. Mater.* **33**, 2006124 (2021) (*cit. on pp. 8, 156*).
- [163] Y. Cao et al., "Correlated insulator behaviour at half-filling in magic-angle graphene superlattices", *Nature* **556**, 80 (2018), [arXiv:1802.00553](https://arxiv.org/abs/1802.00553) (*cit. on pp. 8, 156–158*).
- [164] Z. Hao, A. M. Zimmerman, P. Ledwith, E. Khalaf, D. H. Najafabadi, K. Watanabe, T. Taniguchi, A. Vishwanath, and P. Kim, "Electric field-tunable superconductivity in alternating-twist magic-angle trilayer graphene", *Science* **371**, 1133 (2021), [arXiv:2012.02773](https://arxiv.org/abs/2012.02773) (*cit. on p. 8*).
- [165] L. Wang et al., "Correlated electronic phases in twisted bilayer transition metal dichalcogenides", *Nat. Mater.* **19**, 861 (2020), [arXiv:1910.12147](https://arxiv.org/abs/1910.12147) (*cit. on pp. 8, 159, 256*).
- [166] I. I. Mazin, "Unconventional superconductivity", in *Encyclopedia of condensed matter physics*, edited by T. Chakraborty (Elsevier, 2024), pp. 598–599 (*cit. on p. 9*).
- [167] M. Sigrist and K. Ueda, "Phenomenological theory of unconventional superconductivity", *Rev. Mod. Phys.* **63**, 239 (1991) (*cit. on pp. 9, 84, 87, 97*).
- [168] J. R. Gavaler, "Superconductivity in Nb–Ge films above 22 K", *Appl. Phys. Lett.* **23**, 480 (1973) (*cit. on p. 9*).
- [169] M. L. Cohen and P. W. Anderson, "Comments on the Maximum Superconducting Transition Temperature", in *Aip conf. proc.* Vol. 4, 1 (1972), pp. 17–27 (*cit. on pp. 9, 209*).
- [170] C. Proust and L. Taillefer, "The Remarkable Underlying Ground States of Cuprate Superconductors", *Annu. Rev. Condens. Matter Phys.* **10**, 409 (2019), [arXiv:1807.05074](https://arxiv.org/abs/1807.05074) (*cit. on p. 10*).
- [171] M. Qin, T. Schäfer, S. Andergassen, P. Corboz, and E. Gull, "The Hubbard Model: A Computational Perspective", *Annu. Rev. Condens. Matter Phys.* **13**, 275 (2022), [arXiv:2104.00064](https://arxiv.org/abs/2104.00064) (*cit. on pp. 10, 22, 23*).
- [172] A. Wietek, Y.-Y. He, S. R. White, A. Georges, and E. M. Stoudenmire, "Stripes, Antiferromagnetism, and the Pseudogap in the Doped Hubbard Model at Finite Temperature", *Phys. Rev. X* **11**, 031007 (2021), [arXiv:2009.10736](https://arxiv.org/abs/2009.10736) (*cit. on p. 10*).
- [173] F. Šimkovic, R. Rossi, A. Georges, and M. Ferrero, "Origin and fate of the pseudogap in the doped hubbard model", arXiv preprint (2022), [arXiv:2209.09237](https://arxiv.org/abs/2209.09237) (*cit. on pp. 10, 22*).

- [174] H. v. Löhneysen, A. Rosch, M. Vojta, and P. Wölfle, “Fermi-liquid instabilities at magnetic quantum phase transitions”, *Rev. Mod. Phys.* **79**, 1015 (2007), [arXiv:cond-mat/0606317](#) (*cit. on p. 11*).
- [175] S. Sachdev, “Where is the quantum critical point in the cuprate superconductors?”, *Phys. Status Solidi B* **247**, 537 (2010), [arXiv:0907.0008](#) (*cit. on p. 11*).
- [176] D. Fausti, R. I. Tobey, N. Dean, S. Kaiser, A. Dienst, M. C. Hoffmann, S. Pyon, T. Takayama, H. Takagi, and A. Cavalleri, “Light-Induced Superconductivity in a Stripe-Ordered Cuprate”, *Science* **331**, 189 (2011) (*cit. on p. 11*).
- [177] K. A. Cremin, J. Zhang, C. C. Homes, G. D. Gu, Z. Sun, M. M. Fogler, A. J. Millis, D. N. Basov, and R. D. Averitt, “Photoenhanced metastable c-axis electrodynamic in stripe-ordered cuprate  $\text{La}_{1.885}\text{Ba}_{0.115}\text{CuO}_4$ ”, *PNAS* **116**, 19875 (2019), [arXiv:1901.10037](#) (*cit. on p. 11*).
- [178] A. von Hoegen et al., “Amplification of Superconducting Fluctuations in Driven  $\text{YBa}_2\text{Cu}_3\text{O}_{6+x}$ ”, *Phys. Rev. X* **12**, 031008 (2022) (*cit. on p. 11*).
- [179] S. Fava, G. De Vecchi, G. Jotzu, M. Buzzi, T. Gebert, Y. Liu, B. Keimer, and A. Cavalleri, “Magnetic field expulsion in optically driven  $\text{YBa}_2\text{Cu}_3\text{O}_{6.48}$ ”, *Nature* **632**, 75 (2024), [arXiv:2405.00848](#) (*cit. on p. 11*).
- [180] M. Buzzi et al., “Photomolecular High-Temperature Superconductivity”, *Phys. Rev. X* **10**, 031028 (2020), [arXiv:2001.05389](#) (*cit. on p. 11*).
- [181] M. Buzzi et al., “Phase Diagram for Light-Induced Superconductivity in  $\kappa\text{-(ET)}_2\text{-X}$ ”, *Phys. Rev. Lett.* **127**, 197002 (2021), [arXiv:2106.14244](#) (*cit. on p. 11*).
- [182] M. Mitrano et al., “Possible light-induced superconductivity in  $\text{K}_3\text{C}_{60}$  at high temperature”, *Nature* **530**, 461 (2016), [arXiv:1505.04529](#) (*cit. on pp. 11, 215*).
- [183] M. Budden et al., “Evidence for metastable photo-induced superconductivity in  $\text{K}_3\text{C}_{60}$ ”, *Nat. Phys.* **17**, 611 (2021), [arXiv:2002.12835](#) (*cit. on pp. 11, 215*).
- [184] M. Buzzi, G. Jotzu, A. Cavalleri, J. I. Cirac, E. A. Demler, B. I. Halperin, M. D. Lukin, T. Shi, Y. Wang, and D. Podolsky, “Higgs-Mediated Optical Amplification in a Nonequilibrium Superconductor”, *Phys. Rev. X* **11**, 011055 (2021), [arXiv:1908.10879](#) (*cit. on pp. 11, 74, 215*).
- [185] E. Rowe et al., “Resonant enhancement of photo-induced superconductivity in  $\text{K}_3\text{C}_{60}$ ”, *Nat. Phys.* **19**, 1821 (2023), [arXiv:2301.08633](#) (*cit. on pp. 11, 215*).
- [186] G. Jotzu, G. Meier, A. Cantaluppi, A. Cavalleri, D. Pontiroli, M. Riccò, A. Ardavan, and M.-S. Nam, “Superconducting Fluctuations Observed Far above  $T_c$  in the Isotropic Superconductor  $\text{K}_3\text{C}_{60}$ ”, *Phys. Rev. X* **13**, 021008 (2023) (*cit. on pp. 11, 215*).
- [187] E. Wang, J. D. Adelinia, M. Chavez-Cervantes, T. Matsuyama, M. Fechner, M. Buzzi, G. Meier, and A. Cavalleri, “Superconducting nonlinear transport in optically driven high-temperature  $\text{K}_3\text{C}_{60}$ ”, *Nat. Commun.* **14**, 10.1038/s41467-023-42989-7 (2023), [arXiv:2301.06425](#) (*cit. on pp. 11, 215*).

- [188] J. D. Adelinia, E. Wang, M. Chavez-Cervantes, T. Matsuyama, M. Fechner, M. Buzzi, G. Meier, and A. Cavalleri, “Probing photo-induced granular superconductivity in  $k_3c_{60}$  thin films with an ultrafast on-chip voltmeter”, arXiv preprint (2023), [arXiv:2312.06421](#) (cit. on pp. 11, 215).
- [189] C. J. Eckhardt, S. Chattopadhyay, D. M. Kennes, E. A. Demler, M. A. Sentef, and M. H. Michael, “Theory of resonantly enhanced photo-induced superconductivity”, *Nat. Commun.* **15**, 2300 (2024), [arXiv:2303.02176](#) (cit. on p. 11).
- [190] M. Sato and Y. Ando, “Topological superconductors: a review”, *Rep. Prog. Phys.* **80**, 076501 (2017), [arXiv:1608.03395](#) (cit. on p. 11).
- [191] M. M. Sharma, P. Sharma, N. K. Karn, and V. P. S. Awana, “Comprehensive review on topological superconducting materials and interfaces”, *Supercond. Sci. Technol.* **35**, 083003 (2022), [arXiv:2204.12107](#) (cit. on p. 11).
- [192] S. D. Sarma, M. Freedman, and C. Nayak, “Majorana zero modes and topological quantum computation”, *npj Quantum Inf.* **1**, 15001 (2015), [arXiv:1501.02813](#) (cit. on p. 11).
- [193] O. Gingras, R. Nourafkan, A.-M. S. Tremblay, and M. Côté, “Superconducting Symmetries of  $Sr_2RuO_4$  from First-Principles Electronic Structure”, *Phys. Rev. Lett.* **123**, 217005 (2019), [arXiv:1808.02527](#) (cit. on pp. 11, 84, 85).
- [194] S. Käser, H. U. R. Strand, N. Wentzell, A. Georges, O. Parcollet, and P. Hansmann, “Interorbital singlet pairing in  $Sr_2RuO_4$ : A Hund’s superconductor”, *Phys. Rev. B* **105**, 155101 (2022), [arXiv:2105.08448](#) (cit. on pp. 11, 84, 85).
- [195] J. B. Profe, S. Beck, D. M. Kennes, A. Georges, and O. Gingras, “Competition between  $d$ -wave superconductivity and magnetism in uniaxially strained  $Sr_2RuO_4$ ”, *npj Quantum Mater.* **9**, 53 (2024), [arXiv:2307.10006](#) (cit. on pp. 11, 84).
- [196] I. Esterlis, S. A. Kivelson, and D. J. Scalapino, “A bound on the superconducting transition temperature”, *npj Quantum Mater.* **3**, 59 (2018) (cit. on pp. 12, 209).
- [197] Y. J. Uemura, “Dynamic superconductivity responses in photoexcited optical conductivity and Nernst effect”, *Phys. Rev. Materials* **3**, 104801 (2019), [arXiv:1910.02388](#) (cit. on pp. 12, 208–212, 258).
- [198] T. Hazra, N. Verma, and M. Randeria, “Bounds on the Superconducting Transition Temperature: Applications to Twisted Bilayer Graphene and Cold Atoms”, *Phys. Rev. X* **9**, 031049 (2019) (cit. on pp. 12, 83, 207, 209–211).
- [199] N. Verma, T. Hazra, and M. Randeria, “Optical spectral weight, phase stiffness, and  $T_c$  bounds for trivial and topological flat band superconductors”, *PNAS* **118**, e2106744118 (2021), [arXiv:2103.08540](#) (cit. on pp. 12, 209).
- [200] T. Shi, W. Zhang, and C. A. R. S. de Melo, “Tighter upper bounds on the critical temperature of two-dimensional superconductors and superfluids from the BCS to the Bose regime”, arXiv preprint (2023), [arXiv:2303.10939](#) (cit. on pp. 12, 209).

- [201] Y. Liu et al., “Upper limit of the transition temperature of superconducting materials”, *Patterns* **3**, 100609 (2022) (*cit. on pp. 12, 209*).
- [202] K. Trachenko, B. Monserrat, M. Hutcheon, and C. J. Pickard, “Upper bounds on the highest phonon frequency and superconducting temperature from fundamental physical constantss”, arXiv preprint (2024), [arXiv:2406.08129](https://arxiv.org/abs/2406.08129) (*cit. on pp. 12, 209*).
- [203] M. V. Sadovskii, “Upper Limit for Superconducting Transition Temperature in Eliashberg–McMillan Theory”, *JETP Lett.*, **10**. 1134/s0021364024602409 (2024) (*cit. on pp. 12, 209*).
- [204] J. S. Hofmann, D. Chowdhury, S. A. Kivelson, and E. Berg, “Heuristic bounds on superconductivity and how to exceed them”, *npj Quantum Mater.* **7**, 83 (2022), [arXiv:2105.09322](https://arxiv.org/abs/2105.09322) (*cit. on pp. 12, 207, 209, 210*).
- [205] P. A. M. Dirac, “Quantum mechanics of many-electron systems”, *Proc. R. Soc. London A.* **123**, 714 (1929) (*cit. on p. 15*).
- [206] P. W. Anderson, “More Is Different: Broken symmetry and the nature of the hierarchical structure of science”, *Science* **177**, 393 (1972) (*cit. on p. 15*).
- [207] D. Pines, “Emergent behavior in strongly correlated electron systems”, *Rep. Prog. Phys.* **79**, 092501 (2016), [arXiv:1601.05891](https://arxiv.org/abs/1601.05891) (*cit. on p. 15*).
- [208] S. Kivelson and S. Kivelson, “Understanding complexity”, *Nat. Phys.* **14**, 426 (2018) (*cit. on p. 15*).
- [209] J. P. F. LeBlanc et al., “Solutions of the Two-Dimensional Hubbard Model: Benchmarks and Results from a Wide Range of Numerical Algorithms”, *Phys. Rev. X* **5**, 041041 (2015) (*cit. on pp. 15, 23*).
- [210] K. Lejaeghere et al., “Reproducibility in density functional theory calculations of solids”, *Science* **351**, aad3000 (2016) (*cit. on pp. 15, 17*).
- [211] T. Schäfer et al., “Tracking the Footprints of Spin Fluctuations: A MultiMethod, MultiMessenger Study of the Two-Dimensional Hubbard Model”, *Phys. Rev. X* **11**, 011058 (2021), [arXiv:2006.10769](https://arxiv.org/abs/2006.10769) (*cit. on pp. 15, 23, 44*).
- [212] Y. Chang et al., “Downfolding from ab initio to interacting model Hamiltonians: comprehensive analysis and benchmarking of the DFT+cRPA approach”, *npj Comput. Mater.* **10**, 129 (2024), [arXiv:2311.05987](https://arxiv.org/abs/2311.05987) (*cit. on pp. 15, 20*).
- [213] H. Bruus and K. Flensberg, *Many-body quantum theory in condensed matter physics, An introduction* (Oxford University Press, Oxford, 2004) (*cit. on pp. 16, 23, 26, 27, 29, 31, 68, 100*).
- [214] A. Altland and B. D. Simons, *Condensed Matter Field Theory* (Cambridge University Press, 2010) (*cit. on pp. 16, 23, 41, 60, 62, 81, 93*).
- [215] G. Czycholl, *Solid State Theory, Volume 1: Basics: Phonons and Electrons in Crystals* (Springer Berlin Heidelberg, 2023) (*cit. on pp. 16, 18, 96*).
- [216] P. Hohenberg and W. Kohn, “Inhomogeneous Electron Gas”, *Phys. Rev.* **136**, B864 (1964) (*cit. on p. 17*).

- [217] W. Kohn and L. J. Sham, "Self-Consistent Equations Including Exchange and Correlation Effects", *Phys. Rev.* **140**, A1133 (1965) (*cit. on pp. 17, 106*).
- [218] K. Burke, "Perspective on density functional theory", *J. Chem. Phys.* **136**, 150901 (2012), [arXiv:1201.3679](https://arxiv.org/abs/1201.3679) (*cit. on p. 17*).
- [219] R. M. Martin, *Electronic Structure: Basic Theory and Practical Methods* (Cambridge University Press, 2004) (*cit. on p. 17*).
- [220] D. Bagayoko, "Understanding density functional theory (dft) and completing it in practice", *AIP Adv.* **4**, 127104 (2014) (*cit. on p. 17*).
- [221] K. Burke, "Lies My Teacher Told Me About Density Functional Theory: Seeing Through Them with the Hubbard Dimer", in *Simulating Correlations with Computers*, Vol. 11, edited by E. Pavarini and E. Koch, Modeling and Simulation (Verlag des Forschungszentrum Jülich, 2021) Chap. 3 (*cit. on p. 17*).
- [222] M. Levy, "Universal variational functionals of electron densities, first-order density matrices, and natural spin-orbitals and solution of the  $v$ -representability problem", *PNAS* **76**, 6062 (1979) (*cit. on p. 17*).
- [223] E. H. Lieb, "Density functionals for coulomb systems", *Int. J. Quantum Chem.* **24**, 243 (1983) (*cit. on p. 17*).
- [224] S. F. Sousa, P. A. Fernandes, and M. J. Ramos, "General Performance of Density Functionals", *J. Phys. Chem. A* **111**, 10439 (2007) (*cit. on p. 17*).
- [225] I. Y. Zhang and X. Xu, "On the top rung of Jacob's ladder of density functional theory: Toward resolving the dilemma of SIE and NCE", *WIREs Comput. Mol. Sci.* **11**, 5 (2020) (*cit. on p. 17*).
- [226] J. M. Crowley, J. Tahir-Kheli, and W. A. Goddard, "Resolution of the Band Gap Prediction Problem for Materials Design", *J. Phys. Chem. Lett.* **7**, 1198 (2016) (*cit. on p. 17*).
- [227] F. Aryasetiawan and F. Nilsson, *Downfolding Methods in Many-Electron Theory* (AIP Publishing LLC Melville, New York, 2022) (*cit. on pp. 18, 20, 21, 36, 39*).
- [228] J. Berges, N. Girotto, T. Wehling, N. Marzari, and S. Ponc e, "Phonon Self-Energy Corrections: To Screen, or Not to Screen", *Phys. Rev. X* **13**, 041009 (2023), [arXiv:2212.11806](https://arxiv.org/abs/2212.11806) (*cit. on p. 18*).
- [229] A. Schobert, J. Berges, E. G. C. P. van Loon, M. A. Sentef, S. Brener, M. Rossi, and T. O. Wehling, "Ab initio electron-lattice downfolding: Potential energy landscapes, anharmonicity, and molecular dynamics in charge density wave materials", *SciPost Phys.* **16**, 046 (2024), [arXiv:2303.07261](https://arxiv.org/abs/2303.07261) (*cit. on pp. 18, 158*).
- [230] P. H. Dederichs, S. Bl ugel, R. Zeller, and H. Akai, "Ground States of Constrained Systems: Application to Cerium Impurities", *Phys. Rev. Lett.* **53**, 2512 (1984) (*cit. on p. 18*).
- [231] F. Aryasetiawan, M. Imada, A. Georges, G. Kotliar, S. Biermann, and A. I. Lichtenstein, "Frequency-dependent local interactions and low-energy effective models from electronic structure calculations", *Phys. Rev. B* **70**, 195104 (2004), [arXiv:cond-mat/0401620](https://arxiv.org/abs/cond-mat/0401620) (*cit. on pp. 18, 20, 21*).

- [232] Y. Nomura and R. Arita, “Ab initio downfolding for electron-phonon-coupled systems: Constrained density-functional perturbation theory”, *Phys. Rev. B* **92**, 245108 (2015), [arXiv:1509.01138](#) (cit. on pp. 18, 215).
- [233] A. I. Lichtenstein and M. I. Katsnelson, “Ab initio calculations of quasiparticle band structure in correlated systems: LDA++ approach”, *Phys. Rev. B* **57**, 6884 (1998), [arXiv:cond-mat/9707127](#) (cit. on p. 18).
- [234] M. I. Katsnelson and A. I. Lichtenstein, “LDA++ approach to the electronic structure of magnets: correlation effects in iron”, *J. Phys. Condens. Matter* **11**, 1037 (1999), [arXiv:cond-mat/9808094](#) (cit. on pp. 18, 36).
- [235] T. Wehling, “Projectors, Hubbard  $U$ , Charge Self-Consistency, and Double-Counting”, in *DMFT at 25: Infinite Dimensions*, Vol. 4, edited by E. Pavarini, E. Koch, D. Vollhardt, and A. Lichtenstein, Modeling and Simulation (Verlag des Forschungszentrum Jülich, 2014) Chap. 5 (cit. on p. 18).
- [236] J. Kuneš, “Wannier Functions and Constructions of Model Hamiltonians”, in *The LDA+DMFT: approach to strongly correlated materials*, Vol. 1, edited by E. Pavarini, E. Koch, D. Vollhardt, and A. Lichtenstein, Modeling and Simulation (Verlag des Forschungszentrum Jülich, 2011) Chap. 12 (cit. on p. 18).
- [237] N. Marzari and D. Vanderbilt, “Maximally localized generalized wannier functions for composite energy bands”, *Phys. Rev. B* **56**, 12847 (1997), [arXiv:cond-mat/9707145](#) (cit. on p. 19).
- [238] A. A. Mostofi, J. R. Yates, Y.-S. Lee, I. Souza, D. Vanderbilt, and N. Marzari, “Wannier90: A tool for obtaining maximally-localised Wannier functions”, *Comput. Phys. Commun.* **178**, 685 (2008), [arXiv:0708.0650](#) (cit. on p. 20).
- [239] C. Martins, M. Aichhorn, L. Vaugier, and S. Biermann, “Reduced Effective Spin-Orbital Degeneracy and Spin-Orbital Ordering in Paramagnetic Transition-Metal Oxides:  $\text{Sr}_2\text{IrO}_4$  versus  $\text{Sr}_2\text{RhO}_4$ ”, *Phys. Rev. Lett.* **107**, 266404 (2011) (cit. on p. 20).
- [240] Y. Nomura, M. Kaltak, K. Nakamura, C. Taranto, S. Sakai, A. Toschi, R. Arita, K. Held, G. Kresse, and M. Imada, “Effective on-site interaction for dynamical mean-field theory”, *Phys. Rev. B* **86**, 085117 (2012), [arXiv:1205.2836](#) (cit. on p. 20).
- [241] M. Rösner, E. Şaşıoğlu, C. Friedrich, S. Blügel, and T. O. Wehling, “Wannier function approach to realistic Coulomb interactions in layered materials and heterostructures”, *Phys. Rev. B* **92**, 085102 (2015), [arXiv:1504.05230](#) (cit. on pp. 20, 21).
- [242] M. Hirayama, T. Miyake, and M. Imada, “Derivation of static low-energy effective models by an *ab initio* downfolding method without double counting of Coulomb correlations: Application to  $\text{SrVO}_3$ ,  $\text{FeSe}$ , and  $\text{FeTe}$ ”, *Phys. Rev. B* **87**, 195144 (2013), [arXiv:1211.0597](#) (cit. on p. 20).

- [243] J.-B. Morée, M. Hirayama, M. T. Schmid, Y. Yamaji, and M. Imada, “Ab initio low-energy effective Hamiltonians for the high-temperature superconducting cuprates  $\text{Bi}_2\text{Sr}_2\text{CuO}_6$ ,  $\text{Bi}_2\text{Sr}_2\text{CaCu}_2\text{O}_8$ ,  $\text{HgBa}_2\text{CuO}_4$ , and  $\text{CaCuO}_2$ ”, *Phys. Rev. B* **106**, 235150 (2022), [arXiv:2206.01510](#) (cit. on p. 20).
- [244] M. Springer and F. Aryasetiawan, “Frequency-dependent screened interaction in Ni within the random-phase approximation”, *Phys. Rev. B* **57**, 4364 (1998) (cit. on p. 20).
- [245] M. Casula, P. Werner, L. Vaugier, F. Aryasetiawan, T. Miyake, A. J. Millis, and S. Biermann, “Low-Energy Models for Correlated Materials: Bandwidth Renormalization from Coulombic Screening”, *Phys. Rev. Lett.* **109**, 126408 (2012), [arXiv:1204.4900](#) (cit. on p. 20).
- [246] E. G. C. P. van Loon, M. Rösner, M. I. Katsnelson, and T. O. Wehling, “Random phase approximation for gapped systems: Role of vertex corrections and applicability of the constrained random phase approximation”, *Phys. Rev. B* **104**, 045134 (2021), [arXiv:2103.04419](#) (cit. on p. 20).
- [247] M. Schüler, M. Rösner, T. O. Wehling, A. I. Lichtenstein, and M. I. Katsnelson, “Optimal Hubbard Models for Materials with Nonlocal Coulomb Interactions: Graphene, Silicene, and Benzene”, *Phys. Rev. Lett.* **111**, 036601 (2013), [arXiv:1302.1437](#) (cit. on p. 21).
- [248] E. G. C. P. van Loon, M. Schüler, M. I. Katsnelson, and T. O. Wehling, “Capturing nonlocal interaction effects in the Hubbard model: Optimal mappings and limits of applicability”, *Phys. Rev. B* **94**, 165141 (2016), [arXiv:1605.09140](#) (cit. on p. 21).
- [249] J. Kanamori, “Electron Correlation and Ferromagnetism of Transition Metals”, *Prog. Theor. Phys.* **30**, 275 (1963) (cit. on pp. 21, 22).
- [250] G. Czycholl, *Solid State Theory, Volume 2: Applications: Non-equilibrium, Behavior in External Fields, Collective Phenomena* (Springer Berlin Heidelberg, 2023) (cit. on p. 21).
- [251] J. Hubbard, “Electron correlations in narrow energy bands”, *Proc. R. Soc. London A - Math Phys. Sci.* **276**, 238 (1963) (cit. on p. 22).
- [252] M. C. Gutzwiller, “Effect of Correlation on the Ferromagnetism of Transition Metals”, *Phys. Rev. Lett.* **10**, 159 (1963) (cit. on p. 22).
- [253] H. U. R. Strand, “Valence-skipping and negative- $U$  in the d-band from repulsive local Coulomb interaction”, *Phys. Rev. B* **90**, 155108 (2014), [arXiv:1303.4215](#) (cit. on p. 22).
- [254] E. H. Lieb and F. Y. Wu, “Absence of Mott Transition in an Exact Solution of the Short-Range, One-Band Model in One Dimension”, *Phys. Rev. Lett.* **20**, 1445 (1968) (cit. on p. 22).
- [255] E. H. Lieb and F. Y. Wu, “The one-dimensional Hubbard model: a reminiscence”, *Phys. A: Stat. Mech. Appl.* **321**, 1 (2003), [arXiv:cond-mat/0207529](#) (cit. on p. 22).

- [256] W. Metzner and D. Vollhardt, “Correlated Lattice Fermions in  $d = \infty$  Dimensions”, *Phys. Rev. Lett.* **62**, 324 (1989) (*cit. on pp. 22, 40*).
- [257] D. P. Arovas, E. Berg, S. A. Kivelson, and S. Raghu, “The Hubbard Model”, *Annu. Rev. Condens. Matter Phys.* **13**, 239 (2022), [arXiv:2103.12097](#) (*cit. on p. 22*).
- [258] F. C. Zhang and T. M. Rice, “Effective Hamiltonian for the superconducting Cu oxides”, *Phys. Rev. B* **37**, 3759 (1988) (*cit. on p. 22*).
- [259] H.-C. Jiang and T. P. Devereaux, “Superconductivity in the doped Hubbard model and its interplay with next-nearest hopping  $t''$ ”, *Science* **365**, 1424 (2019), [arXiv:1806.01465](#) (*cit. on p. 22*).
- [260] M. Kitatani, L. Si, O. Janson, R. Arita, Z. Zhong, and K. Held, “Nickelate superconductors—a renaissance of the one-band Hubbard model”, *npj Quantum Mater.* **5**, 59 (2020), [arXiv:2002.12230](#) (*cit. on pp. 22, 128*).
- [261] M. Greiner, O. Mandel, T. Esslinger, T. W. Hänsch, and I. Bloch, “Quantum phase transition from a superfluid to a Mott insulator in a gas of ultracold atoms”, *Nature* **415**, 39 (2002) (*cit. on p. 23*).
- [262] R. Jördens, N. Strohmaier, K. Günter, H. Moritz, and T. Esslinger, “A Mott insulator of fermionic atoms in an optical lattice”, *Nature* **455**, 204 (2008), [arXiv:0804.4009](#) (*cit. on p. 23*).
- [263] R. A. Hart, P. M. Duarte, T.-L. Yang, X. Liu, T. Paiva, E. Khatami, R. T. Scalettar, N. Trivedi, D. A. Huse, and R. G. Hulet, “Observation of antiferromagnetic correlations in the Hubbard model with ultracold atoms”, *Nature* **519**, 211 (2015), [arXiv:1407.5932](#) (*cit. on p. 23*).
- [264] D. Jaksch and P. Zoller, “The cold atom Hubbard toolbox”, *Ann. Phys.* **315**, 52 (2005), [arXiv:cond-mat/0410614](#) (*cit. on p. 23*).
- [265] T. Esslinger, “Fermi-Hubbard Physics with Atoms in an Optical Lattice”, *Annu. Rev. Condens. Matter Phys.* **1**, 129 (2010), [arXiv:1007.0012](#) (*cit. on p. 23*).
- [266] L. Tarruell and L. Sanchez-Palencia, “Quantum simulation of the Hubbard model with ultracold fermions in optical lattices”, *Comptes Rendus. Physique* **19**, 365 (2018), [arXiv:1809.00571](#) (*cit. on pp. 23, 211, 213*).
- [267] A. Avella, *Strongly Correlated Systems, Experimental techniques*, edited by F. Mancini, SpringerLink (Springer, Berlin, Heidelberg, 2015) (*cit. on pp. 23, 24, 88*).
- [268] T. Ayrál, “Nonlocal Coulomb Interactions and Electronic Correlations: Novel Many-Body Approaches”, PhD thesis (Ecole Polytechnique, 2015) (*cit. on pp. 23, 24, 31*).
- [269] R. M. Martin, L. Reining, and D. M. Ceperley, *Interacting Electrons: Theory and Computational Approaches* (Cambridge University Press, 2016) (*cit. on pp. 23, 28, 33, 34, 36, 39, 41, 42*).



- [270] A. A. Abrikosov, "On the Magnetic Properties of Superconductors of the Second Group", *Sov. Phys. JETP* **5**, [*Zh. Eksp. Teor. Fiz.* **32**, 1442 (1957)], 1174 (1957) (*cit. on pp. 27, 70*).
- [271] N. E. Bickers, "Self-Consistent Many-Body Theory for Condensed Matter System", in *Theoretical Methods for Strongly Correlated Electrons*, edited by D. Sénéchal, A.-M. Tremblay, and C. Bourbonnais (2004) Chap. 6 (*cit. on pp. 28, 36, 37*).
- [272] N. Wentzell, G. Li, A. Tagliavini, C. Taranto, G. Rohringer, K. Held, A. Toschi, and S. Andergassen, "High-frequency asymptotics of the vertex function: Diagrammatic parametrization and algorithmic implementation", *Phys. Rev. B* **102**, 085106 (2020), [arXiv:1610.06520](https://arxiv.org/abs/1610.06520) (*cit. on p. 28*).
- [273] F. Aryasetiawan, "Time-dependent exchange-correlation potential in lieu of self-energy", *Phys. Rev. B* **105**, 075106 (2022), [arXiv:2201.02854](https://arxiv.org/abs/2201.02854) (*cit. on p. 29*).
- [274] H. Shinaoka, N. Chikano, E. Gull, J. Li, T. Nomoto, J. Otsuki, M. Wallerberger, T. Wang, and K. Yoshimi, "Efficient ab initio many-body calculations based on sparse modeling of Matsubara Green's function", *SciPost Physics Lecture Notes*, **63** (2022), [arXiv:2106.12685](https://arxiv.org/abs/2106.12685) (*cit. on pp. 30, 45, 46*).
- [275] H. Shinaoka, J. Otsuki, M. Ohzeki, and K. Yoshimi, "Compressing Green's function using intermediate representation between imaginary-time and real-frequency domains", *Phys. Rev. B* **96**, 035147 (2017), [arXiv:1702.03054](https://arxiv.org/abs/1702.03054) (*cit. on pp. 30, 45, 46*).
- [276] H. J. Vidberg and J. W. Serene, "Solving the Eliashberg equations by means of  $N$ -point Padé approximants", *J. Low Temp. Phys.* **29**, 179 (1977) (*cit. on p. 30*).
- [277] J. Schött, I. L. M. Locht, E. Lundin, O. Grånäs, O. Eriksson, and I. Di Marco, "Analytic continuation by averaging Padé approximants", *Phys. Rev. B* **93**, 075104 (2016), [arXiv:1511.03496](https://arxiv.org/abs/1511.03496) (*cit. on p. 30*).
- [278] J. Kaufmann and K. Held, "Ana\_cont: Python package for analytic continuation", *Comput. Phys. Commun.* **282**, 108519 (2023), [arXiv:2105.11211](https://arxiv.org/abs/2105.11211) (*cit. on p. 30*).
- [279] O. Gunnarsson, M. W. Haverkort, and G. Sangiovanni, "Analytical continuation of imaginary axis data using maximum entropy", *Phys. Rev. B* **81**, 155107 (2010), [arXiv:1001.4351v1](https://arxiv.org/abs/1001.4351v1) (*cit. on p. 30*).
- [280] D. Bergeron and A.-M. S. Tremblay, "Algorithms for optimized maximum entropy and diagnostic tools for analytic continuation", *Phys. Rev. E* **94**, 023303 (2016), [arXiv:1507.01012](https://arxiv.org/abs/1507.01012) (*cit. on p. 30*).
- [281] G. J. Krabberger, R. Triebl, M. Zingl, and M. Aichhorn, "Maximum entropy formalism for the analytic continuation of matrix-valued Green's functions", *Phys. Rev. B* **96**, 155128 (2017), [arXiv:1705.08838](https://arxiv.org/abs/1705.08838) (*cit. on p. 30*).
- [282] C. Yue and P. Werner, "Maximum entropy analytic continuation of anomalous self-energies", *Phys. Rev. B* **108**, L220503 (2023), [arXiv:2303.16888](https://arxiv.org/abs/2303.16888) (*cit. on p. 30*).

- [283] R. Levy, J. P. F. LeBlanc, and E. Gull, "Implementation of the maximum entropy method for analytic continuation", *Comput. Phys. Commun.* **215**, 149 (2017), [arXiv:1606.00368](#) (*cit. on p. 30*).
- [284] A. W. Sandvik, "Stochastic method for analytic continuation of quantum Monte Carlo data", *Phys. Rev. B* **57**, 10287 (1998) (*cit. on p. 30*).
- [285] I. Krivenko and M. Harland, "TRIQS/SOM: implementation of the stochastic optimization method for analytic continuation", *Comput. Phys. Commun.* **239**, 166 (2019), [arXiv:1808.00603](#) (*cit. on p. 30*).
- [286] J. Otsuki, M. Ohzeki, H. Shinaoka, and K. Yoshimi, "Sparse modeling approach to analytical continuation of imaginary-time quantum Monte Carlo data", *Phys. Rev. E* **95**, 061302 (2017), [arXiv:1702.03056](#) (*cit. on pp. 30, 46*).
- [287] Y. Motoyama, K. Yoshimi, and J. Otsuki, "Robust analytic continuation combining the advantages of the sparse modeling approach and the Padé approximation", *Phys. Rev. B* **105**, 035139 (2022), [arXiv:2109.08370](#) (*cit. on pp. 30, 46*).
- [288] K. Yoshimi, J. Otsuki, Y. Motoyama, M. Ohzeki, and H. Shinaoka, "SpM: Sparse modeling tool for analytic continuation of imaginary-time Green's function", *Comput. Phys. Commun.* **244**, 319 (2019), [arXiv:1904.02903](#) (*cit. on p. 30*).
- [289] H. Yoon, J.-H. Sim, and M. J. Han, "Analytic continuation via domain knowledge free machine learning", *Phys. Rev. B* **98**, 245101 (2018), [arXiv:1806.03841](#) (*cit. on p. 30*).
- [290] J. Fei, C.-N. Yeh, and E. Gull, "Nevanlinna Analytical Continuation", *Phys. Rev. Lett.* **126**, 056402 (2021), [arXiv:2010.04572](#) (*cit. on pp. 30, 46*).
- [291] K. Nogaki, J. Fei, E. Gull, and H. Shinaoka, "Nevanlinna.jl: A Julia implementation of Nevanlinna analytic continuation", *SciPost Physics Codebases*, **19** (2023), [arXiv:2302.10476](#) (*cit. on pp. 30, 46*).
- [292] S. Iskakov, A. Hampel, N. Wentzell, and E. Gull, "TRIQS/Nevanlinna: Implementation of the Nevanlinna Analytic Continuation method for noise-free data", *Comput. Phys. Commun.* **304**, 109299 (2024), [arXiv:2309.01407](#) (*cit. on p. 30*).
- [293] E. G. C. P. van Loon, A. I. Lichtenstein, M. I. Katsnelson, O. Parcollet, and H. Hafermann, "Beyond extended dynamical mean-field theory: Dual boson approach to the two-dimensional extended Hubbard model", *Phys. Rev. B* **90**, 235135 (2014), [arXiv:1408.2150](#) (*cit. on p. 31*).
- [294] R. T. Scalettar, "Insulator, Metal, or Superconductor: The Criteria", in *The Physics of Correlated Insulators, Metals, and Superconductors*, Vol. 7, edited by E. Pavarini, E. Koch, R. Scalettar, and R. Martin, Modeling and Simulation (Verlag des Forschungszentrum Jülich, 2017) Chap. 2 (*cit. on p. 31*).
- [295] A. V. Chubukov and D. L. Maslov, "First-Matsubara-frequency rule in a Fermi liquid. I. Fermionic self-energy", *Phys. Rev. B* **86**, 155136 (2012), [arXiv:1208.3483](#) (*cit. on p. 33*).

- [296] J. M. Luttinger and J. C. Ward, “Ground-State Energy of a Many-Fermion System. II”, *Phys. Rev.* **118**, 1417 (1960) (*cit. on p. 33*).
- [297] R. Eder, “Analytic Properties of Self-Energy and Luttinger-Ward Functional”, in *Many-Body Methods for Real Materials*, Vol. 9, edited by E. Pavarini, E. Koch, and S. Zhang, Modeling and Simulation (Verlag des Forschungszentrum Jülich, 2019) Chap. 12 (*cit. on pp. 33, 34*).
- [298] C. De Dominicis and P. C. Martin, “Stationary Entropy Principle and Renormalization in Normal and Superfluid Systems. I. Algebraic Formulation”, *J. Math. Phys.* **5**, 14 (1964) (*cit. on p. 34*).
- [299] C. De Dominicis and P. C. Martin, “Stationary Entropy Principle and Renormalization in Normal and Superfluid Systems. II. Diagrammatic Formulation”, *J. Math. Phys.* **5**, 31 (1964) (*cit. on p. 34*).
- [300] G. Baym and L. P. Kadanoff, “Conservation Laws and Correlation Functions”, *Phys. Rev.* **124**, 287 (1961) (*cit. on p. 34*).
- [301] G. Baym, “Self-Consistent Approximations in Many-Body Systems”, *Phys. Rev.* **127**, 1391 (1962) (*cit. on p. 34*).
- [302] Potthoff, “Non-perturbative construction of the Luttinger-Ward functional”, *Condens. Matter Phys.* **9**, 557 (2006), [arXiv:cond-mat/0406671](https://arxiv.org/abs/cond-mat/0406671) (*cit. on pp. 34, 35, 41*).
- [303] E. Kozik, M. Ferrero, and A. Georges, “Nonexistence of the Luttinger-Ward Functional and Misleading Convergence of Skeleton Diagrammatic Series for Hubbard-Like Models”, *Phys. Rev. Lett.* **114**, 156402 (2015), [arXiv:1407.5687](https://arxiv.org/abs/1407.5687) (*cit. on p. 34*).
- [304] R. Eder, “Comment on ‘Non-existence of the Luttinger-Ward functional and misleading convergence of skeleton diagrammatic series for Hubbard-like models’”, arXiv preprint (2014), [arXiv:1407.6599](https://arxiv.org/abs/1407.6599) (*cit. on p. 34*).
- [305] J. Gukelberger, L. Huang, and P. Werner, “On the dangers of partial diagrammatic summations: Benchmarks for the two-dimensional Hubbard model in the weak-coupling regime”, *Phys. Rev. B* **91**, 235114 (2015), [arXiv:1501.04960](https://arxiv.org/abs/1501.04960) (*cit. on pp. 34, 36, 44*).
- [306] A. Stan, P. Romaniello, S. Rigamonti, L. Reining, and J. A. Berger, “Unphysical and physical solutions in many-body theories: from weak to strong correlation”, *New J. Phys.* **17**, 093045 (2015), [arXiv:1503.07742](https://arxiv.org/abs/1503.07742) (*cit. on p. 34*).
- [307] O. Gunnarsson, G. Rohringer, T. Schäfer, G. Sangiovanni, and A. Toschi, “Breakdown of Traditional Many-Body Theories for Correlated Electrons”, *Phys. Rev. Lett.* **119**, 056402 (2017), [arXiv:1703.06478](https://arxiv.org/abs/1703.06478) (*cit. on pp. 34, 35*).
- [308] J. Vučičević, N. Wentzell, M. Ferrero, and O. Parcollet, “Practical consequences of the Luttinger-Ward functional multivaluedness for cluster DMFT methods”, *Phys. Rev. B* **97**, 125141 (2018), [arXiv:1709.10490](https://arxiv.org/abs/1709.10490) (*cit. on p. 34*).

- [309] K. Van Houcke, E. Kozik, R. Rossi, Y. Deng, and F. Werner, “Physical and unphysical regimes of self-consistent many-body perturbation theory”, *SciPost Phys.* **16**, 133 (2024), [arXiv:2102.04508](#) (*cit. on pp. 34, 35*).
- [310] S. Hirata, I. Grabowski, J. V. Ortiz, and R. J. Bartlett, “Nonconvergence of the Feynman-Dyson diagrammatic perturbation expansion of propagators”, *Phys. Rev. A* **109**, 052220 (2024), [arXiv:2312.03157](#) (*cit. on pp. 34, 35*).
- [311] T. Schäfer, G. Rohringer, O. Gunnarsson, S. Ciuchi, G. Sangiovanni, and A. Toschi, “Divergent Precursors of the Mott-Hubbard Transition at the Two-Particle Level”, *Phys. Rev. Lett.* **110**, 246405 (2013), [arXiv:1303.0246](#) (*cit. on p. 35*).
- [312] T. Schäfer, S. Ciuchi, M. Wallerberger, P. Thunström, O. Gunnarsson, G. Sangiovanni, G. Rohringer, and A. Toschi, “Nonperturbative landscape of the Mott-Hubbard transition: Multiple divergence lines around the critical endpoint”, *Phys. Rev. B* **94**, 235108 (2016), [arXiv:1606.03393](#) (*cit. on p. 35*).
- [313] P. Chalupa, P. Gunacker, T. Schäfer, K. Held, and A. Toschi, “Divergences of the irreducible vertex functions in correlated metallic systems: Insights from the Anderson impurity model”, *Phys. Rev. B* **97**, 245136 (2018), [arXiv:1712.04171](#) (*cit. on p. 35*).
- [314] P. Thunström, O. Gunnarsson, S. Ciuchi, and G. Rohringer, “Analytical investigation of singularities in two-particle irreducible vertex functions of the Hubbard atom”, *Phys. Rev. B* **98**, 235107 (2018), [arXiv:1805.00989](#) (*cit. on p. 35*).
- [315] M. Reitner, P. Chalupa, L. Del Re, D. Springer, S. Ciuchi, G. Sangiovanni, and A. Toschi, “Attractive Effect of a Strong Electronic Repulsion: The Physics of Vertex Divergences”, *Phys. Rev. Lett.* **125**, 196403 (2020), [arXiv:2002.12869](#) (*cit. on p. 35*).
- [316] T. Pruschke, W. Metzner, and D. Vollhardt, “On the analyticity of solutions in the dynamical mean-field theory”, *J. Phys. Condens. Matter* **13**, 9455 (2001), [arXiv:arXiv:cond-mat/0105456](#) (*cit. on p. 35*).
- [317] R. Rossi, F. Werner, N. Prokof'ev, and B. Svistunov, “Shifted-action expansion and applicability of dressed diagrammatic schemes”, *Phys. Rev. B* **93**, 161102 (2016), [arXiv:1508.03654](#) (*cit. on p. 35*).
- [318] W. Tarantino, P. Romaniello, J. A. Berger, and L. Reining, “Self-consistent Dyson equation and self-energy functionals: An analysis and illustration on the example of the Hubbard atom”, *Phys. Rev. B* **96**, 045124 (2017), [arXiv:1703.05587](#) (*cit. on p. 35*).
- [319] L. Lin and M. Lindsey, “Variational structure of Luttinger-Ward formalism and bold diagrammatic expansion for Euclidean lattice field theory”, *PNAS* **115**, 2282 (2018), [arXiv:1711.07191](#) (*cit. on p. 35*).
- [320] E. G. C. P. van Loon, F. Krien, and A. A. Katanin, “Bethe-Salpeter Equation at the Critical End Point of the Mott Transition”, *Phys. Rev. Lett.* **125**, 136402 (2020), [arXiv:2002.12745](#) (*cit. on p. 35*).

- [321] S. Isakov and E. Gull, “Phase transitions in partial summation methods: Results from the three-dimensional Hubbard model”, *Phys. Rev. B* **105**, 045109 (2022), [arXiv:2110.06857](#) (*cit. on pp. 35–37, 64*).
- [322] V. Janiš, V. Pokorný, and Š. Kos, “Failure of the Baym-Kadanoff construction to consistently match quantum dynamics with thermodynamic critical behavior”, *Phys. Rev. B* **109**, 075171 (2024), [arXiv:2309.07699](#) (*cit. on pp. 35, 64*).
- [323] S. Adler, F. Krien, P. Chalupa-Gantner, G. Sangiovanni, and A. Toschi, “Non-perturbative intertwining between spin and charge correlations: A “smoking gun” single-boson-exchange result”, *SciPost Phys.* **16**, 054 (2024), [arXiv:2212.09693](#) (*cit. on p. 35*).
- [324] F. Krien, “Conserving dynamical mean-field approaches to strongly correlated systems”, PhD thesis (Universität Hamburg, 2018) (*cit. on p. 35*).
- [325] Y. M. Vilk and A.-M. S. Tremblay, “Non-Perturbative Many-Body Approach to the Hubbard Model and Single-Particle Pseudogap”, *J. Phys. I* **7**, 1309 (1997), [arXiv:cond-mat/9702188](#) (*cit. on p. 35*).
- [326] S. Allen, A.-M. S. Tremblay, and Y. M. Vilk, “Conserving Approximations vs. Two-Particle Self-Consistent Approach”, in *Theoretical Methods for Strongly Correlated Electrons*, edited by D. Sénéchal, A.-M. Tremblay, and C. Bourbonnais (2004) Chap. 8, [arXiv:cond-mat/0110130](#) (*cit. on p. 35*).
- [327] K. Zantout, S. Backes, and R. Valentí, “Two-Particle Self-Consistent Method for the Multi-Orbital Hubbard Model”, *Ann. Phys.* **533**, 2000399 (2021), [arXiv:2008.08098](#) (*cit. on p. 35*).
- [328] C. Gauvin-Ndiaye, C. Lahaie, Y. M. Vilk, and A.-M. S. Tremblay, “Improved two-particle self-consistent approach for the single-band hubbard model in two dimensions”, *Phys. Rev. B* **108**, 075144 (2023), [arXiv:2305.19219](#) (*cit. on pp. 35, 46*).
- [329] K. Van Houcke, E. Kozik, N. Prokof'ev, and B. Svistunov, “Diagrammatic Monte Carlo”, *Physcs. Proc.* **6**, 95 (2010), [arXiv:0802.2923](#) (*cit. on p. 35*).
- [330] J. Li, M. Wallerberger, N. Chikano, C.-N. Yeh, E. Gull, and H. Shinaoka, “Sparse sampling approach to efficient ab initio calculations at finite temperature”, *Phys. Rev. B* **101**, 035144 (2020), [arXiv:1908.07575](#) (*cit. on pp. 35, 45–47*).
- [331] L.-F. Arsenault, P. Sémon, and A.-M. S. Tremblay, “Benchmark of a modified iterated perturbation theory approach on the fcc lattice at strong coupling”, *Phys. Rev. B* **86**, 085133 (2012), [arXiv:1202.5814](#) (*cit. on p. 35*).
- [332] E. G. C. P. van Loon, “Two-particle correlations and the metal-insulator transition: iterated perturbation theory revisited”, *Phys. Rev. B* **105**, 245104 (2022), [arXiv:2110.11116](#) (*cit. on p. 35*).
- [333] F. Aryasetiawan and O. Gunnarsson, “The GW method”, *Rep. Prog. Phys.* **61**, 237 (1998), [arXiv:cond-mat/9712013](#) (*cit. on p. 36*).

- [334] S. Isakov, A. A. Rusakov, D. Zgid, and E. Gull, “Effect of propagator renormalization on the band gap of insulating solids”, *Phys. Rev. B* **100**, 085112 (2019), [arXiv:1812.07027](#) (cit. on p. 36).
- [335] N. E. Bickers, D. J. Scalapino, and S. R. White, “Conserving Approximations for Strongly Correlated Electron Systems: Bethe-Salpeter Equation and Dynamics for the Two-Dimensional Hubbard Model”, *Phys. Rev. Lett.* **62**, 961 (1989) (cit. on pp. 36, 37).
- [336] N. E. Bickers and D. J. Scalapino, “Conserving approximations for strongly fluctuating electron systems. I. Formalism and calculational approach”, *Ann. Phys.* **193**, 206 (1989) (cit. on p. 36).
- [337] N. E. Bickers and S. R. White, “Conserving approximations for strongly fluctuating electron systems. II. Numerical results and parquet extension”, *Phys. Rev. B* **43**, 8044 (1991) (cit. on p. 36).
- [338] D. Manske, *Theory of Unconventional Superconductors* (Springer Berlin Heidelberg, 2004) (cit. on p. 36).
- [339] R. Arita, K. Kuroki, and H. Aoki, “*d*- and *p*-Wave Superconductivity Mediated by Spin Fluctuations in Two- and Three-Dimensional Single-Band Repulsive Hubbard Model”, *J. Phys. Soc. Jpn.* **69**, 1181 (2000), [arXiv:cond-mat/0002440](#) (cit. on pp. 36, 104, 109, 191).
- [340] H. Aoki, “Triplet superconductivity-spin vs. charge fluctuations and fermiology”, *Phys. B: Condens. Matter* **374-375**, 229 (2006) (cit. on p. 36).
- [341] K. Kubo and T. Hotta, “Multipole Ordering and Fluctuations in *f*-Electron Systems”, *J. Phys. Soc. Jpn.* **75**, 232 (2006), [arXiv:cond-mat/0512647](#) (cit. on p. 36).
- [342] K. Kubo and T. Hotta, “Orbital-Controlled Superconductivity in *f*-Electron Systems”, *J. Phys. Soc. Jpn.* **75**, 083702 (2006), [arXiv:cond-mat/0603602](#) (cit. on p. 36).
- [343] T. Dahm and L. Tewordt, “Physical quantities in the normal and *d* wave superconducting states of the Hubbard model for  $\text{YBa}_2\text{Cu}_3\text{O}_{7-y}$ ”, *Phys. C: Supercond.* **246**, 61 (1995) (cit. on p. 36).
- [344] G. Esirgen and N. E. Bickers, “Fluctuation exchange analysis of superconductivity in the standard three-band  $\text{CuO}_2$  model”, *Phys. Rev. B* **57**, 5376 (1998), [arXiv:cond-mat/9711151](#) (cit. on p. 36).
- [345] H. Sakakibara, H. Usui, K. Kuroki, R. Arita, and H. Aoki, “Origin of the material dependence of  $T_c$  in the single-layered cuprates”, *Phys. Rev. B* **85**, 064501 (2012), [arXiv:1112.0964](#) (cit. on p. 36).
- [346] H. Sakakibara, K. Suzuki, H. Usui, K. Kuroki, R. Arita, D. J. Scalapino, and H. Aoki, “First-principles band structure and FLEX approach to the pressure effect on  $T_c$  of the cuprate superconductors”, *J. Phys. Conf. Ser.* **454**, 012021 (2013), [arXiv:1211.1805](#) (cit. on pp. 36, 84).

- [347] H. Kondo and T. Moriya, "Spin Fluctuation-Induced Superconductivity in Organic Compounds", *J. Phys. Soc. Jpn.* **67**, 3695 (1998), [arXiv:cond-mat/9807322](#) (*cit. on p. 36*).
- [348] H. Kino and H. Kontani, "Phase Diagram of Superconductivity on the Anisotropic Triangular Lattice Hubbard Model: An Effective Model of  $\kappa$ -(BEDT-TTF) Salts", *J. Phys. Soc. Jpn.* **67**, 3691 (1998), [arXiv:cond-mat/9807147](#) (*cit. on p. 36*).
- [349] J. Schmalian, "Pairing due to Spin Fluctuations in Layered Organic Superconductors", *Phys. Rev. Lett.* **81**, 4232 (1998), [arXiv:cond-mat/9807042](#) (*cit. on p. 36*).
- [350] M. Mochizuki, Y. Yanase, and M. Ogata, "Ferromagnetic Fluctuation and Possible Triplet Superconductivity in  $\text{Na}_x\text{CoO}_2 \cdot y\text{H}_2\text{O}$ : Fluctuation-Exchange Study of the Multiorbital Hubbard Model", *Phys. Rev. Lett.* **94**, 147005 (2005), [arXiv:cond-mat/0407094](#) (*cit. on pp. 36, 113*).
- [351] K. Yada and H. Kontani, "Origin of Weak Pseudogap Behaviors in  $\text{Na}_{0.35}\text{CoO}_2$ : Absence of Small Hole Pockets", *J. Phys. Soc. Jpn.* **74**, 2161 (2005), [arXiv:cond-mat/0505747](#) (*cit. on p. 36*).
- [352] K. Kuroki, S. Onari, Y. Tanaka, R. Arita, and T. Nojima, "Extended  $s$ -wave pairing originating from the  $a_{1g}$  band in  $\text{Na}_x\text{CoO}_2 \cdot y\text{H}_2\text{O}$ : Single-band  $U$ - $V$  model with fluctuation exchange method", *Phys. Rev. B* **73**, 184503 (2006), [arXiv:cond-mat/0508482](#) (*cit. on p. 36*).
- [353] K. Björnson, A. Kreisel, A. T. Rømer, and B. M. Andersen, "Orbital-dependent self-energy effects and consequences for the superconducting gap structure in multiorbital correlated electron systems", *Phys. Rev. B* **103**, 024508 (2021), [arXiv:2011.04243](#) (*cit. on p. 36*).
- [354] H. Sakakibara, N. Kitamine, M. Ochi, and K. Kuroki, "Possible High  $T_c$  Superconductivity in  $\text{La}_3\text{Ni}_2\text{O}_7$  under High Pressure through Manifestation of a Nearly Half-Filled Bilayer Hubbard Model", *Phys. Rev. Lett.* **132**, 106002 (2024), [arXiv:2306.06039](#) (*cit. on p. 36*).
- [355] G. Esirgen and N. E. Bickers, "Fluctuation-exchange theory for general lattice Hamiltonians", *Phys. Rev. B* **55**, 2122 (1997) (*cit. on p. 36*).
- [356] H. Kontani and K. Ueda, "Electronic Properties of the Trellis-Lattice Hubbard Model: Pseudogap and Superconductivity", *Phys. Rev. Lett.* **80**, 5619 (1998) (*cit. on p. 36*).
- [357] T. Takimoto, T. Hotta, and K. Ueda, "Strong-coupling theory of superconductivity in a degenerate Hubbard model", *Phys. Rev. B* **69**, 104504 (2004), [arXiv:cond-mat/0309575](#) (*cit. on p. 36*).
- [358] K. Kubo, "Pairing symmetry in a two-orbital Hubbard model on a square lattice", *Phys. Rev. B* **75**, 224509 (2007), [arXiv:cond-mat/0702624](#) (*cit. on p. 36*).
- [359] N. D. Mermin and H. Wagner, "Absence of Ferromagnetism or Antiferromagnetism in One- or Two-Dimensional Isotropic Heisenberg Models", *Phys. Rev. Lett.* **17**, 1133 (1966) (*cit. on pp. 39, 80*).

- [360] H. Kontani and M. Ohno, “Effect of a nonmagnetic impurity in a nearly antiferromagnetic Fermi liquid: Magnetic correlations and transport phenomena”, *Phys. Rev. B* **74**, 014406 (2006), [arXiv:cond-mat/0607595](#) (*cit. on p. 39*).
- [361] Q. Sun and G. K.-L. Chan, “Quantum Embedding Theories”, *Accounts Chem. Res.* **49**, 2705 (2016), [arXiv:1612.02576](#) (*cit. on p. 39*).
- [362] M. Vandelli, “Quantum embedding methods in dualspace for strongly interacting electronicsystems”, PhD thesis (Universität Hamburg, 2022) (*cit. on p. 39*).
- [363] A. Georges and G. Kotliar, “Hubbard model in infinite dimensions”, *Phys. Rev. B* **45**, 6479 (1992) (*cit. on pp. 39, 40, 42*).
- [364] A. Georges, “Strongly Correlated Electron Materials: Dynamical Mean-Field Theory and Electronic Structure”, in *Aip conf. proc.* Vol. 715 (2004), pp. 3–74, [arXiv:cond-mat/0403123](#) (*cit. on p. 39*).
- [365] E. Pavarini, E. Koch, A. I. Lichtenstein, and D. Vollhardt, eds., *Dynamical mean-field theory of correlated electrons, Autumn school on correlated electrons*, Vol. 12, Modeling and Simulation (Verlag des Forschungszentrum Jülich, 2022) (*cit. on pp. 39, 42*).
- [366] E. Müller-Hartmann, “Correlated fermions on a lattice in high dimensions”, *Z. Phys. B Condens. Matter* **74**, 507 (1989) (*cit. on p. 40*).
- [367] M. Jarrell, “Hubbard model in infinite dimensions: A quantum Monte Carlo study”, *Phys. Rev. Lett.* **69**, 168 (1992) (*cit. on p. 40*).
- [368] F. J. Ohkawa, “Electron Correlation in the Hubbard Model in  $d = \infty$  Dimension”, *J. Phys. Soc. Jpn.* **60**, 3218 (1991) (*cit. on p. 40*).
- [369] A. C. Hewson, *The Kondo Problem to Heavy Fermions* (Cambridge University Press, 1993) (*cit. on p. 40*).
- [370] A. N. Rubtsov, M. I. Katsnelson, and A. I. Lichtenstein, “Dual fermion approach to nonlocal correlations in the Hubbard model”, *Phys. Rev. B* **77**, 033101 (2008), [arXiv:cond-mat/0612196](#) (*cit. on pp. 41, 44*).
- [371] S. Brener, E. A. Stepanov, A. N. Rubtsov, M. I. Katsnelson, and A. I. Lichtenstein, “Dual fermion method as a prototype of generic reference-system approach for correlated fermions”, *Ann. Phys.* **422**, 168310 (2020), [arXiv:2007.15937](#) (*cit. on pp. 41, 44*).
- [372] Y. Lu and M. W. Haverkort, “Exact diagonalization as an impurity solver in dynamical mean field theory”, *Eur. Phys. J. Special Topics* **226**, 2549 (2017) (*cit. on p. 42*).
- [373] D. Medvedeva, S. Isakov, F. Krien, V. V. Mazurenko, and A. I. Lichtenstein, “Exact diagonalization solver for extended dynamical mean-field theory”, *Phys. Rev. B* **96**, 235149 (2017), [arXiv:1709.09176](#) (*cit. on p. 42*).



- [374] R. Bulla, T. A. Costi, and T. Pruschke, “Numerical renormalization group method for quantum impurity systems”, *Rev. Mod. Phys.* **80**, 395 (2008), [arXiv:cond-mat/0701105](#) (cit. on p. 42).
- [375] S. R. White, “Density matrix formulation for quantum renormalization groups”, *Phys. Rev. Lett.* **69**, 2863 (1992) (cit. on pp. 42, 46).
- [376] D. J. García, K. Hallberg, and M. J. Rozenberg, “Dynamical Mean Field Theory with the Density Matrix Renormalization Group”, *Phys. Rev. Lett.* **93**, 246403 (2004), [arXiv:cond-mat/0403169](#) (cit. on p. 42).
- [377] E. Gull, A. J. Millis, A. I. Lichtenstein, A. N. Rubtsov, M. Troyer, and P. Werner, “Continuous-time Monte Carlo methods for quantum impurity models”, *Rev. Mod. Phys.* **83**, 349 (2011), [arXiv:1012.4474](#) (cit. on p. 42).
- [378] P. Werner, A. Comanac, L. de’Medici, M. Troyer, and A. J. Millis, “Continuous-Time Solver for Quantum Impurity Models”, *Phys. Rev. Lett.* **97**, 076405 (2006), [arXiv:cond-mat/0512727](#) (cit. on p. 42).
- [379] P. Werner and A. J. Millis, “Hybridization expansion impurity solver: General formulation and application to Kondo lattice and two-orbital models”, *Phys. Rev. B* **74**, 155107 (2006), [arXiv:cond-mat/0607136](#) (cit. on p. 42).
- [380] P. Seth, I. Krivenko, M. Ferrero, and O. Parcollet, “TRIQS/CTHYB: A continuous-time quantum Monte Carlo hybridisation expansion solver for quantum impurity problems”, *Comput. Phys. Commun.* **200**, 274 (2016), [arXiv:1507.00175](#) (cit. on pp. 42, 45).
- [381] H. Shinaoka, E. Gull, and P. Werner, “Continuous-time hybridization expansion quantum impurity solver for multi-orbital systems with complex hybridizations”, *Comput. Phys. Commun.* **215**, 128 (2017), [arXiv:1609.09559](#) (cit. on pp. 42, 45).
- [382] C. Melnick, P. Sémon, K. Yu, N. D’Imperio, A.-M. Tremblay, and G. Kotliar, “Accelerated impurity solver for DMFT and its diagrammatic extensions”, *Comput. Phys. Commun.* **267**, 108075 (2021), [arXiv:2010.08482](#) (cit. on p. 42).
- [383] A. N. Rubtsov, V. V. Savkin, and A. I. Lichtenstein, “Continuous-time quantum Monte Carlo method for fermions”, *Phys. Rev. B* **72**, 035122 (2005), [arXiv:cond-mat/0411344](#) (cit. on p. 42).
- [384] E. Gull, P. Werner, O. Parcollet, and M. Troyer, “Continuous-time auxiliary-field Monte Carlo for quantum impurity models”, *Europhys. Lett.* **82**, 57003 (2008), [arXiv:0802.3222](#) (cit. on p. 42).
- [385] S. Sakai, R. Arita, K. Held, and H. Aoki, “Quantum Monte Carlo study for multiorbital systems with preserved spin and orbital rotational symmetries”, *Phys. Rev. B* **74**, 155102 (2006), [arXiv:cond-mat/0605526](#) (cit. on p. 42).
- [386] M. H. Hettler, A. N. Tahvildar-Zadeh, M. Jarrell, T. Pruschke, and H. R. Krishnamurthy, “Nonlocal dynamical correlations of strongly interacting electron systems”, *Phys. Rev. B* **58**, R7475 (1998), [arXiv:cond-mat/9803295](#) (cit. on p. 43).

- [387] A. I. Lichtenstein and M. I. Katsnelson, “Antiferromagnetism and d-wave superconductivity in cuprates: A cluster dynamical mean-field theory”, *Phys. Rev. B* **62**, R9283 (2000), [arXiv:cond-mat/9911320](#) (cit. on p. 43).
- [388] G. Kotliar, S. Y. Savrasov, G. Pálsson, and G. Biroli, “Cellular Dynamical Mean Field Approach to Strongly Correlated Systems”, *Phys. Rev. Lett.* **87**, 186401 (2001), [arXiv:cond-mat/0010328](#) (cit. on p. 43).
- [389] M. Harland, S. Brener, A. I. Lichtenstein, and M. I. Katsnelson, “Josephson lattice model for phase fluctuations of local pairs in copper oxide superconductors”, *Phys. Rev. B* **100**, 024510 (2019), [arXiv:1810.12986](#) (cit. on pp. 43, 77, 78, 81, 84).
- [390] M. Meixner, H. Menke, M. Klett, S. Heinzelmann, S. Andergassen, P. Hansmann, and T. Schäfer, “Mott transition and pseudogap of the square-lattice Hubbard model: Results from center-focused cellular dynamical mean-field theory”, *SciPost Phys.* **16**, 059 (2024), [arXiv:2310.17302](#) (cit. on p. 43).
- [391] T. Ayrál and O. Parcollet, “Mott physics and spin fluctuations: A unified framework”, *Phys. Rev. B* **92**, 115109 (2015), [arXiv:1503.07724](#) (cit. on p. 44).
- [392] T. Ayrál, J. Vučičević, and O. Parcollet, “Fierz Convergence Criterion: A Controlled Approach to Strongly Interacting Systems with Small Embedded Clusters”, *Phys. Rev. Lett.* **119**, 166401 (2017), [arXiv:1706.01388](#) (cit. on p. 44).
- [393] T. Ayrál and O. Parcollet, “Mott physics and collective modes: An atomic approximation of the four-particle irreducible functional”, *Phys. Rev. B* **94**, 075159 (2016), [arXiv:1605.09048](#) (cit. on p. 44).
- [394] A. Toschi, A. A. Katanin, and K. Held, “Dynamical vertex approximation: A step beyond dynamical mean-field theory”, *Phys. Rev. B* **75**, 045118 (2007), [arXiv:cond-mat/0603100](#) (cit. on p. 44).
- [395] H. Kusunose, “Influence of Spatial Correlations in Strongly Correlated Electron Systems: Extension to Dynamical Mean Field Approximation”, *J. Phys. Soc. Jpn.* **75**, 054713 (2006), [arXiv:cond-mat/0602451](#) (cit. on p. 44).
- [396] A. Toschi, G. Rohringer, A. A. Katanin, and K. Held, “Ab initio calculations with the dynamical vertex approximation”, *Ann. Phys.* **523**, 698 (2011), [arXiv:1104.2188](#) (cit. on p. 44).
- [397] C. Taranto, S. Andergassen, J. Bauer, K. Held, A. Katanin, W. Metzner, G. Rohringer, and A. Toschi, “From Infinite to Two Dimensions through the Functional Renormalization Group”, *Phys. Rev. Lett.* **112**, 196402 (2014), [arXiv:1307.3475](#) (cit. on p. 44).
- [398] A. N. Rubtsov, M. I. Katsnelson, and A. Lichtenstein, “Dual boson approach to collective excitations in correlated fermionic systems”, *Ann. Phys.* **327**, 1320 (2012), [arXiv:1105.6158](#) (cit. on p. 44).
- [399] E. A. Stepanov, V. Harkov, and A. I. Lichtenstein, “Consistent partial bosonization of the extended Hubbard model”, *Phys. Rev. B* **100**, 205115 (2019), [arXiv:1908.00536](#) (cit. on p. 44).

- [400] V. Harkov, M. Vandelli, S. Brener, A. I. Lichtenstein, and E. A. Stepanov, "Impact of partially bosonized collective fluctuations on electronic degrees of freedom", *Phys. Rev. B* **103**, 245123 (2021), [arXiv:2102.05425](#) (*cit. on p. 44*).
- [401] M. Vandelli, J. Kaufmann, M. El-Nabulsi, V. Harkov, A. Lichtenstein, and E. Stepanov, "Multi-band D-TRILEX approach to materials with strong electronic correlations", *SciPost Phys.* **13**, 036 (2022), [arXiv:2204.06426](#) (*cit. on p. 44*).
- [402] P. Sun and G. Kotliar, "Extended dynamical mean-field theory and GW method", *Phys. Rev. B* **66**, 085120 (2002), [arXiv:cond-mat/0205522](#) (*cit. on p. 44*).
- [403] S. Biermann, F. Aryasetiawan, and A. Georges, "First-Principles Approach to the Electronic Structure of Strongly Correlated Systems: Combining the GW Approximation and Dynamical Mean-Field Theory", *Phys. Rev. Lett.* **90**, 086402 (2003), [arXiv:cond-mat/0207419](#) (*cit. on p. 44*).
- [404] M. Kitatani, N. Tsuji, and H. Aoki, "FLEX+DMFT approach to the  $d$ -wave superconducting phase diagram of the two-dimensional Hubbard model", *Phys. Rev. B* **92**, 085104 (2015), [arXiv:1505.04865](#) (*cit. on p. 44*).
- [405] M. Kitatani, N. Tsuji, and H. Aoki, "Interplay of Pomeranchuk instability and superconductivity in the two-dimensional repulsive Hubbard model", *Phys. Rev. B* **95**, 075109 (2017), [arXiv:1609.05759](#) (*cit. on p. 44*).
- [406] N. Martin, C. Gauvin-Ndiaye, and A.-M. S. Tremblay, "Nonlocal corrections to dynamical mean-field theory from the two-particle self-consistent method", *Phys. Rev. B* **107**, 075158 (2023), [arXiv:2211.01919](#) (*cit. on pp. 44, 46*).
- [407] K. Zantout, S. Backes, A. Razpopov, D. Lessnich, and R. Valentí, "Improved effective vertices in the multiorbital two-particle self-consistent method from dynamical mean-field theory", *Phys. Rev. B* **107**, 235101 (2023), [arXiv:2211.01400](#) (*cit. on p. 44*).
- [408] O. Simard and P. Werner, "Dynamical mean field theory extension to the nonequilibrium two-particle self-consistent approach", *Phys. Rev. B* **107**, 245137 (2023), [arXiv:2302.14134](#) (*cit. on p. 44*).
- [409] C. Gauvin-Ndiaye, J. Leblanc, S. Marin, N. Martin, D. Lessnich, and A.-M. S. Tremblay, "Two-particle self-consistent approach for multiorbital models: Application to the Emery model", *Phys. Rev. B* **109**, 165111 (2024), [arXiv:2308.14091](#) (*cit. on pp. 44, 46*).
- [410] A. Bera, S. Bera, S. Kalimuddin, S. Gayen, M. Kundu, B. Das, and M. Mondal, "Review of recent progress on THz spectroscopy of quantum materials: superconductors, magnetic and topological materials", *Eur. Phys. J. Special Topics* **230**, 4113 (2021) (*cit. on pp. 45, 74*).
- [411] F. B. Kugler, S.-S. B. Lee, and J. von Delft, "Multipoint Correlation Functions: Spectral Representation and Numerical Evaluation", *Phys. Rev. X* **11**, 041006 (2021), [arXiv:2101.00707](#) (*cit. on p. 45*).

- [412] L. Boehnke, H. Hafermann, M. Ferrero, F. Lechermann, and O. Parcollet, “Orthogonal polynomial representation of imaginary-time Green’s functions”, *Phys. Rev. B* **84**, 075145 (2011), [arXiv:1104.3215](#) (*cit. on p. 45*).
- [413] X. Dong, D. Zgid, E. Gull, and H. U. R. Strand, “Legendre-spectral Dyson equation solver with super-exponential convergence”, *J. Chem. Phys.* **152**, 134107 (2020), [arXiv:2001.11603](#) (*cit. on p. 45*).
- [414] E. Gull, S. Iskakov, I. Krivenko, A. A. Rusakov, and D. Zgid, “Chebyshev polynomial representation of imaginary-time response functions”, *Phys. Rev. B* **98**, 075127 (2018), [arXiv:1805.03521](#) (*cit. on p. 45*).
- [415] W. Ku and A. G. Eguiluz, “Band-Gap Problem in Semiconductors Revisited: Effects of Core States and Many-Body Self-Consistency”, *Phys. Rev. Lett.* **89**, 126401 (2002), [arXiv:cond-mat/0203523](#) (*cit. on p. 45*).
- [416] A. A. Kananenka, J. J. Phillips, and D. Zgid, “Efficient Temperature-Dependent Green’s Functions Methods for Realistic Systems: Compact Grids for Orthogonal Polynomial Transforms”, *J. Chem. Theory Comput.* **12**, 564 (2016) (*cit. on p. 45*).
- [417] M. Kaltak and G. Kresse, “Minimax isometry method: A compressive sensing approach for Matsubara summation in many-body perturbation theory”, *Phys. Rev. B* **101**, 205145 (2020), [arXiv:1909.01740](#) (*cit. on p. 45*).
- [418] E. Moghadas, N. Dräger, A. Toschi, J. Zang, M. Medvidović, D. Kiese, A. J. Millis, A. M. Sengupta, S. Andergassen, and D. D. Sante, “Compressing the two-particle Green’s function using wavelets: Theory and application to the Hubbard atom”, *arXiv preprint* (2024), [arXiv:2407.02454](#) (*cit. on p. 45*).
- [419] E. Sheridan, C. Weber, E. Plekhanov, and C. Rhodes, “Continuous-time quantum Monte Carlo solver for dynamical mean field theory in the compact Legendre representation”, *Phys. Rev. B* **99**, 205156 (2019), [arXiv:1811.12869](#) (*cit. on p. 45*).
- [420] P. Werner, “Quantum Monte Carlo Impurity Solvers”, in *Dynamical Mean-Field Theory of Correlated Electrons*, Vol. 12, edited by E. Pavarini, E. Koch, A. Lichtenstein, and D. Vollhardt, Modeling and Simulation (Verlag des Forschungszentrum Jülich, 2022) Chap. 5 (*cit. on p. 45*).
- [421] N. Chikano, J. Otsuki, and H. Shinaoka, “Performance analysis of a physically constructed orthogonal representation of imaginary-time Green’s function”, *Phys. Rev. B* **98**, 035104 (2018), [arXiv:1803.07257](#) (*cit. on pp. 45, 46*).
- [422] J. Otsuki, M. Ohzeki, H. Shinaoka, and K. Yoshimi, “Sparse Modeling in Quantum Many-Body Problems”, *J. Phys. Soc. Jpn.* **89**, 012001 (2020), [arXiv:1911.04116](#) (*cit. on pp. 45, 46*).
- [423] J. Kaye, K. Chen, and O. Parcollet, “Discrete Lehmann representation of imaginary time Green’s functions”, *Phys. Rev. B* **105**, 235115 (2022), [arXiv:2107.13094](#) (*cit. on pp. 45, 47*).

- [424] J. Kaye, K. Chen, and H. U. Strand, “Libdlr: Efficient imaginary time calculations using the discrete lehmann representation”, *Comput. Phys. Commun.* **280**, 108458 (2022), [arXiv:2110.06765](#) (*cit. on pp. 45, 47*).
- [425] H. Shinaoka, M. Wallerberger, Y. Murakami, K. Nogaki, R. Sakurai, P. Werner, and A. Kauch, “Multiscale Space-Time Ansatz for Correlation Functions of Quantum Systems Based on Quantics Tensor Trains”, *Phys. Rev. X* **13**, 021015 (2023), [arXiv:2210.12984](#) (*cit. on p. 46*).
- [426] M. K. Ritter, Y. Núñez Fernández, M. Wallerberger, J. von Delft, H. Shinaoka, and X. Waintal, “Quantics Tensor Cross Interpolation for High-Resolution Parsimonious Representations of Multivariate Functions”, *Phys. Rev. Lett.* **132**, 056501 (2024), [arXiv:2303.11819](#) (*cit. on p. 46*).
- [427] Y. N. Fernández et al., “Learning tensor networks with tensor cross interpolation: new algorithms and libraries”, arXiv preprint (2024), [arXiv:2407.02454](#) (*cit. on p. 46*).
- [428] A. Eiguren and I. G. Gurtubay, “Helmholtz Fermi surface harmonics: an efficient approach for treating anisotropic problems involving Fermi surface integrals”, *New J. Phys.* **16**, 063014 (2014), [arXiv:1404.6906](#) (*cit. on p. 46*).
- [429] J. Lafuente-Bartolome, I. G. Gurtubay, and A. Eiguren, “Symmetric Helmholtz Fermi-surface harmonics for an optimal representation of anisotropic quantities on the Fermi surface: Application to the electron-phonon problem”, *Phys. Rev. B* **102**, 165113 (2020), [arXiv:2010.06899](#) (*cit. on p. 46*).
- [430] K. Zantout, S. Backes, and R. Valentí, “Effect of Nonlocal Correlations on the Electronic Structure of LiFeAs”, *Phys. Rev. Lett.* **123**, 256401 (2019), [arXiv:1906.11853](#) (*cit. on p. 46*).
- [431] J. Kaye, S. Beck, A. Barnett, L. Van Muñoz, and O. Parcollet, “Automatic, high-order, and adaptive algorithms for Brillouin zone integration”, *SciPost Phys.* **15**, 062 (2023), [arXiv:arXiv:2211.12959](#) (*cit. on p. 46*).
- [432] T. Wang, T. Nomoto, Y. Nomura, H. Shinaoka, J. Otsuki, T. Koretsune, and R. Arita, “Efficient ab initio Migdal-Eliashberg calculation considering the retardation effect in phonon-mediated superconductors”, *Phys. Rev. B* **102**, 134503 (2020), [arXiv:2004.08591](#) (*cit. on pp. 46, 105, 258*).
- [433] T. Wang, M. Hirayama, T. Nomoto, T. Koretsune, R. Arita, and J. A. Flores-Livas, “Absence of conventional room-temperature superconductivity at high pressure in carbon-doped H<sub>3</sub>S”, *Phys. Rev. B* **104**, 064510 (2021), [arXiv:2104.03710](#) (*cit. on pp. 46, 105, 190*).
- [434] T. Wang, T. Nomoto, T. Koretsune, and R. Arita, “Importance of self-consistency in first-principles Eliashberg calculation for superconducting transition temperature”, *J. Phys. Chem. Solids* **178**, 111348 (2023) (*cit. on p. 46*).
- [435] Y. Amiel et al., “Silvanite AuAgTe<sub>4</sub>: a rare case of gold superconducting material”, *J. Mater. Chem. C* **11**, 10016 (2023) (*cit. on pp. 46, 105*).

- [436] S. Poncé, E. Margine, C. Verdi, and F. Giustino, “EPW: Electron–phonon coupling, transport and superconducting properties using maximally localized Wannier functions”, *Comput. Phys. Commun.* **209**, 116 (2016), [arXiv:1604.03525](#) (*cit. on p. 46*).
- [437] H. Lee et al., “Electron–phonon physics from first principles using the EPW code”, *npj Comput. Mater.* **9**, 156 (2023), [arXiv:2302.08085](#) (*cit. on p. 46*).
- [438] H. Mori, T. Nomoto, R. Arita, and E. R. Margine, “Efficient anisotropic Migdal-Eliashberg calculations with an intermediate representation basis and Wannier interpolation”, *Phys. Rev. B* **110**, 064505 (2024), [arXiv:2404.11528](#) (*cit. on pp. 46, 103–105*).
- [439] S. Sumita, M. Naka, and H. Seo, “Fulde-Ferrell-Larkin-Ovchinnikov state induced by antiferromagnetic order in  $\kappa$ -type organic conductors”, *Phys. Rev. Research* **5**, 043171 (2023), [arXiv:2308.14227](#) (*cit. on p. 46*).
- [440] T. Nomoto, T. Koretsune, and R. Arita, “Local force method for the ab initio tight-binding model: Effect of spin-dependent hopping on exchange interactions”, *Phys. Rev. B* **102**, 014444 (2020), [arXiv:2003.11162](#) (*cit. on p. 46*).
- [441] T. Nomoto, T. Koretsune, and R. Arita, “Formation Mechanism of the Helical  $\mathbf{Q}$  Structure in Gd-Based Skyrmion Materials”, *Phys. Rev. Lett.* **125**, 117204 (2020), [arXiv:2003.13167](#) (*cit. on p. 46*).
- [442] Y. Nomura, T. Nomoto, M. Hirayama, and R. Arita, “Magnetic exchange coupling in cuprate-analog  $d^9$  nickelates”, *Phys. Rev. Research* **2**, 043144 (2020), [arXiv:2006.16943](#) (*cit. on p. 46*).
- [443] H. Shinaoka, J. Otsuki, K. Haule, M. Wallerberger, E. Gull, K. Yoshimi, and M. Ohzeki, “Overcomplete compact representation of two-particle Green’s functions”, *Phys. Rev. B* **97**, 205111 (2018), [arXiv:1803.01916](#) (*cit. on p. 46*).
- [444] H. Shinaoka, D. Geffroy, M. Wallerberger, J. Otsuki, K. Yoshimi, E. Gull, and J. Kuneš, “Sparse sampling and tensor network representation of two-particle Green’s functions”, *SciPost Phys.* **8**, 012 (2020), [arXiv:1909.07519](#) (*cit. on p. 46*).
- [445] M. Wallerberger, H. Shinaoka, and A. Kauch, “Solving the Bethe-Salpeter equation with exponential convergence”, *Phys. Rev. Research* **3**, 033168 (2021), [arXiv:2012.05557](#) (*cit. on p. 46*).
- [446] S. Dirnböck, S.-S. B. Lee, F. B. Kugler, S. Huber, J. von Delft, K. Held, and M. Wallerberger, “Overcomplete intermediate representation of two-particle Green’s functions and its relation to partial spectral functions”, *arXiv preprint* (2024), [arXiv:2404.05541](#) (*cit. on p. 46*).
- [447] N. Chikano, K. Yoshimi, J. Otsuki, and H. Shinaoka, “Irbasis: Open-source database and software for intermediate-representation basis functions of imaginary-time Green’s function”, *Comput. Phys. Commun.* **240**, 181 (2019), [arXiv:1807.05237](#) (*cit. on pp. 47, 48*).
- [448] N. Sheng, A. Hampel, S. Beck, O. Parcollet, N. Wentzell, J. Kaye, and K. Chen, “Low-rank Green’s function representations applied to dynamical mean-field theory”, *Phys. Rev. B* **107**, 245123 (2023), [arXiv:2301.07764](#) (*cit. on p. 48*).

- [449] D. J. Scalapino, S. R. White, and S. Zhang, “Insulator, metal, or superconductor: The criteria”, *Phys. Rev. B* **47**, 7995 (1993) (*cit. on pp. 57, 78*).
- [450] S. Peotta and P. Törmä, “Superfluidity in topologically nontrivial flat bands”, *Nat. Commun.* **6**, 8944 (2015), [arXiv:1506.02815](#) (*cit. on pp. 57, 77, 78, 103, 158, 214*).
- [451] L. Liang, T. I. Vanhala, S. Peotta, T. Siro, A. Harju, and P. Törmä, “Band geometry, berry curvature, and superfluid weight”, *Phys. Rev. B* **95**, 024515 (2017), [arXiv:1610.01803](#) (*cit. on pp. 57, 77–79, 103, 158, 214*).
- [452] S. Peotta, K.-E. Huhtinen, and P. Törmä, *Quantum geometry in superfluidity and superconductivity*, 2023, [arXiv:2308.08248](#) (*cit. on pp. 57, 77, 214*).
- [453] V. J. Emery and S. A. Kivelson, “Importance of phase fluctuations in superconductors with small superfluid density”, *Nature* **374**, 434 (1995) (*cit. on pp. 57, 207–209*).
- [454] S. A. Kivelson, “Making high  $T_c$  higher: a theoretical proposal”, *Phys. B: Condens. Matter* **318**, 61 (2002), [arXiv:cond-mat/0109151](#) (*cit. on pp. 57, 207, 209, 214, 257*).
- [455] A. Toschi, M. Capone, and C. Castellani, “Energetic balance of the superconducting transition across the BCS—Bose Einstein crossover in the attractive Hubbard model”, *Phys. Rev. B* **72**, 235118 (2005) (*cit. on pp. 57, 78, 79, 207, 213, 214*).
- [456] G. Singh et al., “Competition between electron pairing and phase coherence in superconducting interfaces”, *Nat. Commun.* **9**, 407 (2018), [arXiv:1704.03365](#) (*cit. on p. 57*).
- [457] J. R. Schrieffer, *Theory of superconductivity*, revised printing, Advanced book program (CRC Press, Boca Raton, 2018) (*cit. on pp. 57, 78, 89, 91, 96*).
- [458] M. Tinkham, *Introduction to superconductivity*, 2nd ed., Dover books on physics (Dover Publications, Mineola, NY, 2004) (*cit. on pp. 57, 64, 65, 67, 69–71, 73, 89, 96*).
- [459] J. F. Annett, *Superconductivity, superfluids, and condensates*, Repr., Oxford master series in physics 5 (Oxford Univ. Press, Oxford [u.a.], 2004), 186 pp. (*cit. on pp. 57, 60–62, 65*).
- [460] A. J. Leggett, *Quantum Liquids: Bose condensation and Cooper pairing in condensed-matter systems* (Oxford University Press Oxford, 2006) (*cit. on pp. 57, 60–62, 65*).
- [461] R. Combescot, *Superconductivity: An Introduction* (Cambridge University Press, 2022) (*cit. on pp. 57, 68, 69, 73*).
- [462] A. Larkin, *Theory of fluctuations in superconductors*, edited by A. A. Varlamov and A. Varlamov, 1. publ. in paperback, International series of monographs on physics 127 (Univ. Press, Oxford, 2009) (*cit. on pp. 57, 62, 64, 79, 80*).

- [463] A. Beekman, L. Rademaker, and J. van Wezel, “An introduction to spontaneous symmetry breaking”, *SciPost Physics Lecture Notes*, **11**, 11 (2019), [arXiv:1909.01820](#) (*cit. on pp. 59, 60, 62, 68, 74, 79–81*).
- [464] L. D. Landau, “On the theory of phase transitions”, *Phys. Z. Sowjet.* **11**, [*Zh. Eksp. Teor. Fiz.* **7**, 19], 26 (1937) (*cit. on pp. 59, 62*).
- [465] S. Elitzur, “Impossibility of spontaneously breaking local symmetries”, *Phys. Rev. D* **12**, 3978 (1975) (*cit. on p. 60*).
- [466] A. J. Leggett and F. Sols, “On the concept of spontaneously broken gauge symmetry in condensed matter physics”, *Found. Phys.* **21**, 353 (1991) (*cit. on p. 61*).
- [467] C. N. Yang, “Concept of Off-Diagonal Long-Range Order and the Quantum Phases of Liquid He and of Superconductors”, *Rev. Mod. Phys.* **34**, 694 (1962) (*cit. on p. 61*).
- [468] O. Penrose, “CXXXVI. On the quantum mechanics of helium II”, *The London, Edinburgh, and Dublin Philosophical Magazine and Journal of Science* **42**, 1373 (1951) (*cit. on p. 61*).
- [469] O. Penrose and L. Onsager, “Bose-Einstein Condensation and Liquid Helium”, *Phys. Rev.* **104**, 576 (1956) (*cit. on p. 61*).
- [470] L. P. Gor’kov, “Microscopic Derivation of the Ginzburg-Landau Equations in the Theory of Superconductivity”, *Sov. Phys. JETP* **9**, [*Zh. Eksp. Teor. Fiz.* **36**, 1918 (1959)], 1364 (1959) (*cit. on p. 62*).
- [471] K. V. Grigorishin, “BCS theory with the external pair potential”, *Phys. Lett. A* **381**, 3089 (2017), [arXiv:1605.07080](#) (*cit. on p. 63*).
- [472] D. J. Thouless, “Perturbation theory in statistical mechanics and the theory of superconductivity”, *Ann. Phys.* **10**, 553 (1960) (*cit. on p. 64*).
- [473] V. L. Ginzburg and L. D. Landau, “On the theory of superconductivity”, *Zh. Eksp. Teor. Fiz.* **20**, 1064 (1950) (*cit. on pp. 64, 67*).
- [474] L. Benfatto, A. Toschi, S. Caprara, and C. Castellani, “Coherence length in superconductors from weak to strong coupling”, *Phys. Rev. B* **66**, 054515 (2002), [arXiv:cond-mat/0109486](#) (*cit. on p. 66*).
- [475] V. L. Ginzburg, “On the Macroscopic Theory of Superconductivity”, *Sov. Phys. JETP* **2**, [*Zh. Eksp. Teor. Fiz.* **29**, 748 (1955)], 589 (1956) (*cit. on p. 67*).
- [476] F. London and H. London, “The electromagnetic equations of the superconductor”, *Proc. R. Soc. London A - Math Phys. Sci.* **149**, 71 (1935) (*cit. on p. 68*).
- [477] A. B. Pippard, “An experimental and theoretical study of the relation between magnetic field and current in a superconductor”, *Proc. R. Soc. London A - Math Phys. Sci.* **216**, 547 (1953) (*cit. on p. 68*).
- [478] C. C. Tsuei and J. R. Kirtley, “Pairing symmetry in cuprate superconductors”, *Rev. Mod. Phys.* **72**, 969 (2000), [arXiv:cond-mat/0004185](#) (*cit. on pp. 71, 84, 88*).



- [479] K. Xu, P. Cao, and J. R. Heath, "Achieving the Theoretical Depairing Current Limit in Superconducting Nanomesh Films", *Nano Lett.* **10**, 4206 (2010) (*cit. on p. 71*).
- [480] A. M. Clogston, "Upper Limit for the Critical Field in Hard Superconductors", *Phys. Rev. Lett.* **9**, 266 (1962) (*cit. on pp. 71, 72*).
- [481] B. S. Chandrasekhar, "A note on the maximum critical field of high-field superconductors", *Appl. Phys. Lett.* **1**, 7 (1962) (*cit. on p. 71*).
- [482] J. M. Lu, O. Zheliuk, I. Leermakers, N. F. Q. Yuan, U. Zeitler, K. T. Law, and J. T. Ye, "Evidence for two-dimensional Ising superconductivity in gated MoS<sub>2</sub>", *Science* **350**, 1353 (2015), [arXiv:1506.07620](#) (*cit. on p. 72*).
- [483] Y. Saito et al., "Superconductivity protected by spin–valley locking in ion-gated MoS<sub>2</sub>", *Nat. Phys.* **12**, 144 (2016), [arXiv:1506.04146](#) (*cit. on p. 72*).
- [484] X. Xi, Z. Wang, W. Zhao, J.-H. Park, K. T. Law, H. Berger, L. Forró, J. Shan, and K. F. Mak, "Ising pairing in superconducting NbSe<sub>2</sub> atomic layers", *Nat. Phys.* **12**, 139 (2016), [arXiv:1507.08731](#) (*cit. on p. 72*).
- [485] J. Lu, O. Zheliuk, Q. Chen, I. Leermakers, N. E. Hussey, U. Zeitler, and J. Ye, "Full superconducting dome of strong Ising protection in gated monolayer WS<sub>2</sub>", *PNAS* **115**, 3551 (2018), [arXiv:1703.06369](#) (*cit. on p. 72*).
- [486] Y. Cao, J. M. Park, K. Watanabe, T. Taniguchi, and P. Jarillo-Herrero, "Pauli-limit violation and re-entrant superconductivity in moiré graphene", *Nature* **595**, 526 (2021), [arXiv:2103.12083](#) (*cit. on p. 72*).
- [487] P. Fulde and R. A. Ferrell, "Superconductivity in a Strong Spin-Exchange Field", *Phys. Rev.* **135**, A550 (1964) (*cit. on p. 72*).
- [488] A. I. Larkin and Y. N. Ovchinnikov, "Nonuniform state of superconductors", *Zh. Eksp. Teor. Fiz.* **47**, 1136 (1964) (*cit. on p. 72*).
- [489] R. Casalbuoni and G. Nardulli, "Inhomogeneous superconductivity in condensed matter and QCD", *Rev. Mod. Phys.* **76**, 263 (2004), [arXiv:hep-ph/0305069](#) (*cit. on pp. 72, 73*).
- [490] J. J. Kinnunen, J. E. Baarsma, J.-P. Martikainen, and P. Törmä, "The Fulde-Ferrell–Larkin–Ovchinnikov state for ultracold fermions in lattice and harmonic potentials: a review", *Rep. Prog. Phys.* **81**, 046401 (2018) (*cit. on pp. 72, 73*).
- [491] D. F. Agterberg, J. S. Davis, S. D. Edkins, E. Fradkin, D. J. V. Harlingen, S. A. Kivelson, P. A. Lee, L. Radzihovsky, J. M. Tranquada, and Y. Wang, "The Physics of Pair-Density Waves: Cuprate Superconductors and Beyond", *Annu. Rev. Condens. Matter Phys.* **11**, 231 (2020) (*cit. on p. 73*).
- [492] A. Himeda, T. Kato, and M. Ogata, "Stripe States with Spatially Oscillating *d*-Wave Superconductivity in the Two-Dimensional  $t - t' - J$ ", *Phys. Rev. Lett.* **88**, 117001 (2002) (*cit. on p. 73*).
- [493] P. A. Lee, "Amperean Pairing and the Pseudogap Phase of Cuprate Superconductors", *Phys. Rev. X* **4**, 031017 (2014), [arXiv:1401.0519](#) (*cit. on p. 73*).

- [494] R. P. Kaur, D. F. Agterberg, and M. Sgrist, “Helical Vortex Phase in the Noncentrosymmetric CePt<sub>3</sub>Si”, *Phys. Rev. Lett.* **94**, 137002 (2005), [arXiv:cond-mat/0408149](#) (*cit. on p. 73*).
- [495] M. D. Croitoru, M. Houzet, and A. I. Buzdin, “In-Plane Magnetic Field Anisotropy of the Fulde-Ferrell-Larkin-Ovchinnikov State in Layered Superconductors”, *Phys. Rev. Lett.* **108**, 207005 (2012), [arXiv:1204.2287](#) (*cit. on p. 73*).
- [496] M. Sgrist, D. F. Agterberg, M. H. Fischer, J. Goryo, F. Loder, S.-H. Rhim, D. Maruyama, Y. Yanase, T. Yoshida, and S. J. Youn, “Superconductors with Staggered Non-centrosymmetry”, *J. Phys. Soc. Jpn.* **83**, 061014 (2014) (*cit. on p. 73*).
- [497] Z. Zheng, M. Gong, Y. Zhang, X. Zou, C. Zhang, and G. Guo, “FFLO Superfluids in 2D Spin-Orbit Coupled Fermi Gases”, *Sci. Rep.* **4**, 6535 (2014) (*cit. on p. 73*).
- [498] S. Mironov and A. Buzdin, “Spontaneous Currents in Superconducting Systems with Strong Spin-Orbit Coupling”, *Phys. Rev. Lett.* **118**, 077001 (2017), [arXiv:1704.04123](#) (*cit. on p. 73*).
- [499] C.-X. Liu, “Unconventional Superconductivity in Bilayer Transition Metal Dichalcogenides”, *Phys. Rev. Lett.* **118**, 087001 (2017), [arXiv:1608.04139](#) (*cit. on p. 73*).
- [500] D. Chakraborty and A. M. Black-Schaffer, “Interplay of finite-energy and finite-momentum superconducting pairing”, *Phys. Rev. B* **106**, 024511 (2022), [arXiv:2205.06276](#) (*cit. on p. 73*).
- [501] S.-B. Zhang, L.-H. Hu, and T. Neupert, “Finite-momentum Cooper pairing in proximitized altermagnets”, *Nat. Commun.* **15**, 1801 (2024), [arXiv:2302.13185](#) (*cit. on p. 73*).
- [502] J. Wosnitza, “FFLO States in Layered Organic Superconductors”, *Ann. Phys.* **530**, 1700282 (2017) (*cit. on p. 73*).
- [503] C. Agosta, “Inhomogeneous Superconductivity in Organic and Related Superconductors”, *Crystals* **8**, 285 (2018) (*cit. on p. 73*).
- [504] R. Lortz, Y. Wang, A. Demuer, P. H. M. Böttger, B. Bergk, G. Zwicknagl, Y. Nakazawa, and J. Wosnitza, “Calorimetric Evidence for a Fulde-Ferrell-Larkin-Ovchinnikov Superconducting State in the Layered Organic Superconductor  $\kappa$ -(BEDT-TTF)<sub>2</sub>Cu(NCS)<sub>2</sub>”, *Phys. Rev. Lett.* **99**, 187002 (2007), [arXiv:0706.3584](#) (*cit. on p. 73*).
- [505] S. Imajo, T. Nomura, Y. Kohama, and K. Kindo, “Emergent anisotropy in the Fulde-Ferrell-Larkin-Ovchinnikov state”, *Nat. Commun.* **13**, 5590 (2022), [arXiv:2110.12774](#) (*cit. on p. 73*).
- [506] H. A. Radovan, N. A. Fortune, T. P. Murphy, S. T. Hannahs, E. C. Palm, S. W. Tozer, and D. Hall, “Magnetic enhancement of superconductivity from electron spin domains”, *Nature* **425**, 51 (2003) (*cit. on p. 73*).

- [507] A. Bianchi, R. Movshovich, C. Capan, P. G. Pagliuso, and J. L. Sarrao, "Possible Fulde-Ferrell-Larkin-Ovchinnikov Superconducting State in CeCoIn<sub>5</sub>", *Phys. Rev. Lett.* **91**, 187004 (2003), [arXiv:cond-mat/0304420](#) (*cit. on p. 73*).
- [508] Y. Matsuda and H. Shimahara, "Fulde-Ferrell-Larkin-Ovchinnikov State in Heavy Fermion Superconductors", *J. Phys. Soc. Jpn.* **76**, 051005 (2007), [arXiv:cond-mat/0702481](#) (*cit. on p. 73*).
- [509] M. Kenzelmann et al., "Evidence for a Magnetically Driven Superconducting Q Phase of CeCoIn<sub>5</sub>", *Phys. Rev. Lett.* **104**, 127001 (2010) (*cit. on p. 73*).
- [510] S. Kitagawa, G. Nakamine, K. Ishida, H. S. Jeevan, C. Geibel, and F. Steglich, "Evidence for the Presence of the Fulde-Ferrell-Larkin-Ovchinnikov State in CeCu<sub>2</sub>Si<sub>2</sub> Revealed Using <sup>63</sup>Cu NMR", *Phys. Rev. Lett.* **121**, 157004 (2018), [arXiv:1810.06135](#) (*cit. on p. 73*).
- [511] C.-w. Cho, J. H. Yang, N. F. Q. Yuan, J. Shen, T. Wolf, and R. Lortz, "Thermodynamic Evidence for the Fulde-Ferrell-Larkin-Ovchinnikov State in the KFe<sub>2</sub>As<sub>2</sub> Superconductor", *Phys. Rev. Lett.* **119**, 217002 (2017), [arXiv:1708.05526](#) (*cit. on p. 73*).
- [512] S. Kasahara et al., "Evidence for an Fulde-Ferrell-Larkin-Ovchinnikov State with Segmented Vortices in the BCS-BEC-Crossover Superconductor FeSe", *Phys. Rev. Lett.* **124**, 107001 (2020), [arXiv:1911.08237](#) (*cit. on p. 73*).
- [513] A. Q. Chen, M. J. Park, S. T. Gill, Y. Xiao, D. Reig-i-Plessis, G. J. MacDougall, M. J. Gilbert, and N. Mason, "Finite momentum Cooper pairing in three-dimensional topological insulator Josephson junctions", *Nat. Commun.* **9**, 3478 (2018), [arXiv:1801.08504](#) (*cit. on p. 73*).
- [514] Z. Zhu et al., "Discovery of segmented Fermi surface induced by Cooper pair momentum", *Science* **374**, 1381 (2021), [arXiv:2010.02216](#) (*cit. on p. 73*).
- [515] X. Liu, Y. X. Chong, R. Sharma, and J. C. S. Davis, "Discovery of a Cooper-pair density wave state in a transition-metal dichalcogenide", *Science* **372**, 1447 (2021), [arXiv:2007.15228](#) (*cit. on p. 73*).
- [516] C.-w. Cho, J. Lyu, C. Y. Ng, J. J. He, K. T. Lo, D. Chareev, T. A. Abdel-Baset, M. Abdel-Hafiez, and R. Lortz, "Evidence for the Fulde-Ferrell-Larkin-Ovchinnikov state in bulk NbS<sub>2</sub>", *Nat. Commun.* **12**, 3676 (2021) (*cit. on p. 73*).
- [517] P. Wan et al., "Orbital Fulde-Ferrell-Larkin-Ovchinnikov state in an Ising superconductor", *Nature* **619**, 46 (2023), [arXiv:2211.07745](#) (*cit. on p. 73*).
- [518] D. Zhao, L. Debbeler, M. Kühne, S. Fecher, N. Gross, and J. Smet, "Evidence of finite-momentum pairing in a centrosymmetric bilayer", *Nat. Phys.* **19**, 1599 (2023) (*cit. on p. 73*).
- [519] S. D. Edkins et al., "Magnetic field-induced pair density wave state in the cuprate vortex halo", *Science* **364**, 976 (2019), [arXiv:1802.04673](#) (*cit. on p. 73*).
- [520] F. Ando, Y. Miyasaka, T. Li, J. Ishizuka, T. Arakawa, Y. Shiota, T. Moriyama, Y. Yanase, and T. Ono, "Observation of superconducting diode effect", *Nature* **584**, 373 (2020) (*cit. on p. 73*).

- [521] M. Nadeem, M. S. Fuhrer, and X. Wang, “The superconducting diode effect”, *Nat. Rev. Phys.* **5**, 558 (2023), [arXiv:2301.13564](#) (*cit. on p. 73*).
- [522] N. F. Q. Yuan and L. Fu, “Supercurrent diode effect and finite-momentum superconductors”, *PNAS* **119**, e2119548119 (2022), [arXiv:2106.01909](#) (*cit. on p. 73*).
- [523] M. E. Fisher, M. N. Barber, and D. Jasnow, “Helicity Modulus, Superfluidity, and Scaling in Isotropic Systems”, *Phys. Rev. A* **8**, 1111 (1973) (*cit. on pp. 73, 78, 79*).
- [524] D. Pekker and C. M. Varma, “Amplitude/Higgs Modes in Condensed Matter Physics”, *Annu. Rev. Condens. Matter Phys.* **6**, 269 (2015), [arXiv:1406.2968](#) (*cit. on p. 74*).
- [525] R. Shimano and N. Tsuji, “Higgs Mode in Superconductors”, *Annu. Rev. Condens. Matter Phys.* **11**, 103 (2020), [arXiv:1906.09401](#) (*cit. on pp. 74, 75*).
- [526] P. W. Higgs, “Broken Symmetries and the Masses of Gauge Bosons”, *Phys. Rev. Lett.* **13**, 508 (1964) (*cit. on pp. 74, 75*).
- [527] P. W. Anderson, “Plasmons, Gauge Invariance, and Mass”, *Phys. Rev.* **130**, 439 (1963) (*cit. on pp. 74–76*).
- [528] R. Matsunaga, Y. I. Hamada, K. Makise, Y. Uzawa, H. Terai, Z. Wang, and R. Shimano, “Higgs Amplitude Mode in the BCS Superconductors  $\text{Nb}_{1-x}\text{Ti}_x\text{N}$  Induced by Terahertz Pulse Excitation”, *Phys. Rev. Lett.* **111**, 057002 (2013), [arXiv:1305.0381](#) (*cit. on p. 74*).
- [529] R. Matsunaga, N. Tsuji, H. Fujita, A. Sugioka, K. Makise, Y. Uzawa, H. Terai, Z. Wang, H. Aoki, and R. Shimano, “Light-induced collective pseudospin precession resonating with Higgs mode in a superconductor”, *Science* **345**, 1145 (2014) (*cit. on p. 74*).
- [530] A. Behrle, T. Harrison, J. Kombe, K. Gao, M. Link, J.-S. Bernier, C. Kollath, and M. Köhl, “Higgs mode in a strongly interacting fermionic superfluid”, *Nat. Phys.* **14**, 781 (2018), [arXiv:1912.01867](#) (*cit. on p. 74*).
- [531] H. Chu et al., “Phase-resolved Higgs response in superconducting cuprates”, *Nat. Commun.* **11**, 1793 (2020), [arXiv:1901.06675](#) (*cit. on p. 74*).
- [532] L. Schwarz et al., “Classification and characterization of nonequilibrium Higgs modes in unconventional superconductors”, *Nat. Commun.* **11**, 287 (2020), [arXiv:1712.0798](#) (*cit. on p. 74*).
- [533] J. Goldstone, “Field theories with «Superconductor » solutions”, *Il Nuovo Cimento* **19**, 154 (1961) (*cit. on p. 74*).
- [534] H. Watanabe, “Counting Rules of Nambu–Goldstone Modes”, *Annu. Rev. Condens. Matter Phys.* **11**, 169 (2020), [arXiv:1904.00569](#) (*cit. on p. 74*).
- [535] C. Timm, *Theory of Superconductivity*, Lecture Notes at TU Dresden, 2023 (*cit. on p. 75*).

- [536] P. Törmä, S. Peotta, and B. A. Bernevig, “Superconductivity, superfluidity and quantum geometry in twisted multilayer systems”, *Nat. Rev. Phys.* **4**, 528 (2022) (*cit. on pp. 77, 103, 158, 210, 214*).
- [537] P. Raychaudhuri and S. Dutta, “Phase fluctuations in conventional superconductors”, *J. Phys. Condens. Matter* **34**, 083001 (2021) (*cit. on pp. 77, 81*).
- [538] D. J. Scalapino, S. R. White, and S. C. Zhang, “Superfluid density and the Drude weight of the Hubbard model”, *Phys. Rev. Lett.* **68**, 2830 (1992) (*cit. on p. 78*).
- [539] P. J. H. Denteneer, G. An, and J. M. J. van Leeuwen, “Helicity modulus in the two-dimensional Hubbard model”, *Phys. Rev. B* **47**, 6256 (1993) (*cit. on p. 78*).
- [540] E. Taylor, A. Griffin, N. Fukushima, and Y. Ohashi, “Pairing fluctuations and the superfluid density through the BCS-BEC crossover”, *Phys. Rev. A* **74**, 063626 (2006), [arXiv:cond-mat/0609187](https://arxiv.org/abs/cond-mat/0609187) (*cit. on pp. 78, 79*).
- [541] E. Gull and A. J. Millis, “Superconducting and pseudogap effects on the interplane conductivity and Raman scattering cross section in the two-dimensional Hubbard model”, *Phys. Rev. B* **88**, 075127 (2013), [arXiv:1304.6406](https://arxiv.org/abs/1304.6406) (*cit. on p. 78*).
- [542] P. T. Reko P. S. Penttilä Kukka-Emilia Huhtinen, “Flat-band ratio and quantum metric in the superconductivity of modified Lieb lattices”, arXiv preprint (2024), [arXiv:2404.12993](https://arxiv.org/abs/2404.12993) (*cit. on pp. 78, 79*).
- [543] X. Hu, T. Hyart, D. I. Pikulin, and E. Rossi, “Geometric and Conventional Contribution to the Superfluid Weight in Twisted Bilayer Graphene”, *Phys. Rev. Lett.* **123**, 237002 (2019), [arXiv:1906.07152](https://arxiv.org/abs/1906.07152) (*cit. on pp. 78, 103, 158, 210, 214*).
- [544] F. Xie, Z. Song, B. Lian, and B. A. Bernevig, “Topology-Bounded Superfluid Weight in Twisted Bilayer Graphene”, *Phys. Rev. Lett.* **124**, 167002 (2020), eprint: [1906.02213](https://arxiv.org/abs/1906.02213) (*cit. on pp. 78, 103, 158, 210, 214*).
- [545] C. Yue, S. Hoshino, A. Koga, and P. Werner, “Unconventional pairing from local orbital fluctuations in strongly correlated  $A_3C_{60}$ ”, *Phys. Rev. B* **104**, 075107 (2021), [arXiv:2103.08925](https://arxiv.org/abs/2103.08925) (*cit. on p. 79*).
- [546] A. P. Levanyuk, “Contribution to the Theory of Light Scattering near the Second-Order Phase-Transition Points”, *Sov. Phys. JETP* **9**, [*Zh. Eksp. Teor. Fiz.* **36**, 810 (1959)], 571 (1959) (*cit. on p. 79*).
- [547] V. L. Levanyuk, “Some Remarks on Phase Transitions of the Second Kind and the Microscopic theory of Ferroelectric Materials”, *Sov. Phys. Solid State* **2**, [*Fiz. Tverd. Tela (Leningrad)* **2**, 2031, 1960], 1824 (1961) (*cit. on p. 79*).
- [548] P. C. Hohenberg, “Existence of Long-Range Order in One and Two Dimensions”, *Phys. Rev.* **158**, 383 (1967) (*cit. on p. 80*).
- [549] G. Palle and D. K. Sunko, “Physical limitations of the Hohenberg-Mermin-Wagner theorem”, *J. Phys. A: Math. Theor.* **54**, 315001 (2021), [arXiv:2107.09714](https://arxiv.org/abs/2107.09714) (*cit. on p. 80*).

- [550] V. L. Berezinskii, “Destruction of Long-range Order in One-dimensional and Two-dimensional Systems having a Continuous Symmetry Group II. Quantum Systems”, *Sov. Phys. JETP* **34**, [*Zh. Eksp. Teor. Fiz.* **61**, 1144 (1972)], 610 (1972) (*cit. on p. 81*).
- [551] J. M. Kosterlitz and D. J. Thouless, “Long range order and metastability in two dimensional solids and superfluids. (Application of dislocation theory)”, *J. Phys. C: Solid State Phys.* **5**, 1124 (1972) (*cit. on p. 81*).
- [552] J. M. Kosterlitz and D. J. Thouless, “Ordering, metastability and phase transitions in two-dimensional systems”, *J. Phys. C: Solid State Phys.* **6**, 1181 (1973) (*cit. on pp. 81, 83*).
- [553] J. M. Kosterlitz, “Kosterlitz–Thouless physics: a review of key issues”, *Rep. Prog. Phys.* **79**, 026001 (2016) (*cit. on pp. 81–83*).
- [554] J. M. Kosterlitz, “The critical properties of the two-dimensional xy model”, *J. Phys. C: Solid State Phys.* **7**, 1046 (1974) (*cit. on p. 83*).
- [555] D. R. Nelson and J. M. Kosterlitz, “Universal Jump in the Superfluid Density of Two-Dimensional Superfluids”, *Phys. Rev. Lett.* **39**, 1201 (1977) (*cit. on p. 83*).
- [556] S. Graser, T. A. Maier, P. J. Hirschfeld, and D. J. Scalapino, “Near-degeneracy of several pairing channels in multiorbital models for the Fe pnictides”, *New J. Phys.* **11**, 025016 (2009), [arXiv:0812.0343](https://arxiv.org/abs/0812.0343) (*cit. on p. 84*).
- [557] H. Ikeda, M.-T. Suzuki, and R. Arita, “Emergent Loop-Nodal  $s_{\pm}$ -Wave Superconductivity in  $\text{CeCu}_2\text{Si}_2$ : Similarities to the Iron-Based Superconductors”, *Phys. Rev. Lett.* **114**, 147003 (2015) (*cit. on p. 84*).
- [558] J. P. L. Faye, P. Sahebsara, and D. Sénéchal, “Chiral triplet superconductivity on the graphene lattice”, *Phys. Rev. B* **92**, 085121 (2015), [arXiv:1505.07890](https://arxiv.org/abs/1505.07890) (*cit. on p. 84*).
- [559] T. Nomoto, K. Hattori, and H. Ikeda, “Classification of “multipole” superconductivity in multiorbital systems and its implications”, *Phys. Rev. B* **94**, 174513 (2016), [arXiv:1607.02716](https://arxiv.org/abs/1607.02716) (*cit. on p. 84*).
- [560] V. L. Berezinskii, “New model of the anisotropic phase of superfluid  $\text{He}^3$ ”, *JETP Lett.* **20**, [*Pis’ma Zh. Eksp. Teor. Fiz.* **20**, 628–631], 287 (1974) (*cit. on pp. 84–86*).
- [561] A. J. Leggett, “A theoretical description of the new phases of liquid  $^3\text{He}$ ”, *Rev. Mod. Phys.* **47**, 331 (1975) (*cit. on pp. 84, 106*).
- [562] J. F. Annett, “Symmetry of the order parameter for high-temperature superconductivity”, *Adv. Phys.* **39**, 83 (1990) (*cit. on pp. 84, 87*).
- [563] C. Platt, “A Common Thread in Unconventional Superconductivity: The Functional Renormalization Group in Multi-Band Systems”, Phd thesis (Julius-Maximilians-Universität Würzburg, 2012) (*cit. on p. 84*).
- [564] J. Linder and A. V. Balatsky, “Odd-frequency superconductivity”, *Rev. Mod. Phys.* **91**, 045005 (2019), [arXiv:1709.03986](https://arxiv.org/abs/1709.03986) (*cit. on pp. 84–86*).

- [565] D. Sénéchal, "Group-Theoretical Classification of Superconducting States", in *Topology, Entanglement, and Strong Correlations*, Vol. 10, edited by E. Pavarini and E. Koch, Modeling and Simulation (Verlag des Forschungszentrum Jülich, 2020) Chap. 13 (cit. on pp. 84, 86).
- [566] A. M. Black-Schaffer and A. V. Balatsky, "Odd-frequency superconducting pairing in multiband superconductors", *Phys. Rev. B* **88**, 104514 (2013), [arXiv:1305.4593](#) (cit. on pp. 85, 86).
- [567] R. M. Geilhufe and A. V. Balatsky, "Symmetry analysis of odd- and even-frequency superconducting gap symmetries for time-reversal symmetric interactions", *Phys. Rev. B* **97**, 024507 (2018) (cit. on pp. 85, 86).
- [568] T. Inui, Y. Tanabe, and Y. Onodera, *Group Theory and Its Applications in Physics* (Springer Berlin Heidelberg, 1990) (cit. on p. 86).
- [569] M. S. Dresselhaus, G. Dresselhaus, and A. Jorio, *Group Theory*, SpringerLink (Springer Berlin Heidelberg, Berlin, Heidelberg, 2008) (cit. on p. 86).
- [570] L. N. Cooper, "Bound Electron Pairs in a Degenerate Fermi Gas", *Phys. Rev.* **104**, 1189 (1956), [arXiv:1709.07650](#) (cit. on p. 90).
- [571] P. Phillips, *Advanced Solid State Physics* (Cambridge University Press, 2012) (cit. on pp. 91, 92).
- [572] I. G. Kaplan, O. Navarro, and J. A. Sánchez, "Exact commutation relations for the Cooper pair operators and the problem of two interacting Cooper's pairs", *Phys. C: Supercond.* **419**, 13 (2005) (cit. on p. 92).
- [573] M. R. Schafroth, S. T. Butler, and J. M. Blatt, "Quasichemical equilibrium approach to superconductivity", *Helv. Phys. Acta* **30**, 93 (1957) (cit. on p. 92).
- [574] A. J. Leggett, "Diatomic molecules and cooper pairs", in *Modern trends in the theory of condensed matter*, Vol. 115, edited by J. A. P. Andrzej Pękalski, Lecture Notes in Physics (1980), pp. 13–27 (cit. on pp. 93, 213).
- [575] P. Nozières and S. Schmitt-Rink, "Bose condensation in an attractive fermion gas: From weak to strong coupling superconductivity", *J. Low Temp. Phys.* **59**, 195 (1985) (cit. on pp. 93, 208, 213).
- [576] P. W. Anderson, "Random-Phase Approximation in the Theory of Superconductivity", *Phys. Rev.* **112**, 1900 (1958) (cit. on p. 94).
- [577] Y. Nambu, "Quasi-Particles and Gauge Invariance in the Theory of Superconductivity", *Phys. Rev.* **117**, 648 (1960) (cit. on p. 94).
- [578] R. D. Mattuck and B. Johansson, "Quantum field theory of phase transitions in Fermi systems", *Adv. Phys.* **17**, 509 (1968) (cit. on pp. 97, 98).
- [579] E. Gull and A. J. Millis, "Pairing glue in the two-dimensional Hubbard model", *Phys. Rev. B* **90**, 041110 (2014), [arXiv:1407.0704](#) (cit. on p. 99).
- [580] D. Poilblanc and D. J. Scalapino, "Calculation of  $\Delta(k, \omega)$  for a two-dimensional  $t - J$  cluster", *Phys. Rev. B* **66**, 052513 (2002), [arXiv:cond-mat/0202180](#) (cit. on p. 99).

- [581] Umamarino, “Eliashberg theory”, in *Emergent Phenomena in Correlated Matter*, Vol. 3, edited by E. Pavarini, E. Koch, and U. Schollwöck, Modeling and Simulation (Verlag des Forschungszentrum Jülich, 2013) Chap. 13 (*cit. on pp. 99, 103, 104*).
- [582] H. Tian et al., “Evidence for Dirac flat band superconductivity enabled by quantum geometry”, *Nature* **614**, 440 (2023) (*cit. on pp. 103, 158*).
- [583] A. B. Migdal, “Interaction between electrons and lattice vibrations in a normal metal”, *Sov. Phys. JETP* **7**, [*Zh. Eksp. Teor. Fiz.* **34**, 1438 (1958)], 996 (1958) (*cit. on p. 104*).
- [584] G. M. Eliashberg, “Interactions between Electrons and Lattice Vibrations in a Superconductor”, *Sov. Phys. JETP* **11**, [*Zh. Eksp. Teor. Fiz.* **38**, 966 (1960)], 696 (1960) (*cit. on p. 104*).
- [585] Y. in’t Veld, M. I. Katsnelson, A. J. Millis, and M. Rösner, “Screening induced crossover between phonon- and plasmon-mediated pairing in layered superconductors”, *2D Mater.* **10**, 045031 (2023), [arXiv:2303.06220](https://arxiv.org/abs/2303.06220) (*cit. on p. 104*).
- [586] P. Morel and P. W. Anderson, “Calculation of the Superconducting State Parameters with Retarded Electron-Phonon Interaction”, *Phys. Rev.* **125**, 1263 (1962) (*cit. on p. 105*).
- [587] M. Simonato, M. I. Katsnelson, and M. Rösner, “Revised Tolmachev-Morel-Anderson pseudopotential for layered conventional superconductors with nonlocal Coulomb interaction”, *Phys. Rev. B* **108**, 064513 (2023) (*cit. on p. 105*).
- [588] W. L. McMillan, “Transition Temperature of Strong-Coupled Superconductors”, *Phys. Rev.* **167**, 331 (1968) (*cit. on pp. 105, 209*).
- [589] P. B. Allen and R. C. Dynes, “Transition temperature of strong-coupled superconductors reanalyzed”, *Phys. Rev. B* **12**, 905 (1975) (*cit. on p. 105*).
- [590] N. F. Berk and J. R. Schrieffer, “Effect of Ferromagnetic Spin Correlations on Superconductivity”, *Phys. Rev. Lett.* **17**, 433 (1966), [arXiv:cond-mat/9812171](https://arxiv.org/abs/cond-mat/9812171) (*cit. on p. 106*).
- [591] B. Raveau, “Strongly correlated electron systems: From chemistry to physics”, *Comptes Rendus. Chimie* **14**, 856 (2011) (*cit. on pp. 110, 111*).
- [592] C. Ahn, A. Cavalleri, A. Georges, S. Ismail-Beigi, A. J. Millis, and J.-M. Triscone, “Designing and controlling the properties of transition metal oxide quantum materials”, *Nat. Mater.* **20**, 1462 (2021) (*cit. on p. 110*).
- [593] D. J. Singh, “Electronic structure of  $\text{NaCo}_2\text{O}_4$ ”, *Phys. Rev. B* **61**, 13397 (2000) (*cit. on p. 111*).
- [594] H. Sakurai, N. Tsujii, O. Suzuki, H. Kitazawa, G. Kido, K. Takada, T. Sasaki, and E. Takayama-Muromachi, “Valence and Na content dependences of superconductivity in  $\text{Na}_x\text{CoO}_2 \cdot y\text{H}_2\text{O}$ ”, *Phys. Rev. B* **74**, 092502 (2006), [arXiv:cond-mat/0511416](https://arxiv.org/abs/cond-mat/0511416) (*cit. on p. 112*).



- [595] M. L. Foo, Y. Wang, S. Watauchi, H. W. Zandbergen, T. He, R. J. Cava, and N. P. Ong, "Charge Ordering, Commensurability, and Metallicity in the Phase Diagram of the Layered  $\text{Na}_x\text{CoO}_2$ ", *Phys. Rev. Lett.* **92**, 247001 (2004), [arXiv:cond-mat/0312174](#) (cit. on p. 112).
- [596] H. Ohta, K. Yoshimura, Z. Hu, Y. Y. Chin, H.-J. Lin, H. H. Hsieh, C. T. Chen, and L. H. Tjeng, "Determination of the Co Valence in Bilayer Hydrated Superconducting  $\text{Na}_x\text{CoO}_2 \cdot y\text{H}_2\text{O}$  by Soft X-Ray Absorption Spectroscopy", *Phys. Rev. Lett.* **107**, 066404 (2011) (cit. on p. 112).
- [597] I. I. Mazin and M. D. Johannes, "A critical assessment of the superconducting pairing symmetry in  $\text{Na}_x\text{CoO}_2 \cdot y\text{H}_2\text{O}$ ", *Nat. Phys.* **1**, 91 (2005), [arXiv:cond-mat/0506536](#) (cit. on p. 112).
- [598] V. I. Anisimov, D. Bukhvalov, and T. M. Rice, "Electronic structure of possible nickelate analogs to the cuprates", *Phys. Rev. B* **59**, 7901 (1999) (cit. on p. 127).
- [599] J. Chaloupka and G. Khaliullin, "Orbital Order and Possible Superconductivity in  $\text{LaNiO}_3/\text{LaMO}_3$  Superlattices", *Phys. Rev. Lett.* **100**, 016404 (2008), [arXiv:1005.1464](#) (cit. on p. 127).
- [600] P. Hansmann, X. Yang, A. Toschi, G. Khaliullin, O. K. Andersen, and K. Held, "Turning a Nickelate Fermi Surface into a Cupratelike One through Heterostructuring", *Phys. Rev. Lett.* **103**, 016401 (2009), [arXiv:0807.0407](#) (cit. on p. 127).
- [601] A. S. Botana and M. R. Norman, "Similarities and Differences between  $\text{LaNiO}_2$  and  $\text{CaCuO}_2$  and Implications for Superconductivity", *Phys. Rev. X* **10**, 011024 (2020) (cit. on p. 127).
- [602] K. Held, L. Si, P. Worm, O. Janson, R. Arita, Z. Zhong, J. M. Tomczak, and M. Kitatani, "Phase Diagram of Nickelate Superconductors Calculated by Dynamical Vertex Approximation", *Front. Phys.* **9**, 810394 (2022), [arXiv:2201.01220](#) (cit. on pp. 127, 128).
- [603] S. Di Cataldo, P. Worm, J. M. Tomczak, L. Si, and K. Held, "Unconventional superconductivity without doping in infinite-layer nickelates under pressure", *Nat. Commun.* **15**, 3952 (2024) (cit. on p. 127).
- [604] Y. Nomura, M. Hirayama, T. Tadano, Y. Yoshimoto, K. Nakamura, and R. Arita, "Formation of a two-dimensional single-component correlated electron system and band engineering in the nickelate superconductor  $\text{NdNiO}_2$ ", *Phys. Rev. B* **100**, 205138 (2019), [arXiv:1909.03942](#) (cit. on pp. 127, 128).
- [605] D. Li, B. Y. Wang, K. Lee, S. P. Harvey, M. Osada, B. H. Goodge, L. F. Kourkoutis, and H. Y. Hwang, "Superconducting Dome in  $\text{Nd}_{1-x}\text{Sr}_x\text{NiO}_2$  Infinite Layer Films", *Phys. Rev. Lett.* **125**, 027001 (2020), [arXiv:2003.08506](#) (cit. on p. 128).
- [606] P. Worm et al., "Spin fluctuations sufficient to mediate superconductivity in nickelates", *Phys. Rev. B* **109**, 235126 (2024), [arXiv:2312.08260](#) (cit. on p. 128).

- [607] S. Di Cataldo, P. Worm, L. Si, and K. Held, “Absence of electron-phonon-mediated superconductivity in hydrogen-intercalated nickelates”, *Phys. Rev. B* **108**, 174512 (2023), [arXiv:2304.03599](#) (*cit. on p. 128*).
- [608] Q. N. Meier, J. B. de Vaulx, F. Bernardini, A. S. Botana, X. Blase, V. Olevano, and A. Cano, “Preempted phonon-mediated superconductivity in the infinite-layer nickelates”, *Phys. Rev. B* **109**, 184505 (2024), [arXiv:2309.05486](#) (*cit. on p. 128*).
- [609] P. Werner and S. Hoshino, “Nickelate superconductors: Multiorbital nature and spin freezing”, *Phys. Rev. B* **101**, 041104 (2020), [arXiv:1910.00473](#) (*cit. on p. 128*).
- [610] F. Lechermann, “Multiorbital Processes Rule the  $\text{Nd}_{1-x}\text{Sr}_x\text{NiO}_2$  Normal State”, *Phys. Rev. X* **10**, 041002 (2020), eprint: [2005.01166](#) (*cit. on p. 128*).
- [611] A. Kreisel, B. M. Andersen, A. T. Rømer, I. M. Eremin, and F. Lechermann, “Superconducting Instabilities in Strongly Correlated Infinite-Layer Nickelates”, *Phys. Rev. Lett.* **129**, 077002 (2022), [arXiv:2202.11135](#) (*cit. on p. 128*).
- [612] B. Kang, C. Melnick, P. Semon, S. Ryee, M. J. Han, G. Kotliar, and S. Choi, “Infinite-layer nickelates as Ni-eg Hund’s metals”, *npj Quantum Mater.* **8**, 35 (2023), [arXiv:2007.14610](#) (*cit. on p. 128*).
- [613] M. Kitatani, L. Si, P. Worm, J. M. Tomczak, R. Arita, and K. Held, “Optimizing Superconductivity: From Cuprates via Nickelates to Palladates”, *Phys. Rev. Lett.* **130**, 166002 (2023), [arXiv:2207.14038](#) (*cit. on p. 128*).
- [614] Y. Zhang et al., “High-temperature superconductivity with zero resistance and strange-metal behaviour in  $\text{La}_3\text{Ni}_2\text{O}_{7-\delta}$ ”, *Nat. Phys.* **20**, 1269 (2024), [arXiv:2307.14819](#) (*cit. on p. 129*).
- [615] L. Wang et al., “Structure Responsible for the Superconducting State in  $\text{La}_3\text{Ni}_2\text{O}_7$  at High-Pressure and Low-Temperature Conditions”, *JACS* **146**, 7506 (2024), [arXiv:2311.09186](#) (*cit. on p. 129*).
- [616] J. Li et al., “Pressure-driven right-triangle shape superconductivity in bilayer nickelate  $\text{La}_3\text{Ni}_2\text{O}_7$ ”, arXiv preprint (2024), [arXiv:2404.11369](#) (*cit. on p. 129*).
- [617] Q. Zhang, Y. Guan, Y. Cheng, L. Min, J. K. Keum, Z. Mao, and M. B. Stone, “Structure and lattice excitations of the copper substituted lead oxyapatite  $\text{Pb}_{9.06(7)}\text{Cu}_{0.94(6)}(\text{PO}_{3.92(4)})_6\text{O}_{0.96(3)}$ ”, *Phys. Rev. Materials* **8**, 014605 (2024), [arXiv:2401.08834](#) (*cit. on pp. 129, 190*).
- [618] Z. Liu et al., “Evidence for charge and spin density waves in single crystals of  $\text{La}_3\text{Ni}_2\text{O}_7$  and  $\text{La}_3\text{Ni}_2\text{O}_6$ ”, *Sci. China Phys., Mech. Astron.* **66**, 217411 (2022), [arXiv:2205.00950](#) (*cit. on p. 129*).
- [619] R. Khasanov, T. J. Hicken, D. J. Gawryluk, L. P. Sorel, S. Bötzel, F. Lechermann, I. M. Eremin, H. Luetkens, and Z. Guguchia, “Pressure-Induced Split of the Density Wave Transitions in  $\text{La}_3\text{Ni}_2\text{O}_{7-\delta}$ ”, arXiv preprint (2024), [arXiv:2402.10485](#) (*cit. on p. 129*).

- [620] K. Chen et al., “Evidence of Spin Density Waves in  $\text{La}_3\text{Ni}_2\text{O}_{7-\delta}$ ”, *Phys. Rev. Lett.* **132**, 256503 (2024), [arXiv:2311.15717](#) (cit. on p. 129).
- [621] Z. Dan, Y. Zhou, M. Huo, Y. Wang, L. Nie, M. Wang, T. Wu, and X. Chen, “Spin-density-wave transition in double-layer nickelate  $\text{La}_3\text{Ni}_2\text{O}_7$ ”, arXiv preprint (2024), [arXiv:2402.03952](#) (cit. on p. 129).
- [622] X. Chen et al., “Electronic and magnetic excitations in  $\text{La}_3\text{Ni}_2\text{O}_7$ ”, arXiv preprint (2024), [arXiv:2401.12657](#) (cit. on p. 129).
- [623] Y. Zhou et al., “Investigations of key issues on the reproducibility of high- $T_c$  superconductivity emerging from compressed  $\text{La}_3\text{Ni}_2\text{O}_7$ ”, arXiv preprint (2023), [arXiv:2311.12361](#) (cit. on p. 129).
- [624] P. Puphal et al., “Unconventional crystal structure of the high-pressure superconductor  $\text{La}_3\text{Ni}_2\text{O}_7$ ”, arXiv preprint (2023), [arXiv:2312.07341](#) (cit. on p. 129).
- [625] X. Chen et al., “Polymorphism in the Ruddlesden–Popper Nickelate  $\text{La}_3\text{Ni}_2\text{O}_7$ : Discovery of a Hidden Phase with Distinctive Layer Stacking”, *JACS* **146**, 3640 (2024), [arXiv:2312.06081](#) (cit. on p. 129).
- [626] N. Wang et al., “Bulk high-temperature superconductivity in the high-pressure tetragonal phase of bilayer  $\text{La}_2\text{PrNi}_2\text{O}_7$ ”, arXiv preprint (2024), [arXiv:2407.05681](#) (cit. on pp. 129, 130).
- [627] S. N. Abadi et al., “Electronic structure of the alternating monolayer-trilayer phase of  $\text{La}_3\text{Ni}_2\text{O}_7$ ”, arXiv preprint (2024), [arXiv:2402.07143](#) (cit. on p. 129).
- [628] H. Wang, L. Chen, A. Rutherford, H. Zhou, and W. Xie, “Long-Range Structural Order in a Hidden Phase of Ruddlesden–Popper Bilayer Nickelate  $\text{La}_3\text{Ni}_2\text{O}_7$ ”, *Inorg. Chem.* **63**, 5020 (2024), [arXiv:2312.09200](#) (cit. on p. 129).
- [629] M. Wang, H.-H. Wen, T. Wu, D.-X. Yao, and T. Xiang, “Normal and Superconducting Properties of  $\text{La}_3\text{Ni}_2\text{O}_7$ ”, *Chinese Phys. Lett.* **41**, 077402 (2024), [arXiv:2406.04837](#) (cit. on p. 130).
- [630] M. Rösner, C. Steinke, M. Lorke, C. Gies, F. Jahnke, and T. O. Wehling, “Two-Dimensional Heterojunctions from Nonlocal Manipulations of the Interactions”, *Nano Lett.* **16**, 2322 (2016) (cit. on p. 156).
- [631] A. Raja et al., “Coulomb engineering of the bandgap and excitons in two-dimensional materials”, *Nat. Commun.* **8**, 15251 (2017) (cit. on p. 156).
- [632] J. M. Pizarro, M. Rösner, R. Thomale, R. Valentí, and T. O. Wehling, “Internal screening and dielectric engineering in magic-angle twisted bilayer graphene”, *Phys. Rev. B* **100**, 161102 (2019), [arXiv:1904.11765](#) (cit. on p. 156).
- [633] P. Stepanov, I. Das, X. Lu, A. Fahimniya, K. Watanabe, T. Taniguchi, F. H. L. Koppens, J. Lischner, L. Levitov, and D. K. Efetov, “Untying the insulating and superconducting orders in magic-angle graphene”, *Nature* **583**, 375 (2020), [arXiv:1911.09198](#) (cit. on p. 156).
- [634] R. Bistritzer and A. H. MacDonald, “Moiré bands in twisted double-layer graphene”, *PNAS* **108**, 12233 (2011), [arXiv:1009.4203](#) (cit. on pp. 156, 158).

- [635] M. R. Koblischka and A. Koblischka-Veneva, “Review of Moiré superconductivity and application of the Roeser-Huber formula”, *Superconductivity* **9**, 100073 (2024) (*cit. on pp. 156, 158*).
- [636] Z.-D. Song and B. A. Bernevig, “Magic-Angle Twisted Bilayer Graphene as a Topological Heavy Fermion Problem”, *Phys. Rev. Lett.* **129**, 047601 (2022), [arXiv:2111.05865](#) (*cit. on p. 158*).
- [637] A. Datta, M. J. Calderón, A. Camjayi, and E. Bascones, “Heavy quasiparticles and cascades without symmetry breaking in twisted bilayer graphene”, *Nat. Commun.* **14**, 5036 (2023), [arXiv:2301.13024](#) (*cit. on p. 158*).
- [638] G. Rai, L. Crippa, D. Călugăru, H. Hu, L. de’Medici, A. Georges, B. A. Bernevig, R. Valentí, G. Sangiovanni, and T. Wehling, “Dynamical correlations and order in magic-angle twisted bilayer graphene”, arXiv preprint (2023), [arXiv:2309.08529](#) (*cit. on p. 158*).
- [639] P. A. Pantaleón, A. Jimeno-Pozo, H. Sainz-Cruz, V. T. Phong, T. Cea, and F. Guinea, “Superconductivity and correlated phases in non-twisted bilayer and trilayer graphene”, *Nat. Rev. Phys.* **5**, 304 (2023), [arXiv:2211.02880](#) (*cit. on pp. 158, 211*).
- [640] J. M. Pizarro, S. Adler, K. Zantout, T. Mertz, P. Barone, R. Valentí, G. Sangiovanni, and T. O. Wehling, “Deconfinement of Mott localized electrons into topological and spin-orbit-coupled Dirac fermions”, *npj Quantum Mater.* **5**, 79 (2020), [arXiv:2001.04102](#) (*cit. on p. 158*).
- [641] L. Crippa, H. Bae, P. Wunderlich, I. I. Mazin, B. Yan, G. Sangiovanni, T. Wehling, and R. Valentí, “Heavy fermions vs doped mott physics in heterogeneous ta-dichalcogenide bilayers”, *Nat. Commun.* **15**, 1357 (2024), [arXiv:2302.14072](#) (*cit. on p. 158*).
- [642] C. N. Lau, M. W. Bockrath, K. F. Mak, and F. Zhang, “Reproducibility in the fabrication and physics of moiré materials”, *Nature* **602**, 41 (2022) (*cit. on p. 159*).
- [643] T. Devakul, V. Crépel, Y. Zhang, and L. Fu, “Magic in twisted transition metal dichalcogenide bilayers”, *Nat. Commun.* **12**, 6730 (2021), [arXiv:2106.11954](#) (*cit. on p. 159*).
- [644] F. Wu, T. Lovorn, E. Tutuc, and A. H. MacDonald, “Hubbard Model Physics in Transition Metal Dichalcogenide Moiré Bands”, *Phys. Rev. Lett.* **121**, 026402 (2018), [arXiv:1804.03151](#) (*cit. on p. 159*).
- [645] J. Zang, J. Wang, J. Cano, A. Georges, and A. J. Millis, “Dynamical Mean-Field Theory of Moiré Bilayer Transition Metal Dichalcogenides: Phase Diagram, Resistivity, and Quantum Criticality”, *Phys. Rev. X* **12**, 021064 (2022), [arXiv:2112.03080](#) (*cit. on p. 159*).
- [646] P. Tschepp et al., “Magnetism and metallicity in moiré transition metal dichalcogenides”, *PNAS* **121**, e2311486121 (2024), [arXiv:2303.13578](#) (*cit. on p. 159*).

- [647] M. Angeli and A. H. MacDonald, “T valley transition metal dichalcogenide moiré bands”, *PNAS* **118**, e2021826118 (2021), [arXiv:2008.01735](#) (*cit. on p. 159*).
- [648] K. Kuroki and R. Arita, “Spin-triplet superconductivity in repulsive Hubbard models with disconnected Fermi surfaces: A case study on triangular and honeycomb lattices”, *Phys. Rev. B* **63**, 174507 (2001), [arXiv:cond-mat/0004381](#) (*cit. on p. 160*).
- [649] K. Kuroki, “Spin-fluctuation-mediated  $d + id'$  pairing mechanism in doped  $\beta$ -MnCl(M=Hf,Zr) superconductors”, *Phys. Rev. B* **81**, 104502 (2010) (*cit. on p. 160*).
- [650] N. Kaushal and E. Dagotto, “Moiré Kanamori-Hubbard model for transition metal dichalcogenide homobilayers”, *Phys. Rev. B* **107**, l201118 (2023), [arXiv:2303.02305](#) (*cit. on p. 160*).
- [651] R. G. Sharma, “Practical Cuprate Superconductors”, in *Springer series in materials science* (Springer International Publishing, 2021), pp. 227–275 (*cit. on p. 189*).
- [652] V. L. Ginzburg, “What problems of physics and astrophysics seem now to be especially important and interesting (thirty years later, already on the verge of XXI century)?”, *Phys. Usp.* **42**, 353 (1999) (*cit. on p. 189*).
- [653] K. Dolui, L. J. Conway, C. Heil, T. A. Strobel, R. P. Prasankumar, and C. J. Pickard, “Feasible Route to High-Temperature Ambient-Pressure Hydride Superconductivity”, *Phys. Rev. Lett.* **132**, 166001 (2024), [arXiv:2310.07562](#) (*cit. on p. 189*).
- [654] E. Snider, N. Dasenbrock-Gammon, R. McBride, M. Debessai, H. Vindana, K. Venkatasamy, K. V. Lawler, A. Salamat, and R. P. Dias, “RETRACTED ARTICLE: Room-temperature superconductivity in a carbonaceous sulfur hydride”, *Nature* **586**, 373 (2020) (*cit. on p. 190*).
- [655] N. Dasenbrock-Gammon et al., “RETRACTED ARTICLE: Evidence of near-ambient superconductivity in a N-doped lutetium hydride”, *Nature* **615**, 244 (2023) (*cit. on p. 190*).
- [656] D. v. d. Marel and J. E. Hirsch, “Room-temperature superconductivity — or not? Comment on *nature* 586, 373 (2020) by E. Snider et al.”, *Int. J. Mod. Phys. B* **37**, 2375001 (2022), [arXiv:2201.07686](#) (*cit. on p. 190*).
- [657] A. V. Sadakov, O. A. Sobolevsky, and V. M. Pudalov, “What led to retraction of the article on room-temperature superconductivity in the journal *nature*: a series of oversights or falsification?”, *Phys. Usp.* **65**, 1313 (2022) (*cit. on p. 190*).
- [658] X. Ming et al., “Absence of near-ambient superconductivity in  $\text{LuH}_{2\pm x}\text{N}_y$ ”, *Nature* **620**, 72 (2023), [arXiv:2303.08759](#) (*cit. on p. 190*).
- [659] D. Garisto, “Superconductivity scandal: the inside story of deception in a rising star’s physics lab”, *Nature*, **10**. 1038/d41586-024-00716-2 (2024) (*cit. on p. 190*).

- [660] S. Lee, J. Kim, S. Im, S. An, Y.-W. Kwon, and K. H. Auh, "Consideration for the development of room-temperature ambient-pressure superconductor (LK-99)", *J. Korean Cryst. Growth Cryst. Technol.* **33**, 61 (2023) (*cit. on p. 190*).
- [661] S. Lee, J.-H. Kim, and Y.-W. Kwon, "The First Room-Temperature Ambient-Pressure Superconductor", arXiv preprint (2023), [arXiv:2307.12008](https://arxiv.org/abs/2307.12008) (*cit. on p. 190*).
- [662] S. Lee, J. Kim, H.-T. Kim, S. Im, S. An, and K. H. Auh, "Superconductor  $\text{Pb}_{10-x}\text{Cu}_x(\text{PO}_4)_6\text{O}$  showing levitation at room temperature and atmospheric pressure and mechanism", arXiv preprint (2023), [arXiv:2307.12037](https://arxiv.org/abs/2307.12037) (*cit. on p. 190*).
- [663] K. Kumar, N. K. Karn, and V. P. S. Awana, "Synthesis of possible room temperature superconductor LK-99:  $\text{Pb}_9\text{Cu}(\text{PO}_4)_6\text{O}$ ", *Supercond. Sci. Technol.* **36**, 10LT02 (2023), [arXiv:2307.16402](https://arxiv.org/abs/2307.16402) (*cit. on p. 190*).
- [664] L. Liu, Z. Meng, X. Wang, H. Chen, Z. Duan, X. Zhou, H. Yan, P. Qin, and Z. Liu, "Semiconducting Transport in  $\text{Pb}_{10-x}\text{Cu}_x(\text{PO}_4)_6\text{O}$  Sintered from  $\text{Pb}_2\text{SO}_5$  and  $\text{Cu}_3\text{P}$ ", *Adv. Funct. Mater.* **33**, 2308938 (2023), [arXiv:2307.16802](https://arxiv.org/abs/2307.16802) (*cit. on p. 190*).
- [665] Q. Hou, W. Wei, X. Zhou, X. Wang, T. Wang, Y. Sun, and Z. Shi, "Synthesis, transport and magnetic properties of Cu-doped apatite  $\text{Pb}_{10-x}\text{Cu}_x(\text{PO}_4)_6\text{O}$ ", *Matter* **6**, 4408 (2023), [arXiv:2308.01192](https://arxiv.org/abs/2308.01192) (*cit. on p. 190*).
- [666] H. Wu, L. Yang, B. Xiao, and H. Chang, "Successful growth and room temperature ambient-pressure magnetic levitation of LK-99", arXiv preprint (2023), [arXiv:2308.01516](https://arxiv.org/abs/2308.01516) (*cit. on p. 190*).
- [667] K. Guo, Y. Li, and S. Jia, "Ferromagnetic half levitation of LK-99-like synthetic samples", *Sci. China Phys., Mech. Astron.* **66**, 107411 (2023), [arXiv:2308.03110](https://arxiv.org/abs/2308.03110) (*cit. on p. 190*).
- [668] S. Zhu, W. Wu, Z. Li, and J. Luo, "First-order transition in LK-99 containing  $\text{Cu}_2\text{S}$ ", *Matter* **6**, 4401 (2023), [arXiv:2308.04353](https://arxiv.org/abs/2308.04353) (*cit. on p. 190*).
- [669] G. S. Thakur, M. Schulze, and M. Ruck, "On the synthesis methodologies to prepare ' $\text{Pb}_9\text{Cu}(\text{PO}_4)_6\text{O}$ ': phase, composition, magnetic analysis and absence of superconductivity", *Supercond. Sci. Technol.* **37**, 015013 (2023), [arXiv:2308.05776](https://arxiv.org/abs/2308.05776) (*cit. on p. 190*).
- [670] C. Liu et al., "Phases and magnetism at microscale in compounds containing nominal  $\text{Pb}_{10-x}\text{Cu}_x(\text{PO}_4)_6\text{O}$ ", *Phys. Rev. Materials* **7**, 084804 (2023), [arXiv:2308.07800](https://arxiv.org/abs/2308.07800) (*cit. on p. 190*).
- [671] K. Kumar, N. Kumar Karn, Y. Kumar, and V. P. S. Awana, "Absence of Superconductivity in LK-99 at Ambient Conditions", *ACS Omega* **8**, 41737 (2023), [arXiv:2308.03544](https://arxiv.org/abs/2308.03544) (*cit. on p. 190*).
- [672] Y. Jiang et al., " $\text{Pb}_9\text{Cu}(\text{PO}_4)_6(\text{OH})_2$ : Phonon bands, localized flat-band magnetism, models, and chemical analysis", *Phys. Rev. B* **108**, 235127 (2023), [arXiv:2308.05143](https://arxiv.org/abs/2308.05143) (*cit. on p. 190*).

- [673] P. Puphal, M. Y. P. Akbar, M. Hepting, E. Goering, M. Isobe, A. A. Nugroho, and B. Keimer, "Single crystal synthesis, structure, and magnetism of  $\text{Pb}_{10-x}\text{Cu}_x(\text{PO}_4)_6\text{O}$ ", *APL Mater.* **11**, 101128 (2023), [arXiv:2308.06256](#) (cit. on pp. 190, 191).
- [674] Z. Lei, C.-W. Lin, I.-N. Chen, C.-T. Chou, Y.-L. Lin, J.-H. Chen, H.-H. Sung, and L.-M. Wang, "The characteristics of Cu-doped lead apatite (LK-99) synthesized with the removal of  $\text{Cu}_2\text{S}$  using ammonia solution: A diamagnetic semiconductor", *APL Mater.* **12**, 021104 (2024), [arXiv:2309.17445](#) (cit. on p. 190).
- [675] M. Singh, P. Saha, K. Kumar, D. Takhar, B. Birajdar, V. P. S. Awana, and S. Patnaik, "Electromagnetic properties of copper doped lead apatite  $\text{Pb}_{10-x}\text{Cu}_x(\text{PO}_4)_6\text{O}$ ", *J. Mater. Sci.* **59**, 1464 (2024), [arXiv:2310.11051](#) (cit. on p. 190).
- [676] T. Habamahoro, T. Bontke, M. Chirom, Z. Wu, J. M. Bao, L. Z. Deng, and C. W. Chu, "Replication and study of anomalies in LK-99 — the alleged ambient-pressure, room-temperature superconductor", *Supercond. Sci. Technol.* **37**, 045004 (2024), [arXiv:2311.03558](#) (cit. on p. 190).
- [677] H. Chen, X. Zhou, Z. Meng, X. Wang, Z. Duan, L. Liu, G. Zhao, H. Yan, P. Qin, and Z. Liu, "Magnetic-Field Response and Giant Electric-Field Modulation of  $\text{Cu}_2\text{S}$ ", *Nano Lett.* **24**, 584 (2024) (cit. on p. 190).
- [678] P. Wang, X. Liu, J. Ge, C. Ji, H. Ji, Y. Liu, Y. Ai, G. Ma, S. Qi, and J. Wang, "Ferromagnetic and insulating behavior in both half magnetic levitation and non-levitation LK-99 like samples", *Quantum Front.* **2**, 10 (2023), [arXiv:2308.11768](#) (cit. on p. 190).
- [679] J. Cabezas-Escases, N. F. Barrera, R. H. Lavroff, A. N. Alexandrova, C. Cardenas, and F. Munoz, "Electronic structure and vibrational stability of copper-substituted lead apatite LK-99", *Phys. Rev. B* **109**, 144515 (2024), [arXiv:2308.01135](#) (cit. on p. 190).
- [680] S. V. Krivovichev and G. Engel, "The Crystal Structure of  $\text{Pb}_{10}(\text{PO}_4)_6\text{O}$  Revisited: The Evidence of Superstructure", *Crystals* **13**, 1371 (2023), [arXiv:2308.04915](#) (cit. on p. 190).
- [681] J. Shen et al., "Phase Stability of Lead Phosphate Apatite  $\text{Pb}_{10-x}\text{Cu}_x(\text{PO}_4)_6\text{O}$ ,  $\text{Pb}_{10-x}\text{Cu}_x(\text{PO}_4)_6(\text{OH})_2$  ( $x = 0, 1$ ), and  $\text{Pb}_8\text{Cu}_2(\text{PO}_4)_6$ ", *Chem. Mater.* **36**, 275 (2023), [arXiv:2308.07941](#) (cit. on p. 190).
- [682] J. Liu, T. Yu, J. Li, J. Wang, J. Lai, Y. Sun, X.-Q. Chen, and P. Liu, "Symmetry breaking induced insulating electronic state in  $\text{Pb}_9\text{Cu}(\text{PO}_4)_6\text{O}$ ", *Phys. Rev. B* **108**, 1161101 (2023), [arXiv:2308.11766](#) (cit. on p. 190).
- [683] K. Ogawa, K. Tolborg, and A. Walsh, "Models of Oxygen Occupancy in Lead Phosphate Apatite  $\text{Pb}_{10}(\text{PO}_4)_6\text{O}$ ", *ACS Energy Lett.* **8**, 3941 (2023) (cit. on p. 190).
- [684] S.-W. Kim, K. Wang, S. Chen, L. J. Conway, G. L. Pascut, I. Errea, C. J. Pickard, and B. Monserrat, "On the dynamical stability of copper-doped lead apatite", *npj Comput. Mater.* **10**, 16 (2024), [arXiv:2309.11541](#) (cit. on p. 190).

- [685] P. K. Jain, “Superionic Phase Transition of Copper(I) Sulfide and Its Implication for Purported Superconductivity of LK-99”, *J. Phys. Chem. C* **127**, 18253 (2023), [arXiv:2308.05222](#) (*cit. on p. 190*).
- [686] P. K. Jain, “Solving the LK-99 puzzle”, *Matter* **6**, 4118 (2023) (*cit. on p. 190*).
- [687] O. Tavakol and T. Scaffidi, “Minimal model for the flat bands in copper-substituted lead phosphate apatite: Strong diamagnetism from multiorbital physics”, *Phys. Rev. B* **109**, 1100504 (2024), [arXiv:2308.01315](#) (*cit. on p. 190*).
- [688] J. Lai, J. Li, P. Liu, Y. Sun, and X.-Q. Chen, “First-principles study on the electronic structure of  $\text{Pb}_{10-x}\text{Cu}_x(\text{PO}_4)_6\text{O}$  ( $x = 0, 1$ )”, *J. Mater. Sci. Technol.* **171**, 66 (2024), [arXiv:2307.16040](#) (*cit. on p. 190*).
- [689] S. M. Griffin, “Origin of correlated isolated flat bands in copper-substituted lead phosphate apatite”, arXiv preprint (2023), [arXiv:2307.16892](#) (*cit. on p. 190*).
- [690] L. Si and K. Held, “Electronic structure of the putative room-temperature superconductor  $\text{Pb}_9\text{Cu}(\text{PO}_4)_6\text{O}$ ”, *Phys. Rev. B* **108**, L121110 (2023) (*cit. on p. 190*).
- [691] H. Bai, J. Ye, L. Gao, C. Zeng, and W. Liu, “Semiconductivity induced by spin-orbit coupling in  $\text{Pb}_9\text{Cu}(\text{PO}_4)_6\text{O}$ ”, *Sci. Rep.* **13**, 21085 (2023) (*cit. on p. 190*).
- [692] L. Celiberti, L. Varrassi, and C. Franchini, “ $\text{Pb}_9\text{Cu}(\text{PO}_4)_6\text{O}$  is a charge-transfer semiconductor”, *Phys. Rev. B* **108**, 1201117 (2023), [arXiv:2310.00006](#) (*cit. on p. 190*).
- [693] D. M. Korotin, D. Y. Novoselov, A. O. Shorikov, V. I. Anisimov, and A. R. Oganov, “Electronic correlations in the ultranarrow energy band compound  $\text{Pb}_9\text{Cu}(\text{PO}_4)_6\text{O}$ : A DFT+DMFT study”, *Phys. Rev. B* **108**, 1241111 (2023), [arXiv:2308.04301](#) (*cit. on p. 190*).
- [694] L. Si, M. Wallerberger, A. Smolyanyuk, S. di Cataldo, J. M. Tomczak, and K. Held, “ $\text{Pb}_{10-x}\text{Cu}_x(\text{PO}_4)_6\text{O}$ : a Mott or charge transfer insulator in need of further doping for (super)conductivity”, *J. Phys. Condens. Matter* **36**, 065601 (2023), [arXiv:2308.04427](#) (*cit. on pp. 190, 191*).
- [695] C. Yue, V. Christiansson, and P. Werner, “Correlated electronic structure of  $\text{Pb}_{10-x}\text{Cu}_x(\text{PO}_4)_6\text{O}$ ”, *Phys. Rev. B* **108**, 1201122 (2023), [arXiv:2308.04976](#) (*cit. on pp. 190, 191*).
- [696] M. M. Hirschmann and J. Mitscherling, “Symmetry-enforced double Weyl points, multiband quantum geometry, and singular flat bands of doping-induced states at the Fermi level”, *Phys. Rev. Materials* **8**, 014201 (2024), [arXiv:2308.03751](#) (*cit. on p. 191*).
- [697] M. Braß, L. Si, and K. Held, “Weyl points and spin-orbit coupling in copper-substituted lead phosphate apatite”, *Phys. Rev. B* **109**, 085103 (2024), [arXiv:2310.09310](#) (*cit. on p. 191*).



- [698] C.-K. Chiu, J. C. Y. Teo, A. P. Schnyder, and S. Ryu, "Classification of topological quantum matter with symmetries", *Rev. Mod. Phys.* **88**, 035005 (2016), [arXiv:1505.03535](#) (cit. on p. 191).
- [699] M. Shimizu, J. Otsuki, and H. O. Jeschke, "Magnetic fluctuations in  $\text{Pb}_9\text{Cu}(\text{PO}_4)_6\text{O}$ ", *Phys. Rev. B* **108**, 1201105 (2023), [arXiv:2308.13557](#) (cit. on p. 191).
- [700] Q. Chen, Z. Wang, R. Boyack, S. Yang, and K. Levin, "When superconductivity crosses over: From BCS to BEC", *Rev. Mod. Phys.* **96**, 025002 (2024), [arXiv:2208.01774](#) (cit. on pp. 208, 212, 213).
- [701] Y. J. Uemura et al., "Universal Correlations between  $T_c$  and  $n_s/m^*$  (Carrier Density over Effective Mass) in High- $T_c$  Cuprate Superconductors", *Phys. Rev. Lett.* **62**, 2317 (1989) (cit. on pp. 208, 210).
- [702] Y. J. Uemura et al., "Basic similarities among cuprate, bismuthate, organic, chevreel-phase, and heavy-fermion superconductors shown by penetration-depth measurements", *Phys. Rev. Lett.* **66**, 2665 (1991) (cit. on pp. 208, 210, 211).
- [703] Y. J. Uemura, "Condensation, excitation, pairing, and superfluid density in high- $T_c$  superconductors: the magnetic resonance mode as a roton analogue and a possible spin-mediated pairing", *J. Phys. Condens. Matter* **16**, S4515 (2004), [arXiv:cond-mat/0406301](#) (cit. on pp. 208, 210, 258).
- [704] L. Sobirey, H. Biss, N. Luick, M. Bohlen, H. Moritz, and T. Lompe, "Observing the Influence of Reduced Dimensionality on Fermionic Superfluids", *Phys. Rev. Lett.* **129**, 083601 (2022) (cit. on p. 210).
- [705] Y. Yu, L. Ma, P. Cai, R. Zhong, C. Ye, J. Shen, G. D. Gu, X. H. Chen, and Y. Zhang, "High-temperature superconductivity in monolayer  $\text{Bi}_2\text{Sr}_2\text{CaCu}_2\text{O}_{8+\delta}$ ", *Nature* **575**, 156 (2019) (cit. on p. 210).
- [706] Y. J. Uemura et al., "Magnetic-field penetration depth in  $\text{K}_3\text{C}_{60}$  measured by muon spin relaxation", *Nature* **352**, 605 (1991) (cit. on pp. 210, 211).
- [707] Y. J. Uemura, L. P. Le, and G. M. Luke, "Muon spin relaxation studies in organic superconductors and organic magnets", *Synthetic Met.* **56**, 2845 (1993) (cit. on pp. 210, 211).
- [708] Y. Nakagawa, Y. Kasahara, T. Nomoto, R. Arita, T. Nojima, and Y. Iwasa, "Gate-controlled BCS-BEC crossover in a two-dimensional superconductor", *Science* **372**, 190 (2021), [arXiv:2012.05707](#) (cit. on pp. 211, 212, 314).
- [709] J. Sous, Y. He, and S. A. Kivelson, "Absence of a BCS-BEC crossover in the cuprate superconductors", *npj Quantum Mater.* **8**, 25 (2023), [arXiv:2210.13478](#) (cit. on pp. 212, 258).
- [710] Q. Chen, Z. Wang, R. Boyack, and K. Levin, "Test for BCS-BEC crossover in the cuprate superconductors", *npj Quantum Mater.* **9**, 27 (2024), [arXiv:2307.08611](#) (cit. on pp. 212, 258).

- [711] M. Keller, W. Metzner, and U. Schollwöck, “Dynamical Mean-Field Theory for Pairing and Spin Gap in the Attractive Hubbard Model”, *Phys. Rev. Lett.* **86**, 4612 (2001) (*cit. on pp. 213, 214*).
- [712] B. Kyung, A. Georges, and A.-M. S. Tremblay, “Potential-energy-driven (BCS) to kinetic-energy-driven (BEC) pairing in the two-dimensional attractive Hubbard model: Cellular dynamical mean-field theory”, *Phys. Rev. B* **74**, 024501 (2006), [arXiv:cond-mat/0508645](https://arxiv.org/abs/cond-mat/0508645) (*cit. on pp. 213, 214*).
- [713] O. Gunnarsson, “Superconductivity in fullerenes”, *Rev. Mod. Phys.* **69**, 575 (1997) (*cit. on p. 215*).
- [714] K. Momma and F. Izumi, “Vesta 3 for three-dimensional visualization of crystal, volumetric and morphology data”, *J. Appl. Crystallogr.* **44**, 1272 (2011) (*cit. on p. 215*).
- [715] T. F. T. Cerqueira, Y.-W. Fang, I. Errea, A. Sanna, and M. A. L. Marques, “Searching Materials Space for Hydride Superconductors at Ambient Pressure”, *Adv. Funct. Mater.*, 2404043 (2024), [arXiv:2403.13496](https://arxiv.org/abs/2403.13496) (*cit. on p. 258*).
- [716] J. P. Ellis, “TikZ Feynman: Feynman diagrams with TikZ”, *Comput. Phys. Commun.* **210**, 103 (2017), [arXiv:1601.05437](https://arxiv.org/abs/1601.05437) (*cit. on p. 314*).

# Acknowledgments

Doing science is a collaborative endeavor that thrives on the exchange of ideas and support from others; it is nearly impossible to perform in isolation. I have had the pleasure of meeting many talented individuals whose thoughts, inspirations, and encouragement have helped me throughout my doctorate. This support has been especially invaluable through the challenges of moving the work space during a global pandemic, remote work, and the subsequent readjustment to in-person meetings. I am deeply grateful to all who have contributed to my academic and personal growth.

First and foremost, I am indebted to my supervisor Tim Wehling who has taught me many invaluable lessons about the mindset of a physicist. Tim's intuition for interesting physical problems is inspiring and motivating to formulate and pursue my own research questions. It has been many years since I joined the group as a student and Tim's mentorship has undoubtedly made me a better scientist.

I am also grateful to Georg Rohringer for taking on my co-supervision after my change to Hamburg. I enjoyed the few but very enriching discussions that we had throughout our joint time in Hamburg.

I want to thank Yusuke Nomura for acting as the second referee of my thesis and for the scientific exchange. I thoroughly enjoyed our discussions, either online or during our in-person meetings in Japan, and I am looking forward to future collaborations.

On the same note, I would like to express my appreciation to Alexander Lichtenstein, Henning Moritz, and Michael Potthoff for partaking in the examination committee.

I sincerely thank Ryotaro Arita for his hospitality during my visit(s) to Japan and his additional mentorship. I really enjoyed (my second time) visiting the group and meeting new and familiar faces again. I am grateful for the opportunities to visit RIKEN and participate in a fully Japanese conference, a truly unique experience.

In addition, I would like to express my gratitude to Giorgio Sangiovanni, Hiroshi Shinaoka, Alessandro Toschi, and Philipp Werner for hosting me during various research visits.

During my time as a graduate student, I had the opportunity to meet many remarkable scientists. I do not have the space to acknowledge them all, but I want to thank the members of the QUASt research unit, FOR 5242 research unit, and CUI:AIM excellence cluster for valuable exchange. I particularly value the

numerous fruitful discussions I had with fellow (former) graduate students Joseph Adelina, Severino Adler, Viktor Christiansson, Maria-Elisabeth Federl, Max Fischer, Felix Gerken, Ioannis Ioannidis, Ming-Chun (Jimmy) Jiang, Fabian Künzel, Hibiki Matsunaga, Michael Meixner, Eva Paprotzki, Matthias Reitner, Emanuele Rossi, Yu Tonghua, Francesco Valiera, Matteo Vandelli, Giovanni de Vecchi, Yann in't Veld, Niklas Wagner, Tianchung Wang, and Paul Worm from all around the world.

I really enjoyed my time in the group and thank everyone for the great working environment, motivational upkeep, and insightful discussions – during our forced time at home, in the office, and on occasional times outside. So, thank you all, Jan Berges, Lara Bremer, Sergey Brener, Edin Kapetanovic, Lennart Klebl, Erik van Loon, Roberto Mozara, Laura Pätzold, José (Chema) Pizarro, Gautam Rai, Siheon Ryee, Arne Schobert, Malte Schüler, Tjark Sievert, and Michael Winter. However, this thanks goes also to the whole institute(s) who contribute to the general engaging atmosphere. On this note, I would also like to express my gratitude for the support by the non-academic staff in Bremen through Sarah Farley, Klaus Bowe, and Beuthner Andreas; as well as in Hamburg by Anna Zharinova and the whole Physnet team!

Special thanks go to Laura, Gautam, Erik, Siheon, Michael, Lennart, my brother Tobias, and my girlfriend Katharina for proof reading parts of my thesis and providing useful feedback.

At the end, I would like to thank my family for their continuing support and motivation. Especially, I want to thank my girlfriend Katharina for her patience, endurance, and love over the past years. I am indebted for your insights on good and clear visual design and for helping me out with some of the illustrations presented in this thesis. Your encouragement and motivation helped me to not lose sanity through times of hard work and you helped me to relax when necessary.

I would like to express my gratitude to Prof. Yoshihiro Iwasa and Dr. Yuji Nakagawa for providing me the data of the Uemura plot from Ref. [708], which is adapted in Fig. 6.1 of this thesis.

I gratefully acknowledge funding by the Cluster of Excellence ‘CUI: Advanced Imaging of Matter’ of the Deutsche Forschungsgemeinschaft (DFG) (EXC 2056, Project ID 390715994), and additional support by DFG research units FOR 5249 (‘QUAST’, Project No. 449872909) and FOR 5242 (WE 5342/7-1, Project No. 449119662).

Feynman diagrams in this thesis have been generated using “TikZ Feynman” [716]. The large language model UHHGPT, as provided by the Universität Hamburg, has been used to improve clarity and coherence of the text in parts of this thesis.

## **Eidesstattliche Versicherung**

Hiermit versichere ich an Eides statt, die vorliegende Dissertationsschrift selbst verfasst und keine anderen als die angegebenen Hilfsmittel und Quellen benutzt zu haben. Sofern im Zuge der Erstellung der vorliegenden Dissertationsschrift generative Künstliche Intelligenz (gKI) basierte elektronische Hilfsmittel verwendet wurden, versichere ich, dass meine eigene Leistung im Vordergrund stand und dass eine vollständige Dokumentation aller verwendeten Hilfsmittel gemäß der Guten wissenschaftlichen Praxis vorliegt. Ich trage die Verantwortung für eventuell durch die gKI generierte fehlerhafte oder verzerrte Inhalte, fehlerhafte Referenzen, Verstöße gegen das Datenschutz- und Urheberrecht oder Plagiate.

## **Declaration of oath\***

I hereby declare in lieu of oath that I have written the present dissertation independently and without illegitimate assistance from third parties. If electronic tools based on generative Artificial Intelligence (gAI) were used in the course of creating the present dissertation, I assure that my own contribution is the focus and that a complete documentation of all used tools is available in accordance with Good Scientific Practice. I bear the responsibility for any incorrect or distorted content generated by the gAI, incorrect references, infringements of data protection and copyright law, or plagiarism.

*\*Only the German text shall be legally binding and prevail.*

Hamburg, den \_\_\_\_\_

\_\_\_\_\_  
Niklas Witt